

Structure and Bonding 183
Series Editor: D. Michael P. Mingos

Virginia Martínez-Martínez
Fernando López Arbeloa *Editors*

Dyes and Photoactive Molecules in Microporous Systems

 Springer

183

Structure and Bonding

Series Editor:

D. Michael P. Mingos, Oxford, UK

Editorial Board Members:

Christine Cardin, Reading, UK

Xue Duan, Beijing, China

Lutz H. Gade, Heidelberg, Germany

Luis Gómez-Hortigüela Sainz, Madrid, Spain

Yi Lu, Urbana, IL, USA

Stuart A. Macgregor, Edinburgh, UK

Joaquin Perez Pariente, Madrid, Spain

Sven Schneider, Göttingen, Germany

Dietmar Stalke, Göttingen, Germany

Aims and Scope

Structure and Bonding is a publication which uniquely bridges the journal and book format. Organized into topical volumes, the series publishes in depth and critical reviews on all topics concerning structure and bonding. With over 50 years of history, the series has developed from covering theoretical methods for simple molecules to more complex systems.

Topics addressed in the series now include the design and engineering of molecular solids such as molecular machines, surfaces, two dimensional materials, metal clusters and supramolecular species based either on complementary hydrogen bonding networks or metal coordination centers in metal-organic framework materials (MOFs). Also of interest is the study of reaction coordinates of organometallic transformations and catalytic processes, and the electronic properties of metal ions involved in important biochemical enzymatic reactions.

Volumes on physical and spectroscopic techniques used to provide insights into structural and bonding problems, as well as experimental studies associated with the development of bonding models, reactivity pathways and rates of chemical processes are also relevant for the series.

Structure and Bonding is able to contribute to the challenges of communicating the enormous amount of data now produced in contemporary research by producing volumes which summarize important developments in selected areas of current interest and provide the conceptual framework necessary to use and interpret mega-databases.

We welcome proposals for volumes in the series within the scope mentioned above. Structure and Bonding offers our authors and readers:

- OnlineFirst publication. Each chapter is published online as it is finished, ahead of the print volume
- Wide dissemination. The chapters and the volume will be available on our platform SpringerLink, one of the largest collections of scholarly content in the world. SpringerLink attracts more than 50 million users at 15.000 institutions worldwide.
- Easy manuscript preparation. Authors do not have to spend their valuable time on the layout of their contribution. Springer will take care of all the layout related issues and will provide support throughout the complete process.

More information about this series at <http://www.springer.com/series/430>

Virginia Martínez-Martínez •
Fernando López Arbeloa
Editors

Dyes and Photoactive Molecules in Microporous Systems

With contributions by

A. A. Alanazi · J. Bujdák · G. Calzaferri ·
E. Coutino-Gonzalez · J. Ferrera-González ·
M. González-Béjar · J. Hofkens · Y. Ishida · R. W. Larsen ·
J. M. Mayers · C. R. McKeithan · A. Natarajan ·
M. Ogawa · J.-M. Oh · M. Pattabiraman · J. Pérez-Prieto ·
M. Roeffaers · U. Ruschewitz · H. A. Schwartz · S. Takagi ·
L. Wojtas · T. Yamaguchi

 Springer

Editors

Virginia Martínez-Martínez
Department of Physical Chemistry
University of the Basque Country
UPV/EHU
Bilbao, Vizcaya, Spain

Fernando López Arbeloa
Department of Physical Chemistry
University of the Basque Country
UPV/EHU
Bilbao, Vizcaya, Spain

ISSN 0081-5993

Structure and Bonding

ISBN 978-3-030-56633-3

<https://doi.org/10.1007/978-3-030-56634-0>

ISSN 1616-8550 (electronic)

ISBN 978-3-030-56634-0 (eBook)

© Springer Nature Switzerland AG 2020

This work is subject to copyright. All rights are reserved by the Publisher, whether the whole or part of the material is concerned, specifically the rights of translation, reprinting, reuse of illustrations, recitation, broadcasting, reproduction on microfilms or in any other physical way, and transmission or information storage and retrieval, electronic adaptation, computer software, or by similar or dissimilar methodology now known or hereafter developed.

The use of general descriptive names, registered names, trademarks, service marks, etc. in this publication does not imply, even in the absence of a specific statement, that such names are exempt from the relevant protective laws and regulations and therefore free for general use.

The publisher, the authors, and the editors are safe to assume that the advice and information in this book are believed to be true and accurate at the date of publication. Neither the publisher nor the authors or the editors give a warranty, expressed or implied, with respect to the material contained herein or for any errors or omissions that may have been made. The publisher remains neutral with regard to jurisdictional claims in published maps and institutional affiliations.

This Springer imprint is published by the registered company Springer Nature Switzerland AG.
The registered company address is: Gewerbestrasse 11, 6330 Cham, Switzerland

Preface

The important progress in materials chemistry offers breakthroughs in the design of devices for a wide range of applications. One of the successful keys in the development of novel systems is the result of the synergy between relevant compounds confined or attached to nanostructured frameworks leading to highly fascinating properties.

In the past century, photochemical reactions or photophysical properties have been extensively studied in homogenous media (gas and liquid phases and solid crystals). However, a different photoresponse can be expected in microheterogeneous systems as a consequence of the limitation of the constrained media imposition and/or specific interactions.

There are many nanostructures of inorganic and/or organic nature to accommodate photofunctional moieties of interest. Generally, (ordered)-nanospaces offer a precise field for photochemical and photophysical processes, able to enhance or provide novel photoinduced phenomena different from those found in solution. Among them, silica-based porous zeolites and layered mineral clays, metal-oxide nanoparticles, carbon-based cyclodextrins, and cucurbiturils, or even those with an organo-inorganic composition such as MOFs frameworks, are the most widely used. Their unique chemical, structural, optical, thermal, and mechanical properties play an important role in the performance, triggered by light as an external stimulus, of the resultant composites. Many compounds, mainly dyes but also ligands, ions, complexes, biomolecules, and metal clusters can surpass their photoactivity under hybridization with different nanostructured materials.

The photoactive function can be intrinsically part of the framework or being a guest molecule. Its incorporation can be performed in many different ways, being either covalently or coordinated attached, or physically embedded in the nanocages of the hosts via a diffusion process loading (from liquid or gas phase), a crystallization inclusion method, or a ship-in-a-bottle synthesis. The followed methodology also influences the final properties of the hybrid material.

Moreover, the important advances in manufacturing techniques allow the production of different types of assemblies such as films, ordered monolayers, nanoparticles, or powder bulk materials, offering a very flexible design for a specific application. Besides, modern characterization techniques and computational tools aid the understanding of their final behavior, leaving room for improvement.

Therefore, the combinations, and hence the final properties, are myriad, being of potential importance for diverse applications ranging from catalysis, lighting, light trapping, transport and energy conversion, memory devices, photonics and optoelectronics, sensing, diagnostics, drug delivery, and other optical and biomedical uses.

This book describes examples of different photo-physicochemical processes and their applications mediated by the supramolecular designs, in which the geometrical constraint imposed by the shape and size of nanostructured cavities and the specific interactions determine the conformation, distance, and orientation between interacting moieties in the ground or excited state. As a result, not only an increase in the photo-, chemical-, and thermal-resistance of the composites is achieved, but also a reduction of non-radiative pathways, a suppression of dye aggregation, a stabilization of metal clusters, a fine-tuning of energy transfer efficiencies, an activation of photoinduced charge transfer or electron hopping, a precise control of photochromism properties, or the generation of anisotropic photoresponses to polarized light. Additionally, enhancement of reaction rates and photoproduct selectivity for several photochemical (intra and inter) reactions in different nanocavities is attained.

The book is organized by the role of the nanostructures to control such phenomena, which directly and indirectly correlate the photofunctions of the systems. The first two chapters are focused on the cooperative effect of zeolites when accommodating dyes and subnanometer metal clusters, respectively; the two following ones exploit MOFs for hosting photoactive guests, non-covalently attached to the voids of porous MOFs, particularly photochromic dyes by post-synthesis loading and Ru(II) polyimines by the crystallization inclusion method. The following three chapters are focused on layered materials, mainly clay minerals, as supports for the intercalation of chromophores in their interlayer space. Next, a chapter is dedicated to the effect of organic nanocages (cyclodextrins, cucurbiturils, and octa-acids) on photophysical activity or photochemical reactions of different photoactive molecules being compared with solutions. The last chapter deals with the synergism between dyes (fluorophores or photosensitizers) and lanthanide (Ln) based-up conversion nanoparticles for potential sensing, imaging, and therapy.

The final aim of this book is to introduce the reader to the advances in the field of photoactive materials based on the combination of photofunctional compounds with a wide range of nanoporous systems or nanoparticles. The design, synthesis, characterization, and applications of these materials are well addressed. All the authors have given in their respective chapters an overview and a future vision of these types

of materials with promising perspectives. We hope that this book entitled “Dyes and Photoactive Molecules in Microporous Systems” attracts the attention of researchers from the materials science and photochemistry fields and serves them as inspiration for the development of new systems with important input, in terms of environment, health, and well-being, into making this world a better place. In our humble opinion, we envision a bright future for the hybrid materials presented in this book and many others waiting to be explored.

Finally, we would like to thank all the authors for their valued scientific contributions, commitment, efforts, and patience. They are the main protagonists of this book. Also, a special thanks to the publisher, Springer, for making this journey so much easier. It was indeed a fruitful and rewarding experience.

Bilbao, Spain
Bilbao, Spain

Virginia Martínez-Martínez
Fernando López Arbeloa

Contents

Guests in Nanochannels of Zeolite L	1
Gion Calzaferri	
Highly Luminescent Metal Clusters Confined in Zeolites	75
Eduardo Coutino-Gonzalez, Maarten Roeffaers, and Johan Hofkens	
Photoactive Molecules within MOFs	105
Heidi Annemarie Schwartz and Uwe Ruschewitz	
Guest-Based Photoactive Porous Materials Based upon Zn-Carboxylate Metal Organic Frameworks	155
Randy W. Larsen, Jacob M. Mayers, Abdulaziz A. Alanazi, Christopher R. McKeithan, and Lukasz Wojtas	
Tuning Emission Properties by Dye Encapsulation into Layered Silicates	185
Yohei Ishida and Shinsuke Takagi	
Resonance Energy Transfer in Hybrid Systems of Photoactive Dye Molecules and Layered Inorganics	205
Juraj Bujdák	
Photofunctions of Dye-Clay Hybrids: Recent Developments	251
Tetsuo Yamaguchi, Jae-Min Oh, and Makoto Ogawa	
Photophysicochemical Processes Directed Within Nano-Containers	321
Mahesh Pattabiraman and Arunkumar Natarajan	
Functional Nanohybrids Based on Dyes and Upconversion Nanoparticles	371
Juan Ferrera-González, María González-Béjar, and Julia Pérez-Prieto	
Index	397

Guests in Nanochannels of Zeolite L



Gion Calzaferri 

Contents

1	Introduction	2
2	Synthesis of Zeolite L	5
3	Guests	6
3.1	Ship-in-a-Bottle Synthesis	12
3.2	Synthesis of Composites Containing Two or More Different Guests	13
4	Functionalization: Stopcocks, Coat, Polymer Brushes	15
4.1	Stopcocks	15
4.2	Functionalization of the Whole Outer Surface	22
5	Patterns of ZL Crystals	23
5.1	Oriented Monolayers	24
5.2	Chains, Files, Hexagonal, and Other Arrangements	26
6	Structure of the Guest-ZL Composites	28
7	Electronic Absorption and Luminescence Properties of the Host-Guest Composites	33
7.1	Absorption and Luminescence Spectra of Organic Guest-ZL Composites	34
7.2	Oscillator Strength	37
7.3	Influence of the Acidity of the Channels on the Guests	39
7.4	Exciton Coupling of Organic Guests	43
8	ZL as a Catalyst	48
9	Artificial Photonic Antenna Systems for Light Harvesting, Transport, and Trapping	49
9.1	Communication with the Outside World	56
10	Biological and Biomedical Applications	59
11	Summary	62
	References	63

Abstract Zeolite L (ZL) is a unique host. It accepts a large number of different guests inside of its nanochannels and allows specific modification of its surface. This is due to the combination of its chemical, structural, optical, and mechanical properties. The resulting composites have been investigated in a surprisingly broad field of applications, ranging from catalysis, lubricant technology, pigments, sensing, optics, optoelectronics, biology, drug delivery, diagnostics, and even human

G. Calzaferri (✉)

Department of Chemistry and Biochemistry, University of Bern, Bern, Switzerland

e-mail: gion.calzaferri@dcb.unibe.ch

medicine. ZL seems to be the only known thermally and mechanically stable material with linear channels of about 1 nm diameter, where the size of the particles and, hence, the length of the channels can be tuned in the range from about 30 nm up to 20,000 nm, which can be synthesized as crystals of different morphology such as discs, barrels, and elongated tubes. We discuss the synthesis of ZL, the many guests that have been inserted, the functionalization of the channel entrances with stopcocks and decoration of the coat, and different patterns created with ZL crystals. Much progress has been made in understanding the structure of guest-ZL composites. ZL has been used in catalysis and for creating artificial photonic antenna systems for light harvesting, transport, and trapping. The advances using ZL composites for diagnostics and for biological and biomedical applications are impressive. This remarkable evolution justifies to devote this article to zeolite L.

Keywords Breast cancer · Catalysis · Cluster · Diagnostics · Drug delivery · Dyes · FRET · Host-guest composites · Luminescence · Pigments · Rare earth · Sensing · Supramolecular chemistry · Zeolite

1 Introduction

The opportunities for creating nanochannel-based host-guest materials and for realizing organizational patterns with specific properties are immensely diverse [1–4]. Assemblies, polymers, crystals, and biological structures bearing nanochannels have been known and studied for decades [5–9]. Examples of nanochannel materials are cyclodextrins, urea-based assemblies, zeolites, zeotypes, mesoporous silica, collagens, organic nanochannels, carbon nanotubes, metal oxide nanochannels, and metal organic frameworks [5–15]. They have been investigated as hosts for molecules, complexes, ions, or clusters under a great variety of conditions. This gives a vague impression regarding the infinite number of combinations and hence objects with different properties that can be realized. Current research regarding such hosts and the resulting composites concerns catalysis, waste disposal, lubricants, pigments, sensing, optics, nonlinear and micro optics, electronics, optoelectronics, solar energy utilization, biology, cosmetics, sunscreen, drug delivery, diagnostics, and medicine. In these applications the chemical, structural, optical, and mechanical properties of the host are essential.

This article is dedicated to zeolite L as a host for guests comprising metal cations, metal clusters, metal complexes, organic cations, and neutral organic molecules. What is special about zeolite L? We show that the combination of chemical, structural, optical, and mechanical properties makes zeolite L – which we abbreviate as ZL, for simplicity – a unique host for creating distinct composites by accepting a large variety of guests and by allowing specific surface modification. Such composites have therefore been investigated in a surprisingly broad field of applications,

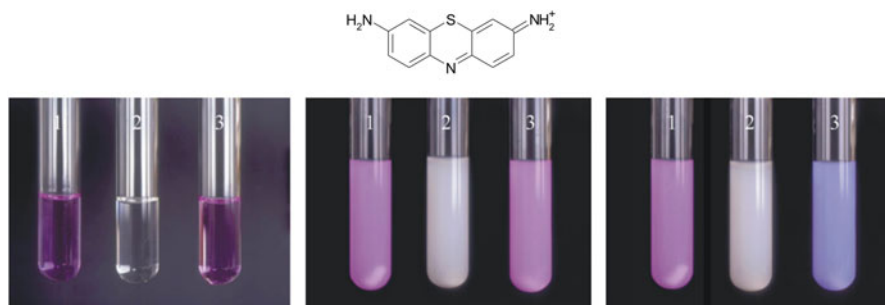


Fig. 1 Observation made when 600 nm sized ZL particles are added to a solution of the cationic molecule thionine (TH⁺) shown on the top. Left: we see two test tubes, 1 and 3, containing 4 mL of a 2×10^{-6} M aqueous solution of TH⁺. The test tube 2 in the middle contains pure water and serves as a reference. Middle: Addition of 2 mL of a ZL suspension (2 g ZL in 100 mL water) to each of these test tubes causes immediate color change, indicating the formation of TH⁺ aggregates in the test tubes 1 and 3. Right: Test tube 3 was heated to gentle boiling for about 1 min and then cooled to r.t. The color change is striking. It demonstrates the formation monomers. We next add at r.t. a few drops of a 0.1 M hypochlorite solution. The effect is striking. The color of the sample in test tube 1 bleaches rapidly, but nothing happens to sample 3. This experiment can be used as a convenient and fast probe to check the success of a ZL synthesis [17, 20]. Adapted with permission from [20] Copyright Elsevier

ranging from catalysis, lubricant technology, pigments, sensing, optics, optoelectronics, biology, drug delivery, diagnostics, and even human medicine. ZL seems to be the only known thermally and mechanically stable material with linear channels of about 1 nm diameter where the size of the particles and, hence, the length of the channels can be tuned in the range from about 30 nm up to 20,000 nm and which can be synthesized as crystals of different morphology such as discs, barrels, and elongated tubes. This means that crystals consisting of about 250 up to 10^8 strictly parallel channels are available. The anionic framework of ZL allows inserting cationic species by means of ion exchange and neutral species from the gas phase or from dispersions, using an appropriate liquid phase, and it enables attaching reversible or covalently bound functionalities [14–16].

My interest in ZL as a host started with an observation we made in the simple test tube experiment illustrated in Fig. 1. Left: Two test tubes, 1 and 3, contain a diluted aqueous solution of thionine (TH⁺). Sample 2 is pure water and serves as a reference. Middle: We add a portion of a ZL suspension. The immediate color change indicates the formation of TH⁺ aggregates at the surface of the particles. Right: We now heat test tube 3 with a Bunsen burner. Another color change is observed. It is the color of monomers. We next add (at room temperature) a few drops of a 0.1 M hypochlorite solution. The effect is striking. The color of the sample in test tube 1 bleaches rapidly, but nothing happens to sample 3. This means that the TH⁺ slipped into the ZL channels upon heating where they are present as monomers and where they are protected against bleaching by the anionic hypochlorite. The latter cannot enter the negatively charged channels of ZL. The hypochlorite, however, rapidly bleaches the

TH^+ at the outer ZL surface in sample 1. We have two effects: avoidance of aggregate formation and protection. Spectroscopic evidence supports the interpretation [17]. The properties of ZL are fundamentally different from those observed with zeolite Y (ZY). TH^+ exchanged zeolite Y results in pink-colored samples characteristic for H aggregates of this dye. The color changes from pink to blue when drying TH^+ZY and back to pink upon rehydration. This means that TH^+ within the supercages of zeolite Y is present as monomers when the zeolite is dry and as H-aggregated dimers when it is wet, [18] while TH^+ is present as monomer within the channels of ZL, independent of whether the sample is “wet” or “dry.” Details of the structure of $\text{TH}^+\text{-ZL}$ was revealed many years after these observations were made [19]. The more we learned about the properties of ZL as a host, the more we were surprised by its unique properties for creating highly organized systems [14–16, 20, 21]. The important progress regarding the understanding of the structure of host-guest composites was made possible by the availability of advanced computational tools, modern powder diffraction techniques, and luminescence microscopy [1]. The remarkable evolution justifies devoting this article to zeolite L.

ZL is a so-called large pore 12-membered ring zeolite with one-dimensional channel system. It was discovered by Breck and Flaningan (1968) as synthetic material and observed many years later in nature by Artioli and Kvick [10, 11, 22]. ZL possesses circular pore aperture with a crystallographic diameter of 0.71 nm. It belongs to the low-silica zeolites with a molar composition of $(\text{M}^+)_9([\text{AlO}_2]_9[\text{SiO}_2]_{27})_x\text{nH}_2\text{O}$, where M^+ are monovalent cations, usually K^+ . The framework of ZL possesses therefore anionic properties which are compensated by, e.g., alkali ions. The latter can be exchanged to some extent by other cations. We represent the structure of ZL and features of its morphology in Fig. 2 in a more intuitive way that allows imaging important properties. Precise structural data can be found in references [12, 23, 24].

The number of channels n_{CH} of a crystal of diameter d_Z that run parallel to the c-axis can be estimated using Eq. (1):

$$n_{ch} = 0.268(d_Z)^2; d_Z \text{ in units of nm.} \quad (1)$$

This means, for example, that a crystal with a diameter of 600 nm features nearly 10^5 strictly parallel channels. It also means that the number of channels per surface area n_{CH}/cm^2 is 4.3×10^{13} . The number n_{uc} of u.c. of a ZL crystal of length l_Z and diameter d_Z can be estimated as expressed in Eq. (2):

$$n_{uc} = 0.356d_Z^2l_Z; d_Z, l_Z \text{ in units of nm.} \quad (2)$$

From this follows that a ZL crystal of 100 nm length and diameter consists of 2,680 channels and 35,700 u.c. and one of 1,000 nm length and 600 nm diameter consists of 96,400 channels and 1.28×10^6 u.c. The void space, provided by the channels with respect to the total volume of a crystal, is about 26% [25].

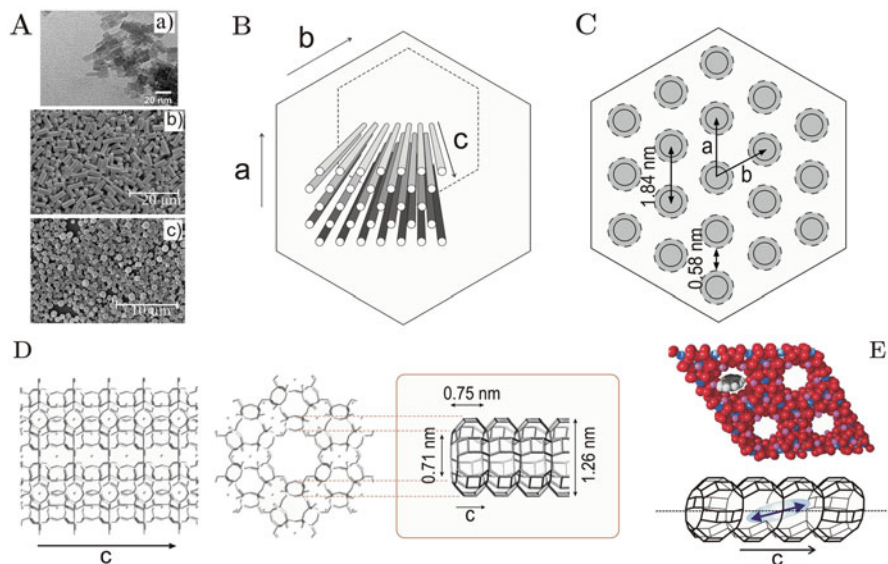


Fig. 2 Morphology and structure of ZL. (A) Images of three ZL samples: (a) TEM image of nanosized particles with average length and diameter of 30 nm; (b) SEM image of crystals with an average length of 6,000 nm; (c) disc-shaped crystals on a glass substrate. (B) Schematic view of the 1D parallel channels (depicted as gray tubes). Vectors a , b , and c are primitive vectors; a and b make an angle of 60° and are perpendicular to c . Each channel is surrounded by six neighbors. (C) Representation of the basal plane of ZL. The pore openings are shown as solid lines. The dashed lines represent the largest channel diameter. The center-to-center distance between two adjacent channels is 1.84 nm, and the shortest distance is 0.58 nm. (D) Side and top view of a channel. c is the primitive vector coinciding with the channel axis. We see on the right that a u.c. is 0.75 nm long, the pore opening is 0.71 nm wide, and the largest diameter in the channel is 1.26 nm. The lines of the left and the middle part of this scheme represent oxygen bridges between Si and Si/Al, while the lines of the framed scheme connect the Si/Al atoms. (E) Van der Waals picture of a guest molecule entering a channel and schematic side view of a channel with a dye molecule inside. The double arrow indicates an example of the orientation of the electronic transition dipole moment of the dye

2 Synthesis of Zeolite L

An important property of ZL is that samples can be synthesized in a large variety of sizes and morphologies, spanning a volume range of eight orders of magnitude, all of them with the same hexagonal structure consisting of linear 1 nm channels. Only technical grade ZL is commercially available. This is an unfortunate limitation because many interesting experiments and applications depend critically on the size, the morphology, and the chemical purity of the crystals. The synthesis of laboratory amounts of ZL crystals in a large size range and different morphology from disc-shaped, barrel, and elongated crystals is relatively easy, however, and can be performed in poly(tetrafluoroethylene) (PTFE) bottles placed in a tight PTFE pressure vessel that supports temperature of up to about 180°C and pressures up to

about 16 bar. The size of the crystals can be tuned between 30 nm and 10,000 nm. The hexagonal ZL crystals, which typically feature approximately cylindrical morphology, can be obtained with various aspect ratios ranging from elongated to barrel- and disc-shaped using this method [26, 27].

It is interesting that variations of ZL synthesis procedure including studies regarding the mechanism of formation of the crystals continue to attract interest of researchers despite of the fact that the first synthesis goes back to the 1968 report of Breck and Flanigen [10, 11]. The reason for this is that the large scale of different applications under investigation demand for different specific morphologies, sizes, and purities of the crystals and that the properties and size distribution of the resulting crystals depend critically on small changes of the reaction conditions which are the chemical compositions of alumina, silica, potassium hydroxide, water, the temperature, and the reaction time. It is also influenced by stirring and different types of additives. The parameters which influence size, morphology, as well as size and shape distribution are still only partially understood [28–38]. Hydrothermal synthesis of high-quality ZL crystals with tunable size and morphology using microwave heating was reported. Crystals of different length and shape have been obtained in this manner [39].

Assembling zeolite crystals into well-defined macroscopic structures is of particular interest, considering that zeolites are ideal host materials for a large variety of molecules, complexes, and clusters. In device chemistry, a high degree of supramolecular organization is important for attaining the desired macroscopic properties. A possibility for achieving such organization is the controlled assembly of the ZL crystals into oriented structures and the preparation of mono-directional materials.

3 Guests

It may be surprising, to learn how many different guest and combinations of guest have been inserted into the 1 nm channels of ZL. Methods that have been used are cation exchange, insertion of neutral guest from the gas phase and from an inert solvent, pressure-supported insertion, and ship-in-a-bottle synthesis. We list the currently known guest in Tables 1, 2, and 3. It seems that template synthesis procedures have not been very successful for the preparation of well-defined ZL composites.

ZL allows, through geometrical constraints, the realization of extremely high concentrations of well-oriented molecules that behave essentially as monomers or as very weakly interacting monomers. A 30 nm × 30 nm crystal can host 5,000 guests that occupy 2 u.c., and a 60 nm × 60 nm crystal can host up to 40,000 guests of this size. It is convenient to introduce a parameter bearing information on the dye concentration but based on the purely geometrical (space-filling) properties of ZL as a host (i.e., showing to what extent the ZL channels are filled with guests). The loading or occupation probability p of a guest-ZL composite is defined by Eq. (3):

Table 1 Cationic guests that have been inserted into the channels of ZL

Inorganic cations			
H ⁺ , Li ⁺ , Na ⁺ , K ⁺ , Cs ⁺ , Ag ⁺ , Tl ⁺ , Mg ²⁺ , Ca ²⁺ , Pt ²⁺ , Cd ²⁺ , Sn ²⁺ , Co ²⁺ , ¹⁰⁰ In ³⁺ , Eu ³⁺ , Tb ³⁺ , Er ³⁺ , Yb ³⁺ , Nd ³⁺			
Organic cations			
Th ⁺		Acr ⁺	
Py ⁺		MeAcr ⁺	
PyGY ⁺		ProFl ⁺	
PyB ⁺		AY ⁺	
Ox ⁺		AO ⁺	
DEOx ⁺		AF ⁺	
Ox1 ⁺		BDP ⁺	
DASP ⁺		MV ²⁺	
			MC ⁺
			PC20 ⁺
			PC21 ⁺
			BTMPI ⁺
			PIC ⁺
			SQ III R = CH ₃ SQ(JG9) R = (CH ₂) ₃ CH ₃
			ST1, ST2, ST3 R1=R2=H R1=OMe, R2=Br R1=Br, R2=Br
			IMZ ⁺

$$p = \frac{\text{number of occupied sites}}{\text{total number of sites}}. \quad (3)$$

The symbol n_s represents the number of u.c. occupied by a guest. It can, for example, be equal to 1, 2, or 3, but n_s is not necessarily an integer. The loading p ranges from 0 for an empty ZL to 1 for a fully loaded one. The concentration $c(p)$ of a guest-ZL composite can be expressed as a function of p by means of Eq. (4): [14]

$$c(p) = 0.752 \frac{p}{n_s} \left(\frac{\text{mol}}{\text{L}} \right). \quad (4)$$

This means, for example, that the maximum concentration of a guest that occupies 2 u.c. amounts to 0.376 mol/L. Many samples with high loading have been prepared. The MV²⁺-ZL was probably the first composite reported with such a high loading [40]. Entropy decrease accompanying the buildup of such highly ordered composites has been analyzed [20, 41, 42]. The insertion kinetics leading to homogeneous filling could nicely be monitored using the two cationic dyes Py⁺

Table 2 Neutral guests that have been inserted into the channels of ZLAr, Xe, N₂, O₂, H₂O, CH₃OH, CH₃CH₂OH, benzene, toluene and many other small guests.Metal cluster M_n and M_nN_n; M, N are Ag, Ni, Pt, Sn, Co, Mo, Ru, Rh

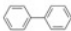
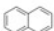


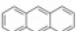
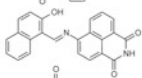

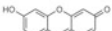

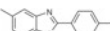
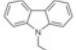
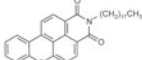

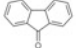

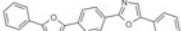

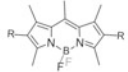
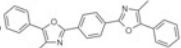

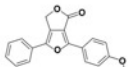

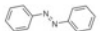
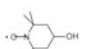


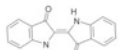
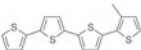
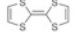



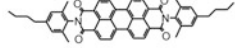
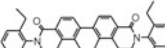
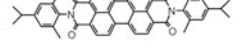









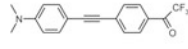
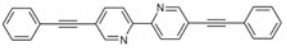
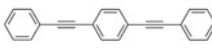
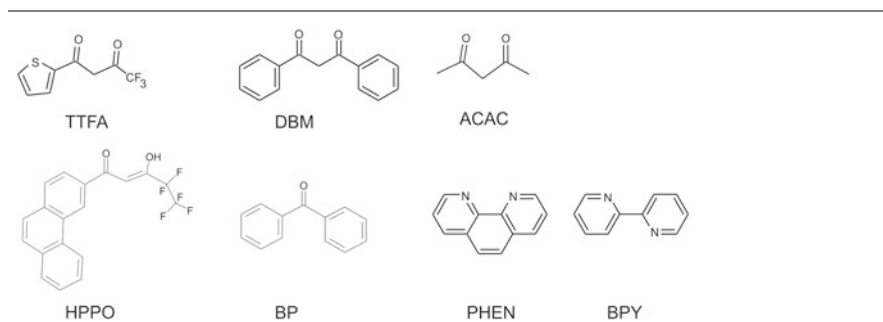
BP		Naphthalene		NY43	
pTP		Anthracene		JCG65	
DPH		ResH		Hostasol Red	
PBOX		N-Ethyl-carbazole		HY3G	
MBOXE		Fluorenone		LYF083	
POPOP		DCS		Bodipy (R = H, alkyl aryl)	
DMPOPOP		Stilbene		Furo-Furanone	
isoviolanthrone		Azobenzene		Hydroxy-TEMPO	
SG 5		DANS		Indigo	
DM4T		TTF			
dmpa-XP		tdc-XP			
DXP		b-DXP			
DEXP		ip-DXP			
tb-DXP		dm-DXP			
dmp-DXP		m-DXP			
o-bone-DXP		dm-XP			
bone-DXP		tb-DXT			
tb-DXQ		Tol2			
Bpy2		BPB			

Table 3 Ligands used in the ship-in-the-bottle synthesis of organolanthanide complexes within the channels of ZL

and Ox^+ (Table 1), which are of nearly identical size and shape, as donor-acceptor pair in a Förster resonance energy transfer (FRET) experiment [43]. The time needed for homogeneous filling depends on the length of the channels, the type of guests, and the reaction conditions [16, 43, 44]. This allows to freeze non-equilibrated states for inspection purposes by simply cooling the samples to room temperature, a method popular for measuring and presenting luminescence microscopy images; see, e.g., Fig. 3 in [45], Fig. 20 in [14], or Figs. 4 and 5 in [46]. This should, however, not be misinterpreted in the sense that achieving homogenous filling is difficult, which is usually not the case, but has probably been assumed in [47]; homogenous filling is usually just a question of choosing appropriate conditions. Composites with the highest possible packing, based on barrel-shaped crystals of about 500 nm length, namely, 1.5 fluorenone (Table 3) per u.c., have been prepared by Tabacchi et al. and used for structural analysis [48]. High-pressure studies of fluorenone-ZL composites revealed an impressive stability even at GPa pressures, evidencing a pressure-induced strengthening of the interaction between the fluorenone carbonyl group and the ZL potassium cations, thus indicating a way to the realization of, e.g., optical devices able to maintain their functionality under extreme conditions [49].

We use the value of p , Eq. (3), for denoting a system as follows: a composite name, such as guest-ZL.05 or dye-ZL.25, indicates a guest loading (occupation probability) of the ZL host of 0.05 or 0.25, respectively. A comparison of the length of four representative dyes with the length of the u.c. of ZL is shown in Fig. 3. This allows to state that HR molecules demand 2 u.c.; hence $n_s = 2$. DMPOPOP and DXP occupy about 3 u.c.; hence $n_s \approx 2.5$ to 3 is a meaningful measure, while $n_s \approx 3.5$ applies for tb-DXP. The occupation probability p based on such arguments is a rough but useful measure and can be used as a guideline. More precise information can be obtained using theoretical and experimental structural analysis data [40, 47–49].

Most synthesis procedures for obtaining guest-ZL composites start from $(\text{M}^+)_{9}([\text{AlO}_2]_{9}[\text{SiO}_2]_{27})_x\text{nH}_2\text{O}$, with potassium as the monovalent cation M^+ . Up to a maximum of 3.6 out of the 9 M^+ cations per u.c. can be exchanged. Table 1 lists

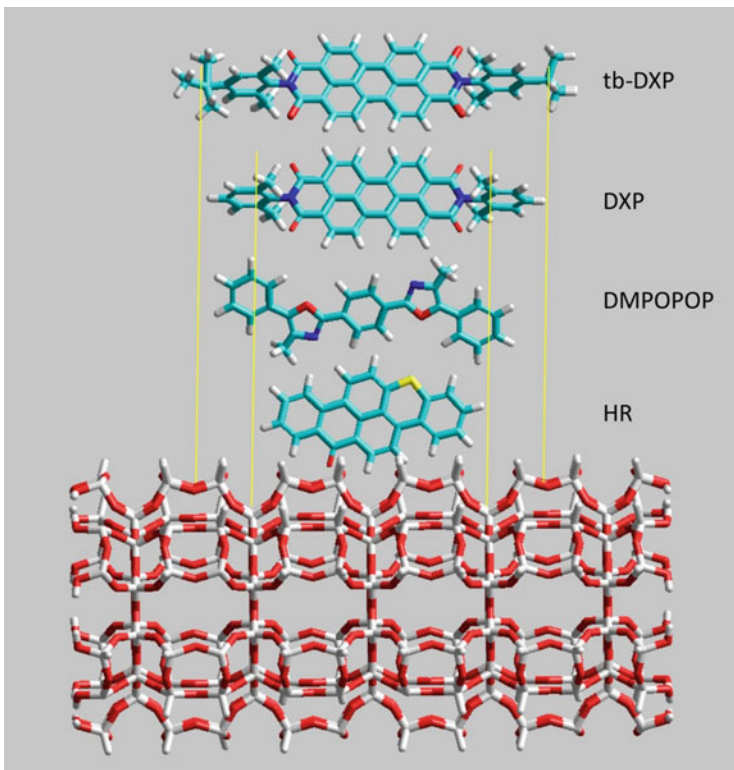


Fig. 3 Comparison of the length, indicated in brackets, of four dyes with the u.c. length of ZL: HR (1.5 nm), DMPOPOP (2.0 nm), DXP (2.1 nm), and tb-DXP (2.6 nm). The inner two yellow vertical lines mark the 1.5 nm length of 2 u.c. and the outer ones the 2.25 nm length of 3 u.c

cations that have been inserted. Exchange by monovalent cations is usually fast and easy. Divalent cations enter sometimes very fast and sometimes more reluctantly. Not more than one trivalent cation per u.c. can be exchanged, and the preparation conditions must be selected with care. They play an important role in the ship-in-a-bottle synthesis of rare earth complexes. The cations listed in Table 1 are usually not the only guest in the channels. Very often water molecules are present. Potassium is the most frequent co-cation, and care has to be taken to control the amount of the often less wanted protons. The insertion temperature is limited by the thermal stability of the guests and by the boiling point of the solvent. It can sometimes be extended by using a poly(tetrafluoroethylene) (PTFE) bottle placed in a tight PTFE pressure vessel that supports temperature of up to about 180°C and pressures up to 16 bar, similar as used for ZL synthesis. The maximum temperature that can be used for the insertion of neutral guests is limited by their temperature stability and goes up to a maximum of about 300°C. The insertion temperature of many perylene diimide dyes, as an example, was 260°C [16]. Water is removed by usually moderate heating

under vacuum prior to the insertion of neutral guests [50]. Neutral guests that have been inserted are reported in Table 2.

Some molecules remain typically adsorbed at the outer surface of the ZL crystals independent of the synthesis procedure. It is therefore often necessary to remove them in order to obtain the desired product. Different procedures have been used successfully, depending on the guest. Anions cannot enter the channels of ZL unless they form ion pairs. This means that molecules at the outer surface can be destroyed by using an oxidizing agent such as hypochlorite [26] (see, e.g., Fig. 1) or by applying dithionite as a reducing agent [51]. The molecules inside of the channels are not accessible to anionic species unless drastic conditions are applied. A common method used to remove objects from the outer surface is washing the samples with a solvent that is not or only slowly capable of entering the channels and passing the guest. Examples are 1-butanol [50, 52] and DCM [16], but also washing solutions containing an appropriate detergent can be used to remove the molecules on the outer surface [14, 53].

A molecule that can enter a channel can also exit, if no measures are taken to avoid this process, depending on the environmental conditions. An illustrative example is the observation that the speed to substitute resorufin (ResH, Table 2) located inside of the channels by solvent molecules depends on their size. The following pattern was observed at r.t.: water \gg methanol $>$ ethanol $>$ 1-propanol \geq 1-butanol. The reason is that water molecules can pass the ResH inside of the narrow channels, while 1-propanol and especially 1-butanol cannot [52]. The displacement of para-terphenyl (pTP, Table 2) by water was observed to be reversible. Exposure of pTP-ZL composites to laboratory air at rt. of about 20% relative humidity causes the pTP to leave the channels and to adsorb at the outer surface of the ZL crystals. Interestingly, the pTP slips back into the channels upon drying the samples at about 200°C. This process can be repeated many times [54]. It is interesting to compare this observation with the behavior of fluorenone. It was observed that this molecule is not substituted by water despite of the fact that it is smaller than pTP or similar molecules which are displaced [55]. The reason for this behavior was not understood at the time of its discovery. The puzzle was solved by performing extensive first-principles investigations on the fluorenone inside ZL, both at dry conditions and in the presence of water. It turned out that the interaction of the fluorenone carbonyl group with the ZL extra framework potassium cations is responsible for the dye stabilization in the ZL nanochannels. The interaction with potassium extra framework cations stabilizes the carbonylic dye fluorenone inside the nanochannels, leading to a water-resistant dye-ZL composite. A selection of the resulting structures calculated for dry conditions is shown in Fig. 4. The fluorenone is strongly bound to one K^+ via the carbonyl oxygen in the minimum energy structure seen in the bottom panels. Contact to two K^+ seen in the upper left panel is only 2.1 kcal/mol less stable. On the contrary, the upper right panel represents a configuration in which the carbonyl group of the dye does not interact with the potassium cation. Such a configuration is much less stable than the minimum structure. The comparison demonstrates that configurations in which the carbonyl group is not in contact with K^+ are strongly energetically disfavored with respect to

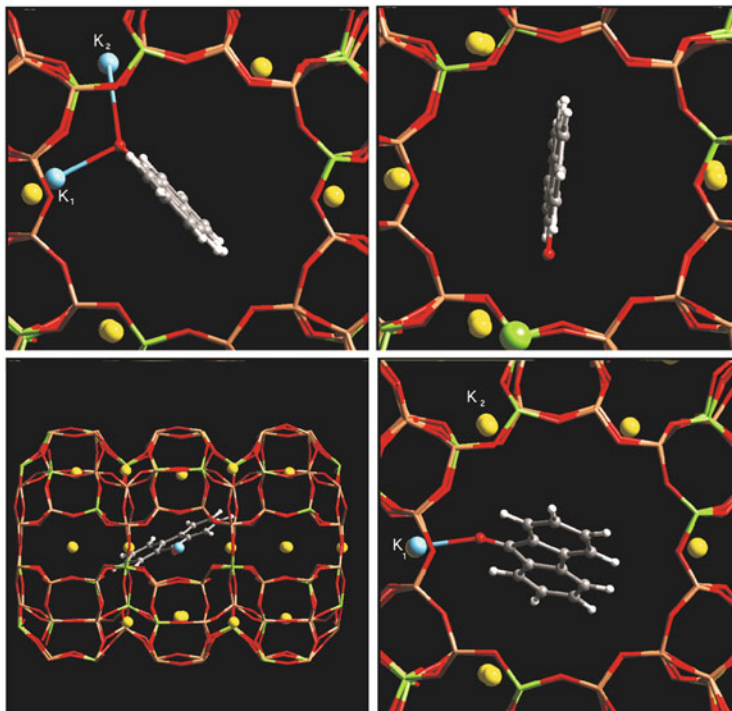


Fig. 4 Structure of fluorenone in the ZL channels. Bottom panels: Most stable structure. Upper left panel: Contact to two K^+ . This structure is slightly less stable with respect to the structure with one $C=O \dots K^+$ contact seen in the bottom panels. Upper right panel: configuration in which the carbonyl group does not interact with the K^+ . It is much less stable than the minimum structure shown in the bottom panels. Color code: brown, Si; red, O; green, Al; gray, C; white, H; yellow, K^+ ; blue, K^+ interacting with oxygen. The green sphere indicates the Al atom closest to the $C=O$ oxygen [56]. Adapted with permission from [56], Copyright American Chemical Society

those exhibiting coordination to K^+ . This understanding represents a general principle [56].

3.1 Ship-in-a-Bottle Synthesis

In situ formation of species within the channels of ZL is possible by adsorbing suitable precursors that can be transformed into the final guest. Complexes have been synthesized inside the channels of ZL by means of the “ship-in-a-bottle” synthesis, pioneered by Lunsford et al. in the early 1980s [57]. This synthesis principle has been used successfully for the preparation of many host-guest composites [58–60]. The ship-in-a-bottle procedure has been widely used for the preparation of catalytically active metal and bimetallic clusters in ZL, such as Pt, PtSn, PtCo, Ru,

RhNi, and MoCo [61–69]. Lanthanide complexes have been prepared inside the channels of ZL using the ligands reported in Table 3. The principle is to first exchange the monovalent cations, most often K^+ , by the lanthanide ion Ln^{3+} (Eu^{3+} , Tb^{3+} , Er^{3+} , Yb^{3+} , Nd^{3+}). The samples are then dried, and the ligand is added either from the gas phase or from an inert solvent such as n-hexane. The material must be protected from humidity if high luminescent yield is envisaged. Key for success is that the ligands are able to diffuse deeply into the channels and, in many cases, that they are small enough to pass each other inside. This is usually easier for nanosized or disc-shaped ZL crystals. Different procedures have been used depending on the envisaged properties [70–77].

3.2 *Synthesis of Composites Containing Two or More Different Guests*

The properties of ZL composites containing more than one type of guests can differ radically from those containing only one type of guests. We should distinguish between guests that cannot pass each other inside of the tiny channels and guests that can pass each other.

3.2.1 **Guests That Cannot Pass Each Other**

Many of the guests listed in Tables 1 and 2 are too bulky for gliding past each other inside the channels as depicted in Fig. 5a. This is especially true for most molecules the length of which surpasses the length of 1 u.c. which is 0.75 nm. Simultaneous insertion of a mixture of two different guests is a simple possibility for, e.g., doping a main component with some other molecules as illustrated in the “random synthesis” scheme of Fig. 5. It was, e.g., used for studying the insertion kinetics of the two cationic dyes Py^+ and Ox^+ by means of cation exchange [43]. The sequential insertion of guests as illustrated in the “sequential synthesis” scheme of Fig. 5 allows preparing many types of composites bearing a rich variety of properties. It was first reported for cationic dyes [78] and soon extended to neutral dyes and combination of neutral and cationic dyes leading to “sandwich”-type arrangements [16, 54]. Sequential insertion is successful for molecules which cannot glide past each other inside the channels as explained in the scheme in Fig. 5. The first step consists of inserting a chosen amount of a species mol1 either by ion exchange, or by gas phase adsorption, or from a solvent, depending on its properties. This leads to a material we name mol1-ZL. After removing species which might eventually be adsorbed at the outer surface, the second species (mol2) is inserted. Insertion conditions have to be chosen such that mol1 will not leave the channels or decompose during the process. Once at least one mol2 has entered each channel on both sides, the mol1 cannot escape

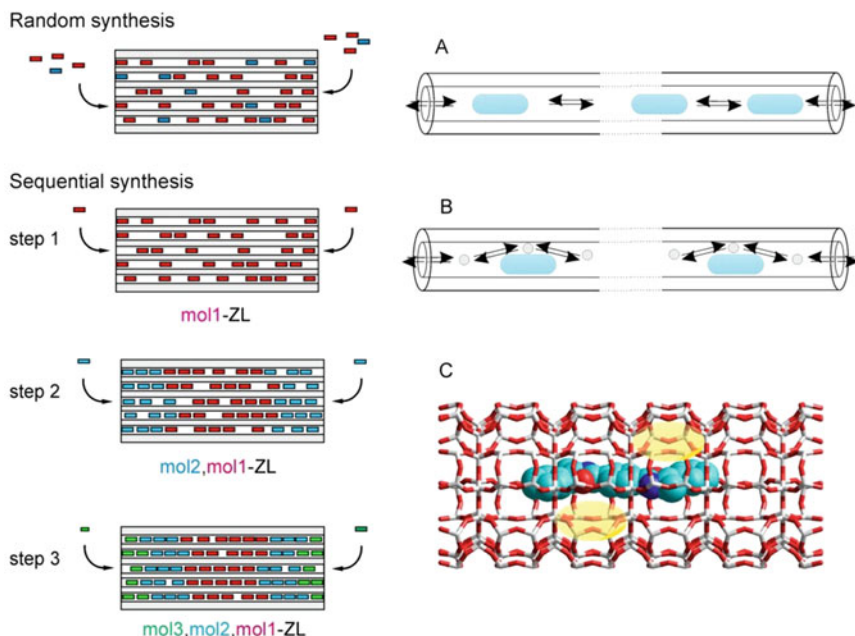


Fig. 5 Preparation of composites containing two or more different guests. Left: Synthesis using guests that are too bulky for gliding past each other inside the channels. We show on top how two different guests can be inserted simultaneously, either in about equal amounts or one in excess and the other as dopant. Below: A scheme for sequential insertion is sketched. Step 1 illustrates the insertion of the first guest mol1, resulting in the mol1-ZL composite. A next guest mol2 is inserted in the second step. The mol2 pushes the mol1 deeper into the channels, because the molecules cannot glide past each other; the resulting composite is a mol2,mol1-ZL sandwich composite. This process can be repeated in step 3. It stops once the channels are filled. Right: Two types of co-guest are illustrated. (a) Sketch of guests that cannot pass each other inside of the channels. (b) Small co-guest such as oxygen, water, methanol, and others can very often pass the bulkier guest molecules. The reversibility allows either to add or to remove them from a mol-ZL composite. Scheme (c) illustrates a larger co-guest (yellow) which cannot be removed. Such co-guest must be inserted before the larger guests are added. They can be used to tune the properties of the “main” guest molecules

anymore. The mol2 pushes the mol1 deeper into the channels, because they cannot pass each other. The sample obtained after this step is named as mol2,mol1-ZL. The same procedure can be repeated for mol3, with the resulting material being mol3,mol2,mol1-ZL sandwich. The different insertion procedures can be combined: for example, a cationic mol1 is inserted by means of ion exchange. A neutral mol2 is then embedded by gas phase adsorption or from an appropriate solvent and so on. Materials with more than three different types of dyes can be prepared if desired. Many such composites have been prepared and characterized [14–16, 46, 54, 79, 80].

3.2.2 Guests That Can Pass Each Other

Small molecules such as H_2 , O_2 , N_2 , Cl_2 , H_2O , CH_3O , toluene, and others can often pass bulkier guest inside of the channels and can thus modify properties of the composites in many ways. This is, e.g., important for using ZL in catalysis [81]. An interesting example that explains the importance of controlling the co-guests is the behavior of ResH (Table 2). This molecule is strongly fluorescent in solution in its anionic form Res^- . The fluorescence was observed to be completely quenched when the molecule was inserted into the channels of ZL using a procedure that results in a fully hydrated composite [52]. The properties of Res-ZL composites change dramatically, however, if prepared under different conditions so that completely dehydrated Res-ZL results, which is observed to be strongly luminescent [82]. Scheme (b) in Fig. 5 illustrates such situations. Different properties result if a small co-guest must first be positioned in the well of the channel in a way that larger guest inserted afterward can slip past them. Once both guests, the smaller and the bulkier one, are inside, the smaller guest remains trapped in his trench, as exemplified in Scheme (c) of Fig. 5. An example of such a situation is IMZ^+ (Table 1) which has frequently been used in order to substitute some of the 3.6 per u.c. charge compensation K^+ located in the channels [16, 83].

4 Functionalization: Stopcocks, Coat, Polymer Brushes

Hydroxy groups are distributed all over the external surface of ZL crystals. This provides an opportunity for functionalization by means of covalent bonds. The base and coat hydroxy groups, furthermore, show distinctly different reactivity. This can be understood by comparing them as illustrated in Fig. 6. The figure explains that the channel entrances are exclusively located at the base. The red lines point to the base of the SEM image of a ZL crystal and connect it with the drawing on the left showing the hexagonally arranged channel entrances and the sketch which shows how the channel entrances can be functionalized selectively with stopcocks. The scheme illustrates a situation where the channels are filled with two different guests, arranged in a sandwich structure. The yellow line connects the coat of a ZL crystal, seen in the SEM image, with the coat in the scheme which is functionalized by binding the yellow objects to the OH groups located at the surface [14, 15, 20].

4.1 Stopcocks

The stopcock principle was invented for selective modification of the ZL channel entrances [84, 85]. A simple scheme of the stopcock principle is illustrated in Fig. 7a. The head of these molecules is too large to enter the channels. Since stopcock

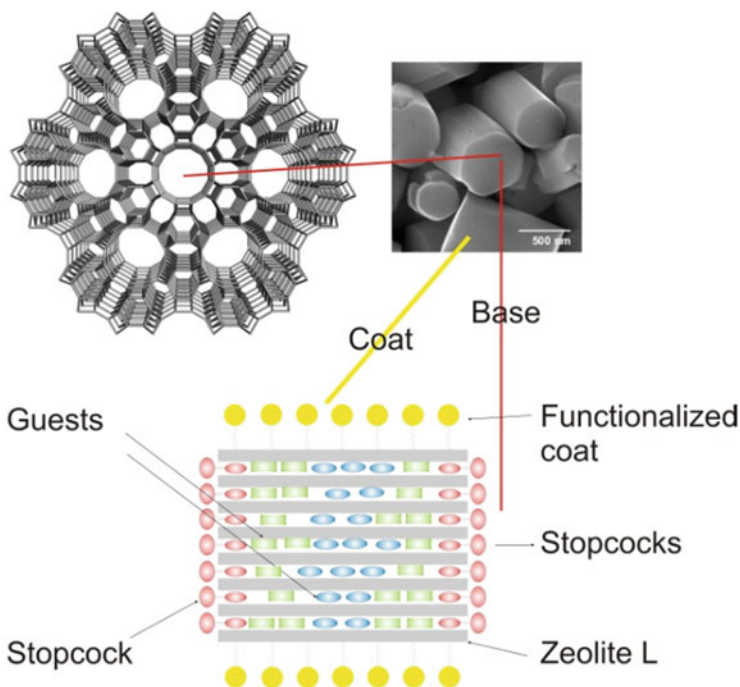


Fig. 6 Chemical properties of the base and the coat of ZL crystals. Upper: The channel entrances are exclusively located at the base, the structure of which is shown on the left. Guests cannot penetrate the ZL via the coat which is tightly sealed with respect to any molecules. Both, base and coat bear, however, OH groups which can be used for functionalization. Lower: The scheme illustrates that the channels can be filled with, e.g., two different guests, arranged in a sandwich structure. Next the channel entrances can be modified with stopcocks shown as red objects. And finally, also the coat can be functionalized by binding the yellow objects to the OH groups located at its surface

molecules are located at the interface between the interior of a ZL crystal and the surroundings, they can be considered as mediators for communication between dye molecules located inside of the nanochannels and objects outside of the crystals. Luminescent stopcocks can be used, e.g., to extract or inject electronic excitation energy into or from the ZL crystals by means of FRET. Stopcock molecules can also prevent penetration of small molecules such as oxygen and water or hinder encapsulated molecules, cluster, and cations from leaving the channels. The dye molecules BTRX and B493/503 (Table 4) were used in the first successful demonstration of the stopcock principle. Their head consists of a BODIPY fluorophore, and their label is a succinimidyl ester. Key to success was the choice of appropriate reaction conditions. The molecules can be dissolved in small amounts in cyclohexane which promotes the succinimidyl ester to slip into the ZL channels where it is stabilized. This led to the first known antenna system which allowed extracting excitation energy from donors located inside of the channels by means of FRET and also injecting electronic

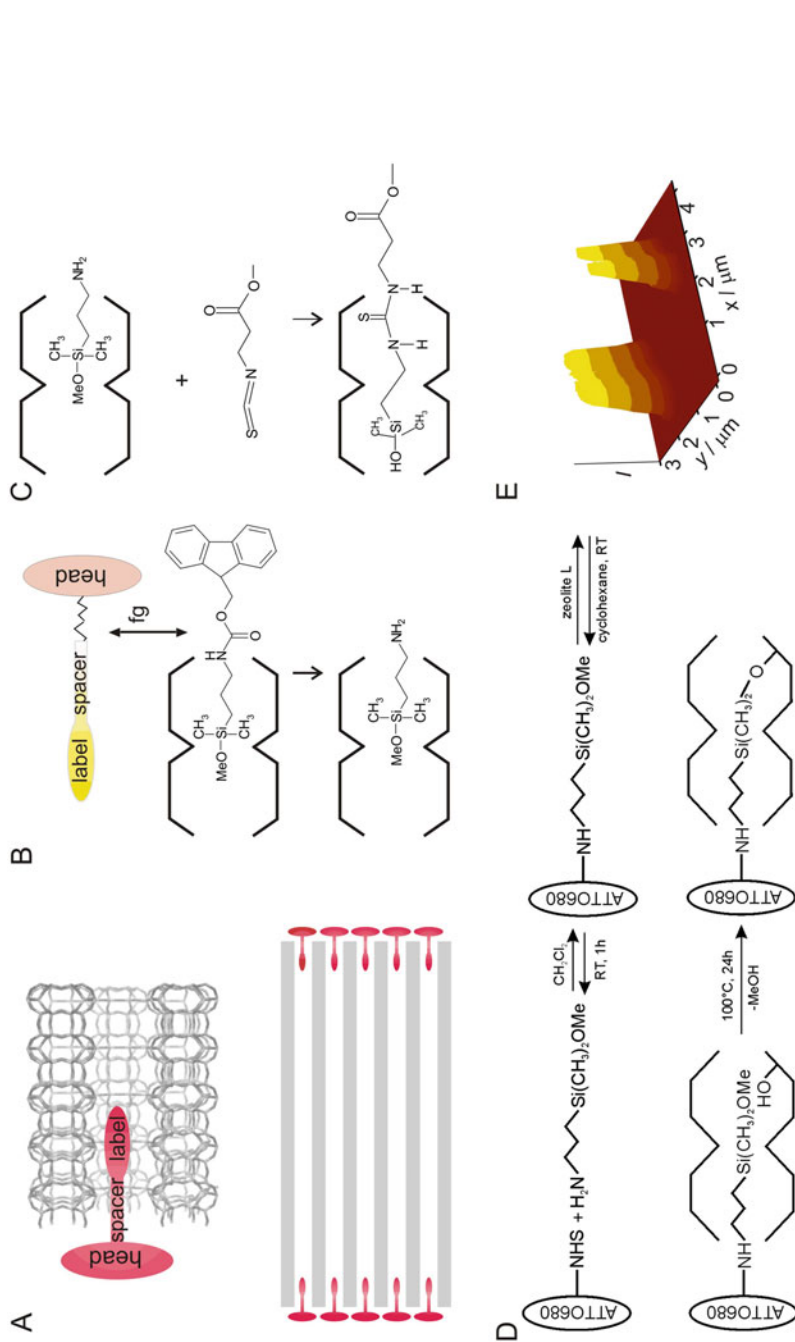


Fig. 7 Stopcock principle. (a) A channel entrance with a schematically represented stopcock molecule consisting of a label pointing into the channel, a spacer, and a head which is too large to enter a channel. The scheme below shows a representation of a ZL crystal plugged with stopcock molecules at all channel entrances. (b) The head of the stopcock is bound to the spacer using a functional group fg such that it can be split off, leaving a reactive amino group that can be used in a next functionalization step. We show this for Fmoc-APMS as stopcock molecule [87]. (c) The amino group is reacted with methyl-3-isothiocyanatopropionate, resulting in carboxyester groups which can be used, e.g., for reacting with DNA [88]. (d) Reaction principle used to covalently bind the ATTO680 amino-reactive dye to the end of a channel, as an example [89]. (e) Confocal fluorescence microscopy image of an ATTO680 functionalized crystal. The relative fluorescence intensity distribution shows that the dye is located at both ends of a ZL crystal [89]

Table 4 Stopcocks

MJ65		Oc1		AnH ₂ T ₄	
RAMC		Terpy		ZnPc n=2,3,4 R=-SiMe ₃ , -NCS, -imidazolium cation]	
Cy02702		H0385		D291	
MFG		BNCO		Ru-ph4-TMS	
B493/503		TRH		BTRX	
ATTO-495-NHS		ATTO-520-NHS		ATTO-565-NHS	
ATTO-610-NHS		MATMS		ATTO-680-NHS	
APMS-FMOC		PAH		TSPCU	
AETES		APTES		DEGAC	
CPTES		TES-PCN		MPTMS	
CP-TMS		Melmz+Sil		GOP-TMS	
C18TES				Bulmz+Sil	

excitation energy from the stopcocks to acceptors located inside of the nanochannel [86]. The reason why the succinimidyl ester was so successful in stabilizing these composites was not well understood at the time of discovery. It is, however, analogous to the stabilization mechanism of fluorenone explained in Fig. 4, namely, via the interaction of the carbonyl group with the ZL extra framework potassium cations [56].

It is interesting that the $-\text{Si}(\text{CH}_3)_2\text{-OH}$ group can act as convenient label, which seems to be hold inside the channels by binding to the potassium cations, similarly as the carbonyl groups. This was used for modifying the channel entrances with amino groups as exemplified in Fig. 7b. Again, key to success is to use the right reaction conditions. The anchored amino group that can be reacted to incorporate other functional groups is seen in Fig. 7c. Fmoc-APMS was used in the first successful demonstration of this principle [87]. (There is a printing mistake in the formula 1 of the Fmoc-APMS, reported in [87]; an O atom is missing.) The number of resulting amino groups linked to the ZL after performing the reaction shown in Fig. 7b was determined by a quantitative ninhydrin colorimetric reaction [90] and compared to the calculated number of channel entrances. The spatial distribution was analyzed by adding the strongly luminescent amino-reactive ATTO610-NHS (Table 4). The N-hydroxysuccinimidyl ester (NHS) group of this molecule is well known to react selectively with primary amino groups in high yield, giving an amide bond. The spatial distribution of the luminescence seen in Fig. 8a shows that the dye is located exclusively on the base of the crystals. This was used to synthesize antenna composites containing DXP inside of the channels acting as donors and ATTO610 as acceptors at the channel entrances [89]. The interpretation of the result in Fig. 8a is

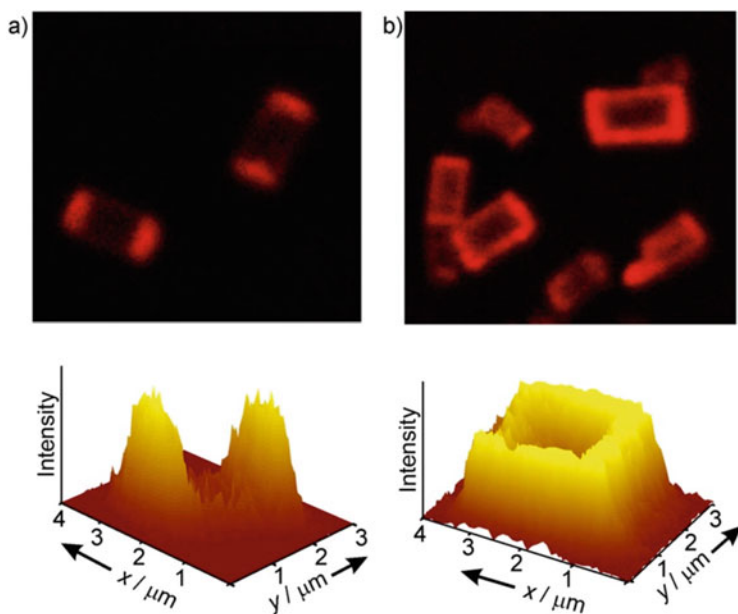


Fig. 8 Confocal fluorescence microscopy images of ZL single crystals. (a) Two crystals functionalized with APMS and coupled to the strongly fluorescing dye ATTO610-NHS. We also show the relative intensity distribution of one of these crystals (bottom). (b) Several crystals with ATTO610-NHS coupled to crystals functionalized with APTES (top) and the corresponding relative intensity distribution of one of these crystals (bottom). Both samples, (a) and (b), are modified with the same amount of dye; therefore the overall fluorescence intensity of the single crystals is similar [87]. Adapted with permission from [87] Copyright Wiley VCH

accentuated when comparing it with the result of the following procedure. Fmoc-APTES, bearing the bulky triethoxysilyl group, was used instead of Fmoc-APMS in the surface modification reaction of ZL under otherwise the same conditions, leading to about the same total amount of $-\text{NH}_2$ groups at the ZL surface, as revealed by the ninhydrin test. The spatial distribution of the amino group was again tested, by reacting the samples with ATTO610-NHS. The confocal fluorescence microscopy images of these samples are shown in Fig. 8b. The difference between the results obtained with the monomethoxysilane APMS and the triethoxysilane APTES is striking. The overall fluorescence intensity of single crystals of both samples is about the same, since the same number of amino groups is available, but the distribution of the amino groups on the ZL surface is completely different: while Fmoc-APMS is observed only at the base of the crystals, Fmoc-APTES is observed to be present over the whole surface. The only way to explain this is by assuming that the smaller $-\text{Si}(\text{CH}_3)_2\text{-OH}$ can enter the channels where it is stabilized, while the more bulky triethoxysilyl cannot. We should add that alternative reagents based on silanol and silylether functional groups for channel modification have been reported [91]. The reaction shown in Fig. 7d is another way of using the $-\text{Si}(\text{CH}_3)_2\text{-OH}$ group for anchoring a molecule at the channel entrance [89]. Amino functionalization of the whole surface was, e.g., used for decorating the ZL with cyclodextrin [92].

The fact that the bulky triethoxysilyl group is too large for entering the ZL channels can be used to fix a stopcock with an appropriate tail and spacer irreversibly to the channel entrance by reacting it with the OH groups present. This was demonstrated using the triethoxysilylated coumarin dye (TSPCU) seen in Fig. 9 [93].

The insertion of TCPCU was performed in CH_2Cl_2 as a solvent. The molecule is not fixed after this step as can be observed by dispersing the material in ethanol immediately after the insertion. Leaching of dye occurs under these conditions, indicating reversibility of this first step. Irreversible fixation was obtained by refluxing the samples in toluene. This procedure leads to the formation of covalent siloxane bonds between the triethoxysilyl and the silanol groups at the entrances of the ZL channels. Again, appropriate choice of the solvent for the insertion step and details of the reaction condition are crucial. Fluorescence from the dye was observed only at the base planes of the cylindrical ZL crystals, indicating selective modification of the channel entrances, similar as seen in Fig. 8a. When ZL crystals containing Py^+ were reacted with TCPCU as indicated above, energy transfer from the

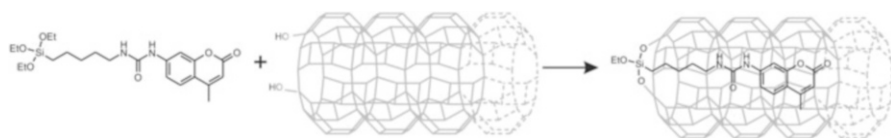


Fig. 9 Selective modification of ZL channel entrances with triethoxysilylated coumarin TSPCU. TCPCU is first inserted and then fixed by reacting the Si-OEt with OH groups located at the channel entrances [93]

coumarin to Py^+ was observed [93]. An interesting extension regarding the versatility of the stopcock principle is achieved by transforming the amino group into carboxyester functionalization as indicated in Fig. 7c using a reaction reported in [94]. The carboxyester functionalization extends the number of chemicals that can be attached to the crystals, for example, DNA [88]. Proof of principle was reported by reacting the so-prepared carboxyester-functionalized ZL with Texas Red hydrazide (TRH, Table 4) and by performing confocal fluorescence microscopy analysis. The results are similar to those seen in Fig. 8a. Energy transfer from donor molecules located inside of the channels to the Texas Red at the channel entrances was observed in samples loaded with Py^+ , which in this case acts as a donor, before modifying the channel entrances [95]. The possibility to selectively modify the base was combining with micro contact printing (mCP) technique. A stepwise procedure allowed modifying the two bases of the ZL crystals selectively with different functionalities [96]. Stopcocks can be very useful for sealing the channels. While stopcocks such as AETES, CPTES (Table 4), and similar may be sufficient for fixing spacious guest from leaving the channels, larger labels and spacers are needed for keeping small guests inside or to prevent penetration of small molecules such as oxygen. Stopcocks bearing imidazolium as label such as Melmi⁺Sil, Bulmi⁺Sil (Table 4), and similar have been shown to be very useful for such purposes [77, 97–99]. Our understanding of stopcocks as closure molecules was much improved by a theoretical study which provided microscopic-level structural information on modified ZL. The interaction of the tail group of the representative molecules AETES⁺ and BuImz⁺Sil (Table 4) with the inner surface of ZL channels, their space filling properties, and the number and quality of the siloxane bonds which fix the stopcock irreversibly at the channel entrance was elucidated [100]. One of the results of this study is that BuImz⁺Sil acts like a cork on a bottle: it seals the ZL channel from the inside, while two AETES⁺ per channel entrance are needed for obtaining a similar effect. The Connolly surface representations shown in Fig. 10, indicating the accessible surface area, are particularly informative: upon bonding of BuImz⁺Sil, the channel entrance is completely blocked. The same effect is observed

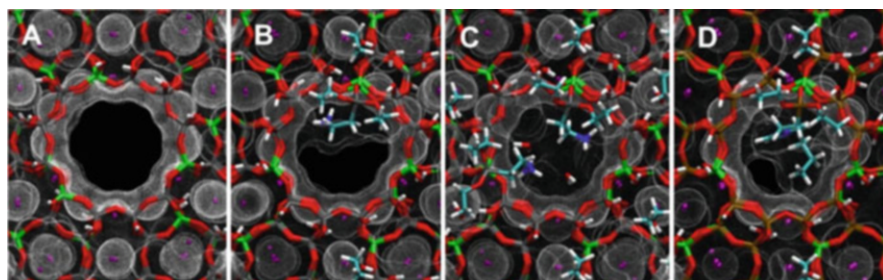


Fig. 10 Connolly surfaces (shown as white dots), indicating the accessible surface area. Atoms are shown as stick models. (a) Unmodified ZL. (b) One AETES⁺ attached to ZL. (c) Two AETES⁺ attached to ZL. (d) BuImz⁺Sil attached to ZL [100]. Adapted with permission from [100] © Wiley VCH

if two AETES⁺ molecules are attached. We do expect that complete sealing is also achieved by using TCPCU (Fig. 9), as another example. The ability of guest molecules to access the channel interior is strongly diminished for larger molecules even with one AETES⁺ molecule attached.

4.2 *Functionalization of the Whole Outer Surface*

Functionalization of the whole surface of ZL and of ZL composites is often desirable for achieving specific properties such as avoidance of agglomeration of the particles, solubilization in a specific environment, and refractive index matching, for attaching reactive groups, and for obtaining biocompatibility or bio-reactivity. Methods rely essentially on reactions with the surface OH groups of ZL. Popular reagents are AETES, APTES, MPTMS, CPTES, MeImz⁺Sil, and BuImz⁺Sil, but also DEGAC, MATMS, and PAH have been used [16, 92, 99, 101–104]. Two principles for obtaining surface modification are illustrated in Fig. 11; optimal choice of the solvent and details of the reaction conditions are important for achievement of the desired result. Reaction (a) illustrates modification of stopcock-modified composites where the stopcocks have no affinity to the modifying reagent. Reaction (b) includes sealing the channel entrances. This means that the molecules must bear a tail which has good affinity to the channel entrance and a base which is not reactive in the self-organization step. Change of the solvent may be necessary for the fixation step. For example, ZL can be functionalized with APTES leading to amino-functionalized particles, or it can be reacted with BuImz⁺Sil leading to composites bearing very different properties.

Progress regarding selective surface modification has been reported by several authors. The site-selective immobilization of dyes and different proteins recognizing entities at the surface of ZL crystals using mild radical nitroxide exchange reactions opens interesting possibilities for obtaining new properties [105, 106]. De Cola et al. reported that modification of ZL with magnetically active Fe₃O₄ particles can be achieved by simply mixing the ZL with a large excess of Fe₃O₄ nanoparticles in water [107]. A novel type of ZL/polymer hybrid material was obtained by Studer et al. who described the preparation of polymer brush particles using surface-functionalized ZL crystals as macro initiators in controlled radical polymerization processes. Copolymerization of a photo-cleavable monomer and subsequent spin trapping of functionalized nitroxides under UV irradiation lead to a variety of highly functionalized ZL-based core-shell particles in a modular approach. These ZL/polymer hybrids feature a softer surface and higher densities of functionalities, in comparison to crystals modified with monolayers, and thus exhibit a higher capability to interact [108, 109].

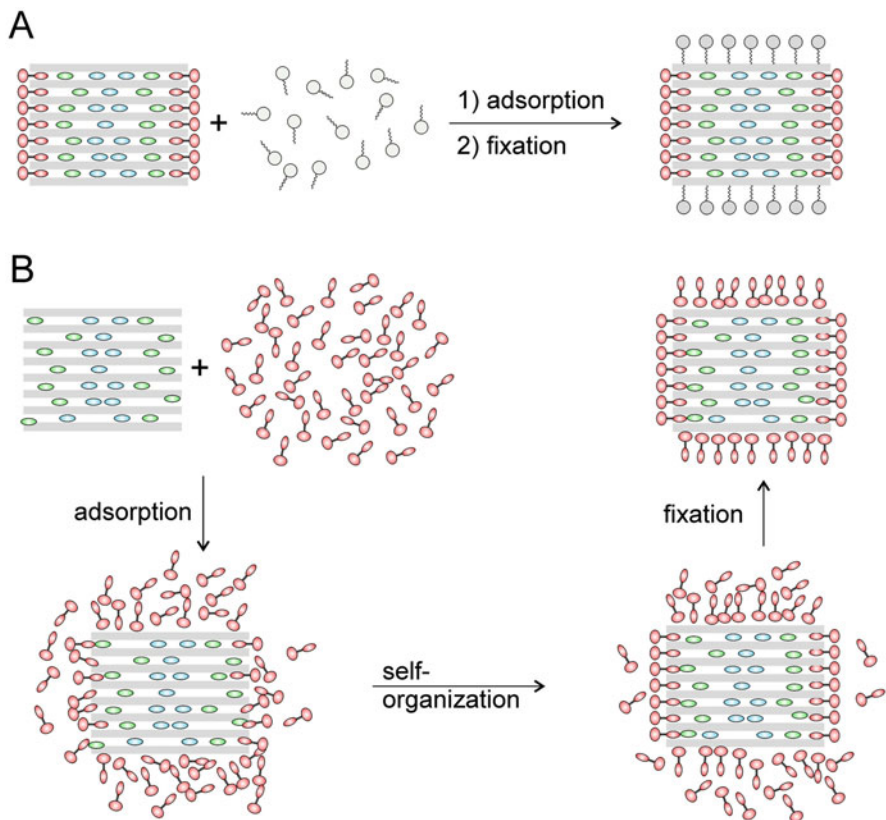


Fig. 11 Two principles for obtaining surface modification. (a) Modification of stopcock-modified composites where the stopcocks have no affinity to the modifying reagent. (b) Sealing the channel entrances and modification of the coat using the same reagent

5 Patterns of ZL Crystals

Hierarchically organized structures, presenting successive ordering from the molecular up to mm or cm scale, are of great interest. They allow establishing direct relationship between the molecular arrangements and the macroscopic properties. A high degree of supramolecular organization is important in device chemistry, for attaining the desired macroscopic qualities. Possibilities for achieving such organization are the self-assembly of the zeolite crystals into oriented structures, the embodiment into nanofibers, contact with biological objects, solubilization in polymer matrices, and the preparation of mono-directional materials. Self-assembly can be guided by applying stopcock functionalization of ZL crystals that may contain different kind of guests. The beauty of this approach is that single building blocks can be connected in such a way that they can keep their individual properties but in addition, through controlled assembly, generate new functions not present in the

separate components. This allows the generation of novel materials with individual nano-characteristics that can be translated into macroscopic properties. Some early examples of such self-assembly patterns are reported in Fig. 12.

5.1 Oriented Monolayers

The arrangements that attracted most interest are dense monolayers of ZL crystals with the *c*-axis oriented perpendicularly with respect to the surface. The preparation of dense monolayers of zeolite crystals in the nanometer to micrometer size regime was originally motivated by the desire to designing chemical structures on electrode surfaces that redefine the chemical and physical microenvironment in which heterogeneous electron transfer reactions occur [118–122]. The first high-quality dense monolayer was achieved with crystals of zeolite A of rather perfect cubic morphology [123]. Strongly luminescent silver sulfide quantum dots were prepared in the first ship-in-a-bottle synthesis on such a zeolite A monolayer [124]. The preparation of oriented ZL monolayers presented an additional challenge with respect to the cubic zeolite A layers. The first successful preparation of such oriented ZL monolayers illustrated in Fig. 12b was reported simultaneously by G. Calzaferri et al. and by K. B. Yoon et al. in the same issue of *Angewandte* [111, 112]. This initiated much interest because this pattern can be used in optical and electro-optical experiments, for selective gas separation membranes, chemical sensors, micro contact transfer printing, as well as studying cell adhesion or neuron properties, both of biological and biomedical interest. Different ways for obtaining such monolayers have been explored. Disc-shaped crystals are easier to handle than elongated ones. The narrower the size distribution and the more perfect the morphology of the crystals, the higher the quality of the monolayers. The general principles for monolayer preparation reported in refs. [111, 123, 125] remain valid. Li et al. reported an interesting method for obtaining highly luminescent and transparent ZL monolayers [126]. A variety of preparation techniques, including utilization of strong magnetic fields or optical tweezer forces, have been investigated in order to meet special needs [73, 76, 109, 123–136]. Subsequent insertion of guests into the channels and addition of stopcocks are, however, only possible if the free channel openings are not blocked or damaged during the preparation of the monolayer [111]. A special example concerns the suppression of luminescence quenching of a ruthenium complex by oxygen. The Ru²⁺ complex (Ru-ph4-TMS, Table 4) has a tail which nicely fits into the channels of ZL. The head is positively charged and can therefore bind electrostatically to the negatively charged channel entrance, as illustrated in Fig. 13. The van der Waals model indicates that the size of the head is such that it plugs the channels quantitatively and the center to center distance of 18.4 Å between two channel entrances ensures that there is enough space for the heads of adjacent Ru-ph 4-TMS stopcocks. It is well known that the luminescence of such Ru complexes is quenched by O₂ via a diffusion-controlled collision [137–

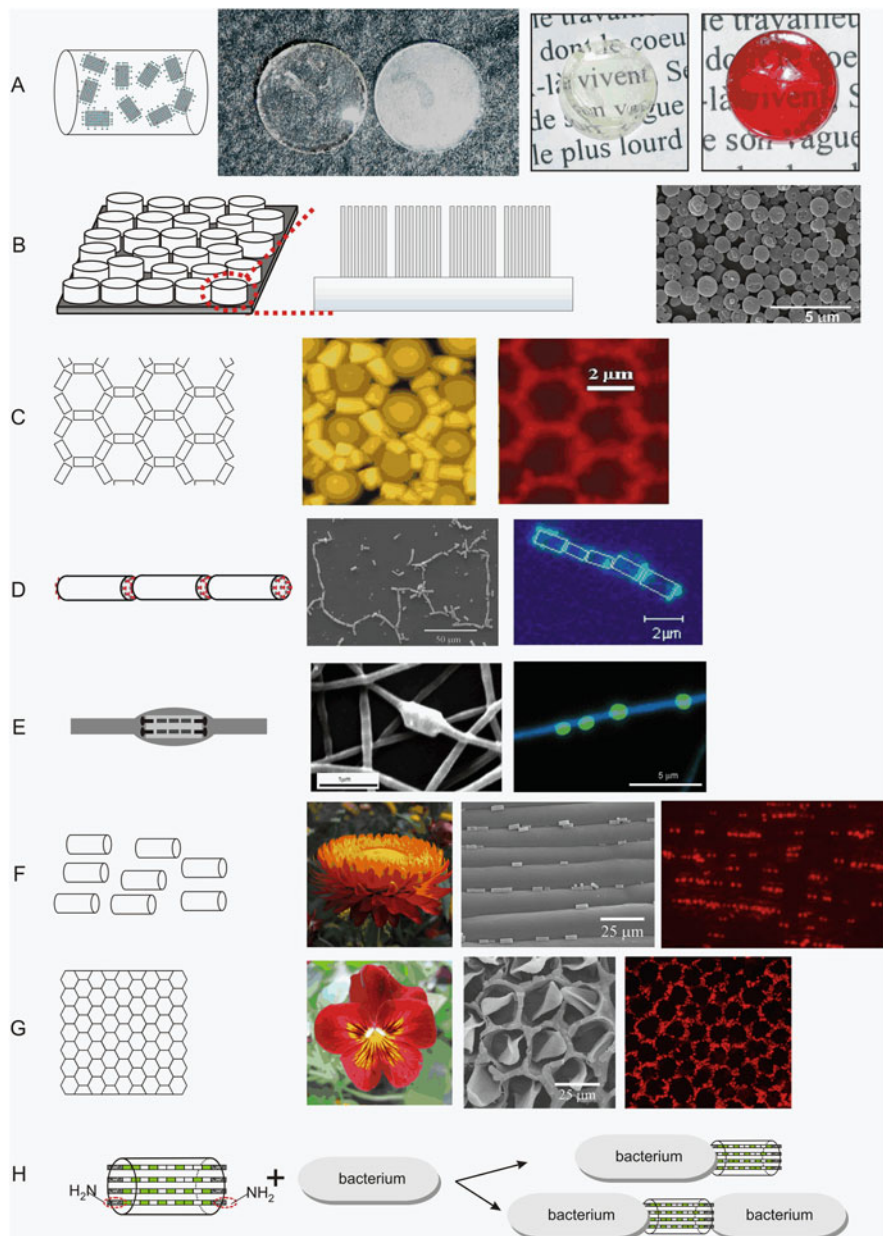


Fig. 12 Solubilization and self-assembly examples of ZL crystals. (a) Refractive index matching of ZL crystals embedded in a polymer matrix [103, 110]. (b) Monolayer of oriented ZL crystals standing on their base [111, 112, 129]. (c) Crystals arranged in a hexagonal pattern by a surface tension-driven self-assembly process on a PDMS/PS film, as well as by using breath figure formation and soft lithography techniques [113, 114]. (d) Crystals modified with D291 [101] and with AnH₇T₈ (blue) [46] at their base, assembled as chains. (e) Electrospun nanofibers embedding dye-ZL crystals. The crystals are oriented along the fiber axis [115]. (f) ZL crystals oriented by the elongated epidermis cell walls of a strawflower [116]. (g) Self-assembly of ZL crystals on biological self-cleaning surfaces. The ZL is located on top of the epidermis cell walls of a horned pansy. They are thus arranged in hexagonal patterns [116]. (h) Self-assembly of amino stopcock-functionalized ZL crystals with bacteria [117]

139]. Interestingly, this luminescence quenching is much weaker when Ru-ph4-TMS is bound to ZL in a dichloromethane suspension.

The explanation is that this is due to the delocalization of the emitting $^3\text{MLCT}$ state over the tail of the bpy-ph4 ligand which is located inside of the channels and thus shielded by the ZL. This hinders the O_2 in making successful collisions with the tail [140]. An even larger shielding effect can be observed when the Ru-ph4-TMS stopcocks are attached to a ZL monolayer. The luminescence lifetime of the attached Ru-ph4-TMS stopcock was measured to be nearly the same under O_2 and under N_2 atmosphere under these conditions [127]. The emission spectra of the (Ru-ph4-TMS)-ZL monolayer in N_2 and in O_2 atmosphere are shown in the lower part of Fig. 13. The time delay between the curves shown is 200 ns. The great similarity of both emission spectra is remarkable. The lifetime in O_2 and in N_2 atmosphere is about the same as that of the free complex in solution under N_2 atmosphere ($\tau = 1,207$ ns). This means that the ZL host provides an excellent shielding of the emitting $^3\text{MLCT}$ state of Ru-ph4-TMS, preventing collisions between the O_2 quencher and the sensitive tail of the stopcock. This also supports the interpretation that the excited state is essentially localized on the ph4 tail [141]. Disc-shaped crystals with an average length of 250 nm and an aspect ratio, length to diameter, of 0.3 have been used for the preparation of the oriented monolayers used in these experiments. The oriented ZL monolayers were prepared according to the procedure described in [111], using CP-TMS (Table 4) as covalent linker.

De Cola et al. applied successfully micro contact printing (MCP) [142] to obtain well-ordered and uniformly oriented ZL monolayers on conductive surfaces without any chemical modification of the ZL or the substrate [131]. They created particular patterns with ZL crystals that were filled with a fluorescent dye. A similar technique was used for realizing spatial controlled channel entrances functionalization of disc-shaped ZL nanocrystals with two different functionalities. A stepwise procedure allowed modifying specifically both bases of the ZL crystals: one with a suitable chemical group, e.g., ATTO-565, and the other one with a functionalized nano-object, e.g., magnetic iron oxide nanoparticles [135].

5.2 Chains, Files, Hexagonal, and Other Arrangements

ZL crystals have been arranged in different patterns, some of which are illustrated in Fig. 12. The size, the aspect ratio, and the quality of the ZL particles, but also their surface modification, are factors which determine type and quality of patterns that can be created. The formation of files, Fig. 12d, is promoted by appropriate stopcock modification so that the interaction between the stopcocks of two crystals approaching each other is stronger than any other interactions [101, 143, 144]. Elongated chains can be obtained using electrospinning of a polymer, Fig. 12e [115], and self-assembled nanofibers of fluorescent dye-ZL crystals [145]. Hexagonal patterns, Fig. 12c, have been obtained using a surface tension-driven auto-assembly process

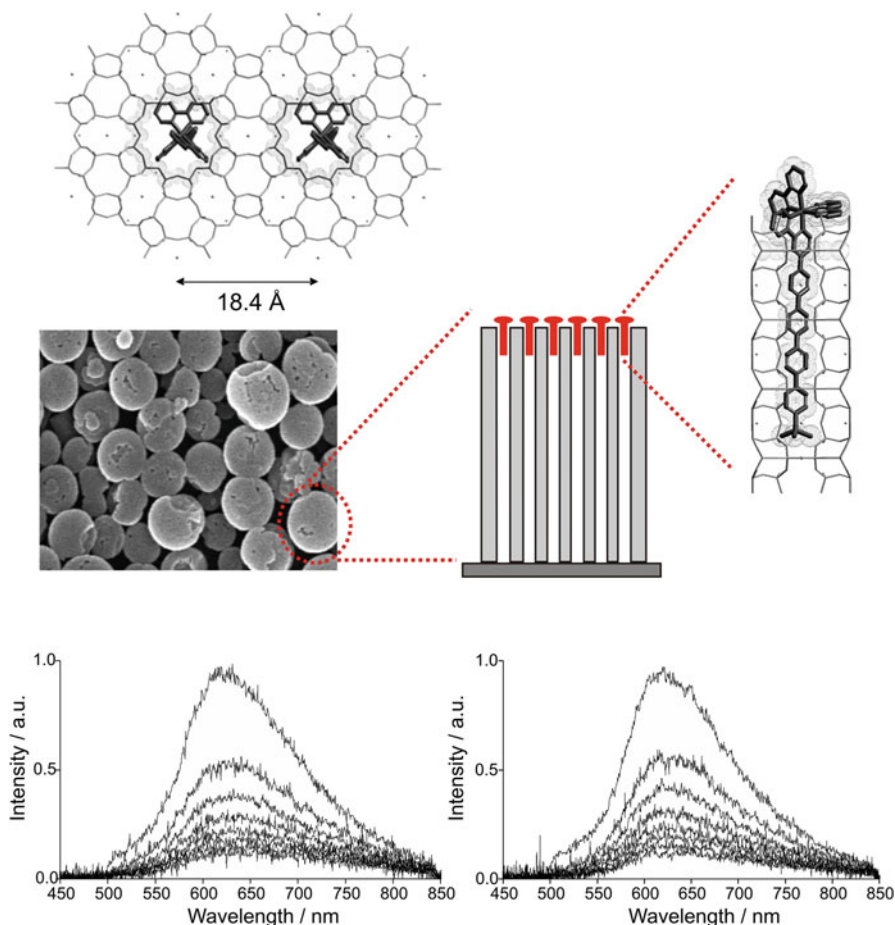


Fig. 13 Suppression of luminescence quenching due to protection by the ZL. Top: Electrostatic binding of positively charged stopcock molecules Ru-ph4-TMS to the negatively charged ZL channel entrance. The distance between two channel openings is indicated. Middle: We see on the left side a SEM image of a ZL monolayer. The diameter of the crystals is about 600 nm. The cartoon in the middle illustrates the orientation of the channels with respect to the surface plane. The van der Waals interaction illustrates the protection of the tail which penetrates into a channel. Bottom: Time-resolved emission spectra of a (Ru-ph4-TMS)-ZL monolayer in toluene under O_2 (left) and under N_2 (right) atmosphere. The spectra were recorded at room temperature under excitation at 460 nm. The delay increment between consecutive spectra is 200 ns [127]

[113] or by immersing petals of different flowers into a suspension containing dye-ZL crystals, Fig. 12g [116]. Hashimoto et al. examined the preparation of close-packed monolayers on large areas. They prepared unidirectional alignment in the horizontal packing structures (parallel alignment), Fig. 12f, by employing pre-grooved substrates [132]. Utilization of optical tweezer [146], optical assembly of bio-hybrid micro-robots [147], or opto-mechanically assisted assembly of

surface-functionalized ZL hybrids [109] for the construction of complex functional ZL patterns are innovative approaches for obtaining fascinating arrangement.

6 Structure of the Guest-ZL Composites

The structure of the host ZL is well known [12, 23, 24, 148]. This provides a sound basis for elucidating the structure and interactions of the guests within the host. The current powerful techniques available to study host-guest compounds have been reviewed by Tabacchi [1]. The presence of guests usually lowers the symmetry of the objects, thus complicating structural characterization of the confined species with standard crystallographic methods. These limitations have been overcome in modern crystallographic techniques which can integrate single crystal, powder, and neutron diffraction data with pair distribution function analyses. This has allowed, as an example, to determine the structure of self-assembled composites of ZL with the perylene diimide dye tb-DXP, revealing the fundamental host-guest interactions at atomistic level [44]. Vibrational spectroscopy (IR, Raman, INS) are prime techniques for elucidating host-guest interaction pattern [40, 44, 55]. Confocal luminescence spectroscopy tells us the orientation of the electronic transition dipole moment (ETDM) which is directly connected to the orientation of the molecules with respect to the channels [14, 149, 150]. Electronic absorption and luminescence properties of the guests are sensitive and sometimes very sensitive to interactions of the guests with the environment and on the guest-guest distances and orientations as we shall discuss in the next two chapters. Computational studies are of overwhelming importance for advancing our understanding of host-guest systems. They enable to capture structural and dynamical features and provide explanations otherwise difficult or impossible to gather directly from experiments [44, 49, 56, 79, 151–160]. Calculations, combined with experiments, have shown that dye-ZL composites can withstand GPa pressures without alteration in the organization of the guests. This is an important information regarding the extension of the application of ZL-based optical devices [49, 160, 161].

Newsam presents in 1989 the complete structure results of powder neutron diffraction studies of a dehydrated potassium ZL at 298 and 78 K and of the same ZL at 78 K containing, on average, one molecule of perdeuteriobenzene/u.c [148]. He observed that little change in structure accompanies dehydration, benzene sorption, or temperature change in the range of 298 to 78 K. The non-framework K^+ configuration shows only subtle changes over the range of conditions studied. Perdeuteriobenzene was observed at 78 K in “capping” positions above the channel wall K^+ . Simple atom-atom potential modeling of the benzene site based on the structural results yields only a small activation barrier to benzene molecule reorientation.

It was a surprise to observe that nearly every u.c. could be filled with one methylviologen cation MV^{2+} using room temperature ion exchange, despite of the fact that the length of this molecule exceeds by far the 0.75 nm length of a u.c. This

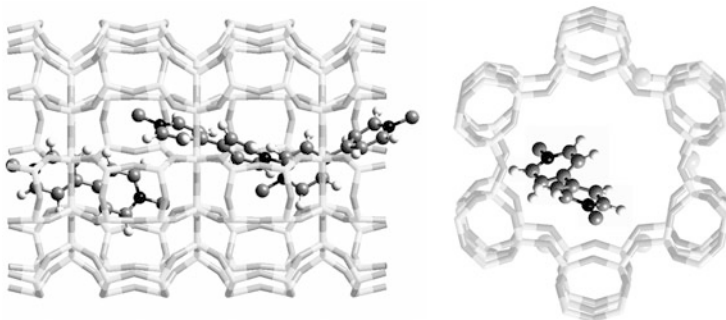


Fig. 14 Location of MV^{2+} inside a channel of ZL. Left: Side view of the channel depicting a likely arrangement of the molecules along the channel. Right: Top view along the channel axis showing one possible position and orientation of a molecule and the atom labeling scheme [40]

means that two MV^{2+} must share part of the volume of a u.c., but how? The puzzle was solved by applying Rietveld refinement of X-ray data and molecular modeling. It turned out that the angle between the main molecular axis of MV^{2+} and the c -axis of the ZL is 27° with the MV^{2+} lying along the channel wall, as illustrated in Fig. 14. This tilt makes it possible to have a MV^{2+} cation in each cage, despite the fact that the MV^{2+} is longer than the repeat distance along the channel of the ZL. The MV^{2+} cannot be in a periodic chain along the channel axis. Neighboring MV^{2+} must, therefore, be rotated around the sixfold axis, which does increase the distances between the cations. For a rotation of 120° (threefold screw axis), the intermolecular contacts $MV^{2+} \dots MV^{2+}$ along the c -axis have normal values of 3.3–3.4 Å. The close contact with the channel wall is the result of weak MV^{2+} -zeolite interactions. This finding was supported by IR and Raman spectroscopic data [40].

The, at the time of finding [55], surprising observation that fluorenone is not substituted by water in a fluorenone-ZL composite could be explained as a result of extensive first-principles investigations. It turned out that the interaction of the fluorenone carbonyl group with the ZL extra framework potassium cations is responsible for the dye stabilization in the ZL nanochannels; see Fig. 4 [56]. Arletti et al. prepared composites with maximally packed fluorenone molecules, namely, 1.5 molecules per u.c., and elucidate their structure by integrated multi-technique analyses. They thus discovered the first quasi 1D supramolecular nano-ladders running along the ZL channels. Spatial and morphological control provided by the nanoporous matrix combined with a complex blend of strong dye-ZL and weaker dye-dye van der Waals interactions is the origin of this unique architecture, which is also stabilized by the hydrogen bond network of co-adsorbed water molecules surrounding the dye nano-ladder and penetrating between its rings [48, 49].

TH^+ -ZL stands for the beginning of my interest in dye-ZL composites; see Fig. 1. It is very satisfying that the structure of the TH^+ -ZL composites has been elucidated by Arletti et al. despite of the fact that the configuration of ZL with its high sixfold symmetry and the maximum loading of about 0.27 TH^+ per u.c. makes Rietveld structural refinement difficult. The authors succeeded in elucidating the geometry

and the localization of the TH^+ , despite of this difficulty. They found that TH^+ is aligned parallel to the 12MR and located on the mirror planes parallel to the *c*-axis. Water molecules interact strongly with the dye and form a kind of solvent-matrix tube shaped around the TH^+ [19].

Perylene dyes have been used in many dye-ZL composites because of their spectroscopic properties and their chemical robustness which allow preparing systems with a large variety of interesting properties [14, 16, 46, 83, 87, 159, 162–164]. Knowing details regarding the structural characteristics of such composites is therefore important. Hence, it is satisfactory that Gigli et al. have been able to establish a microscopically detailed picture of a hybrid composite of ZL with the perylene diimide tb-DXP at both hydrated and anhydrous conditions by applying integrating experiments with different time scale and radiation source (IR, XRPD, total scattering), including first-principles DFT modeling [44]. A graphical representation of the results is seen in Fig. 15. The asymmetric positioning of the dye in

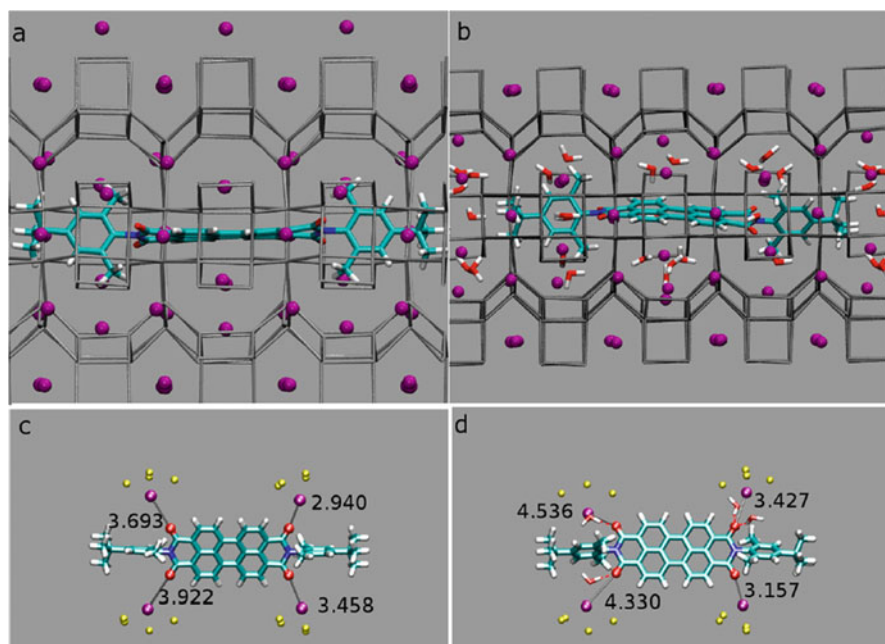


Fig. 15 Structure of a hybrid tb-DXP-ZL composite. (a) Graphical representation of the minimum energy structure of the anhydrous tb-DXP-ZL system. Only the Al/Si atoms of the framework (gray sticks) are represented. C atoms are represented in cyan, N in blue, O in red, and H in white. The K^+ are shown as purple spheres. (b) Optimized structure of the hydrated tb-DXP-ZL. (c) The tb-DXP molecule extracted from the optimized anhydrous system, along with the four closest potassium cations. (d) The tb-DXP molecule extracted from the optimized hydrated system. Also shown are the four closest K^+ and the water molecules hydrogen bonded (red-dashed lines) to the carbonyl oxygen atoms. The framework oxygen atoms (yellow spheres) close to the potassium cations are shown as well in (c) and (d). In panels c and d, the four shortest $\text{K}^+\cdots\text{OCO}$ distances (in Å) are indicated [44]. Adapted with permission from [44] Copyright American Chemical Society

the ZL channel is determined by two factors: shape volume constraints and relative strength of competitive interactions among confined species. This work deepens the understanding of host-guest interactions in dye-ZL composites, a key requirement to master the finely tuned mechanisms governing supramolecular organization in confined nano-spaces.

The orientation of oxonine Ox⁺ and pyronine Py⁺ inside of channels of ZL crystals was investigated by means of fluorescence microscopy and single-crystal imaging. The result was a cone-shaped distribution of the ETDM with a half-cone angle of 72° [149]. This result was not well understood based on geometrical arguments because the ZL structure gives room for only two possible arrangements of the molecules' long axis: a half-cone angle of up to 40° for Ox⁺ and an angle of about 90° with respect to the *c*-axis of ZL. The measurements were therefore reinvestigated by probing Ox⁺-ZL composites using two-photon fluorescence polarimetric microscopy. The result obtained over several points measured on several crystals was a half-cone angle distribution of 70–85°, thus confirming the result of the initial study [165]. How can this be? The puzzle was solved using first-principles quantum chemical, molecular dynamics calculations [153]. It turned out that an angle in the range of 70–85° is not an energetically favored orientation, and it might only be visited transiently by Ox⁺ at room temperature. The results of the calculations suggested different ways to interpret the optical microscopy data, namely, the experimental results derive from the superposition of differently oriented Ox⁺. The most stable orientation in the hydrated system, which corresponds to the optical microscopy experiment conditions, is 88°. However, other conformations, with Ox⁺ nearly aligned to the channel, are quite close in energy and can be easily accessed at room temperature. Following this argument, the actual distribution of Ox⁺ inside the ZL channel is understood to result from a larger portion of Ox⁺ molecules perpendicularly oriented and a smaller fraction approximately aligned to the channel. The optical microscopy data are therefore interpreted as the resultant, i.e., the “vector sum” of components arising from an Ox⁺ population characterized by non-uniform orientation, mainly perpendicular to the channel but contaminated by a fraction of molecules approximately aligned to the channel. The results for Py⁺ are similar [153]. Even though the parallel orientation is not the equilibrium arrangement for the hydrated Ox⁺-ZL composite, the low mobility of Ox⁺ in the presence of water makes it likely that a small though appreciable number of Ox⁺ molecules could remain frozen in such an arrangement for some time. Moreover, the low Ox⁺ mobility, detected along the simulations, is in line with the experimental observation that diffusion of Ox⁺ inside ZL is very slow even at 100°C [43]. Furthermore, such a fraction of nearly parallel Ox⁺ and Py⁺ is responsible for the J aggregate coupling observed in ZL, a fact which cannot be understood otherwise [166]. This demonstrates the enormous power of the combination of confocal microscopy and advanced computational techniques for understanding the structure of guest-host composites.

The electronic S₀-S₁ (1La) transition of methylacridine MeAcr⁺ is relatively weak and oriented parallel to the *y*-axis, as indicated in Fig. 16a), while the more intense S₀-S₂ is parallel to *z* (1Lb). Both transitions are of π-π* type

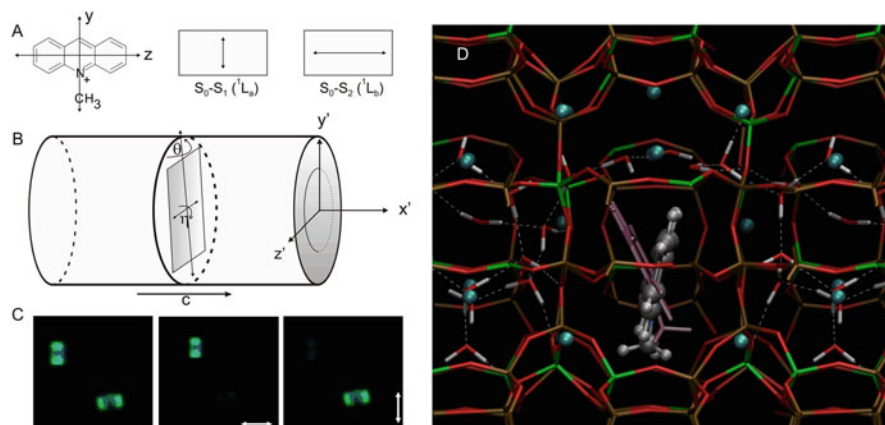


Fig. 16 Structure of the MeAcr⁺-ZL composite. Definition of the orientation of the S₀-S₁ (¹L_a) and S₀-S₂ (¹L_b) electronic transition dipole moment (ETDM). The angles η and θ describe the orientation of MeAcr⁺ inside of the ZL channels. (a) MeAcr⁺ is sketched as rectangle, and the orientations of the ETDMs are indicated as double arrows. The drawing (b) shows the position in the (y',z') plane which corresponds to the angles $(\eta, \theta) = (90^\circ, 90^\circ)$. (c) Fluorescence microscopy images of two MeAcr⁺-ZL crystals with a length of about 2 μm : left, observed without polarizer; middle and right, observed through a polarizer, the orientation of which is indicated by the double arrow [128]. (d) Superposition of the minimum energy structures of the MeAcr⁺-ZLx18H₂O composite (with MeAcr⁺ in ball-and-stick representation, C gray, N blue, H white) and of dry MeAcr⁺-ZL (with MeAcr⁺ in pink, stick representation). Color codes: Si brown; O red; Al green; K cyan; H white. The dashed lines represent hydrogen bonds [154]

[167, 168]. Absorption spectra of the S₀-S₂ band have been measured on oriented MeAcr⁺-ZL monolayers [128]. These data allow to interpret the single-crystal fluorescence microscopy observations seen in Fig. 16c. We observe that the crystal parallel to the x'-axis vanishes if the polarizer is set in this orientation and the crystal perpendicular to x' vanishes if the polarizer is turned by 90°. The question regarding the equilibrium orientation of the dye was fully resolved by performing extensive computational studies. They showed that among the different possible orientations of the dye, the most stable structures are characterized by large η and θ values, close to 90°, at both dry and hydrated conditions. This is illustrated in Fig. 16d where the ball-and-stick representation refers to hydrated conditions while the pink, stick representation refers to dry MeAcr⁺-ZL. Analysis of these results showed that the most stable orientation of MeAcr⁺, which features both its long and short molecular axes nearly perpendicular to the channel axis, is mainly determined by dye-ZL electrostatic interactions but also depends on the co-solvent water. The perpendicular arrangement implies dye confinement in a single ZL cell and allows the nearby cells to be fully occupied by water molecules as in pristine ZL structures. The dye is not hydrogen bonded to water or to the ZL framework oxygens, and it is hydrophobically solvated by water molecules [154].

We already mentioned that high-pressure studies of fluorenone-ZL composites revealed an impressive stability even at GPa pressures, evidencing a pressure-

induced strengthening of the interaction between the fluorenone carbonyl group and the ZL potassium cations, thus indicating a way to the realization of, e.g., optical devices able to maintain their functionality under extreme conditions [49]. The high baric stability of the ZL framework was confirmed in a compressibility behavior and pressure-induced over-hydration study [161].

7 Electronic Absorption and Luminescence Properties of the Host-Guest Composites

The electronic properties of the guests are influenced by interactions with the host, with the charge compensating cations, with co-guests, by interactions between the guests, and by the spatial restrictions imposed by the host. It is important to distinguish between the influence of such interactions on spectroscopic data and the frequently present influences of physical effects such as light-scattering, light-guiding, and self-absorption which is usually followed by re-emission, in order to avoid misinterpretation. Pure ZL crystals do not show any electronic absorption in the visible and in the near UV up to about 200 nm or even 180 nm. The weak vibration overtone absorption present in the near IR must be considered in near IR absorption and luminescence spectroscopy. Diffuse reflectance techniques are popular for measuring electronic absorption and luminescence spectra. Measurements on very thin layers covered by a refractive index matching polymer or oil allow analyzing and, if desired, suppressing intra-particle effects such as self-absorption, saturation of single particles of samples with high loading, or wave-guiding processes. These processes may affect considerably the shape of the spectra, the luminescence quantum yields, and luminescence decay [20, 46, 169–172]. The influence of extra- and intra-particle self-absorption and re-emissions on the shape of the spectra and the luminescence quantum yield has been discussed in detail [171]. These effects do not concern the luminescence properties of rare earth-ZL composites because for them self-absorption is usually negligible. The nature of the cations that must compensate 3.6 negative charges per u.c. is of considerable importance. Their impact depends on the type and concentration of the co-solvent which has been water in most cases investigated so far. Little is known regarding the influence of organic co-guests such as n-octane and similar. The heavy atom effect [173], which enhances singlet to triplet intersystem crossing and thus triplet emission, was studied by Ramamurthy et al. The authors compared the influence of alkali cations and of Tl^+ on the phosphorescence yield of naphthalene and related aromatic guest in zeolite X and Y. They observed a decrease of $S_0 \leftarrow S_1$ emission accompanied with an increase of the phosphorescence yield in the following order: $Li^+ \approx Na^+ \approx K^+ < Rb^+ < Cs^+ \ll Tl^+$ [174, 175]. This corroborates with the Z^4 increase of the efficiency of spin-orbit coupling with the atomic number Z [176]. Similar studies for ZL are missing. It seems, however, reasonable to assume that a basically similar heavy atom effect should apply. Hashimoto et al. observed

enhanced phosphorescence lifetime even at room temperature for 9-ethylcarbazole, which tightly fits into the ZL channels. They reported dimer formation for anthracene and for naphthalene, as observed by excimer emission. The photo-physics of anthracene and naphthalene in ZL was observed to be remarkably different from that in solution and also different from that in large-pore faujasite zeolites where the framework exerts only weak conformational control over the guest molecules [177]. More attention has been devoted to the influence of co-cations on Brønsted acidity and its impact on luminescence properties, as will be discussed in Sect. 7.3.

7.1 Absorption and Luminescence Spectra of Organic Guest-ZL Composites

The conformational control of the ZL framework over the guest molecules leads to enhanced luminescence yields for guests if conformational flexibility is responsible for deactivation pathways [14]. The shape of the absorption spectra is often less influenced by the host than one might perhaps expect. Figure 15 illustrates the microscopically detailed picture of tb-DXP inside of the ZL channels, as established using different experimental techniques and DFT modeling. This is an ideal situation for a comparison of the absorption spectra of the perylene dyes tb-DXP (blue), tb-DXT (green), and tb-DXQ in solution with the spectra of the corresponding dye-ZL composites. We present it in Fig. 17. The finding that the vibronic structure, known to be characteristic for perylene dyes in solution, Fig. 17a), is also present in the ZL composites, Fig. 17b, reflecting an observation valid for many other dye-ZL composites. We therefore discuss it in more detail by marking and comparing the positions of the 0–0', 0–1', 0–2', and 0–3' transitions, which can be identified easily in spectra of diluted samples of these dyes, both in solution (Fig. 17a) and in the dye-ZL samples (Fig. 17b). The broadening of the spectra of the dye-ZL composites with respect to the solution spectra is smaller than one might expect. The uncertainty of the band positions is small for the 0–0' transition. It increases with increasing energy because the bands are not fully resolved. It also increases from tb-DXP to tb-DXT to tb-DXQ but it is not larger in the dye-ZL composites. Their energy can be sufficiently well determined to justify the conclusions presented below. We should add that the same is seen for all 11 PDIs reported in [16]. The numerical values of the positions and of the energy differences $\Delta E[\nu' - (\nu' + 1)]$ between the 0– ν' and the 0–($\nu' + 1$) transitions are reported in Table 5. The comparison of the spectra of the dyes in solution and in ZL reveals that the broadening is small, that the shift of the 0–0' transition is small, and that the vibronic pattern seen in solution is preserved for the three dyes after intercalation into the nanochannels of ZL. This is remarkable. The data collected in Table 5 allow the conclusion that the energy difference $\Delta E[\nu' - (\nu' + 1)]$ between the 0– ν' and the 0–($\nu' + 1$) transitions is the same in solution and in ZL, within the experimental uncertainty. These observations signify that the part of the molecules responsible for the $S_0 \rightarrow S_1$ (π – π^*) is not

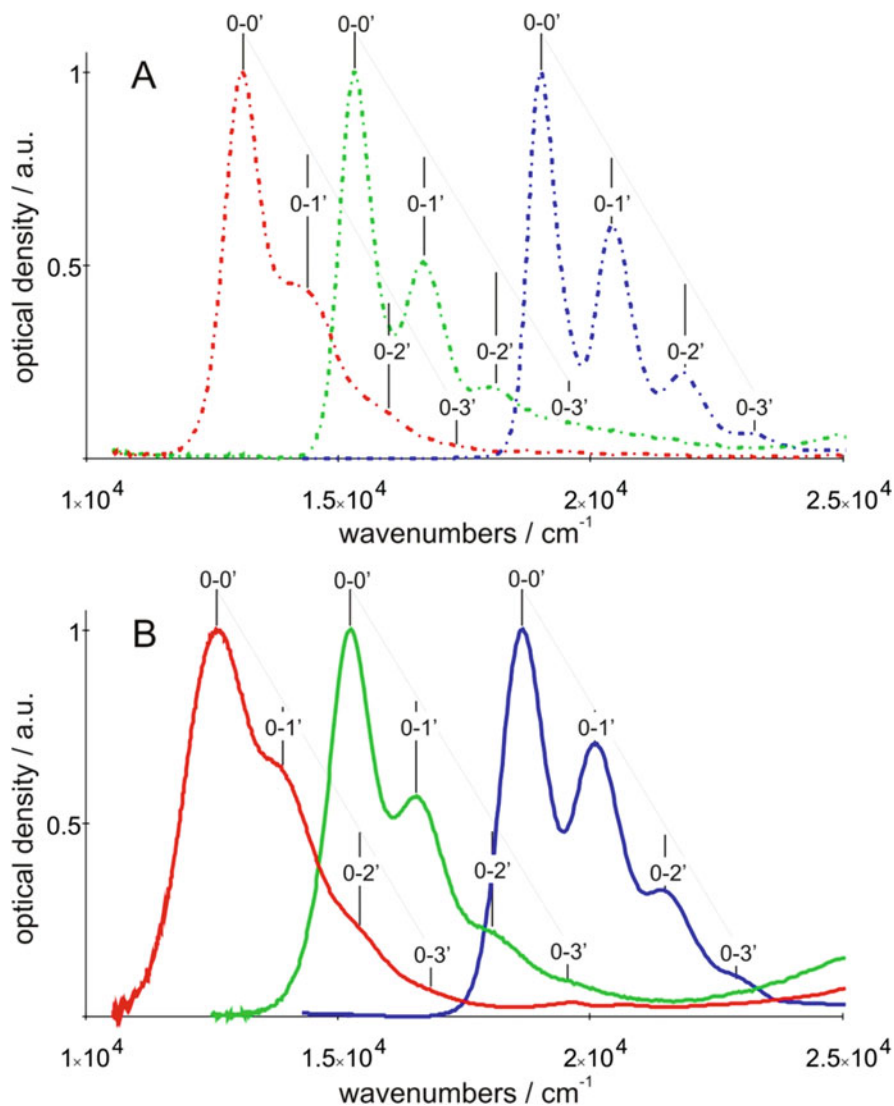


Fig. 17 Comparison of the $S_1 \leftarrow S_0$ ($\pi-\pi^*$) vibronic structure of tb-DXP, blue; tb-DXT, green; and tb-DXQ, red [16]. (a) Spectra were measured in 5×10^{-6} M DCM solutions (dash-dot). (b) The spectra of the dye-ZL composites (low loading in the order of 0.002, ambient conditions) (solid) were recorded using the thin layer OGS technique [178]

affected by the host, including the co-solvent water. This fully agrees with the results reported in Fig. 15 and the finding that the carbonyl groups of these dyes bind to the zeolite extra framework potassium cations [44].

We now discuss the spectra of MeAcr^+ -ZL. The first $\pi-\pi^*$ ($S_1 \leftarrow S_0$) transition, which establishes the S_1 state from which the cationic dye Me-Acr^+ emits, is weak

Table 5 Vibronic bands of tb-DXP, tb-DXT, and tb-DXQ in DCM and in ZL

Transition	tb-DXP (DCM)	ΔE [$\nu' - (\nu' + 1)$]	tb-DXT (DCM)	ΔE [$\nu' - (\nu' + 1)$]	tb-DXQ (DCM)	ΔE [$\nu' - (\nu' + 1)$]
0-0'	19,010	–	15,290	–	13,020	–
0-1'	20,410	1,400	16,670	1,380	14,290	1,270
0-2'	21,830	1,420	17,990	1,320	15,870	1,580
0-3'	23,150	1,320	19,460	1,470	17,240	1,415
Transition	tb-DXP- ZL	ΔE [$\nu' - (\nu' + 1)$]	tb-DXT- ZL	ΔE [$\nu' - (\nu' + 1)$]	tb-DXQ- ZL	ΔE [$\nu' - (\nu' + 1)$]
0-0'	18,660	–	15,240	–	12,580	–
0-1'	20,080	1,420	16,560	1,320	13,790	1,210
0-2'	21,370	1,290	17,990	1,430	15,630	1,590
0-3'	22,780	1,410	19,460	1,470	16,810	1,430

$\Delta E[\nu' - (\nu' + 1)]$ is the energy difference between the $0 - \nu'$ and the $0 - (\nu' + 1)$ transitions. Energies are in $[\text{cm}^{-1}]$ [16]

(0.023, $\epsilon(415 \text{ nm}) = 4,000 \text{ M}^{-1} \text{ cm}^{-1}$), while the second one ($S_2 \leftarrow S_0$) is of high intensity (0.19, $\epsilon(357 \text{ nm}) = 21,400 \text{ M}^{-1} \text{ cm}^{-1}$). Both corresponding ETDMs are in the molecular plane perpendicular to each other, as explained in Fig. 16. In Me-Acr⁺-ZL composites, both are located in a plane perpendicular to the channel axis [154]. Polarized absorption and fluorescence properties have been investigated on oriented MeAcr⁺-ZL monolayers [128]. These facts make Me-Acr⁺ special, and it is interesting to compare the absorption and the fluorescence spectra in aqueous solution and in hydrated composites. We show the data in Fig. 18. The presence of characteristic vibronic features in all spectra in solution and in the MeAcr⁺-ZL composite is remarkable. They differ little and are equally present in the excitation spectrum. Since the shifts in peak position between the spectra in these environments are small, it is sufficient to indicate them by means of vertical lines for the aqueous solution spectra. The same holds for the numerical values of the $0 - \nu'$ and the $0 - \nu''$ transitions and for the energy difference between the $0 - \nu'$ and the $0 - (\nu' + 1)$ transitions $\Delta E[\nu' - (\nu' + 1)]$, and for the energy difference between the $0 - \nu''$ and the $0 - (\nu'' + 1)$ transitions $\Delta E[\nu'' - (\nu'' + 1)]$ (Table 6). We observe that the vibrational energies are all in the same range of about $1,200 \text{ cm}^{-1}$. This means that all of them are most probably related to aromatic C–H bending and/or C–C stretching vibrations. The nearly perfect mirror symmetry between the $S_0 \rightarrow S_1$ absorption and the $S_0 \leftarrow S_1$ fluorescence bands, and the well-developed vibrational features, indicates that there is very little difference between the shape of the potential energy curves of the S_0 , the S_1 , and the S_2 states. This means that the minimum positions of the S_0 and the S_2 potentials are about identical while that of the S_1 is slightly displaced with respect to the previous two and that this holds similarly for Me-Acr⁺ dissolved in water and confined within the ZL nanochannels. The observations we have presented for the perylene-ZL and for the MeAcr⁺-ZL composites reflect the properties of many dyes confined within the nanochannels of ZL. We refer to Fig. 11 of [178], where a comparison of the absorption, fluorescence, and excitation spectra of a 10^{-6} M Ox^+ solution in MeOH and of Ox^+ -ZL composites measured using the

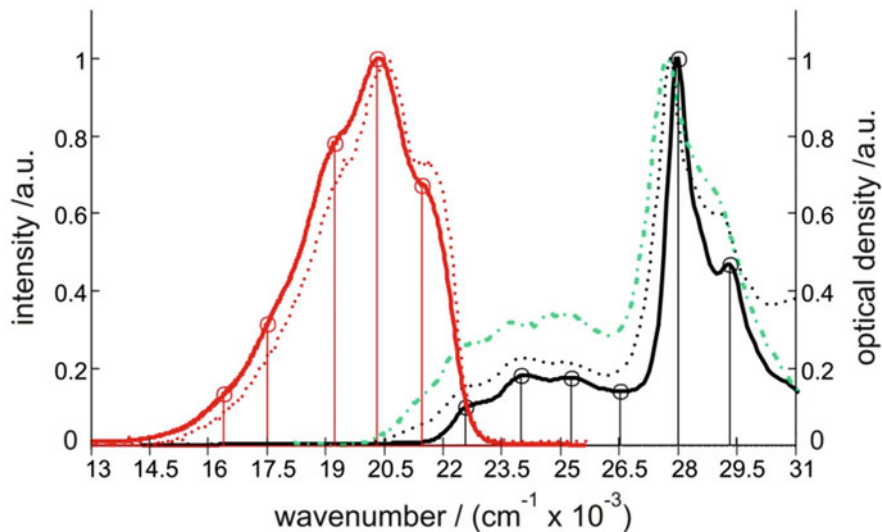


Fig. 18 Absorption (black), fluorescence (red), and excitation (green) spectra of MeAcr^+ in solution and confined within the channels of ZL [154]. The solid lines show the absorption and the fluorescence spectra of a 2.8×10^{-6} M MeAcr^+ solution in water. The absorption and fluorescence spectra of a MeAcr^+ -ZL composite with a loading of $p = 0.01$ are dotted, and the excitation spectrum of the same sample (observed at 560 nm) is dash-dotted. They were recorded using thin layer OGS technique [178]

OGS technique is reported. The electronic and especially the luminescence properties of some organic guests and those of all rare earth guests are sensitive or even very sensitive to the presence of protons, namely, the Brönsted acidity. We discuss this in Sect. 7.3.

7.2 Oscillator Strength

We introduce the notion of the oscillator strength f because we will need it below. The value of f provides a mean to get a feeling for the intensity of light absorption and luminescence of dye-ZL composites. The oscillator strength f can be calculated from the absorption spectrum according to Eq. (5), where $\bar{\nu}$ is the wavenumber in cm^{-1} of the electronic transition $S_0 \rightarrow S_1$ and $\epsilon(\bar{\nu})$ is the extinction coefficient in $\text{M}^{-1} \text{cm}^{-1}$ at wavenumber $\bar{\nu}$ [179].

$$f = 4.319 \times 10^{-9} \text{M cm}^2 \int \epsilon(\bar{\nu}) d\bar{\nu} \quad (5)$$

Table 6 Numerical values extracted from the aqueous solution spectra shown in Fig. 18 [154]

Electronic transitions	Absorption	Energy [10^3 cm^{-1}]	$\Delta E[\nu'-(\nu'+1)]$ [10^3 cm^{-1}]	Fluorescence	Energy [10^3 cm^{-1}]	$\Delta E[\nu'-(\nu'+1)]$ [10^3 cm^{-1}]
S_0-S_1 (1L_a)	0-0'	22.7		0'-0	22.7	
	0-1'	24.0	1.3	0'-1	21.5	1.2
	0-2'	25.3	1.3	0'-2	20.3	1.2
	0-3'	26.5	1.2	0'-3	19.2	1.1
				0'-4	17.5	1.3
				0'-5	16.3	1.2
S_0-S_2 (1L_b)	0-0''	28.0	$\Delta E[\nu''-(\nu''+1)]$			
	0-1''	29.3	1.3			

The magnitude of f of organic dyes is often in the order of 1 but can also be larger. For the cyanine dye PC21⁺, one finds a value of 1.4, and for the perylene dyes DXP and similar, it is 0.76. Assuming a ZL particle of 30 nm size, fully loaded with a dye with $f = 1$ that occupies 3 u.c., we find an oscillator strength of up to 3,000. This is a very large value. It can be compared, e.g., with the oscillator strength of 11, reported for a GaAs quantum-sized particle of about 7 nm diameter, consisting of roughly 20,000 atoms [180]. This simple reasoning does not apply for dye-ZL particles larger than about 100 nm because then saturation phenomena and inner filter effects complicate the situation [181].

7.3 Influence of the Acidity of the Channels on the Guests

The structure of the water organization inside the channels of ZL was studied by Fois and Tabacchi in detail and compared with its MOF mimic [182]. Water is the most frequent co-guest in the ZL host-guest composites that have been investigated so far. Brønsted acidity is therefore an issue in all these composites. We illustrate its importance by the following simple argument. A total of 3.6 mobile positive charges, contributed, e.g., by 3.6 potassium cations, are present on average in each u.c. in the same volume that is used by the guests. Twenty-one water molecules are present in this volume in a fully hydrated composite. Replacing one of the 3.6 positive charges by a proton means that the ratio of the hydronium concentration to water molecules $[H_3O^+]/[H_2O]$ is 1:21. This means that the Brønsted acidity in such a nanochannel corresponds to that of 2.5 M hydrochloric acid. Attention is therefore advised if composites are washed with pure water in order to remove some unwanted molecules or ions from its surface because the pure water should be considered as a 10^{-7} to 10^{-6} M H_3O^+ solution. Such a procedure, hence, favors insertion of the often unwanted protons, according to Eq. (6), where M^+ is a charge compensating cation such as K^+ [14].



It is important to have a measure for the proton activity $a_{H_3O^+}$ inside the nanochannels of ZL. Such a measure is provided by dyes which can be inserted into the channels and which show distinctly different absorption or fluorescence spectra depending on the pH of the environment. We can argue as follows. The stoichiometry of ZL with monovalent cations M^+ that contains some protons is $M^+_{9-x}H^+_x(SiO_2)_{27}(AlO_2)_9 \times nH_2O$ where n equals 21 in fully hydrated samples. This means that the number of water molecules in an acid base reaction of dye molecules D located inside of the ZL channels, Eq. (6), cannot be considered as being constant. This is expressed in Eq. (8), where K_a is the acidity constant expressed by means of the activities a of the corresponding species.

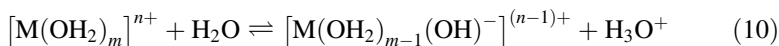


$$K_a = \frac{a_{DH^+}}{a_D} \frac{a_{H_2O}}{a_{H_3O^+}} \quad (8)$$

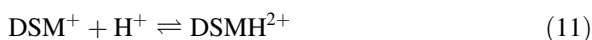
Solving Eq. (8) for the proton activity and expressing the result in terms of concentrations and activity coefficients γ , we obtain:

$$a_{H_3O^+} = \frac{[DH^+]}{[D]} \frac{[H_2O]}{K_a} \frac{\gamma_{DH^+} \gamma_{H_2O}}{\gamma_D} \quad (9)$$

This means that proton activity inside of the zeolite channels can be obtained by measuring the ratio $[DH^+]/[D]$ by means of electronic absorption spectroscopy. The change of the number of water molecules in the protonation reaction (Eq. (7)) can be taken into account. It is not so important for fully hydrated zeolite but can become very important in partially hydrated materials. The ratio of the activity coefficients γ is not known. It is, however, reasonable to assume that it is essentially constant if different dyes are used for probing the proton activity so that a meaningful comparison of the values is possible. This procedure has many applications in different fields, including biology [176]. It is well known that positive metal ion gives acidic solutions in water according to Eq. (10) [183]:



A consequence of this is that the proton activity inside of the ZL channels depends on the nature of the charge compensation cations. Values for some cations have been measured using the spectral response of pH-sensitive dyes [172, 184], typically the reaction of DSMI in Eq. (11); see Table 7:



The influence of the charge compensating metal cations is large [83, 172, 178]. Table 7 shows that the high acidity inside the channels cannot be controlled

Table 7 pK_a values of aqueous solutions of metal ions and pH values measured inside the channels of ZL, using Dsm^+ as indicator^a

Cation	pK_a^b cation in water	pH inside the channels of ZL
Li ⁺	13.6	3.4
K ⁺ \approx Na ⁺	14.0	3.4
Cs ⁺	–	3.7
Mg ²⁺	11.2	2.8
Ca ²⁺	12.7	3.1

^aLoading of Dsm^+ : 0.06 per u.c., T = 298 K, [172]

^b[183], 3.6 equivalents of the corresponding cations per u.c. were in the main channel of ZL

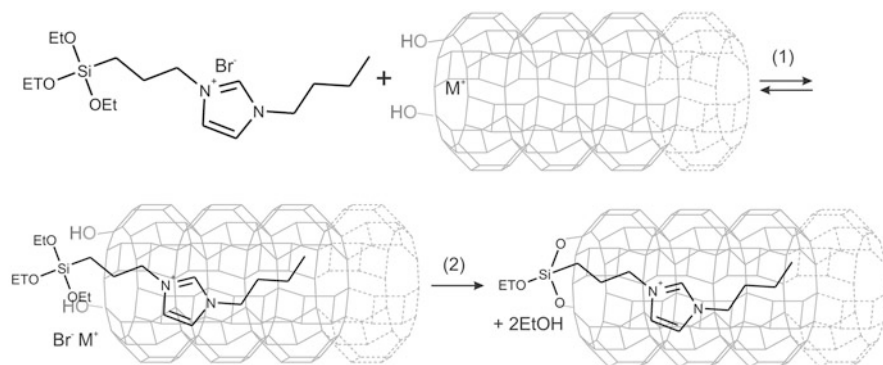


Fig. 19 Selective modification of the ZL channel entrance; (1) sonication at r.t, (2) fixation at 60°C [77, 93]

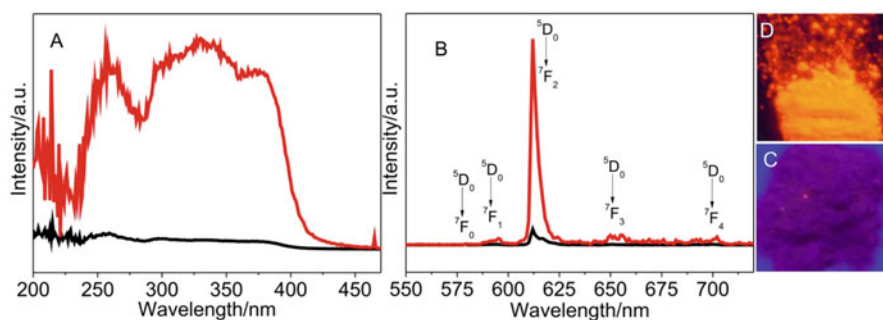


Fig. 20 Excitation spectra monitored at 612 nm (A) and emission spectra (B) excited at 345 nm of [Eu³⁺L_n]-NZL (black) and BuImz⁺Sil-([Eu³⁺L_n]-NZL) (red) observed at r.t. The typical Eu³⁺ emission bands are indicated. (C) and (D) Images of the two samples taken under near UV excitation: (C) [Eu³⁺L_n]-NZL. (D) BuImz⁺Sil-([Eu³⁺L_n]-NZL) [77]. Adapted with permission from [77] Copyright Wiley VCH

sufficiently by changing the charge compensating metal cations. However, substituting, e.g., a fraction of the 3.6 charge compensating metal cations by an organic cation can have much impact. An enormous increase of the luminescence intensity was observed when attaching the BuImz⁺Sil stopcock to nanosized ZL (NZL) composites, the channels of which contained Eu³⁺(L_n), if L was a β-diketonate (TTFA or DBM, Table 3) [77]. The imidazolium salt was used because it bears a positively charged part which easily enters the negatively charged NZL-channel upon exchanging a cation present in the neighborhood and because the bulky triethoxysilane moiety can react with the OH groups present at the channel entrances. The modification reaction was performed as reported in Fig. 19; see also Fig. 9.

We name the composites [Eu³⁺L_n]-NZL, where L is equal to TTFA (Table 3), and composites modified with the stopcock: BuImz⁺Sil-([Eu³⁺L_n]-NZL). Figure 20 shows a result of this surprising observation. We first note that the shape of the excitation spectra, observed at the 612 nm (⁵D₀ → ⁷F₂) Eu³⁺ emission, is identical

for both samples but differs enormously in intensity. The shape corresponds to the absorption band of TTFA. The about 100 times larger emission intensity of the stopcock modified samples is manifested when comparing the red and the black emission bands. The photographic images (C) and (D) provide an intuitive impression of the effect exerted by the stopcock modification. Similar observations were made when using DBM as a ligand.

What is the reason for this unexpected important luminescence enhancement? It is known that protonation of diketonates competes with full coordination to Eu^{3+} and that incomplete coordination affects the luminescence yield. Both TTFA and DBM can be protonated under the acidic environment of hydrated ZL. DBM to an even larger extent, as its $\text{p}K_{\text{a}}$ value is larger than that of TTFA, with values of 8.95 and 6.33, respectively. This provides the explanation for the remarkable influence of the stopcock modification with BuImz^+Sil on the luminescence intensity of the β -diketonate-based composites. It is caused by a decrease of the proton activity inside of the NZL channels. Each stopper attached to the channel entrance exchanges one of the cations that control the proton strength, as explained above. The effect is enhanced by the fact that the imidazolium acts as a weak base [185, 186]. The effect weakens with increasing size of the ZL crystals. The ratio of channel entrances and u.c. of a ZL crystal of equal length and diameter d in nm is equal to $1.485/d$. This means that, for example, a 30 nm NZL consists of about 20 times more u.c. than channel entrances. It is, however, useful to remember that the BuImz^+Sil also acts like a cork on a bottle: it seals the ZL channel as illustrated in Fig. 10 [100]. Li et al. applied the understanding provided by these observations for designing highly sensitive rare earth-ZL composites as sensing devices for detecting basic molecules [99, 187].

Hostasol Red (HR, Table 2) is a solvatochromic dye of brilliant color. It can be inserted easily into the channels of ZL where its bright fluorescence is largely quenched, essentially because of protonation in the first excited state [172, 178]. It is remarkable that exchange of only one half out of the 3.6 charge compensating potassium cations per u.c. by the imidazolium cation IMZ^+ (Table 3) causes a jump from about 3% fluorescence quantum yield observed in potassium HR-ZL composites to a yield of nearly 100% [83]. The reason is the same, as we have seen above in Fig. 20 upon addition of the BuImz^+Sil stopcock to $[\text{Eu}^{3+}\text{TTFA}_n]\text{-NZL}$. IMZ^+ reduces the proton activity inside the channels of ZL sufficiently, so that the quenching caused by excited state protonation is suppressed. We indicate the number and type of charge compensating cations as follows: $\text{ZL}_p((3.6-x)\text{M1}^+, x\text{M2}^+)$, where p is the loading of HR; see Eqs. (3) and (4). Figure 21 shows representative data that illustrate the influence of IMZ^+ on HR-ZL composites. The bathochromic shift of the absorption and fluorescence bands manifests the solvatochromism of HR. The photographic images give a visual impression on the influence of the IMZ^+ . It is remarkable that the color and the luminescence intensity of the sample $\text{HR-ZL}_{.5}\text{-}(2.6 \text{ K}^+, 1.0\text{IMZ}^+)$ did not change upon prolonged immersion in water [83].

IMZ^+ is the only organic cation the influence of which on the properties of guest-ZL composites was studied to some extent as substitute for part of the charge compensating metal cation. Many other options exist, still waiting to be explored, with the potential of fundamentally influencing properties of many guest-ZL composites.

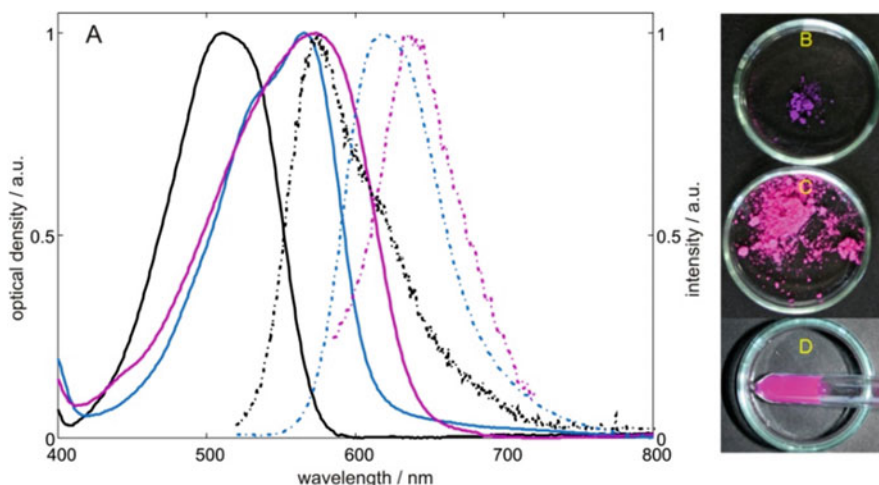


Fig. 21 Absorption (solid), fluorescence (dash-dot) spectra, and colors of HR in different environments. (a) spectra: (black) 10^{-6} M solution in DCM; (pink) HR-ZL.5(K⁺), and (blue) HR-ZL.5 (3.1 K⁺, 0.5IMZ⁺). All fluorescence spectra were excited at 490 nm. Spectra of the dye-ZL composites were measured as OGS. Photographic images taken under ambient conditions: (b) HR-ZL.5(3.6 K⁺) after exposure to ambient air. (c) HR-ZL.5(2.6 K⁺, 1.0IMZ⁺) after exposure to ambient air. (d) HR-ZL.5-(2.6 K⁺, 1.0IMZ⁺) that was left for 2 weeks in water; the color and luminescence of this sample did not change during this time [83]

7.4 Exciton Coupling of Organic Guests

Hashimoto studied the behavior of naphthalene and anthracene located inside of the channels of ZL. The spectroscopic feature of these composites was a clear sign of exciton coupling [177]. Exciton coupling was later observed for several composites consisting of neutral and of cationic guests [15, 46, 155, 162, 166, 181]. Different possibilities for packing the guests are schematically illustrated in Fig. 22. It shows that the so-called H- and J-exciton coupling is possible for small molecules (a)1' and (a)1'', respectively. The limited space provided by the channels favors J-coupling, (see (a)4) for larger molecules if their shape allows for a sufficiently small distance between their ETDMs. The double arrows indicate the direction of the ETDM of the first allowed electronic transition of the guests. The figure also illustrates that molecular engineering can be applied to fine-tune the distance between the chromophores, for example, by covalently binding optically inert spacers to the end of the chromophores as seen in b and b'.

The Davydov coupling strength β_c between two molecules $(A^* \dots A) \leftrightarrow (A \dots A^*)$, with A^* denoting an electronically excited molecule A , can be calculated by using Eq. (12) [181, 188, 189].

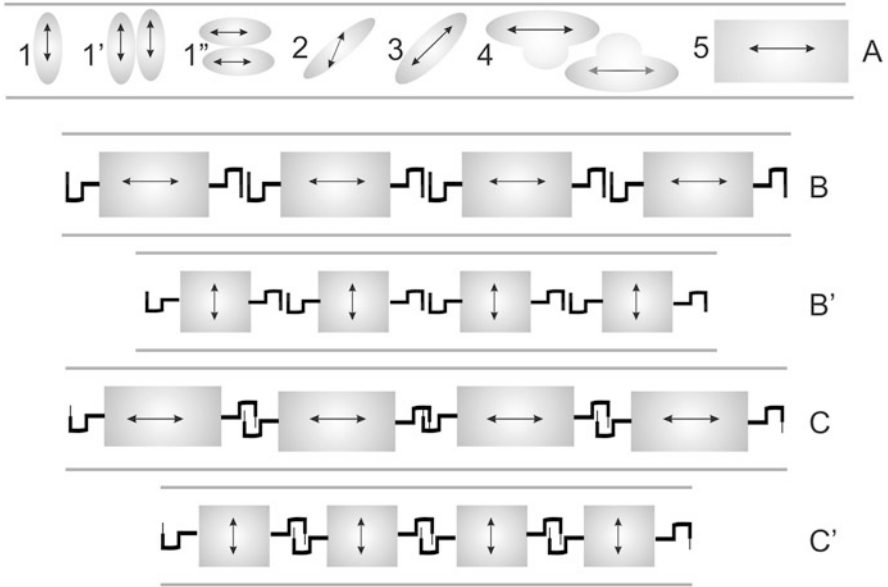


Fig. 22 Molecules in the channels of ZL. The double arrows indicate the direction of the ETDM of the first allowed electronic transition. **(a)** Representative orientations of molecules and sketch of pairs ready for exciton coupling. **(b)** Orientation of molecules which align their ETDM parallel and **(b')** perpendicular to the channel axis and which have no exciton interaction because optically inert spacers keep them at sufficiently large distance. **(c)** Orientation of molecules which align their ETDM parallel and **(c')** perpendicular to the channel axis and which are so close that Davydov coupling is important [15, 181]

$$\beta_C = AD \times \frac{\kappa}{R^3} \times \frac{f}{\Delta E} \times \frac{1}{n^2} \quad (12)$$

The value of the constant AD is equal to $1.615 \times 10^{-18} \text{ m}^2 \text{ cm}^{-1}$ if we express β_C in cm^{-1} . The magnitude of the interaction β_C caused by exciton coupling, and hence the resulting splitting of the levels, depends on the oscillator strength f , Eq. (5), the relative orientation κ of two neighboring ETDM explained in Fig. 23a, and the distance R between the interacting ETDM. The expression for κ can be simplified in the present case as $\kappa = 1 - 3\cos^2(\theta)$, where θ is the angle between two adjacent ETDMs. The coupling is largest for in-line orientation ($\theta = 0^\circ$, $\kappa = -2$), leading to J-coupling, while H-coupling occurs at essentially parallel arrangement ($\theta = 90^\circ$, $\kappa = 1$). β_C further depends on the electronic excitation energy ΔE and on the refractive index n of the environment. The validity of Eq. (12) depends on the condition that the distance between the ETDM of two involved molecules is large with respect to the length of the ETDM. It can be shown that the length l_{μ^*} of the ETDM can be expressed as follows, where the value of the parameter *const* is equal to $3.036 \times 10^{-6} \text{ cm}^{0.5}$; the oscillator strength f is dimensionless [181]:

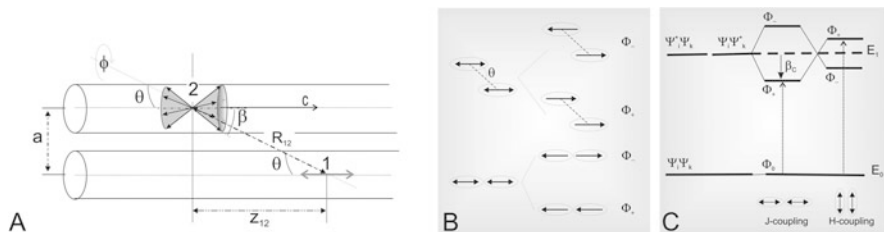


Fig. 23 (a) Relative orientation of the ETDMs of the donor 1 and of the acceptor 2 located in a neighboring channel. The center to center distance a between two adjacent ZL channels amounts to 1.84 nm. (b) Phase relation and energy level diagram, shown for $\phi = 0$. Left: Phase relation which describes the interaction caused by the ETDM between the electronically excited state configurations $A_i^* \dots A_k$ and $A_i \dots A_k^*$. (c) Energy level diagram showing the exciton splitting of two chromophores caused by the configuration interaction due to the ETDM. This interaction naturally causes only a splitting of electronically excited states and has no consequences on the ground state. The different splitting of the excited state levels for ETDM oriented collinear and for those which are parallel, as represented by means of double arrows, is due to the angle dependence of κ . The allowed electronic transitions are indicated by the dotted arrows

$$l_{\mu^*} = \text{const} \sqrt{\frac{f}{\Delta E}} \quad (13)$$

From Eq. (13) we find, as an example, the length of the ETDM of an organic molecule absorbing light at 500 nm with oscillator strength one to be 0.215 nm. This means that the distance R between the ETDM of two adjacent molecules in a nanochannel of interest here is usually large enough, so that Eq. (12) can be considered as a good approximation. We show in Fig. 23 schematically different orientations and packing of dye molecules in a 1D channel. The double arrows indicate the direction of the ETDM of the first allowed electronic transition. The inverse power to the third distance dependence of the coupling strength β_c allows to deduce that molecular engineering can be applied for fine-tuning the distance between the chromophores, e.g., by covalently binding optically inert spacers at the end of the chromophores as illustrated in Fig. 22. From Eq. (12) we know, e.g., that the value of β_c decreases by a factor of 3.375 if the distance between two interacting ETDM is augmented from $2/3R$ to R . This possibility for fine-tuning has been tested for perylene dyes [16, 162]. The wave functions $\Psi_i\Psi_k$ and $\Psi_i^*\Psi_k$, $\Psi_i\Psi_k^*$ in Fig. 23 describe the ground state and the electronically excited states of the pairs $(A_i \dots A_k)$, and Φ_- and Φ_+ describe the corresponding exciton states. We refer for a more detailed discussion to the chapter “Theoretical Background” of [181] and the Appendix SI2 of [190].

Exciton splitting of molecules located in adjacent channels is too small for being easily detected. This can be deduced from the data reported in Fig. 24 where we show (left) the magnitude of the Davydov coupling strength β_c and of the resulting spectral shift (right) as a function of the distance R for representative values for the oscillator strength f and for the electronic excitation energy ΔE . The red lines in this

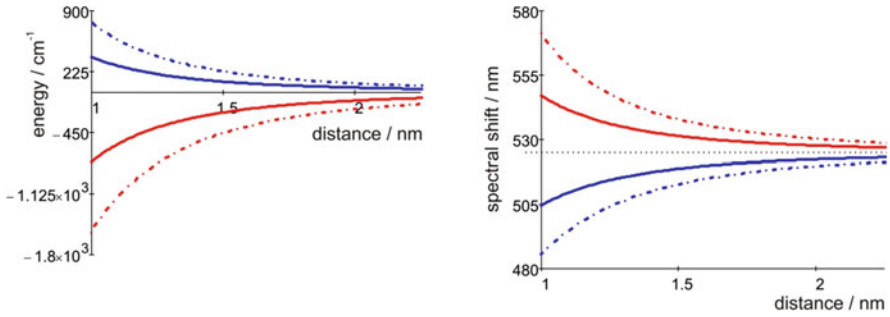


Fig. 24 Exciton splitting of the stationary states Φ_- and Φ_+ and spectral shift of the $0-0'$ transition as a function of separation (center to center distance of the ETDMs), calculated for $f = 0.95$, $\Delta E = 20,000 \text{ cm}^{-1}$, and $n = 1.45$. Red lines: $\theta = 0$, which means J-coupling. Blue lines: $\theta = \pi/2$, which means H-coupling. The solid lines describe exciton interaction between two neighbors, while the dash-dot lines describe the interaction between many chromophores located at equal distances. Electronic transitions to the higher lying states are forbidden for J-aggregate coupling [181, 189]

Fig. correspond to values calculated for $\theta = 0$ which means J-coupling. The blue lines refer to $\theta = \pi/2$ which means H-coupling. The solid lines describe exciton interaction between two neighbors, while the dash-dot lines describe the interaction between many chromophores located at equal distances. We note that the shortest distance between two chromophores in two adjacent ZL channels is 1.84 nm. Inspection of Fig. 24 indicates that the Davydov splitting at this distance is too small for being an important feature at room temperature for both H- and J-coupling. Low-temperature spectroscopy would be needed in order to observe it. Corresponding experiments have not been known so far. The interaction and, hence, the spectral shift increase, however, fast with decreasing distance. It is already important for distances equal to the length of 2 u.c., which is 1.5 nm. It is therefore not surprising that exciton coupling has been observed on DXP-ZL composites [162].

We illustrate this in Fig. 25. The figure shows DXP molecules inside of a schematically drawn ZL channel. A guess based on a van der Waals image indicates that the shortest distance between two molecule centers at highest possible packing corresponds to about 2 u.c. or a bit less. This means a shortest distance of about 1.4 nm. Calculating the exciton splitting for DXP leads to 220 cm^{-1} for two neighbors and 440 cm^{-1} for many, which corresponds to a bathochromic shift of 6 nm and 12 nm, respectively. This seems to only slightly underestimate the spectral shift that has been observed [162]. It is interesting to study the fluorescence microscopy images of DXP-ZL crystals where the loading was stopped before the guest could reach an equilibrated state with homogenous distribution along the channels. Freezing not equilibrated states is easy because loading occurs at high temperature usually about 260° [16]. This leads to samples with dense packing at both ends of the crystals and large distances between samples in the inner part of the crystals. This technique has been used very frequently for studying many different dye-ZL crystals; see, e.g., [14, 15, 46]. Epi-fluorescence micrographs of a DXP-ZL

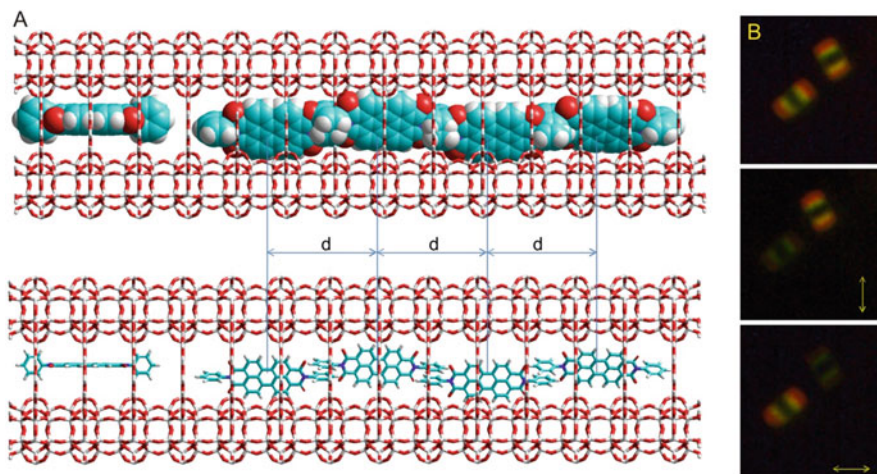


Fig. 25 DXP inside of a schematically drawn ZL channel and fluorescence micrographs of DXP-ZL. **(a)** Scheme of one DXP molecule and of densely packed DXP inside of a ZL channel. Upper: van der Waals representation of DXP; Lower: stick representation. The distances d are roughly equal to the length of 2 u.c. which means 1.5 nm. O, red; C, blue; H, white; Si or Al, light gray. **(b)** Epi-fluorescence micrographs of a DXP-ZL crystal. The double arrows indicate that the corresponding images were taken through a polarizer at 90° and at 0° , respectively. Loading of the samples was stopped before the guest could reach an equilibrated state with homogenous distribution along the channels. Dense packing at both ends of the crystals leads to J-coupling seen as red color. Green dominates in the middle part where the distance between the DXP is large and where therefore no coupling takes place [162]

crystal prepared in this way are seen in Fig. 25b. The double arrows indicate that the corresponding images were taken through a polarizer at 0° and at 90° , respectively. We observe prominent J-coupling seen as red color at both ends of the crystals, while green dominates in the middle part where the distance between the DXP is large and where therefore no coupling takes place. The red sections represent areas where DXP molecules undergo J-coupling. Orange regions correspond to regions where free molecule and aggregates are present, while the green zone contains only non-interacting dyes. Energy transfer from monomers to J-aggregates is thought to occur in the orange areas. It is possible to suppress J-coupling of perylene dyes by adding a sufficiently bulky and long substituent at both ends of these molecules. The structure of highly packed tb-DXP-ZL has been explored as we have seen in Fig. 15 [44]. From this we know that the center to center distance for this composites amounts to about 3 u.c. which means that the interaction β_C caused by exciton coupling, Eq. (12), is smaller than about 50 cm^{-1} . This is much less than the value of kT which amounts to 207 cm^{-1} . It is therefore too small to be detected at room temperature even for many interacting dyes in extended structures.

J-aggregates show many interesting properties [191–194]. It is, however, difficult to achieve large exciton coherence length, because disorder causes shortening [192, 195, 196]. ZL appears to be an excellent host for preparing exciton composites

of large coherence length with a variety of molecules of appropriate shape. No research directing into this has, however, been communicated so far. Hence, this field remains largely unexplored. Studies similar to those reported by Arletti et al. on the high-pressure behavior of dye-ZL hybrid materials for fluorenone as a host, who observed a remarkable resilience of the supramolecular organization of dye molecules hyper-confined in ZL channels, however, bear the potential for rapidly exploring this kind of new optical materials [49].

8 ZL as a Catalyst

It is remarkable that ZL, which can be used for protecting molecules from photochemically and thermally induced degradation by preventing diffusion controlled processes and also by inhibiting intramolecular movements such as an intramolecular rotation which may result in an unstable conformation, has also the ability for acting as an excellent support for catalytically active metal clusters. It has also the ability for acting itself as a catalyst as, e.g., seen in the selective *p*-chlorination of biphenyl in ZL [81] or as proactive agent to extend the lifetime of commercial lubricants by protecting the performance additives from depletion and adsorbing the acid formed during oxidation [197]. ZL has been investigated as support for catalytically active Pt [61, 68, 198]. Bimetallic PtSn particles supported by a ZL host were found to exhibit higher activity and selectivity for isobutane dehydrogenation and resistance to deactivation than simply Pt-based composites [62]. Cho et al. observed that incorporation of tin into Pt cluster, consisting of 5–7 atoms inside potassium ZL, changed the adsorption properties of hydrogen and xenon due to the formation of bimetallic nanoparticles and caused an important improvement of *n*-hexane aromatization. Their data show that cluster formation occurred without pore blockage [63]. The hydrogenation of citral using Ru clusters prepared from different precursors and supported by ZL was tested. Different selectivity depending on the preparation procedures and, hence, also on the size and location of the Ru clusters was observed [64]. It is well known that the final selectivity of an active metal can be modified by employing an adequate support which interacts with the metal or by adding a second component which acts as a promoter. This understanding has been used in a study regarding Pt clusters prepared in ZL hosts of varying morphology and channel lengths. The authors observed that the morphology and the channel length of ZL have important influence on the performance of Pt-ZL catalysts used for the aromatization of *n*-octane. Catalysts with a larger fraction of small metal clusters inside the pores were found to be more active for a longer time. The metal distribution in the ZL is optimum for intermediate crystal size. When the crystal is too long, Pt particles can be transported outside of the zeolite during the pretreatments. By contrast, when the crystal is too small, the outer surface area dominates, and a large fraction of metal particles is deposited outside the pores [65]. The reason for the exceptional catalytic performance of Pt-ZL composites suppressing coke formation in aromatization of hexane has been elucidated by Davis et al. using

isotope labeling experiments. They found that the dehydrocyclization reaction of hexane over Pt-ZL composites is controlled by hexane entry into the wider lobes of the ZL channels where the Pt clusters reside. In contrast to non-microporous-supported Pt catalysts, the tiny windows of the ZL channels allow hexane to pass through one by one to the larger lobes containing the Pt clusters. This controlled diffusion of hexane is the reason for the high stability and selectivity of the catalyst, most likely because it inhibits the bimolecular reactions that lead to coke formation and catalyst deactivation [199]. Roduner et al. studied the structure, size, hydrogen uptake, and magnetic properties of Pt cluster in ZL [66, 67]. The activity of disc-shaped and of nanosized ZL supports for bimetallic RhNi clusters was compared in a study regarding metal-ZL-catalyzed hydrogen production in biogas reforming processes [39]. Restructuring of the metal cluster, at least in the initial phase of activity, is expected to occur. This has been very nicely demonstrated in an experiment where atomic layer deposition was used to synthesize PtCo clusters of 0.6–0.8 nm diameter inside of the ZL channels. Restructuring during the aromatization process of n-heptane leads to improved and impressing performance during the initial 5 h reaction time [69]. ZL with its one-dimensional channels shows excellent catalytic performances in the selective hydrogenation and aromatization. The small pore size, however, strongly hinders the diffusion of bulky molecules in bimetallic ZL supported clusters used for hydrodesulphurization (HDS) of FCC gasoline. This leads to the idea to combine the properties of the nanoporous ZL with those of mesoporous MCM-41 and to decorate this with bimetallic MoCo clusters. The so-obtained composites showed very interesting multifunctional performances in the HDS reaction of full-range FCC gasoline [200, 201].

9 Artificial Photonic Antenna Systems for Light Harvesting, Transport, and Trapping

An artificial photonic antenna is an organized multi-component arrangement in which several chromophores absorb the incident light and channel the electronic excitation energy to a common acceptor component [202]. We observed that ZL can be used as a host for organizing different chromophores into well-defined patterns [78, 203]. The question aroused if this could be used for preparing materials consisting of appropriately chosen chromophores organized by ZL as a host to mimic important properties of the natural antenna system of green plants which consists of several hundred chlorophyll molecules closely packed in a hydrophobic environment. The results of our calculations, which were based on a homogeneous Markoffian random walk of FRET (Förster Resonance Energy Transfer) [204, 205] processes, in which each energy transfer step is incoherent and occurs from a thermalized initial state, were so encouraging that we decided to study its implication in a systematic way and to design and realize artificial antenna systems based on ZL as an organizing and stabilizing host [151]. The orientation inside the channels of the

dyes Py^+ and Ox^+ , used as example donor-acceptor pair in this study, was not known at this time and was later found to be more complex than assumed. Fluorescence microscopy combined with single-crystal imaging [149], two-photon fluorescence polarimetric microscopy [165], and extensive first-principles investigations led to the result that different preferential orientations must be considered in the presence or absence of water because of the dominant stabilization of either the host or the guest, respectively. Optical microscopy data might therefore be reinterpreted as the vector sum of components arising from a population of molecules with non-uniform orientation [153]. This understanding does not affect the essentials of the procedure and the derived consequences reported in [151], but they affect some details of the numerical outcome. Py^+ and Ox^+ are very nice donor-acceptor pair for demonstrating many aspects of FRET resulting from their organization inside of the ZL channels. We illustrate this by reporting an early experiment in Fig. 26 [78]. This was the first demonstration that the insertion of dye molecules, which penetrate the hexagonal ZL crystals from both sides, into the linear channels of ZL can be observed by means of a fluorescence microscope. Micro crystals of $0.95\ \mu\text{m}$ in diameter and $1.5\ \mu\text{m}$ in length were used. One of them is shown in the electron microscopy image 1 of Fig. 26. Fluorescence microscope image 2 shows a crystal after Py^+ insertion by means of cation exchange in aqueous dispersion during 5 min, boiling temperature. The characteristic green fluorescence can be observed at both ends of the cylinder, while the section in the middle remains dark. During this short exchange time, the dye molecules, coming from both sides, only penetrate a small part of the inside. After an exchange time of 2 h, the fluorescent areas have become larger because the dyes on both sides have moved further inside, image 3. The sample was then exchanged with an Ox^+ solution for 2 h. The resulting stacking is made visible by the green emission of Py^+ in the inside and the yellow emission of Ox^+ near the bottom and the top surface in the image 4. This demonstrates that the Py^+ was pushed deeper into the channels by the Ox^+ in a process we have introduced in Fig. 5. The location of Ox^+ can be seen more clearly in image 5, where Ox^+ was excited selectively [78].

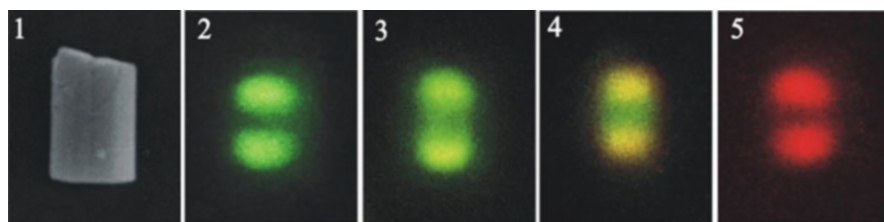


Fig. 26 Illustration of the insertion of first Py^+ followed by Ox^+ into the channels of ZL resulting in an antenna composite. (1) Electron microscopy image of a $1.5\text{-}\mu\text{m}$ -long ZL crystal. (2–5) True color fluorescence microscopy pictures of dye-loaded ZL crystals, observed at r.t. (2–4) Fluorescence after excitation of only Py^+ . (2) After 5 min exchange with Py^+ , (3) after 2 h exchange with Py^+ , (4) after additional 2 h exchange with Ox^+ . (5) The same as (4) but after specific excitation of only Ox^+ [78]

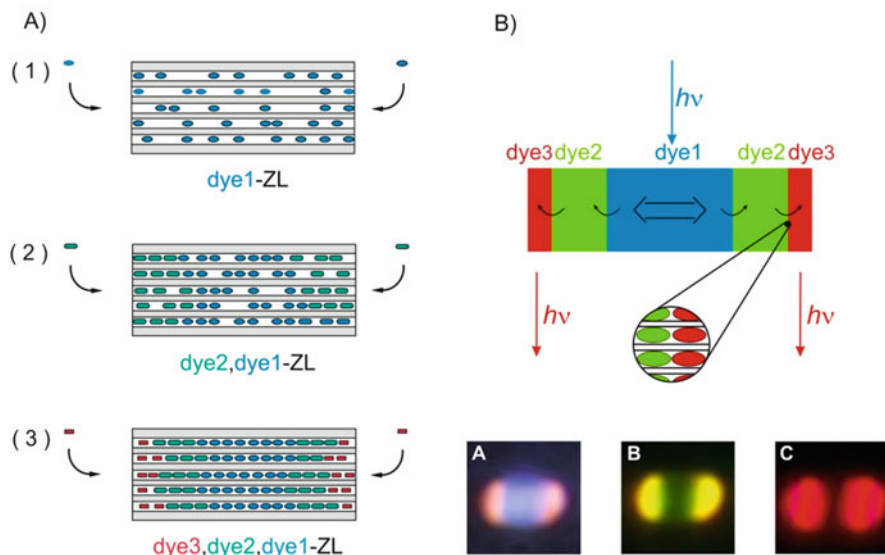


Fig. 27 Preparation and structure of the first three-dye antenna sandwiches acting for light harvesting and transport by means of FRET. (a) The blue emitting POPOP (or in other experiments MBOXE or DMPOPOP; Table 2) is first inserted from the gas phase in step (1). Py⁺ is then inserted by means of cation exchange from an aqueous dispersion. It pushes in this step (2) the dye1 deeper into the channels. Ox⁺ was chosen as dye3 in step (3). It is inserted in the same way as Py⁺, using again cation exchange, by pushing the dyes that are already inside even deeper into the channels. (b) The result of this synthesis of a bi-directional three-dye photonic antenna is explained and illustrated. Upper: Explanation of the principle of the so-prepared bi-directional three-dye photonic antenna. The enlarged section shows the organization of individual dye molecules at the domain boundary between the dye2 and dye3. Lower: Fluorescence microscopy images of an Ox⁺,Py⁺, POPOP-ZL crystal of 2,000 nm length upon selective excitation of (a) POPOP at 330–385 nm, (b) Py⁺ at 470–490 nm, and (c) Ox⁺ at 545–580 nm. The excitation light was eliminated by appropriate cutoff filters in front of the CCD camera: (a) cutoff: 410 nm, (b) cutoff 515 nm, (c) cutoff 605 nm [21, 54]

The geometrical constraints imposed by the ZL host determine the organization of the dyes. This allows for sequential insertion of different guests, resulting in organized pattern, as we have illustrated in Fig. 26. Applying this principle soon led to the first artificial photonic antenna composite consisting of three different dyes: blue-green-red, ranging from about 350–600 nm in light absorption and transportation of the energy to an emitting state with 620 nm maximum emission [54]. Essentials of these first three dye antenna experiments are explained in Fig. 27 where we show on the left (a) the synthesis principle which leads to an organizational pattern realized in composites which we sometimes name as sandwich materials. The upper part of Fig. 27b illustrates a thus prepared composite crystal loaded with a blue, a green, and a red dye, the red one presenting the emitting state. After selective excitation of the blue dye in the middle, energy transfer (FRET) takes place to both ends of the crystal where the dye3 emits red fluoresces. The lower part of this

figure shows fluorescence microscopy images of such a photonic antenna. We observe that after selective excitation of dye1 (POPOP), located in the middle part, the light energy is carried spectrally from the blue to green (dye2, Py⁺) to red (dye3, Ox⁺) and spatially from the crystal center to its both ends. The stacking of the dyes in the crystal can be seen in microscopy images taken on an approximately 2,000-nm-long crystal. Image A shows the fluorescence observed after selective excitation of the POPOP and applying a 410 nm cutoff filter in front of the monitoring CCD camera. The middle of the crystal shows the blue fluorescence of POPOP, while the red emission of Ox⁺ appears at both ends. Between these two zones, the superposition of the fluorescence of all three dyes results in emission of white light. The fluorescence, after selective excitation of the Py⁺ and applying a 515 nm cutoff filter, is seen in image B. The yellow emission is due to superposition of the green Py⁺ and the red Ox⁺ fluorescence. Image c, finally, shows the emission of Ox⁺ after selective excitation of only Ox⁺ and applying a 605 nm cutoff filter. These three microscopy images show very nicely the sequence of the inserted dyes in the channels, although the limited resolution available at this time did not allow distinguishing more clearly between the different regions [21, 25, 54].

A more efficient three-dye antenna composite can be realized using the combination DMPOPOP,tb-DXP,HR-ZL. The scheme seen in Fig. 28a explains the structure of this composite. It shows that in this case the red-emitting dye is located in the middle of the crystal in contrast to the sandwich seen in Fig. 27. This means that the excitation energy is transported via FRET from both sides of the crystal to the middle. The spectroscopic data in Fig. 28b shows that the shape of the fluorescence band, observed under excitation at $\lambda = 360$ nm, corresponds to that of HR,

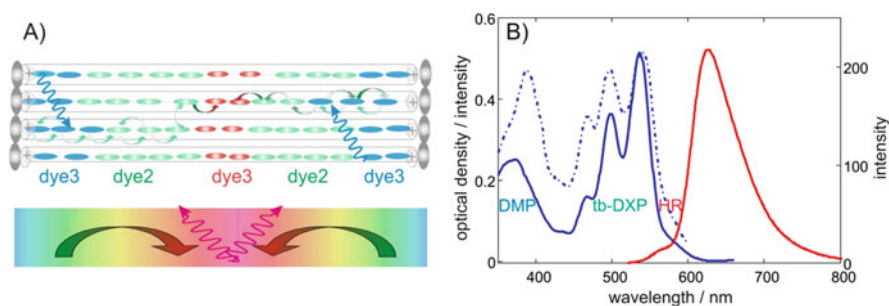


Fig. 28 Advanced three-dye antenna sandwiches acting for light harvesting and transport by means of FRET. (a) The chromophores are embedded in the channels of the host material in a process similar to that shown in Fig. 27a. Here, however, the red dye3 is inserted first, followed by dye2 and finally dye3 resulting in the dye1,dye2,dye3-ZL composite. The channels are plugged with stop-cock molecules (gray) to prevent guests from escaping. The scheme also illustrates how the blue and the green dyes act as donors, the green ones further as transmitter, to channel the absorbed incoming light to the red acceptors, located in the middle part of the channels, which finally release the accumulated excitation energy as red luminescence. (b) Electronic spectra of the three-color antenna system DMPOPOP,tb-DXP,HR-ZL, measured as OGS. Absorption spectrum (blue, solid line); excitation spectrum observed at $\lambda = 680$ nm (blue, dash-dot); luminescence spectrum observed upon excitation at $\lambda = 360$ nm (red, solid line) [16]

with a small feature at shorter wavelength stemming from the tb-DXP. The band looks identical under excitation at $\lambda = 490$ nm. The excitation spectrum, observed at $\lambda = 680$ nm, shown as blue dash-dot line, follows the absorption spectrum drawn as blue solid line. The intensity of the short-wavelength contribution, mainly stemming from the absorption of DMPOPOP, is larger than expected. This is probably caused by the scattering contribution at short wavelength, which is much lower in the range of emission of the HR acceptor [16]. Alternative ways for preparing interesting photonic antenna composites base on ZL as a host have been reported [79, 206]. Bañuelos et al. prepared a four-dye antenna composite base on ZL as a host [80].

The first report on a time-space and spectrally resolved characterization of a photonic antenna was published in 2001 [50]. It was achieved in the laboratory of R. Pansu, ENS Cachan, and was made possible thanks to the favorable properties of dye2,dye1-ZL antenna composite. Measurements of similar type became then soon common standard; see, e.g., [162, 166, 178]. We explain the early experiment by means of Fig. 29, where part (a) shows the size and organization of the composite. The length of the ZL crystal is seen in the electron microscopy image; it amounts to 2,600 nm. The host was in a first step filled with Ox^+ using cation exchange. The so-prepared composite was then dried under vacuum. The DMPOPOP, which we name DMP in the figure in order to shorten the name, was then added under vacuum conditions using the double ampoule method reported in [54]. The scanning confocal fluorescence microscopy images from left to right show the emission along the channels for DMP upon excitation at 330–385 nm and observed through a polarizer oriented parallel to the long axis, as indicated by the white double arrow, while the image in the middle was observed when the polarizer was turned into vertical position, as indicated by the yellow double arrow. The image seen on the right was observed without a polarizer upon excitation of the Ox^+ at 545–580 nm. The intensity profile on the left of Fig. 29a was observed when scanning the emission at 470 nm along the crystal axis, upon excitation at 320 nm. The profile in the middle was observed when monitoring the emission at 610 nm after excitation at 320 nm, while the profile on the right was seen when the sample was excited at 490 nm. The data show that the organization of the dyes inside the crystal corresponds to the scheme seen in (a). They also beautifully illustrate the energy transfer from the DMP to the Ox^+ , and they show that the energy migration length of excited Ox^+ is not sufficient to fill the 2,600-nm-long crystals homogeneously, in accordance with theoretical considerations [151]. The fact that the ETDM of DMP and of Ox^+ is oriented nearly perpendicular to each other inside a channel is optimal for these experiments, but it is of course not optimal for efficient FRET from DMP to Ox^+ . The hexagonal structure of the host has, however, as a consequence that each channel is surrounded by six neighbor channels which still allow for important FRET, as has already been explained [151] more explicitly in Fig. 8 of [15]. Figure 29b reports the first part of the *Luminescence* dynamics. The blue line represents the fluorescence decay of DMP, observed on a crystal that contains only this dye, hence DMP-ZL, excited at 320 nm and observed at 470 nm. The average lifetime was 1.78 ns. The decay of Ox^+ can be observed at 600 nm on a single DMP,

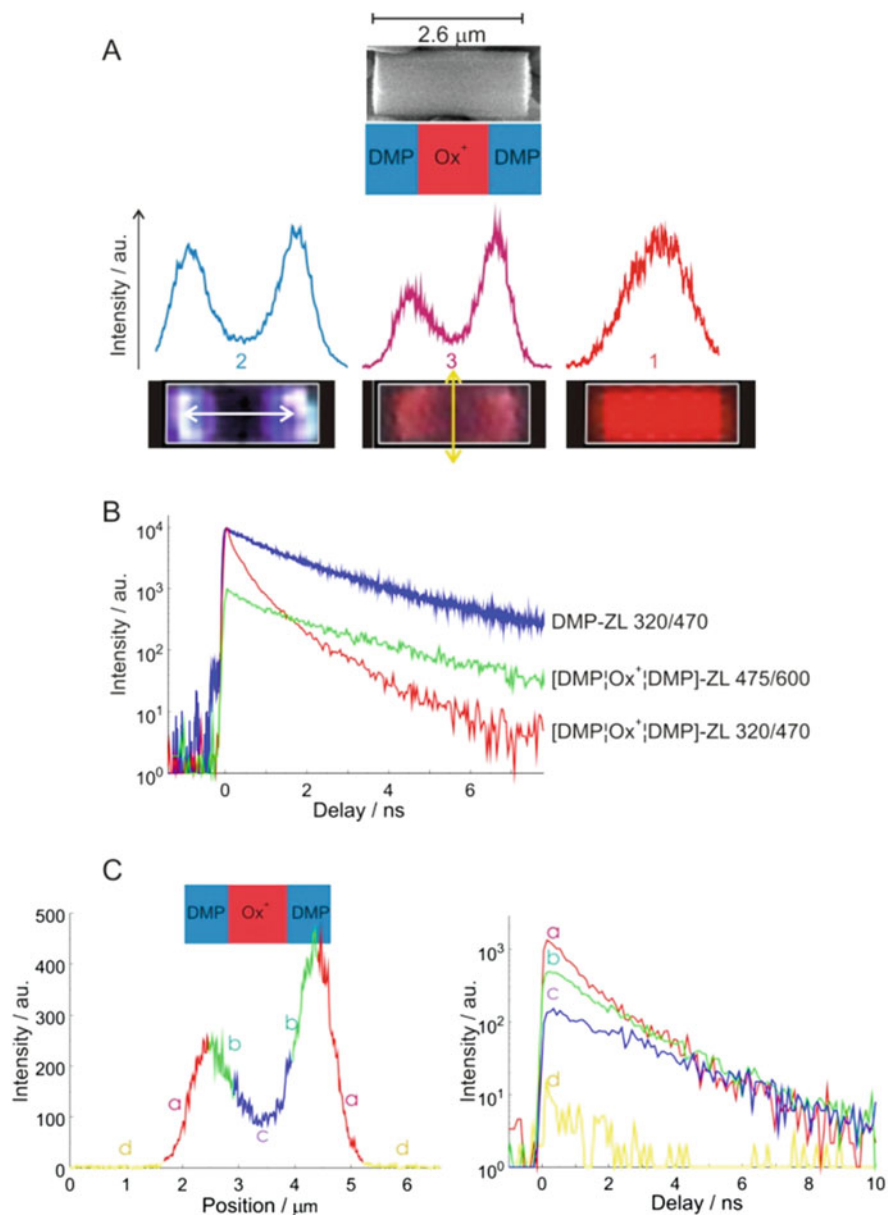


Fig. 29 Time, space, and spectrally resolved characterization of a photonic dye₂,dy₁-ZL antenna. (a) Size and organization of the composite. The length of the ZL crystal, seen in the electron microscopy image, is 2,600 nm. The scheme indicates that the ZL host is in a first step filled with Ox⁺ followed by addition of DMP, resulting in a composite we name DMP,Ox⁺-ZL. The scanning confocal fluorescence microscopy images from left to right show the emission along the channels for DMP upon excitation at 330–385 nm and observed through a polarizer oriented parallel to the long axis, as indicated by the white double arrow. The image in the middle is observed when the polarizer is turned into vertical position, as indicated by the yellow double arrow. The image seen on the right is observed without a polarizer upon excitation of the Ox⁺ at 545–580 nm. The intensity

Ox^+ -ZL crystal because DMP does not absorb light at the 495 nm excitation wavelength used. It is shown as green line and bears an average fluorescence lifetime of 1.71 ns. The decay of DMP, seen as red line in a DMP, Ox^+ -ZL crystal excited at 320 nm and observed at 470 nm, is more complex and has an average fluorescence lifetime of 300 ps. The reason for this short lifetime is that energy transfer takes place from excited DMP to Ox^+ . The reduction of the excited donor lifetime expectancy by a factor of 6 means that 83% of the absorbed photons are transferred from excited DMP to Ox^+ by means of FRET. Figure 29c reports on the second part of the *Luminescence* dynamics, namely, the luminescence decay observed at different position of a DMP, Ox^+ -ZL crystal, namely, outside of the crystal (d, yellow), at the border at both sides (a, red), roughly at both phase boundaries DMP/ Ox^+ (b, green), and in the middle (c, blue), upon excitation at 320 nm. The observation of the emission was chosen above 660 nm to make sure that no DMP emission was eventually mixed in. The yellow signal outside of the crystal is due to noise and scattered photons. The red signal, observed at the border of the crystal, originates from excited Ox^+ molecules that are very close to the DMP molecules. They have a fast rise time and decay. The rise time is somewhat slower if we move further into the crystal (green), and it is substantially delayed in the middle part of the crystal (blue). The presence of a slow rise time and of a delayed decay shows that Ox^+ fluorescence is excited via FRET through DMP. The spatial dependence of this effect beautifully demonstrates the dynamics of the energy transfer and energy migration from the border of the crystal to the center. The rise of the fluorescence intensity of an acceptor excited via FRET by a donor can be well seen in a different experiment made with Ox^+ , Py^+ -ZL composites similar to those shown in Fig. 26, where Py^+ is the donor and Ox^+ the acceptor. This has been reported in Fig. 11 of [169]. The dyes Ox^+ and Py^+ have been proven for being useful in many additional FRET experiments. We mention the transfer of electronic excitation energy between randomly mixed dye molecules in the channels of zeolite [170] and optical spectroscopy experiments on dye-ZL crystals organized as oriented monolayers [128], and we



Fig. 29 (continued) profile on the left is observed when scanning the emission at 470 nm along the crystal axis, upon excitation at 320 nm. That in the middle is observed when monitoring the emission at 610 nm after excitation at 320 nm, while the profile on the right is seen when the sample is excited at 490 nm. **(b, c)** show the luminescence decay of composites in a confocal microscope excited with 1.2-ps pulses. **(b)** Decay observed as an average over the whole crystal. Blue: Decay of the DMP fluorescence at 470 nm when a DMP-ZL sample is excited at 320 nm. Green: Decay of the Ox^+ luminescence upon excitation at 495 nm and observation at 600 nm of a DMP, Ox^+ -ZL composite. Red: Decay of the DMP luminescence observed at 470 nm when a DMP, Ox^+ -ZL composite is excited at 320 nm. **(c)** Time- and space-resolved confocal microscopy results for a DMP, Ox^+ -ZL composite. The decay of the Ox^+ emission is similar to that in **(b)** but with the different regions indicated by different letters and colors (d, yellow; a, red; b, green; and c, blue). The corresponding decay of the luminescence of Ox^+ (at $\lambda \geq 660$ nm) when a DMP, Ox^+ -ZL composite is excited at 320 nm at the positions indicated on the left [50]. Adapted with permission from [50] Copyright Wiley VCH

refer to articles where also other dye combinations for achieving important FRET functionalities have been discussed [14, 15, 46, 181, 207].

Out of the many possible applications of such ZL-based FRET-composites that have been discussed in the literature, we refer only to utilization in luminescent solar concentrators (LSC). A LSC is a wave-guiding plate containing luminescent chromophores [208, 209]. Light enters the face of the plate, is absorbed, and is subsequently emitted at longer wavelength. The luminescent light is trapped by total internal reflection and guided to the edges of the plate, where it can be converted to electricity by a photovoltaic cell. Because the edge area of the plate is much smaller than the face area, the LSC operates as a concentrator of light. It has been well understood for more than 30 years that a major reflection loss in such a device is caused by the overlap between the absorption and emission spectra of the chromophores [208–214]. A way to minimize this loss is to use specific antenna material as illustrated in Fig. 28 [16]. Absorption and emission spectra are separated by employing a large amount of a strongly absorbing dye and very little emitting dye. This system bears important properties needed for an LSC. An important prerequisite is that light scattering can be suppressed quantitatively in the region of emission, because even weak scattering results in very severe losses. This criterion seems so far to be only partially fulfilled by ZL-based composites, despite of remarkable progress that has been made [16, 99, 103, 110, 215]. The emitting HR used in the composite shown in Fig. 28 cannot be considered as ideal, as already discussed in [16]. More research, and advanced chemical engineering, is needed for finding an optimal emitting dye. It seems also necessary to study the influence of the co-guest regarding the long-time stability of the material in order to meet the hard conditions faced in outdoor application. Monolayers of oriented ZL-based composites, as reported in Fig. 12, can be used to prepare optically strongly anisotropic layers, thus reducing reflection losses considerably [15]. This option is waiting to be explored. The wavelength range that has been covered so far by ZL-based antenna composites extends from the near UV to about 700 nm. Extension to 850 nm or even 900 nm looks possible but remains challenging. It seems that the materials known are not far away from being ready for realizing stable and efficient LSC devices. The research and technological effort needed for arriving there should, nevertheless, not be underestimated.

9.1 Communication with the Outside World

The stopcocks reported in Table 4 can be used for sealing the nanochannels of ZL crystals partially or completely regarding matter exchange with the environment. They can be used for binding individual crystals into chains or to arrange crystals perpendicularly to a surface, thus forming dense monolayers of oriented crystals. The stopcock-driven self-assembling of ZL crystals into uniformly oriented layers can be extended using cooperative interaction of a ligand function reacting with metal cations [76]. Some of the stopcocks in Table 4 consist of a part which can be

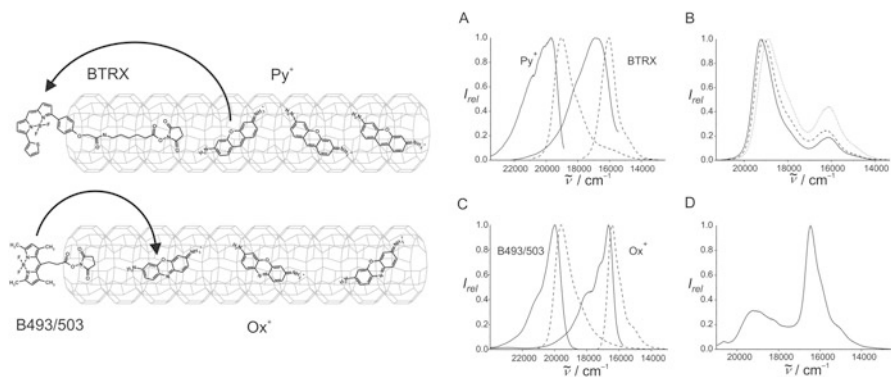


Fig. 30 Trapping energy from and injecting energy into dye-ZL nano antenna. Left: The upper arrangement schematizes ZL channels filled with Py^+ ; the ends of the channels are modified with BTRX stopcocks. The lower arrangement schematizes Ox^+ -ZL with the ends of the channels plugged with B493/503. Right: (a) Fluorescence (dash) and fluorescence excitation (solid) spectra of Py^+ -ZL and of BTRX-ZL. (b) Fluorescence spectra of the BTRX- $\{\text{Py}^+$ -ZL $\}$ observed upon selective excitation of Py^+ at $22,000 \text{ cm}^{-1}$. Three different Py^+ loadings were recorded: $p = 0.02$ (solid), $p = 0.06$ (dashed), $p = 0.10$ (dotted). (c) Fluorescence (dashed) and fluorescence excitation (solid) spectra of Ox^+ -ZL and of B493/503-ZL. (d) Fluorescence spectra of the B493/503- $\{\text{Ox}^+$ -ZL $\}$. All spectra are scaled to the same height [86]. Adapted with permission from [86] Copyright Wiley VCH

regarded as a luminescent label. This functionality is ideal for establishing communication from the inside of the channels to the outside or vice versa. The first report on such a communication was published in a paper entitled “Trapping Energy from and Injecting Energy into Dye-Zeolite Nanoantennae” [86]. We show the essentials of this early experiment in Fig. 30.

Energy transfer experiments were performed on the two different systems shown on the left side of Fig. 30. The Py^+ /BTRX system which we name BTRX- $\{\text{Py}^+$ -ZL $\}$ was used to investigate FRET from Py^+ inside of the ZL channels to the BTRX stopcocks and the B493/503- $\{\text{Ox}^+$ -ZL $\}$ system to investigate FRET from B493/503 stopcocks to Ox^+ molecules inside the ZL channels. ZL nanocrystals with a size of about 30 nm were used. The optical properties of Py^+ -ZL and of BTRX modified nanocrystals are shown in Fig. 30a. The spectral overlap integral between the fluorescence spectrum of Py^+ and the excitation spectrum of BTRX is large – a prerequisite for effective energy transfer. Py^+ -ZL composites with three different occupational probabilities $p = 0.02$, $p = 0.06$, and $p = 0.10$ were modified with two BTRX stopcocks per channel. Py^+ was selectively excited at $22,000 \text{ cm}^{-1}$. Figure 30b shows the resulting fluorescence spectra. We can clearly see the fluorescence band of BTRX at $16,000 \text{ cm}^{-1}$. It is the result of FRET from the excited Py^+ , located inside, to the BTRX stopcocks located at both ends of the channels. An increase of the donor concentration leads to a decrease of the mean donor-acceptor and mean donor-donor separation. It is expected that this results in more effective FRET, which is what we observe. The bathochromic shift of the Py^+ emission band is caused by self-absorption and re-emission [20, 171]. The reverse of this external

trapping is injection of electronic excitation energy. This was performed on the B493/503- $\{\text{Ox}^+\text{-ZL}\}$ shown on the left side of Fig. 30, lower. Again, we first characterized the $\text{Ox}^+\text{-ZL}$ and the nanocrystals modified with B493/503 separately, as seen in Fig. 30c. The spectral overlap integral between the emission spectrum of B493/503 and the excitation spectrum of Ox^+ is favorable for FRET. The B493/503- $\{\text{Ox}^+\text{-ZL}\}$ composite was investigated by selectively exciting the B493/503 stopcocks at $21,740\text{ cm}^{-1}$. The resulting emission spectrum seen in Fig. 30d shows that impressive energy transfer takes place from the B493/503 stopcocks to the Ox^+ located inside of the channels and emitting strongly at $16,000\text{ cm}^{-1}$. This marked the beginning of many successful experiments with luminescent stopcocks. Luminescent metal complexes as stopcock objects such Ru-ph4-TMS [216] and ZnPc [217, 218] were used as donor and acceptor chromophores, respectively, while Ir^{3+} complexes were investigated for the creation of photo- and electro-responsive properties [219]. Also quantum dots were tested as chromophores at the channel entrances for FRET properties [220]. Communication between a dye located inside of the channels and a stopcock-acceptor dye was explored by attaching biotin to a DMPOPOP-ZL by using sequential functionalization similar as seen in Fig. 30. Addition of a weak-binding antigen modified with ATTO-488 leads to important FRET features, thus proving that bio-labels based on dye-ZL composites have interesting properties as phototherapeutic agents [46, 181]. Luisa De Cola extended this by showing that bio-conjugate dye-ZL composites can be used as labels in protein microarrays [221]. Embedding stopcock- $\{\text{dye-ZL}\}$ composites into polymers by applying electrospinning resulted in highly interesting nanofiber-FRET communication systems using Cy02702 as a stopcock [222] and in a sophisticated combination to white light-emitting fibers [215].

The preparation of robust ZL monolayers of ZL crystals on a glass substrate with open channels on the free ends, we have discussed in Sect. 5.1, allows creating mono-directional antenna properties [111]. The consecutive insertion of two different dyes which cannot glide past each other as a result of spatial restrictions is the basis for the preparation of an antenna system capable of efficiently transporting electronic excitation energy. The consecutive insertion also allows to insert a dye and in a next step to plug the channel ends on the free part of the crystals standing on the substrate with a desired stopcock, acting either as an acceptor in FRET experiments or as a donor. The Py^+/Ox^+ pair has been used for testing this in the experiments reported in Fig. 31. To an oriented ZL monolayer, seen in the upper part of this figure, Py^+ was inserted by cation exchange followed by insertion of Ox^+ , resulting in the pattern seen in Scheme (a). The spectra illustrate that considerable energy transfer from the electronically excited Py^+ to the Ox^+ occurs after selective excitation of the Py^+ . We have discussed that extension beyond the interior of the ZL is achieved by selectively positioning molecules at the entrances. Here we show that this can be realized in a completely anisotropic way. Two different stopcock dyes have been used. ATTO-520, after selective excitation of at 460 nm, acts as injector to the acceptors Ox^+ located inside of the ZL nanochannels, as seen in Fig. 30b. The reverse is the case for the Cy02702 stopcock, which captures the electronic excitation energy of the selectively excited Py^+ located inside of the ZL channels, Fig. 30c.

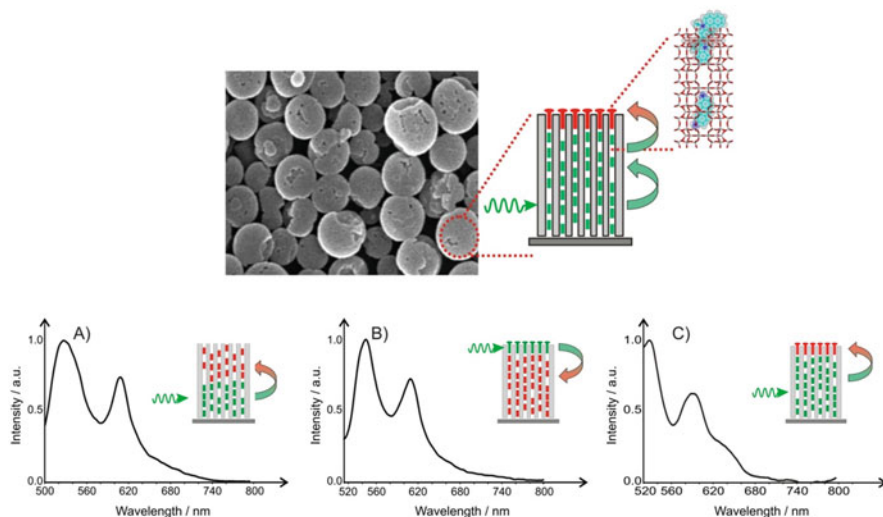


Fig. 31 FRET in oriented dy1,dye2-ZL, and stopcock-{dye-ZL} monolayers. Upper: We see on the left a SEM image of a ZL monolayer, the diameter of the disc-shaped crystals is in the order of 600 nm. The right part shows a scheme of a ZL crystal standing on a substrate which contains a luminescent chromophore and which is plugged with a stopcock. We also see a magnification of one channel. Lower: The schemes explain the different organizational pattern for which the emission spectra are reported. They emphasize that the investigated samples consist of correspondingly modified ZL crystals arranged as oriented monolayers on a glass plate. The spectra of the three samples have been scaled to the same height at the maxima. (a) Ox^+, Py^+ -ZL L monolayer. The emission spectrum was recorded after selective excitation of Py^+ at 460 nm. (b) ATTO-520- $\{\text{Ox}^+ - \text{ZL}\}$ monolayer. The emission spectrum was recorded after selective excitation of ATTO-520 at 460 nm. (c) Cy02702- $\{\text{Py}^+ - \text{ZL}\}$ monolayer. The emission spectrum was recorded after selective excitation of Py^+ at 460 nm [111]. Adapted with permission from [111] Copyright Wiley VCH

These were the first unidirectional antenna systems reported in literature [111]. Spectroscopy allows characterizing the remarkable optical anisotropy properties of such layers [46, 128]. Different organizational patterns have been explored by preparing oriented ZL monolayers with a functional linker who coordinates lanthanide ions [73]. Potential applications in optoelectronics, sensing, drug delivery, biological, biomedical applications, or solar energy devices of such highly organized systems have been discussed and are waiting for being explored [15, 98, 99, 109, 136, 223].

10 Biological and Biomedical Applications

Research regarding the utilization of ZL-based composites for biological and biomedical applications has been pioneered by Luisa De Cola. It was initiated by the discovery of anisotropic self-assembly of the nonpathogenic bacteria (*Escherichia coli*) with ZL composites. The bacteria bind selectively to the amino-functionalized

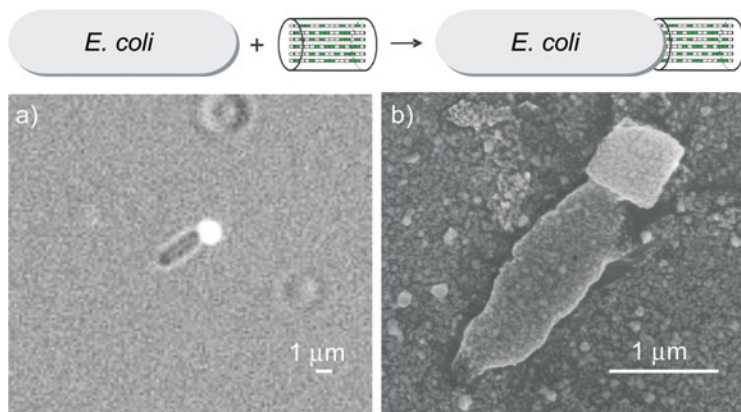


Fig. 32 Assembly of 1:1 ZL/bacterium, which we name bacteria- $\{\text{Py}^+\text{-ZL}\}$ assembly, in PBS buffer solution. Image a) was taken upon white and blue light illumination in an optical microscope. b) SEM image of the assembly after evaporation of the solvent and subsequent coating with silver [117]. Adapted with permission from [117] Copyright Wiley VCH

channel ends [117]. Selective amino functionalization of the channel entrances of ZL crystals, which were loaded with Py^+ as luminescent label, was realized using the reaction procedure explained in Fig. 7b [87]. The bacteria- $\{\text{Py}^+\text{-ZL}\}$ assembly was observed to be stable, presumably owing to electrostatic interactions. Fluorescence microscopy was employed in solution to characterize the assembly. The $\text{Py}^+\text{-ZL}$ can be easily detected in the aggregate, because of its characteristic green luminescence. We show this in Fig. 32a. Analysis performed on dry samples by using scanning electron microscopy (SEM) confirmed the solution results (Fig. 32b). It is interesting to note that the bacteria- $\{\text{Py}^+\text{-ZL}\}$ assembly is able to live under the physiological conditions. The organism is able to “swim” in the solution even with the heavy 1,000 nm ZL load. Self-assembly of two bacteria, one at each end, with a functionalized 1,000 nm ZL as the junction was observed when using an excess of bacteria [117]. These observations were later used for testing a novel scheme based on optical trapping to fabricate living micro-robots. A holographic optical tweezers allowed three-dimensional manipulation in real time. The assembly of living micro-robots consisted of a rod-shaped prokaryotic bacterium and a single elongated ZL crystal [147]. The abovementioned discovery was also used to test if photoactive ZL composites could eventually serve for targeting, labeling, and killing antibiotic-resistant bacteria. ZL crystals were loaded with DXP, as a luminescent label, amino functionalized at the channel ends as discussed above, and decorated with a silicon(IV) phthalocyanine dihydroxide as a photosensitizer that forms toxic singlet oxygen upon red light irradiation. This composite targets antibiotic-resistant *Escherichia coli* and *Neisseria gonorrhoea*, thus opening encouraging possibilities for the development of new photosensitizer composites for phototherapy [224].

Cell functions are affected by the way the cells interact with extracellular matrix. The many contact points between cells and a surface influence the information

transfer between the living cell and the matrix. This was explored in experiments with disc-shaped ZL, loaded with DXP as fluorescent label, and amino-functionalized channel entrances by the method as reported in Fig. 7b. One part of the amino-functionalized ZL crystals was further functionalized with d-penicillamine, and the other portion was reacted with l-penicillamine (penicillamine is a bioactive chelating agent). The so-modified composites were organized as monolayers on a glass substrate, similar as reported in Fig. 12b). This allowed studying stereo-controlled interactions of the obtained enantiomorphous substrate with different cell types. The authors made the remarkable observation that this strategy can be employed for the separation of primary cells and cancerogenic cells [136, 225]. We have already seen that ZL is a biocompatible crystalline aluminosilicate. The possibility for completely sealing the channel entrances as explained in Figs. 9, 10, and 19 was used successfully to prepare encapsulated $^{111}\text{In}^{3+}$ in nano-ZL, the surface of which can be further decorated as explained in Fig. 6, for scintigraphic imaging [97]. This was the first report of *in vivo* experiments with ZL composites. It demonstrated the feasibility of a new strategy for the radiolabeling using porous nanocontainers. Studer et al. reported in an article entitled “Site-Specific Immobilization of Proteins at ZL Crystals by Nitroxide Exchange Reactions” that surface nitroxide exchange reactions are well suited for a site-selective modification of ZL crystals. They have shown that the nitroxide exchange is a reversible process that can be conducted under mild, physiological conditions at the ZL surface. Proteins can be immobilized site-specifically to ZL crystals by covalent bond formation or by using his-tag, streptavidin-tag, or concanavalin A-mannose interactions [106]. We have already mentioned studies regarding bioconjugated fluorescent ZL composites as labels in protein microarrays [221]. Drug delivery into living cells was demonstrated using multifunctional ZL. The host was filled with a model drug, 4',6-diamidino-2-phenylindole (DAPI), and functionalized with DNA oligonucleotides. The release kinetics of DNA and of the guest molecules into living cells was studied to prove the multiple-drug-delivery ability of the system. The release kinetics of the two molecules and the localization of the nanocontainers were monitored by imaging them by confocal microscopy. The two emissions, the blue and the red, could be followed independently from each other to give information about the fate of the components inside of living cells. This was the first example in literature of using ZL crystals as multifunctional nanocontainers to simultaneously deliver DNA oligonucleotides and organic molecules into living cells. The system can be regarded as a prototype for the development of novel nanoparticles for drug delivery and gene therapy [163]. The preparation of density gradients made of bifunctional disc-shaped ZL crystals, loaded with guest molecules, on glass surfaces and the realization of “Janus” density gradient surfaces reported by Kehr et al. appears as an important extension of this [226]. The authors observed that more cells adhered on the density gradient of biopolymer-coated ZL than on uncoated ones, and they found that cells gradually internalized the guest-ZL from the underlying density gradient containing bifunctional ZL crystals. This means that ZL acted as nanocontainer by transporting the guest molecules housed within its channels into the cells through cellular uptake.

This serves as a proof of principle for surface-mediated drug delivery [226]. Silica-based nanomaterials are largely explored for biomedical applications. We have seen that ZL-based composites emerged as potent biomedical tools for imaging applications and as a platform for cell growth and interactions, since they show defined shape and size distributions and allow for both encapsulation of luminescent guests and exohedral surface modification. It is remarkable that the targeting action and fast cancer cell uptake of nanosized guest-ZL was observed for nanocrystals functionalized with Ctxb antibodies. This suggests feasibility of designing novel theranostic tools based on such composites [227]. Following this internalization, studies on disc-shaped ZL composites with DXP as guest using human cells were performed, because understanding the interaction between the ZL nanoparticles and cells is imperative for improving their potentialities. The intracellular trafficking and internalization kinetics of ZL into breast cancer cells and normal epithelial mammary cells were analyzed using scanning electron microscopy, confocal luminescence microscopy, and transmission electron microscopy. The uptake was observed to depend on the cell type. It was faster and more efficient in breast cancer cells, with a higher number of ZL particles being internalized by cancer cells over time, compared to that in the epithelial mammary cells. TEM results showed that the internalized nanoparticles were mainly localized in the cell vacuoles. SEM analysis revealed that cell internalization of ZL was faster in breast cancer cells when compared to normal breast cells, with some particles being already internalized after 5 min of incubation. Internalization of ZL by the normal epithelial mammary cells was slower, and, even after 60 min of incubation, only a small number of nanoparticles were internalized. The same behavior was observed by confocal fluorescence microscopy and TEM analyses. This evidenced that breast cancer cells internalize a higher number of ZL nanoparticles than epithelial mammary cells, with the particles being mainly localized in the vacuoles in both of the cell lines. The use of endocytic pharmacological inhibitors suggests that ZL is internalized by the cells by means of a caveolin-mediated process since dynasore significantly inhibited the uptake [164]. These are important results. They demonstrate the enormous potential of ZL-based composites for contributing to the elucidation of biological and biomedical processes.

11 Summary

The discoverers of zeolite L, Breck and Flanigen, would be surprised and delighted to learn about the world of properties, composites, science, and applications that have emerged from their invention and the fact that there is much more expected to come. Zeolite L seems to be the only known thermally and mechanically stable material with linear channels of about 1 nm diameter where the size of the particles and, hence, the length of the channels, can be tuned in the range from about 30 nm up to about 20'000 nm which can be synthesized as crystals of different morphology such as discs, barrels, and elongated tubes.

The combination of chemical, structural, and mechanical properties makes ZL a unique host for creating distinct composites by accepting inorganic, organic, and biologically relevant guests and by allowing specific surface modification. Such composites have therefore been investigated in a surprisingly broad field of applications, ranging from catalysis, lubricant technology, pigments, sensing, optics, optoelectronics, biology, drug delivery, diagnostics, and human medicine. This effort underlines the fact that hierarchically organized structures, presenting successive ordering from the molecular up to mm or cm scale, are of great interest. They allow establishing direct relationship between the molecular arrangements and the macroscopic world. ZL has been used for creating artificial photonic antenna systems for light harvesting, transport, and trapping. Much progress has been made in understanding the structure of guest-ZL composites. The advances in using ZL composites for diagnostics and for biological and biomedical applications are impressive.

Unfortunately, only technical grade ZL material is commercially available. This makes it difficult for many laboratories to perform experiments with appropriate ZL crystals. It would be desirable to find the following qualities of chemically pure ZL with narrow size distribution on the market on laboratory amounts: nanosized ZL (about 50 nm), disc-shaped ZL with flat surfaces, barrel-shaped ZL in the range of 600 nm, and cylinder-shaped ZL of about 1,500 nm or 2000 nm length. It is easy to predict that this would much enhance progress in the field of science and application of ZL as a host.

Acknowledgments I would like to thank Professors Ettore Fois and Gloria Tabacchi for important suggestions and for many excellent and inspiring discussions.

References

1. Tabacchi G (2018) Supramolecular organization in confined nanospaces. *ChemPhysChem* 19:1249–1297
2. Ramamurthy V, Inoue Y (2011) Supramolecular photochemistry, controlling photochemical processes. Wiley, Hoboken. ISBN: 978-0-470-23053-4
3. Ikigaki K, Okada K, Tokudome Y, Toyao T, Falcaro P, Doonan CJ, Takahashi M (2019) MOF-on-MOF: oriented growth of multiple layered thin films of metal–organic frameworks. *Angew Chem Int Ed* 58:6886–6890
4. Ozin GA, Arsenault AC (2005) Nanochemistry: a chemical approach to nanomaterials. RSC, Cambridge. ISBN: 0-85404-664-X
5. Ramamurthy V (1991) Photochemistry in organized and constrained media. VCH, New York. ISBN: 0-89537-775-2
6. Valtchev V, Mintova S, Tsapatsis M (2009) Ordered porous solids, recent advances and prospects. Elsevier, Oxford. ISBN: 978-0-444-53189-6
7. Cejka J, van Bekkum H, Corma A, Schüth F (2007) Studies in surface science and catalysis. In: Introduction to zeolite science and practice, vol 168. 3rd edn. Elsevier, Amsterdam. ISBN: 78-0-444-53063-9
8. Laeri F, Schüth F, Simon U, Wark M (2003) Host-guest systems based on nanoporous crystals. Wiley, Weinheim. ISBN: 3-527-30501-7

9. Wenz G (1994) Cyclodextrins as building blocks for supramolecular structures and functional units. *Angew Chem Int Ed* 33:803–822
10. Breck DW (1974) Zeolite molecular sieves. Wiley, New York. ISBN: 0-471-09985-6
11. Ernst S, Weitkamp J (1994) Synthesis of large pore aluminosilicates. *Catal Today* 19:27–67
12. International Zeolite Association. <http://www.iza-structure.org/databases>
13. Langley PJ, Hulliger J (1999) Nanoporous and mesoporous organic structures: new openings for materials research. *Chem Soc Rev* 28:279–291
14. Calzaferri G, Huber S, Maas H, Minkowski C (2003) Host–guest antenna materials. *Angew Chem Int Ed* 42:3732–3758
15. Calzaferri G (2012) Nanochannels: hosts for the supramolecular organization of molecules and complexes. *Langmuir* 28:6216–6231
16. Cao P, Khorev O, Devaux A, Sägesser L, Kunzmann A, Ecker A, Häner R, Brühwiler D, Calzaferri G, Belsler P (2016) Supramolecular organization of dye molecules in zeolite L channels: synthesis, properties, and composite materials. *Chem Eur J* 22:4046–4060
17. Calzaferri G, Gfeller N (1992) Thionine in the cage of zeolite L. *J Phys Chem* 96:3428–3435
18. Ramamurthy V, Sanderson DR, Eaton DF (1993) Control of dye assembly within zeolites: role of water. *J Am Chem Soc* 115:10438–10439
19. Gigli L, Arletti R, Vitillo JG, Alberto G, Martra G, Devaux A, Vezzalini G (2015) Thionine dye confined in zeolite L: synthesis location and optical properties. *J Phys Chem C* 119:16156–16165
20. Calzaferri G, Brühwiler D, Megelski S, Pfenniger M, Pauchard M, Hennessy B, Maas H, Devaux A, Graf U (2000) Playing with dye molecules at the inner and outer surface of zeolite L. *Solid State Sci* 2:421–447
21. Calzaferri G, Pauchard M, Maas H, Huber S, Khatyr A, Schaafsma T (2002) Photonic antenna system for light harvesting, transport and trapping. *J Mater Chem* 12:1–13
22. Artioli G, Kvick Å (1990) Synchrotron X-ray Rietveld study of perlielite, the natural counterpart of synthetic zeolite-L. *Eur J Mineral* 2:749–760. <https://doi.org/10.1127/ejm/2/6/0749>
23. Baerlocher C, Meier WM, Olson DH (2001) Atlas of zeolite framework types. 5th edn. Elsevier, Amsterdam
24. Ohsuna T, Slater B, Gao F, Yu J, Sakamoto Y, Zhu G, Terasaki O, Vaughan W, Qiu S, Catlow CRA (2004) Fine structures of zeolite-Linde-L: surface structures, growth unit and defects. *Chem Eur J* 10:5031–5040
25. Calzaferri G, Maas H, Pauchard M, Pfenniger M, Megelski S, Devaux A (2002) Supramolecularly organized luminescent dye molecules in the channels of zeolite L. In: Neckers DC, von Bünau G, Jenks WS (eds) *Advances in photochemistry*, vol 27. Wiley, Hoboken, pp 1–50. ISBN: 0-471-21451-9
26. Megelski S, Calzaferri G (2001) Tuning the size and shape of zeolite L based inorganic/organic host/guest composites for optical antenna systems. *Adv Funct Mater* 11:277–286
27. Zabala Ruiz A, Brühwiler D, Ban T, Calzaferri G (2005) Synthesis of zeolite L: tuning size and morphology. *Monatsh Chem* 136:77–89
28. Tsapatsis M, Lovallo M, Okubo T, Davis ME, Sadakata M (1995) Characterization of zeolite L nanoclusters. *Chem Mater* 7:1734–1741
29. Larlus O, Valtchev VP (2004) Control of LTL-type zeolite crystals. *Chem Mater* 16:3381–3389
30. Lee YJ, Lee JS, Yoon KB (2005) Synthesis of long zeolite-L crystals with flat facets. *Microporous Mesoporous Mater* 80:237–246
31. Brent R, Anderson MW (2008) Fundamental crystal growth mechanism in zeolite L revealed by atomic force microscopy. *Angew Chem Int Ed* 47:5327–5330
32. Brent R, Lobo AJW, Lewis DW, Anderson MW (2010) Modifying the crystal habit of zeolite L by addition of an organic space filler. *J Phys Chem C* 114:18240–18246
33. Itani L, Bozhilov KN, Clet G, Delmotte L, Valtchev V (2011) Factors that control zeolite L crystal size. *Chem Eur J* 17:2199–2210

34. Lupulescu AI, Kumar M, Rimer JD (2013) A facile strategy to design zeolite L crystals with tunable morphology and surface architecture. *J Am Chem Soc* 135:6608–6617
35. Ban T, Takamura M, Morikawa M, Ohya Y (2013) Comparison of organic ligand effects on morphology control between disc-like zeolite L crystals and zeolite A and W crystals. *Mater Chem Phys* 137:1067–1072
36. Wang Y, Lv T, Ma Y, Tian F, Shi L, Liu X (2016) Synthesis and characterization of zeolite L prepared from hydrothermal conversion of magadiite. *Microporous Mesoporous Mater* 228:86–93
37. Cho HS, Hill AR, Cho M, Miyasaka K, Jeong K, Anderson MW, Ku Kang J, Terasaki O (2017) Directing the distribution of potassium cations in zeolite-LTL through crown ether addition. *Cryst Growth Des* 17:4516–4521
38. Li S, Li J, Dong M, Fan S, Zhao T, Wang J, Fan W (2019) Strategies to control zeolite particle morphology. *Chem Soc Rev* 48:885–907
39. Gartzia-Rivero L, Bañuelos J, Izquierdo U, Barrio V, Bizkarra K, Cambra JF, López-Arbeloa I (2014) Microwave synthesis of LTL zeolites with tunable size and morphology: an optimal support for metal-catalyzed hydrogen production from biogas reforming processes. *Part Part Syst Charact* 31:110–120
40. Hennessy B, Megelski S, Marcolli C, Shklover V, Bärlocher C, Calzaferri G (1999) Characterization of methylviologene in the channels of zeolite L. *J Phys Chem B* 103:3340–3351
41. Calzaferri G (2017) Entropy in multiple equilibria, theory and applications. *Phys Chem Chem Phys* 19:10611–10621
42. Calzaferri G (2018) Entropy in multiple equilibria, compounds with different sites. *Phys Chem Chem Phys* 20:29070–29084
43. Pfenniger M, Calzaferri G (2000) Intrazeolite diffusion kinetics of dye molecules in the nanochannels of zeolite L monitored by energy transfer. *ChemPhysChem* 1:211–216
44. Gigli L, Arletti R, Tabacchi G, Fabbiani M, Vitillo JG, Martra G, Devaux A, Miletto I, Quartieri S, Calzaferri G, Fois E (2018) Structure and host-guest interactions of perylene-diimide dyes in zeolite L nanochannels. *J Phys Chem C* 122:3401–3418
45. Maas H, Khatyr A, Calzaferri G (2003) Phenoxazine dyes in zeolite L, synthesis and properties. *Microporous Mesoporous Mater* 65:233–242
46. Calzaferri G, Lutkouskaya K (2008) Mimicking the antenna system of green plants. *Photochem Photobiol Sci* 7:879–910
47. Viani L, Minoia A, Cornil J, Beljonne D, Egelhaaf HJ, Gierschner J (2016) Resonant energy transport in dye-filled monolithic crystals of zeolite L: modeling of inhomogeneity. *J Phys Chem C* 120:27192–27200
48. Gigli L, Arletti R, Tabacchi G, Fois E, Vitillo JG, Martra G, Agostini G, Quartieri S, Vezzalini G (2014) Close-packed dye molecules in zeolite channels self-assemble into supramolecular nanoladders. *J Phys Chem C* 118:15732–15743
49. Gigli L, Arletti R, Fois E, Tabacchi G, Quartieri S, Dmitriev V, Vezzalini G (2018) Unravelling the high-pressure behaviour of dye-zeolite L hybrid materials. *Crystals* 8 (79):1–22
50. Pauchard M, Huber S, Méallet-Renault R, Maas H, Pansu R, Calzaferri G (2001) Time- and space-resolved luminescence of a photonic dye-zeolite antenna. *Angew Chem Int Ed* 40:2839–2842
51. Woodtli P, Giger S, Müller P, Sägeser L, Zucchetto N, Reber MJ, Ecker A, Brühwiler D (2018) Indigo in the nanochannels of zeolite L: towards a new type of colorant. *Dyes Pigments* 149:456–461
52. Brühwiler D, Gfeller N, Calzaferri G (1998) Resorufin in the channels of zeolite L. *J Phys Chem B* 102:2923–2929
53. Brühwiler D, Calzaferri G, Torres T, Ramm JH, Gartmann N, Dieu LQ, López-Duarte I, Martínez-Díaz MV (2009) Nanochannels for supramolecular organization of luminescent guests. *J Mater Chem* 19:8040–8067

54. Pauchard M, Devaux A, Calzaferri G (2000) Dye-loaded zeolite L sandwiches as artificial antenna systems for light transport. *Chem Eur J* 6:3456–3470
55. Devaux A, Minkowski C, Calzaferri G (2004) Electronic and vibrational properties of fluorenone in the channels of zeolite L. *Chem Eur J* 10:2391–2408
56. Fois E, Tabacchi G, Calzaferri G (2010) Interactions, behavior, and stability of fluorenone inside zeolite nanochannels. *J Phys Chem C* 114:10572–10579
57. DeWilde W, Peeters G, Lunsford JH (1980) Synthesis and spectroscopic properties of tris(2,2'-bipyridine)ruthenium in zeolite Y. *J Phys Chem* 84:2306–2310
58. Lainé P, Lanz M, Calzaferri G (1996) Limits of the in situ synthesis of tris(2,2'-bipyridine) ruthenium(II) in the supercages of zeolite Y. *Inorg Chem* 35:3514–3518
59. Alvaro M, Fornés V, García S, García HScaiano JC (1998) Intrazeolite photochemistry. 20. Characterization of highly luminescent europium complexes inside zeolites. *J Phys Chem B* 102:8744–8750
60. Corma A, Garcia H (2004) Supramolecular host-guest systems in zeolites prepared by ship-in-a-bottle synthesis. *Eur J Inorg Chem* 6:1143–1164
61. Joshi PN, Bandyopadhyay R, Awate SV, Shiralkar VP, Rao BS (1994) Influence of physico-chemical parameters on n-hexane dehydrocyclization over Pt/LTL zeolites. *React Kinet Catal Lett* 53:231–236
62. Cortright RD, Dumesic JA (1995) L-zeolite-supported platinum and platinum/tin catalysts for isobutane dehydrogenation. *Appl Catal A Gen* 129:101–115
63. Choa SJ, Ryoob R (2004) Characterization of PtSn nanoparticles in KL zeolite and n-hexane aromatization activity. *Catal Lett* 97:71–75
64. Alvarez-Rodriguez J, Guerrero-Ruiz A, Rodriguez-Ramos I, Arcoya-Martin A (2005) Modifications of the citral hydrogenation selectivities over Ru/KL-zeolite catalysts induced by the metal precursors. *Catal Today* 107–108:302–309
65. Trakarnroek S, Jongpatiwut S, Rirksomboon T, Osuwan S, Resasco DE (2006) n-Octane aromatization over Pt/KL of varying morphology and channel lengths. *Appl Catal A Gen* 313:189–199
66. Jensen C, Buck D, Dilger H, Bauer M, Phillipp F, Roduner E (2013) Maximum hydrogen chemisorption on KL zeolite supported Pt clusters. *Chem Commun* 49:588–590
67. Jensen C, Slagereen J, Jakes P, Eichel RA, Roduner E (2013) Support effects on hydrogen desorption, isotope exchange, chemical reactivity, and magnetism of platinum nanoclusters in KL zeolite. *J Phys Chem C* 117:22732–22745
68. Xu D, Wu B, Ren P, Wang S, Huo C, Zhang B, Guo W, Huang L, Wen X, Qin Y, Yang Y, Li Y (2017) Controllable deposition of Pt nanoparticles into a KL zeolite by atomic layer deposition for highly efficient reforming of n-heptane to aromatics. *Cat Sci Technol* 7:1342–1350
69. Wang S, Xu D, Zhu D, Zhao B, Guan H, Qin Y, Wu B, Yangang Y, Liad Y (2020) Elucidating the restructuring-induced highly active bimetallic Pt-Co/KL catalyst for the aromatization of n-heptane. *Chem Commun* 56:892–895
70. Wang YG, Guo Z, Li HR (2007) Highly luminescent host-guest based on zeolite lanthanide complexes. *J Rare Earths* 25(Special Issue):283–285
71. Monguzzi A, Macchi G, Meinardi F, Tubino R, Burger M, Calzaferri G (2008) Sensitized near infrared emission from lanthanide-exchanged zeolites. *Appl Phys Lett* 92:123301-1–123301-3
72. Wang Y, Li H, Gu L, Gan Q, Li Y, Calzaferri G (2009) Thermally stable luminescent lanthanide complexes in zeolite L. *Microporous Mesoporous Mater* 121:1–6
73. Wang Y, Li H, Feng Y, Zhang H, Calzaferri G, Ren T (2010) Orienting zeolite L microcrystals with a functional linker. *Angew Chem Int Ed* 49:1434–1438
74. Li H, Cheng W, Wang Y, Liu B, Zhang W, Zhang H (2010) Surface modification and functionalization of microporous hybrid material for luminescence sensing. *Chem Eur J* 16:2125–2130

75. Mech A, Monguzzi A, Meinardi F, Mezyk J, Macchi G, Tubino R (2010) Sensitized NIR erbium(III) emission in confined geometries: a new strategy for light emitters in telecom applications. *J. Am Chem Soc* 132:4574–4576
76. Cao P, Li H, Zhang P, Calzaferri G (2011) Self-assembling zeolite crystals into uniformly oriented layers. *Langmuir* 27:12614–12620
77. Li P, Wang Y, Li H, Calzaferri G (2014) Luminescence enhancement after adding stoppers to europium(III) nanozeolite L. *Angew Chem Int Ed* 53:2904–2909
78. Gfeller N, Megelski S, Calzaferri G (1998) Transfer of electronic excitation energy between dye molecules in the channels of zeolite L. *J Phys Chem B* 102:2433–2436
79. Insuwan W, Rangsiwatananon K, Meeprasert J, Namuangruk S, Surakhot Y, Kungwan N, Jungsuttiwong S (2017) Combined experimental and theoretical investigation on fluorescence resonance energy transfer of dye loaded on LTL zeolite. *Microporous Mesoporous Mater* 241:372–382
80. Gartzia-Rivero L, Bañuelos J, López-Arbelo I (2017) Photoactive nanomaterials inspired by nature: LTL zeolite doped with laser dyes as artificial light harvesting systems. *Materials* 10 (495):1–13
81. Botta A, Buysch HJ, Puppe L (1991) Selective *p*-chlorination of biphenyl in L zeolites. *Angew Chem Int Ed* 30:1689–1690
82. Hashimoto S, Moon HR, Yoon KB (2007) Optical microscopy study of zeolite-dye composite materials. *Microporous Mesoporous Mater* 101:10–18
83. Devaux A, Calzaferri G, Belsler P, Cao P, Brühwiler D, Kunzmann A (2014) Efficient and robust host–guest antenna composite for light harvesting. *Chem Mater* 26:6878–6885
84. Calzaferri G (2001) Dye loaded zeolite material, Patent US 6,932,919 B2, granted 2005
85. Calzaferri G (2005) Dye loaded zeolite material containing devices, Patent US 7,372,012 B2, granted 2008
86. Maas H, Calzaferri G (2002) Trapping energy from and injecting energy into dye-zeolite Nanoantennae. *Angew Chem Int Ed* 41:2284–2288
87. Huber S, Calzaferri G (2004) Sequential functionalization of the channel entrances of zeolite L crystals. *Angew Chem Int Ed* 43:6738–6742. Printing mistake in formula 1 of FMOc-APMS an O atom is missing. For the correct formula see Fig. 7B and Table 4 of this publication
88. Laurent A, Debart F, Lamb N, Rayner B (1997) Esterase-triggered fluorescence of fluorogenic oligonucleotides. *Bioconj Chem* 8:856–861
89. Huber S, Calzaferri G (2004) Energy transfer from dye-zeolite L antenna crystals to bulk silicon. *ChemPhysChem* 5:239–242
90. Kaiser E, Colescott RL, Bossinger CD, Cook PI (1970) Color test for detection of free terminal amino groups in the solid-phase synthesis of peptides. *Anal Biochem* 34:595–598
91. Beierle JM, Roswanda R, Erne PM, Coleman AC, Browne WR, Feringa BL (2013) An improved method for site-specific end modification of zeolite L for the formation of zeolite L and gold nanoparticle self-assembled structures. *Part Part Syst Charact* 30:273–279
92. Szarpak-Jankowska A, Burgess C, De Cola L, Huskens J (2013) Cyclodextrin-modified zeolites: host–guest surface chemistry for the construction of multifunctional nanocontainers. *Chem Eur J* 19:14925–14930
93. Ban T, Brühwiler D, Calzaferri G (2004) Selective modification of the channel entrances of zeolite L with triethoxysilylated coumarin. *J Phys Chem B* 108:16348–16352
94. Phuong T, Khac-Minh T, Thi Van Ha N, Thi Ngoc Phuong H (2004) Synthesis and antifungal activities of phenylenedithioureas. *Bioorg Med Chem Lett* 14:653–656
95. Li H, Devaux A, Popovic Z, De Cola L, Calzaferri G (2006) Carboxyester functionalized dye-zeolite L host-guest materials. *Microporous Mesoporous Mater* 95:112–117
96. Kehr NS, Ergün B, Lülff H, De Cola L (2014) Spatially controlled channel entrances functionalization of zeolites L. *Adv Mater* 26:3248–3252
97. Tsotsalas MM, Kopka K, Luppi G, Wagner S, Law MP, Schäfers M, De Cola L (2010) Encapsulating $^{111}\text{In}^{3+}$ in nanocontainers for scintigraphic imaging: synthesis, characterization, and in vivo biodistribution. *ACS Nano* 4:342–348

98. Zhang J, Gong S, Yu J, Li P, Zhang X, He Y, Zhou J, Shi R, Li H, Peng A, Wang J (2017) Thermally stable white emitting Eu^{3+} complex@nanozeolite@luminescent glass composite with high CRI for organic-resin-free warm white LEDs. *ACS Appl Mater Interfaces* 9:7272–7281
99. Li H, Li P (2018) Luminescent materials of lanthanoid complexes hosted in zeolites. *Chem Commun* 54:13884–13893
100. Tabacchi G, Fois E, Calzaferri G (2015) Structure of nanochannels entrances in stopcock-functionalized zeolite L composites. *Angew Chem Int Ed* 54:11112–11116
101. Bossart O, Calzaferri G (2006) Organisation and solubilisation of zeolite L crystals. *Chimia* 60:179–181
102. Devaux A, Popovic Z, Bossart O, De Cola L, Kunzmann A, Calzaferri G (2006) Solubilisation of dye-loaded zeolite L nanocrystals. *Microporous Mesoporous Mater* 90:69–72
103. Suárez S, Devaux A, Bañuelos J, Bossart O, Kunzmann A, Calzaferri G (2007) Transparent zeolite-polymer hybrid materials with tunable properties. *Adv Funct Mater* 17:2298–2306
104. Busby M, Kerschbaumer H, Calzaferri G, De Cola L (2008) Orthogonally bi-functional fluorescent zeolite-L micro-crystals. *Adv Mater* 20:1614–1618
105. Schulte B, Tsotsalas M, Becker M, Studer A, De Cola L (2010) Dynamic microcrystal assembly by nitroxide exchange reactions. *Angew Chem Int Ed* 49:6881–6884
106. Becker M, De Cola L, Studer A (2011) Site-specific immobilization of proteins at zeolite L crystals by nitroxide exchange reactions. *Chem Commun* 47:3392–3394
107. Fibikar S, Luppi G, Martínez-Junza V, Clemente-León M, De Cola L (2015) Manipulation and orientation of zeolite L by using a magnetic field. *ChemPlusChem* 80:62–67
108. Buscher T, Barroso Á, Denz C, Studer A (2015) Synthesis and photo-postmodification of zeolite L based polymer brushes. *Polym Chem* 6:4221–4229
109. Barroso Á, Buscher T, Ahlers K, Studer A, Denz C (2018) Optomechanically assisted assembly of surface-functionalized zeolite-L-based hybrid soft matter. *Part Part Syst Charact* 35(1800041):1–6
110. Li H, Ding Y, Cao P, Liua H, Zheng Y (2012) Preparation and luminescence of transparent zeolite L-polymer hybrid materials. *J Mater Chem* 22:4056–4059
111. Zabala Ruiz A, Li H, Calzaferri G (2006) Organizing supramolecular functional dye-zeolite crystals. *Angew Chem Int Ed* 45:5282–5287
112. Seok Lee J, Lim H, Ha K, Cheong H, Yoon KB (2006) Facile monolayer assembly of fluorophore containing zeolite rods in uniform orientations for anisotropic photoluminescence. *Angew Chem Int Ed* 45:5288–5292
113. Yunus S, Spano F, Patrinoiu G, Bolognesi A, Botta C, Brühwiler D, Zabala Ruiz A, Calzaferri G (2006) Hexagonal network organization of dye-loaded zeolite L crystals by surface-tension driven autoassembly. *Adv Funct Mater* 16:2213–2217
114. Vohra V, Bolognesi A, Calzaferri G, Botta C (2009) Multilevel organization in hybrid thin films for opto electronic applications. *Langmuir* 25:12019–12023
115. Cucchi I, Spano F, Giovanella U, Catellani M, Varesano A, Calzaferri G, Botta C (2007) Fluorescent electrospun nanofibres embedding dye-loaded zeolite crystals. *Small* 3:305–309
116. Bossart O, Calzaferri G (2008) Selfassembly of zeolite L crystals on biological self-cleaning surfaces. *Microporous Mesoporous Mater* 109:392–397
117. Popovic Z, Otter M, Calzaferri G, De Cola L (2007) Self-assembling living systems with functional nanomaterials. *Angew Chem Int Ed* 46:6188–6191
118. Li Z, Lai C, Mallouk TE (1989) Self-assembling trimolecular redox chains at zeolite Y modified electrodes. *Inorg Chem* 28:178–182
119. Rolison D (1990) Zeolite-modified electrodes and electrode-modified zeolites. *Chem Rev* 90:867–878
120. Calzaferri G, Hädener K, Li JW (1991) Quasi-reversible silver zeolite electrode by photochemical modification. *Chem Commun* 9:653–654
121. Li J, Calzaferri G (1993) Silver zeolite 4A modified electrodes: intrazeolite effect. *Chem Commun* 18:1430–1432

122. Li JW, Pfanner K, Calzaferri G (1995) Silver-zeolite-modified electrodes: an intrazeolite electron transport mechanism. *J Phys Chem* 99:2119–2126
123. Lainé P, Seifert R, Giovanoli R, Calzaferri G (1997) Convenient preparation of close-packed monograin-layers of pure zeolite A microcrystals. *New J Chem* 21:453–460
124. Leiggener C, Calzaferri G (2004) Monolayers of zeolite A containing luminescent silver sulfide clusters. *ChemPhysChem* 5:1593–1596
125. Yoon KB (2007) Organization of zeolite microcrystals for production of functional materials. *Acc Chem Res* 40:29–40
126. Cao P, Wang Y, Li H, Yu X (2011) Transparent, luminescent, and highly organized monolayers of zeolite L. *J Mater Chem* 21:2709–2714
127. Albuquerque RQ, Zabala Ruiz A, Li H, De Cola L, Calzaferri G (2006) Luminescence quenching measurements on zeolite L monolayers. In: *Proceedings of SPIE, photonics for solar energy systems*, vol 6197, p 61970B 1-5
128. Huber S, Ruiz AZ, Li H, Patrinoiu G, Botta C, Calzaferri G (2007) Optical spectroscopy of inorganic-organic host-guest nanocrystals organized as oriented monolayers. *Inorg Chim Acta* 360:869–875
129. Li HR, Wang YG, Zhang WJ, Liu BY, Calzaferri G (2007) Fabrication of oriented zeolite L monolayers employing luminescent perylenediimide-bridged Si(OEt)₃ precursor as the covalent linker. *Chem Commun* 27:2853–2854
130. Wang Y, Li H, Liu B, Gan Q, Dong Q, Calzaferri G, Sun Z (2008) Fabrication of oriented zeolite L monolayer via covalent molecular linkers. *J Solid State Chem* 181:2469–2472
131. Cucinotta F, Popovic Z, Weiss EA, Whitesides GM, De Cola L (2009) Microcontact transfer printing of zeolite monolayers. *Adv Mater* 21:1142–1145
132. Hashimoto S, Samata K, Shoji T, Taira N, Tomita T, Matsuo S (2009) Preparation of large-scale 2D zeolite crystal array structures to achieve optical functionality. *Microporous Mesoporous Mater* 117:220–227
133. Woerdemann M, Gläsener S, Hörner F, Devaux A, De Cola L, Denz C (2010) Dynamic and reversible organization of zeolite L crystals induced by holographic optical tweezers. *Adv Mater* 22:4176–4179
134. Matsunaga C, Uchikoshi T, Suzuki TS, Sakka Y, Matsuda M (2013) Fabrication of the c-axis oriented zeolite L compacts using strong magnetic field. *Mater Lett* 93:408–410
135. Kehr NS, Ergün B, Lülff H, De Cola L (2014) Spatially controlled channel entrances functionalization of zeolite L. *Adv Mater* 26:3248–3252
136. Kehr NS, Atay S, Ergün B (2015) Self-assembled monolayers and nanocomposite hydrogels of functional nanomaterials for tissue engineering applications. *Macromol Biosci* 15:445–463
137. Demas JN, Harris EW, McBride RP (1977) Energy transfer from luminescent transition metal complexes to oxygen. *J Am Chem Soc* 99:3547–3551
138. Coutant MA, Payra P, Dutta PK (2003) Oxygen transport in zeolite Y measured by quenching of encapsulated tris(bipyridyl)ruthenium. *Microporous Mesoporous Mater* 60:79–90
139. Payra P, Dutta PK (2003) Development of a dissolved oxygen sensor using tris(bipyridyl) ruthenium (II) complexes entrapped in highly siliceous zeolites. *Microporous Mesoporous Mater* 64:109–118
140. Albuquerque RQ, Popovic Z, De Cola L, Calzaferri G (2006) Luminescence quenching by O₂ of a Ru²⁺ complex attached to zeolite L. *ChemPhysChem* 07:1050–1053
141. Amouyal E, Mouallem-Bahout M, Calzaferri G (1991) Excited states of M(II,d⁶)-4-phenylterpyridine complexes; electron localization. *J Phys Chem* 95:7641–7649
142. Kumar A, Biebuyck HA, Whitesides GM (1994) Patterning self-assembled monolayers: applications in materials science. *Langmuir* 10:1498–1511
143. Popović Z, Busby M, Huber S, Calzaferri G, De Cola L (2007) Assembling micro crystals through cooperative nano scale interactions. *Angew Chem Int Ed* 46:8898–8902
144. Becker M, De Cola L, Studer A (2013) Assembly of linear chains consisting of alternating silica beads and zeolite L crystals by nitroxide exchange reactions. *J Mater Chem C* 1:3287–3290

145. Vohra V, Bolognesi A, Calzaferri G, Botta C (2010) Self-assembled nanofibers of fluorescent zeolite L crystals and conjugated polymer. *Langmuir* 26:1590–1593
146. Veiga-Gutiérrez M, Woerdemann M, Prasetyanto E, Denz C, De Cola L (2012) Optical-tweezers assembly-line for the construction of complex functional zeolite L structures. *Adv Mater* 24:5199–5204
147. Barroso Á, Landwerth S, Woerdemann M, Alpmann C, Buscher T, Becker M, Studer A, Denz C (2015) Optical assembly of bio-hybrid micro-robots. *Biomed Microdevices* 17:1–8
148. Newsam JM (1989) Structures of dehydrated potassium zeolite L at 298 and 78 K and at 78 K containing sorbed perdeuteriobenzene. *J Phys Chem* 93:7694–7769
149. Megelski S, Lieb A, Pauchard M, Drechsler A, Glaus S, Debus C, Meixner AJ, Calzaferri G (2001) Orientation of fluorescent dyes in the nanochannels of zeolite L. *J Phys Chem B* 105:25–35
150. Sprung C, Weckhuysen BM (2015) Differences in the location of guest molecules within zeolite pores as revealed by multilaser excitation confocal fluorescence microscopy: which molecule is where? *J Am Chem Soc* 137:1916–1928
151. Gfeller N, Calzaferri G (1997) Energy migration in dye-loaded hexagonal microporous crystals. *J Phys Chem B* 101:1396–1408
152. Bussemer B, Munsel D, Wunscher H, Mohr GJ, Grummt UW (2007) Electronic properties of neutral dyes in the channels of zeolite L: a combined spectroscopic and quantum chemical study. *J Phys Chem B* 111:8–15
153. Fois E, Tabacchi G, Calzaferri G (2012) Orientation and order of xanthene dyes in the one-dimensional channels of zeolite L: bridging the gap between experimental data and molecular behavior. *J Phys Chem C* 116:16748–16799
154. Fois E, Tabacchi G, Devaux A, Belser P, Bruhwiler D, Calzaferri G (2013) Host-guest interactions and orientation of dyes in the one-dimensional channels of zeolite L. *Langmuir* 29:9188–9198
155. Manzano H, Gartzia-Rivero L, Bañuelos J, López-Arbeloá I (2013) Ultraviolet–visible dual absorption by single BODIPY dye confined in LTL zeolite nanochannels. *J Phys Chem C* 117:13331–13336
156. Zhou X, Wesolowski TA, Tabacchi G, Fois E, Calzaferri G, Devaux A (2013) First-principles simulation of the absorption bands of fluorenone in zeolite L. *Phys Chem Chem Phys* 15:159–167
157. Insuwan W, Rangsriwatananon K, Meeprasert J, Namuangruk S, Surakhot Y, Kungwan N, Jungsuttiwong S (2014) Combined experimental and theoretical investigation on photophysical properties of trans-azobenzene confined in LTL zeolite: effect of cis-isomer forming. *Microporous Mesoporous Mater* 197:348–357
158. Van Speybroeck V, Hemelsoet K, Joos L, Waroquier M, Bell RG, Catlow CRA (2015) Advances in theory and their application within the field of zeolite chemistry. *Chem Soc Rev* 44:7044–7111
159. Tabacchi G, Calzaferri G, Fois E (2016) One-dimensional self-assembly of perylene-diimide dyes by unidirectional transit of zeolite channel openings. *Chem Commun* 52:11195–111598
160. Arletti R, Fois E, Gigli L, Vezzalini G, Quartieri S, Tabacchi G (2017) Irreversible conversion of a water–ethanol solution into an organized two-dimensional network of alternating supra-molecular units in a hydrophobic zeolite under pressure. *Angew Chem Int Ed* 56:2105–2109
161. Gigli L, Vezzalini G, Quartieri S, Arletti R (2019) Compressibility behavior and pressure-induced over-hydration of zeolite K–AlSi–L. *Microporous Mesoporous Mater* 276:160–166
162. Busby M, Devaux A, Blum C, Subramaniam V, Calzaferri G, De Cola L (2011) Interactions of perylene bisimide in the one-dimensional channels of zeolite L. *J Phys Chem C* 115:5974–5988
163. Lülff H, Bertucci A, Septiadi D, Corradini R, De Cola L (2014) Multifunctional inorganic nanocontainers for DNA and drug delivery into living cells. *Chem Eur J* 20:10900–10904

164. Vilaça N, Totovao R, Prasetyanto EA, Miranda-Gonçalves V, Morais-Santos F, Fernandes R, Figueiredo F, Bañobre-López M, Fonseca AM, De Cola L, Baltazar F, Neves IC (2018) Internalization studies on zeolite nanoparticles using human cells. *J Mater Chem B* 6:469–476
165. Gasecka A, Dieu LQ, Brühwiler D, Brasselet S (2010) Probing molecular order in zeolite L inclusion compounds using two-photon fluorescence polarimetric microscopy. *J Phys Chem B* 114:4192–4198
166. Busby M, Blum C, Tibben M, Fibikar S, Calzaferri G, Subramaniam V, De Cola L (2008) Time, space, and spectrally resolved studies on J-aggregate interactions in zeolite L nanochannels. *J Am Chem Soc* 130:10970–10976
167. Matsuoka Y, Yamaoka K (1979) Film dichroism. II. Linearly polarized absorption spectra of acridine dyes in stretched poly(vinyl alcohol) films. *Bull Chem Soc Jpn* 52:3163–3170
168. Matsuoka Y (1980) Film dichroism. 4. Linear dichroism study of orientation behaviour of planar molecules in stretched poly(vinyl alcohol) film. *J Phys Chem* 84:1361–1366
169. Yatskou MM, Meyer M, Huber S, Pfenniger M, Calzaferri G (2003) Electronic excitation energy migration in a photonic dye-zeolite antenna. *ChemPhysChem* 4:567–587
170. Lutkouskaya K, Calzaferri G (2006) Transfer of electronic excitation energy between randomly mixed dye molecules in the channels of zeolite L. *J Phys Chem B* 11:5633–5638
171. Devaux A, Calzaferri G, Miletto I, Cao P, Belser P, Brühwiler D, Khorev O, Häner R, Kunzmann A (2013) Self-absorption and luminescence quantum yields of dye-zeolite L composites. *J Phys Chem C* 117:23034–23047
172. Albuquerque RQ, Calzaferri G (2007) Proton activity inside the channels of zeolite L. *Chem Eur J* 13:8939–8952
173. Kasha M (1953) Collisional perturbation of spin-orbit coupling and the mechanism of fluorescence quenching. A visual demonstration of the perturbation. *J Chem Phys* 20:71–74
174. Caspar JV, Ramamurthy V, Corbin DR (1990) The location of organic guests within X-type faujasite zeolites via external heavy-atom induced phosphorescence. *Coord Chem Rev* 97:225–236
175. Ramamurthy V, Caspar JV, Corbin DR, Schlyer BD, Maki AH (1990) Triplet-state photophysics of naphthalene and α,ω -diphenylpolyenes included in heavy-cations-exchanged zeolites. *J Phys Chem* 94:3391–3393
176. Valeur B (2002) *Molecular fluorescence, principles and applications*. Wiley, Weinheim. ISBN: 3-527-29919-X
177. Hashimoto S, Hagiri M, Matsubara N, Tobita S (2001) Photophysical studies of neutral aromatic species confined in zeolite L: comparison with cationic dyes. *Phys Chem Chem Phys* 3:5043–5051
178. Calzaferri G, Méallet-Renault R, Brühwiler D, Pansu R, Dolamic I, Diemel T, Adler P, Li H, Kunzmann A (2011) Designing dye-nanochannel antenna hybrid materials for light harvesting, transport and trapping. *ChemPhysChem* 12:580–594
179. Kuhn H, Försterling HD (2000) *Principles of physical chemistry*. Wiley, Chichester
180. Alén B, Bosch J, Granados D, Martínez-Pastor J, García JM, González L (2007) Oscillator strength reduction induced by external electric fields in self-assembled quantum dots and rings. *Phys Rev B* 75:045319-1–045319-7
181. Calzaferri G, Devaux A (2011) Manipulation of energy transfer processes within the channels of L-zeolite. In: Ramamurthy V, Inoue Y (eds) *Supramolecular photochemistry; controlling photochemical processes*. Wiley, Hoboken., ISBN: 978-0-470-23053-4, Chapter 9, pp 285–387
182. Fois E, Tabacchi G (2019) Water in zeolite L and its MOF mimic. *Z Krist Cryst Mater* 234 (7–8):495–511
183. Hawkes SJ (1996) All positive ions give acid solutions in water. *J Chem Educ* 73:516–517
184. Bussemer B, Dreiling I, Grummt UW, Mohr GJ (2009) Spectroscopic and quantum chemical study of the Brønsted acid sites in zeolite L channels with acidochromic cyanine dyes. *J Photochem Photobiol A Chem* 204:90–96

185. Klähn M, Seduraman A, Wu P (2011) Proton transfer between tryptophan and ionic liquid solvents studied with molecular dynamics simulations. *J Phys Chem B* 115:8231–8241
186. Lu Y, Moganty SS, Schaefer JL, Archer LA (2012) Ionic liquid-nanoparticle hybrid electrolytes. *J Mater Chem* 22:4066–4072
187. Li P, Zhang Y, Wang Y, Wang Y, Li H (2014) Luminescent europium(III)- β -diketonate complexes hosted in nanozeolite L as turn-on sensors for detecting basic molecules. *Chem Commun* 50:13680–13682
188. Davydov AS (1964) The theory of molecular excitons. *Usp Fiz Nauk* 82:393–448
189. Calzaferri G (2008) Energy transfer in nanochannels. *Il Nuovo Cimento* 123(B):1337–1367
190. Winiger CB, Langenegger SM, Calzaferri G, Häner R (2015) Formation of two homochromophoric H-aggregates in DNA assembled alternating dye stacks. *Angew Chem Int Ed* 54:3643–3647
191. McRae EG, Kasha M (1964) The molecular exciton model. In: *Physical progress in radiation biology*. Academic Press, New York, pp 23–42
192. Kobajashi T (1996) *J-aggregates*. World Scientific, Singapore
193. Lenhard JR, Hein BR (1996) Effects of J-aggregation on the redox levels of a cyanine dye. *J Phys Chem* 100:17287–17296
194. Sola-Llano R, Fujita Y, Gómez-Hortigüela L, Alfayate A, Uji-i H, Fron E, Toyouchi S, Pérez-Pariente J, López-Arbeloa I, Martínez-Martínez V (2018) One-directional antenna systems: energy transfer from monomers to J-aggregates within 1D nanoporous aluminophosphates. *ACS Photonics* 5:151–157
195. Bakalis LD, Knoester J (1999) Pump-probe spectroscopy and the exciton delocalization length in molecular aggregates. *J Phys Chem B* 103:6620–6628
196. Koti ASR, Taneja J, Periasamy N (2003) Control of coherence length and aggregate size in the J-aggregate of porphyrin. *Chem Phys Lett* 375:171–176
197. Zaarour M, El Siblani H, Arnault N, Boullay P, Mintova S (2019) Zeolite nanocrystals protect the performance of organic additives and adsorb acid compounds during lubricants oxidation. *Materials* 12(2830):1–12
198. Roduner E (2018) Superatom chemistry: promising properties of near-spherical noble metal clusters. *Phys Chem Chem Phys* 20:23812–23826
199. Azzam KG, Jacobs G, Shafer WD, Davis BH (2010) Aromatization of hexane over Pt/KL catalyst: role of intracrystalline diffusion on catalyst performance using isotope labeling. *J Catal* 270:242–248
200. Huo Q, Gong Y, Dou T, Zhao Z, Pan H, Deng F (2010) Novel micro- and mesoporous composite molecular sieve assembled by zeolite L nanocrystal and its performance for the hydrodesulfurization (HDS) of fluid catalytic cracking (FCC) gasoline. *Energy Fuel* 24:3764–3771
201. Liu B, Zhao Z, Wang D, Liu J, Chen Y, Li T, Duan A, Jiang G (2015) A theoretical study on the mechanism for thiophene hydrodesulfurization over zeolite L-supported sulfided CoAMo catalysts: insight into the hydrodesulfurization over zeolite-based catalysts. *Comput Theor Chem* 1052:47–57
202. Venkata Rao K, Jain A, George SJ (2014) Organic–inorganic light-harvesting scaffolds for luminescent hybrids. *J Mater Chem C* 17:3055–3064
203. Binder F, Calzaferri G, Gfeller N (1995) Dye molecules in zeolites as artificial antenna. *Sol Energy Mater Sol Cells* 38:175–186
204. Förster T (1946) Energiewanderung und Fluoreszenz. *Naturwissenschaften* 6:166–175
205. Förster T (1948) Zwischenmolekulare Energiewanderung und Fluoreszenz. *Ann Phys* 2:55–75
206. Gartzia-Rivero L, Bañuelos J, López-Arbeloa I (2015) Excitation energy transfer in artificial antennas: from photoactive materials to molecular assemblies. *Int Rev Phys Chem* 34:515–556
207. Köppe R, Bossart O, Calzaferri G, Sariciftci NS (2007) Advanced photon harvesting concepts for low energy gap organic solar cells. *Sol Energy Mater Sol Cells* 91:986–995
208. Goetzberger A, Greubel W (1977) Solar energy conversion with fluorescent collectors. *Appl Phys* 14:123–139

209. Markvart T, Danos L, Fang L, Parel T, Soleimani N (2012) Photon frequency management for trapping & concentration of sunlight. *RSC Adv* 2:3173–3179
210. Batchelder JS, Zewail AH, Cole T (1979) Luminescent solar concentrators. 1: theory of operation and techniques for performance evaluation. *Appl Opt* 18:3090–3110
211. Kittidachachan P, Danos L, Meyer TJ, Alderman N, Markvart T (2007) Photon collection efficiency of fluorescent solar collectors. *Chimia* 61:780–786
212. Debije MG, Verbunt PP (2012) Thirty years of luminescent solar concentrator research: solar energy for the built environment. *Adv Energy Mater* 2:12–35
213. Correia SFH, Frias AR, Fu L, Rondão R, Pecoraro E, Ribeiro SJL, André PS, Ferreira RAS, Carlos LD (2018) Large-area tunable visible-to-near-infrared luminescent solar concentrators. *Adv Sustain Syst* 1800002:1–9. <https://doi.org/10.1002/adsu.201800002>
214. Dienel T, Bauer C, Dolamic I, Brühwiler D (2010) Spectral-based analysis of thin film luminescent solar concentrators. *Sol Energy* 84:1366–1369
215. Vohra V, Calzaferri G, Destri S, Pasini M, Porzio W, Botta C (2010) Toward white light emission through efficient two step energy transfer in hybrid nanofibers. *ACS Nano* 4:1409–1416
216. Bossart O, De Cola L, Welter S, Calzaferri G (2004) Injecting electronic excitation energy into an artificial antenna system through a Ru²⁺ complex. *Chem Eur J* 10:5771–5775
217. Dieu LQ, Devaux A, López-Duarte I, Martínez-Díaz MV, Brühwiler D, Calzaferri G, Torres T (2008) Novel phthalocyanine based stopcock for zeolite L. *Chem Commun* 10:1187–1198
218. López-Duarte I, Dieu LQ, Dolamic I, Martínez-Díaz MV, Torres T, Calzaferri G, Brühwiler D (2011) On the significance of the anchoring group in the design of antenna materials based on phthalocyanine stopcocks and zeolite L. *Chem Eur J* 17:1855–1862
219. Cucinotta F, Guenet A, Bizzari C, Mróz W, Botta C, Milián-Medina B, Gierschner J, De Cola L (2014) Energy transfer at the zeolite L boundaries: towards photo- and electroresponsive materials. *ChemPlusChem* 79:45–57
220. Ramachandra S, Popović ZD, Schuermann KC, Cucinotta F, Calzaferri G, De Cola L (2011) Förster resonance energy transfer in quantum dot–dye loaded zeolite L nanoassemblies. *Small* 10:1488–1494
221. Li Z, Luppi G, Geiger A, Josel H-P, De Cola L (2011) Bioconjugated fluorescent zeolite L nanocrystals as labels in protein microarrays. *Small* 7:3193–3201
222. Vohra V, Devaux A, Dieu LQ, Scavia G, Catellani M, Calzaferri G, Botta C (2009) Energy transfer in fluorescent nanofibers embedding dye-loaded zeolites L crystals. *Adv Mater* 21:1146–1150
223. Li P, Yang D, Li H (2016) Luminescence ethylenediamine sensor based on terbium complexes entrapment. *Dyes Pigments* 132:306–309
224. Strassert CA, Otter M, Albuquerque RQ, Höne A, Vida Y, Maier B, De Cola L (2009) Photoactive hybrid nanomaterial for targeting, labeling, and killing antibiotic-resistant bacteria. *Angew Chem Int Ed* 48:7928–7931
225. El-Gindi J, Benson K, De Cola L, Galla HJ, Kehr NS (2012) Cell adhesion behavior on enantiomerically functionalized zeolite L monolayers. *Angew Chem Int Ed* 51:3716–3720
226. Kehr A, Motealleh AH (2016) Schäfer, cell growth on (“janus”) density gradients of bifunctional zeolite L crystals. *ACS Appl Mater Interfaces* 8:35081–35090
227. Marega R, Prasetyanto EA, Michiels C, De Cola L, Bonifazi D (2016) Fast targeting and cancer cell uptake of luminescent antibody-nanozeolite bioconjugates. *Small* 12:5431–5441

Highly Luminescent Metal Clusters Confined in Zeolites



Eduardo Coutino-Gonzalez, Maarten Roeffaers, and Johan Hofkens

Contents

1	Confined Functional Metal Clusters	77
1.1	Synthesis Strategies Developed for the Stabilization of Metal Clusters	78
1.2	Luminescent DNA Encapsulated Silver Clusters	78
1.3	Peptide-Protected Silver Clusters	80
1.4	Polymer-Encapsulated Silver Clusters	81
1.5	Silver Clusters Confined in Hard Template-Based Inorganic Systems	81
2	Luminescent Silver Clusters Confined in Zeolites	82
2.1	Early Studies on Silver-Exchanged Zeolites	82
2.2	Synthesis Strategy to Confine Luminescent Silver Clusters in Zeolites	83
2.3	Structure-to-Properties Relationship of Silver Clusters Confined in Zeolites	85
2.4	Tailoring the Optoelectronic Properties of Silver Clusters Confined in Zeolites	86
3	Characterization of Silver Clusters Confined in Zeolites	87
3.1	UV-VIS and FT-IR Spectroscopy	87
3.2	X-Ray-Based Techniques and Theoretical Modeling	89
3.3	Fluorescence Spectroscopy and Microscopy	91
3.4	Electron Microscopy	91
3.5	Electron Spin Resonance (ESR) Spectroscopy and Thermogravimetric Analysis (TGA)	92
4	Applications of Luminescent Silver-Containing Zeolites	94
4.1	Phosphors for Lighting Applications	94
4.2	Humidity Sensors	95
4.3	Optoelectronic Devices	96
4.4	Encoded Information Carriers	96
5	Other Luminescent Metal Clusters and Perovskite Quantum Dots Confined in Zeolites	97
6	Concluding Remarks	99
	References	100

E. Coutino-Gonzalez (✉)
Centro de Investigaciones en Óptica, A. C., León, Guanajuato, Mexico
e-mail: ecoutino@cio.mx

M. Roeffaers
cMACS, Department of Microbial and Molecular Systems, KU Leuven, Heverlee, Belgium

J. Hofkens
Chem&Tech, Molecular Imaging and Photonics, KU Leuven, Leuven, Belgium

Abstract The synthesis of functional metal clusters has attracted the attention of scientists from diverse fields over the past decades, due to promising optical properties associated with such structures, particularly their luminescence properties. However, the synthesis of sub-nanometer metal clusters consisting of few atoms is not straightforward due to the tendency of the clusters to aggregate, and thus rapidly losing their peculiar optical features. One strategy to achieve the stabilization of luminescent metal clusters is the use of zeolite frameworks that possess the appropriate molecular-sized pores and cages to confine metal clusters. Their cation-exchange capacities facilitate the uptake of metal ions, and after an activation procedure (heat treatment, photoactivation, X-ray irradiation), the formation of highly luminescent metal clusters is promoted, whose size and optical properties are controlled by the confinement environment. In this chapter, an up-to-date overview of synthesis strategies to stabilize luminescent metal clusters (particularly silver clusters) will be given, emphasizing the use of zeolites as confinement scaffolds. Moreover, several characterization strategies utilized in the study of silver clusters confined in zeolites will be discussed, focusing on the challenging nature of this task and the need for combinatorial approaches. Finally, emerging applications of luminescent silver-zeolite systems will be discussed.

Keywords Cation exchange · Confined spaces · Luminescent silver clusters · Self-assembly · Ship-in-a-bottle strategy · Zeolites

Abbreviations

DFT	Density functional theory
EDX	Energy dispersive X-ray
EQE	External quantum efficiency
ESR	Electron spin resonance
EXAFS	Extended X-ray absorption fine structure
FAU	Faujasite zeolite
FT-IR	Fourier transformed infrared
HAADF-STEM	High-angle annular dark-field scanning transmission electron microscopy
LED	Light emitting diode
LTA	Linde type A zeolite
LTL	Linde type L zeolite
MOF	Metal organic framework
MOR	Mordenite zeolite
NIR	Near infrared
NUV	Near ultraviolet
OLED	Organic light emitting diode
RHO	Rho zeolite
SOD	Sodalite zeolite
TEM	Transmission electron microscopy

TGA	Thermogravimetric analysis
UV-Vis	Ultraviolet-visible
WLED	White light emitting diode
XAFS	X-ray absorption fine structure
XEOL	X-ray-excited optical luminescence
XPS	X-ray photoelectron spectroscopy
XRD	X-ray diffraction
ZSM-5	Zeolite Socony Mobil-5

1 Confined Functional Metal Clusters

Metal clusters consisting of only several to tens of metal atoms possess unique properties that are different from those found in metal nanoparticles and bulk metal. Due to their electronic configuration and discrete energy levels, metal clusters exhibit peculiar electronic and optical properties [1, 2], such as molecule-like energy gaps [3, 4], strong photoluminescence [5, 6], and high catalytic activity [7–9]. Recently, many efforts to study metal clusters with multifunctional properties have been carried. Hence, these small structures might help to understand the missing link between atomic and nanoparticle metal behavior [10]. However, their direct experimental analysis is not always straightforward. Small metal clusters tend to aggregate and thus rapidly form larger nanoparticles [11], whereas the typical sub-nanometer size structures of such small metal clusters hinder their analysis [12]. An alternative to overcome this problem is the stabilization of metal clusters by different hosts. For instance, organic molecules such as thiolates [13, 14] or DNA [15, 16] have been widely utilized, whereas template-based inorganic scaffolds such as glasses [17] and zeolites [18, 19] are often used. However, the influence of the confinement scaffolds on the physicochemical properties of the oligoatomic metal clusters needs to be taken into consideration. It is well documented that the unique properties of metal clusters are related to their size, charge, shape, and interaction with their environment [20, 21]. For instance, the fluorescent emission of gold clusters encapsulated in DNA strands could be adjusted from the near infrared (IR) to the ultraviolet (UV) region by changing their core size. Gold clusters ranging from Au₃₁, Au₂₃, Au₁₃, Au₈, and Au₅ showed near IR, red, green blue, and UV emission, respectively [22, 23]. On the other hand, a relationship between gold metal cluster size and catalytic activity in the oxidation of CO and thiophenol has been demonstrated [9, 24]. It was found that gold clusters containing about 10 gold atoms were the species with the most catalytic activity, whereas larger Au clusters showed very low or no catalytic activity.

Next to functional gold cluster, a growing number of studies on sub-nanometer sized copper and silver clusters have also appeared. For instance, the synthesis of small oligoatomic copper clusters in microemulsions has been reported [25]. Photoluminescence was observed in copper clusters with less than 10 Cu

atoms, whereas larger copper nanostructures did not show emission. In a different study, a clear relationship between the luminescence properties and the clusters size was demonstrated in heat-treated [19] and photoactivated [18, 26] silver clusters confined in zeolitic matrices. Their optical properties were shown to be strongly influenced by the host crystal structure, the silver content, and the nature of the remaining counter-balancing ions. Remarkably, these silver cluster zeolite composites displayed high photo- and chemical-stability and high external quantum efficiencies (the external quantum efficiency of a luminescent material is defined as the ratio of the number of photons emitted to the number of photons absorbed by a material, this measure takes into account losses associated with the absorption of photons by non-emissive species, like, for instance, in this case, silver ions and impurities associated with the starting material) [27], making them very attractive, for instance, as phosphor materials for several applications, such as in fluorescent lamps and as upconverter materials in solar cells.

1.1 Synthesis Strategies Developed for the Stabilization of Metal Clusters

The selective synthesis of metal clusters is heavily hindered by the inevitable sintering tendency of metal clusters leading to the formation of larger nanoparticles with the subsequent loss of their peculiar optical properties. Throughout the years, many strategies have been explored to synthesize well-defined metal clusters. For instance, mass-selected oligoatomic silver clusters in gas phase have been widely investigated [1, 2, 28, 29]. Combining experimental and theoretical analysis, the optical properties and molecular transitions of such small isolated clusters have been studied. However, as these synthesis conditions are not ideal for most common applications, alternative stabilization protocols are required. The high coordination affinity of silver atoms with lone-pair electrons such as in nitrogen has been successfully exploited by using cytosine-rich DNA strands as a scaffold for small silver clusters [15]. Similarly, polyphosphates, peptides, or polymers have been utilized as stabilizing agents for the fabrication of silver clusters. Recently, the use of rigid confinement scaffolds, such as glasses and zeolites, have been also demonstrated. These strategies will be further discussed in the following sections using representative examples focusing on silver clusters.

1.2 Luminescent DNA Encapsulated Silver Clusters

Deoxyribonucleic acid (DNA) strands, especially the cytosine base, have shown strong affinity for Ag ions. In the pioneering work of Petty and Dickson [15], the fabrication of the first DNA-templated luminescent Ag nanoclusters was demonstrated (Fig. 1). Small silver subnanoclusters (<10 atoms) were produced by

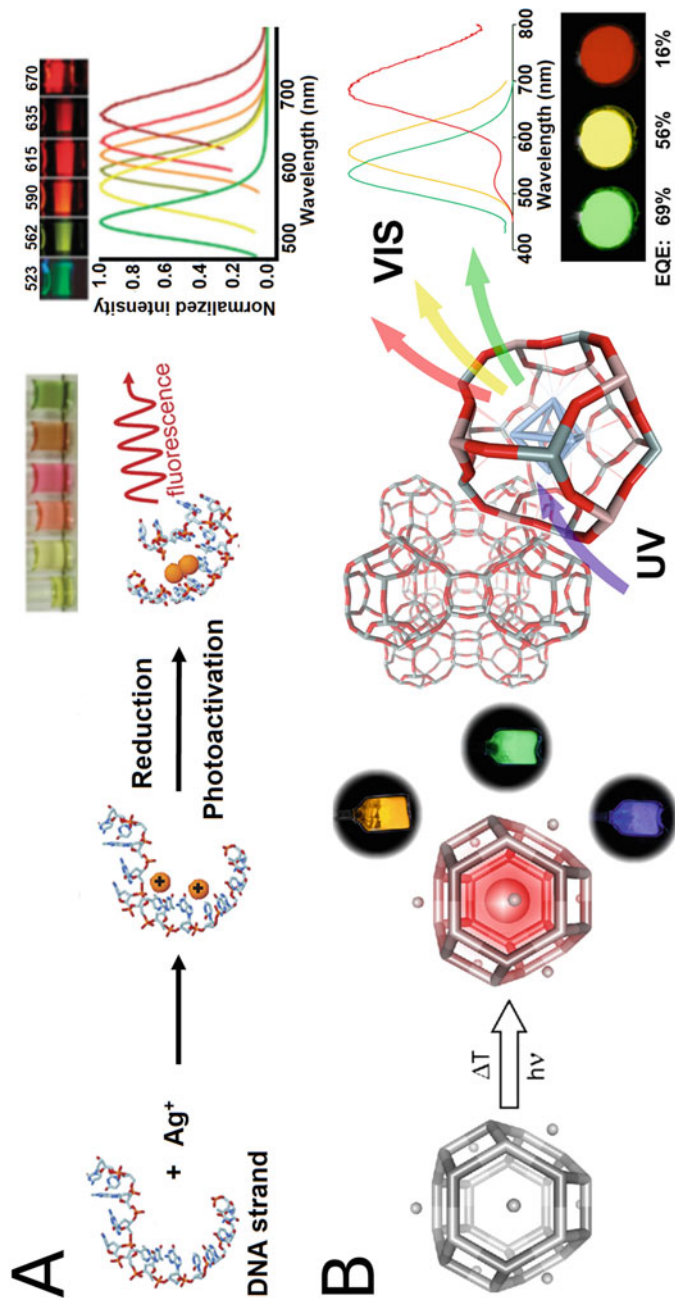


Fig. 1 Synthesis strategies used for the fabrication of luminescent silver clusters using organic (a) and inorganic scaffolds (b). Adapted from references [27, 30]. Copyright 2012, The Royal Society of Chemistry. Copyright 2013 American Chemical Society

chemical reduction, using sodium borohydride as reducing agent, of the attached Ag ions into a specific DNA sequence. This work opened up the possibilities for tailoring the optical and electronic properties of sub-nanometer silver clusters by controlling the stoichiometry of the initial reactants. From this study, several reports related to the fabrication, characterization, and applications of luminescent DNA-templated silver clusters appeared during the past decade [31–34]. These new emerging materials have found multiple applications, mostly as single molecule fluorophores [16], biolabels [35], intracellular staining agents [36], and (bio)chemical sensors [30]. At present, the structure of the silver clusters encapsulated in DNA strands is mostly studied by combinatorial approaches using HPLC-mass spectrometry, single crystal XRD, XAFS, IR, DFT, and UV-Vis spectroscopy [30]. However, up to now, there is no consensus about the correlation between the different emission colors observed in these samples and their structures. In a recent study [37] carried by Copp and collaborators, a dependence of fluorescent wavelength emissions on the number of silver atoms confined in DNA templates was proposed. They suggested that a magic number of silver atoms resulted in “magic emission bands.” Green emission was correlated to Ag_4^{n+} species, whereas Ag_6^{m+} clusters were suggested as being responsible of the red emission. These assumptions should be taken with caution, since, as already demonstrated by several groups [15, 16, 36], the functionality of DNA-templated silver clusters is influenced by several factors. Nevertheless, this pioneering work [37] might set the basis of a more rational approach for studying luminescent DNA-templated silver clusters.

1.3 Peptide-Protected Silver Clusters

Analogous to the production of luminescent silver clusters in DNA templates, the use of peptides to stabilize and generate luminescent silver clusters was introduced by Makarava and collaborators [38]. In this work, the fabrication of water-soluble organic-inorganic hybrid nanoclusters composed of silver and thioflavin T with remarkable fluorescent properties was reported. Different types of peptides were then explored, for instance, luminescent silver nanoclusters protected by glutathione spanning the entire visible range (blue-, green-, yellow-, and red-emitting species), and luminescence quantum yields over 60% were reported by Le Guevel and co-workers [39]. In a different study, the photoemission mechanism of carboxylate-protected silver nanoclusters was elucidated by Chen and collaborators [40]. They attributed the emission observed in Ag-carboxylate nanoclusters to ligand-to-metal charge transfer from silver in the carboxylate complex to the Ag atoms in the core of the clusters and the subsequent radiative relaxation. Based on these findings, the authors proposed a molecular-level design of luminescent Ag-carboxylate probes for different applications, such as in optoelectronics. On the other hand, the development of luminescent thiolate-capped silver nanoclusters has been explored [41]. Yang and collaborators [42] were able to elucidate the molecular structure of a yellow-emitting thiolate-protected Ag_{14} cluster by using

single crystal X-ray diffraction analysis. A metal core containing Ag_6^{4+} species encapsulated within a cubic arrangement of the thiolated template was then proposed.

1.4 Polymer-Encapsulated Silver Clusters

One of the most versatile strategies to fabricate luminescent water-soluble silver clusters is based on the utilization of synthetic polymers as encapsulating and stabilizing agents. The first evidence of the fabrication of polymer-encapsulated silver clusters was presented by Henglein [43], in this study silver ions were reduced in the presence of sodium poly(phosphate), as consequence colloidal particles containing silver clusters were generated. In subsequent reports, this concept was further developed, and synthetic polymers of different nature were used [44, 45]. However, the first study dealing with the fabrication of luminescent long-lived polymer-encapsulated silver clusters was carried by Dickson and Zheng [46], by using second and fourth-generation OH-terminated dendrimers as scaffolds and photon irradiation as activation procedure. They were able to synthesize luminescent silver nanoclusters ($\text{Ag}_2\text{--Ag}_8$) with emission maxima ranging between 500 and 650 nm. The use of these materials as biological labels was then suggested. In a different report carried by Diez and co-workers [47], the tunability of the emission of silver nanoclusters encapsulated in poly(methyl methacrylic acid, PMAA) by varying the polarity of the solvent was demonstrated. This work set the basis for the use of these materials for molecular sensing. In the majority of the previous examples, UV-Vis irradiation was mostly used as activation tool to generate well-defined silver clusters with narrowed size distribution. The use of chemical reducing agents was employed to a lesser extent since less specificity in the formation of the silver cluster was observed (mixture of silver clusters and nanoparticles). An example of an alternative and selective method to synthesize fluorescent polymer-protected Ag clusters was presented by Xu and Suslik [48]. By using a sonochemical approach and varying the synthetic conditions, it was possible to control the optical properties of silver clusters encapsulated in PMAA polymers. Due to the recent developments in the synthesis of polymer-encapsulated luminescent silver clusters, multiple applications have been proposed for these materials such as bioimaging, chemical and biosensing, single molecule studies, and catalysis.

1.5 Silver Clusters Confined in Hard Template-Based Inorganic Systems

Inspired by the work performed by scientists centuries ago on stained glass, several research groups started to explore the fabrication of well-defined silver clusters in

glassy substrates. One of the first reports on the optical properties of silver clusters in silica-based glasses was performed by Borsella and co-workers [49]. In this study different silver ion concentrations and gases used during the heat treatment of the samples were tested. A plausible formation mechanism was attributed to the creation of defects on the glass structure generated by the ion implantation technique, such defects served as nucleation sites to trigger the formation of luminescent silver clusters (<8 Ag atoms). In the same report, the use of these materials in optoelectronic applications was suggested. Since this report, different groups started to investigate the influence of the initial composition of the glass matrix on the optical properties of the formed silver clusters, for instance, the use of oxyfluoride [50], lanthanide-containing [51], and metal co-doped glassy substrates [52]. Next to the use of traditional activation techniques, researchers started to look for more controlled synthesis conditions for the fabrication of luminescent silver clusters in glassy substrates. Combinatorial approaches in which X-ray irradiation, heat treatment, and photon-induced activation [53–55] are employed, emerged as alternative activation procedures to fabricate, in a more controlled fashion, luminescent silver clusters in glassy substrates with specific functionalities. On the other hand, microporous materials have been pointed as suitable materials to stabilize sub-nanometer metal clusters; for instance, zeolites (Fig. 1) have been used as scaffolds for the fabrication of silver clusters and nanoparticles over the past five decades [56]. Recently, a novel type of microporous functional materials, metal organic frameworks (MOFs), were postulated as potential candidates to serve as scaffolds for the confinement of functional luminescent metal clusters and nanoparticles. This is exemplified in the work of Falcaro and Furukawa [57], in which a MOF material was doped with lanthanides ions (Eu^{3+} , Tb^{3+}) to generate a red emitting material. On the other hand, several attempts have been carried to fabricate metal nanoparticles within MOFs nanocavities. This was recently achieved in a study by Ameloot and collaborators [58] in which MOFs were used as photoactive matrices for the generation of metallic silver microstructures. In a different example, the rational design of the ligand prior to MOF assembly to encapsulate palladium nanoparticles was applied to fabricate advanced heterogeneous catalysts [59]. It is expected that these types of functional materials (metal doped MOFs) will emerge as a viable route for the fabrication of luminescent metal clusters as illustrated by recent reports [60, 61].

2 Luminescent Silver Clusters Confined in Zeolites

2.1 *Early Studies on Silver-Exchanged Zeolites*

Zeolites are aluminosilicate materials with a molecularly sized cages arrangement which makes them perfect candidates to accommodate sub-nanometer silver clusters, whereas their high cation exchange capacity facilitates the uptake of silver ion precursors within their pores and cages. A subsequent reduction step (heat treatment, Photoactivation X-ray irradiation) converts metal cations into oligoatomic clusters,

whose sizes and shapes are controlled by the dimensional restrictions induced by the zeolite framework. Moreover, the negative charge of the zeolite framework and the coordinating properties of the lattice oxygen atoms provide an additional stabilization of (partially charged) silver clusters.

Silver-exchanged zeolites were first reported in the early 60s by Ralek and collaborators [62]. In this study, a visual color change in the zeolite samples with respect to the silver loading and water content was observed. Nevertheless, at that time no explanation for this phenomenon was proposed. After this report, two groups started to study silver-exchanged zeolites independently. Seff and collaborators [63] initiated the detailed structural characterization of silver-loaded zeolites using X-ray diffraction experiments and proposed their use as chemical sensors, whereas Jacobs and co-workers [64] studied the silver clusters formation mechanisms in zeolites by analyzing their redox processes. One of the first studies on the photoluminescence characterization of silver-exchanged zeolites was reported by Ozin and collaborators [65]. In this study blue and green emission colors were observed in silver-loaded faujasite zeolites having different silver contents. Later, Calzaferri and co-workers [66] reported the formation of luminescent quantum-sized silver sulfide clusters in Linde Type A (LTA) zeolites. In this report, the formation of emissive species was achieved by the photosensitization of silver clusters by halides. More recently, the characterization of fluorescence in heat-treated silver-exchanged zeolites was carried out [19]; herein the emissive features of silver-exchanged zeolites were attributed to the presence of partially reduced small oligoatomic silver clusters. In Table 1 a compilation of photophysical properties of silver clusters confined in zeolites is displayed, including steady-state and time-resolved photoluminescence results.

2.2 Synthesis Strategy to Confine Luminescent Silver Clusters in Zeolites

Space-confinement of silver clusters in zeolites is a versatile method to stabilize highly luminescent silver clusters using a ship-in-a-bottle approach. Starting from a variety of zeolite topologies with different silicon-to-aluminum ratios and alkali metal ions (i.e., sodium, potassium, lithium), silver uptake is accomplished through cation exchange by immersing zeolite precursors (in powder form) in silver nitrate solutions of different concentrations (to study the effect of zeolite silver loading), the cation exchange step is employed to replace the counter-balancing ions present in the zeolites by silver ions. Once the zeolites have been exchanged with silver ions, a subsequent activation step is required to promote the formation of luminescent silver clusters; such activation can be achieved by heat treatment, X-ray irradiation, and Photoactivation [18, 19, 68]. As a result of the activation, partially reduced silver clusters are formed through different pathways where the required electrons needed for metal ion reduction are provided by the zeolite framework oxygen (resulting in

Table 1 Photophysical properties of luminescent silver-zeolite composites

Ag-zeolite	Exc/Em (nm)	Lifetime	EQE (%)	Comments	Ref.
Ag-FAUY	308/483 334/530	–	–	Ag content: 2.5–34.0 wt %	[65]
Ag ₂ S-LTA	280/490 280/530 280/650	–	–	Ag content: 4.0–25.0 wt %	[66]
Ag ₂ S-LTA	280/620 280/650	81 μs (for the orange-red luminescent samples)	–	Emission profiles were recorded at 78, 173, and 223 K, Ag content: 0.2–25.0 wt%	[67]
Ag-LTA	375/540	0.1, 1, 4 ns	–	Photoactivation by UV illumination, Ag content: 8.1 wt% ^a	[18]
Ag-FAU Ag-LTA	300–350/ 550 450/690	<0.5, 1.0–2.5 ns, 3.5–6.5 ns for the green emitting species, 115 μs, 835 μs for the red emitting species	–	Ag content: 2.6–40.7 wt % ^a	[19]
Ag-FAU Ag-LTA	340/550 420/690	–	20–69 1–20	Ag content: 2.6–40.7 wt % ^a	[27]
Ag-FAU Ag-LTA	320/550 420/660	0.60, 3.30 ns Ag-FAU, 0.35, 1.60, 4.10 ns Ag-LTA (green emitters) 0.38, 2.50 ns Ag-LTA (orange-red emitters)	–	Samples synthesized by X-ray irradiation, Ag content: 13.4–32.7 wt% ^a	[68]
Ag-LTA	342/855	21 μs	–	Ag content: 7.3–36.6 wt %	[69]
Ag-LTA	260/450 260/580 420/650	0.80 ns, 3.5 ns, 24 μs, 270 μs for green/yellow emitting species, 0.90 ns, 5.20 ns for orange/red emitting species	1–62	Partially lithium exchanged LTA zeolites were employed in this study, Ag content: 4.8–40.7 wt% ^a	[70]
Ag-SOD	320/540 330/600 360/640	–	–	Thermal activation at 250°C, Ag content: 11 & 89 wt%	[71]
Ag-FAUX	271/550 311/550	–	20.8	Ag content: 2–53 wt%	[72]
Ag-FAU Ag-LTA	340/550 420/690	–	3–99	Ag content: 2.6–40.7 wt % ^a	[73]
Ag-FAU	313/573	341 ns, 491 ns, 553 ns, 556 μs	5.9–17.8	X-ray activation of nano-sized zeolite crystals, Ag content: 10 wt%	[74]

(continued)

Table 1 (continued)

Ag-zeolite	Exc/Em (nm)	Lifetime	EQE (%)	Comments	Ref.
Ag-LTA	250–255/ 510–605 270–285/ 510–605	–	4–52	Partially and fully lithium exchanged LTA zeolites were employed in this study, Ag content: 2.6–40.7 wt% ^a	[75]
Ag-LTA	310/560	0.08 ns, 0.9 ns, 3.4 ns, 34 ns, 409 μ s	–	Ag content: 13.4 wt%	[76]
Ag-FAUY	365/450–650	–	–	Heat treatment from 200–950°C, 0.5×10^{-3} to 0.1 M of AgNO ₃	[77]
Ag-FAUY	230/448 320/503	–	41	Effect of co-existing cations, 1.20–92.1% Ag-exchange ratio	[78]
Ag-S-LTA	340/450–600	0.18 ns, 0.99 ns, 2.63 ns, 7.41 ns, 20.9 ns, 34.3 μ s	19–30	Sulfur-containing zeolites, Ag content: 6.3 wt% ^a	[79]

^aTheoretical values based on a dehydrated basis, assuming a complete uptake of silver ions by the zeolite host

local lattice damage) and/or by oxygen of the hydration water present in the zeolites [19, 27]. Several parameters (Fig. 2) are of paramount importance to achieve the formation of luminescent silver clusters in zeolites. Regarding the starting zeolite material, the presence of cages and cavities of appropriate dimensions will limit the size of the formed clusters, next to this, the silicon-to-aluminum ratio plays an important role since this will dictate the cation exchange capacity of the zeolites. Moreover, the counter-balancing cations present in the zeolite topologies is also an important parameter to consider.

2.3 Structure-to-Properties Relationship of Silver Clusters Confined in Zeolites

One of the ultimate goals in the study of functional metal clusters is the correlation between their atomic scale organization and physicochemical properties. In the case of luminescent silver clusters confined in zeolites, a detailed structural and electronic characterization is required to understand the size-to-structure functional relationship and for rational material optimization [80]. However, the analysis of such sub-nanometer species is challenging due to the sensitivity of silver clusters and zeolite frameworks to radiation damage imposed by highly energetic beam probes used in high-resolution techniques [68, 80]. A recent report demonstrated that by

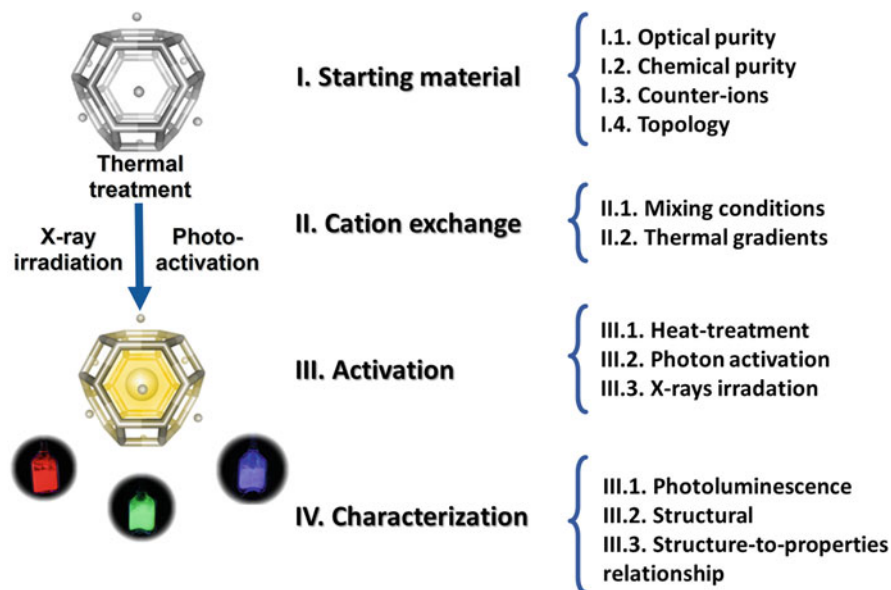


Fig. 2 Synthesis strategy (highlighting the main parameters) utilized to confine and characterize luminescent silver clusters in zeolites

using combinatorial and multidisciplinary approaches the exact nature of luminescent silver clusters in LTA zeolites was unraveled by X-ray-excited optical luminescence-EXFAS (XEOL-EXAFS), DFT, and photoluminescence experiments [81]. This task had remained elusive for over more than four decades; therefore, this report may pave the way for the development of rational design rules for confining luminescent silver and other metal clusters in zeolites.

2.4 Tailoring the Optoelectronic Properties of Silver Clusters Confined in Zeolites

The versatility of the Ag-zeolite multicomponent system is directly related to the intrinsic and complex tunability of the system as a whole [82]. There are several key zeolite parameters, which confer peculiar optical properties to the clusters, such as, the framework Si/Al ratio, choice of counter-balancing ions, silver loading, and zeolite topology (Fig. 2). De Cremer and collaborators systematically evaluated the effect of zeolite topology, silver loading, and counter-balancing cation on the luminescence color displayed by Ag-LTA and Ag-FAU zeolites, observing that green and red emitters were mainly found in Ag-LTA zeolite, whereas for Ag-FAU samples green and yellow emitters were observed [19]. Later, the external quantum efficiency (EQE) of Ag-LTA and Ag-FAU samples was evaluated,

showing that Ag-FAU zeolites were the best performing materials with EQEs reaching 69%, whereas Ag-LTA zeolites displayed a modest EQE of 16% [27]. The quest for optimizing the luminescence performance of Ag-zeolites derived in a recent study where by fine-tuning the synthesis parameters of silver-exchanged FAU zeolites EQEs reaching 100% were reported [73]. As for Ag-LTA systems, several attempts were performed to push EQEs toward industrial appealing values. One approach that rendered promising results was the use of lithium as counterbalancing cations in Ag-LTA zeolites [70], where maximum EQEs values of about 62% were recorded together with a dynamical emission color response controlled by water present in the zeolites. This report opened up the possibility of developing switchable optoelectronic responses in Ag-LTA materials. This was later studied at the atomic scale by EXAFS experiments, revealing that water and framework oxygen ligands strongly affect the organization of silver clusters valence electrons causing the peculiar on-off photoluminescence switching of the materials [83].

3 Characterization of Silver Clusters Confined in Zeolites

Deciphering the physicochemical properties of silver clusters confined in zeolites is fundamental for the understanding of the different processes behind cluster formation and their functional properties. More importantly, the detailed structural characterization allows researchers to deeply understand the structure-to-properties relationship, which provides the fundamental basis for silver clusters optimization for different applications. Because the optical, electronic, and catalytic properties of sub-nanometer silver clusters are strongly linked to their size, composition, morphology, and electronic state, several experimental techniques have been applied to perform the characterization of silver clusters confined in zeolites. It is worth to mention that due to the small size of silver clusters contained in zeolite matrices, some techniques that are normally applied in the characterization of larger silver nanoparticles are not suitable for the study of sub-nanometer-sized silver clusters. In this section, we briefly revise common characterization techniques employed in the analysis of silver-exchanged zeolites using representative examples. These include UV-VIS-NIR and X-ray spectroscopy, electron microscopy, theoretical modeling, fluorescence microscopy, EPR spectroscopy, and thermogravimetric analysis (Fig. 3).

3.1 UV-VIS and FT-IR Spectroscopy

Sub-nanometer silver clusters present a molecular-like behavior due to their special electronic structure which consists of discrete energy levels, resulting in the generation of optical transitions with absorbance bands that can be monitored by UV-Vis spectroscopy. This technique has been successfully applied in the characterization of

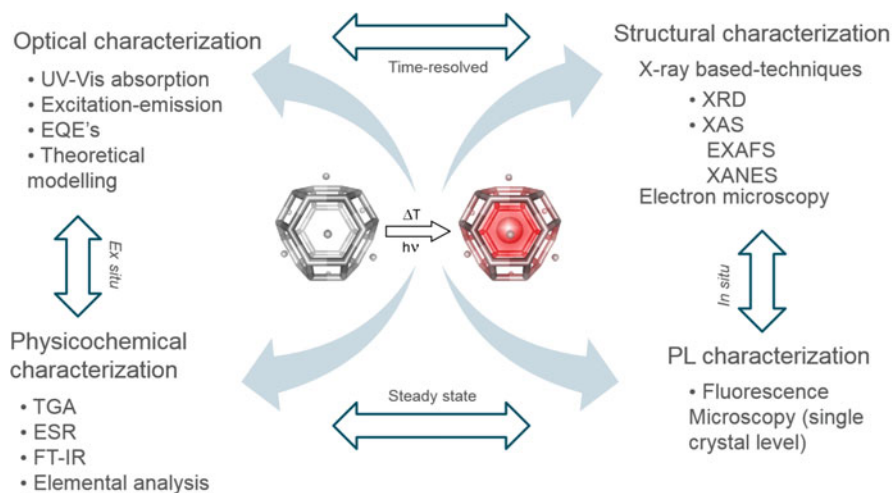


Fig. 3 Characterization techniques employed in the study of luminescent silver clusters confined in zeolites

the different silver species formed in zeolite matrices. For instance, the cause of the yellow color of activated silver-containing LTA zeolites was thoroughly studied by Calzaferri and collaborators [84–97]. They showed that upon activation under high vacuum, silver-exchanged LTA zeolites turned yellow at room temperature and brick-red at 200°C and that all absorption bands appearing in the UV-Vis region were dependent on the hydration of the Ag ions. They explain this dynamical change of colors as electronic transitions from the lone pairs of oxygen atoms of the zeolite framework to the empty 5 s orbital of the Ag ions (ligand-to-metal charge transfer, LMCT). In a different study, a correlation between the tentative positions of silver ions in the zeolite lattice with respect to their electronic transitions was reported [85] based on a full UV-Vis spectral characterization and molecular orbital characterization. In this study, the water dependence of the silver clusters absorption bands was also observed.

The detailed investigation on the interactions of the different silver species contained in zeolite matrices and their environments under different reducing gases was explored by Baumann and co-workers [86] by means of IR transmission spectroscopy. They proved that at different stages of silver clusters formation, interactions of certain gases (CO, CO₂) with different silver species gave rise to structural changes and kinetics of clusters formation. In a subsequent study, Bo and Kevan [87] demonstrated by far-infrared experiments that the transformation between silver ionic clusters and silver metal nanoparticles in RHO zeolites could be cycled by reduction and oxidation reactions. Even further, the analysis performed by Wang and collaborators [88], in which in situ FT-IR spectroscopy was employed to probe the locations of silver ions in silver-exchanged LTA zeolites, showed evidence of different silver species inside the zeolite framework. Although it is difficult to find direct evidence for the different interactions between silver clusters

and the zeolite framework by FT-IR spectroscopy, this analytical tool provides indirect information that could be helpful, for instance, in the analysis of the role of water on the optical properties of silver loaded zeolites.

3.2 X-Ray-Based Techniques and Theoretical Modeling

X-ray diffraction (XRD) is a useful tool used for determining the atomic and molecular structure of a crystal, in which the crystalline atoms cause the diffraction of an X-ray beam into many specific directions. By measuring these angles and intensities of the diffracted beams, the density of electrons within the crystal structure can be estimated. From this electron density, the mean positions of the atoms in the crystal structure can be determined, as well as their chemical bonds and degree of disorder. XRD has been one of the preferred characterization techniques to study the crystalline and well-ordered structures of natural and synthetic zeolites. This type of analysis has been extended to metal exchanged zeolites, for instance, a detailed review on the extraframework metal cation distributions in faujasite zeolites through XRD was recently published [89]. In the case of silver-containing LTA zeolites, the dynamical change of colors that resulted from the heat treatment of silver-exchanged LTA zeolites was systematically studied via XRD by two different research groups. Kim and Seff [63] attributed this color change to the presence of partially reduced octahedral Ag_6 clusters within the sodalite cages of the zeolite framework, whereas Jacobs and collaborators [90] suggested that the coloration was due to the presence of linear Ag_3 clusters. Further investigation on Ag-LTA samples pointed out that the formation of silver clusters with different sizes could be achieved by varying the initial silver loading [19]. Next to silver-exchanged LTA zeolites, other zeolite topologies containing different silver species, mostly utilized for catalytic applications, have been analyzed by XRD. For instance, Lee and collaborators [91] reported the formation of Ag_2^{2+} , Ag_3^+ , Ag_3^{2+} silver clusters in faujasite zeolites dehydrated under oxygen flow. In a similar study, Kim and co-workers determined the crystal structure of fully Ag-exchanged faujasite zeolites under reducing environments [92], they found the presence of larger silver clusters (Ag_4^+ , Ag_8^{m+}) when the samples were exposed to a H_2 gas flow.

X-ray absorption fine structure (XAFS) has also been widely applied in the characterization of silver-exchanged zeolites (Fig. 4). This technique provides information at atomic scale in structures lacking long-range order (such as sub-nanometer clusters), including metal-to-metal and metal-to-ligand bonding, as well as for estimating the cluster nuclearity. By using this technique metallic and cationic silver clusters composed of 2–8 Ag atoms such as dimers (Ag_2), trimers (Ag_3^+) and hexamers (Ag_6^{+4}) have been reported for silver-exchanged zeolites [93–95]. Additionally, XAFS studies have revealed the great influence that the confinement scaffold (zeolite topology) possesses on the physicochemical properties of silver clusters [96, 97]. However, the data interpretation of the results obtained by XAFS on silver-exchanged zeolites should be performed with caution, a recent study

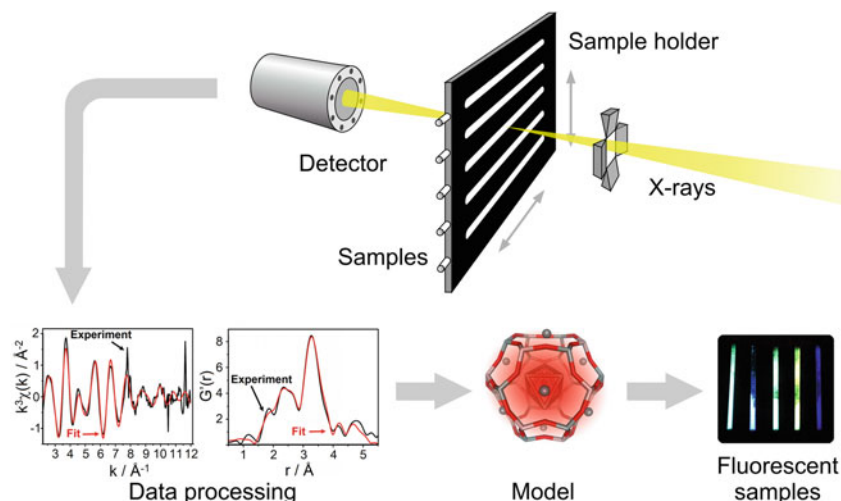


Fig. 4 Schematic representation of the use of EXAFS technique to characterize luminescent silver clusters confined in zeolites. Adapted from Ref. [82]. Copyright 2017 American Chemical Society

showed the great influence that the X-ray beam can have in the dynamics of formation/destruction of luminescent silver clusters in LTA and FAU zeolites [68]. Recently the characterization of luminescent silver clusters confined in LTA zeolites using a combination of X-ray-excited optical luminescence and extended X-ray absorption fine structure (XEOL-EXAFS) pointed to the presence of tetrahedral silver clusters in the center of sodalite cages, suggesting that their optical properties originate from a confined two-electron superatom quantum system [81]. This study highlights the usefulness of this combinatorial approach in deciphering the exact structure of the luminescence silver species. Additionally, X-ray-based characterization techniques such as energy-dispersive X-ray spectroscopy (EDX) and X-ray photoelectron spectroscopy (XPS) have been employed to monitor the electronic states and perform the elemental analysis of silver-exchanged zeolites [98, 99].

Complementary to the structural, electronic, and compositional information obtained by X-ray-based techniques, theoretical modeling is a powerful tool that can be applied to elucidate the physicochemical properties of silver clusters in zeolites and predict, in a quantitative way, the impact that different factors will have on their optical properties. At present, due to the complexity of the Ag-zeolite systems, few studies dealing with the theoretical modeling of the optical properties of silver clusters confined in zeolites have been reported. A representative example is the work carried by Cuong and collaborators [100]. Starting from fully silver-exchanged LTA zeolites, they predicted the absorption bands of two possible emitting species. However, this study was not compared to experimental data to further confirm the validity of the model.

3.3 *Fluorescence Spectroscopy and Microscopy*

Silver-exchanged zeolites have been extensively studied because of their promising catalytic properties [90]. Colored ionic silver complexes were reported as responsible for their catalytic properties [85]; however, these complexes presented poor luminescent properties at room temperature. Kanan and collaborators reported the luminescence properties of silver-containing zeolites under liquid nitrogen conditions [101]. They attributed the photoluminescence activity to the presence of Ag dimers, trimers, and tetramers species in different zeolite topologies (LTA, FAU, ZSM-5) and established a correlation between different emission bands and silver cluster size. One of the first photoluminescence studies on silver-exchanged zeolites at room temperature was presented by De Cremer and co-workers [18], in which individual silver-containing zeolite crystals were photo-activated using a fluorescence microscope set-up. The formation of highly luminescent green emitting species in Ag-LTA was demonstrated. Subsequently, the same group reported the characterization of fluorescence in heat-treated silver-exchanged zeolites [19]. In this study, different types of emitters with characteristic luminescence colors were observed, depending on the nature of the counter-balancing ions present in the zeolite framework, the silver loading and the zeolite topology. Green, yellow, and red emission colors were tentatively assigned to partially reduced Ag_3^{n+} and Ag_6^{m+} clusters. The first evidence of the influence of metal-guest and zeolite-host features on the luminescence properties of these types of materials was presented in this work.

The spectral evolution of the emission bands observed in silver-exchanged zeolites during thermal treatment under different gas atmospheres was studied in detail in a different report [102]. By using an in-situ heating stage mounted on a fluorescence microscope, the process of thermally induced silver cluster formation could be followed in detail, as well as the effect of hydration/rehydration on the emission color of the formed clusters. In a latter study [27], the different factors that could affect the luminescent performance of silver-loaded materials were assessed in a quantitative way by measuring external quantum efficiencies (EQE); in the same report a reduction-oxidation procedure to improve their luminescence performance and water stability was described.

3.4 *Electron Microscopy*

Transmission electron microscopy (TEM) is a very powerful technique to characterize the structure and composition of materials at the atomic scale. However, the use of electron microscopy is limited in aluminosilicate mesoporous matrices due to the extreme sensitivity of these materials toward electron beam irradiation under high vacuum conditions [103]. In the case of silver-exchanged zeolites, it is of

paramount importance to determine the atomic positions of the silver atoms in the zeolitic framework. Such knowledge could allow the understanding of the relationship between the structure and the physicochemical properties of these sub-nanometer structures. Unfortunately, silver-exchanged zeolites are extremely sensitive to damage caused by the electron beam, especially in the case of topologies having a relatively low Si/Al ratio such as LTA and FAU zeolites. During one of the first high-resolution TEM (HR-TEM) studies on silver-exchanged zeolites (FAUX, LTA, LTL, MOR, RHO), a particular effect was observed [104]. The formation of silver nanowires as a result of the reduction of silver cations incorporated in the zeolite frameworks by the incident electron beam was reported. This new approach to synthesize silver nanowires was later applied for the fabrication of well-defined silver nanoparticles in LTA and FAU zeolites [105]. In this report, a twofold mechanism, in which the electron beam irradiation performed the breaking of chemical bonds in the zeolite framework and simultaneously a rapid diffusion of Ag cations in the amorphous materials occurred, resulting in the aggregation of larger silver nanoparticles from silver cations and clusters. Recently, high-angle annular dark-field scanning transmission electron microscopy (HAADF-STEM) was used to image individual Ag atoms in LTA zeolites [106]. An octahedral Ag_6 cluster was clearly visualized in the sodalite cages of fully exchanged heat-treated Ag-LTA zeolites. HAADF-STEM images yielded an intensity which scales with the atomic number Z and the thickness of the sample [107]. Therefore, the silver atoms appeared with higher intensity in comparison to the elements of the zeolite framework (Si, Al, and O). The use of aberration-corrected TEM at relatively low electron doses opened new avenues to study silver-exchanged zeolites at atomic scales, as illustrated by the work of Altantzis and collaborators, where the structure of luminescent silver clusters confined in FAU zeolites was unraveled (Fig. 5) [80].

3.5 Electron Spin Resonance (ESR) Spectroscopy and Thermogravimetric Analysis (TGA)

ESR experiments on silver-exchanged zeolites have provided valuable information related to the structure and magnetic properties of silver clusters, as well as their location, stability, and reactivity with different ligands. For instance, the stabilization of Ag_2^+ , Ag_3^{2+} , and Ag_6^{n+} species have been reported on Ag-LTA zeolites under γ irradiation, depending on the silver loading and dehydration conditions [108, 109]. Whereas, Ag_6^{n+} clusters have been exclusively observed in hydrogen-reduced samples [110]. The formation of these paramagnetic species was related to the electron capture from diamagnetic precursors such as Ag_3^+ or Ag_6^{2+} . ESR analysis has also contributed to the elucidation of the formation mechanisms of silver clusters in zeolites. For instance, Michalik and Kevan described the silver clustering in the sodalite cage of Ag-LTA zeolites based on ESR analysis [109]. The

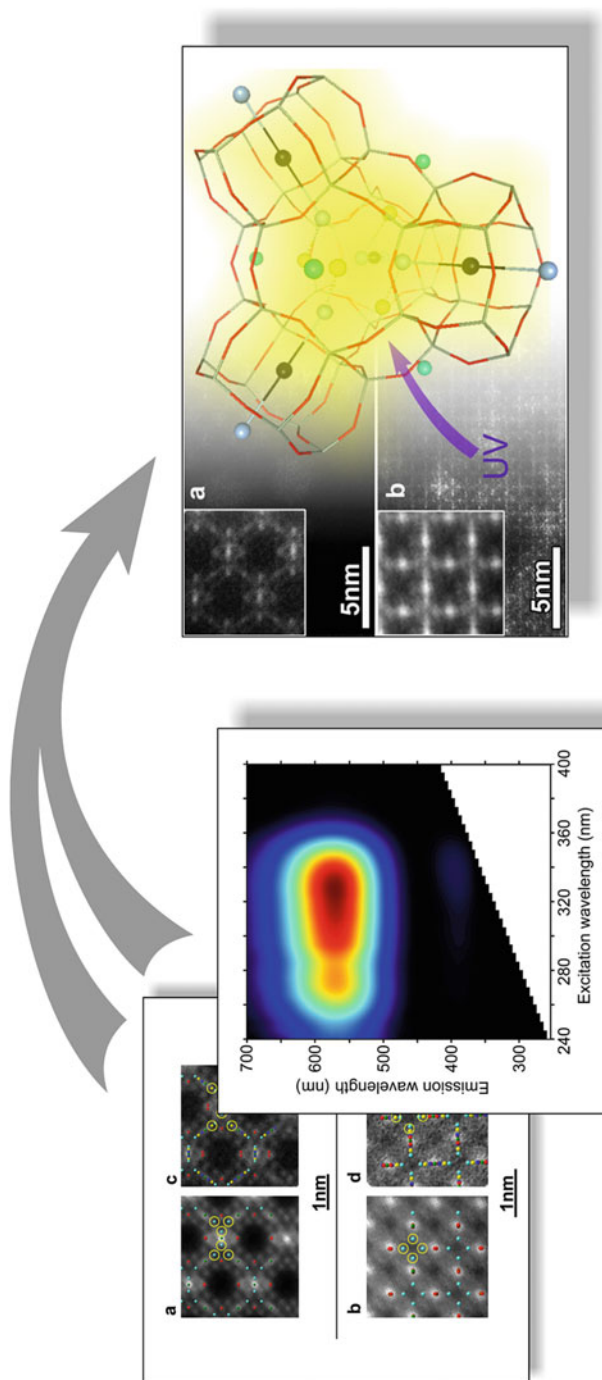


Fig. 5 Combined HAADF-STEM, XRD, and photoluminescence approach followed to decipher the structure of Ag clusters confined in FAU zeolites. Adapted from Ref. [80]. Copyright 2016 American Chemical Society

dynamical formation of trimers and hexamers Ag clusters in silver-exchanged zeolites was proposed depending on the silver content. The formation of trimer Ag species was observed in samples having low silver loadings, whereas the appearance of the hexamer Ag clusters was attributed to the interaction of two trimer species within the sodalite cages of silver-exchanged LTA zeolites containing higher silver loadings. ESR has been mainly applied to obtain information related to the behavior of silver clusters in zeolites during catalytic reactions. Nevertheless, in a recent report, the use of ESR as a tool to elucidate the electronic properties of luminescent silver-exchanged LTA samples was demonstrated [19]. In this work, the presence of partially reduced paramagnetic Ag_6^+ silver clusters in Ag-LTA samples was associated with the red emission observed in this particular sample.

TGA is an auxiliary technique utilized to investigate the water content at different temperatures in silver-exchanged zeolites [102]. The results obtained by this technique have contributed to the analysis of the relationship between silver clusters and their environment (ligands). For instance, based on X-ray diffraction and TGA evidence, the debate about the electrons source involved in the synthesis of thermally auto-reduced silver clusters in zeolites was clarified [19].

Although several characterization techniques employed in the study of silver clusters confined in zeolite matrices have been discussed in the previous sections, there is no a universal technique to deal with this task, a more combinatorial approach is needed to decipher the physicochemical properties and formation mechanisms of such small metal entities. The use of a particular technique above others is determined by the approach employed and the information required. Most of the above revised characterization techniques have been used to try to correlate the structure-to-luminescence properties relationship of silver-exchanged zeolites and establish the basis of more rational design and synthesis of multifunctional silver clusters in zeolite matrices.

4 Applications of Luminescent Silver-Containing Zeolites

4.1 Phosphors for Lighting Applications

Luminescent silver-zeolite composites display interesting emissive properties, such as large Stokes shifts, high external quantum efficiencies, and large photostability, among others. Depending on the zeolite topology, the presence of specific counter balancing ions, and the silver loading, different emissive silver species can be created upon thermal treatment, with spectral properties ranging from blue to red. Therefore, this new class of photostable luminescent materials with tunable emission colors offers interesting perspectives as wavelength converters in fluorescent lamps and LEDs (Fig. 6). To date, several publications and patents have demonstrated the high applicability of these versatile materials to be implemented in light emitting devices [19, 27, 73, 111–113]. Recent efforts have been directed to the synthesis of single-phase white emitting phosphors with absorption in the NUV region.



Fig. 6 Silver-zeolite-based phosphors and lanthanide-based commercial phosphors under 254 nm illumination (left). Working fluorescent lamp prototype using green-emitting silver-zeolite phosphor materials (right)

Representative studies have been reported where the use of silver-zeolites or silver-sulfur-zeolites has rendered into the fabrication of white-emissive LED prototypes [77, 79]. We might be witnesses, in a very close future, of the first generation of light emitting devices based on silver-exchanged zeolite phosphors, which could represent a breakthrough toward the gradual replacement of lanthanide-based phosphors in light emitting devices.

4.2 Humidity Sensors

The ability of Ag clusters confined in zeolites to optically respond to external stimuli can be utilized in sensing applications. For instance, several reports have suggested the use of silver-zeolites as vapor sensors based on their absorption response to hydration levels [114], leading to samples with different colors depending on their water content. The luminescence response of silver-zeolites toward the presence of water has been also observed [102]. Where the exposure of silver-zeolite samples to high-humidity environments led to a quenching of the luminescence. This process was demonstrated to be fully reversible and a subsequent drying step by mild heating showed the reestablishment of their original luminescent properties. Up to now the sensing characteristics of silver clusters confined in zeolites were based on a “positive or negative” response using the depletion/activation of their luminescence properties. However, in a recent study, the dynamic emission color change of silver clusters stabilized in LTA (containing lithium as counter balancing ion) zeolites with respect to their hydration level was shown (Fig. 7) [70]. This major improvement in the stimuli-to-response process could have direct implications in the use of these materials as luminescence-based humidity sensors at macro and micro scale.

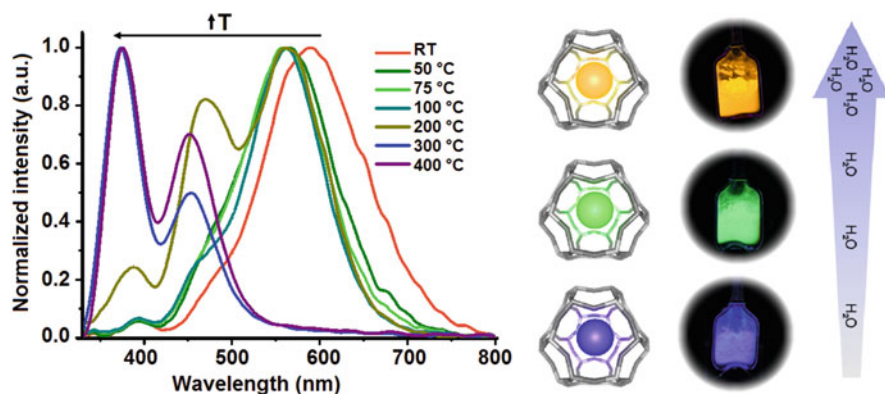


Fig. 7 Luminescence response of silver clusters confined in lithium-containing LTA zeolites toward water content. Adapted from Ref. [70]. Copyright 2015, The Royal Society of Chemistry

4.3 Optoelectronic Devices

Besides the use of luminescent silver-containing zeolites as secondary emissive phosphors in LED devices, such materials have been also tested in hybrid organic/inorganic light-emitting diodes (OLEDs) as recently demonstrated by Kennes and collaborators (Fig. 8) [115], where luminescent silver-exchanged zeolites were embedded in polyvinyl carbazole (PVK). It was observed that the use of silver-exchanged zeolites as emitters in a single-layer OLED led to electroluminescence bands that clearly differ from pristine PVK OLEDs and the typical photoluminescence behavior of silver-zeolites. Moreover, a clear dependence between the zeolite silver loading and the electroluminescence intensity was recorded. A follow-up study of the electroluminescence mechanism of silver-zeolite-based OLEDs addressed the role of the polymer matrix, zeolite framework, and counter-ions present in the zeolites on the OLED performance. Based on the obtained results, a silver-exchanged-based OLED device displaying a voltage polarity dependent color was achieved [116]. These studies are paving the way for a new type of easily tunable hybrid and cost-effective OLEDs using silver-exchanged zeolites as the emissive materials.

4.4 Encoded Information Carriers

The photoactivation of silver clusters in single zeolite crystals has been recently demonstrated (Fig. 9, upper panel). These new types of optically encoded microcarriers were created using a two-photon activation process with near-infrared light [26]. It was suggested that the formation of bright silver clusters was accomplished through the photochemical reduction of the silver ions (serving as counter

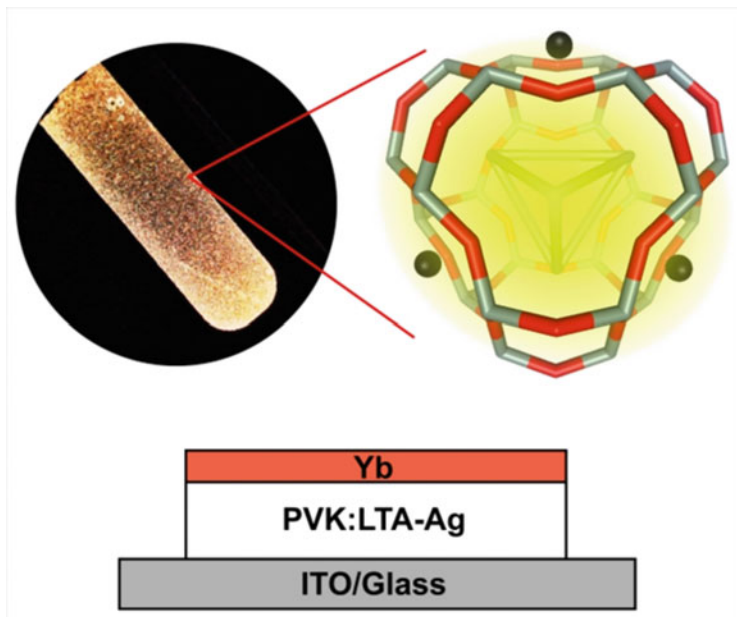


Fig. 8 Schematic representation of a silver-zeolite composite-based LED (ZEOLED). Taken from Ref. [70]. Copyright 2017 Wiley-VCH GmbH & Co. KGaA, Weinheim

balancing ions in the zeolite framework) present in non-irradiated samples. Very high writing resolutions, down to the diffraction limit, were obtained as well as an excellent readability due to the positive contrast imaging and brightness stability of the emissive clusters. By using this strategy, several advanced matrix codes were generated in different layers of individual zeolite microcarriers demonstrating an excellent 3D resolution. Therefore, these materials open new opportunities for built-in safety and quality labels to prevent counterfeiting, for instance, in bank notes. Moreover, this strategy has also been extended to other confinement hosts (using silver clusters as guests) such as polymers and glass matrices [117–119] and at different photoactivation scales (Fig. 9, lower panel).

5 Other Luminescent Metal Clusters and Perovskite Quantum Dots Confined in Zeolites

The ship-in-a-bottle strategy to confine luminescent silver clusters in zeolites has been extended to other metal precursors, such as the case of lead clusters. In a recent study, the self-assembly and confinement of highly luminescent lead (Pb) clusters into the molecular-sized cavities of LTA zeolites was demonstrated [120].

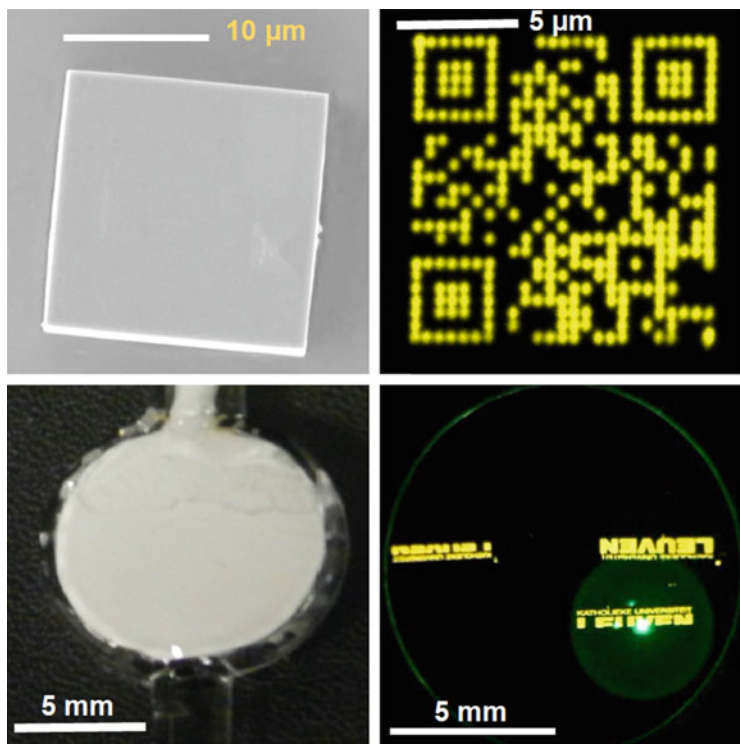


Fig. 9 Photoactivation of silver clusters confined in LTA zeolites at micro (upper panel) and macro (lower panel) scale. Adapted from Ref. [26]. Copyright 2010 Wiley-VCH GmbH & Co. KGaA, Weinheim

Pb-LTA samples displayed an intense deep-blue emission with external quantum efficiencies up to 69%, where a tetrahedral lead cluster (Pb₄) with unusually short Pb – Pb distances and hydroxyl ligands was identified as responsible for the luminescence properties. An alternative approach to incorporate luminescent species into zeolite frameworks was reported by Ruivo and collaborators, where Na₂SO₄, NaCl, and LTA zeolite precursors were ball-milled and treated at high temperatures under a reductive atmosphere [121]. The samples displayed a transformation from LTA to SOD (sodalite) framework combined with the confinement of orange luminescent sulfide species, tentatively related to S⁻² and S₄⁻² emitting centers, extending the myriad of opportunities to chalcogenide species. Later on, the incorporation of silver cations into luminescent sulfur-zeolites resulted in the fabrication of white emitting silver-sulfur zeolites, displaying a remarkable color tunability [79]. This report opened up several avenues to fabricate luminescent hybrid species (metal/chalcogenide) within the molecularly-size cavities of zeolites. Continuing with the strategy to confine luminescent inorganic hybrid materials in zeolites, recent reports have pointed toward the use of zeolites as stabilizing scaffolds for the

fabrication of luminescent perovskite quantum dots, conferring them additional physicochemical stability, a pertinent issue in the development of perovskites. A facile two-step synthesis procedure for the fabrication of luminescent and color-tunable CsPbX₃-zeolite FAUY composite phosphors was recently shown, where perovskites quantum dots were encapsulated within the porous zeolite matrix [122, 123]. The use of such phosphors was also demonstrated in the fabrication of white-light-emitting diodes (WLEDs), with composite materials reaching luminescence quantum efficiencies of 81% [124]. The perovskite-zeolite composites displayed a significant improved resistance to elevated temperatures, water, and intensive laser illumination as compared to bare luminescent perovskite quantum dots.

6 Concluding Remarks

Several aspects related to the synthesis, characterization, and potential applications of luminescent metal clusters (particularly the case of highly luminescent silver clusters) confined in zeolite matrices were addressed in this chapter. Due to the recent advances in the intricate host-guest chemistry of zeolites, it has been possible to design and synthesize functional metal clusters with specific size, geometry, and charge within their porous framework. For the case of silver-zeolite composites, this development has resulted in the fabrication of a wide palette of emitting clusters spanning the whole visible spectrum displaying high external quantum efficiencies (close to 100%), great chemical and photostability, and responsive optical properties. Altogether, these useful optical properties could be applied for the development of smart sensing devices and more efficient (and cost-effective) phosphors for down conversion in lighting applications. Though to date, the relationship between the electronic and structural properties of such metal nanostructures has not been fully understood. This is mainly due to the challenges associated with the characterization of such clusters at the nanoscale. To overcome this problem, complementary and holistic approaches have been developed and applied to understand the different phenomena that govern the electronic and optical properties of luminescent silver clusters confined in zeolites at the atomic scale. Ultimately, the deep understanding obtained will allow the development of rational design rules for confining silver and other metal clusters in zeolites. There is still a long way to go to arrive at a clear image of how the electronic and structural features of silver clusters stabilized in zeolites influence their optical properties; however, innovative studies have recently paved the way to achieve such goals. Finally, it is expected that the scientific community will get inspired by the approach followed to confine luminescence metal clusters in zeolites which will ultimately trigger the development of related nanostructured materials, such as the case of luminescent perovskite quantum dots stabilized in zeolites, for which the first examples have been recently reported.

Acknowledgments ECG gratefully acknowledges the support provided by CONACYT-Ciencia Básica fund through the project A1-S-44458.

References

1. Felix C, Harbich W, Buttet J, Rabin I, Schulze W, Ertl G (1999) *Chem Phys Lett* 313:105–109
2. Lecoutre S, Rydlo A, Felix C, Buttet J, Gilb S, Harbich WJ (2011) *Chem Phys* 134:074302–074308
3. Murray RW (2008) *Chem Rev* 108:2688–2720
4. Quinn BM, Laaksonen T, Ruiz V, Liljeroth P (2008) *Chem Soc Rev* 37:1836–1846
5. Xu H, Suslick KS (2010) *Adv Mater* 22:1078–1082
6. Kang X, Zhu MZ (2019) *Chem Soc Rev* 48:2422–2457
7. Turner M, Golovko VB, Vaughan OPH, Abdulkin P, Berenguer-Murcia A, Tikhov MS, Johnson BFG, Lambert RM (2008) *Nature* 454:981–983
8. Xu S, Xiao FS, Purnell SK, Alexeev O, Kawi S, Deutsch SE, Gates BC (1994) *Nature* 372:346–348
9. Corma A, Concepcion P, Boronat M, Sabater MJ, Navas J, Yacaman MJ, Larios E, Posadas A, Lopez-Quintela MA, Bucetta D, Mendoza E, Guilera G, Mayoral A (2013) *Nature* 5:775–781
10. Morse MD (1986) *Chem Rev* 86:1049–1109
11. Guzzi L, Beck A, Horvath A, Horvath D (2002) *Top Catal* 19:157–163
12. Diez I, Rass RHA (2011) *Nanoscale* 3:1963–1970
13. Link S, Beeby A, Fitzgerald S, El-Sayed MA, Schaaff TG, Whetten RL (2002) *J Phys Chem B* 106:3410–3415
14. Negishi Y, Nobusada K, Tsukuda T (2005) *J Am Chem Soc* 127:5261–5270
15. Petty JT, Zheng J, Hud NV, Dickson RM (2004) *J Am Chem Soc* 126:5207–5212
16. Vosch T, Antoku Y, Hsiang JC, Richards CI, Gonzalez JI, Dickson RM (2007) *Proc Natl Acad Sci* 104:12616–12621
17. Eichelbaum M, Rademann K, Hoell A, Tatchev DM, Weigel W, Stoßer R, Pacchioni G (2008) *Nanotechnology* 19:135701–135709
18. De Cremer G, Antoku Y, Roeffaers MBJ, Sliwa M, Van Noyen J, Smout S, Hofkens J, De Vos D, Sels B, Vosch T (2008) *Angew Chem Int Ed* 47:2813–2816
19. De Cremer G, Coutino-Gonzalez E, Roeffaers MBJ, Moens B, Ollevier J, Van der Auweraer M, Schoonheydt R, Jacobs PA, De Schryver F, Hofkens J, De Vos D, Sels B, Vosch T (2009) *J Am Chem Soc* 131:3049–3056
20. Lu Y, Chen W (2012) *Chem Soc Rev* 41:3594–3623
21. Wilcoxon JP, Abrams BL (2006) *Chem Soc Rev* 35:1162–1194
22. Zheng J, Zhang CW, Dickson RM (2004) *Phys Rev Lett* 93:077402(1)–077402(4)
23. Zheng J, Nicovich PR, Dickson RM (2007) *Annu Rev Phys Chem* 58:409–431
24. Haruta M (1997) *Catal Today* 36:153–166
25. Vazquez-Vazquez C, Banobre-Lopez M, Mitra A, Lopez-Quintela MA, Rivas J (2009) *Langmuir* 25:8208–8216
26. De Cremer G, Sels BF, Hotta J, Roeffaers MBJ, Bartholomeeusen E, Coutino-Gonzalez E, Valtchev V, De Vos D, Vosch T (2010) *Adv Mater* 22:957–960
27. Coutino-Gonzalez E, Roeffaers MBJ, Dieu B, De Cremer G, Leyre S, Hanselaar P, Fyen W, Sels B, Hofkens J (2013) *J Phys Chem C* 117:6998–7004
28. Bonacic-Koutecky V, Veyret V, Mitric R (2001) *J Chem Phys* 115:10450–10460
29. Harb M, Rabilloud F, Simon D, Rydlo A, Lecoutre S, Conus F, Rodrigues V, Felix CJ (2008) *Chem Phys* 129:194108–194109
30. Choi S, Dickson RM, Yu J (2012) *Chem Soc Rev* 41:1867–1891

31. O'Neill PR, Velazquez LR, Dunn DG, Gwinn EG, Fyngenson DK (2009) *J Phys Chem C* 113:4229–4233
32. Patel SA, Richards CI, Hsiang JC, Dickson RM (2008) *J Am Chem Soc* 130:11602–11603
33. Gwinn EG, O'Neill PR, Guerrero AJ, Bouwmeester D, Fyngenson DK (2008) *Adv Mater* 20:279–283
34. Petty JT, Story SP, Hsiang JC, Dickson RM (2013) *J Phys Chem Lett* 4:1148–1155
35. Yu J, Choi S, Dickson RM (2009) *Angew Chem Int Ed* 48:318–320
36. Choi S, Yu J, Patel SA, Tzeng YL, Dickson RM (2011) *Photochem Photobiol Sci* 10:109–115
37. Copp SM, Schultz D, Swasey S, Pavlovich J, Debord M, Chiu A, Olsson K, Gwinn EG (2014) *J Phys Chem Lett* 5:959–963
38. Makarava N, Parfenov A, Baskakov IL (2005) *Biophys J* 89:572–580
39. Le Guevel X, Spies C, Daum N, Jung G, Schneider M (2012) *Nano Res* 5:379–387
40. Chen Y, Yang T, Pan H, Yuang Y, Chen L, Liu M, Zhang K, Zhang S, Wu P, Xu J (2014) *J Am Chem Soc* 136:1686–1689
41. Rao TUB, Nataraju B, Pradeep T (2010) *J Am Chem Soc* 132:16304–16307
42. Yang H, Lei J, Wu B, Wang Y, Zhou M, Xia A, Zheng L, Zheng N (2013) *Chem Commun* 49:300–302
43. Henglein A (1989) *Chem Phys Lett* 154:473–476
44. Mostafavi M, Keghouche N, Delcourt MO (1990) *Chem Phys Lett* 169:81–84
45. Ershov BG, Henglein AJ (1998) *Phys Chem B* 102:10663–10666
46. Zheng J, Dickson RM (2002) *J Am Chem Soc* 124:13982–13983
47. Diez I, Pussa M, Kulmala S, Jiang H, Walther A, Goldmann AS, Muller AHE, Ikkala O, Ras RHA (2009) *Angew Chem Int Ed* 48:2122–2125
48. Xu H, Suslick KS (2010) *ACS Nano* 4:3209–3214
49. Borsella E, Cattaruzza E, De Marchi G, Gonella F, Mattei G, Mazzoldi P, Battadin G, Polloni RJ (1999) *Non-Cryst Solids* 245:122–128
50. Kuznetsov AS, Cuong NT, Tikhomirov VK, Jivanescu M, Stesmans A, Chibotaru LF, Velázquez JJ, Rodríguez VD, Kirilenko D, Van Tendeloo G, Moshchalkov VV (2012) *Opt Mater* 34:616–621
51. Guo H, Wang XF, Chen JD, Fang L (2010) *Opt Express* 18:18900–18905
52. Shestakov MV, Chen X, Baekelant W, Kuznetsov AS, Tikhomirov VK, Hofkens J, Moshchalkov VV (2014) *RSC Adv* 4:20699–20703
53. Chen S, Akai T, Kadono K, Yazawa T (2001) *Appl Phys Lett* 79:3687–3689
54. Espiau de Lamaestre R, Bea H, Bernas H, Belloni J, Marignier JL (2007) *Phys Rev B* 76:205431-1–205431-17
55. Bourhis K, Royon A, Papon G, Bellec M, Petit Y, Canioni L, Dussauze M, Rodriguez V, Binet L, Caurant D, Treguer M, Videau J-J, Cardinal T (2013) *Mater Res Bull* 48:1637–1644
56. Sun T, Seff K (1994) *Chem Rev* 27:857–870
57. Falcaro P, Furukawa S (2012) *Angew Chem Int Ed* 47:8431–8433
58. Ameloot R, Roefsaers MJB, De Cremer G, Vermoortele F, Hofkens J, Sels BF, De Vos D (2011) *Adv Mater* 51:1788–1791
59. Chen L, Chen H, Luque R, Li Y (2014) *Chem Sci* 5:3708–3714
60. Houk RJT, Jacobs BW, El Gabaly F, Chang NN, Talin AA, Graham DD, House SD, Robertson IM, Allendorf MD (2009) *Nano Lett* 9:3413–3418
61. Jonckheere D, Coutino-Gonzalez E, Baekelant W, Bueken B, Reinsch H, Stassen I, Fenwick O, Richard F, Samorì P, Ameloot R, Hofkens J, Roefsaers MJB, De Vos D (2016) *J Mater Chem C* 4:4259–4268
62. Ralek M, Jiru P, Grubner O, Beyer H (1962) *Collect Czechoslov Chem Commun* 27:142
63. Kim Y, Seff K (1977) *J Am Chem Soc* 99:7055–7057
64. Beyer H, Jacobs PA, Uytterhoeven JB (1976) *Chem Soc Faraday Trans* 72:674–685
65. Ozin GA, Hughes F (1983) *J Phys Chem* 87:94–97
66. Bruhwiler D, Seifert R, Calzaferri G (1999) *J Phys Chem B* 103:6397–6399
67. Bruhwiler D, Leiggener C, Glaus S, Calzaferri G (2002) *J Phys Chem B* 106:3770–3777

68. Coutino-Gonzalez E, Grandjean D, Roeffaers MBJ, Kvashnina K, Fron E, Dieu B, De Cremer G, Lievens P, Sels B, Hofkens J (2014) *Chem Commun* 50:1350–1352
69. Lin H, Imakita K, Rong-Gui SC, Fujii M (2014) *J Appl Phys* 116:013509–013505
70. Coutino-Gonzalez E, Baekelant W, Grandjean D, Roeffaers MBJ, Van der Auweraer M, Vosch T, Bovet N, Fron E, Aghakhani MS, Lievens P, Sels B, Hofkens J (2015) *J Mater Chem C* 3:11857–11867
71. Lin H, Imakita K, Fuji M, Prokof'ev VY, Gordina NE, Said B, Galarneau A (2015) *Nanoscale* 7:15665–15671
72. Johan E, Yamauchi Y, Matsue N, Itagaki Y, Aono H (2016) *J Ceram Soc Jpn* 124:70–73
73. Fenwick O, Coutino-Gonzalez E, Grandejan D, Baekelant W, Richard F, Bonacchi S, De Vos D, Lievens P, Roeffaers MBJ, Hofkens J, Samorì P (2016) *Nat Mater* 15:1017–1022
74. Taiji K, Iso Y, Isobe T (2018) *J Lumin* 196:214–220
75. Baekelant W, Aghakani S, Coutino-Gonzalez E, Kennes K, D'Acapito F, Grandjean D, Van der Auweraer M, Lievens P, Roeffaers MBJ, Hofkens J, Steele JA (2018) *J Phys Chem Lett* 9:5344–5350
76. Fron E, Aghakhani S, Baekelant W, Grandjean D, Coutino-Gonzalez E, Van der Auweraer M, Roeffaers MBJ, Lievesn P, Hofkens J (2019) *J Phys Chem C* 123:0630–10638
77. Yao DC, Xu S, Wang YG, Li HR (2019) *Mater Chem Front* 3:1080–1084
78. Johan E, Kanda Y, Matsue N, Itagaki Y, Aono H (2019) *J Lumin* 213:482–488
79. Baekelant W, Romolini G, Sun L, De Ras M, Fron E, Moreira T, Viola C, Ruivo A, Laia CAT, Martens J, Martin C, Woong-Kim C, Van der Auweraer M, Roeffaers MBJ, Hofkens J, Coutino-Gonzalez E (2020) *Methods Appl Fluoresc* 8:024004(1)–024004(9)
80. Altantzis T, Coutino-Gonzalez E, Martinez GT, Abakumov AA, van Tendeloo G, Roeffaers MBJ, Bals S, Hofkens J (2016) *ACS Nano* 10:7604–7611
81. Grandjean D, Coutino-Gonzalez E, Cuong NT, Fron E, Baekelant W, Aghakhani MS, Schlexer P, D'Acapito F, Banerjee D, Roeffaers MBJ, Nguyen MT, Hofkens J, Lievens P (2018) *Science* 361:686–690
82. Coutino-Gonzalez E, Baekelant W, Steele J, Woong-Kim C, Roeffaers MBJ, Hofkens J (2017) *Acc Chem Res* 50:2353–2361
83. Aghakhani S, Grandejan D, Baekelant D, Coutino-Gonzalez E, Fron E, Kvashnina K, Roeffaers MBJ, Hofkens J, Sels B, Lievens P (2018) *Nanoscale* 10:11467–11476
84. Seifert R, Kunzmann A, Calzaferri G (1998) *Angew Chem Int Ed* 37:1522–1524
85. Seifert R, Rytz R, Calzaferri G (2000) *J Phys Chem A* 104:7473–7483
86. Baumann J, Beer R, Calzaferri G, Waldeck B (1989) *J Phys Chem* 93:2292–2302
87. Bo X, Kevan L (1991) *J Phys Chem* 95:1147–1151
88. Wang P, Yang SW, Kondo JN, Domen K, Baba T (2003) *Chem Lett* 32:792–793
89. Frising T, Leflaive P (2008) *Microporous Mesoporous Mater* 114:27–63
90. Jacobs PA, Uytterhoeven JB, Beyer HK (1979) *J Chem Soc Faraday Trans* 75:109–118
91. Lee HS, Kim Y, Seff K (2000) *Microporous Mesoporous Mater* 41:49–59
92. Kim SY, Kim Y, Seff K (2003) *J Phys Chem B* 107:6938–6945
93. Matsuoka M, Ju WS, Yamashita H, Anpo M (2001) *J Synchrotron Radiat* 8:613–615
94. Matsuoka M, Ju WS, Yamashita H, Anpo M (2003) *J Photochem Photobiol A* 160:43–46
95. Miyanaga T, Hoshino H, Endo H, Sakane H (1999) *J Synchrotron Radiat* 6:442–444
96. Minayaga T, Hoshino H, Endo H (2001) *J Synchrotron Radiat* 8:557–559
97. Suzuki Y, Miyanaga T, Hoshino H, Matsumoto N, Aina T (2005) *Phys Scr T115:765–768*
98. Aspromonte SG, Mizrahi MD, Schneeberger FA, Lopez JMR, Boix AV (2013) *J Phys Chem C* 117:25433–25442
99. Mayoral A, Anderson PA (2007) *Nanotechnology* 18:165708
100. Cuong NT, Nguyen HMT, Nguyen MT (2013) *Phys Chem Chem Phys* 15:15404–15415
101. Kanan SM, Kanan MC, Patterson HH (2003) *Curr Opin Solid State Mater* 7:443–449
102. De Cremer G, Coutino-Gonzalez E, Roeffaers MBJ, De Vos DE, Hofkens J, Vosch T, Sels BF (2010) *ChemPhysChem* 11:1627–1631
103. Yuan ZY, Zhou W, Parvulescu V, Su BL (2003) *J Electron Spectrosc* 129:189–194

104. Edmondson MJ, Zhou W, Sieber SA, Jones IP, Gameson I, Anderson PA, Edwards PP (2001) *Adv Mater* 13:1608–16011
105. Sasaki Y, Suzuki T (2009) *Mater Trans* 50:1050–1053
106. Mayoral A, Carey T, Anderson PA, Lubk A, Diaz I (2011) *Angew Chem Int Ed* 50:11230–11233
107. Pennycook SJ (1992) *Annu Rev Mater Sci* 22:171–195
108. Morton JR, Preston KF (1998) *J Magn Reson* 68:121–128
109. Michalik J, Kevan L (1986) *J Am Chem Soc* 108:4247–4253
110. Hermerschmidt D, Haul D (1980) *Ber Bunsenges Phys Chem* 84:902–907
111. Vosch T, Sels BF, Roeffaers MBJ, Hofkens J, De Vos DE, De Cremer G (2009) Patent application: WO 2009006707
112. Vosch T, Sels BF, Roeffaers MBJ, Hofkens J, De Vos DE, De Cremer G (2009) Patent application: WO 2009006710
113. Baekelant W, Coutino-Gonzalez E, Steele J, Roeffaers MBJ, Hofkens J (2017) *ACS Energy Lett* 2:2491–2497
114. Alcantara GP, Ribeiro LES, Alves AF, Andrade CMG, Fruett F (2017) *Microporous Mesoporous Mater* 247:34–45
115. Kennes K, Coutino-Gonzalez E, Martin C, Baekelant W, Roeffaers MBJ, van der Auweraer M (2017) *Adv Funct Mater* 27:1606411(1)–1606411(8)
116. Kennes K, Martin C, Baekelant W, Coutino-Gonzalez E, Fron E, Roeffaers MBJ, Hofkens J, Van der Auweraer M (2019) *ACS Appl Mater Inter* 11:12179–12183
117. Kunwar P, Hassinen J, Bautista G, Ras RHA, Toinoven J (2016) *Sci Rep* 6:23998(1)–23998(6)
118. Kunwar P, Hassinen J, Bautista G, Ras RHA, Toinoven J (2014) *ACS Nano* 8:11165–11171
119. Royon A, Bourhis K, Bellec M, Papon G, Bousquet B, Deshayes Y, Cardinal T, Canioni L (2010) *Adv Mater* 22:5282–5286
120. Baekelant W, Aghakhani S, Coutino-Gonzalez E, Grandjean D, Kennes K, Jonckheere D, Fron E, D'Acapito F, Longo A, Lievens P, Roeffaers MBJ, Hofkens J (2018) *J Phys Chem C* 122:13953–13961
121. Ruivo A, Coutino-Gonzalez E, Santos MM, Baekelant W, Fron E, Roeffaers MBJ, Pina F, Hofkens J, Laia CAT (2018) *J Phys Chem C* 122:14761–147770
122. Sun J-Y, Rabouw FT, Yang X-F, Huang X-Y, Jing X-P, Ye S, Zhang Q-Y (2017) *Adv Funct Mater* 27:1704371(1)–1704371(8)
123. Ye S, Sun J-Y, Han Y-H, Zhou Y-Y, Zhang Q-Y (2018) *ACS Appl Mater Interfaces* 10:24656–24664
124. Li R, Wei Z, Zhao H, Yu H, Fang X, Fang D, Li J, He T, Chen R, Wang X (2018) *Nanoscale* 10:22766–22774

Photoactive Molecules within MOFs



Heidi Annemarie Schwartz and Uwe Ruschewitz

Contents

1	General Introduction	107
1.1	Photochromism	108
1.2	Solvatochromism	110
1.3	Metal–Organic Frameworks	112
1.4	Implementing Photoswitches into MOFs	113
2	Switch@MOF Systems	116
2.1	Stilbenes in MOFs	116
2.2	Azobenzene and Its Derivatives in MOFs	117
2.3	Diarylethenes in MOFs	134
2.4	Spiropyrans in MOFs	136
2.5	Spirooxazines in MOFs	142
3	Conclusion and Future Perspectives	146
	Appendix	149
	References	149

Abstract Photochromic molecules have been considered to be applied in responsive functional materials. Recently, the combination of a porous host matrix and these photoactive species has become an emerging field of research. Especially the use of crystalline nanoporous metal-organic frameworks (MOFs) as host materials has proven to be very promising. The combination of crystallinity and the ability to be systematically functionalized is one of the main advantages of these porous host materials. The resulting switch@MOF hybrid systems exhibit fascinating and even surprising properties ranging from the “simple” possibility of solid-state switching to remote control gas uptake and conductance photoswitching. After a short

H. A. Schwartz
Institute of General, Inorganic and Theoretical Chemistry, University of Innsbruck, Innsbruck,
Austria
e-mail: heidi.schwartz@uibk.ac.at

U. Ruschewitz (✉)
Department of Chemistry, University of Cologne, Cologne, Germany
e-mail: uwe.ruschewitz@uni-koeln.de

introduction to photochromism, solvatochromism, and MOFs, this chapter discusses the formation and the developments of these switch@MOF materials and the recent advances in exploitation of the light-induced structural changes.

Keywords 2-Phenylazopyridine · Azobenzenes · Diarylethenes · Hybrid materials · Metal-organic frameworks (MOFs) · Photochromism · Porous coordination polymers · Solid-state switching · Solvatochromism · Spirooxazines · Spiropyrans · Stilbenes · Thin MOF films

Abbreviations

AZB	Azobenzene
BET	Brunauer-Emmett-Teller
BSP	1-(2-hydroxy-ethyl)-3,3-dimethyl-indolino-6'-nitrobenzospiroopyran
<i>c</i>	Closed
COF	Covalent-organic framework
CT	Charge-transfer
<i>d</i>	Day(s)
DAE	Diarylethenes
DC	Direct current
DFT	Density functional theory
DMF	<i>N,N'</i> -dimethylformamide
DSC	Difference scanning calorimetry
DTE	Dithienylethenes
EDS/EDX	Energy dispersive X-ray spectroscopy
EDTM	Electric dipole transition moment
EtOH	Ethanol
<i>ext</i>	Extinction
<i>h</i>	Hour(s)
HKUST	Hong Kong University of Science and Technology
IR	Infrared
IR-MOF	Isorecticular MOF
IRRA	Infrared reflection-absorption
<i>irrad</i>	Irradiated
JUC	Jilin University China
LED	Light-emitting diode
LPE	Liquid phase epitaxial growth
<i>max</i>	Maximum
MC	Merocyanine
MeOH	Methanol
MIL	Matériaux de l'Institut Lavoisier
<i>min</i>	Minute or minimal
MOF	Metal-organic framework
<i>nm</i>	Nanometer

NMR	Nuclear magnetic resonance
<i>o</i>	Open
<i>oF</i>	4 <i>H</i> , 4 <i>H'</i> -octafluoro
PAP	2-phenylazopyridine
PCN	Porous coordination network
PCP	Porous coordination polymer
PDF	Pair distribution function
PEG	Poly(ethylene glycol)
<i>pF</i>	Perfluoro
PIZOF	Porous interpenetrated zirconium-organic frameworks
PM	Porous material
PSS	Photostationary state
QCM	Quartz crystal microbalance
SBU	Secondary building unit
SEM	Scanning electron microscopy
SP	Spiropyran
SP-Nitro	1,3,3-trimethyl-indolino-6'-nitrobenzo-pyrylospiran
SP-O	1,3,3-trimethyl-indolino-naphtho-spirooxazine
SURMOF	Surface-mounted MOF
<i>tF</i>	<i>Ortho</i> -tetrafluoro
TGA	Thermogravimetric analysis
ToF-SIMS	Time-of-flight secondary ion mass spectrometry
UHPLC	Ultra-high-performance liquid chromatography
UiO	Universitetet i Oslo
UV	Ultra-violet
vis	Visible (light)
XPS	X-ray photoelectron spectroscopy
XR(P)D	X-ray (powder) diffraction
ϵ^0	Elution power
λ	Wavelength

1 General Introduction

The synthesis and design of smart materials has become a central point of research in recent years. Especially responsive systems have been investigated, as they can be applied, e.g., as sensor materials and memory devices or when implemented in medical applications. In general, responsive materials react in different ways upon an external stimulus: they can change their magnetic properties and their electrical conductivity, or, most importantly, they can change their absorption properties. Considering the latter, light is one of the most attractive stimuli, as it is a cheap and constantly available stimulus, which is desirable for possible applications. When

light causes changes of the absorption properties, this phenomenon is called photochromism.

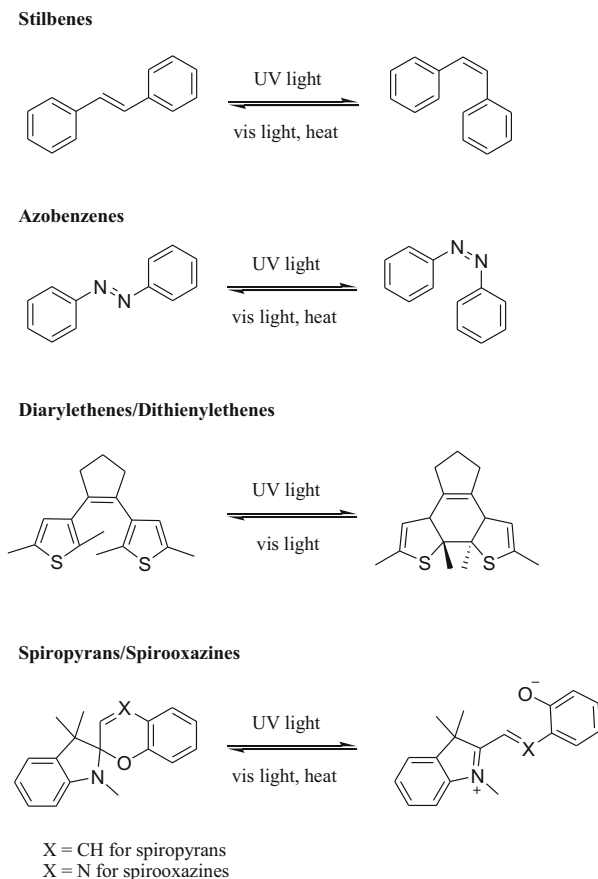
Since most of the photochromic molecules only show very limited photoswitching in the pristine solid, the majority of investigations on their photochromic properties has been performed in solution. As an example, spiropyrans with substantial light-induced structural changes have almost exclusively been investigated in solution [1–4], when embedded in polymers [5–9] or nanoporous materials [10–12]. Several efforts were being made to incorporate the photoactive part into zeolites, silica matrices, or polymers to form smart materials. About 20 years ago, *Caro* and co-workers started to implement the photoactive moiety as a guest molecule into a porous host matrix (porous material, PM) [13]. In a first attempt, the authors embedded azobenzene into nanoporous zeolites, forming the first photoswitch@PM composite material. In addition to other azobenzene@zeolite materials [14, 15], also spiropyran@zeolite composites were synthesized [16–18]. For both types of switches, photochromic properties of the switchable part were observed, making these hybrid compounds promising candidates for the development of functional materials. Another elegant way to obtain these smart materials is the embedment of photochromic dyes into metal-organic frameworks (MOFs) to form functional switch@MOF composites. MOFs represent a class of porous materials with a high crystallinity combined with the ability to be systematically functionalized, opening a wide range of applications.

This chapter will give an overview of switch@MOF systems with the photoactive part being non-covalently attached to the MOF scaffold. Firstly, the terms photochromism, solvatochromism and metal-organic frameworks will be briefly introduced, and finally, as the main part of this chapter, the hitherto known switch@MOF hybrid systems will be thoroughly discussed.

1.1 Photochromism

The phenomenon of photochromism was firstly discovered by *Fritzsche* [19], when he observed bleaching of an orange-colored tetracene solution in the daylight that retrieved its color overnight. Almost 100 years later in the 1950s, *Hirshberg* [20] was the first to define photochromism as the reversible transformation of a molecular species between two isomers A and B with different absorption properties upon irradiation with electromagnetic radiation of a specific wavelength. Here, reorganization of the ground state can be either achieved by light, such molecules that are called P-type chromophores, or by heat supply, which makes these molecules T-type chromophores [21]. Two different types of photochromism are distinguished: positive and negative photochromism. The photochromism is called positive, if the thermodynamically more stable species A is found to be non- or slightly colored, while the irradiated one B is deeply colored. Here, $\lambda_{\max}(\text{B})$ of the irradiated moiety is red-shifted in comparison to $\lambda_{\max}(\text{A})$ of the ground state. If $\lambda_{\max}(\text{A}) > \lambda_{\max}(\text{B})$, the photochromism is called inverse, antidromic, or negative [21].

Fig. 1 Photoisomerization processes of commonly used photochromic compounds in hybrid switch@MOF materials. Isomerization is caused by irradiating the ground state (left) with light of a specific wavelength resulting in the formation of the excited state, which is depicted on the right. Reorganization of the ground state is either achieved by light of another wavelength and/or by heat supply



Photochromism is known for both inorganic and organic compounds. In the following, we will set our focus on organic photoswitches. For organic compounds, the photoresponse depends on the nature of the photochromic molecule. Different kinds of structural changes occur and may vary from simple isomerization processes to transfer reactions and bond breaking. For that reason, these photoswitches are divided into different types with respect to their photoresponse. The two relevant types for this review with exemplary representatives are discussed in the following. Photochromic compounds, which are commonly used in switch@MOF hybrid systems, are depicted in Fig. 1.

- *E/Z* isomerization
E.g., stilbenes [22], azobenzenes [23–25]
- Ring-opening/ring-closing (pericyclic reactions)
E.g., spiroopyrans [26, 27] and spirooxazines [28], diarylethenes [29], fulgides [30]

For stilbenes and azobenzenes, irradiation with UV light causes an *E*-to-*Z* conversion of the molecules, for spiropyrans/spirooxazines and diarylethenes/dithienylethenes (denoted as DAE and DTE in the following), light exposure results in ring opening or ring closure to yield the excited state, respectively. Spiropyrans and spirooxazines are switched between their closed, colorless spiropyran form (denoted as SP form) and the open, deeply colored merocyanine form (denoted as MC form). The isomerization process is accompanied by a drastic increase in the dipole moment. In contrast to that, DAEs/DTEs exhibit ring closure of the *o*-DAE/DTE to the *c*-DAE/DTE (*o* denotes open- and *c* closed-ring form, respectively). The isomerization processes are shown in Fig. 1. For a more detailed description of the switching mechanisms, we refer to the literature, e.g., by *Bouas-Laurent and Dürr* [21] and others [22, 23, 25, 29, 31–34].

The light-induced structural changes require a certain degree of spatial freedom and are strongly related to the type of isomerization. For many DAEs/DTEs, photoswitching is even possible in the pure solids for both crystalline powders and single crystals, since the light triggered re-organization between the ground and the excited state is almost non-spacious [35]. In contrast to that, azobenzenes and their fluorinated derivatives differ significantly in size of the *E* and *Z* isomers [36]. Consequently, the photochromic response in the solid state is limited or even completely suppressed. A similar case is found for spiropyrans and spirooxazines. Despite of few exceptions (e.g., when deposited as thin films [37–39], at very low temperatures [40] or when irradiated with intense UV light [41]), the SP-to-MC isomerization is sterically hindered in the pristine solid materials. This limited applicability remains a challenging task, as the dissolved state is obviously disadvantageous for the construction and design of functional materials.

Since the light-induced structural changes cause alterations in absorption properties (color change), dipole moment, and/or refractive index [42], photochromic compounds are intensively studied as they are expected to pave the way to new responsive materials. The first example of an application of a spiropyran composite was realized in 1989 by *Rentzepis and Parthenopoulos*, who published a spiropyran-based three-dimensional optical data storage device [5]. Additionally, photochromic compounds were employed as synthetic molecular machines [43–46], whose most famous representatives were awarded with the Nobel Prize in 2016 [47]. Ever since, several efforts for the construction of responsive functional materials have been made, also with an increasing interest in MOFs as host matrices for the photochromic dye.

1.2 Solvatochromism

The class of spiropyrans and spirooxazines shows solvent-dependent absorption maxima of the excited species, which is referred to as solvatochromism. As *Reichhardt* comprehensively dealt with solvent effects in organic chemistry, his

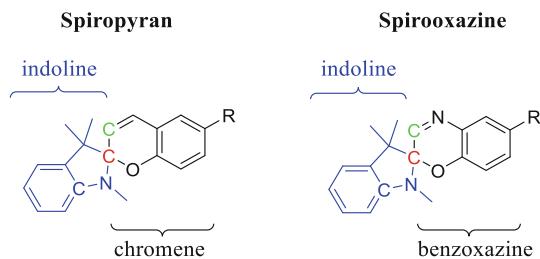


Fig. 2 Structures of spiropyrans and spirooxazines in their closed SP form. The indoline part is colored in blue; the chromene, respectively, benzoxazine part is colored in black. The C_{Spiro} atom is highlighted in red and the chromene/benzoxazine carbon in green

definitions will be briefly described in the following. For more details, we refer to the literature [48].

A molecule is designated as solvatochrome, if the absorption band of this molecule dissolved in solvents of different polarity shows alterations with respect to position, shape, and intensity. In particular interest of this work, only changes in position are examined: with increasing polarity of the solvent, the absorption maxima may be red- (bathochromic) or blue-shifted (hypsochromic), which is denoted as negative solvatochromism for the latter and positive solvatochromism for the former. These alterations originate from solute-solvent interactions, such as dipole-dipole or hydrogen bonding interactions, etc. By these interactions, the energy gap between the ground and the excited state is modified. Here, the effect on the spectra is primarily dependent on the dye and its type of transition. For spiropyrans and spirooxazines, the electronic transitions of interest are $\pi \rightarrow \pi^*$ and $n \rightarrow \pi^*$, as well as charge-transfer absorptions. Both molecules form the so-called merocyanine form upon UV light irradiation, which has already been described earlier. Merocyanines are part of the class of the intramolecular ionic meropolymethine dyes, which are located in between the polyenes and polymethines [49, 50].

Those compounds, which merocyanines belong to, have an electron-donating group A, which is linked by a conjugated system B to the electron accepting group C. In case of the molecules depicted in Fig. 2, the N-atom of the indoline part represents the electron-donating group and the O-atom of the chromene/benzoxazine unit the electron accepting group. Because of this specific structure, two mesomeric electronic states are formed: $A - B - C \leftrightarrow A^+ - B - C^-$. Obviously, the electronic transition is an intramolecular charge-transfer between the electron donating group A and the electron accepting group C. For this reason, dipole moments of the ground state and excited state differ significantly. In case of spiropyrans and spirooxazines, irradiation with UV light triggers a change in the electronic distribution and, consequently, the formation of a dipolar solute. As a result of this, two intramolecular electronic transitions occur, when the species is either dissolved in a nonpolar or in a polar solvent [51–53]. Depending on the type of molecule, the energy gap of the ground and the excited state is either reduced in size or enlarged with increasing solvent polarity, which causes blue- or red-shifted absorption bands, respectively. In

particular for spiropyrans, an increase in solvent polarity causes blue-shifted absorption bands. Consequently, the electronic structure of the excited species shifts from a polymethine-like state to a polyene-like state by increasing the solvent's polarity [32, 48]. For spirooxazines, both types of solvatochromism have been observed, mainly dependent on the substitution of the benzoxazine ring [54].

Both photochromic and solvatochromic properties are mostly observed in solution and only rarely in the pure solids. Therefore, encapsulation of photoswitchable dye molecules into a (porous) host matrix seems to be of great potential, since the single molecules are separated from each other in a confined environment, which, in turn, might influence the optical properties of the incorporated species.

1.3 Metal-Organic Frameworks

Since the publication of MOF-5 by *Yaghi* and co-workers in 1999 [55], the interest in metal-organic frameworks (MOFs) has increased rapidly [56]. MOFs are hybrid materials consisting of inorganic nodes, mostly metal cations or metal-oxo-clusters, which are linked by organic linker molecules with at least two functional groups, forming a two- or three-dimensional framework with potential voids [57]. These compounds were already described before 1999 [58–62], but MOF-5 somehow gave the starting point of this research area. The schematic construction of MOFs is exemplarily described for MOF-5 (see Fig. 3): the inorganic Zn_4O^{6+} cluster and the carboxylate function of the organic terephthalate anion form a secondary building unit (SBU). By connecting these SBUs by the linker molecules into three dimensions, the framework of MOF-5 with accessible voids is generated.

Especially because of their potential voids, MOFs are extremely promising candidates for both industry and science. If accessible, these pores offer various applications for, e.g., gas adsorption [63, 64], separation of gases [65, 66] and liquids

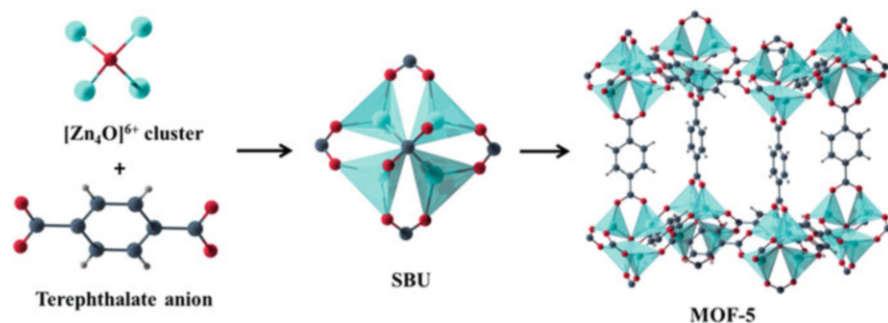


Fig. 3 Schematic construction of MOF-5 from Zn_4O^{6+} clusters and terephthalate anions forming a 3D framework structure with accessible voids. Crystallographic data used for this figure were taken from *Yaghi* and co-workers [55]. Color code: turquoise, zinc cations; red, oxygen anions; grey, carbon; white, hydrogen

[66–68], heterogeneous catalysis [69], drug encapsulation and delivery [70, 71], incorporation of fluorescent dyes [72, 73], and electronic devices [74, 75]. Even structure elucidation of organic molecules via embedment into a MOF framework has been shown by *Fujita* and co-workers, who established this as “crystalline sponge method” [76–83]. Detailed information on possible industrial applications of MOFs can be found in several reviews [84, 85]. Also in modern physics concerning, e.g., semiconductors, MOFs started to gain more and more attention [86].

These diverse applicabilities are the result of the structural design of MOFs. The linker molecules as well as the metal nodes can be variably designed. *Yaghi* and co-workers synthesized isorecticular MOFs (IR-MOFs), which show similar network topologies by simultaneous elongation and modification of the linker molecules [87]. That way, pore diameters up to 98 Å were realized [88]. However, further elongation of the linker molecule does not always lead to larger pores, but to interpenetration, which has been observed, e.g., for PIZOFs (porous interpenetrated zirconium-organic frameworks) [89]. With respect to potential applications such as chemical sensors, smart membrane separation or data storage devices, MOFs as thin films are preferable to powder MOFs. The thin film approach allows to fabricate devices and, additionally, films possess a more flexible design than bulk materials. For the production of thin MOF films, various methods have been developed [90–92]. Rather straightforward ways are spin-coating a suspension of MOF crystals onto a specific surface [93, 94], direct growth of MOF films on surfaces by solvothermal methods [95, 96] or controlled layer-by-layer synthesis. The latter are referred to as surface-mounted MOFs – SURMOFs [97].

The systematic design and functionalization of MOF pores, as well as the opportunity to prepare MOFs as thin films, make this class of materials promising candidates to control the guest uptake, host-guest interactions, and, additionally, guest-guest interactions.

While most applications since 1999 focus on gas adsorption and storage, the field of photoactive MOFs has been given only more attention in recent years and is now a growing field of research. This is not surprising, since MOFs appear to be ideal host matrices for photoactive molecules. In the following, these guest@MOF materials will be introduced in a general way. First, methods on how to incorporate the photochromic guest molecules and how to characterize the resulting hybrid materials are described. In a second step, different switch@MOF systems will be introduced, starting with the rather simple photochromic dye stilbene. Each section will always start with the work published on crystalline bulk materials and will then, if available, continue with thin film materials.

1.4 Implementing Photoswitches into MOFs

The construction of switch@MOF hybrid materials can be achieved by either *extrinsic* or *intrinsic* introduction of the photoactive part, respectively. In 2016,

Gascon and co-workers presented a comprehensive review on this topic, assigning the photoactive function to either being a part of the framework itself as *intrinsic* or being a guest molecule as *extrinsic* introduction to the MOF [98]. Further reviews on this topic have been published [99–106]. Generally, it is possible to introduce the photoactive functionality in four different ways, which will be shortly described in the following:

1. Intrinsic introduction

- (a) The photoactive part is part of the linker backbone itself.
- (b) The photoactive part is a substituent of the linker.
- (c) The photoactive part is coordinatively immobilized inside the MOF scaffold.

2. Extrinsic introduction

- (d) The photochromic dye is inserted as a non-covalently attached guest molecule inside the MOF lattice.

For the intrinsic introduction, three ways are distinguished: Firstly, the photochromic moiety is part of the linker backbone itself. As aforesaid, the light-induced isomerization processes often require a certain degree of spatial freedom. Hence, large structural change, e.g., *E/Z* isomerization, is sterically hindered [107] or even leads to a collapse of the framework in such systems [108, 109]. Therefore, only few studies have been published with promising functionalities [110–112]. Secondly, the photochromic unit is introduced as a substituent of the linker [113]. Here, both bulk materials and thin films have been successfully prepared [112, 114–116]. It has been demonstrated that the uptake amount of gases can be controlled by light [114, 117]. Particularly for thin films with azobenzene side groups, the diffusion properties [118, 119], permeation and separation factor of membranes [120], or the proton-conduction of guest molecules [121] was remote-controlled by light. In a recently published work, *Heinke* and co-workers were even able to show that switching of the enantioselective adsorption capacity by light is possible [122]. However, isomerization processes are hindered in some cases [123]. Moreover, the high synthetic efforts to obtain such functionalized linker molecules is the major drawback, which limits broad applications of photoactive MOFs constructed that way. The latter also applies to coordinative immobilization of the photoswitch, which has been presented by *Shustova* and co-workers [124] for spiropyran and diarylethene derivatives.

Via extrinsic introduction, the photoactive moieties are embedded as guest molecules inside the MOF pores. This strategy is challenging, as the mobility triggers a significantly more complex situation than the guest being fixed at the MOF scaffold. For instance, the degree of filling (guest-guest interactions) and the physicochemical environment given by the MOF voids (host-guest interactions) are expected to affect the preferable orientation and configuration of the guest molecule and the photostationary state (PSS).

With respect to extrinsic inclusion, at least four different methods for incorporation were described in the literature:

(a) Loading via diffusion processes:

The MOF is dispersed in a solution of the photochromic dye. Here, the host material is loaded via diffusion of the guest molecules into the MOF pores. A possible disadvantage of this method is that the solvent molecules may remain together with the chromophore inside the pores. Hence, resulting properties might not exclusively originate from the MOF host, and care must be taken to remove all residual solvent molecules after the loading process.

(b) Loading via melting processes:

The activated MOF and the dye are mixed and heated to the melting point of the respective guest molecule. Subsequently, the molten dye will enter the pores of the host lattice. Here, no solvent molecules have to be excluded in further considerations.

(c) Loading via gas phase loading processes:

The activated MOF and the dye are thoroughly ground and heated under reduced pressure to the sublimation point of the photochromic molecule. Here, the guest molecules are embedded into the host material via the gas phase. Hence, no solvent molecules have to be considered. However, sublimation temperatures must be chosen carefully so that embedded dye molecules are not removed again and no residual guest outside the MOF pores remains. Additionally, care must be taken to avoid thermal decomposition of the photochromic dye and the MOF.

(d) Loading via crystallization inclusion:

MOF precursors and the photochromic dye form the switch@MOF composite in a one pot synthesis. During the construction of the MOF network, the switches used in the starting solution are integrated simultaneously. Obviously, this is a time-saving method. Anyhow, chromophores with non-coordinating substituents must be chosen to avoid competing effects with the linker molecules. Furthermore, solvent molecules remaining together with the chromophore inside the pores might occur in this synthesis procedure. Similar to loading via diffusion processes, care must be taken to remove all solvent molecules afterwards.

All these loading procedures were used to synthesize various switch@MOF systems with fascinating and even surprising properties. In a next step, the resulting systems must be thoroughly analyzed. Adequate characterization of these functional materials is indispensable to understand the occurring optical properties. Here, different methods were applied, all regarding to Incorporation, Composition, and resulting Effects, so that *Ruschewitz* and co-workers named it the ICE-principle [152]. In Table 1, the different methods used for the characterization of switch@MOF systems together with the obtainable information are summarized. The categorization refers to the literature discussed in Chap. 2 “Switch@MOF Systems.”

Since the first synthesis and investigation of a hybrid switch@MOF systems, not only the variety of these systems increased from comparably simple to complex dye molecules, but also the characterization of the obtained materials evolved in a way that the interaction of host and guest molecule is now understood in more detail. In the course of the following chapter, various synthesis as well as methodological

Table 1 Methods used to characterize switch@MOF systems following the ICE-principle

Incorporation/successful embedment	Composition of the hybrid material	Effects/investigations on the resulting properties
XRD, XRPD	Elemental analysis	UV/vis spectroscopy
DSC	XPS	IRRA, IR spectroscopy
Leaching	DSC/TGA measurements	Raman spectroscopy
	¹ H NMR spectroscopy	BET
	UHPLC	QCM
	ToF-SIMS	Gas permeance
	SEM	Luminescence spectroscopy
	BET	DC measurements
	EDX/EDS	DFT calculations

approaches are presented, which have continued to develop up to the most recent work and, thus, led to a significantly better understanding of the resulting optical properties of these switch@MOF materials. However, even today not all aspects are understood. These limitations will be discussed in the conclusion section.

2 Switch@MOF Systems

Various switch@MOF systems with fascinating properties were synthesized. As photoactive part different photochromic dyes have been incorporated into both bulk materials and thin films. In the following, the resulting composites will be presented, always starting with bulk materials followed by thin films.

2.1 Stilbenes in MOFs

2.1.1 Bulk Material

The first switching system consisting of a photochromic dye and a metal-organic framework was described by *Fujita* and co-workers in 2010 [125]. They used a porous coordination network (PCN; this is an alternative term for MOF) built up from the tris(4-pyridyl)triazine ligand and ZnI₂. The *as synthesized* network $[(ZnI_2)_3(C_{18}H_{12}N_6)_2] \times (C_6H_5NO_2)_n$ was soaked into a solution containing *Z*-stilbene in cyclohexane. Initially, the pale PCN crystals turned bright yellow, which already indicated the successful embedment of the dye. By elemental analyses, the authors confirmed the inclusion of one molecule *Z*-stilbene per formula unit of the PCN. Additionally, diffuse reflectance UV/vis spectroscopy verified the successful inclusion, since a new charge-transfer (CT) band at approximately 450 nm was observed, which the authors attributed to the proximity of the guest molecule with the PCN ligand inside the network.

The formed *Z*-stilbene@PCN was suspended in cyclohexane and irradiated with light of a wavelength of 400–500 nm for several hours. Remarkably, this resulted in a nearly 100% *Z*-to-*E* photoconversion without the formation of any photo-induced by-products (e.g., dihydrophenanthrene or photooxidized products). Selective isomerization of *Z*- to *E*-stilbene only occurred in the presence of the PCN. In absence of the network or the single network components (ligand or ZnI₂), no photo-conversion was found. Furthermore, after removal of the stilbene@PCN crystals, the isomerization stopped and by adding pyrene as a blocking agent to the reaction mixture, a slower photo-conversion was observed. The *E/Z* ratio increases faster within the crystals than in the supernatant. Therefore, the authors concluded that *Z*-to-*E* photoisomerization exclusively occurs within the pores of the PCN. Additionally, the *E*-stilbene within the pores exchanges with the unreacted *Z*-stilbene in the supernatant solution.

Conclusively, these results demonstrate the successful photo-conversion inside the pores of a PCN with a selective formation of *E*-stilbene without any photo-induced by-products and, thus, demonstrate the first photoswitching of a photochromic dye inside a porous coordination network/MOF.

2.2 Azobenzene and Its Derivatives in MOFs

2.2.1 Bulk Material

In contrast to stilbenes, several studies have been published on azobenzene and derivatives incorporated in MOFs, both in bulk materials and in thin films. In the following, the results will be presented in order of their publication date. It should be emphasized that the first work by *Kitagawa* and co-workers was published ca. 2 years after the pioneering work of *Fujita* and co-workers on stilbene@PCN (Sect. 2.1.1).

In 2012, *Kitagawa* and co-workers expanded the field of switch@MOF systems to azobenzene (AZB) as photoactive part [126]. Via a gas-phase loading process, *E*-AZB was incorporated into the flexible porous coordination polymer (PCP \equiv MOF) [(Zn₂(terephthalate)₂(triethylenediamine))]_n (also referred to as DMOF-1) [127]. By elemental and thermogravimetric analyses, the composition of AZB@DMOF-1 (the authors denoted this hybrid material as 1 \supset AB) was determined. Additionally, XRPD measurements on the composite material showed a change of the host structure originating from the successful inclusion of the photochromic dye. The XRPD patterns of pure DMOF-1 and AZB-loaded DMOF-1 are depicted in Fig. 4a, b, respectively.

In comparison to benzene@DMOF-1, a similar diffraction pattern of AZB@DMOF-1 is observed, where the connectivity of the overall framework is preserved, but a rhombic net is formed [127]. The authors concluded that the change from a tetragonal to an orthorhombic crystal system accompanied by a shrinkage of the cell volume was a result of the AZB embedment.

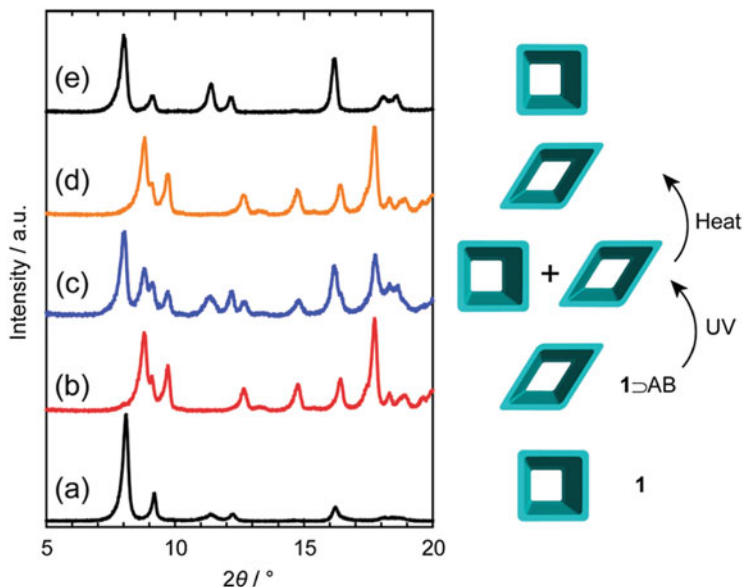
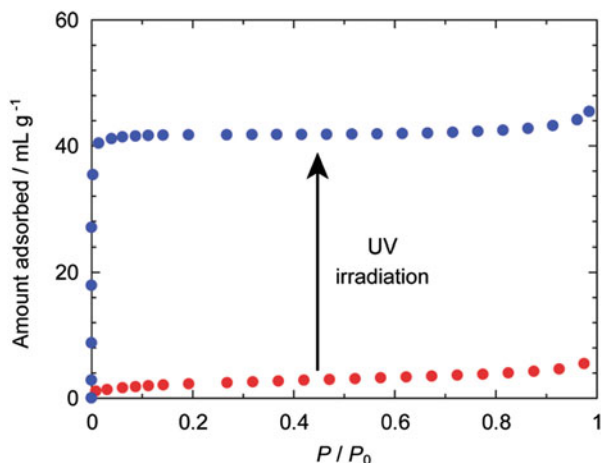


Fig. 4 Left: XRPD patterns of (a) unloaded DMOF-1, (b) AZB@DMOF-1, (c) AZB@DMOF-1 after UV light irradiation, (d) irradiated AZB@DMOF-1 after heating at 120°C, and (e) the adduct of unloaded DMOF-1 with Z-stilbene. Right: Schematic illustrations of the host structure. Reprinted (adapted) with permission from Ref. [126], copyright 2012 American Chemical Society

Upon light irradiation, the *E/Z* isomerization of AZB inside the MOF pore occurred, resulting in a structural transformation of the flexible host material to a superposition of the two patterns originating from the tetragonal and the orthorhombic structures (depicted in Fig. 4c). Thus, *Kitagawa* and co-workers presented the first example of a light-induced switching of a MOF structure. Furthermore, a *Z/E* ratio of 38:62 was determined from NMR spectroscopic measurements (^1H NMR), which is close to the photostationary state (PSS) of AZB in solution. As expected, the light-induced structural changes are time-dependent reaching the saturation at ~ 6 h UV light irradiation for the *Z* isomer. Remarkably, an enhanced stability of the *Z* isomer was observed: after keeping the irradiated sample in the dark at 25°C for 1 month, more than 80% of the *Z* isomer remained, indicating a higher activation energy for the $Z \rightarrow E$ transformation in the MOF pores compared to the isomerization in solution. This means, the molecular properties of AZB, i.e., the thermodynamic stability of the less stable *Z* isomer, are influenced by the encapsulation.

To examine the responsive functionality of the occurring structural transformations, the incorporated AZB was used to switch the N_2 gas adsorption properties of the nanoporous host DMOF-1 by light. The nonirradiated species showed (almost) no nitrogen uptake, probably because of a pore blockage caused by the guest *E*-AZB (see Fig. 5, red dots). After irradiation with UV light, the $E \rightarrow Z$ conversion resulted in a remarkable increase of the N_2 adsorption amount due to the significant structural change of the host framework (Fig. 5, blue dots). By heat supply, the N_2 uptake was

Fig. 5 N_2 adsorption isotherms at 77 K for AZB@DMOF-1 before (red) and after irradiation with UV light (blue). Reprinted (adapted) with permission from Ref. [126], copyright 2012 American Chemical Society



reversed showing the remote control of gas uptake and release. To sum up, a new strategy of guest-to-host transmission was presented highlighting the potential of the combination of MOFs and photochromic dyes as functional smart materials.

One year later, in 2013, *Kitagawa* and co-workers used a poly(ethylene glycol) functionalized azobenzene (denoted as PEG-AZB) to form a photoresponsive reversible encapsulation-release system [128]. Here, the dye molecule was dissolved in various solvents and DMOF-1 [127] was added to the respective reaction mixture. Only for ethanol, a successful incorporation of the functionalized azobenzene was observed: After the addition of the MOF host to the PEG-AZB-ethanol mixture, the initially yellow solution immediately turned colorless. The successful inclusion of PEG-AZB in DMOF-1 was confirmed by DSC measurements: The resulting yellow precipitate did not show any signal, which could be assigned to the melting of neat PEG-AZB. These findings were corroborated by NMR spectroscopy.

Photoswitching of PEG-AZB from its *E* to its *Z* form requires a certain degree of sterical freedom due to the large substituents. Consequently, UV light irradiation caused the release of the guest molecules in its (almost) linear *E* form, and, thus, an increased concentration of the *Z* isomer was detected in the supernatant solution. By visible light, the $Z \rightarrow E$ conversion was reversed and the guest was encapsulated into the MOF again. The light-induced encapsulation and release are shown in Fig. 6.

Almost at the same time, *Ruschewitz* and co-workers started their investigations on azobenzene embedded in different non-flexible MOFs [129–131]. Particularly, they examined the influence of various MOF structures on the photochromic properties of the incorporated guest molecule. As host materials, MOF powders of type MOF-5 [55], MIL-68(In) [132], and MIL-68(Ga) [132], as well as MIL-53(Al) [133] and MIL-53(Ga) [134], were chosen, and azobenzene was loaded via the gas phase to exclude any solvent molecule from all further considerations. The successful incorporation of the photoactive molecule was confirmed by both XRPD and elemental analyses. By the latter, also the amount of embedded AZB was quantified.

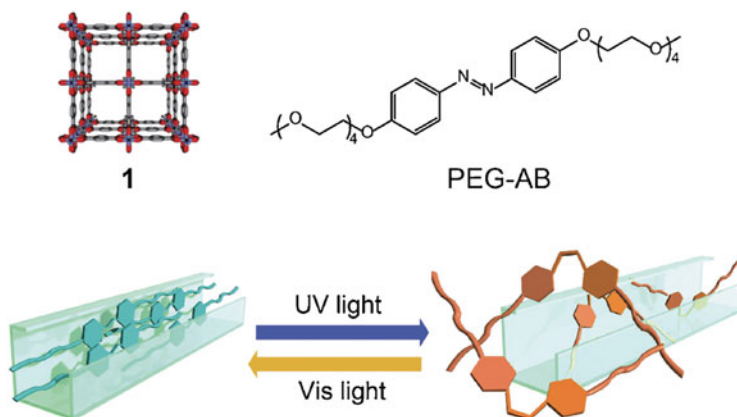


Fig. 6 Schematic illustration of DMOF-1 (denoted as **1**), the photochromic guest molecule PEG-AZB, and the light-induced encapsulation and release of PEG-AZB in DMOF-1. Reprinted (adapted) with permission from Ref. [127], copyright 2013 Chemical Society of Japan

X-ray powder diffraction is an elegant way to follow the incorporation process, since for non-flexible MOFs the embedment is accompanied by a modulation of the reflection intensities. This is caused by the changed electron density arising from the guest molecules inside the MOF pores, while the reflection positions remain unaffected. On the contrary, for flexible MOFs such as the MIL-53 family [133, 134] or DMOF-1 [127] described earlier, inclusion of a guest molecule may cause the so-called breathing effect and typically significant changes of the diffraction pattern with respect to intensities and 2θ positions are observed. Furthermore, if the dye is not completely embedded, additional reflections of the guest moiety would be visible in the respective XRPD pattern. In Fig. 7, the comparison of unloaded and loaded MOF-5 is depicted, showing the modulation of intensities upon guest loading, especially visible for the third reflection.

The light-induced *E*-to-*Z* conversion was quantified by means of IR spectroscopy, since the *E* and *Z* isomer exhibit distinguishable IR bands. For $\text{AZB}_{0.66}@\text{MIL-68}(\text{In})$, 30% of the *Z* isomer was found, whereas 27% for $\text{AZB}_{0.66}@\text{MIL-68}(\text{Ga})$ and 25% for $\text{AZB}_5@\text{MOF-5}$ were reported. Surprisingly, no photoswitching was observed for MIL-53(Al) as host material at all. To understand the reasons for the inhibited isomerization in MIL-53(Al) from a structural point of view, the authors conducted high resolution synchrotron powder diffraction measurements to solve the structures of $\text{AZB}_{0.66}@\text{MIL-68}(\text{Ga})$ and $\text{AZB}_{0.5}@\text{MIL-53}(\text{Al})$. The resulting crystal structures are shown in Fig. 8.

Obviously, the *E*-to-*Z* isomerization of AZB in MIL-53(Al) is sterically hindered, whereas no such hindrance is found in MIL-68(Ga). As a consequence, the size and the shape of the host pores as well as the orientation and the amount of the incorporated azobenzene molecules within these pores significantly influence the light response of the resulting photoswitch@MOF systems.

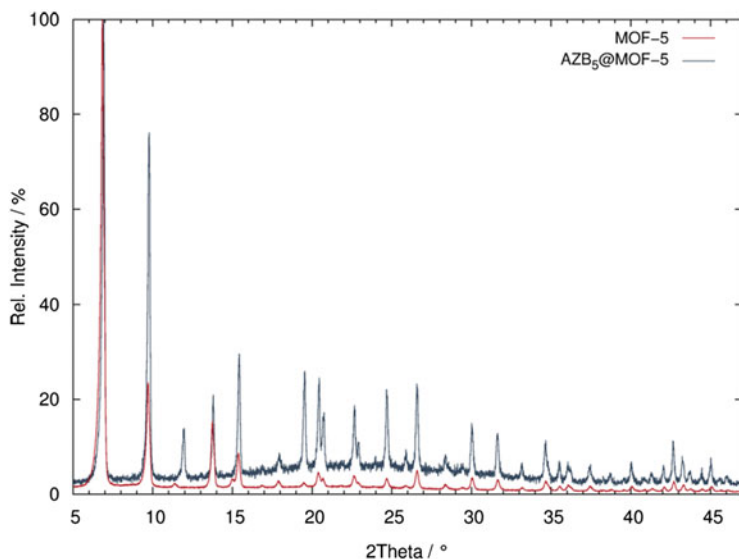


Fig. 7 XRPD patterns of unloaded MOF-5 (red) and MOF-5 loaded with azobenzene (blue). Reprinted (adapted) with permission from Ref. [129], copyright 2013 American Chemical Society

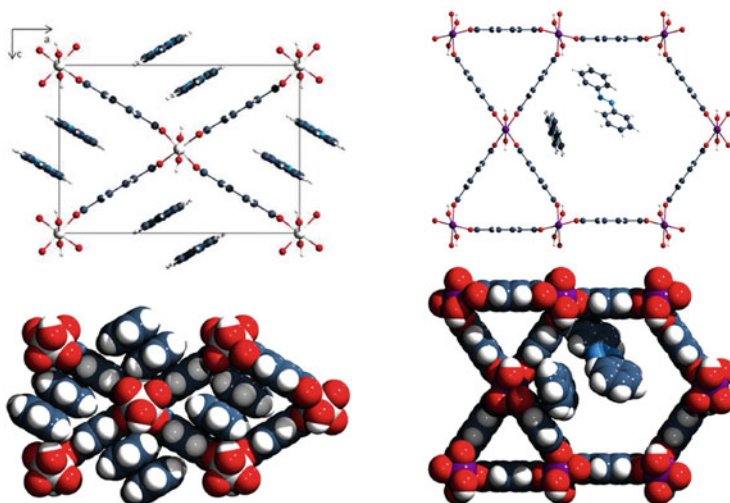


Fig. 8 Left: (top) Unit cell of $\text{AZB}_{0.5}@\text{MIL-53}(\text{Al})$ along [010], (bottom) space-filling representation. Right: (top) view of the crystal structure of $\text{AZB}_{0.66}@\text{MIL-68}(\text{Ga})$ in a view along [001], (bottom) space-filling representation. Reprinted (adapted) with permission from Ref. [129], copyright 2013 American Chemical Society

Most azobenzene-containing materials, such as most polymers or organic solvents, have strong absorption bands in the mid-IR range, especially in the so-called fingerprint region between 600 cm^{-1} and $1,500\text{ cm}^{-1}$ and, thus, making them virtually nontransparent for IR light. As a result, the AZB photoswitching has only rarely been investigated by vibrational spectroscopy. Therefore, *Ruschewitz* and co-workers presented one of these rare examples of precise AZB vibrational data [129].

Generally, azobenzene is switched between its two isomers by irradiation with UV light. However, the necessity of UV light that might interfere with the host matrix is a severe drawback. Additionally, the absorption bands of *E*- and *Z*-azobenzene overlap, which leads to photostationary states so that a complete transformation of one isomer to the other is not possible. By modifying azobenzene with suitable substituents, separation of the absorption bands might be achieved [135], e.g., introduction of fluorine atoms in the phenyl rings of AZB. For *tF*-AZB, photostationary states with almost quantitative switching (91% *Z* and 86% *E*) were reached, when dissolved in acetonitrile [136]. Remarkably, these isomerization processes are triggered by light in the visible region. Hence, UV light is no longer obligatory to induce the *E*-to-*Z* transformation and vice versa [136].

As a consequence, *Ruschewitz* and co-workers extended their work to the incorporation of fluorinated azobenzenes into MOFs [137]. Fifteen new photochromic hybrid materials were synthesized via a gas phase loading process. As host materials, the authors chose MOF-5 [55], MIL-68(In) [132], MIL-68(Ga) [132], MIL-53(Al) [133], and MIL-53(Ga) [134], similar to their investigations on pristine azobenzene [129]. As photochromic part, various fluorinated azobenzenes were embedded, namely, *ortho*-tetrafluoroazobenzene (*tF*-AZB), 4*H*, 4*H'*-octafluoroazobenzene (*oF*-AZB), and perfluoroazobenzene (*pF*-AZB), and their optical properties inside the host scaffolds were studied. The authors confirmed the successful guest inclusion by XRPD measurements and proved that *pF*-AZB_{0.34}@MIL-53(Al) and *pF*-AZB_{3.57}@MOF-5 did not release any guest molecules at ambient conditions by DSC/TG analyses. In a next step, the crystal structure of *pF*-AZB_{0.34}@MIL-53(Al) was solved in order to understand the underlying host-guest interactions and the associated photochromic properties, as in contrast to AZB embedded in MIL-53(Al), an *E*-to-*Z* isomerization of *pF*-AZB occurred within this MOF host. Solving the crystal structure of such composite materials is not straightforward, since possible disorder of the guest must be considered. Therefore, low temperature measurements are to be preferred, and, additionally, the initial state of the dye molecule should be close to 100% *E* or *Z*. Both requirements are met for the mentioned system leading to the crystal structure shown in Fig. 9. *pF*-AZB perfectly fits into the pores of MIL-53(Al), taking the respective *van der Waals* radii into account. However, in contrast to AZB_{0.5}@MIL-53(Al) the occupancy of the guest sites in the pores of the MOF is significantly lower in *pF*-AZB_{0.34}@MIL-53(Al), thus giving the guests in the latter more space for the photoswitching process.

Additionally, the authors thoroughly studied the underlying host-guest interactions (Fig. 9, right). Firstly, O – H...F interactions (shortest O – H...F distance: 213 pm) seem to dominate, and only weak O – H... π interactions are observed

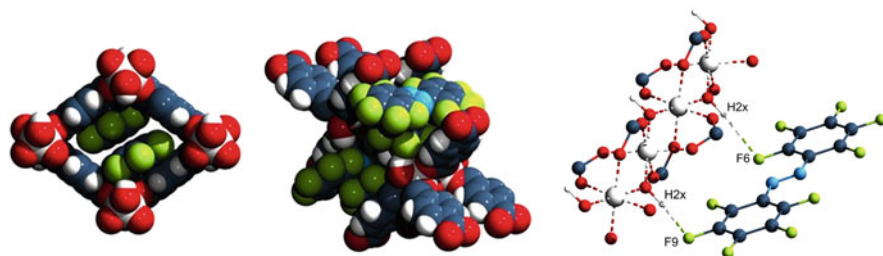


Fig. 9 (Left) space-filling presentation of the crystal structure of pF -AZB_{0.34}@MIL-53(Al) in a view along [100]; (middle) side view with an “opened” channel; (right) details of the crystal structure emphasizing some of the underlying host-guest interactions. Reprinted (adapted) with permission from Wiley and Sons, Ref. [137]; copyright 2019 Wiley-VCH

Table 2 Maximum amounts of the E and Z isomers for the investigated guest@MOF composites, reached by illumination with $\lambda = 405$ nm and $\lambda = 532$ nm, respectively

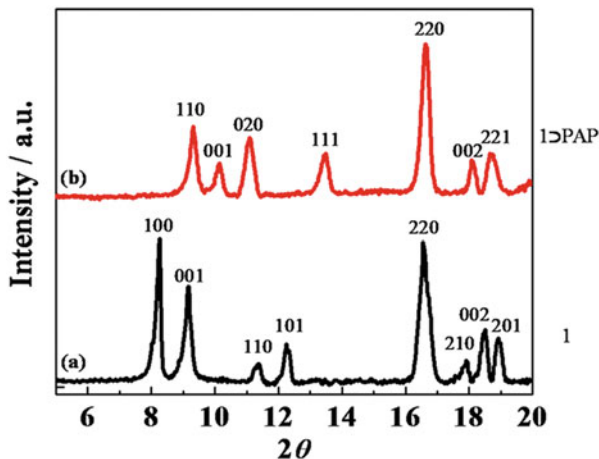
	AZB max. E /max. Z , [initial state]	tF -AZB max. E /max. Z , [initial state]	oF -AZB max. E /max. Z , [initial state]	pF -AZB max. E /max. Z , [initial state]
MOF-5	100%/25% [100% E]	93%/82% [52% E]	n.d. [62–88% E]	100%/50% [80% E]
MIL-53 (Al)	100%/0% [100% E]	90%/100% [37% E]	100%/56% [99% E]	100%/little Z [100% E]
MIL-53 (Ga)	100%/n.d. [100% E]	90%/94% [37% E]	n.d. [little Z]	100%/n.d. [100% E]
MIL-68 (Ga)	100%/27% [100% E]	96%/93% [45% E]	n.d. [62–88% E]	100%/40% [87% E]
MIL-68 (In)	100%/30% [100% E]	95%/95% [51% E]	88%/90% [62% E]	100%/79% [55% E]

Reprinted (adapted) with permission from Wiley and Sons, Ref. [137]; copyright 2019 Wiley-VCH
n.d. not determined

(shortest O – H...C distance: 281 pm compared to 265 pm in AZB_{0.50}@MIL-53(Al) [129]) originating from the high degree of fluorination of the pF -AZB guest and the inversion of its quadrupole moment [138]. Secondly, the phenyl rings are arranged almost directly one above each other with only a very small shift, which is in-between a stacked and an offset-stacked arrangement [139] being also the result of the inverted quadrupole moment of the perfluorinated ring. This was confirmed by a small shift in the frequency of $\tilde{\nu}$ (C=C) from 1,506 cm⁻¹ in the IR spectrum of unloaded MIL-53(Al) to 1,513 cm⁻¹ in the IR spectrum of pF -AZB_{0.34}@MIL-53(Al). Besides the determination of host-guest interactions, IR spectroscopy allows for a direct quantitative analysis of the switching process by tracking the E and Z bands of the different azobenzenes, respectively. The results of these investigations are summarized in Table 2.

It is a very remarkable result of this work that for tF -AZB embedded in different MOF hosts almost quantitative photoswitching (>90%) is found in a solid-state

Fig. 10 XRPD pattern of (a) unloaded DMOF-1 (black) and (b) DMOF-1 loaded with PAP (red). Reprinted (adapted) with permission from Ref. [140], copyright 2019 American Chemical Society. (<https://pubs.acs.org/doi/abs/10.1021/acsomega.8b00903>; further permissions related to the material excerpted should be directed to the ACS)

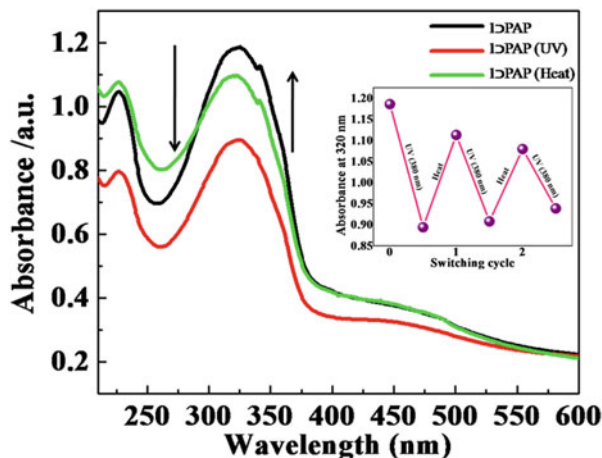


material by illumination with green and blue light without the need of UV light. Even more, the system consisting of *tF*-AZB and MIL-68(In) exhibits no significant fatigue upon several switching cycles, making this composite material promising for future applications. Thus, the authors presented the first guest@MOF systems with almost quantitative switching and detailed investigations on the underlying host-guest interactions to explain the optical properties of these materials from a structural point of view.

In ongoing studies, *Agarkar* and *Das* started to investigate the azobenzene derivative 2-phenylazopyridine (PAP) and focused their work on DMOF-1 [127] as host scaffold in a first step [140], mainly following the work of *Kitagawa* and co-workers [126] on AZB@DMOF-1. Because of the structural similarity of PAP and AZB, the authors expected a similar light-induced guest-to-host structural transmission, which had already been observed for the AZB@DMOF-1 composite upon UV light irradiation [126]. Accordingly, the dye molecule in its *E* form was embedded into the MOF framework by adsorption through melting and the successful guest inclusion was confirmed by a leaching experiment. Here, the PAP@DMOF-1 (denoted as 1 \supset PAP by the authors) sample was mixed with chloroform. PAP is known to be highly soluble in chloroform, hence, non-inserted molecules would be detectable by UV/vis spectroscopy.

No absorption band was observed, thus verifying the complete embedment of PAP. Additional XRPD measurements were performed, showing the successful formation of PAP@DMOF-1. In Fig. 10, the diffraction patterns of unloaded DMOF-1 (black) and loaded DMOF-1 (red) are depicted. Upon guest inclusion, the original tetragonal unit cell changes to an orthorhombic one, which was also found by *Kitagawa* and co-workers [126]. Additionally, IR spectra were recorded and the representative N=N stretching vibration indicated a non-coordinative mode of the dye molecule. Similar to the hitherto presented switch@MOF systems, the PAP@DMOF-1 composite material exhibits photochromic behavior as well. The light-induced *E*-to-*Z* conversion was triggered by UV light (380 nm), whereas

Fig. 11 UV/vis spectra of PAP@DMOF-1 (black), PAP@DMOF-1 after irradiation with UV light (red), and after heat treatment (green). In the inset three switching cycles of PAP@DMOF-1 (pink) are shown. Reprinted (adapted) with permission from Ref. [140], copyright 2019 American Chemical Society. (<https://pubs.acs.org/doi/abs/10.1021/acsomega.8b00903>; further permissions related to the material excerpted should be directed to the ACS)



reconversion was achieved by heat treatment at 60°C, which is similar to the results achieved for pristine PAP. The absorption spectra of PAP@DMOF-1 before and after irradiation with UV light as well as heat supply are depicted in Fig. 11. Additionally, experiments on the fatigue resistance were performed. Here, a significant decrease in absorption was observed after three cycles (see Fig. 11, inset). The ^1H NMR studies gave a photostationary state of 25:75 *Z/E* ratio, which slightly differs from the results of *Kitagawa* and co-workers [126].

It is most remarkable that in contrast to AZB@DMOF-1, the DMOF-1 host scaffold remains unaltered upon the light-induced isomerization of PAP. The authors explained this nonresponsive behavior by an interaction of the pyridine-N atom of PAP with the paddle-wheel unit of the MOF and suggested a partial replacement of DABCO (one of the two ligands used for the construction of DMOF-1). Further, they assumed that the interactions between AZB and DMOF-1 are stronger than those between PAP and the MOF. Nevertheless, nitrogen adsorption isotherms of PAP@DMOF-1 before and after UV light treatment were collected, which revealed a small N_2 uptake, which was related to the conformational change of the guest moiety.

In a following work, *Agarkar* and *Das* used the same guest molecule (PAP) but studied the photochromic behavior when combined with well-known MOF-5 [55] as host material [141]. The resulting PAP@MOF-5 (denoted as MOF-5 \supset PAP by the authors) hybrid material was investigated with respect to its optical properties and the influence of the conformational transformation of the embedded guest molecule on the surrounding host matrix. The loading procedure, confirmation of completeness of embedment as well as the study of the non-coordinating mode of PAP inside MOF-5 were performed analogously to their previously reported study and corroborated the successful formation of PAP@MOF-5. The orange-colored host-guest composite was analyzed with respect to its photochromic behavior by UV/vis

Fig. 12 UV/vis spectra of PAP@MOF-5 before (black), after irradiation with UV light (red), and after heat treatment (green). In the inset, three switching cycles of PAP@MOF-5 (pink) are shown. Reprinted from Ref. [141], copyright 2019 with permission from Elsevier

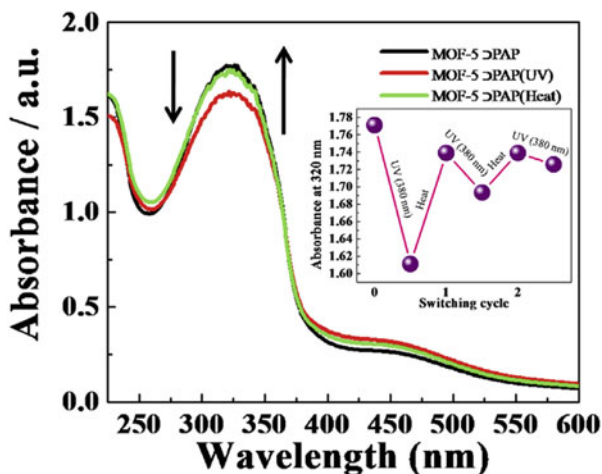
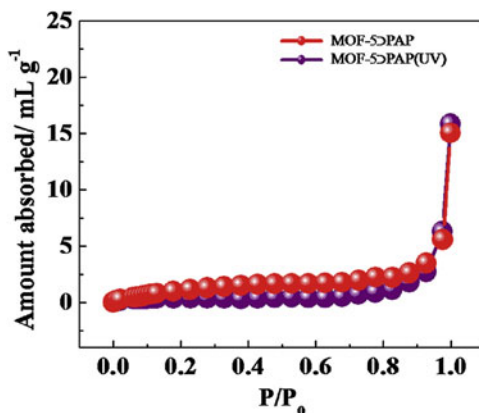


Fig. 13 Nitrogen adsorption isotherms at 77 K for PAP@MOF-5 before (red) and after irradiation with UV light (purple). Reprinted from Ref. [141], copyright 2019 with permission from Elsevier



spectroscopy. In Fig. 12, the UV/vis spectra of PAP@MOF-5 are shown both before and after irradiation with UV light (380 nm) as well as heat treatment (60°C).

Upon UV light irradiation, only a small amount of *E*-PAP converts to its *Z* form, possibly originating from steric hindrance inside the MOF scaffold. Reconversion of the *E* isomer was only partially achieved. The low fatigue resistance is already visible after three switching cycles (see Fig. 12, inset). The authors suggested photobleaching as well as geometrical hindrance as reasons for the low reversibility of switching. The former has already been found for AZB@MIL-53(Al) by Ruschewitz and co-workers [129]. However, it should be noted that the pores of MOF-5 are much larger than those of MIL-53(Al). Therefore, this behavior remains somewhat unexpected. In additional nitrogen adsorption measurements, no significant difference in the N₂ amount was observed before and after irradiating PAP@MOF-5 with UV light (see Fig. 13), which supports the results obtained from UV, IR, and ¹H NMR studies.

2.2.2 Thin Films

In 2016, *Zhang* and co-workers presented the first photochromic guest-encapsulated MOF thin film and studied the resulting photochromic properties [142]. The authors used a modified liquid phase epitaxial growth (LPE) method to insert plain azobenzene directly into a MOF thin film of type HKUST-1 (HKUST denotes Hong Kong University of Science and Technology) [143] to form *E*-AZB@HKUST-1. Both the schematic in situ layer-by-layer growth of the functional thin film and the light-induced isomerization process of AZB inside these thin films are depicted in Fig. 14.

The resulting *E*-AZB@HKUST-1 thin films were thoroughly studied using XRD, IRRAS, SEM, EDS, and XPS. The combined results of these measurements confirmed the successful AZB inclusion and, additionally, “an effective encapsulation with 20%” AZB was calculated from the EDS data [142]. In a next step, the authors investigated the photoisomerization of AZB inside the HKUST-1 thin film on an OH-functionalized quartz glass. In contrast to plain AZB powder, a different absorbance was observed for the composite material, see Fig. 15, top, which was not further commented by the authors. When irradiated with UV light for varying times, the absorption band at approx. 270 nm decreases, indicating the successful *E*-to-*Z* conversion of AZB inside the MOF pores (see Fig. 15, bottom). The reversibility was shown by exposure to visible light. Here, the intensity of the absorption band at approx. 270 nm increased again. Moreover, the temperature dependent emission properties of the hybrid thin films were measured, which further proved the formation of the composite material.

Heinke and co-workers also prepared thin MOF films of type HKUST-1 and loaded these films with plain azobenzene and *tF*-azobenzene [144]. Instead of a

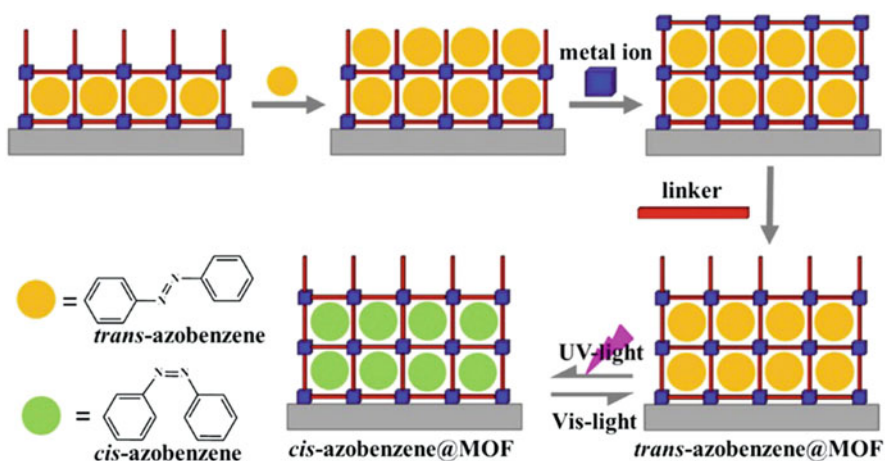


Fig. 14 Schematic presentation of the in situ layer-by-layer growth of AZB@HKUST-1 thin films and photoinduced *E*(*trans*)-to-*Z*(*cis*) conversion of AZB inside the MOF pores. Reprinted (adapted) with permission of Ref. [142]. Copyright 2016 American Chemical Society

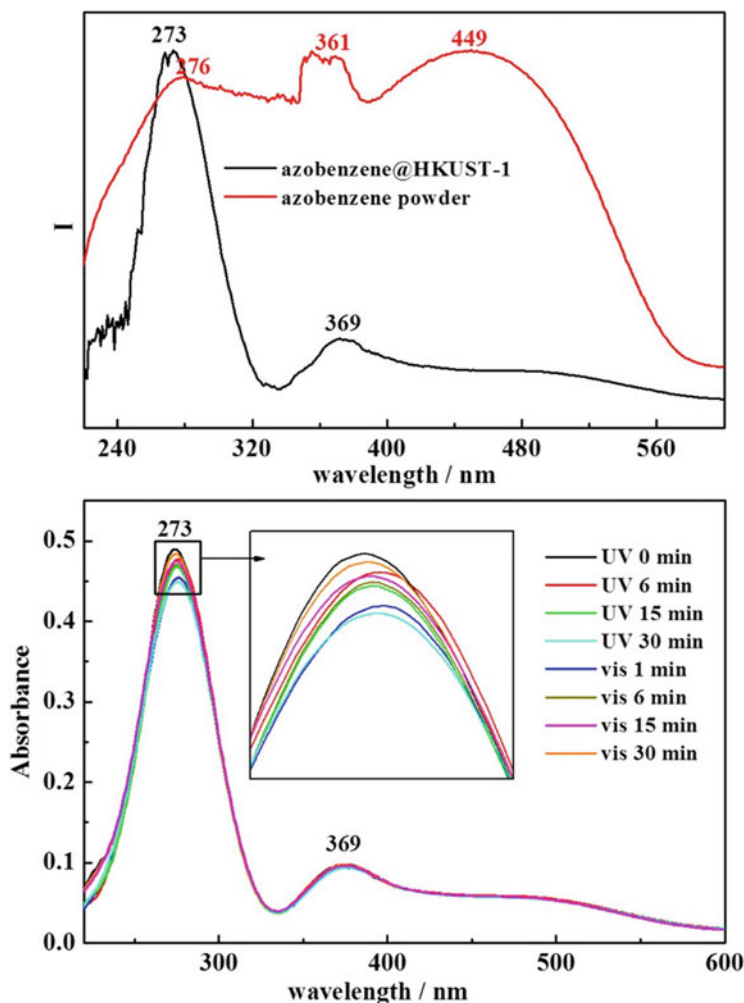


Fig. 15 Top: UV/vis spectra of pristine AZB powder (red) and an AZB@HKUST-1 thin film (black). Bottom: absorbance spectra of AZB@HKUST-1 thin films after irradiation with UV and visible light with different irradiation times. Reprinted (adapted) with permission of Ref. [142]. Copyright 2016 American Chemical Society

gas-phase loading process or a direct incorporation during the thin film synthesis, they chose diffusion of both guest molecules from an ethanolic solution into the host matrix. In a first step, AZB as the photoswitchable part was thoroughly examined by a variety of methods. The successful embedment of AZB was confirmed by UV/vis (Fig. 16a) and IR spectroscopy (Fig. 16d) as well as by XPS (Fig. 16e) and XRD measurements. Additionally, depth profiles measured by Time-of-Flight Secondary Ion Mass Spectrometry (ToF-SIMS) proved the homogeneity of the AZB@HKUST-1 thin films, which are depicted in Fig. 16f.

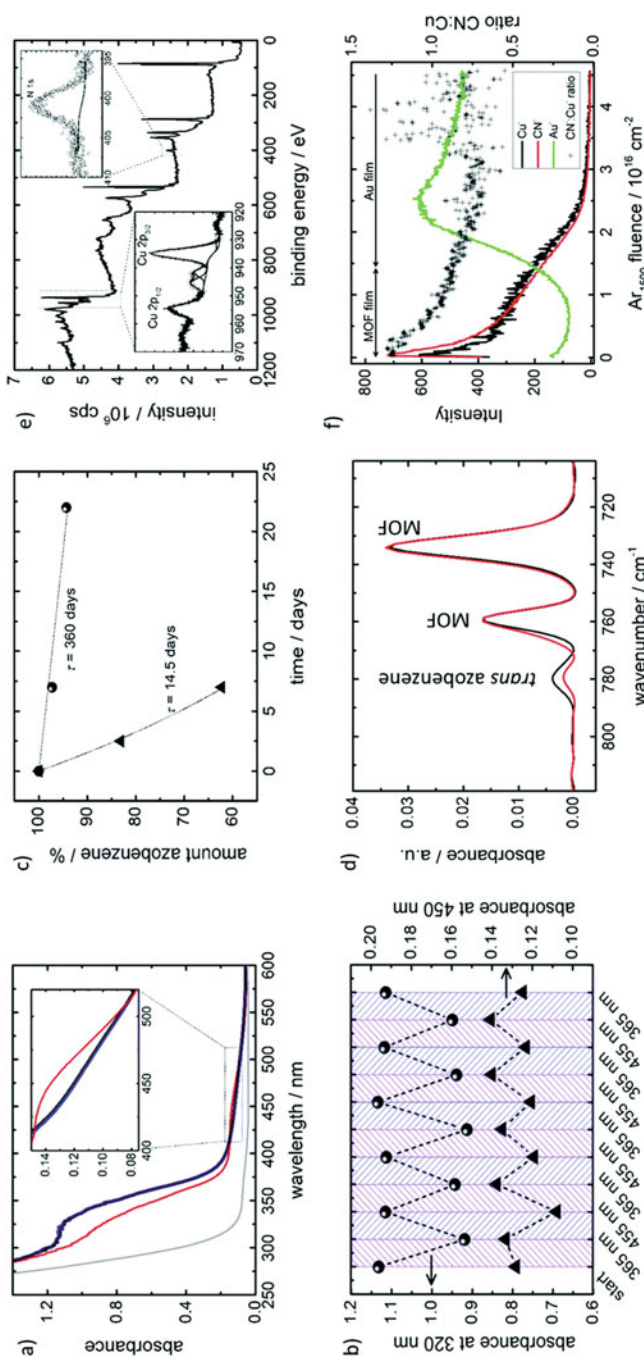


Fig. 16 Spectroscopic studies of AZB in thin films of type HKUST-1. (a) UV-vis spectra: pure HKUST-1 (grey), AZB@HKUST-1 before (black), and after irradiation with UV light (red) and blue light (455 nm, blue). (b) Absorbance at 320 nm (spheres) and at 450 nm (triangles) after the repeated irradiation with 365 nm and 455 nm for 5 min each. (c) Relative amount of AZB, determined from the absorbance at 320 nm after long-term storage of AZB@HKUST-1 thin films in air at room temperature (spheres) and at 60°C (triangles), respectively. The dotted lines show exponential fits with the depletion (or desorption) time constants τ . (d) IRRA spectra: pristine *E* state (black), after UV light irradiation, *Z* state (red). The area of the band at about 780 cm^{-1} , which is attributed to *E*-AZB, is 0.039 a.u. in the *E* state and 0.013 a.u. in the *Z* state. (e) XPS spectrum. (f) ToF-SIMS depth profiles. Left axis: signal intensities of Cu (both isotopes, black line), CN (corresponds to AZB, red), and gold clusters (green) plotted against erosion beam (argon clusters) fluence as a measure of depth. Right axis: normalized ratio of CN:Cu signals (black crosses). Due to the inhomogeneous film thickness and roughness, the transition from AZB@HKUST-1 (red and black) to the gold substrate (green) is smeared. Reprinted (adapted) with permission of Ref. [144]. Copyright 2017 The Royal Society of Chemistry

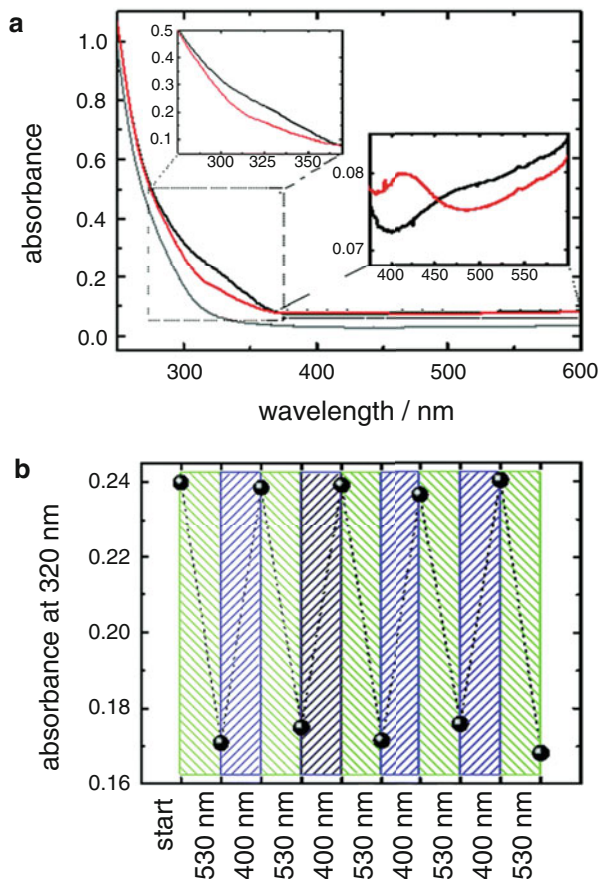
When embedded inside the MOF thin films, AZB undergoes photochromism, which was followed by UV/vis spectroscopy (see Fig. 16a): UV light irradiation causes the *E*-to-*Z* conversion (365 nm; red line), while after irradiation with blue light (455 nm; blue line), a spectrum almost identical to the spectrum of the pristine *E*-AZB-loaded SURMOF is obtained. The photostability as well as fatigue resistance was studied through several cycles of UV light and visible light irradiation, respectively. The authors found the intensity shifts of both the *E* and *Z* isomers to be stable with no significant bleaching, see Fig. 16b). Similar to Ruschewitz and co-workers [129], IR spectroscopy was applied to determine the switching yield. Here, the amount of *E*-AZB decreases from 100% to 35% (65% *Z*-AZB) after UV light irradiation, which is similar to results obtained for thin films with AZB side groups as substituents of a MOF linker [120]. Furthermore, AZB only slowly desorbs from the host framework, as determined from long-term storage experiments at room temperature and at 60°C (see Fig. 16c). Thus, AZB@HKUST-1 represents a rather stable switch@MOF hybrid system.

Based on the results of Ruschewitz and co-workers [137] on fluorinated azobenzenes, the authors chose *tF*-AZB as a potential guest molecule. As described before, the isomerization processes of *tF*-AZB can be triggered with visible light, hence no UV light is necessary [136]. Moreover, *tF*-AZB exhibits both a larger thermal stability and a higher switching yield. The latter originates from the electronic structures of the isomers: The energies for the $n\text{-}\pi^*$ bands of the *E* and *Z* isomer markedly differ as well as the respective excitation wavelengths.

For *tF*-AZB@MOF thin films, a light response similar to *tF*-AZB dissolved in ethanol is observed upon illumination with 400 nm and 530 nm. Photoswitching is reversible for five switching cycles without significant fatigue. Both the light response and reversibility of switching are depicted in Fig. 17a, b.

In order to study the functional response of the obtained (*tF*-)AZB@HKUST-1 thin films, gas uptake and release experiments were performed before and after irradiation with the polar molecule 1,4-butanediol: the initial argon flow was enriched with butanediol during the uptake measurements, and the gas uptake was detected via a quartz crystal microbalance (QCM) [145]. The results of these measurements before and after UV light irradiation are shown in Fig. 18. After reaching the equilibrium uptake amount of *E*-AZB@HKUST-1, the sample was irradiated with 365 nm for 20 min. The light-induced *E*-to-*Z* isomerization of AZB caused an increase of the butanediol uptake of approx. 8% [144], similar to photoswitchable SURFMOFs with azobenzene side-groups [120, 146]. The changing uptake of butanediol in these experiments was assumed to derive from the different dipole moments of *E*- and *Z*-AZB, which is 0 D in *E*-AZB and 3 D in *Z*-AZB [34]. Similar experiments were performed on *tF*-AZB@HKUST-1 thin films. Even though an increase of the butanediol uptake was found, the total amount was significantly smaller, probably as a result of a smaller amount of *tF*-AZB embedded inside the MOF host. To sum up, Heinke and co-workers were the first to present photoswitchable thin films with azobenzene and *tF*-azobenzene as non-covalently attached guest molecules, which were used to remote control the gas uptake amount.

Fig. 17 (a) UV/vis spectra of *tF*-AZB@HKUST-1 thin films before (black lines) and after irradiation with visible light (530 nm, red lines). In grey, unloaded HKUST-1 is shown; (b) switching cycles of *tF*-AZB@HKUST-1 after repeated irradiation with 530 nm and 400 nm. Reprinted with permission from Ref. [144]. Copyright 2017 The Royal Society of Chemistry



Also in 2017, *Caro* and co-workers presented their studies on photoswitchable MOF membranes containing azobenzene as photoactive unit and UiO-67 as host matrix (UiO denotes Universitetet i Oslo) [95]. In contrast to *Heinke* and co-workers [144], the authors applied a synthetically much easier but rarely described approach to grow the MOF ultrathin films. For the first time, they solvothermally synthesized a submicrometer-sized thin UiO-67 membrane on an α -Al₂O₃ support. To avoid cracking of this membrane, AZB insertion was performed via diffusion from acetone. Residual AZB was washed off by dipping the membrane in a fresh acetone solution. Afterwards, the composite thin film was dried in air to remove the solvent to exclusively elucidate the AZB-MOF interactions. In a reference experiment, bulk UiO-67 was loaded with AZB via a gas phase loading process.

N₂ sorption isotherms of pristine and loaded UiO-67 membranes showed an AZB loading without any free space left inside the MOF's pores. Therefore, switching of AZB from its *E* to *Z* isomer is sterically hindered. It is not surprising that for this fully loaded MOF membrane no gas flux is observed, see Fig. 19a. As a consequence, the authors desorbed some azobenzene in order to achieve photoswitching of the dye

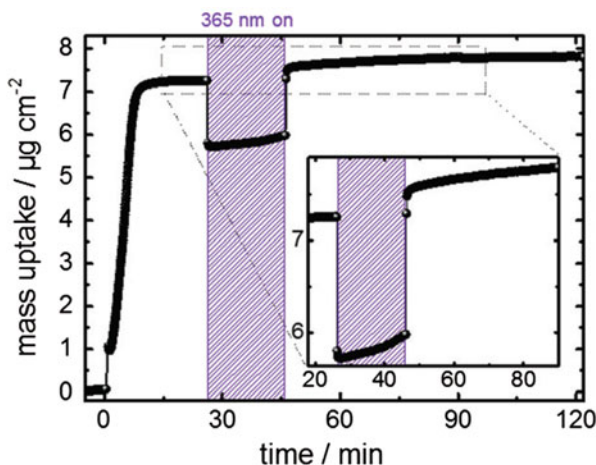


Fig. 18 Uptake of 1,4-butanediol by an AZB-loaded HKUST-1 thin film measured by QCM [145]. After ca. 25 min, when the equilibrium uptake of 1,4-butanediol by the thin film in the *E* state is reached, the sample is irradiated with UV light. The *E*-to-*Z* isomerization results in an increase of the butanediol uptake by Δm . The instantaneous decrease and increase of the determined apparent mass, when switching the light on and off, are most likely caused by a small (local) temperature increase during light irradiation resulting in changes of the resonance frequency of the QCM. Reprinted with permission from Ref. [144]. Copyright 2017 The Royal Society of Chemistry

molecule and thus, gas transport of probe molecules. By controlled thermal desorption, which was directly followed by CO₂ permeance measurements at 353 K under in situ UV light irradiation (365 nm), photoswitching as well as gas transport was realized. Here, the maximum switchable amount of AZB directly corresponds to a drastic increase in CO₂ permeance. Analogous measurements on bulk AZB@UiO-67 corroborate the results on the ultrathin films.

In a next step, the membrane with the ideal AZB-filling was used to remote control the membrane permeation of a H₂:CO₂ mixture by light. Figure 19b depicts the reversible gas permeation after irradiation with UV light (365 nm) and visible light (455 nm). Interestingly, the light-induced *E*-to-*Z* conversion causes an increase in CO₂ permeation. When present in its *E* state, the H₂/CO₂ separation factor is 14.7, which the authors suggested to originate from gating processes rather than electrostatic effects [114]. After irradiation with UV light and the concomitant formation of the *Z* state, a H₂/CO₂ selectivity of 10.1 and a higher CO₂ permeance are reached. Additionally, the H₂ permeance also increases slightly upon *E*-to-*Z* conversion of AZB inside UiO-67 and decreases vice versa, which indicates gating processes. As a consequence of size changes of the AZB moiety upon isomerization [14], the thus reduced effective pore diameter is assumed to cause the changing separation factors of 10.1:14.7.

To understand the mechanism of AZB@UiO-67 switching, UV/vis and IR spectroscopic measurements were applied. From UV/vis spectroscopic data, 12% of the AZB molecules inside the host matrix were determined to be switchable.

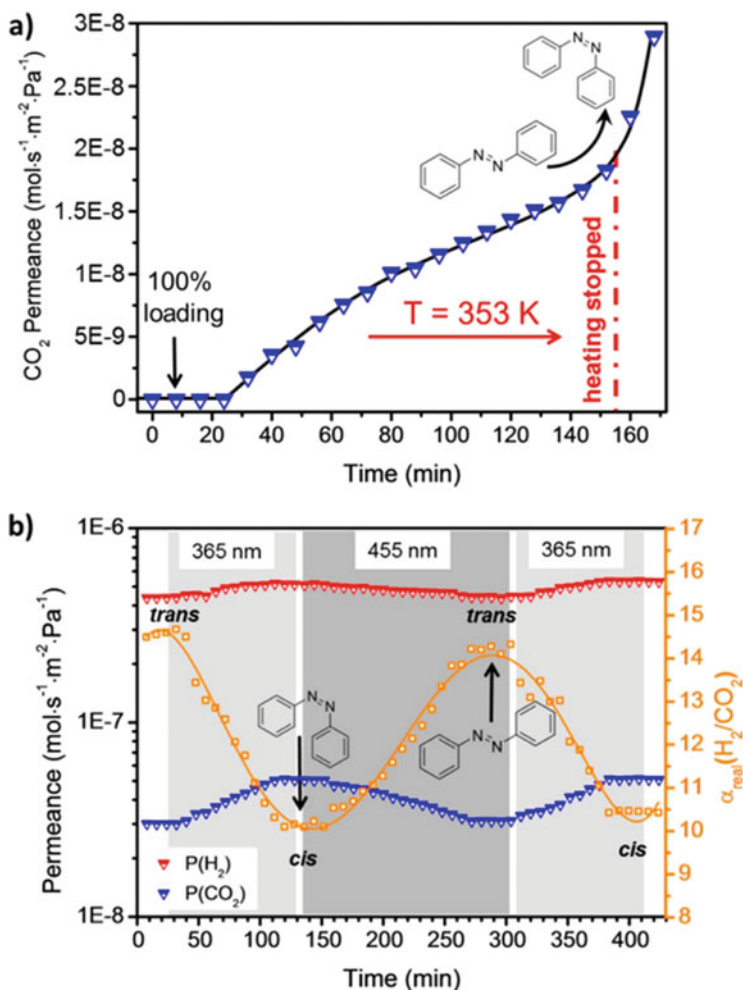


Fig. 19 (a) Controlled thermal desorption of AZB from an ultrathin UiO-67 membrane starting with a fully loaded membrane without any permeance. The desorption of AZB was indirectly monitored by the increasing CO₂ permeance. During the in situ desorption of AZB, the LED was constantly irradiating the top layer of the AZB@UiO-67 membrane with 365 nm, inducing the *E* (*trans*)-to-*Z* (*cis*) conversion. The indicator of the maximal switchable amount of AZB inside the MOF was the rapid increase in CO₂ permeance after a certain AZB desorption, where the heating was stopped (dashed red line). (b) Reversible gas permeation of an equimolar H₂/CO₂ mixture upon in situ reversible switching of AZB in UiO-67 at a constant reduced AZB loading. The sample is irradiated with 365 nm, causing *E*-to-*Z* isomerization, and 455 nm, causing the retransformation. While the permeation of H₂ (red) remains almost constant, the CO₂ permeation (blue) significantly increases upon *E*-to-*Z* switching. This causes large changes of the separation factor (orange). Reprinted with permission from Ref. [95]. Copyright 2017 American Chemical Society

Based on IR spectroscopy, the authors proposed formation of π -stacking complexes of *E*-azobenzene with the BPDC linkers at the pore entrances. Upon irradiation, these complexes change from an *E*-AZB stacking to a *Z*-AZB stacking. *E* and *Z* isomer profoundly differ in size and dipole moment, and thus, the MOF pore window opens and closes with great efficacy. With these results, *Caro* and co-workers were the first group that could show that an impressive separation factor for gases can be achieved with a switch@MOF composite with non-covalently attached guest molecules.

2.3 Diarylethenes in MOFs

2.3.1 Bulk Materials/Single Crystals

Stilbenes and azobenzenes are rather simple photoswitches with comparatively small changes in their absorption properties, which are almost invisible for the human eye. Replacement of these dyes with photochromic units that undergo both drastic geometrical changes and large alterations in their spectral profiles could be of great potential to remote control MOF pore properties.

In 2013, *Benedict* and co-workers were the first group to study the photochromic behavior of a dye molecule meeting these requirements inside a MOF. Already described DMOF-1 [127] was synthesized and single crystals of this material were loaded with the dithienylethene 1,2-bis(2,5-dimethyl-thien-3-yl)-perfluorocyclopentene [147, 148] (denoted as DTE) via a melting process [149]. The initially formed DTE@DMOF-1 hybrid material shows no optical difference compared to plain DMOF-1 (Fig. 20a, c).

Upon UV light exposure (365 nm), the colorless DTE@DMOF-1 crystals immediately turn dark red, exhibiting strong linear dichroism for incident light, presumably originating from DTE alignment inside the MOF host. In Fig. 20, top, polarized light images along [001] and [100] and the corresponding absorption spectra, Fig. 20, bottom, are shown. The authors found the orientation of the electric dipole transition moment to be responsible for the coloration. For the DTE@DMOF-1 single crystals, the dichroic ratio was calculated to be 0.29. Consequently, the DTE guest molecule (and its corresponding electric dipole transition moment, EDTM) is preferentially aligned approx. 28° from the [001] axis in the *ac* plane.

Unfortunately, the structural characterization of the DTE@DMOF-1 single crystal was not successful due to a combination of inhomogeneous loading and positional disorder of the guest molecule (note: DMOF-1 crystallizes with a high tetragonal symmetry). By ^1H NMR spectroscopy, the amount of DTE loaded into DMOF-1 was found to vary significantly, making an accurate structure solution impossible.

Although switching of DTE inside DMOF-1 can be repeated many times, the initial open-ring state is not completely retrieved, even after long exposure times with visible light. Furthermore, the generation of the colored species occurs faster

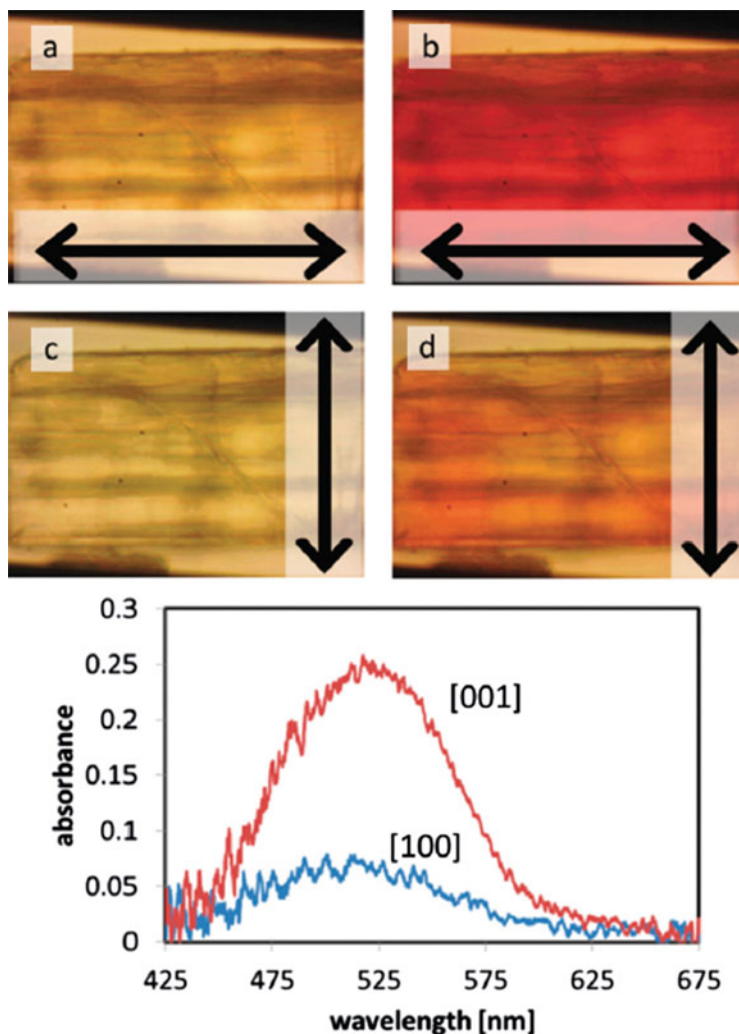


Fig. 20 (Top) polarized light images of DTE@DMOF-1 single crystals before (**a** and **c**) and after irradiation with UV light (365 nm, **b** and **d**). The plane of polarization for **a** and **b** ([001]) and **c** and **d** ([100]) is marked with a double arrow; (bottom) polarized absorption spectra of a DTE@DMOF-1 crystal after UV light irradiation. Reprinted (adapted) with permission from Ref. [149]. Copyright 2013 The Royal Society of Chemistry

than the reversion to the colorless form. In contrast to, e.g., azobenzenes, the photoconversion of DTE between its open and closed form is exclusively triggered by light, making these molecules highly stable towards temperature changes. Also, when embedded in DMOF-1, DTE exhibits excellent thermal stability, when kept in the dark for 1 month. To summarize, *Benedict* and co-workers presented the first example of an advanced composite with clearly separated absorption bands and a

high thermal stability of the embedded photochromic guest. Indeed, this class of photochromic hybrid materials offers a great potential to study thermally stable photoswitches inside MOFs both in bulk form and as thin films.

2.4 Spiroyrans in MOFs

2.4.1 Bulk Materials

Diarylethenes and dithienylethenes are one example of photochromic dyes with clearly separated absorption bands. Significant spectral changes are also observed for spiroyrans upon UV light irradiation: While the open spiropyran (SP) form does not show an absorption band in the visible region and is mostly colorless, the corresponding merocyanine (MC) possesses a strong absorption band and is, therefore, deeply colored [26, 27]. Interestingly, the absorption properties of the excited MC are highly dependent on the surrounding medium [21, 150, 151], which is referred to as solvatochromism [48] (thoroughly described in Sect. 1.2). The solvatochromism of MC in solvents of different polarity is depicted in Fig. 21, right. Both photochromic and solvatochromic responses make spiroyrans particularly interesting for MOF insertion: on the one hand, a photochromic material can be obtained, and on the other hand, direct polarity investigations of the MOF host can be conducted.

Following these considerations, *Ruschewitz* and co-workers began their studies on the simple nitro-substituted spiropyran 1,3,3-trimethyl-indolino-6'-nitrobenzopyrylospiran in 2017, denoted as SP-Nitro [152] (note: the first to describe a spiropyran@MOF system were *Zhu* and co-workers [93], but they used a MOF thin film, which will be described subsequently). Via a gas phase loading process, SP-Nitro was combined with MOF-5 [55], MIL-68(In) [132], MIL-68(Ga) [132], and MIL-53(Al) [133]. The successful insertion was confirmed by XRPD



Fig. 21 Left: photography of compounds SP-Nitro@MOF-5 (1), SP-Nitro@MIL-68(In) (2), SP-Nitro@MIL-68(Ga) (3), and SP-Nitro@MIL-53(Al) (4) after irradiation with UV light ($\lambda = 365$ nm, 1 min). Right: photography of SP-Nitro dissolved in solvents of varying polarity after irradiation with UV light ($\lambda = 365$ nm, 1 min). Reprinted (adapted) with permission from Ref. [152]. Copyright 2017 American Chemical Society

measurements, tracing modulations in the reflection intensities, while the peak positions remained mainly unaltered. For SP-Nitro@MIL-53(Al), surface adsorption instead of embedment into the MOF pores was found and verified via XPS studies.

Remarkably, in MOF-5 the open MC form of the inserted spiropyran is already present without UV light treatment. Since MC-Nitro exhibits a drastically higher dipole moment than its ground state counterpart (SP form), the chemical environment of the MOF-5 pore was suggested to be rather polar and, therefore, preferred by molecules with a high dipole moment such as merocyanines. Upon UV light exposure, an increase in the MC absorption for SP-Nitro@MOF-5 indicated proceeding formation of the MC moiety, which is referred to as positive photochromism. For host lattices of the MIL-68 series, no MC absorption band was found directly after loading. SP-to-MC conversion occurred for all SP-Nitro@MIL-68 composites upon UV light excitation, and, similar to MOF-5 as host material, positive photochromism was observed for the spiropyran embedded in the respective porous host. The successful isomerization of the closed SP form to its open MC form was traced both by UV/vis and IR spectroscopic measurements.

Interestingly, the absorption properties of MC-Nitro strongly depend on the MOF scaffold (see Fig. 21, left). When embedded in MOF-5, MC-Nitro shows an absorption comparable to being dissolved in methanol or ethanol. For hosts of the MIL-68 family, an absorption resembling that of an acetone solution is observed. For MC-Nitro, surface-bound on MIL-53(Al), the absorption is similar to that of a toluene solution. Remarkably, solvatochromic behavior cannot only be observed in solution but also in the solid state. Both the ability to successfully isomerize from the closed spiropyran to the open merocyanine form and the dependence of the absorption properties on the respective host lattice pretty much resemble the behavior of SP-Nitro in solution. Therefore, the authors denoted MOFs as *solid solvents* for these dye molecules and were the first to describe a combined photochromic and solvatochromic response of a dye molecule inside a MOF host.

Taking advantage of SP-Nitro's solvatochromic response inside the different MOFs, the authors classified the polarity of MOF-5, MIL-68(In/Ga), and MIL-53(Al) according to the elutrope series of *Snyder* [153] by applying SP-Nitro as a polarity sensor. By doing so, MOF-5 represents the most polar porous material, followed by MIL-68(In), MIL-68(Ga), and MIL-53(Al). Please note that for MIL-53(Al) only surface adsorption has to be considered. The correlation between the polarity of MOFs and solvents is shown in Fig. 22.

In a subsequent study, the authors performed detailed IR und UV/vis measurements to monitor the photostability of the inserted spiropyran upon prolonged and repetitive UV light treatment. However, only little fatigue resistance was found for both cases, making the applicability of the nitro-substituted spiropyran in functional materials difficult.

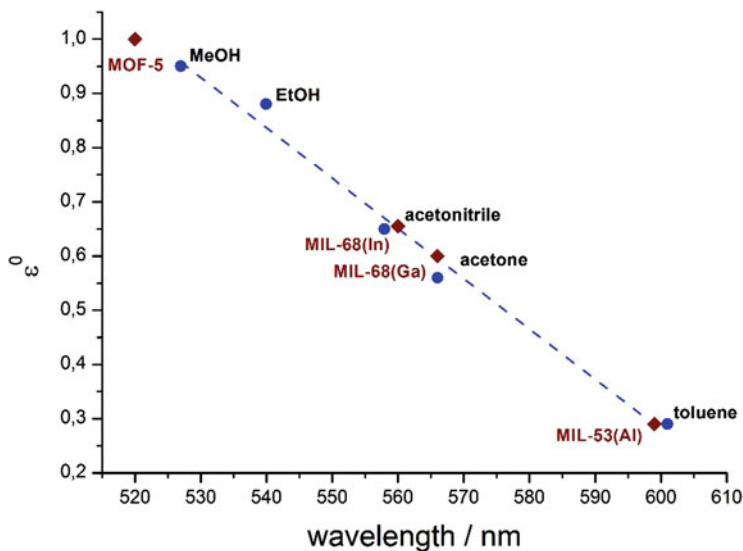


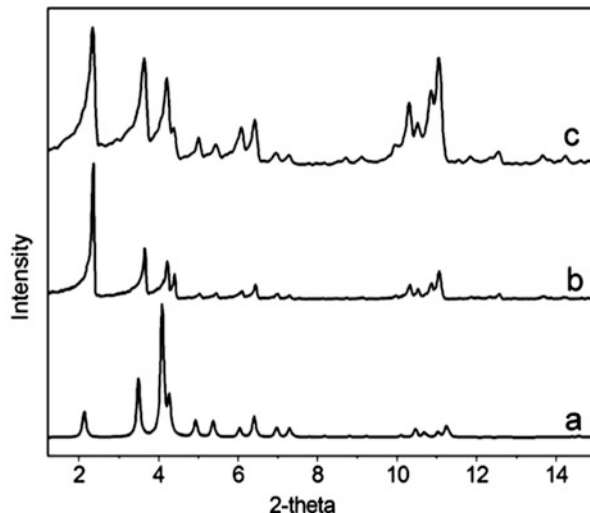
Fig. 22 Plot of the wavelength of the absorption maxima of MC-Nitro dissolved in different solvents (blue dots) versus the elution power ϵ^0 on alumina taken from *Snyder* [153], classifying the polarity of the respective MOFs (red diamonds). The values of irradiated SP-Nitro dissolved in different solvents (blue dots) were linearly fitted (dashed blue line). Reprinted (adapted) with permission from Ref. [152]. Copyright 2017 American Chemical Society

2.4.2 Thin Films

Already in 2012, *Zhu* and co-workers started their investigations on a spiro pyran@MOF composite [93]. Instead of a bulk MOF material, the object of the presented work was the formation of a spiro pyran@MOF thin film. In occasion of that, the precursors for an indium trimesate-based MOF and, as a new method of dye insertion, the guest molecule, namely, 1-(2-hydroxy-ethyl)-3,3-dimethylindolino-6'-nitrobenzospiro pyran (denoted as BSP), were dispersed in a H₂O-DMF mixture and reacted in a microwave. Subsequently, the formed composite was spin-coated on quartz glass. The resulting MOF thin films were designated as BSP@JUC-120, with JUC-120 representing a new analogue of MIL-100, which is typically formed with trivalent Al, Fe, and Cr cations [167–169]. The successful synthesis was confirmed by XRPD measurements. The diffraction pattern of JUC-120 matches the calculated pattern of MIL-100(Cr) in all apparent peak positions (see Fig. 23a, b, respectively). When loaded with BSP, no substantial differences are observed in comparison to the unloaded JUC-120 thin film. The peak positions remain unaffected, while slight changes in the reflection intensities are found (Fig. 23c), which indicate the successful embedment of the photochromic dye.

In a next step, the authors determined the pore diameters of the accessible voids of JUC-120, which are suitable for BSP inclusion and, most importantly, light-induced conversion processes. In further measurements on thermal stability, surface

Fig. 23 XRD patterns of (a) MIL-100(Cr) (calculated data), (b) as-synthesized powder of JUC-120, and (c) the BSP@JUC-120 thin film. Reprinted (adapted) with permission from Ref. [93]. Copyright 2012 American Chemical Society



morphology and gas adsorption/desorption, the authors thoroughly studied this new guest@MOF composite.

All switch@MOF systems described and presented up to now exhibited positive photochromism: i.e., in the ground state, the switch is colorless or almost colorless, whereas irradiation with light of a specific wavelength causes the formation of a thermodynamically less stable species with an absorption band in the visible range of light. Consequently, the absorption maximum of the excited state is positioned at longer wavelengths than the respective maximum of the ground state.

In contrast to that, for BSP@JUC-120 a negative, reverse or antidromic photochromism is reported for the first time. Surprisingly, the BSP@JUC-120 thin films are already deeply colored before UV light irradiation. After exposure to UV light, the initially deeply colored films turn colorless (see Fig. 24a). The films revert to their initial colored state, when kept in the dark. In order to study the switching process, in situ UV/vis spectra were recorded (see Fig. 24b). Before UV light treatment, an absorption maximum at 556 nm and a small blue-shifted shoulder were observed, which could clearly be attributed to the open merocyanine form of BSP showing that the open merocyanine form is stabilized inside JUC-120. Upon UV light irradiation, the absorption maximum at 556 nm decreases indicating the proceeding population of the closed spiropyran form of BSP. The authors explained this negative photochromism, where the usually stable SP form represents a metastable state, by a rather polar environment given by the MOF pores. Similar findings have already been published, e.g., by Wark and co-workers [18], who implemented a spiropyran into a zeolite matrix and also found the open merocyanine form to be stabilized in the initial state.

To probe the ability of the BSP@JUC-120 thin films to be implemented in devices, the authors performed fluorescence spectroscopic measurements on fading and fatigue resistance. The photorelaxation from MC-to-SP proceeds slowly,

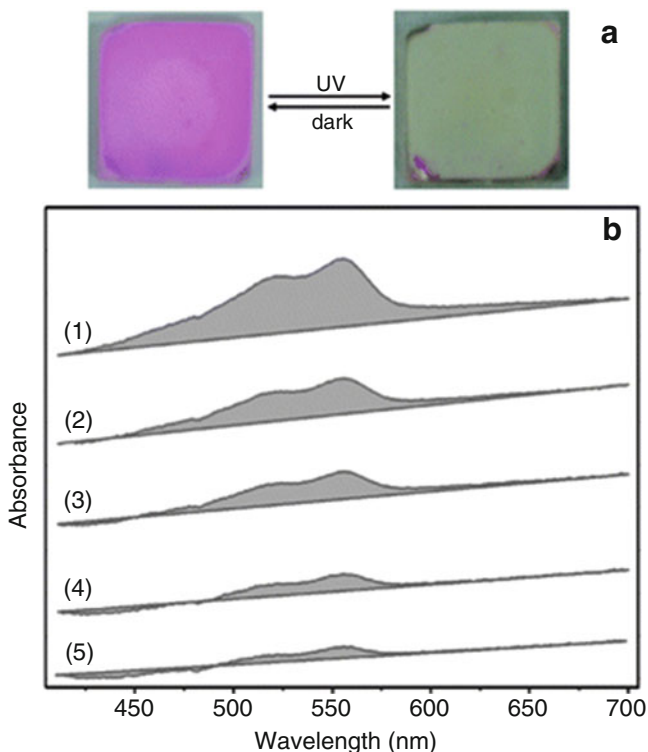


Fig. 24 (a) Photographic images of the BSP@JUC-120 thin films before (left) and after irradiation with UV light (right); (b) UV/vis spectra of the BSP@JUC-120 thin films before (1) and after UV light exposure at different times: (2) 2 min, (3) 5 min, (4) 10 min, and (5) 20 min. Reprinted (adapted) with permission from Ref. [93]. Copyright 2012 American Chemical Society

pointing to strong host-guest interactions between the open form of the spiropyran and the MOF scaffold. It has to be stated that a negligible influence of the temperature during the measurements was observed, showing the thermal stability of the composite. Moreover, the system displays high reversibility of its photochromism. In conclusion, the authors presented an unusual way of forming a switch@MOF system by a direct insertion of the chromophore during the host synthesis. However, most fascinating is the type of photochromism that was observed, making BSP@JUC-120 thin films the only known MOF material exhibiting negative photochromism.

All hitherto described functionalities resulting from the combined properties of a switchable dye and a MOF host focused on the optical response of these systems and, additionally, on how this response could be used for gas separation or transport. In a recent work, *Heinke* and co-workers extended the possible applications of these hybrid materials to the controlled switchability of conductance [154]. In earlier studies, it was demonstrated that the SP-to-MC conversion results in an increased conductivity of single spiropyran molecules [155] and spiropyran monolayers

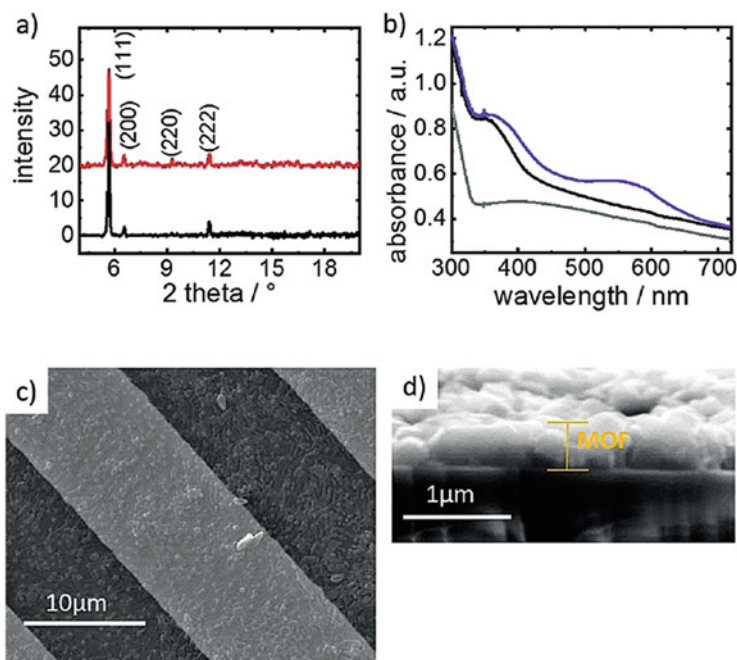


Fig. 25 (a) XRD patterns of unloaded (black) and SP-Nitro-loaded UiO-67 (red); (b) UV/vis spectra of UiO-67 (grey), SP-Nitro-loaded UiO-67 before (black), and after UV light irradiation for 5 min (violet); top view (c) and cross-sectional image (d) of the SP-Nitro@UiO-67 thin films on interdigitated gold electrodes recorded by SEM. Reprinted (adapted) with permission from Wiley and Sons, Ref. [154]; copyright 2019 Wiley-VCH

[156]. Moreover, by the combination of spiropyran with conducting polymers, a conductivity switching by a factor of 2.5 was achieved [157]. Based on these considerations, the nitro-substituted spiropyran SP-Nitro, which had already successfully been incorporated in MOFs [152], was chosen and loaded via a diffusion process into a MOF thin film of type UiO-67 [170]. The successful insertion of SP-Nitro into the pores of the host lattice was confirmed by XRPD measurements. In Fig. 25a, the diffraction patterns of unloaded (black) and loaded UiO-67 (red) are shown. Obviously, the peak positions remain unaffected. However, a significant intensity increase of the (220) peak is found, which indicates the successful guest inclusion. In reference experiments with bulk UiO-67, this peak was also mainly affected upon guest inclusion. Since no additional reflections are present, residual spiropyran on the MOF surface can be excluded in both cases. In addition, the authors performed SEM measurements to show the homogenous morphology of the thin films (see Fig. 25c, d). Furthermore, the results of EDX measurements indicated 7.5 embedded spiropyran molecules per unit cell of the MOF.

Upon irradiation with UV light, an absorption band at ~550 nm appears, which can clearly be assigned to the open MC form (see Fig. 25b). Hence, SP-to-MC conversion is possible inside the pores of UiO-67. Initially after loading, the

SP-Nitro@UiO-67 thin films are colorless, whereas light exposure causes the isomerization process and the films become colored. Thus, the closed spiropyran form is exclusively present in the dark. The switching yield was determined by IR spectroscopy, yielding 70% MC form upon irradiation with UV light.

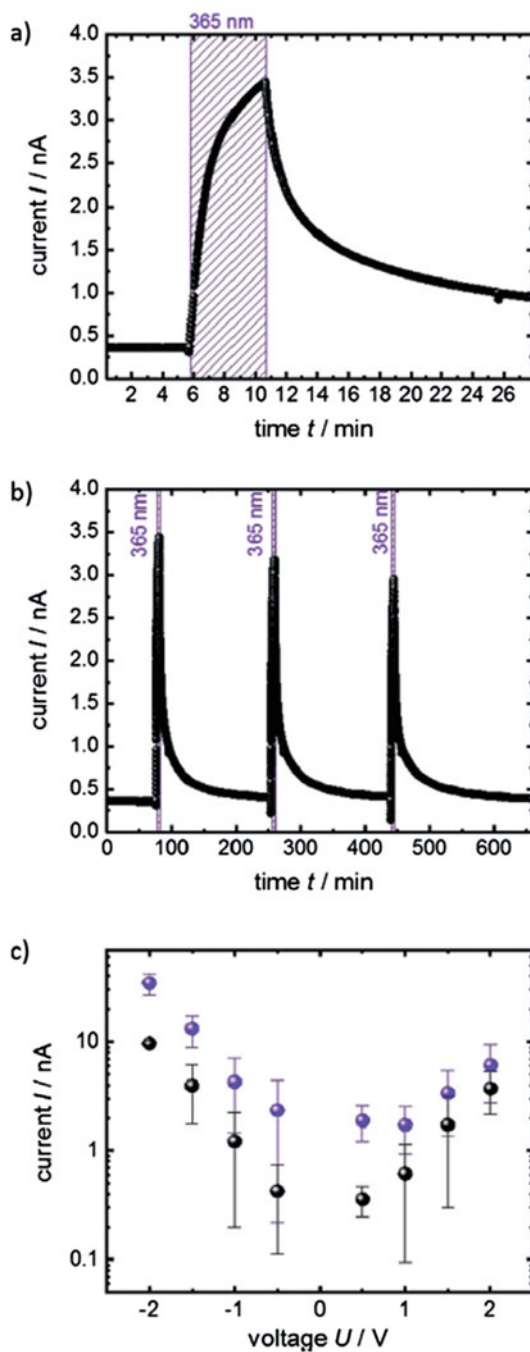
In order to study the conduction properties of the presented material via DC measurements, thin films of SP-Nitro@UiO-67 were prepared on interdigitated gold electrodes. The results of these measurements are depicted in Fig. 26. In the initial state with spiropyrans being exclusively present in their SP form, almost no current is observed (see Fig. 26a). Upon UV light exposure ($\lambda = 365$ nm), the conductivity increases by a factor of ten as a result of the SP-to-MC conversion. When turning off the UV light, reconversion to the ground state is accompanied by a decreasing current. This conductance photoswitching was repeated for three consecutive cycles (see Fig. 26b) with a slightly decreasing conductivity, which the authors explained with the known fatigue of spiropyrans [158]. In Fig. 26c the current-voltage characteristic of SP-Nitro@UiO-67 is depicted. The current increases over the whole voltage range, when the sample is exposed to UV light. The details of the underlying charge transfer processes were examined precisely in accompanying DFT calculations. Instead of a ballistic transport, charge hopping is present. For the MC moieties, the electronic coupling is stronger than for the SP species. Therefore, an increased charge hopping rate is found, when SP-Nitro is converted to its open merocyanine form. The stronger electronic coupling and the hole injection from the gold electrodes result in efficient electron hole conduction. In conclusion, this SP-Nitro@UiO-67 thin film represents the first example for reversible photoswitching of the electronic properties of a hybrid MOF material.

2.5 Spirooxazines in MOFs

2.5.1 Bulk Materials

For spiropyrans, prolonged UV light irradiation results in photodegradation predominantly via a bimolecular process, which involves the triplet excited state of the spiropyran moiety [159]. Bimolecular processes are related to the concentration of spiropyran molecules. By immobilization of single dyes on, e.g., supports, those processes are easily suppressed [160]. *Diamond* and co-workers observed an increased fatigue resistance of spiropyran dyes being immobilized in comparison to those in the dissolved state [161]. Nonetheless, spiropyrans show comparably low fatigue resistance in comparison to other photochromic molecules. For instance, spirooxazines, structurally related molecules, exhibit a significantly higher photoresistance and reversibility of switching than most of the spiropyrans. Both dye molecules only differ structurally by an additional nitrogen atom in the spiropyran chromene ring, which is denoted as benzoxazine part for spirooxazines. However, in contrast to spiropyrans, the synthesis and also publications on spirooxazines went almost unnoticed, even though this class of photochromic

Fig. 26 Conductance switching of SP-Nitro@UiO-67 thin films. (a) Current at a DC voltage of +1 V; the sample was irradiated with UV light (365 nm) for 5 min. (b) Current at the same conditions during three consecutive cycles of UV light irradiation for 5 min; (c) current-voltage characteristics of SP-Nitro@UiO-67 before (SP form, black) and after (MC form, violet) irradiation with UV light. Reprinted (adapted) with permission from Wiley and Sons, Ref. [154]; copyright 2019 Wiley-VCH



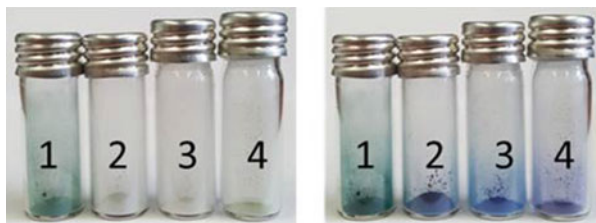


Fig. 27 Photographic images of SP-O@MOF-5 (1), SP-O@MIL-68(In) (2), SP-O@MIL-68(Ga) (3), and SP-O@MIL-53(Al) (4) before (left) and after (right) irradiation with UV light. Reprinted (adapted) with permission from Wiley and Sons, Ref. [163]; copyright 2020 Wiley-VCH

compounds is known since the 1960s [162]. Only with the description of the extraordinary photostability of 1,3,3-trimethylindolino-naphthospirooxazine (denoted as SP-O) by *Chu* in 1983 [162] these molecules gained more attention. Similar to spiropyrans, spirooxazines convert to the strongly colored merocyanine form upon irradiation with UV light. Depending on substituents and the surrounding medium, the excited species shows an absorption maximum with an asymmetric shape and a blue- or red-shifted shoulder [33] in the range 480–670 nm. Spirooxazines are known to show positive and negative solvatochromism, which is dependent on the substituents. The photochromic and solvatochromic response combined with an enhanced photostability make spirooxazines very promising candidates for insertion into porous hosts, e.g., spirooxazine@MOF composite materials.

For this reason, *Ruschewitz* and co-workers started investigations on SP-O embedded in different MOF hosts [163]. Similar to their work published on azobenzenes, its fluorinated derivatives [129, 137], and spiropyrans [152], the authors chose MOF-5 [55], MIL-68(In) [132], MIL-68(Ga) [132], and MIL-53(Al) [133] as suitable host matrices with respect to pore size and adsorption properties. The incorporation of the spirooxazine SP-O was achieved via a gas phase loading process to exclude the influence of solvent molecules on all further investigations. The successful embedment was confirmed by XRPD for MOF-5, MIL-68(In) and MIL-68(Ga), respectively. However, similar to the results on SP-Nitro [152], no modulation in the reflection intensities nor a significant change in their 2θ values was observed for MIL-53(Al) as host material. Again, the results of XPS measurements prove a surface adsorption of SP-O on MIL-53(Al), whereas the photoswitchable molecule is incorporated inside the other MOF hosts of this study. Via a combined analysis using XPS and DSC/TGA data, the composition of the hybrid systems was determined, and, additionally, strong host-guest interactions were found.

In order to study the photochromic response and the photostability and reversibility of switching, detailed UV/vis and IR spectroscopic measurements were performed. All hybrid compounds exhibit positive photochromism. In Fig. 27, the change in color upon UV light irradiation is depicted. Notably, the embedment of SP-O into MOF-5 already causes stabilization of the excited merocyanine isomer in the initial state, which is in agreement with the results on SP-Nitro@MOF-5

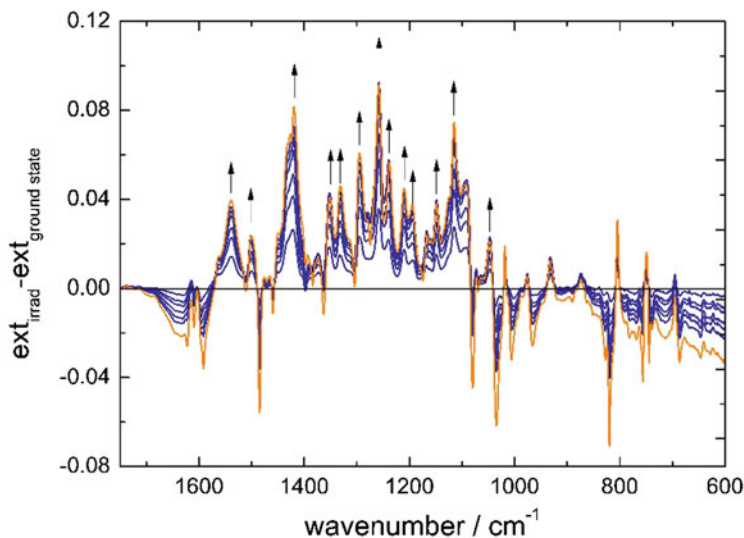


Fig. 28 Difference IR spectra of SP-O@MOF-5. The spectrum for the longest irradiation time (UV light: $\lambda = 365$ nm, 720 min) is colored in orange; the direction of increasing bands is marked with arrows. Reprinted (adapted) with permission from Wiley and Sons, Ref. [163]; copyright 2020 Wiley-VCH

[152]. Furthermore, the absorption bands of the excited isomer are increasingly blue-shifted from MOF-5 to MIL-68(In/Ga) and MIL-53(Al). With respect to the solvatochromic response of SP-O, MOF-5 represents the most polar host lattice followed by the MIL-68 family and MIL-53(Al) (note: here, SP-O is only surface-adsorbed). This MOF polarity order nicely substantiates the results on SP-Nitro@MOF composites (see Fig. 22) [152].

Subsequently, the authors studied the photostability and the fatigue resistance of these SP-O@MOF systems by IR and UV/vis spectroscopy. Since exposure to UV light causes a decrease of the SP and an increase of the MC bands, IR spectroscopy was applied to monitor the light-induced changes. That way, the successful isomerization was proven and, moreover, for the first time IR data of the excited merocyanine isomer of SP-O were assigned to the respective vibrational bands. In Fig. 28, the difference spectra of SP-O@MOF-5 are shown. Here, the authors subtracted the spectrum of the nonirradiated material from the spectra collected after different irradiation times to obtain $\text{ext}_{\text{irrad}} - \text{ext}_{\text{ground state}}$ (changing bands are colored in blue and the difference spectrum for maximal irradiation times is colored in orange). Notably, for an irradiation time of 720 min, maximal changes are found, which clearly shows that no photodegradation occurs even after such long exposure times. This finding was further supported by UV/vis measurements. Hence, this system shows an extraordinarily high photoresistance upon prolonged irradiation.

All studied SP-O@MOF materials exhibit reversible photochromism upon thermal treatment (room temperature for several minutes) or irradiation with visible

light. The latter was found to be more efficient to trigger the MC-to-SP conversion than thermal treatment. Consequently, the open merocyanine form is thermally stabilized when inserted in the different MOF hosts. However, this stabilization seems to depend on the type of the MOF scaffold. The reasons for that have not been elucidated so far.

With this work, *Ruschewitz* and co-workers were the first to develop hybrid switch@MOF systems containing spirooxazines, which show a high photostability and reversibility of switching. Both properties are obligatory for the construction of functional materials, and, therefore, these SP-O@MOF systems are of high potential for future applications.

3 Conclusion and Future Perspectives

The tailored design and synthesis of smart materials is a challenging task in modern materials chemistry. In this respect, MOFs have attracted a tremendous interest in recent years, since these porous materials can be synthesized in a LEGO-like manner starting from metal cations and organic linkers. The isorecticular approach by *Yaghi* and co-workers [87] is a perfect example of this fascinating branch of materials science.

When combining these versatile MOFs with the numerous photochromic mainly organic molecules that were developed in the last decades, an almost uncountable number of potential responsive materials might result. Table 3 gives a summary of the hybrid systems consisting of a photochromic dye embedded in a MOF reported up to now and Fig. 29 shows a sketch of how these materials are constructed in general. Of course, there are other ways to incorporate the photochromic functionality within MOFs, e.g., as substituents of the linker or part of the linker's

Table 3 Summary of the switch@MOF systems reported up to now (B: bulk material; TF: thin films)

	Stilbene	AZB	Fluorinated AZB	PAP	DTE	SP	SP- O
Zn-based PCN	B						
DMOF-1		B		B	B		
MOF-5		B	B	B		B	B
MIL-68(In)		B	B			B	B
MIL-68(Ga)		B	B			B	B
MIL-53(Al)		B	B			B ^a	B ^a
MIL-53(Ga)		B	B				
HKUST-1		TF	TF				
UiO-67		TF				TF	
JUC-120 (MIL-100 analogue)						TF	

^aOnly surface-adsorbed

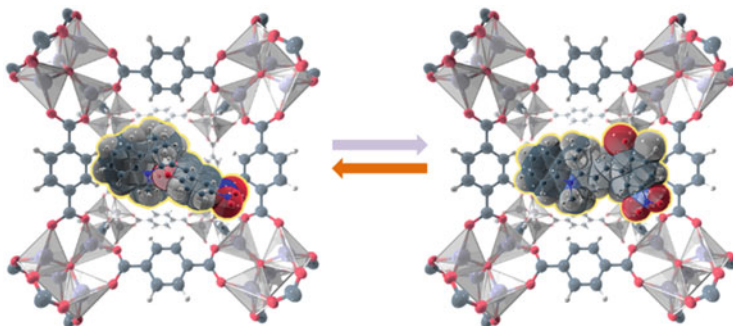


Fig. 29 Schematic illustration of a switch@MOF system before and after irradiation with UV light. The light-induced isomerization process is allowed inside the host lattice due to the spatial separation of the guests

backbone. But these approaches do not utilize the great variety of possible MOF hosts as well as photochromic guests, not to mention the high synthetic efforts that are needed to construct such systems.

It was the aim of this chapter to introduce the reader into the developing field of photochromic dyes non-covalently attached to the voids of porous MOFs. Synthetic procedures as well as methods, how to characterize these new responsive materials, were addressed. It is surely challenging to get detailed information about these guest@MOF systems due to the high mobility of the embedded guest molecules. How can we be sure that the guest is embedded in the pores of the MOFs and not just adsorbed on the surfaces of MOF particles? How can we quantify the loading? Can we get structural information on the embedment of the guest within the voids of a specific MOF, and what are the underlying host-guest and maybe – for high loadings – guest-guest interactions?

However, most fascinating are the properties of the resulting hybrid materials: remote control of gas uptake and release, light-triggered changes of absorption properties – already visible by drastic color changes to the naked eye – solvatochromic behavior of a dye within a specific MOF pore that resembles the behavior of these dyes in solvents and led to the description of MOFs as “solid solvents” [152] or the reversible photoswitching of electronic conductivity [154] to name a few.

It is surprising that the research on switch@MOF systems only started in 2010 with the pioneering work of *Fujita* and co-workers [125], who embedded stilbene in a porous coordination network, which is another term for a MOF. Within less than 10 years, the methods and materials described in this chapter were developed. Not very surprisingly, most work was done on azobenzene, probably still the best investigated photochromic dye molecule. However, by functionalization of azobenzene, i.e., fluorination or PEG substituents, interesting materials were obtained, which, as an example, allowed an almost quantitative photoswitching [137]. Moreover, also other examples of photochromic dyes were embedded in MOFs, i.e., diarylethenes, spiropyrans, and spirooxazines. Each of them has specific

advantages – high thermal stability, high fatigue resistance, etc. – which were described in the respective sections.

It should be stressed here that the embedment of photochromic dyes into porous hosts is not restricted to MOFs, as also COFs (covalent organic frameworks), cyclodextrin cages, or zeolites are suitable candidates. Notably, the first work on the latter is dated back to the late 1990's [13], a few years before MOFs entered the scientific world. And for current applications, photochromic dyes embedded in/being part of polymeric layers are probably still the best choice. But none of these alternative hosts show the high versatility of MOFs.

Surely, there are also disadvantages of photochromic dyes embedded as non-covalently attached guests in MOF hosts. The difficulties in obtaining detailed information about the highly mobile guests have already been mentioned. Additionally, the low thermal stability of these hybrid materials might be considered as a drawback, as the embedded guests will leave the MOF matrix upon heating. However, long-term investigations on thin films of type HKUST-1 with embedded azobenzene proved that at least at room temperature this material is stable for several months, whereas upon heating to 60°C its integrity suffers significantly. However, it should be stated that azobenzene is the most volatile guest used in these investigations and with the other less volatile guests the thermal stability increases.

What are the tasks and aims of this research field for the future? As was already presented in this chapter, the use of high-quality thin films seems to be indispensable for possible applications. And here is still a high need for further developments, as the large variety of MOF structures available as bulk materials (single crystals, powders) cannot be synthesized to the same extent as thin films. Nevertheless, investigations on bulk switch@MOF systems are still necessary, as in most cases they paved the way for the development of functional responsive thin film materials. That is, new MOFs as hosts for such switch@MOF hybrid materials need to be developed and tested, which influence the photochromic properties of the embedded dyes by specific spatial or electronic situations. On the other hand, there is still a large variety of interesting photochromic molecules, which have not been investigated as possible guests for incorporation into MOFs, e.g., fulgides. Indeed, almost every month a new and interesting photochromic dye molecule is published, which might be an interesting candidates for a guest@MOF system, e.g., the recently published iminothioindoxyls [164]. Another approach only poorly being addressed up to now, is the directed embedment of two or more guests in a MOF matrix, as also specific guest-guest interactions like charge-transfer or electron hopping will lead to materials with new and fascinating properties.

Nevertheless, it is our deepest conviction that more detailed information about the structures of these switch@MOF systems is needed to develop them further, as from these structures the underlying host-guest and guest-guest interactions can be deduced and, at best, be used to design new hybrid materials with improved properties. At the moment, the structural information is low and mainly restricted to results of high-resolution synchrotron powder diffraction data. However, this approach is difficult due to the high mobility of the guests and their possible disorder in high-symmetric hosts. Therefore, more local probes like solid-state NMR or total

X-ray diffraction combined with PDF (pair distribution function) are obligatory to extract as much structural information as possible. This approach has already been used successfully for other systems [165, 166]. With this additional information, we envision a bright future for the switch@MOF hybrid materials presented in this book chapter.

Appendix

This book chapter was completed in October 2019 and covers almost all the literature available at that time. As MOFs as hosts for photoactive molecules are a very fast developing field of research, it was not possible to include the many interesting papers published after this deadline.

References

1. Li C, Zhang Y, Hu J, Cheng J, Liu S (2010) *Angew Chem Int Ed* 49:5120–5124
2. Liao B, Long P, He B, Yi S, Ou B, Shen S, Chen J (2013) *J Mater Chem C* 1:3716–3721
3. Chen J, Zeng F, Wu S, Zhao J, Chen Q, Tong Z (2008) *Chem Commun* 13:5580–5582
4. Zhu L, Zhu M-Q, Hurst JK, Li ADQ (2005) *J Am Chem Soc* 127:8968–8970
5. Parthenopoulos DA, Rentzepis PM (1989) *Science* 245:843–845
6. Chung D-J, Ito Y, Imanishi Y (1994) *J Appl Polym Sci* 51:2027–2033
7. Moniruzzaman M, Sabey CJ, Fernando GF (2007) *Polymer* 48:255–263
8. Allcock HR, Kim C (1991) *Macromolecules* 24:2846–2851
9. Oh YJ, Nam JA, Al-Nahain A, Lee S, In I, Park SY (2012) *Macromol Rapid Commun* 33:1958–1963
10. Kundu PK, Olsen GL, Kiss V, Klajn R (2014) *Nat Commun* 5:3588 (1–9)
11. Samanta D, Galaktionova D, Gemen J, Shimon LJW, Diskin-Posner Y, Avram L, Král P, Klajn R (2018) *Nat Commun* 9:641 (1–9)
12. Wang D, Zhao W, Wei Q, Zhao C, Zheng Y (2018) *ChemPhotoChem* 2:403–415
13. Marlow F, Hoffmann K, Caro J (1997) *Adv Mater* 9:567–570
14. Weh K, Noack M, Hoffmann K, Schröder K-P, Caro J (2002) *Microporous Mesoporous Mater* 54:15–26
15. Hoffmann K, Resch-Genger U, Marlow F (2000) *Microporous Mesoporous Mater* 41:99–106
16. Casades I, Alvaro M, García H, Pillai MN (2002) *Photochem Photobiol Sci* 1:219–223
17. Casades I, Constantine S, Cardin D, García H, Gilbert A, Márquez F (2000) *Tetrahedron* 56:6951–6956
18. Schomburg C, Wark M, Rohlfing Y, Schulz-Ekloff G, Wöhrle D (2001) *J Mater Chem* 11:2014–2021
19. Fritzsche J, Hebd CR (1867) *Seances Acad Sci* 69:1035–1038
20. Hirshberg Y, Hebd CR (1950) *Seances Acad Sci* 116:903–904
21. Bouas-Laurent H, Dürr H (2001) *Pure Appl. Chem* 73:639–665
22. Waldeck DH (1991) *Chem Rev* 91:415–436
23. Hartley GS (1937) *Nature* 140:281–281
24. Hartley GS (1938) *J Chem Soc*:633–642
25. Robertson JM (1939) *J Chem Soc*:232–236

26. Fischer E, Hirshberg Y (1952) *J Chem Soc*:4522–4524
27. Chaudé O, Rumpf R, Hebd CR (1953) *Seances Acad Sci* 236:697–699
28. Berkovic G, Krongauz V, Weiss V (2000) *Chem Rev* 100:1741–1754
29. Irie M (2000) *Chem Rev* 100:1685–1716
30. Yokoyama Y (2000) *Chem Rev* 100:1717–1739
31. Kortekaas L, Browne WR (2019) *Chem Soc Rev* 48:3406–3424
32. Klajn R (2014) *Chem Soc Rev* 43:148–184
33. Lokshin V, Samat A, Metelitsa AV (2002) *Russ Chem Rev* 71:893–916
34. Hartley GS, Le Fèvre RJW (1939) *J Chem Soc*:531–535
35. Irie M (2010) *Photochem Photobiol Sci* 9:1535–1542
36. Hermann D, Schwartz HA, Ruschewitz U (2017) *ChemistrySelect* 2:11846–11852
37. Lukyanov BS, Metelitsa AV, Voloshin NA, Alexeenko YS, Lukyanova MB, Vasilyuk GT, Maskevich SA, Mukhanov EL (2005) *Int J Photoenergy* 7:17–22
38. Rezvanova AA, Frolova LA, Troshin PA (2016) *Mendeleev Commun* 26:26–28
39. Ubukata T, Fujii S, Arimatsu K, Yokoyama Y (2012) *J Mater Chem* 22:14410–14417
40. Harada J, Kawazoe Y, Ogawa K (2010) *Chem Commun* 46:2593–2595
41. Gentili PL, Nocchetti M, Miliani C, Favaro G (2004) *New J Chem* 28:379–386
42. Natali M, Giordani S (2012) *Chem Soc Rev* 41:4010–4029
43. Bléger D (2016) *Macromol Chem Phys* 217:189–198
44. Lee C-L, Liebig T, Hecht S, Bléger D, Rabe JP (2014) *ACS Nano* 8:11987–11993
45. Kumar K, Knie C, Bléger D, Peletier MA, Friedrich H, Hecht S, Broer DJ, Debije MG, Schenning APHJ (2016) *Nat Commun* 7:11975 (1-8)
46. Zhao F, Bonasera A, Nöchel U, Behl M, Bléger D (2018) *Macromol Rapid Commun* 39:1700527 (1–5)
47. Koumura N, Zijlstra RWJ, van Delden RA, Harada N, Feringa BL (1999) *Nature* 401:152–155
48. Reichardt C (2003) *Solvents and solvent effects in organic chemistry*. Wiley, Weinheim
49. Dähne S, Leupold D, Nikolajewski HE, Radeaglia R (1965) *Zeitschrift für Naturforsch B* 20:1006–1007
50. Radeaglia R, Dähne S (1970) *J Mol Struct* 5:399–411
51. Brady JE, Carr PW (1985) *J Phys Chem* 89:5759–5766
52. Brunschwig BS, Ehrenson S, Sutin N (1987) *J Phys Chem* 91:4714–4723
53. Bayliss NS, McRae EG (1954) *J Phys Chem* 58:1002–1006
54. Metelitsa AV, Lokshin V, Micheau JC, Samat A, Guglielmetti R, Minkin VI (2002) *Phys Chem Chem Phys* 4:4340–4345
55. Li H, Eddaoudi M, O’Keeffe M, Yaghi OM (1999) *Nature* 402:276–279
56. Tan J-C, Civalieri B (2015) *CrystEngComm* 17:197–198
57. Batten SR, Champness NR, Chen X-M, Garcia-Martinez J, Kitagawa S, Öhrström L, O’Keeffe M, Suh MP, Reedijk J (2013) *Pure Appl Chem* 85:1715–1724
58. Abrahams BF, Hoskins BF, Michail DM, Robson R (1994) *Nature* 369:727–729
59. Hoskins BF, Robson R (1989) *J Am Chem Soc* 111:5962–5964
60. Li H, Eddaoudi M, Thomas A, Groy L, Yaghi OM (1998) *J Am Chem Soc* 120:8571–8572
61. Kondo M, Yoshitomi T, Matsuzaka H, Kitagawa S, Seki K (1997) *Angew Chem Int Ed* 36:1725–1727
62. Ninclaus C, Serre C, Riou D, Férey G (1998) *C R Acad Sci Ser IIC* 1:551–556
63. Zlotea C, Campesi R, Cuevas F, Leroy E, Dibandjo P, Volkringer C, Loiseau T, Férey G, Latroche M (2010) *J Am Chem Soc* 132:2991–2997
64. Suh MP, Park HJ, Prasad TK, Lim D-W (2012) *Chem Rev* 112:782–835
65. Wu H, Reali RS, Smith DA, Trachtenberg MC, Li J (2010) *Chem A Eur J* 16:13951–13954
66. Li J-R, Sculley J, Zhou H-C (2012) *Chem Rev* 112:869–932
67. Alaerts L, Maes M, Giebler L, Jacobs PA, Martens JA, Denayer JFM, Kirschhock CEA, De Vos DE (2008) *J Am Chem Soc* 130:14170–14178
68. Maes M, Vermoortele F, Alaerts L, Couck S, Kirschhock CEA, Denayer JFM, De Vos DE (2010) *J Am Chem Soc* 132:15277–15285

69. Lee J, Farha OK, Roberts J, Scheidt KA, Nguyen ST, Hupp JT (2009) *Chem Soc Rev* 38:1450–1459
70. Horcajada P, Chalati T, Serre C, Gillet B, Sebrie C, Baati T, Eubank JF, Heurtaux D, Clayette P, Kreuz C, Chang J-S, Hwang YK, Marsaud V, Bories P-N, Cynober L, Gil S, Férey G, Couvreur P, Gref R (2010) *Nat Mater* 9:172–178
71. Horcajada P, Serre C, Vallet-Regí M, Sebban M, Taulelle F, Férey G (2006) *Angew Chem Int Ed* 45:5974–5978
72. Tu M, Reinsch H, Rodríguez-Hermida S, Verbeke R, Stassin T, Egger W, Dickmann M, Dieu B, Hofkens J, Vankelecom I, Stock N, Ameloot R (2018) *Angew Chem* 131:2445–2449
73. Dolgoplova EA, Moore TM, Ejegbavwo OA, Pellechia PJ, Smith MD, Shustova NB (2017) *Chem Commun* 53:7361–7364
74. Stavila V, Talin AA, Allendorf MD (2014) *Chem Soc Rev*:5994–6010
75. Allendorf MD, Schwartzberg A, Stavila V, Talin AA (2011) *Chem A Eur J* 17:11372–11388
76. Inokuma Y, Arai T, Fujita M (2010) *Nat Chem* 2:780–783
77. Brkljača R, Schneider B, Hidalgo W, Otálvaro F, Ospina F, Lee S, Hoshino M, Fujita M, Urban S (2017) *Molecules* 22:211 (1–9)
78. Lee S, Hoshino M, Fujita M, Urban S (2017) *Chem Sci* 8:1547–1550
79. Inokuma Y, Matsumura K, Yoshioka S, Fujita M (2017) *Chem An Asian J* 12:208–211
80. Zigon N, Kikuchi T, Ariyoshi J, Inokuma Y, Fujita M (2017) *Chem An Asian J* 12:1057–1061
81. Sakurai F, Khutia A, Kikuchi T, Fujita M (2017) *Chem A Eur J* 23:15035–15040
82. Hoshino M, Khutia A, Xing H, Inokuma Y, Fujita M (2016) *IUCr J* 3:139–151
83. Inokuma Y, Yoshioka S, Ariyoshi J, Arai T, Hitora Y, Takada K, Matsunaga S, Rissanen K, Fujita M (2013) *Nature* 495:461–466
84. Czaja AU, Trukhan N, Müller U (2009) *Chem Soc Rev* 38:1284–1293
85. Mueller U, Schubert M, Teich F, Puetter H, Schierle-Armdt K, Pastré J (2006) *J Mater Chem* 16:626–636
86. Mezenov YA, Krasilin AA, Dzyuba VP, Nominé A, Milichko VA (2019) *Adv Sci* 6:1900506 (1–15)
87. Eddaoudi M, Kim J, Rosi N, Vodak D, Wachter J, O’Keeffe M, Yaghi OM (2002) *Science* 295:469–472
88. Deng H, Grunder S, Cordova KE, Valente C, Furukawa H, Hmadeh M, Gandara F, Whalley AC, Liu Z, Asahina S, Kazumori H, O’Keeffe M, Terasaki O, Stoddart JF, Yaghi OM (2012) *Science* 336:1018–1023
89. Schaate A, Roy P, Preusse T, Lohmeier SJ, Godt A, Behrens P (2011) *Chem A Eur J* 17:9320–9325
90. Falcaro P, Ricco R, Doherty CM, Liang K, Hill AJ, Styles MJ (2014) *Chem Soc Rev* 43:5513–5560
91. Zhuang JL, Terfort A, Wöll C (2015) *Coord Chem Rev* 307:391–424
92. Li Y-S, Bux H, Feldhoff A, Li G-L, Yang W-S, Caro J (2010) *Adv Mater* 22:3322–3326
93. Zhang F, Zou X, Feng W, Zhao X, Jing X, Sun F, Ren H, Zhu G (2012) *J Mater Chem* 22:25019–25026
94. Zhuang J-L, Ceglarek D, Pethuraj S, Terfort A (2011) *Adv Funct Mater* 21:1442–1447
95. Knebel A, Sundermann L, Mohmeyer A, Strauß I, Friebe S, Behrens P, Caro J (2017) *Chem Mater* 29:3111–3117
96. Li Y-S, Liang F-Y, Bux H, Feldhoff A, Yang W-S, Caro J (2010) *Angew Chem Int Ed* 49:548–551
97. Shekhah O, Wang H, Kowarik S, Schreiber F, Paulus M, Tolan M, Sternemann S, Evers F, Zacher D, Fischer RA, Wöll C (2007) *J Am Chem Soc* 129:15118–15119
98. Castellanos S, Kapteijn F, Gascon J (2016) *CrystEngComm* 18:4006–4012
99. Jones CL, Tansell AJ, Easun TL (2016) *J Mater Chem A* 4:6714–6723
100. Dolgoplova EA, Rice AM, Martin CR, Shustova NB (2018) *Chem Soc Rev* 47:4710–4728
101. Mukhopadhyay RD, Praveen VK, Ajayaghosh A (2014) *Mater Horiz* 1:572–576
102. Russew M-M, Hecht S (2010) *Adv Mater* 22:3348–3360

103. Wang L, Li Q (2018) *Chem Soc Rev* 47:1044–1097
104. Coudert F-X (2015) *Chem Mater* 27:1905–1916
105. Juan-Alcañiz J, Gascon J, Kapteijn F (2012) *J Mater Chem* 22:10102–10118
106. Schwartz HA, Ruschewitz U, Heinke L (2018) *Photochem Photobiol Sci* 17:864–873
107. Schaate A, Dühren S, Platz G, Lilienthal S, Schneider AM, Behrens P (2012) *Eur J Inorg Chem*:790–796
108. Epley CC, Roth KL, Lin S, Ahrenholtz SR, Grove TZ, Morris AJ (2017) *Dalton Trans* 46:4917–4922
109. Zhang J, Wang L, Li N, Liu J, Zhang W, Zhang Z, Zhou N, Zhu X (2014) *CrystEngComm* 16:6547–6551
110. Khayyami A, Philip A, Karppinen M (2019) *Angew Chem* 131:13534–13538
111. Zheng Y, Sato H, Wu P, Jeon HJ, Matsuda R, Kitagawa S (2017) *Nat Commun* 8:100 (1–6)
112. Dolgoplova EA, Galitskiy VA, Martin CR, Gregory HN, Yarbrough BJ, Rice AM, Berseneva AA, Ejegbavwo OA, Stephenson KS, Kittikhunnatham P, Karakalos SG, Smith MD, Greytak AB, Garashchuk S, Shustova NB (2019) *J Am Chem Soc* 141:5350–5358
113. Modrow A, Zargarani D, Herges R, Stock N (2011) *Dalton Trans* 40:4217–4222
114. Park J, Yuan D, Pham KT, Li J-R, Yakovenko A, Zhou H-C (2012) *J Am Chem Soc* 134:99–102
115. Yu X, Wang Z, Buchholz M, Füllgrabe N, Grosjean S, Bebensee F, Bräse S, Wöll C, Heinke L (2015) *Phys Chem Chem Phys* 17:22721–22725
116. Healey K, Liang W, Southon PD, Church TL, D’Alessandro DM (2016) *J Mater Chem A* 4:10816–10819
117. Modrow A, Zargarani D, Herges R, Stock N (2012) *Dalton Trans* 41:8690–8696
118. Heinke L, Cakici M, Dommaschk M, Grosjean S, Herges R, Bräse S, Wöll C (2014) *ACS Nano* 8:1463–1467
119. Heinke L (2017) *J Phys D Appl Phys* 50:193004 (1–18)
120. Wang Z, Knebel A, Grosjean S, Wagner D, Bräse S, Wöll C, Caro J, Heinke L (2016) *Nat Commun* 7:13872 (1–7)
121. Müller K, Helfferich J, Zhao F, Verma R, Kanj AB, Meded V, Bléger D, Wenzel W, Heinke L (2018) *Adv Mater* 30:1706551 (1–7)
122. Kanj AB, Bürck J, Grosjean S, Bräse S, Heinke L (2019) *Chem Commun* 55:8776–8779
123. Wang Z, Heinke L, Jelic J, Cakici M, Dommaschk M, Maurer RJ, Oberhofer H, Grosjean S, Herges R, Bräse S, Reuter K, Wöll C (2015) *Phys Chem Chem Phys* 17:14582–14587
124. Williams DE, Martin CR, Dolgoplova EA, Swifton A, Godfrey DC, Ejegbavwo OA, Pellechia PJ, Smith MD, Shustova NB (2018) *J Am Chem Soc* 140:7611–7622
125. Ohara K, Inokuma Y, Fujita M (2010) *Angew Chem Int Ed* 49:5507–5509
126. Yanai N, Uemura T, Inoue M, Matsuda R, Fukushima T, Tsujimoto M, Isoda S, Kitagawa S (2012) *J Am Chem Soc* 134:4501–4504
127. Dybtsev DN, Chun H, Kim K (2004) *Angew Chem Int Ed* 43:5033–5036
128. Uemura T, Washino G, Yanai N, Kitagawa S (2013) *Chem Lett* 42:222–223
129. Hermann D, Emerich H, Lepski R, Schaniel D, Ruschewitz U (2013) *Inorg Chem* 52:2744–2749
130. Ruschewitz U, Hermann D (2010) *Z Anorg Allg Chem* 636:2068
131. Ruschewitz U, Hermann D (2012) *Z Anorg Allg Chem* 638:1574
132. Volkringer C, Meddouri M, Loiseau T, Guillou N, Marrot J, Férey G, Haouas M, Taulelle F, Audebrand N, Latroche M (2008) *Inorg Chem* 47:11892–11901
133. Loiseau T, Serre C, Huguenard C, Fink G, Taulelle F, Henry M, Bataille T, Férey G (2004) *Chem A Eur J* 10:1373–1382
134. Volkringer C, Loiseau T, Guillou N, Férey G, Elkaïm E, Vimont A (2009) *Dalton Trans* 53:2241–2249
135. Wegner HA (2012) *Angew Chem Int Ed* 51:4787–4788
136. Bléger D, Schwarz J, Brouwer AM, Hecht S (2012) *J Am Chem Soc* 134:20597–20600

137. Hermann D, Schwartz HA, Werker M, Schaniel D, Ruschewitz U (2019) *Chem A Eur J* 25:3606–3616
138. Hernández-Trujillo J, Vela A (1996) *J Phys Chem* 100:6524–6530
139. Hunter CA, Lawson KR, Perkins J, Urch CJ (2001) *J Chem Soc Perkin Trans 2*:651–669
140. Das D, Agarkar H (2018) *ACS Omega* 3:7630–7638
141. Agarkar H, Das D (2019) *J Mol Struct* 1184:435–442
142. Fu W-Q, Liu M, Gu Z-G, Chen S-M, Zhang J (2016) *Cryst Growth Des* 16:5487–5492
143. Chui SS-Y, Lo SM-F, Charmant JPH, Orpen AG, Williams ID (1999) *Science* 283:1148–1150
144. Müller K, Wadhwa J, Singh Malhi J, Schöttner L, Welle A, Schwartz H, Hermann D, Ruschewitz U, Heinke L (2017) *Chem Commun* 53:8070–8073
145. Johannsmann D (2015) *The quartz crystal microbalance in soft matter research*. Springer, Basel
146. Wang Z, Grosjean S, Bräse S, Heinke L (2015) *ChemPhysChem* 16:3779–3783
147. Kobatake S, Yamada T, Uchida K, Kato N, Irie I (1999) *J Am Chem Soc* 121:2380–2386
148. Yamada T, Kobatake S, Irie M (2000) *Bull Chem Soc Jpn* 73:2179–2184
149. Walton IM, Cox JM, Coppin JA, Linderman CM, Patel DGD, Benedict JB, Ren H, Zhu G (2013) *Chem Commun* 49:8012–8014
150. Florea L, Hennart A, Diamond D, Benito-Lopez F (2012) *Sensors Actuators B Chem* 175:92–99
151. Florea L, McKeon A, Diamond D, Benito-Lopez F (2013) *Langmuir* 29:2790–2797
152. Schwartz HA, Olthof S, Schaniel D, Meerholz K, Ruschewitz U (2017) *Inorg Chem* 56:13100–13110
153. Snyder LR (1983) *High performance liquid chromatography*. Academic Press, New York
154. Garg S, Schwartz H, Kozłowska M, Kanj AB, Müller K, Wenzel W, Ruschewitz U, Heinke L (2019) *Angew Chem Int Ed* 58:1193–1197
155. Darwish N, Aragonès AC, Darwish T, Ciampi S, Díez-Pérez I (2014) *Nano Lett* 14:7064–7070
156. Kumar S, van Herpt JT, Gengler RYN, Feringa BL, Rudolf P, Chiechi RC (2016) *J Am Chem Soc* 138:12519–12526
157. Jiang G, Song Y, Guo X, Zhang D, Zhu D (2008) *Adv Mater* 20:2888–2898
158. Tork A, Boudreau F, Roberge M, Ritcey AM, Lessard RA, Galstian TV (2001) *Appl Opt* 40:1180–1186
159. Sakuragi M, Aoki K, Tamaki T, Ichimura K (1990) *Bull Chem Soc Jpn* 63:74–79
160. Whelan J, Wojtyk JTC, Buncl E (2008) *Chem Mater* 20:3797–3799
161. Radu A, Byrne R, Alhashimi N, Fusaro M, Scarmagnani S, Diamond D (2009) *J Photochem Photobiol A Chem* 206:109–115
162. Chu NYC (1983) *Can J Chem* 61:300–305
163. Schwartz HA, Werker M, Tobeck C, Christoffels R, Schaniel D, Olthof S, Meerholz K, Kopacka H, Huppertz H, Ruschewitz U (2020) *ChemPhotoChem* 4:195–206
164. Hoorens MWH, Medved' M, Laurent AD, Di Donato M, Fanetti S, Slappendel L, Hilbers M, Feringa BL, Buma WJ, Szymanski W (2019) *Nat Commun* 10:2390 (1–11)
165. Bendeif E-E, Gansmuller A, Hsieh K-Y, Pillet S, Woike T, Zobel M, Neder RB, Bouazaoui M, El Hamzaoui H, Schaniel D (2015) *RSC Adv* 5:8895–8902
166. Hsieh K-Y, Bendeif E-E, Gansmuller A, Pillet S, Woike T, Schaniel D (2013) *RSC Adv* 3:26132–26141
167. Volkringer C, Popov D, Loiseau T, Férey G, Burghammer M, Riekel C, Haouas M, Taulelle F (2009) *Chem Mater* 21:5695–5697
168. Horcajada P, Surlblé S, Serre C, Hong DY, Seo YK, Chang JS, Grenèche JM, Margiolaki I, Férey G (2007) *Chem Commun*:2820–2822
169. Férey G, Serre C, Mellot-Draznieks C, Millange F, Surlblé S, Dutour J, Margiolaki I (2004) *Angew Chem Int Ed* 43:6296–6301
170. Cavka JH, Jakobsen S, Olsbye U, Guillou N, Lamberti C, Bordiga S, Lillerud KP (2008) *J Am Chem Soc* 130:13850–13851

Guest-Based Photoactive Porous Materials Based upon Zn-Carboxylate Metal Organic Frameworks



Randy W. Larsen, Jacob M. Mayers, Abdulaziz A. Alanazi,
Christopher R. McKeithan, and Lukasz Wojtas

Contents

1	Introduction	156
1.1	Metal Organic Frameworks	156
1.2	Photoactive Metal Organic Frameworks	158
1.3	Transition Metal Polyimines as Photoactive Guests	159
2	Ruthenium(II) Polyimines as Photoactive Guests Within Zn-Based Polyhedral MOFs ...	160
2.1	Zn-Carboxylate-Based Polyhedral MOFs	160
2.2	Encapsulation of RuBpy Within USF2 and HKUST-1(Zn) (RuBpy@USF2 and RuBpy@HKUST-1(Zn))	161
3	RuBpy Templated MOFs	166
3.1	The RWLC-1 and RWLC-2 Templated MOFs	167
3.2	The RWLC-3 Templated MOF	171
3.3	The RWLC-5 Templated MOF	174
3.4	The RWLC-6 Templated MOF	177
4	Conclusions and Future Perspectives	180
	References	181

Abstract Metal organic framework (MOF) materials are attractive candidates for the development of solar energy applications due to the modularity of design, high porosity, and ease of functionalization of these materials. The encapsulation of photoactive guests into porous MOFs is a particularly attractive strategy for the development of photosensitive MOFs. This chapter is focused on the encapsulation of Ruthenium polyimine-type complexes into MOFs due to their high stability,

R. W. Larsen (✉), J. M. Mayers, C. R. McKeithan, and L. Wojtas
Department of Chemistry, University of South Florida, Tampa, FL, USA
e-mail: rwlarsen@usf.edu

A. A. Alanazi
Department of Chemistry, University of South Florida, Tampa, FL, USA

Department of Chemistry, Sattam Bin Abdulaziz University, Al Kharj, Saudi Arabia

robust photophysical properties, and excited state tuneability. It has now been demonstrated that Ru(II)tris(2,2'-bipyridine) (RuBpy) can exhibit a templating effect in the formation of the resultant metal organic framework (MOF) materials. A number of new topologies have now been synthesized using Zn(II) ions and carboxylate ligands in which the encapsulated RuBpy clusters exhibit unique photophysical properties. In this chapter, the relationship between MOF cavities and the RuBpy photophysical properties is reviewed. Two polyhedral MOFs (RuBpy@HKUST-1(Zn) and RuBpy@USF2) and five RuBpy templated MOFs (RWLC-1,-2,-3,-5 and -6) are discussed in terms of cavity influence on excited state population and decay pathways.

Keywords 2,2'-Bipyridine · Metal building block · Metal organic frameworks · Metal to ligand charge transfer states · Photophysics · Ruthenium(II) polyimines

Abbreviations

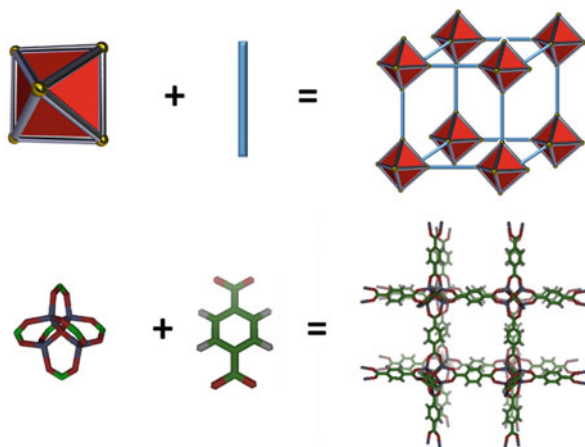
BDC	Benzene 1,4-dicarboxylate
BTCA	Benzene-1,3,5 carboxylate
BTE	1,3,5-Tris(carboxyphenylethynyl)benzene
LF	Ligand field state
MBB	Metal building block
MLCT	Metal to ligand charge transfer
MOF	Metal organic framework
POM	Polyoxometalate
RuBpy	Ru(II)tris(2,2'-bipyridine)
RuBpy	Ru(II)tris(2,2'-bipyridine)
TCPB	1,3,5-Tris(4-carboxyphenyl)benzene

1 Introduction

1.1 Metal Organic Frameworks

Metal organic frameworks (MOFs) constitute a class of functional porous materials that provide an extensive foundation through which a wide range of applications can be developed including, but not limited to, gas storage and separation, heterogeneous catalysis, drug delivery, sensors, environmental remediation, and light harvesting [1–5]. The MOF class of materials feature high porosity, a wide array of structural topologies, ease of synthesis, and tunable functionality [3, 6–8]. The versatility of MOFs is due to the fact that these materials contain molecular building blocks (MBBs) composed of metal coordination complexes linked through multidentate organic ligands (Fig. 1) [9, 10]. The key advantage associated with MOFs includes the fact that the geometry of the MBB can be tuned, the organic

Fig. 1 Top – Diagrammatic representation of the modular nature associated with MOF assembly. Bottom – Components of MOF-5 including the linear benene-1,4-dicarboxylate and the Zn-O metal building block



ligands connecting the MBBs can be functionalized, and the scale can be selected from nano- to mesoporous. These factors allow for extraordinary versatility in structure, and function not available in other porous materials such as zeolites, porous Si, or hydrogels. In terms of structural diversity, these materials extend from discrete nanoscale polyhedral to large extended porous networks. These networks, with nanoscale cavities, are of particular importance to guest-based functional materials since the cavities can accommodate a wide variety of guest molecules. Examples of MOF networks include numerous zeolite topologies [11, 12], quartz diamond [13], perovskites [14, 15], rutile [16], and feldspar [17] to name only a few.

The most notable applications for MOFs have been in the area of gas storage and separations [18, 19]. One of the earliest targets for MOF gas storage was H_2 due to the potential for MOFs to serve as a hydrogen supply for hydrogen-oxygen fuel cells. The weight percent of H_2 storage has been reported as high as 10% for MOF-5 and SNU-6 at 77 K [20]. A more recent effort has been focused on CO_2 sequestration for use in remediation of greenhouse gasses with Mg-MOF-74 having one of the largest uptakes (5.3 mg/g at 40°C) [21]. Other gas storage applications include toxic industrial chemicals (TICs) such as NO_x , CO, SO_2 , and Cl_2 as well as other energy-related gases including CH_4 [22]. Various MOFs have also been the target for heterogeneous catalyst development centered primarily on oxidation reactions [23]. Catalytic sites can be either engineered into the framework through the MBBs or organic linkers (metalloporphyrins) or encapsulated within the large interior cavities. The MOF channels and windows can modulate the diffusion of both reactants and products to and from the catalytic sites.

1.2 Photoactive Metal Organic Frameworks

Photoactive MOFs are of particular importance for the development of efficient light-harvesting materials. Two general strategies have been employed in the development of photoactive MOFs (Fig. 2). The first utilizes the metal cluster MBBs and/or the framework ligands as the photoactive element of the MOF. Photoactive framework MOFs typically contain lanthanides as part of the MBB and/or porphyrin-based organic linkers, both of which are photochemically active [24–26]. Many of these materials have been developed for sensor applications as the luminescent properties of the lanthanide clusters are highly sensitive to the nature of the coordinated ligands [27]. Alternatively, a wide variety of MOFs have been synthesized and characterized in which the ligands connecting the MBBs are composed of free base or metalloporphyrins [28, 29]. These materials are of particular interest since the porphyrin macrocycles making up the framework can contain open metal sites for catalysis, and many photoactive active porphyrins are available. In the case of framework-based catalysts, the target reactant diffuses through the windows and channels of the photoexcited MOF, undergoes photochemical transformation, and then diffuses back into the bulk solvent. The advantages of this type of MOF catalyst include a high density of catalytic sites, ease of access for photochemical reactants, and framework tunability toward specific photochemical reactants. The drawbacks, however, include nonspecific photochemistry as the reactants can simply interact with the ligands/MBB which reduces the ability to utilize pore selectivity and difficulty in the design and synthesis of MOFs with new photoactive ligands and/or building blocks.

Photocatalytic MOFs in which a photoactive guest molecule is encapsulated within the cavities of the material have also been developed. Examples of this type

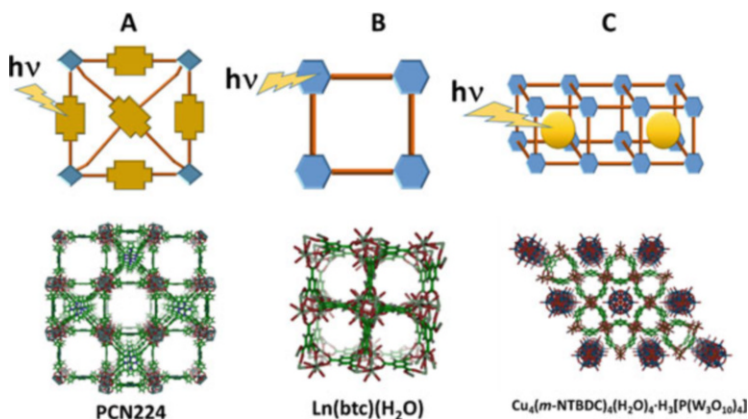


Fig. 2 Top – Diagrammatic representation of the various strategies for the development of photoactive MOFs. Bottom – Examples of photoactive MOFs. (a) MOF containing photoactive bridging ligands, (b) MOF containing photoactive MBBs, and (c) MOF containing photoactive guest molecules

of photocatalyst have been reported in which the encapsulated guest includes Keggin-type polyoxometalates encapsulated within an HKUST-1(Cu) framework [30–33], free base and metalloporphyrins encapsulated within both rhoZMOF and HKUST-1(Zn) [34–36], and Ru(II) polyimines encapsulated in pillared 2D sheet materials [37]. This type of photoactive MOF offers several advantages including a wide range of photoactive guests available for encapsulation; the windows leading to the photoexcited guest can be tuned for greater reactant selectivity, and a large library of MOFs exists that can be exploited for guest encapsulation.

1.3 Transition Metal Polyimines as Photoactive Guests

Transition metal polyimines and related compounds are an important class of photoactive guests due to their overall stability, relatively high molar extinction coefficients in the visible region of the optical spectrum ($>10,000 \text{ M}^{-1} \text{ cm}^{-1}$), and relatively long-lived metal-to-ligand charge transfer states (MLCT) [38, 39]. The most widely investigated of the transition metal polyimines is [Ru(II)(2,2'-bipyridine)₃]²⁺ (RuBpy). The excited state photophysics of the RuBpy complex serves as a general model for transition metal polyimines. Excitation of the RuBpy in the visible region ($\sim 450 \text{ nm}$) leads to formation of an ¹MLCT state in which electron density is delocalized from the Ru(II) center to the 2,2'-bipyridine ligands (Fig. 3) [40]. The ¹MLCT state rapidly decays ($\sim \text{ps}$) to a set of three closely spaced ³MLCT states through an efficient spin-orbit coupling. Additional ³MLCT states are also present that are $\sim 850 \text{ cm}^{-1}$, $\sim 2,450 \text{ cm}^{-1}$, and $\sim 3,100 \text{ cm}^{-1}$ above the triplet state manifold. The lowest energy ³MLCT state manifold decays back to the singlet ground state through both radiative and non-radiative pathways. The observed

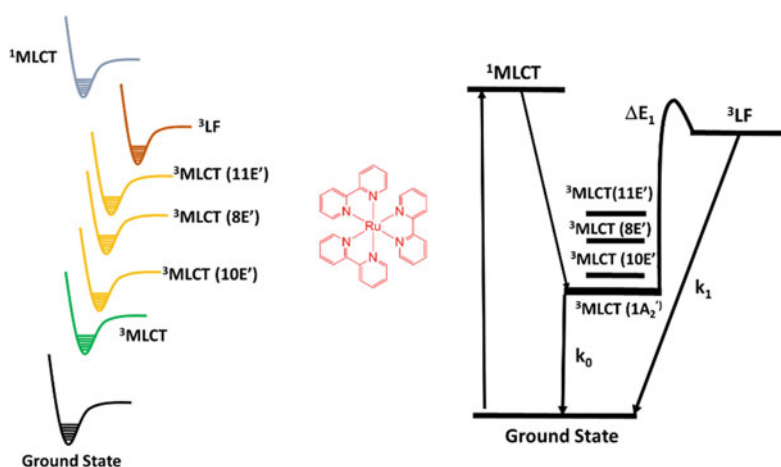


Fig. 3 Summary of the excited state decay pathways for RuBpy

decay rate (emission decay rate) is on the order of ~ 600 ns in deaerated solution and is sensitive to both temperature and solvent. A metal-centered ligand field state (^3LF) can also be thermally populated from the lower-energy $^3\text{MLCT}$ manifold through an energy barrier of $\sim 3,500$ cm^{-1} . The ^3LF state has antibonding with respect to the Ru-N bonds and decays non-radiatively with a fast decay constant of $\sim 1 \times 10^{13}$ s^{-1} [41].

2 Ruthenium(II) Polyimines as Photoactive Guests Within Zn-Based Polyhedral MOFs

2.1 Zn-Carboxylate-Based Polyhedral MOFs

Zinc(II) carboxylate MOFs are a class of porous materials composed of polyhedral cages which share common vertices and windows into adjacent cavities. A wide variety of Zn(II) and Cu(II) polyhedral MOFs have been synthesized and characterized and are one of the earliest examples of reticular porous materials. Among the most widely known polyhedral MOFs are the IRMOFs developed by Omar Yaghi [42]. The IRMOF series share a common cubic topology constructed from linear organic linkers of various sizes linking Zn oxide clusters. The isorecticular approach allows for the development of frameworks that includes a wide range of cavity and window diameters [43, 44]. Another polyhedral framework, while not originally synthesized with Zn(II) ions, is HKUST-1 whose Zn analog has shown promising properties in the development of photocatalytic materials. The HKUST-1 framework was among the first nanoporous materials with regard to crystallinity which could be chemically functionalized unlike the more widely utilized inorganic zeolites [45]. The HKUST-1 topology incorporates Cu-Cu paddle wheel MBBs which are a common building unit in high-performing multifunctional materials including NU-111 [46], PCN-14 [47], and NOTT-115 [48]. The HKUST-1(Zn) framework is isostructural with HKUST-1(Cu) and is composed of dinuclear Zn(II) paddle wheel MBBs connected from benzene-1,3,5-dicarboxylate (BTCA) to form a 3,4-connected cubic framework (*tbo* – net topology) [31, 45]. The HKUST-1(Zn) contains three cavities whose shapes can be approximated as rhombihexahedron of 13 Å diameter ($1,278$ Å³ volume), octahemioctahedron of 11 Å diameter (696 Å³ volume), and tetrahedron of 5 Å diameter (65 Å³ volume). Another topology isostructural with HKUST-1(Zn) is USF2 which is a polyhedral MOF composed of dinuclear Zn-paddle wheel MBBs also connected through trimesic acid linkers resulting in a Pm-3m cubic symmetry [49]. The resulting framework can be viewed as a tiling of 3D space with two faceted polyhedrals (cuboctahedron and octahemioctahedron) with an edge skeleton cube. The largest cavity in USF2 can be viewed as a cuboctahedron with diameter of ~ 15 Å with small windows of ~ 9 Å.

2.2 Encapsulation of RuBpy Within USF2 and HKUST-1(Zn) (RuBpy@USF2 and RuBpy@HKUST-1(Zn))

One of the early examples of photoactive transition metal polyimine guest encapsulation within a MOF was RuBpy encapsulated within the Zn-carboxylate MOF USF2 (RuBpy@USF2) [50]. These materials were prepared at room temperature using a so-called crystallization inclusion technique in which the guest is present during MOF synthesis. In the presence of RuBpy, the synthesis of USF2 produces orange crystals with the same unit cell as the parent USF2. The RuBpy cations could not be crystallographically resolved within the framework, but their presence within the MOF framework is confirmed from the photophysical properties. The most probable cavity for encapsulation is the cuboctahedron with a diameter of ~ 15 Å as the diameter of the RuBpy is ~ 12 Å. The RuBpy has also been encapsulated within an isostructural HKUST-1(Zn) MOF, also via a “ship-in-a-bottle” strategy (Fig. 4). Like the RuBpy@USF2 MOF, the RuBpy was not crystallographically resolved.

The steady-state emission spectrum of RuBpy@USF2 is hypsochromically shifted relative to RuBpy in ethanol (598 nm vs. 604 nm, respectively), similar to what has been observed for RuBpy encapsulated within ZeoliteY, while a bathochromic shift is observed for RuBpy@HKUST-1(Zn) (612 nm vs. 604 nm, respectively) (Fig. 5) [51, 52]. The hypsochromic shift observed in the RuBpy@USF2 is consistent with limited stabilization of the large excited state dipole moment (associated with formation of the MLCT state) possibly due to

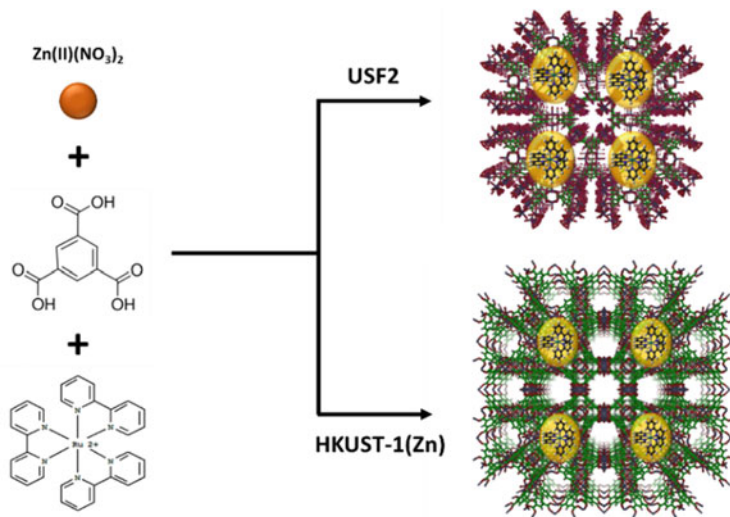


Fig. 4 Diagram illustrating the encapsulation of RuBpy within both USF2 and the isostructural HKUST-1(Zn) MOF

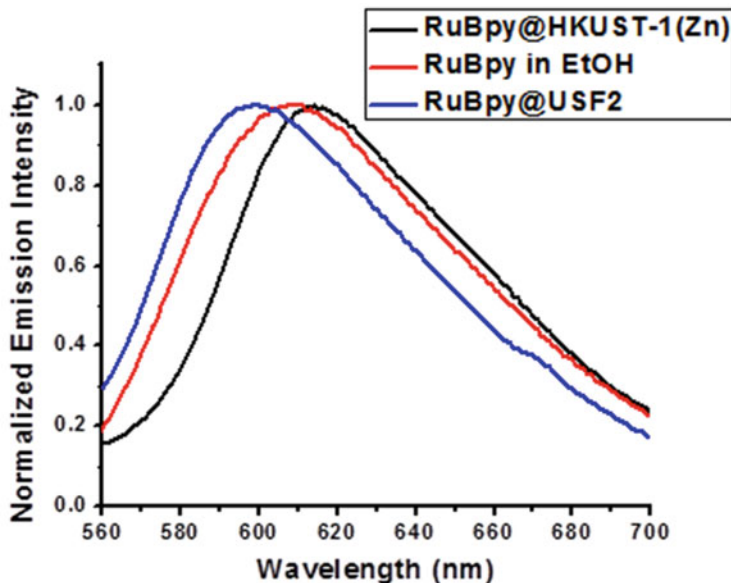


Fig. 5 Overlay of the steady-state emission spectra of RuBpy in ethanol, RuBpy@USF2 and RuBpy@HKUST-1(Zn)

differences in cavity micropolarity. Thus, emission takes place from an unrelaxed $^3\text{MLCT}$ state of the encapsulated RuBpy. In addition, the USF2 cavities are partially cationic due to the incomplete coordination of specific periodic Zn-paddle wheels. This partial charge may also result in the destabilization of the $^3\text{MLCT}$ leading to an increase in energy and a hypsochromic shift in emission. The similarities between the cavities that are most likely to host the RuBpy guests in both USF2 and HKUST-1(Zn) would suggest similar emission profiles if limited solvent reorganization was the primary factor in destabilizing the $^3\text{MLCT}$ state. Since the RuBpy@HKUST-1(Zn) emission is actually bathochromically shifted rather than hypsochromically shifted as in RuBpy@USF2, the partial charge associated with the USF2 framework is most likely responsible for the destabilization (i.e., the HKUST-1(Zn) framework is neutral).

In order to better understand the effects of encapsulation on the physical properties of the emitting $^3\text{MLCT}$ states, the emission spectrum can be analyzed using the spectral profile $I(E)$ which represents the ratio of the intensity at ν to the intensity at the energy gap, E_{00} , according to:

$$I(E) = \sum_{n=0}^N \sum_{m=0}^M [(E_{00} - nh\omega_M - mh\omega_L)/E_{00}]^4 (e^{-SM}/n!) \times (e^{-SL}/m!) \exp \left[-4\text{Ln}2(E - E_{00} + nh\omega_M + mh\omega_L/\Delta\nu_{1/2})^2 \right] \quad (1)$$

Table 1 Parameters obtained upon fitting of the steady-state emission spectra of RuBpy@USF2, RuBpy@HKUST-1(Zn), and RuBpy in ethanol to Eq. (1)

Species	E_{00} (cm^{-1})	$h\omega_M$ (cm^{-1})	$h\omega_L$ (cm^{-1})	S_M	S_L	$\Delta\nu_{1/2}$ (cm^{-1})	Reference
RuBpy in EtOH	16,781	1,258	355	0.64	0.73	1,617	[50]
RuBpy@USF-2	16,814	1,257	129	0.65	0.10	1,561	[50]
RuBpy@HKUST-1(Zn)	16,359	1,207	279	0.60	0.10	1,511	[51]

where $\Delta\nu_{1/2}$ is the full width at half maximum, n and m are the vibrational quantum numbers for medium, and low-frequency acceptor vibrational modes, S_M and S_L are the corresponding vibronic coupling factors (Huang-Rhys factors), and $h\omega_M$ and $h\omega_L$ are the average vibrational frequencies of the acceptor modes [53]. In the case of RuBpy complexes, the ground and lowest energy $^3\text{MLCT}$ states are coupled through medium-frequency $\nu(\text{Bpy})$ ring stretching modes, low-frequency ring torsional modes, and lower frequency Ru-N stretching modes [53]. The data for the fits to RuBpy in ethanol, RuBpy@USF2, and RuBpy@HKUST-1(Zn) are summarized in Table 1. The data indicate that the E_{00} values are consistent with the observed emission maxima indicating that the energy difference between the lowest energy potential energy well associated with the $^3\text{MLCT}$ manifold is responsible for the observed emission energy rather than overall changes in the vibrational manifolds. The most significant differences between the RuBpy@USF2 and RuBpy@HKUST-1(Zn) are in the low-frequency Huang-Rhys coupling factors and the average low-frequency coupling modes. The Huang-Rhys factors are related to both the nuclear displacement of the excited state (ΔQ) and the frequencies of the coupling modes according to Eq. (2):

$$S = \mu(1/2)(h\omega/\hbar)(\Delta Q)^2 \quad (2)$$

where μ is the reduced mass of the vibration system, and $h\omega$ is the frequency of the coupling vibrational mode. The nuclear displacement terms of the Huang-Rhys factors can be utilized to determine the extent to which the excited state potential surfaces associated with the encapsulated RuBpy are perturbed by encapsulation. This may be accomplished by rearranging Eq. (2) and taking a ratio of the displacement terms according to Eq. (3):

$$(\Delta Q_{\text{MOF}})/\Delta Q_{\text{Sol}} = (S^{\text{MOF}}h\omega_{\text{sol}}/S^{\text{Sol}}h\omega_{\text{MOF}})^{1/2} \quad (3)$$

where ΔQ_{MOF} and ΔQ_{Sol} are the excited state displacement term for the RuBpy encapsulated within the MOF and RuBpy in solution, respectively, S^{MOF} and S^{Sol} are Huang-Rhys factors obtained from the fits of the steady-state emission data and $h\omega_{\text{MOF}}$ and $h\omega_{\text{Sol}}$ are the frequencies of the coupling modes, also obtained from the steady-state emission fits. The ratio of the displacements, determined using either the medium- or low-frequency coupling modes, provides information regarding the

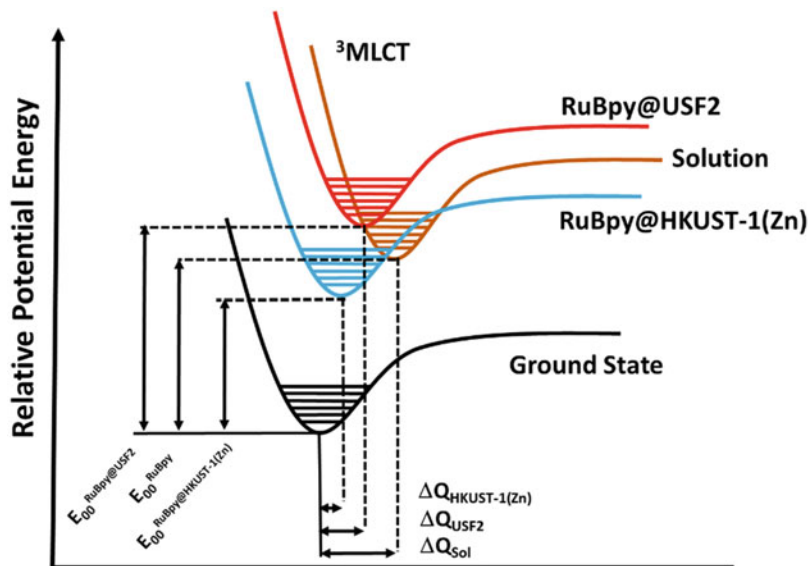


Fig. 6 Diagram illustrating the displacement of the excited state potential surfaces of RuBpy@USF2 and RuBpy@HKUST-1(Zn), relative to RuBpy in solution

effects of encapsulation on the distortion of the RuBpy complex. The ratios calculated from RuBpy@USF2 and RuBpy@HKUST-1(Zn) indicate smaller displacements for both systems relative to RuBpy in solution by 0.6 and 0.4, respectively (see Fig. 6).

The corresponding lifetimes of RuBpy@USF2 and RuBpy@HKUST-1(Zn) are also quite unique from RuBpy in solution (Fig. 7). In the case of RuBpy@USF2, the RuBpy emission could be fit to a single exponential function giving a lifetime significantly longer than for RuBpy in solution ($\tau_{\text{USF2}} = 1,200$ ns vs. $\tau_{\text{Sol}} = 614$ ns). In contrast, the RuBpy@HKUST-1(Zn) emission is best fit to a biexponential function with $\tau_{\text{short}} = 133$ ns and $\tau_{\text{long}} = 744$ ns.

Fitting the emission decay rate constants as a function of temperature to the excited state decay model described in Fig. 3 provides details regarding the excited state decay pathways according to:

$$k_{\text{obs}} = k_0 + k_1 \times \exp(-\Delta E_1/k_B T) \quad (4)$$

where k_0 is the rate constant associated with relaxation from the $^3\text{MLCT}$ to the singlet ground state and is the sum of the radiative (k_r) non-radiative (k_{nr}) decay constants, k_1 is the non-radiative rate constant for the decay of the ^3LF to the ground state, ΔE_1 is the energy barrier required to access the ^3LF state from the $^3\text{MLCT}$ state, and k_B is Boltzmann's constant.

Analysis of the data in Table 2 provides insights as to the differences in emission lifetimes between the two materials and RuBpy in solution. In the case of the

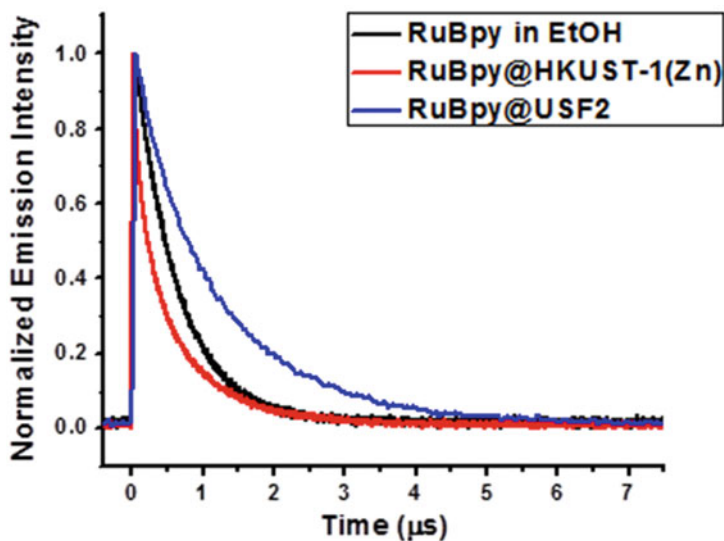


Fig. 7 Overlay of the emission decays of RuBpy in ethanol, RuBpy@USF2, and RuBpy@HKUST-1(Zn)

Table 2 Parameters obtained upon fitting of the emission lifetimes of RuBpy@USF2, RuBpy@HKUST-1(Zn), and RuBpy in ethanol to Eq. (4)

Species	k_0 (s^{-1})	k_1 (s^{-1})	ΔE_1 (cm^{-1})	τ (ns)	Reference
RuBpy in EtOH	5.6×10^5	5.1×10^{13}	3,661	614	[50]
RuBpy@USF-2	5.5×10^5	1.5×10^{15}	4,593	1,200	[50]
RuBpy@HKUST-1 Short lifetime	3.4×10^6	2.9×10^{13}	3,255	133	[51]
RuBpy@HKUST-1 Long lifetime	7.2×10^5	1.4×10^{12}	3,033	744	[51]

RuBpy@USF2, the reduced observed decay rate is attributed to an increase in the barrier to access the 3LF state by $\sim 1,000$ cm^{-1} , while the decay rate constant from the 3MLCT to the ground state is unaffected. The increase in ΔE_1 is likely the result of confinement that does not allow for expansion of the complex associated with population of the 3LF state. With regard to the slow decay of the RuBpy@HKUST-1 (Zn), the k_0 value is only slightly higher than that of RuBpy in solution or RuBpy@USF2, while the barrier to access the 3LF state becomes sufficiently large as to preclude occupancy altogether. In this case, the ΔE_1 value is actually the barrier to access other MLCT states that are slightly higher in energy than the 3MLCT manifold [54, 55]. This is also observed for RuBpy encapsulated within zeolite Y cages in which a ΔE_1 of ~ 820 cm^{-1} is observed that is attributed to the barrier to access a fourth 3MLCT that lies above the lowest-energy three state 3MLCT manifold. For the RuBpy@HKUST-1(Zn), the ΔE_1 value is much higher than the energy gap between the 3MLCT state manifold and the fourth 3MLCT state observed

in Zeolite Y and instead is due to a barrier accessing MLCT states that are higher in energy than the fourth MLCT state including additional singlet-in-character MLCT states [54]. This observation further suggests that the cavity being occupied by RuBpy in RuBpy@HKUST-1(Zn) is quite distinct from that in RuBpy@USF2 despite the similarities in MOF structure.

The fast decay associated with RuBpy@HUKUST-1(Zn) exhibits a k_0 that is nearly an order of magnitude larger than what is observed for RuBpy in solution and a k_1 and ΔE_1 that are similar to solution values. These observations are consistent with RuBpy@HKUST-1(Zn) containing a population of RuBpy that is located in regions of the framework that have larger volumes (defect regions) or at specific surface sites. These sites allow for access to the ^3LF state as well as quenching of the $^3\text{MLCT}$ either from other bound RuBpy complexes (self-quenching) or possibly other unknown exogenous quenchers.

3 RuBpy Templated MOFs

The motivation behind MOF templating arises from the desire to produce novel topologies with unique properties, which are not accessible through direct synthetic methods, and is a common methodology in MOF synthesis. The templating molecule has been suggested to interact with the framework precursors through weak forces such as Van der Waals interactions, hydrogen bonding, and electrostatic contacts [56]. In some cases, the templating molecule may remain as a guest within the templated MOF structure. Generally, templating molecules can be divided into seven classes including solvents, organic molecules, inorganic salts, coordination complexes, surfactants, polymers, and gas molecules [57]. The templating effects of solvent on MOF synthesis have been well documented. For example, Bharadwaj et al. reported the synthesis of several different Pb(II) MOFs varying only in the relative concentrations of water and various alcohols [58]. Zaworotko et al. reported the synthesis of two topologies, USF3 and USF4, which differed in the presence of benzene or chlorobenzene templating molecules, respectively [59].

Inorganic compounds may also serve as effective templating agents. One class of transition metal complex that has demonstrated a templating ability for MOFs are the polyoxometalates (POMs). These polyoxoanions have a wide range of applications due to their physical and chemical properties imparted by the diversity in metal composition. Liu and Hu have developed a synthetic method which combines the catalytic activity of $\text{H}_3\text{PW}_{12}\text{O}_{40}$ with the high surface area and stability of MOFs to produce cubic and octahedral crystals of the MOF NENU-3a ($\text{Cu}_{12}(\text{BTCA})_8 \cdot \text{H}_3\text{PW}_{12}\text{O}_{40}$) [60]. The POM interaction with the MOF precursors is critical for the nucleation processes required to form NENU-3a. Keggin-type POMs have also shown potential for serving as templating molecules producing novel host-guest applications in dye adsorption and photochemistry [61].

The RuBpy and related Ru(II) polyimine complexes are emerging as an important class of transition metal templating agents for the synthesis of photoactive MOFs for

light harvesting and photocatalytic applications. Recently, the templating effects of RuBpy-type complexes have been exploited to produce a number of novel RuBpy-MOFs in which the Ru(II) cation is crystallographically resolved. For many of these MOFs, the frameworks do not form in the absence of the Ru(II) complexes [62–65].

3.1 The RWLC-1 and RWLC-2 Templated MOFs

Under solvothermal conditions, a solution containing RuBpy, Zn(II) cations, and 1,3,5-tris(4-carboxyphenyl)benzene (TCPB) produces two MOFs in the same reaction vessel (Fig. 8) [62]. One of the MOFs, designated RWLC-1, contains two RuBpy cations encapsulated within a large cavity formed from the linkage of TCPB with Zn_2OH clusters. The framework consists of chains of Zn_2OH clusters, along a [001] direction, linked alternately by the carboxylate groups of the TCPB and hydrogen bonds between the OH^- and carboxylate groups. The linkage results in formation of hexagonal channels which are interrupted by TCPB ligands forming cavities which encompass two RuBpy cations separated by counter ions (either Cl^- or PF_6^-). The RWLC-2 structure is a 3,6-connected net with TCPB ligands and Zn_3OH clusters (composed of three Zn ions bridged by three carboxylate ligands with an OH^- group in the center) at the corresponding vertices.

The photophysical properties of both RWLC-1 and RWLC-2 are somewhat similar to RuBpy@HKUST-1(Zn) and RuBpy@USF2. With regard to the steady-state emission, RWLC-1 displays a hypsochromic shift, relative to RuBpy in solution (583 nm for RWLC-1 vs. 606 nm for RuBpy in solution) that is similar to RuBpy@USF2, while RWLC-2 displays a large bathochromic shift more closely

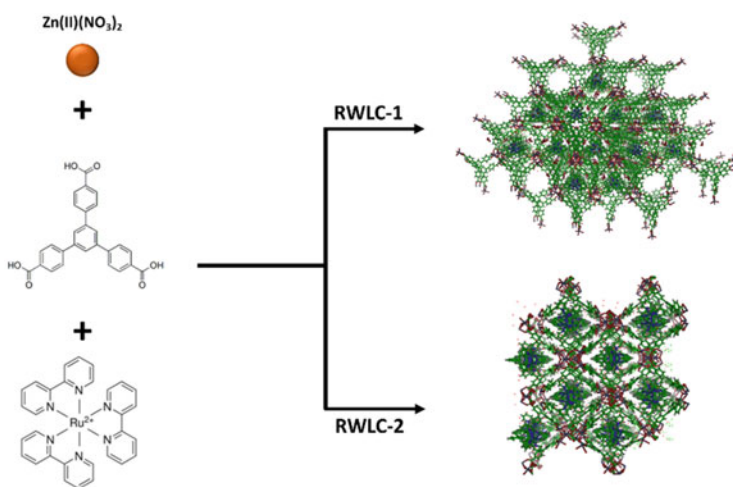


Fig. 8 Diagram illustrating the RuBpy templated formation of RWLC-1 and RWLC-2 MOFs

Fig. 9 Overlay of the steady-state emission spectra of RuBpy in ethanol, RWLC-1, and RWLC-2

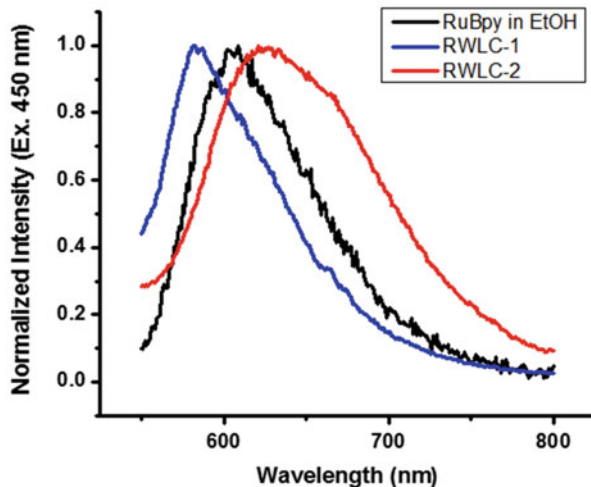


Table 3 Parameters obtained upon fitting of the steady-state emission spectra of RWLC-1, RWLC-2 and RuBpy in ethanol to Eq. (1)

Species	E_{00} (cm^{-1})	$h\omega_M$ (cm^{-1})	$h\omega_L$ (cm^{-1})	S_M	S_L	$\Delta\nu_{1/2}$ (cm^{-1})	Reference
RuBpy in EtOH	16,781	1,258	355	0.64	0.73	1,617	[50]
RWLC-1	17,364	1,589	463	0.62	0.68	1,726	[62]
RWLC-2	16,213	1918	347	0.55	0.73	2,668	[62]

resembling RuBpy@HKUST-1(Zn) (626 nm for RWLC-2 vs. 606 nm for RuBpy in solution) (Fig. 9). Although the steady-state emission data resemble those of the polyhedral MOFs, the Franck-Condon parameters are quite distinct (Table 3). Specifically, the Huang-Rhys parameters are quite similar to those of RuBpy in ethanol indicating that confinement within these MOFs does not distort either the ground or excited state potential surfaces. The shifts in the emission spectra are then likely to be due to differences in the ability of the MOF cavities to stabilize (RWLC-2) or destabilize (RWLC-1) the emitting $^3\text{MLCT}$ states due to electrostatic interactions with the framework MBBs and/or solvent effects.

In the case of RWLC-2, the crystal structure demonstrates that the encapsulated RuBpy cations are located within channels $\sim 9 \text{ \AA}$ [62]. The crystallographic data also shows electron density in this region consistent with disordered water molecules. The bathochromic shift is then consistent with the polar solvent stabilizing the excited state dipole movement associated with the $^3\text{MLCT}$ manifold thus lowering the excited state energy. In the case of RWLC-1, two RuBpy cations are closely packed within the hexagonal cavities with little access to solvent molecules. Rather, the two RuBpy cations are separated by either PF_6^- or Cl^- anions which appear to

Fig. 10 Overlay of the emission decays of RuBpy in ethanol and the RuBpy templated MOFs RWLC-1 and RWLC-2

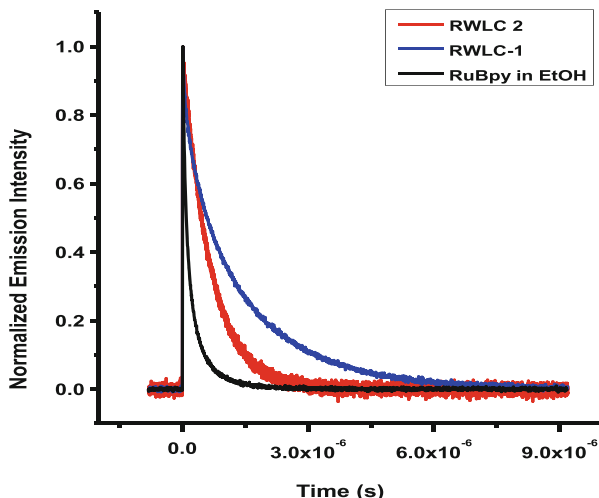


Table 4 Parameters obtained upon fitting of the emission lifetimes of RWLC-1, RWLC-2, and RuBpy in ethanol to Eq. (4)

Species	k_0 (s^{-1})	k_1 (s^{-1})	ΔE_1 (cm^{-1})	τ (ns)	Reference
RuBpy in EtOH	5.6×10^5	5.1×10^{13}	3,661	614	[50]
RWLC-1	3.8×10^6	2.7×10^{13}	3,753	237	[62]
Short lifetime					
RWLC-1	5.3×10^5	2×10^{10}	2,566	1,600	[62]
Long lifetime					
RWLC-2	4.0×10^6	1.3×10^{13}	3,256	171	[62]
Short lifetime					
RWLC-2	7.6×10^5	2×10^{10}	2,198	797	[62]
Long lifetime					

destabilize the 3MLCT state manifold much like the charge associated with the USF2 framework discussed above.

The normalized emission decays for RWLC-1 and RWLC-2 are displayed in Fig. 10. For both materials, the emission decays could be fit to biexponential decay functions. This is somewhat surprising since the crystal structures show only a single population of RuBpy in each material. The RWLC-1 and RWLC-2 MOFs both exhibit populations with lifetimes longer than that observed for RuBpy in ethanol (1,600 ns and 797 ns for RWLC-1 and -2, respectively, and making up 72% of the total population for both MOFs, relative to 614 ns for RuBpy in EtOH). Examination of the decay parameters (see Table 4) demonstrates that the relaxation from the low-lying 3MLCT is unaffected by encapsulation of the RuBpy, while the parameters associated with the thermal population of the 3LF state are quite distinct from RuBpy in solution. Specifically, the ΔE_1 values for RWLC-1 and RWLC-2 (2,566 cm^{-1} and 2,198 cm^{-1} , respectively) are significantly lower than that observed for RuBpy in solution (3,661 cm^{-1}) which should result in a much shorter

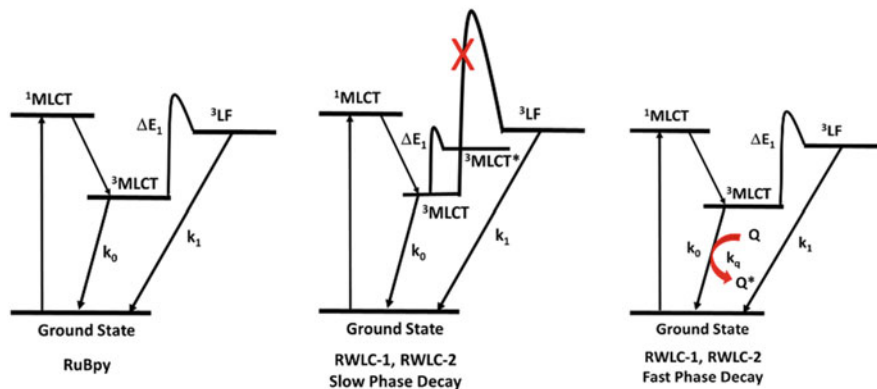


Fig. 11 Proposed energy level diagram for the fast and slow phase decays associated with RuBpy encapsulated within RWLC-1 and RWLC-2, relative to RuBpy in EtOH

lifetime of the RuBpy if the ΔE_1 was attributed to thermal access to the ^3LF state. The fact that the observed emission lifetime is actually longer than RuBpy in solution suggests that the barrier to access the ^3LF is sufficiently high as to prevent any significant population of the state. The values of k_1 associated with RWLC-1 and RWLC-2 are also several orders of magnitude lower than that of RuBpy in solution. These data are consistent with a model in which a population of RuBpy is encapsulated within cavities of the RWLC-1 and RWLC-2 frameworks that restrict access to the ^3LF state. Thus, the ΔE_1 value then represents the barrier to access $^3\text{MLCT}$ states that are higher in energy than the emitting $^3\text{MLCT}$ manifold and the nearby fourth $^3\text{MLCT}$ state (see Fig. 11). Computational studies together with single crystal emission of RuBpy have identified two singlet-like MLCT states which are $\sim 2,442\text{ cm}^{-1}$ and $\sim 3,096\text{ cm}^{-1}$ above the lowest energy $^3\text{MLCT}$ manifold consistent with this hypothesis [54, 55].

What is somewhat striking is the differences between the longer lifetimes of RWLC-1 and RWLC-2 which is almost twofold (1,600 ns for RWLC-1 and 797 ns for RWLC-2). Closer examination of the relaxation parameters reveals two components that contribute to the faster decay for RWLC-2. The first is the ΔE_1 value for RWLC-2 which is $\sim 400\text{ cm}^{-1}$ lower than for RWLC-1, while the values for k_1 are identical. The lower barrier allows for a greater population of the fast-decaying $^3\text{MLCT}^*$ state in RWLC-2. The second is the decay rate constant for the $^3\text{MLCT}$ state manifold (k_1) which is also slightly faster for RWLC-2. Thus, both the higher-energy $^3\text{MLCT}$ population and the emitting $^3\text{MLCT}$ relaxation rate contribute to the overall increase in decay rate. These perturbations are likely due to differences in solvent interactions between the RuBpy cations within the RWLC-2 cavities, relative to RWLC-1 [62].

Examination of the decay parameters for short lifetime component for both RWLC-1 and RWLC-2 is consistent with a population of RuBpy that is located in a less confined environment as evident by the similarity in k_1 and ΔE_1 between the

MOFs and RuBpy in ethanol. In contrast, the decay rate constant for the relaxation of the $^3\text{MLCT}$ to the singlet ground state (k_0) is nearly an order of magnitude larger for RWLC-1 and RWLC-2 relative RuBpy in solution suggesting a quenching process involving either self-quenching (RuBpy complexes encapsulated in close proximity) or the presence of as yet unidentified quenching molecules co-encapsulated with the RuBpy cations.

3.2 The RWLC-3 Templated MOF

The reaction of Zn(II) cations with a smaller 1,4-benzene dicarboxylate (BDC) ligand in dimethylformamide produces the well-known MOF-5 material [66]. The MOF-5 framework exhibits a zeolite-like topology with $[\text{Zn}_4\text{O}]^{6+}$ groups organized into an octahedral array of BDC ligands to form a porous cubic framework of space group (Fm-3 m) [66]. The MOF-5 framework exhibits a surface area of $\sim 3,500 \text{ m}^2 \text{ g}^{-1}$ and a pore volume of 1.2 cm^3 . In the presence of RuBpy cations, the MOF-5 reaction conditions produce a distinctive templated MOF, RWLC-3, which consists of a twofold interpenetrated pillared honeycomb network (Fig. 12) [63]. The two *bnb* networks are interconnected through Zn-O coordination interactions between adjacent Zn clusters. The single *bnb* network consists of trigonal Zn paddlewheel clusters at the honeycomb network vertices that are connected by the BDC ligands. The honeycomb layers are axially connected at the vertices by BDC ligands ultimately forming the three-dimensional *bnb* network. The framework is overall negatively charged with charge balance achieved by the RuBpy cations

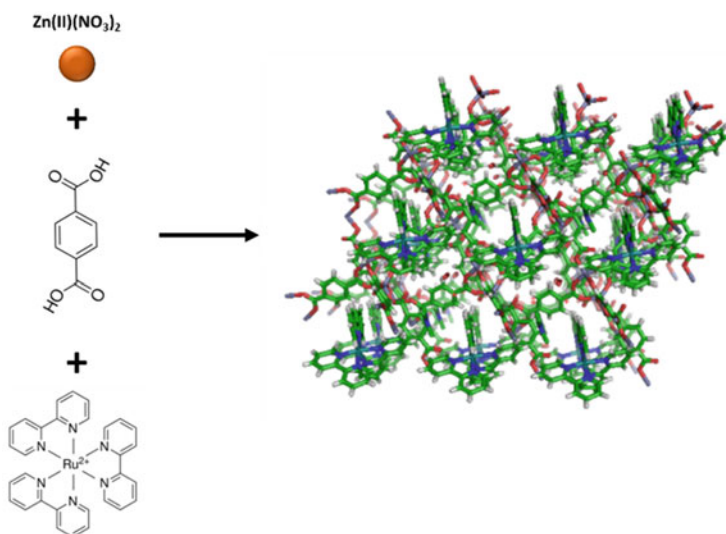


Fig. 12 Diagram illustrating the RuBpy templated formation of RWLC-3 MOF

Fig. 13 Overlay of the steady-state emission spectra of RuBpy in ethanol and RuBpy in RWLC-3

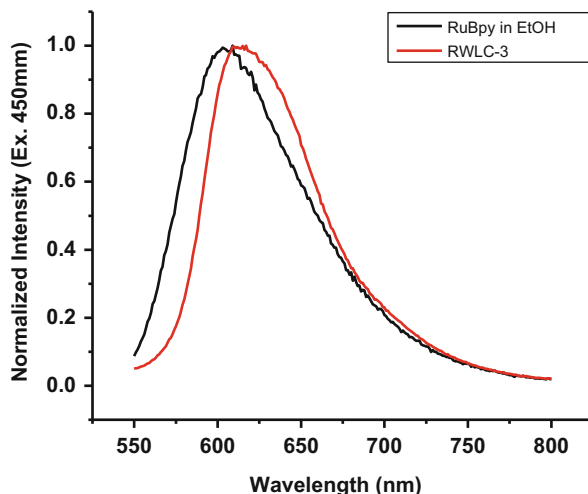


Table 5 Parameters obtained upon fitting of the steady-state emission spectra of RWLC-3 and RuBpy in ethanol to Eq. (1)

Species	E_{00} (cm^{-1})	$h\omega_M$ (cm^{-1})	$h\omega_L$ (cm^{-1})	S_M	S_L	$\Delta\nu_{1/2}$ (cm^{-1})	Reference
RuBpy in EtOH	16,781	1,258	355	0.64	0.73	1,617	[50]
RWLC-3	16,524	2,471	846	0.14	0.19	1,072	[63]

located within the channels. The RuBpy cations are disordered over two well-resolved positions around the inversion center.

The steady-state emission of RWLC-3 is bathochromically shifted by ~ 6 nm which is considerably less than the bathochromic shift observed for RWLC-2 (~ 20 nm relative to RuBpy in EtOH) and opposed to the hypsochromic shift observed for RWLC-1 (~ 23 nm relative to RuBpy in EtOH) (Fig. 13). Examination of the Franck-Condon parameters (Table 5) reveals significant differences in the $^3\text{MLCT}$ state properties relative to the other Zn-carboxylate MOFs specifically with regard to the average medium- and low-frequency coupling modes and the Huang-Rhys parameters (from Eqs. (1) and (2)). The reduction in the E_{00} value indicates stabilization of the $^3\text{MLCT}$ state dipole through interactions with the framework and/or co-encapsulated solvent molecules (disordered). The coupling factors suggest significant differences in excited state potential well displacement much like RuBpy@HKUST-1(Zn) with a $(\Delta Q_{\text{MOF}}/\Delta Q_{\text{Sol}}) \sim 0.3$ (see Eq. (2) and (3)) (Fig. 14).

Like the RWLC-1 and RWLC-2 templated frameworks, the RWLC-3 emission lifetime is best fit to a biexponential function with a short lifetime of 120 ns (58% of the population) and a longer lifetime of 453 ns (42% of the population) (Fig. 15). However, the longer lifetime differs considerably from the other RuBpy encapsulated/templated Zn-carboxylate MOFs in that the magnitude is less than that observed for RuBpy in ethanol (453 ns for RWLC-3 vs. 614 ns for RuBpy in

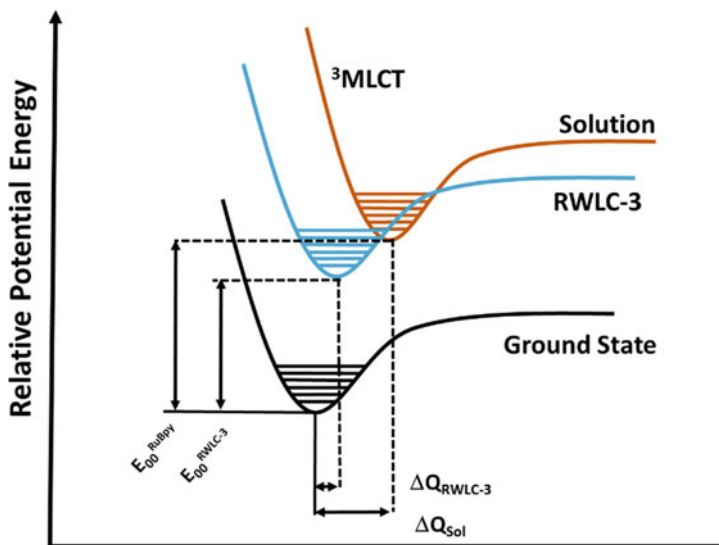


Fig. 14 Diagram illustrating the displacement of the excited state potential surfaces of RWLC-3, relative to RuBpy in solution

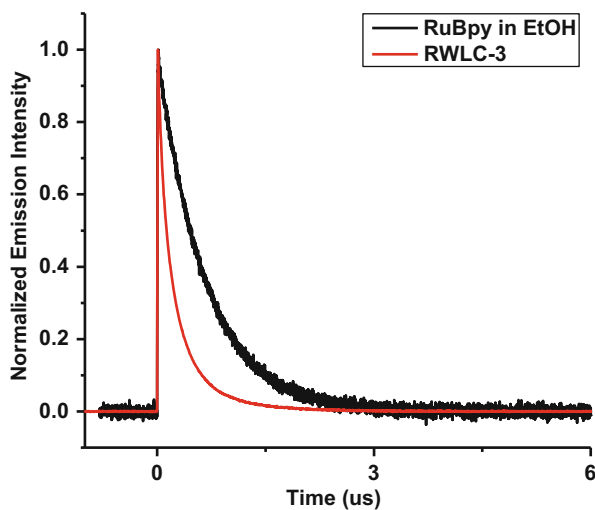


Fig. 15 Overlay of the emission decays of RuBpy in ethanol and the RuBpy templated MOFs RWLC-3

EtOH). The results are quite similar to what has been observed in the RuBpy@ZeoliteY in which the emission lifetime is slightly shorter than that of RuBpy in water (530 ns for RuBpy@ZeoliteY vs. 600 ns for RuBpy in EtOH) [51]. In the case of RuBpy@ZeoliteY, the argument for the lifetime centered on the hypothesis that the barrier to access the ^3LF state is sufficiently high as to preclude

Table 6 Parameters obtained upon fitting of the emission lifetimes of RWLC-3, RuBpy@ZeoliteY and RuBpy in ethanol

Species	k_0 (s^{-1})	k_1 (s^{-1})	ΔE_1 (cm^{-1})	τ (ns)	Reference
RuBpy in EtOH	5.6×10^5	5.1×10^{13}	3,661	614	[50]
RWLC-3 Fast phase	5.4×10^6	1.2×10^{14}	3,624	120	[63]
RWLC-3 Slow phase	3×10^5	1×10^{11}	1,779	453	[63]
RuBpy@ZeoliteY	3.8×10^5	1×10^8	890	530	[51]

occupation and that emission originated from a fourth 3MLCT located at $\sim 900\text{ cm}^{-1}$ above the lowest-energy 3MLCT manifold [51]. From the temperature dependence of the lifetimes (summarized in Table 6), the decay parameters are found to be similar to those for RuBpy@ZeoliteY indicating a similar relaxation pathway with slight differences in cavity environment. The results further highlight the differences in cavity environments between the RWLC-1 and RWLC-2 MOFs and the RWLC-3 MOF with the RWLC-1, -2 cavities providing environments allowing access to singlet in character MLCT states higher in energy than the lowest-energy 3MLCT states and RWLC-3 in which relaxation occurs from the fourth 3MLCT state.

3.3 The RWLC-5 Templated MOF

In order to modify the functional properties of RWLC-3 including framework stability, an attempt was made to replace the Zn(II) cations in the framework with the isoelectronic Cd(II). Using Cd(II) in place of Zn(II) cations in the presence of RuBpy and BDC produces a MOF distinct from the RWLC-3 framework. The Cd framework (RWLC-5) contains RuBpy cations within an anionic framework constructed from $Cd_2Cl_2(COO)_4$ clusters linked through the BDC ligands [65]. The Cd MBB contains bidentate coordination of two carboxylate groups and can be simplified as a 4-connected node similar to a paddlewheel motif. The framework can be summarized as a 4-connected unimodal net of a CdS/CdSO₄ topology. A characteristic feature of this framework is the presence of channels running along the [101] direction with chains of RuBpy cations formed through π - π (between adjacent RuBpy cations) and CH- π interactions (RuBpy cations and the framework ligands). The RuBpy cations are further immobilized between two negatively charged framework metal clusters. The structure also contains disordered water molecules in sites that are within an H-bonding distance with a framework carboxylate and a RuBpy cation with $\sim 34\%$ of these sites being occupied by water molecules. The RWLC-5 framework is stable under drying conditions and in the presence of various solvents including water. No loss in crystallinity is observed over long periods of dry storage (up to 1 year).

The steady-state emission of RWLC-5 is bathochromically shifted by $\sim 24\text{ nm}$ relative to RuBpy in ethanol (630 nm for RWLC-5 vs. 606 nm for RuBpy in EtOH)

Fig. 16 Overlay of the steady-state emission spectra of RuBpy in ethanol and RWLC-5

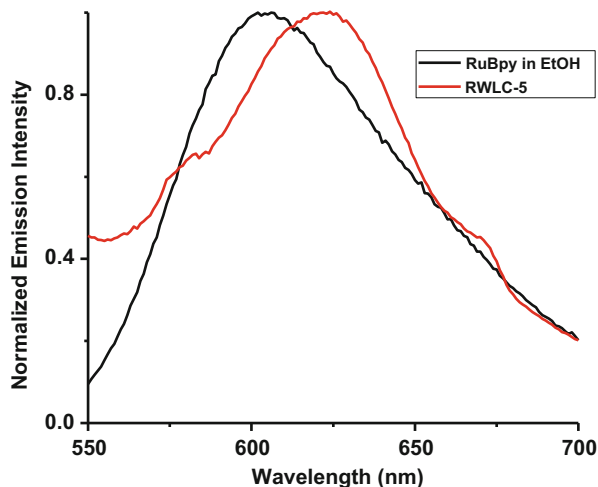
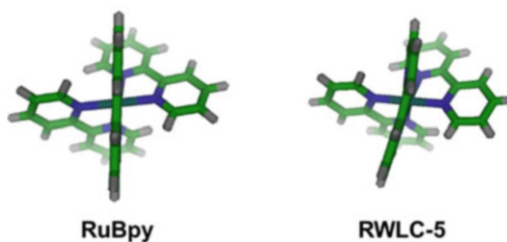


Table 7 Parameters obtained upon fitting of the steady-state emission spectra of RWLC-5 and RuBpy in ethanol to Eq. (1)

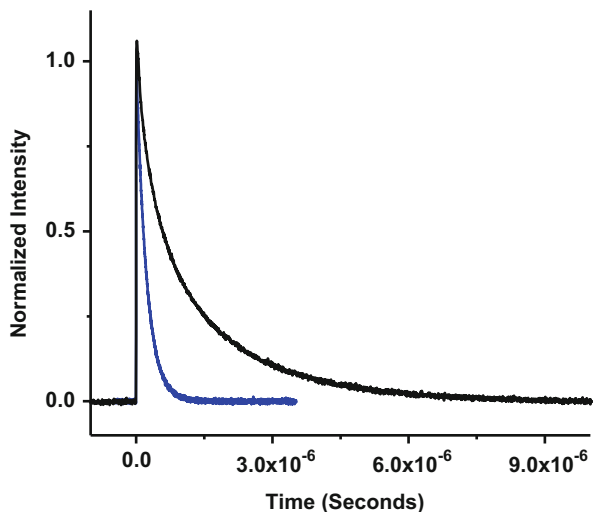
Species	E_{00} (cm^{-1})	$h\omega_M$ (cm^{-1})	$h\omega_L$ (cm^{-1})	S_M	S_L	$\Delta\nu_{1/2}$ (cm^{-1})	Reference
RuBpy in EtOH	16,781	1,258	355	0.64	0.73	1,617	[50]
RWLC-5	15,915	1,738	636	0.31	0.1	1,463	[65]

Fig. 17 Comparison of the structure of RuBpy and RuBpy encapsulated within RWLC-5



similar to RWLC-2 and RuBpy@HKUST-1(Zn) indicating the stabilizing effect of the cavity on the lower-energy $^3\text{MLCT}$ manifold (Fig. 16). The Franck-Condon parameters also indicate a smaller displacement of the $^3\text{MLCT}$ state relative to the ground state (Table 7) relative to RuBpy in ethanol with a $(\Delta Q_{\text{MOF}}/\Delta Q_{\text{Sol}})$ of ~ 0.4 . Unlike with the other RuBpy encapsulated MOFs described here, the X-ray data is of sufficiently high quality to reveal distortions of the 2,2'-bipyridine rings within the encapsulated RuBpy. These distortions are greater for one of the three 2,2'-bipyridine rings (Fig. 17). Preliminary ZINDO/S calculations (data not shown) are consistent with the bathochromic shift being due, at least in part, to these

Fig. 18 Overlay of the emission decays of RuBpy in ethanol and the RuBpy templated MOFs RWLC-5



structural perturbations. It is likely that similar structural perturbations take place in the other members of the RWLC series although the X-ray data is not of sufficient quality to definitively make this determination.

The emission lifetime data for RWLC-5 is displayed in Fig. 18 and is also best fit to a biexponential decay function. The lifetimes obtained from the fits are 126 ns (62% of the population) and 1,167 ns (38% of the population). Unlike the other members of the RWLC series or the Zn-polyhedral MOFs, the emission lifetimes (both short lifetime component and longer lifetime component) display no temperature dependence. The absence of temperature dependence indicates that there are no thermally accessible excited states above or below the lowest-energy $^3\text{MLCT}$ manifold. Of particular interest is the fact that the population of RuBpy cations giving rise to the slow phase lifetime is nearly equivalent to the population of water molecules observed in sites within hydrogen bonding distance to one of the RuBpy 2,2'-bipyridine rings. Thus, it is likely that the hydrogen bonding interaction modulates the non-radiate decay rate from the lowest-energy $^3\text{MLCT}$ manifold to the ground state most likely through alterations to the coupling vibronic density of states.

In the case of the fast phase decay, a k_0 of $6.9 \times 10^6 \text{ s}^{-1}$ is obtained from the lifetime fit which is consistent with quenching of the lowest $^3\text{MLCT}$ manifold, similar to the other members of the RWLC class of templated MOFs. As the population of RuBpy exhibiting the short lifetime is $\sim 62\%$ and the occupancy of the RuBpy in the crystal lattice is $>85\%$, the quenching is likely due to self-quenching of neighboring RuBpy cations that are not influenced by the water-hydrogen bonding interactions.

3.4 The RWLC-6 Templated MOF

The previous series of RWLC RuBpy templated MOFs utilized small benzene carboxylate-type ligands and Zn(II) or Cd(II) metal nodes which produced small cavities with crystallographically resolved RuBpy encapsulated within these cavities. In order to determine if RuBpy could template MOFs with larger cavities, a synthesis was performed using the larger 1,3,5-tris-carboxyphenylethynyl benzene (BTE) ligand which shares the same geometrical arrangement of carboxylate groups as the BTCA ligand used in the synthesis of HKUST-1(Zn) but expands the length of the linker. Under solvothermal conditions, the presence of Zn(II) cations and the BTE ligand forms MOF-180 with cavities of $15 \text{ \AA} \times 23 \text{ \AA}$ forming a *qom* network [67]. However, in the presence of RuBpy under similar conditions, a distinct RWLC-6 MOF is formed consisting of five metal Zn-clusters (Zn(II)/COO-(BTE)/OH-/H₂O) connected through BTE ligands (Fig. 19) [64]. The structure is doubly interpenetrated with RuBpy located in cavities between two negatively charged Zn clusters. The RuBpy is disordered over an inversion symmetry element with Ru atoms located approximately on the inversion center with the occupancy of Ru close to 100% (refined space occupancy $\sim 85\%$). The framework charge appears to be negative with the presence of two OH⁻ groups in the cluster. The negative charge is balanced by the encapsulated RuBpy cations. The presence of electron density in crystalline voids indicates the presence of disordered solvent.

The steady-state emission of RWLC-6 is hypsochromically shifted from RuBpy in solution similar to RWLC-1 and RuBpy@USF2 (601 nm for RWLC-6 vs. 606 nm for RuBpy in EtOH) (Fig. 20) [64]. The hypsochromic shift is likely a result of the disordered solvent molecules and/or environmental effects, similar to what has been described for RuBpy@USF2 [50]. Interestingly, the Franck-Condon parameters are nearly identical to those observed for RuBpy in ethanol suggesting no significant

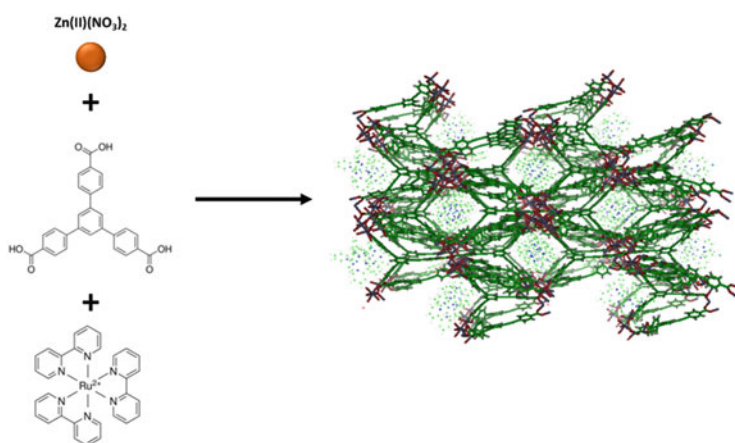


Fig. 19 Diagram illustrating the RuBpy templated formation of RWLC-6 MOF

Fig. 20 Overlay of the steady-state emission spectra of RuBpy in ethanol and RWLC-6

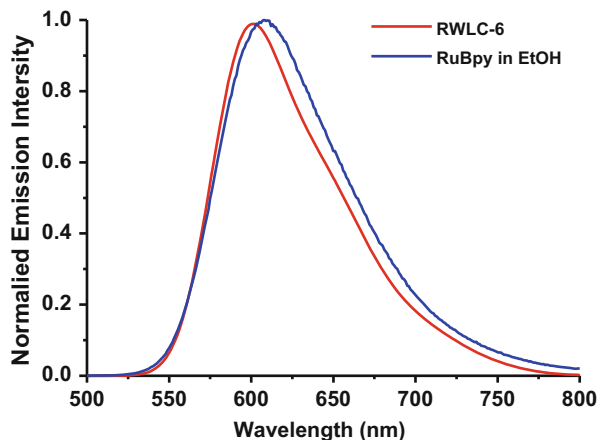


Table 8 Parameters obtained upon fitting of the steady-state emission spectra of RWLC-6 and RuBpy in ethanol to Eq. (1)

Species	E_{00} (cm ⁻¹)	$h\omega_M$ (cm ⁻¹)	$h\omega_L$ (cm ⁻¹)	S_M	S_L	$\Delta\nu_{1/2}$ (cm ⁻¹)	Reference
RuBpy in EtOH	16,781	1,258	355	0.64	0.73	1,617	[50]
RWLC-6	16,927	1,257	391	0.67	0.68	1,396	[64]

Table 9 Parameters obtained upon fitting of the emission lifetimes of RWLC-6 and RuBpy in ethanol

Species	k_0 (s ⁻¹)	k_1 (s ⁻¹)	ΔE_1 (cm ⁻¹)	τ (ns)	Reference
RuBpy in EtOH	5.6×10^5	5.1×10^{13}	3,661	614	[50]
RWLC-6 Fast phase	2.2×10^6	2.4×10^7	454	216	[64]
RWLC-6 Slow phase	5.5×10^5	2.3×10^{14}	3,084	1,032	[64]

perturbations to either the ground or ³MLCT manifold of states. These results are similar to RWLC-1 and RWLC-2 (Table 8).

The emission decay of the RWLC-6 is also best fit using a biexponential function with a short lifetime population having a $\tau \sim 216$ ns (24% of the population) and a longer lifetime population having a $\tau \sim 1,032$ ns (76% of the population) with decay parameters summarized in Table 9 (Fig. 21). The kinetic parameters are quite distinct from other members of the RWLC series. For example, the short lifetime populations in RWLC-1,2 and 3 all have ΔE_1 and k_1 values in the range of what is observed for RuBpy in solution but have k_0 values much larger than RuBpy in solution. This is entirely consistent with a population of RuBpy in which confinement does not restrict access to the ³LF but experience a quenching process that deactivates the lowest-energy ³MLCT manifold possibly by self-quenching with neighboring RuBpy cations. This is clearly not the case for the short lifetime population in

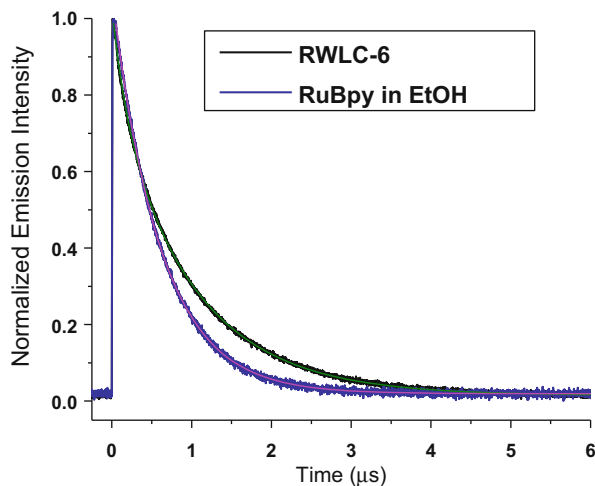


Fig. 21 Overlay of the emission decays of RuBpy in ethanol and the RuBpy templated MOFs RWLC-6

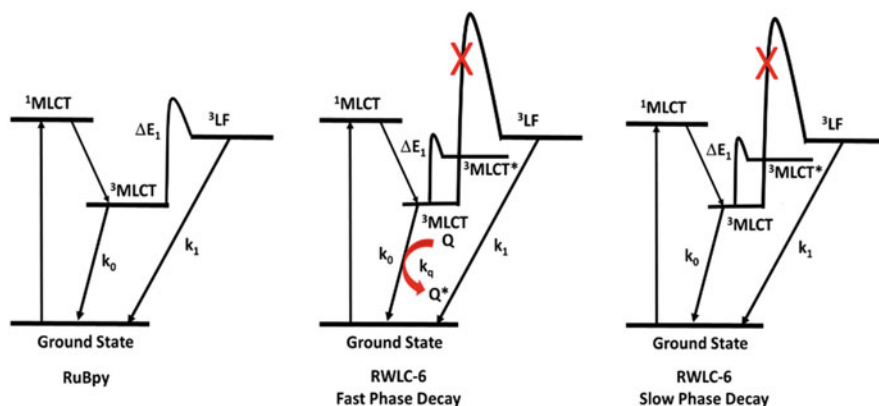


Fig. 22 Proposed energy level diagram for the fast and slow phase decays associated with RuBpy encapsulated within RWLC-6 relative to RuBpy in EtOH

RWLC-6 in which the ΔE_1 and k_1 values are significantly reduced, and the value of k_0 is increased by a factor of ~ 2 . The short lifetime population associated with RWLC-6 is likely one in which the barrier to access the ^3LF state is sufficiently high as to preclude occupation, and the ΔE_1 represents the barrier to access a fourth $^3\text{MLCT}$ (above the emitting $^3\text{MLCT}$ manifold) instead. The increase in k_0 is consistent with RuBpy cations associated with the short lifetime population being in close proximity and undergoing self-quenching (Fig. 22).

The corresponding long lifetime population exhibits a ΔE_1 value in between what is observed for RuBpy in solution and that of the lowest singlet in character MLCT states observed in RWLC-1 and RWLC-2. The fact that the lifetime is greatly

extended for this population indicates that the ΔE_1 barrier is actually that accessing the singlet in character MLCT states and the observed emission decay results from relaxation from both the lowest-energy $^3\text{MLCT}$ manifold and higher-energy $^1/3\text{MLCT}$ excited states. In addition, the k_0 value is also nearly identical to that observed for RuBpy in solution indicating a relaxation from the $^3\text{MLCT}$ is relatively unperturbed.

4 Conclusions and Future Perspectives

The ability to encapsulate photoactive guests, particularly Ru(II) polyimines, into porous MOF frameworks is an important advance in the development of new photoactive/photoresponsive materials. The increasing number of photoactive guest-MOFs is also providing a unique opportunity to examine the mechanisms through which encapsulation within varying cavity types can modulate the photophysics of the photoactive guest. The summary presented here of RuBpy encapsulation within Zn-carboxylate-based MOFs provides insights into such mechanisms. Several general features are evident. First, the energy associated with the emitting $^3\text{MLCT}$ depends on both the accessibility of the RuBpy to solvent within the cavities and to the overall framework charge. Second, in nearly all cases, encapsulation increases the barrier to access the ^3LF , which should lead to stabilization of the RuBpy ligands. In addition, other MLCT states, including a fourth $^3\text{MLCT}$ state above the emitting $^3\text{MLCT}$ state manifold and other high-energy $^1/3\text{MLCT}$ states, become accessible and modulate the rate of emission decay. Finally, in nearly all cases, the emission decays could be fit to a biexponential function indicating two populations of encapsulated RuBpy with a population of short lifetime RuBpy cations that appear to have quenched $^3\text{MLCT}$ manifolds. The longer lifetimes are associated with populations of RuBpy in structurally confined cavities that are not accessible to either exogenous quenchers or neighboring RuBpy allowing for self-quenching. These observations provide an important framework from which a more detailed analysis of cavity structure-photophysical modulation relationships can be performed.

The results summarized in this chapter provide a foundation for understanding the effects of encapsulation of transition metal cations on their corresponding photophysics. With the present catalog of MOFs with well-resolved RuBpy cations, it is now possible to examine the molecular details that modulate the electronic states of the encapsulated guest. Specifically, the relationship between structural distortions associated with RuBpy encapsulation and the observed photophysics can now be compared with intermolecular interactions between the RuBpy and elements of the framework. The overall intent is to utilize cavity-RuBpy photophysical relationships in order to produce light-responsive materials “by design.” These studies also provide a platform through which to modulate the photophysical properties of other transition metal complexes through encapsulation within MOF-type materials.

References

1. Zhou H-C, Long JR, Yaghi OM (2012) Introduction to metal–organic frameworks. *Chem Rev* 112(2):673–674
2. Moulton B, Zaworotko MJ (2001) From molecules to crystal engineering: supramolecular isomerism and polymorphism in network solids. *Chem Rev* 101(6):1629–1658
3. Eddaoudi M, Moler DB, Li H, Chen B, Reineke TM, O’Keeffe M, Yaghi OM (2001) Modular chemistry: secondary building units as a basis for the design of highly porous and robust metal–organic carboxylate frameworks. *Acc Chem Res* 34(4):319–330
4. Li J-R, Sculley J, Zhou H-C (2012) Metal–organic frameworks for separations. *Chem Rev* 112(2):869–932
5. Horcajada P, Gref R, Baati T, Allan PK, Maurin G, Couvreur P, Férey G, Morris RE, Serre C (2012) Metal–organic frameworks in biomedicine. *Chem Rev* 112(2):1232–1268
6. Paillaud J-L, Harbuzaru B, Patarin J, Bats N (2004) Extra-large-pore zeolites with two-dimensional channels formed by 14 and 12 rings. *Science* 304(5673):990
7. Cook TR, Zheng Y-R, Stang PJ (2013) Metal–organic frameworks and self-assembled supramolecular coordination complexes: comparing and contrasting the design, synthesis, and functionality of metal–organic materials. *Chem Rev* 113(1):734–777
8. Cheetham AK, Férey G, Loiseau T (1999) Open-framework inorganic materials. *Angew Chem Int Ed* 38(22):3268–3292
9. Brant JA, Liu Y, Sava DF, Beauchamp D, Eddaoudi M (2006) Single-metal-ion-based molecular building blocks (MBBs) approach to the design and synthesis of metal–organic assemblies. *J Mol Struct* 796(1):160–164
10. Corma A (1997) From microporous to mesoporous molecular sieve materials and their use in catalysis. *Chem Rev* 97(6):2373–2420
11. Davis ME (2002) Ordered porous materials for emerging applications. *Nature* 417:813–821
12. Corma A, Davis ME (2004) Issues in the synthesis of crystalline molecular sieves: towards the crystallization of low framework-density structures. *ChemPhysChem* 5(3):304–313
13. Song L, Wang Y-J, Chai W-X (2019) A diamond-type metal-organic framework based on nano-sized [Cu₈(μ₄-I)₆(PPh₃)₄]₂⁺ clusters and cyanide-ion linkers: design, structure and luminescent property. *Inorg Chem Commun* 104:190–196
14. Mitzi DB (2019) Introduction: perovskites. *Chem Rev* 119(5):3033–3035
15. Saparov B, Mitzi DB (2016) Organic–inorganic perovskites: structural versatility for functional materials design. *Chem Rev* 116(7):4558–4596
16. Bourikas K, Kordulis C, Lycourghiotis A (2014) Titanium dioxide (anatase and rutile): surface chemistry, liquid–solid interface chemistry, and scientific synthesis of supported catalysts. *Chem Rev* 114(19):9754–9823
17. Huskić I, Pekov IV, Krivovichev SV, Friščić T (2016) Minerals with metal-organic framework structures. *Sci Adv* 2(8):e1600621
18. Li B, Wen H-M, Zhou W, Chen B (2014) Porous metal–organic frameworks for gas storage and separation: what, how, and why? *J Phys Chem Lett* 5(20):3468–3479
19. Ma S, Zhou H-C (2010) Gas storage in porous metal–organic frameworks for clean energy applications. *Chem Commun* 46(1):44–53
20. Goldsmith J, Wong-Foy AG, Cafarella MJ, Siegel DJ (2013) Theoretical limits of hydrogen storage in metal–organic frameworks: opportunities and trade-offs. *Chem Mater* 25(16):3373–3382
21. Zhang Z, Zhao Y, Gong Q, Li Z, Li J (2013) MOFs for CO₂ capture and separation from flue gas mixtures: the effect of multifunctional sites on their adsorption capacity and selectivity. *Chem Commun* 49(7):653–661
22. Britt D, Tranchemontagne D, Yaghi OM (2008) Metal-organic frameworks with high capacity and selectivity for harmful gases. *Proc Natl Acad Sci* 105(33):11623

23. Dhakshinamoorthy A, Asiri AM, Garcia H (2017) Tuneable nature of metal organic frameworks as heterogeneous solid catalysts for alcohol oxidation. *Chem Commun* 53 (79):10851–10869
24. Black CA, Costa JS, Fu WT, Massera C, Roubeau O, Teat SJ, Aromí G, Gamez P, Reedijk J (2009) 3-D lanthanide metal-organic frameworks: structure, photoluminescence, and magnetism. *Inorg Chem* 48(3):1062–1068
25. Parker D, Dickins RS, Puschmann H, Crossland C, Howard JAK (2002) Being excited by lanthanide coordination complexes: aqua species, chirality, excited-state chemistry, and exchange dynamics. *Chem Rev* 102(6):1977–2010
26. Allendorf MD, Bauer CA, Bhakta RK, Houk RJT (2009) Luminescent metal-organic frameworks. *Chem Soc Rev* 38(5):1330–1352
27. Rocha J, Carlos LD, Paz FAA, Ananias D (2011) Luminescent multifunctional lanthanides-based metal-organic frameworks. *Chem Soc Rev* 40(2):926–940
28. Lee J, Farha OK, Roberts J, Scheidt KA, Nguyen ST, Hupp JT (2009) Metal-organic framework materials as catalysts. *Chem Soc Rev* 38(5):1450–1459
29. Huh S, Kim S-J, Kim Y (2016) Porphyrinic metal-organic frameworks from custom-designed porphyrins. *CrystEngComm* 18(3):345–368
30. He Z, Pang Q, Rankine D, Sumby CJ, Zhang L, Doonan CJ, Li Q (2013) Encapsulation of polyoxometalates within layered metal-organic frameworks with topological and pore control. *CrystEngComm* 15(45):9340–9343
31. Chui SSY, Lo SMF, Charmant JPH, Orpen AG, Williams ID (1999) A chemically functionalizable nanoporous material [Cu₃(TMA)₂(H₂O)₃]_n. *Science* 283(5405):1148–1150
32. Song J, Luo Z, Britt DK, Furukawa H, Yaghi OM, Hardcastle KI, Hill CL (2011) A multiunit catalyst with synergistic stability and reactivity: a polyoxometalate-metal organic framework for aerobic decontamination. *J Am Chem Soc* 133(42):16839–16846
33. Wee LH, Wiktor C, Turner S, Vanderlinden W, Janssens N, Bajpe SR, Houthoofd K, Van Tendeloo G, De Feyter S, Kirschhock CEA, Martens JA (2012) Copper benzene tricarboxylate metal-organic framework with wide permanent mesopores stabilized by keggin polyoxometallate ions. *J Am Chem Soc* 134(26):10911–10919
34. Alkordi MH, Liu Y, Larsen RW, Eubank JF, Eddaoudi M (2008) Zeolite-like metal-organic frameworks as platforms for applications: on metalloporphyrin-based catalysts. *J Am Chem Soc* 130(38):12639–12641
35. Larsen RW, Wojtas L, Perman J, Musselman RL, Zaworotko MJ, Vetromile CM (2011) Mimicking heme enzymes in the solid state: metal-organic materials with selectively encapsulated heme. *J Am Chem Soc* 133(27):10356–10359
36. Larsen RW, Miksovskaja J, Musselman RL, Wojtas L (2011) Ground- and excited-state properties of Zn(II) tetrakis(4-tetramethylpyridyl) porphyrin specifically encapsulated within a Zn (II) HKUST metal-organic framework. *J Phys Chem A* 115(42):11519–11524
37. Sen R, Koner S, Bhattacharjee A, Kusz J, Miyashita Y, Okamoto K-I (2011) Entrapment of [Ru (bpy)₃]²⁺ in the anionic metal-organic framework: novel photoluminescence behavior exhibiting dual emission at room temperature. *Dalton Trans* 40(26):6952–6960
38. Balzani V, Juris A, Venturi M, Campagna S, Serroni S (1996) Luminescent and redox-active polynuclear transition metal complexes. *Chem Rev* 96(2):759–834
39. Meyer TJ (1986) Photochemistry of metal coordination complexes: metal to ligand charge transfer excited states. *Pure Appl Chem* 58(9):1193–1206
40. Strouse GF, Schoonover JR, Duesing R, Boyde S, Jones Jr WE, Meyer TJ (1995) Influence of electronic delocalization in metal-to-ligand charge transfer excited states. *Inorg Chem* 34 (2):473–487
41. Caspar JV, Meyer TJ (1983) Photochemistry of MLCT excited states. Effect of nonchromophoric ligand variations on photophysical properties in the series cis-Ru(bpy)₂L₂²⁺. *Inorg Chem* 22(17):2444–2453
42. Rosi NL, Eckert J, Eddaoudi M, Vodak DT, Kim J, Keeffe M, Yaghi OM (2003) Hydrogen storage in microporous metal-organic frameworks. *Science* 300(5622):1127

43. Furukawa H, Go YB, Ko N, Park YK, Uribe-Romo FJ, Kim J, O’Keeffe M, Yaghi OM (2011) Isoreticular expansion of metal–organic frameworks with triangular and square building units and the lowest calculated density for porous crystals. *Inorg Chem* 50(18):9147–9152
44. Yaghi OM, O’Keeffe M, Ockwig NW, Chae HK, Eddaoudi M, Kim J (2003) Reticular synthesis and the design of new materials. *Nature* 423(6941):705–714
45. Bourne SA, Lu J, Mondal A, Moulton B, Zaworotko MJ (2001) Self-assembly of nanometer-scale secondary building units into an undulating two-dimensional network with two types of hydrophobic cavity. *Angew Chem Int Ed* 40(11):2111–2113
46. Farha OK, Wilmer CE, Eryazici I, Hauser BG, Parilla PA, O’Neill K, Sarjeant AA, Nguyen ST, Snurr RQ, Hupp JT (2012) Designing higher surface area metal–organic frameworks: are triple bonds better than phenyls? *J Am Chem Soc* 134(24):9860–9863
47. Ma S, Sun D, Simmons JM, Collier CD, Yuan D, Zhou H-C (2008) Metal-organic framework from an anthracene derivative containing nanoscopic cages exhibiting high methane uptake. *J Am Chem Soc* 130(3):1012–1016
48. Yan Y, Blake AJ, Lewis W, Barnett SA, Dailly A, Champness NR, Schröder M (2011) Modifying cage structures in metal–organic polyhedral frameworks for H₂ storage. *Chem Eur J* 17(40):11162–11170
49. Lu J, Mondal A, Moulton B, Zaworotko MJ (2001) Polygons and faceted polyhedra and nanoporous networks. *Angew Chem Int Ed* 40(11):2113–2116
50. Larsen RW, Wojtas L (2012) Photophysical studies of Ru(II)tris(2,2′-bipyridine) confined within a Zn(II)-trimesic acid polyhedral metal-organic framework. *J Phys Chem A* 116(30):7830–7835
51. McKeithan CR, Mayers JM, Wojtas L, Larsen RW (2018) Photophysical studies of Ru(II)tris(2,2′-bipyridine) encapsulated within the ZnHKUST-1 metal organic framework. *Inorg Chim Acta* 483:1–5
52. Lainé P, Lanz M, Calzaferri G (1996) Limits of the in situ synthesis of Tris(2,2′-bipyridine) ruthenium(II) in the supercages of zeolite Y. *Inorg Chem* 35(12):3514–3518
53. Caspar JV, Meyer TJ (1983) Photochemistry of tris(2,2′-bipyridine)ruthenium(2+) ion (Ru(bpy)₃2+). Solvent effects. *J Am Chem Soc* 105(17):5583–5590
54. Komada Y, Yamauchi S, Hirota N (1988) Phosphorescence properties of lower emitting states of [Ru(bpy)₃](ClO₄)₂. *J Phys Chem* 92:6511–6518
55. Heully JL, Alary F, Boggio-Pasqua M (2009) Spin-orbit effects on the photophysical properties of Ru(bpy)₃2+. *J Chem Phys* 131(18):184308
56. Dhotel A, Chen Z, Delbreilh L, Youssef B, Saiter J-M, Tan L (2013) Molecular motions in functional self-assembled nanostructures. *Int J Mol Sci* 14(2):2303–2333
57. Liu Y, Goebel J, Yin Y (2013) Templated synthesis of nanostructured materials. *Chem Soc Rev* 42(7):2610–2653
58. Santra A, Bharadwaj PK (2014) Solvent-induced structural diversity of partially fluorinated, stable Pb(II) metal–organic frameworks and their luminescence properties. *Cryst Growth Des* 14(3):1476–1485
59. Zhang Z, Zaworotko MJ (2014) Template-directed synthesis of metal–organic materials. *Chem Soc Rev* 43(16):5444–5455
60. Liu Y, Liu S, He D, Li N, Ji Y, Zheng Z, Luo F, Liu S, Shi Z, Hu C (2015) Crystal facets make a profound difference in polyoxometalate-containing metal–organic frameworks as catalysts for biodiesel production. *J Am Chem Soc* 137(39):12697–12703
61. Xie J (2008) Investigation of inorganic–organic hybrid materials containing polyoxometalate cluster anions and organic dye cations. *J Coord Chem* 61(24):3993–4003
62. Whittington CL, Wojtas L, Larsen RW (2014) Ruthenium(II) tris(2,2′-bipyridine)-templated zinc(II) 1,3,5-tris(4-carboxyphenyl)benzene metal organic frameworks: structural characterization and photophysical properties. *Inorg Chem* 53(1):160–166
63. Whittington CL, Wojtas L, Gao WY, Ma S, Larsen RW (2015) A new photoactive Ru(II)tris(2,2′-bipyridine) templated Zn(II) benzene-1,4-dicarboxylate metal organic framework: structure and photophysical properties. *Dalton Trans* 44(12):5331–5337

64. McKeithan CR, Wojtas L, Larsen RW (2019) Photophysical properties of the [Ru(2,2'-bipyridine)₃]²⁺ templated metal organic framework, RWLC-6. *Inorg Chim Acta* 496:119034
65. Larsen RW, Mayers JM, Wojtas L (2017) A novel photo-active Cd:1,4-benzene dicarboxylate metal organic framework templated using [Ru(II)(2,2'-bipyridine)₃]²⁺: synthesis and photophysics of RWLC-5. *Dalton Trans* 46(37):12711–12716
66. Li H, Eddaoudi M, O’Keeffe M, Yaghi OM (1999) Design and synthesis of an exceptionally stable and highly porous metal-organic framework. *Nature* 402:276
67. Furukawa H, Ko N, Go YB, Aratani N, Choi SB, Choi E, Yazaydin AÖ, Snurr RQ, O’Keeffe M, Kim J, Yaghi OM (2010) Ultrahigh porosity in metal-organic frameworks. *Science* 329(5990):424

Tuning Emission Properties by Dye Encapsulation into Layered Silicates



Yohei Ishida and Shinsuke Takagi

Contents

1 Emission of Dyes	186
2 Layered Silicates	187
3 Photochemical Property and Layered Materials	189
4 Complex of Dyes and Layered Silicates	190
5 Photochemical Properties of Dyes in/on Layered Silicates	192
6 Emission Enhancement of Dyes in/on Layered Silicates (Surface-Fixation Induced Emission (S-FIE))	196
7 Color Tuning of Dyes in/on Layered Silicates	198
8 Reversible Environment-Responsiveness of Dyes in/on Layered Silicates	199
9 Summary	201
References	202

Abstract This chapter describes the emission behavior of molecules on the surface of layered materials. Emission properties of molecules depend on their surrounding environment. Even in homogeneous environments, this emission behavior depends on solvent effects such as viscosity, permittivity, polarity, and so on. While the chemical reaction media provided by layered materials is the analog of solvent effects, the effect of layered materials induces important changes in the properties of the molecule. For example, the emission intensity could be enhanced 100 times by the complex formation with layered materials. Despite the drastic effect of layered materials on the photochemical properties of molecules, the use of layered materials is limited due to some factors. One of these factors is the complicated complex formation behavior of molecules on layered materials. This sometimes includes

Y. Ishida
Division of Material Science and Engineering, Faculty of Engineering, Hokkaido University,
Hokkaido, Japan
e-mail: ishida-yohei@eng.hokudai.ac.jp

S. Takagi (✉)
Department of Applied Chemistry, Graduate Course of Urban Environmental, Sciences, Tokyo
Metropolitan University, Tokyo, Japan
e-mail: takagi-shinsuke@tmu.ac.jp

segregation and aggregation that induce changes in photochemical properties. In recent decades, the intrinsic photochemical properties of molecules on layered materials were clarified by the progress in techniques to prepare complexes between molecules and layered materials. These examples will be described in this chapter.

Keywords Chromism · Emission · Fluorescence · Layered materials · Synthetic clay · Transition probability

Abbreviations

<i>p</i> -TMPyP	Tetrakis(N-methylpyridinium-4-yl)porphyrin
AFM	Atomic force microscopy
AIE	Aggregation-induced emission
CEC	Cation exchange capacity
DMF	Dimethylformamide
SSA	Saponite
S-FIE	Surface-fixation induced emission
TPAB	1,3,5-Tris[(<i>N</i> -pyridinium)aniline-4-yl]-benzene
XRD	X-ray diffraction

1 Emission of Dyes

This section briefly describes the main photophysical processes of chromophores. The energy diagram of a molecule is shown in Fig. 1. Before absorbing light, the molecule exists at an electronically ground state (S_0). When the temperature is low enough, the vibrational state of the molecule is supposed to be $\nu = 0$. An electronically excited state (S_n ($\nu = 0, 1, 2, \dots$)) is produced when the molecule absorbs light. Absorption is governed by the transition probability rule [1, 2]. In the case that

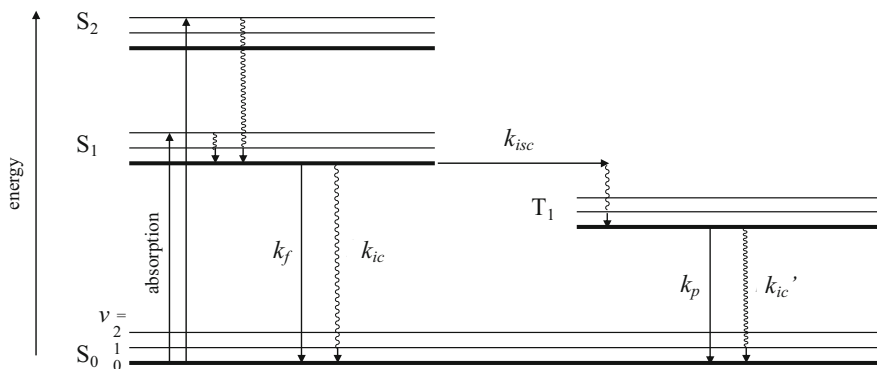


Fig. 1 An exemplar state energy diagram for molecular organic photochemistry

the produced excited state is thermally activated ($\nu \geq 1$), thermal relaxation to $\nu = 0$ occurs. According to Kasha's rule [1], relaxation from S_n ($n \geq 2$) to S_1 is fast. In general, the lowest excited state (S_1 ($\nu = 0$)) is the active electronically excited state. Several processes are possible from the active electronically excited state (S_1 ($\nu = 0$)). These processes include thermal deactivation to the electronically ground state (S_0 ($\nu = 0, 1, 2, \dots$)), radiative deactivation to the electronically ground state (S_0 ($\nu = 0, 1, 2, \dots$)), and an intersystem crossing to the triplet state, as shown in Fig. 1. The rate constants are expressed as k_{ic} , k_{fl} , and k_{isc} , respectively. The rate constants are governed by the rules in transition probability [2, 3] such as the Franck-Condon factor. Each molecule has its own individual rate constants. The quantum yield (Φ) is an important parameter for these processes. The emission from S_1 is called fluorescence. In the case of fluorescence quantum yield (Φ_f), Φ_f is the ratio m/n where n is the absorbed photon number and m is the emitted photon number. Φ_f is expressed as $k_{fl}/(k_{fl} + k_{ic} + k_{isc})$. As is the case with the S_1 state, the T_1 state deactivates through thermal and radiative processes. According to the energy gap law [4], T_1 state tends to suffer thermal deactivation; thus, to observe emission from T_1 , a low temperature condition is necessary in general. Emission between states with the same spin quantum number is called fluorescence, whereas that with a different spin quantum number is called phosphorescence. In this chapter, the effects of layered materials on the processes shown in Fig. 1, especially on emission behavior, are described. Change in the energy state affects the emission wavelength that is the emission color. On the contrary, change in transition probabilities affects the emission quantum yield.

2 Layered Silicates

Layered materials [5–9] are host materials with a two-dimensional structure. Clay minerals, graphene, layered double hydroxide, and so on are typical layered materials. Clay minerals are aluminum phyllosilicates, sometimes with iron, magnesium, and alkali metals in the structure. In this chapter, we focused on synthetic saponites because they are commonly used and well characterized. Their characteristic features include (1) nanostructured flat sheets that can be formed by elements with a high Clarke number, (2) negatively or positively charged surfaces, (3) exfoliation or stacking ability of individual nanosheets depending on the surrounding conditions, (4) an interlayer space whose volume can be reversibly changed, and (5) optical transparency in solution when the particle size is small (<50 nm) and the concentration is not too high. The molecules on the surface can change their structure, intramolecular vibrational motion, and so on, which could then alter their photochemical properties.

Particularly in the case of artificially synthesized clay, the composition is clear and purity is quite high. Sumecton SA (Kunimine, Japan) and Laponite (BYK, Germany) are commercially available clays. The composition of Sumecton SA is $[(Si^{4+}_{7.2}Al^{3+}_{0.8})(Mg_6)O_{20}(OH)_4]^{-0.8} 0.8Na^+$, and its structure is shown as Fig. 2a.

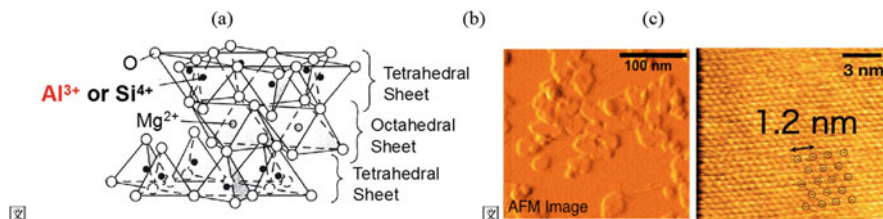


Fig. 2 (a) Unit structure of synthetic saponite. This unit is two-dimensionally connected and forms disc-shaped particles. Replacement of Si^{4+} with Al^{3+} affords an anionic charge in the structure. (b) AFM image of clay particles. (c) AFM image of the surface of a clay particle and the ideal distribution of anionic charge

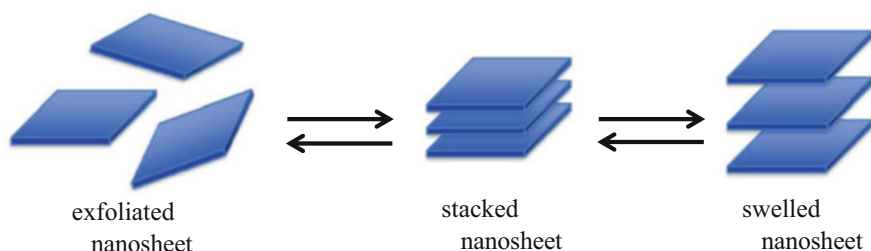


Fig. 3 The exfoliated, stacked, and swelled state of clay nanosheets

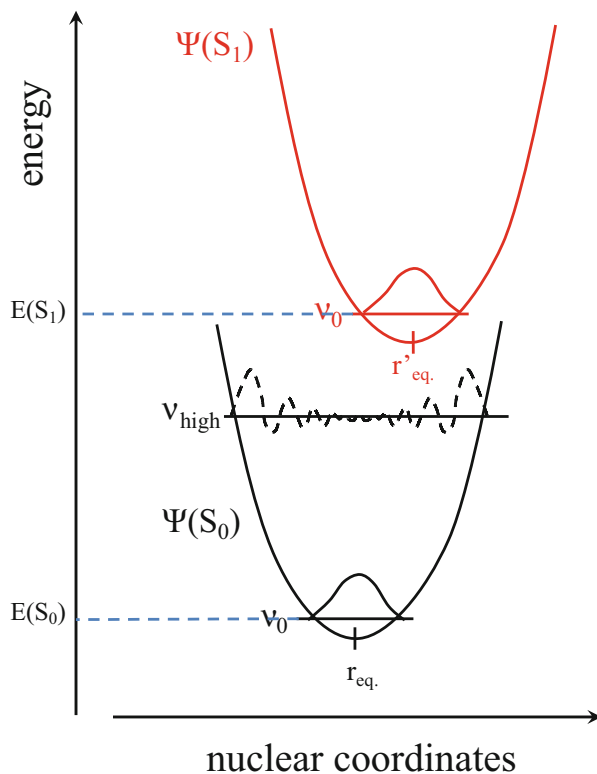
Isomorphous substitution of Si^{4+} with Al^{3+} in the tetrahedral layer produces anionic charges in the structure. The unit structure can be extended widely in two dimensions. In this case, the average intercharge distance on the clay surface is calculated to be 1.2 nm in the hexagonal array because the cation exchange capacity (CEC) is 0.997 meq g^{-1} and the theoretical surface area is $7.5 \times 10^2 \text{ m}^2 \text{ g}^{-1}$. In the case of Sumecton SA, there are few silanol groups on the siloxane surface, whereas a silanol group exists at the edge. Because of these features of clay, guest molecules can interact with clay by electrostatic, hydrophobic, and van der Waals interactions.

While clay nanosheets tend to stack especially in the solid state, they can swell or exfoliate into a single nanosheet in solution. In the case of Sumecton SA, the nanosheets completely exfoliate in water. Reversibility between the exfoliated and stacked state is a unique structural property of layered materials (Fig. 3). In special cases, nanosheets can be scrolled like a cigar [10, 11]. These structural changes are related to the photochemical behavior of the adsorbed guest molecules.

3 Photochemical Property and Layered Materials

The properties of a molecule are affected by its surrounding field. Especially in the case of photochemical properties, the effect of the surrounding field is large. Effects on (1) molecular structure, (2) solvation, (3) intermolecular interactions, and so on are expected. The typical potential curves for the S_0 and S_1 state are shown in Fig. 4. This figure is analogous to the Jablonski diagram shown in Fig. 1. For diatomic molecules, the horizontal axis indicates the interatomic distance. In the case of typical molecules, it indicates a molecular structure that is multi-dimensional. In the figure, r_{eq} and r'_{eq} indicate the most stable structure for S_0 and S_1 , respectively. Because the electronic state between S_0 and S_1 is different, their most stable structure is not the same ($r_{\text{eq}} \neq r'_{\text{eq}}$). At the S_1 state in Fig. 4, there are two relaxation pathways. One is radiative and the other is nonradiative deactivation. The probability is governed by the overlap of wave functions between (S_1, ν_0) and ($S_0, \nu_0, 1, 2, \dots$) for radiative deactivation. On the contrary, this is governed by the overlap of wave functions between (S_1, ν_0) and (S_0, ν_{high}) for nonradiative deactivation. Depending on the surrounding chemical reaction field, the value of r_{eq} , r'_{eq} , $E(S_0)$, and $E(S_1)$ in Fig. 4 and even the shape of $\Psi(S_0)$ and $\Psi(S_1)$ are affected. These effects of the

Fig. 4 Potential energy curve for the S_0 and S_1 states



chemical reaction field around the molecule change the photochemical properties of the molecule such as absorption wavelength, fluorescence wavelength, absorption coefficient, and fluorescence quantum yield. For example, when $\Delta E (= |E(S_0) - E(S_1)|)$ is decreased, the absorption and fluorescence wavelength are shortened, and fluorescence quantum yield tends to decrease because of the energy gap law [12–17]. On the other hand, when $\Delta r (= |r_{eq.} - r_{eq.}|)$ is decreased, the fluorescence quantum yield tends to be large, because the overlap of wave functions between (S_1, ν_0) and (S_0, ν_0) and that between (S_1, ν_0) and (S_0, ν_{high}) become large and small, respectively.

How do layered silicates as a chemical reaction field affect the photochemical property of a molecule? The major effects of layered silicates are as follows. (1) The molecule itself suffers changes in molecular structure and its molecular motion. It is expected that the molecular structure becomes more planar and its motion is suppressed on the surface of the layered silicate, because of the flat surface of the layered silicates at the atomic level. (2) The molecule is in a high local concentration and tends to form aggregates. Molecular aggregation also affects photochemical properties because of the interaction between transition dipole moments. The details of these effects will be described in the next section.

4 Complex of Dyes and Layered Silicates

The dye molecule and layered silicates form complexes through attractive interactions such as electrostatic and hydrophobic interactions. In the case of saponite that is a typical anionic layered silicate, cationic molecules can be adsorbed on the surface of layered silicates mainly by the electrostatic interactions. For example, it is well known that methylene blue (Fig. 5) is easily adsorbed on layered silicates in an aqueous solution or dispersion [18–22]. Complex formation behavior can be monitored by UV-vis absorption measurements. The absorption spectra of methylene blue change with the time after mixing each solution [19, 22] as can be seen in Fig. 5. In this system, there is an interaction between the layered silicate and methylene blue as well as between methylene blue molecules, leading to the formation of aggregates. In the case of organic molecules, aggregates are easily formed on the layered silicate surface in aqueous suspension, mainly because of hydrophobic interactions. Typical aggregates are H- and J-type aggregates, which are non-emissive and emissive, respectively [18]. Although an assembly including H- and J-type aggregates on layered silicates is unique, even for J-aggregates, the excited lifetime of the molecule on layered silicates tends to be short; therefore, molecules on layered silicates are less photochemically active in general. Many researchers have felt that it is difficult to use layered silicates as a platform to construct photochemical reaction systems and photo-functional materials.

In recent years, techniques to control the assembly of structures on layered silicates have been developed [7, 23–32]. In the suitable combination of anionic saponite and tetrakis(N-methylpyridinium-4-yl)porphyrin (*p*-TMPyP), aggregation

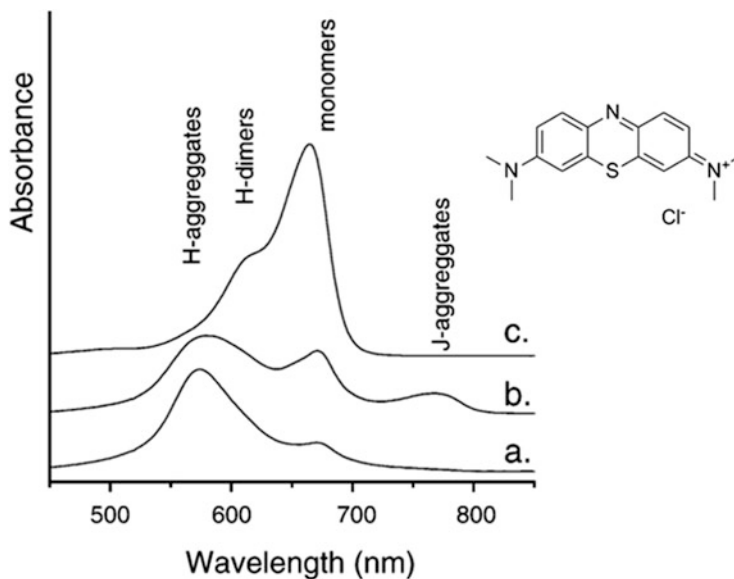


Fig. 5 Visible spectra of methylene blue in Kunipia montmorillonite dispersion and aqueous solution. The spectra of the dispersion measured at 1 min (a) and 24 h (b) after mixing the dye solution with the clay dispersion are compared with the MB solution (c). The dye concentration is 2.5 $\mu\text{mol/L}$ and the ratio dye/clay = 0.05 mmol/g. Reproduced with permission from Elsevier [19]

was found to be completely suppressed [23, 24, 29]. In this system, porphyrin was adsorbed on the surface of saponite at up to 100% vs. the cation exchange capacity of the clay (CEC) without any aggregation. The absorption spectra of *p*-TMPyP with a loading range of 10–150% vs. CEC are shown in Fig. 6. As observed, up to 100% vs. CEC, the spectral shape was the same, indicating non-aggregate formation. Above 100% vs. CEC, a new band appears in the absorption spectra at shorter wavelength ascribed to non-adsorbed dye species. When the adsorption rate is 100% vs. CEC, the average intermolecular distance of *p*-TMPyP is 2.4 nm for a typical saponite. In addition to absorption behavior, fluorescence does not suffer concentration quenching in the case of *p*-TMPyP [33, 34]. The mechanism to suppress aggregate formation on saponite is rationalized as follows. The inter-anionic charge distance on the saponite surface is calculated to be 1.2 nm based on the hexagonal array, and the inter-cationic distance in *p*-TMPyP is around 1.03 nm. Because of the good electrostatic matching between saponite and *p*-TMPyP, the interaction between saponite and *p*-TMPyP is quite strong. Therefore, aggregation between *p*-TMPyP and *p*-TMPyP is suppressed (Fig. 7). Because the relative interchange charge-matching plays an important role, this mechanism is called the “size-matching effect” [7, 23–32]. This complex, *p*-TMPyP, is photochemically active and subjected to physicochemical observation.

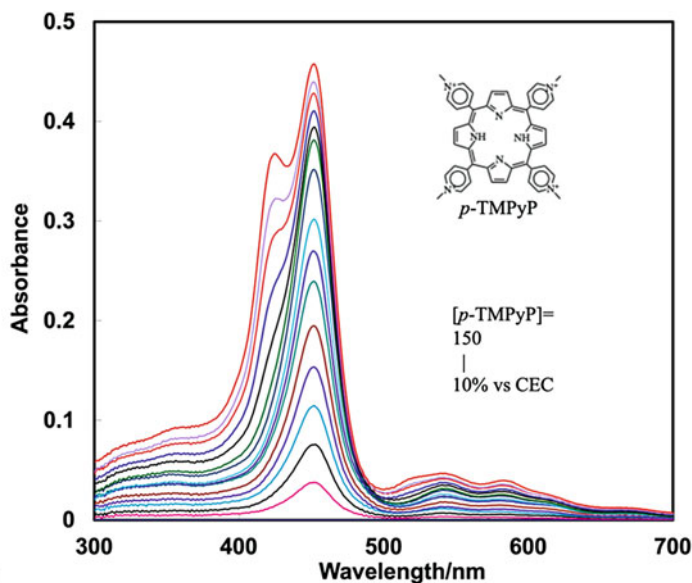


Fig. 6 Absorption spectra of SSA-*p*-TMPyP complex at various concentrations of *p*-TMPyP up to 150% vs. CEC

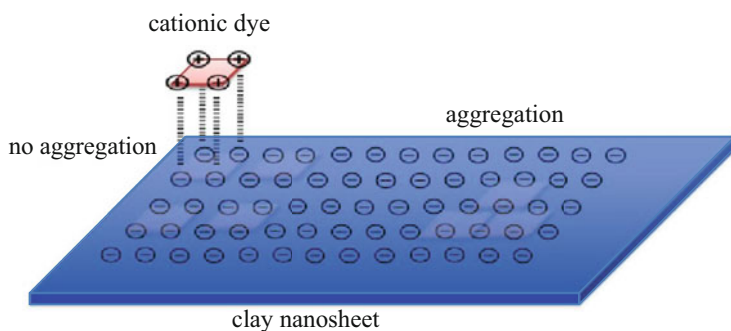


Fig. 7 Size-matching effect for clay-dye complexes

5 Photochemical Properties of Dyes in/on Layered Silicates

The photophysical features of a molecule on layered silicates are much different compared to that in solution. For example, a large red shift in absorption spectra is observed for porphyrin derivatives upon complex formation with saponite [23, 24, 29, 35–37]. The absorption spectra of porphyrin derivatives on the surface and between the sheets (intercalated) are shown in Fig. 8. Surprisingly, the λ_{max} of MgTMPyP reaches 500 nm by complex formation with saponite [38]. Systematic

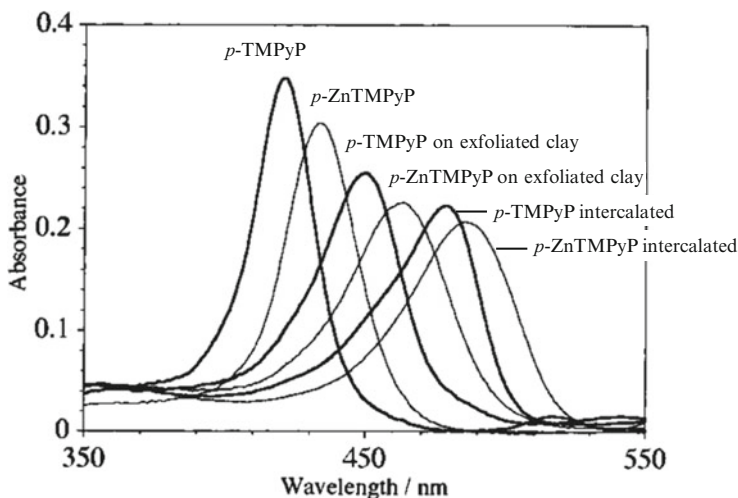


Fig. 8 Absorption spectra of cationic porphyrins with clay and without clay in the Soret band region. [synthetic saponite] = 500 mg L⁻¹, [porphyrin] = 1.0 × 10⁻⁶ M (0.8% vs. CEC). Porphyrins are *p*-TMPyP and *p*-ZnTMPyP. Reproduced with permission from the American Chemical Society with a slight modification [64]

experiments using a series of porphyrin derivatives directly confirmed that a flattening in the molecular structure of the porphyrin molecule is the dominant mechanism for the spectral shift on the saponite surface [31]. Because the flatness of saponite is quite high, such effect is expected to be larger than that of other host materials.

In addition to absorption behavior, other photochemical properties are also affected by complex formation with layered silicates. The most stationary stable structure, as well as the motion of the molecule, should be affected by adsorption. The intramolecular motion of the molecule on layered silicates surface is expected to be restricted similarly as the molecule at low temperature or in a “frozen” state. In fact, suppression of nonradiative deactivation was observed for many cases on layered silicates [39–46]. On the contrary, the radiative deactivation process could be enhanced because of an increase in the Franck-Condon factor [39, 46]. These factors directly change the fluorescence behavior of the molecule. The resulting fluorescence quantum yield (ϕ_f) is expressed as in Eq. (1).

$$\phi_f = k_{fl} / (k_{ic} + k_{fl} + k_{isc}) \quad (1)$$

To enhance the ϕ_f , an increase in k_{fl} and/or a decrease in $k_{ic} + k_{isc}$ is necessary. k_{fl} and $k_{ic} + k_{isc}$ can be calculated using the values of ϕ_f and fluorescence lifetimes (τ) according to Eqs. (2) and (3).

$$k_{fl} = \phi_f / \tau \quad (2)$$

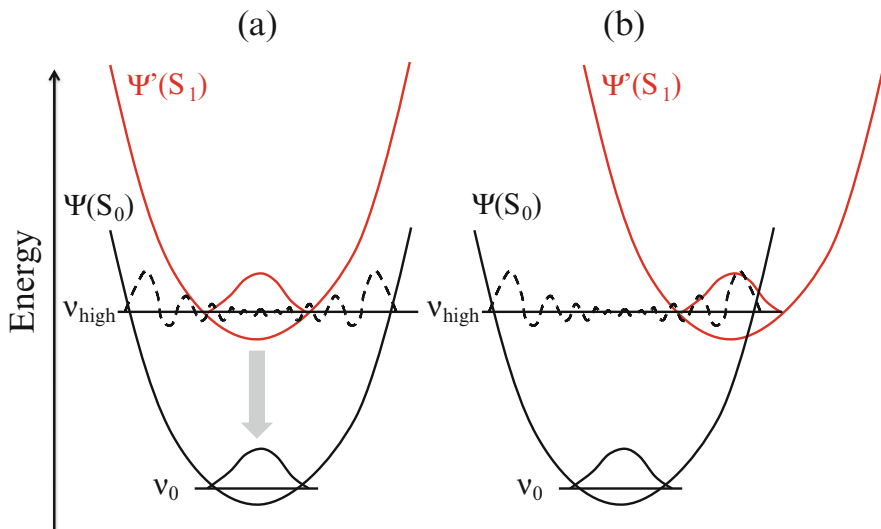
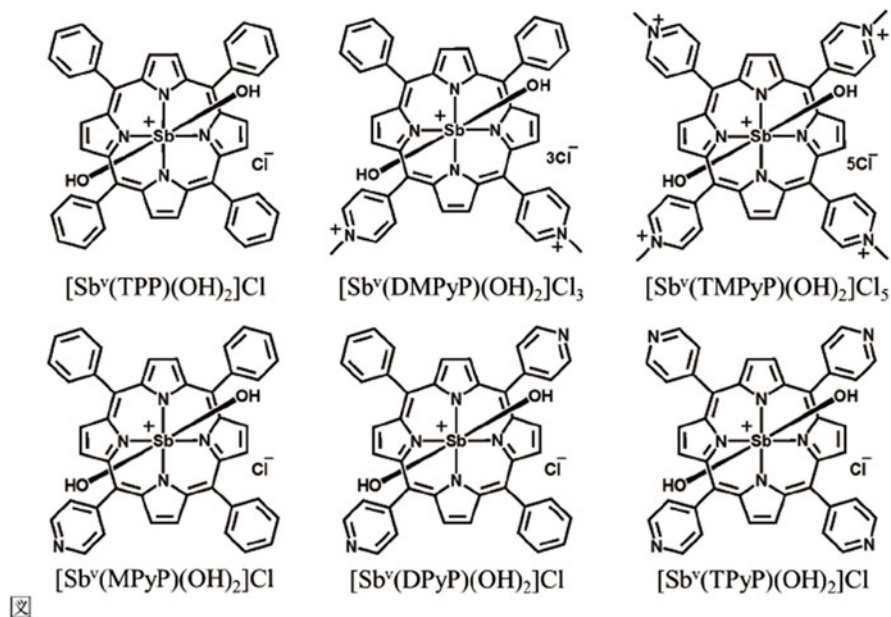


Fig. 9 Plausible conceptual potential energy curves of the ground and excited states of a molecule (a) on saponite and (b) in solution. Reproduced with permission from the Royal Society of Chemistry with a slight modification [41]

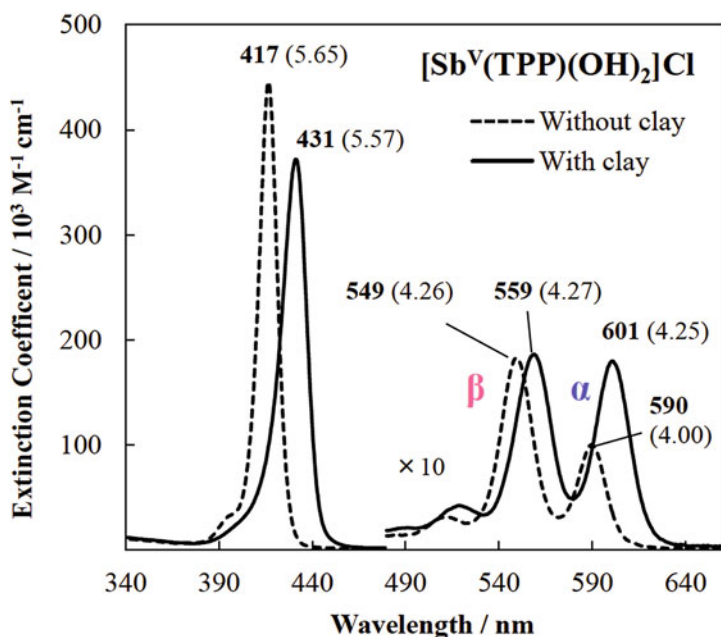
$$k_{ic} + k_{isc} = k_{fl}/\phi_{fl} - k_{fl} \quad (3)$$

The effect of the saponite surface on these parameters has been examined for several molecules. The effect of adsorption on saponite was discussed using potential energy curves. Of course, this model is too simple, and it is useful for qualitative discussion. The plausible conceptual potential energy curves for a molecule in the electronically ground and excited state on saponite (a) and in solution (b) are shown in Fig. 9. On saponite (a), it is expected that the stationary stable structure of the excited state is similar to that of the ground state, because the molecule is fixed on the saponite surface, especially in the case of a cationic molecule. In such a case, k_{fl} and k_{ic} tend to be large and small, respectively, compared to the case in solution (b). In Fig. 9, although the curve shape is expressed in the same manner, it is also expected that the curve shape becomes sharper by the complex formation with saponite. These effects can induce various changes in the photochemical properties of the molecule.

Other than the absorption spectral shift as shown in Fig. 8, an interesting effect of clay nanosheet according to Fig. 9 was observed for Sb(V)porphyrins. The absorption spectra of Sb(V)porphyrin derivatives in solution (a) and on saponite (b) are shown in Fig. 10 [40, 41]. The absorption coefficient is shown in parentheses. In many cases, the intensity of the α band was increased by complex formation with saponite. In other cases, an apparent increase in the absorption coefficient was observed [34]. These examples indicate that the potential energy surface of molecules is much affected by complex formation with saponite. In the next section, the effect of saponite on emission behavior will be detailed.



☒



☒

Fig. 10 Top: Structures of dihydroxo(5,10,15,20-tetraphenylporphyrinato)antimony(V) chloride ($[\text{Sb}^{\text{V}}(\text{TPP})(\text{OH})_2]^{1+}$), dihydroxo[5,10-diphenyl-15,20-di(*N*-methyl-pyridinium-4-yl)porphyrinato]antimony(V) trichloride ($[\text{Sb}^{\text{V}}(\text{DMPyP})(\text{OH})_2]^{3+}$), dihydroxo[5,10,15,20-tetrakis(*N*-methyl-pyridinium-4-yl)porphyrinato]-antimony(V) pentachloride ($[\text{Sb}^{\text{V}}(\text{TMPyP})(\text{OH})_2]^{5+}$), dihydroxo[5,10,15-triphenyl-20-mono(4-pyridyl)-porphyrinato]antimony(V)chloride ($[\text{Sb}^{\text{V}}(\text{MPyP})(\text{OH})_2]^{1+}$), dihydroxo[5,15-diphenyl-10,20-di(4-pyridyl)porphyrinato]antimony(V) chloride

6 Emission Enhancement of Dyes in/on Layered Silicates (Surface-Fixation Induced Emission (S-FIE))

In general, observation and analysis of molecules on a solid surface is not easy because they undergo various complicated phenomena such as aggregation [12]. On using the size-matching effect, the photochemical behavior of adsorbed molecules becomes simple. As monomeric species can be easily obtained even on solid surfaces using the size-matching effect, the intrinsic photochemical properties of monomer molecules on solid surfaces can be observed and studied. In recent years, studies have shown that the fluorescence intensity is highly enhanced by complex formation in layered silicates in general. One of the early examples of this effect is the fluorescence enhancement of methyl viologen on clay reported by C. Detellier et al. [47, 48]. While methyl viologen is not emissive in aqueous solution, it becomes emissive when adsorbed on the clay surface. Although the fluorescence suffers concentration quenching as the adsorption density increases, it is still enhanced by more than hundred times. After this discovery, the size-matching effect was established, and since then many examples of the fluorescence enhancement effect in layered silicates have been found. In Fig. 11, the fluorescence enhancement behavior of 1,3,5-tris[(*N*-pyridinium)aniline-4-yl]-benzene (TPAB) by complex formation with saponite is shown [49]. The fluorescence quantum yield (ϕ_f) increased from 0.077 to 0.42 on complexation with clay. In this case, the radiative rate constant (k_{fl}) increased from $0.081 \times 10^9 \text{ s}^{-1}$ to $0.13 \times 10^9 \text{ s}^{-1}$, and the nonradiative rate constant (k_{ic}) decreased from $0.97 \times 10^9 \text{ s}^{-1}$ to $0.19 \times 10^9 \text{ s}^{-1}$, respectively. In this case, the effects of saponite on both k_{fl} and k_{ic} enhance the fluorescence intensity. Such fluorescence enhancement behavior was named “surface-fixation induced emission (S-FIE)” [46]. Nowadays, another type of emission behavior named “aggregation-induced emission (AIE)” receives a lot of attention from the viewpoint of biological and chemical probes and optoelectronic systems [50–52]. In the case of AIE, the suppression of vibrational motion leading to the radiationless dissipation of the exciton energy in an aggregation state could play an important role in emission enhancement. Although S-FIE has some similarities to AIE in terms of the actual phenomenon and mechanism, each process possesses different advantages. In the case of S-FIE, the photophysical observation and analysis is easy, because the sample solution is transparent and the photochemical behavior is simple. It should be noted that the fluorescence decay curve can be analyzed by single exponential

Fig. 10 (continued) ($[\text{Sb}^{\text{V}}(\text{DPyP})(\text{OH})_2]^{1+}$), and dihydroxo[5,10,15,20-tetra(4-pyridyl)porphyrinato]antimony(V) chloride ($[\text{Sb}^{\text{V}}(\text{TPyP})(\text{OH})_2]^{1+}$). Bottom: The absorption spectra of $[\text{Sb}^{\text{V}}(\text{TPP})(\text{OH})_2]^{1+}$ in solution and on saponite. The absorption coefficient ($\log \epsilon$) is shown in parentheses. Reprinted with permission from *J. Phys. Chem. A*, 2013, 117, 7823–7832 with a slight modification. Copyright (2013) American Chemical Society. Reproduced with permission from The Royal Society of Chemistry with a slight modification [41]

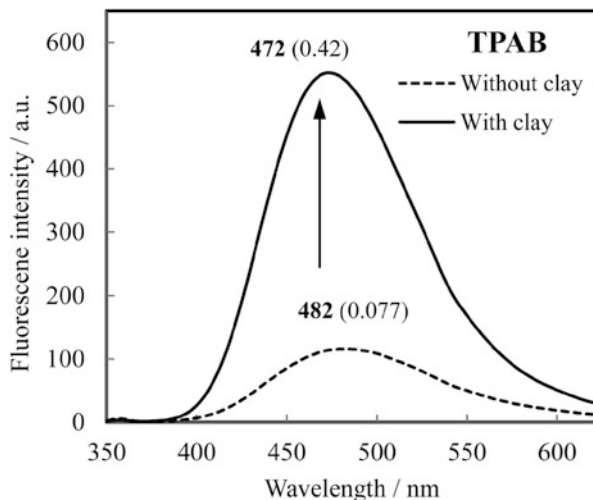


Fig. 11 The fluorescence enhancement behavior of 1,3,5-tris[*N*-pyridinium]aniline-4-yl]-benzene (TPAB) by complexing with clay. Reproduced with permission from the American Chemical Society with a slight modification [49]

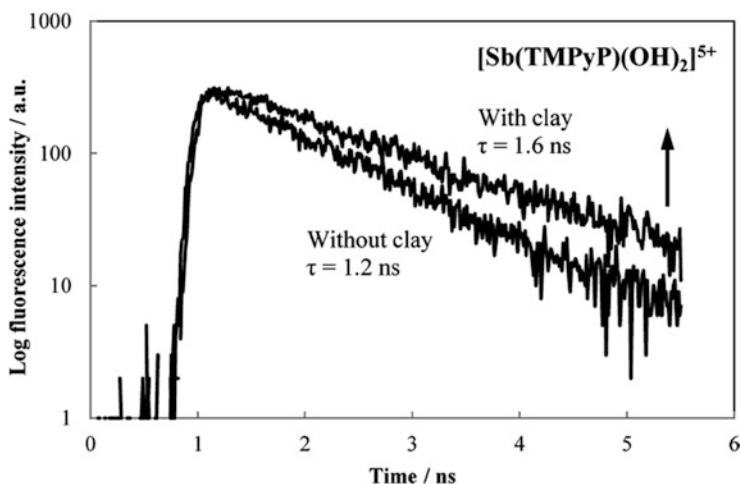


Fig. 12 Fluorescence decay profile and fluorescence lifetimes (τ) of porphyrins excited with and without clay in water. The porphyrin loadings on the clay surface were 5×10^{-4} molecules nm^{-2} . Reproduced with permission from the American Chemical Society with a slight modification [40]

fitting as shown in Fig. 12. Studies on the presence of this effect in various molecules showed that k_{nr} increased in many cases and k_f sometimes increased by complexing with clay depending on the type of molecule [38]. Two theories, namely, structure

resembling effect and structure fixing effect, were proposed to explain the fluorescence enhancement behavior in clay [38].

The photochemical property should strongly depend on the surrounding environment such as a solution, solid surface, mesopore, and so on. So far, it has been difficult to discuss the photochemical properties in such media. The layered silicate surface is expected to be an ideal media to explore the effect of the chemical reaction field. The authors expect that novel methods for X-fixation induced emission ($X = \text{glass, metal, zeolite, MOF, and so on}$) will be discovered. It should be noted that the behavior of the solid surface is unique not only for emission properties but also for chemical reactions. The photo-isomerization reaction [53], artificial light harvesting system, and artificial photosynthetic system have been examined on layered silicate surface.

7 Color Tuning of Dyes in/on Layered Silicates

The spectral shift in the absorption spectra of layered silicates was described in Sect. 5. Similarly, the spectral shift in the emission spectra is also possible, and thus, layered silicates can tune the emission color of molecules. The typical procedure to tune the emission color requires organic synthesis, where the synthetic process is determined based on the precise design. This process is expensive and time-consuming, while complexation with clay is quite simple. The example of fluorescence color change is shown in Figs. 13 and 14 [43]. For $m\text{-B}^{\text{III}}\text{TMPySp}$ and $p\text{-B}^{\text{III}}\text{TMPySp}$, color changes from green to yellow and from orange to red were observed, respectively.

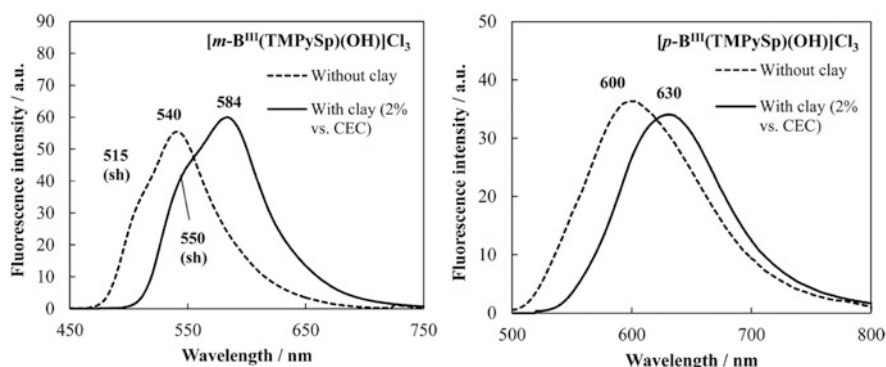


Fig. 13 Fluorescence spectra normalized by absorbance at excitation wavelength. The excitation wavelengths are 370 and 400 nm for $m\text{-B}^{\text{III}}\text{TMPySp}$ and 398 and 426 nm for $p\text{-B}^{\text{III}}\text{TMPySp}$ without and with the saponite in water, respectively. Fluorescence maxima values ($\lambda_{\text{fl}}/\text{nm}$) are shown in spectra. [subporphyrin] = 1.0×10^{-7} M (Loading levels of the subporphyrins were 2.0% versus CEC of the saponite.). Reproduced with permission from the American Chemical Society with a slight modification [43]

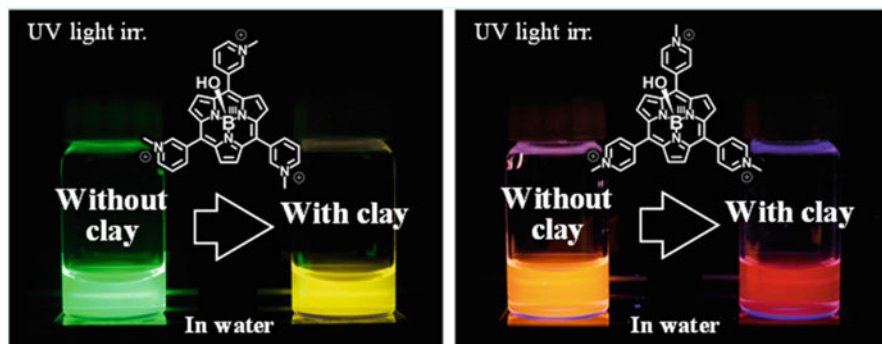


Fig. 14 Changes in fluorescence color of *m*-B^{III}TMPySp and *p*-B^{III}TMPySp without and with the saponite excited at 365 nm in water. [B^{III}TMPySp] = 2.7×10^{-6} M (0.4% versus CEC of the saponite)

8 Reversible Environment-Responsiveness of Dyes in/on Layered Silicates

The complex formed by layered silicates and guest molecules is considered as a supramolecular system. Thus, it is expected that the structure is flexible and responds to environmental change. For example, a change in the adsorption orientation angle of molecules on the saponite surface (Fig. 15) was reported [54–58]. Planar aromatic

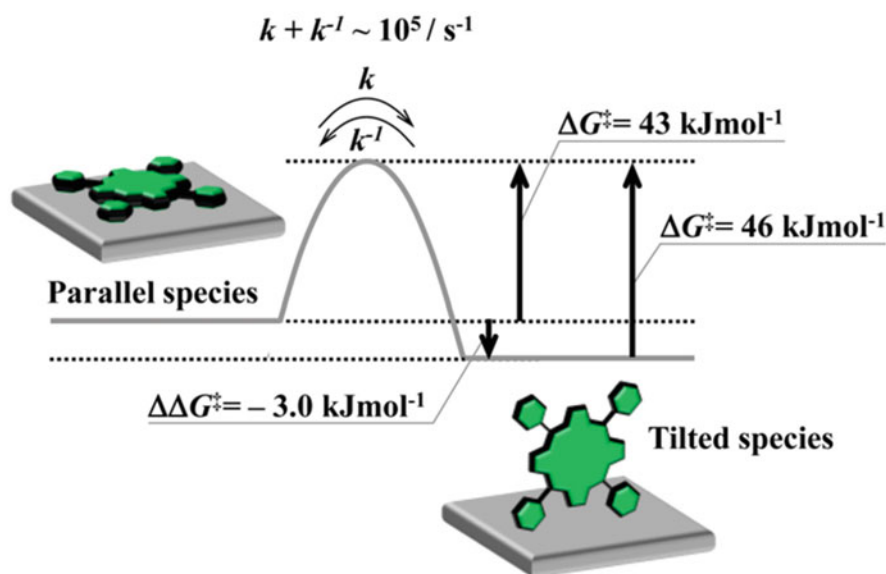


Fig. 15 Energy diagram of the transition between the parallel and tilted adsorbed species in the ground state at 300 K, revealed by static and kinetic studies. Reproduced with permission from the American Chemical Society with a slight modification [58]

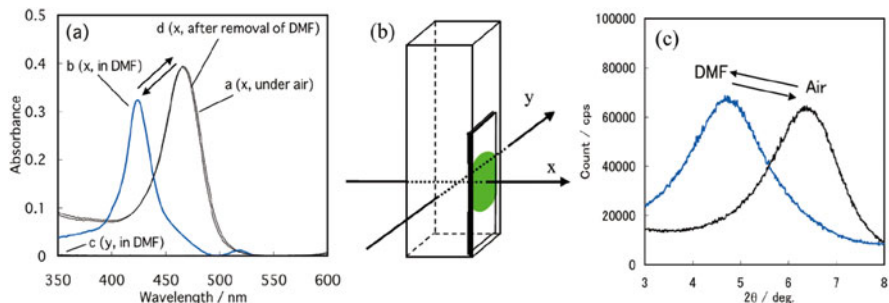


Fig. 16 (a) Absorption spectra of porphyrin-clay film from the x-direction under air (line a), from the x- and y-directions in DMF (lines b and c), and from the x-direction after removal of DMF and drying (line d). (b) Setup for absorption measurement. (c) XRD pattern of clay-porphyrin membrane covered with DMF and under air

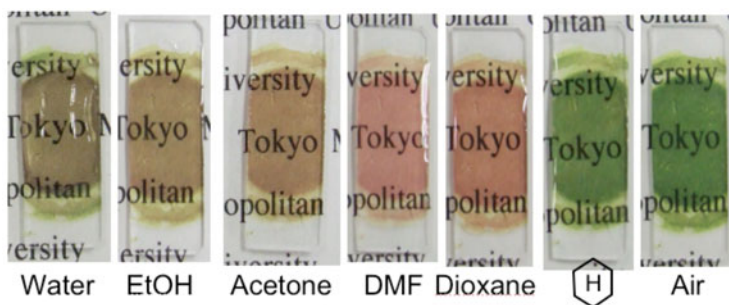


Fig. 17 Picture of porphyrin-clay membrane on the glass. The film is covered by various solvents. Reproduced with permission from the American Chemical Society with a slight modification [59]

molecules tend to be adsorbed in a way where the aromatic system of the molecule and silicate surface are parallel to each other, mainly due to the hydrophobic interaction between them in aqueous solution. By changing the solvent composition, it was found that the adsorption orientation was no longer parallel [54–58]. In a parallel adsorption state, the adsorbed molecule experiences the steric effect of the surface. On the other hand, in a non-parallel (tilted) adsorption state, the adsorbed molecule does not experience such steric effect of the surface, and the situation is similar to that in the bulk solution.

By exploiting the reversible change in molecular orientation, environmentally responsive materials can be constructed, because orientation change can induce a color change. For example, dye-clay complexes have been reported to exhibit solvatochromic [59] and chromism effects, based on changes in humidity [60]. Transparent films composed of these dye-clay complexes can be used as sensors. The absorption spectra of the porphyrin-clay film covered by dimethylformamide (DMF) in air are shown in Fig. 16a. The color of the porphyrin-clay films changes between green and brown, depending on the surrounding solvents, as can be seen in Fig. 17. The change in absorption was completely

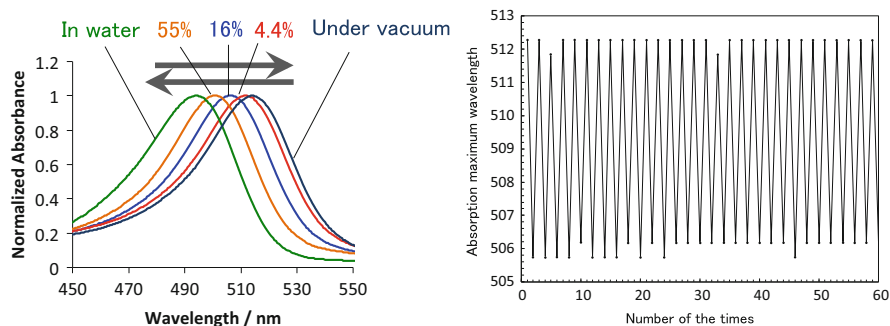


Fig. 18 Absorption spectra of MgTMPyP/saponite hybrid film under vacuum or in wet air and (a) the stability for repeated chromism. Reproduced with permission from the American Chemical Society with a slight modification [60]

synchronized with the change in interlayer distance, as can be seen in Fig. 16c. As this chromism does not include atomic bond fission and rearrangement, consequently the reversibility and repeating stability are expected to be quite high. The chromism behavior of Mg porphyrin-clay membrane is shown in Fig. 18. In this case, the chromism reversibility is demonstrated (Fig. 18).

9 Summary

All molecules are affected by their surrounding environment. For homogeneous systems, physicochemical studies are easy to perform and have been conducted extensively, for example, the solvent effects. Undoubtedly, the properties of the dye differ depending on the chemical reaction field mainly in heterogeneous systems such as gas phase, liquid phase, micelles, vesicles, reverse micelles, solid surfaces, layered compounds, mesoporous materials, zeolites, and solid phase. Heterogeneous materials complicate various phenomena due to their non-uniformity and are not easy to study scientifically. However, since layered compounds provide a flat surface at the atomic level, the physicochemical study becomes rather easy, compared to other heterogeneous chemical reaction fields. In the past, research on such heterogeneous chemical reaction fields progressed in the field of application and industrial use, while academic understanding was delayed. The authors believe that layered silicates can aid in the development of both the basic science and application-based aspects. In this chapter, we have focused on the monomolecular nature of dyes, but the aggregate structure of dyes on layered silicates is also interesting. In fact, an artificial photosynthesis system [61–63] based on the arranging an artificial light harvesting system [64–70] and molecular photocatalysts [62, 71] has been reported. In this chapter, we mainly discussed saponites as layered silicates, but there are many other types of layered compounds, including layered semiconductors that exhibit

redox activity [72–76] and graphene [77–79]. The role of layered compounds is an ever-expanding field of chemistry.

References

1. Kasha M (1950) *Discuss Faraday Soc* 9:14–19
2. Turro NJ (1991) *Modern molecular photochemistry*. University Science Books, Mill Valley
3. Lakowicz JR (2006) *Principles of fluorescence spectroscopy*. Springer, Berlin
4. Englman R, Jortner J (1970) *Mol Phys* 18:145–164
5. Ogawa M, Kuroda K (1995) *Chem Rev* 95:399–438
6. Takagi K, Shichi T (2000) *J Photochem Photobiol C* 1:113–130
7. Takagi S, Eguchi M, Tryk DA, Inoue H (2006) *J Photochem Photobiol C* 7:104–126
8. Ogawa M, Ide Y, Okada T (2010) *Chem Asian J* 7:1980–1992
9. Nakato T, Kawamata J, Takagi S (2017) *Inorganic nanosheets and nanosheet-based materials (fundamentals and applications of two-dimensional systems)*. Springer, Berlin
10. Tong Z, Takagi S, Shimada T, Tachibana H, Inoue H (2006) *J Am Chem Soc* 128:684–685
11. Ma R, Sasaki T (2010) *Top Appl Phys* 117:135–146
12. Lin S (1970) *J Chem Phys* 53:3766–3767
13. Maiti M, Danger BR, Steer RP (2008) *J Phys Chem A* 112:5824–5833
14. Wilson JS, Chawdhury N, Al-Mandhary MR, Younus M, Khan MS, Raithby PR, Köhler A, Friend RH (2001) *J Am Chem Soc* 123:9412–9417
15. Christensen RL, Goyette M, Gallagher L, Duncan J, DeCoster B, Lugtenburg J, Jansen FJ, Hoef IVD (1999) *J Phys Chem A* 103:2399–2407
16. Grosshenny V, Harriman A, Romero FM, Ziessel R (1996) *J Phys Chem* 100:17472–17484
17. Hochstrasser RM, Marzzacco C (1968) *J Chem Phys* 49:971–984
18. Bujdák J (2018) *J Photochem Photobiol C* 35:108–133
19. Bujdák J (2006) *Appl Clay Sci* 34:58–73
20. Czimerová A, Bujdák J, Gáplovský A (2004) *Colloids Surf A Physicochem Eng Asp* 243:89–96
21. Schoonheydt RA, Heughebaert L (1992) *Clay Miner* 27:91–100
22. Neumann MG, Schmitt CC, Gessner F (1996) *J Colloid Interface Sci* 177:495–501
23. Takagi S, Shimada T, Yui T, Inoue H (2001) *Chem Lett* 30:128
24. Takagi S, Shimada T, Eguchi M, Yui T, Yoshida H, Tryk DA, Inoue H (2002) *Langmuir* 18:2265
25. Eguchi M, Takagi S, Tachibana H, Inoue H (2004) *J Phys Chem Solids* 65:403–407
26. Takagi S, Konno S, Aratake Y, Masui D, Shimada T, Tachibana H, Inoue H (2011) *Microporous Mesoporous Mater* 141:38–42
27. Egawa T, Watanabe H, Fujimura T, Ishida Y, Yamato M, Masui D, Shimada T, Tachibana H, Yoshida H, Inoue H, Takagi S (2011) *Langmuir* 27:10722
28. Takagi S, Shimada T, Ishida Y, Fujimura T, Masui D, Tachibana H, Eguchi M, Inoue H (2013) *Langmuir* 29:2108–2119
29. Fujimura T, Shimada T, Hamatani S, Onodera S, Sasai R, Inoue H, Takagi S (2013) *Langmuir* 29:5060–5065
30. Ohtani Y, Ishida Y, Ando Y, Tachibana H, Shimada T, Takagi S (2014) *Tetrahedron Lett* 55:1024–1027
31. Auwärter W, Écija D, Klappenberger FN, Barth JV (2015) *Nat Chem* 7:105
32. Yui T, Takagi K, Inoue H (2018) *J Photochem Photobiol A Chem* 363:61–67
33. Ishida Y, Shimada T, Tachibana H, Inoue H, Takagi S (2012) *J Phys Chem A* 116:12065–12072

34. Ishida Y, Fujimura T, Masui D, Shimada T, Tachibana H, Inoue H, Takagi S (2012) *Clay Sci* 15:169–174
35. Chernia Z, Gill D (1999) *Langmuir* 15:1625
36. Kuykendall VG, Thomas JK (1990) *Langmuir* 6:1350
37. Ishida Y, Masui D, Shimada T, Tachibana H, Inoue H, Takagi S (2012) *J Phys Chem C* 116:7879–7885
38. Takagi S, Konno S, Ishida Y, Ceklovsky A, Masui D, Shimada T, Tachibana H, Inoue H (2010) *Clay Sci* 14:235–239
39. Tokieda D, Tsukamoto T, Ishida Y, Ichihara H, Shimada T, Takagi S (2017) *J Photochem Photobiol A Chem* 339:67–79
40. Tsukamoto T, Shimada T, Takagi S (2013) *J Phys Chem A* 117:7823–7832
41. Tsukamoto T, Shimada T, Takagi S (2015) *RSC Adv* 5:8479–8485
42. Hagiwara S, Ohtani Y, Takagi S, Shimada T (2015) *Clay Sci* 19:63–66
43. Tsukamoto T, Shimada T, Takagi S (2016) *ACS Appl Mater Interfaces* 8:7522–7528
44. Kudo N, Tsukamoto T, Tokieda D, Shimada T, Takagi S (2018) *Chem Lett* 47:636–639
45. Nakazatoa R, Shimada T, Ohtani Y, Ishida T, Takagi S (2018) *Tetrahedron Lett* 59:2459–2462
46. Ishida Y, Shimada T, Takagi S (2014) *J Phys Chem C* 118:20466–20471
47. Villemure G, Detellier C, Szabo AG (1986) *J Am Chem Soc* 108:4658–4659
48. Villemure G, Detellier C, Szabo AG (1991) *Langmuir* 7:1215–1221
49. Tsukamoto T, Shimada T, Takagi S (2013) *J Phys Chem C* 117:2774–2779
50. Hong Y, Lam JWY, Tang BZ (2009) *Chem Commun* 29:4332–4353
51. Hong Y, Lam JWY, Tang BZ (2011) *Chem Soc Rev* 40:5361–5388
52. Xie S, Wong AYH, Chen S, Tang BZ (2019) *Chem Eur J* 25:5824–5847
53. Umemoto T, Ohtani Y, Tsukamoto T, Shimada T, Takagi S (2014) *Chem Commun* 50:314–316
54. Eguchi M, Takagi S, Inoue H (2006) *Chem Lett* 35:14–15
55. Eguchi M, Tachibana H, Takagi S, Tryk DA, Inoue H (2007) *Bull Chem Soc Jpn* 80:1350–1356
56. Eguchi M, Shimada T, Tryk DA, Inoue H, Takagi S (2013) *J Phys Chem C* 117:9245–9251
57. Eguchi M, Watanabe Y, Ohtani Y, Shimada T, Takagi S (2014) *Tetrahedron Lett* 55:2662–2666
58. Eguchi M, Shimada T, Inoue H, Takagi S (2016) *J Phys Chem C* 120:7428–7434
59. Takagi S, Shimada T, Masui D, Tachibana H, Ishida Y, Tryk DA, Inoue H (2010) *Langmuir* 26:4639–4641
60. Fujimura T, Shimada T, Sasai R, Takagi S (2018) *Langmuir* 34:3572–3577
61. Takagi S, Eguchi M, Inoue H (2006) *Langmuir* 22:1406–1408
62. Tsukamoto T, Shimada T, Takagi S (2018) *ACS Omega* 3:18563–18571
63. Tsukamoto T, Shimada T, Shiragami T, Takagi S (2015) *Bull Chem Soc Jpn* 88:578–583
64. Takagi S, Tryk DA, Inoue H (2002) *J Phys Chem B* 106:5455–5460
65. Eguchi M, Tachibana H, Takagi S, Inoue H (2007) *Res Chem Intermed* 33:191
66. Ishida Y, Shimada T, Masui D, Tachibana H, Inoue H, Takagi S (2011) *J Am Chem Soc* 133:14280–14286
67. Ishida Y, Shimada T, Takagi S (2013) *J Phys Chem C* 117:9154–9163
68. Ohtani Y, Shimada T, Takagi S (2015) *J Phys Chem C* 119:18896–18902
69. Ohtani Y, Kawaguchi S, Shimada T, Takagi S, Shinsuke H (2017) *J Phys Chem C* 121:2052–2058
70. Suzuki S, Tatsumi D, Tsukamoto T, Honna R, Shimada T, Inoue H, Takagi S (2018) *Tetrahedron Lett* 59:528–531
71. Tatsumi D, Tsukamoto T, Honna R, Hoshino S, Shimada T, Takagi S (2017) *Chem Lett* 30:128–129
72. Wang L, Sasaki T (2014) *Chem Rev* 114:9455
73. Sakai N, Ebina Y, Takada K, Sasaki T (2004) *J Am Chem Soc* 126:5851
74. Sonotani A, Shimada T, Takagi S (2017) *Chem Lett* 46:499–501
75. Sano K, Sonotani A, Tatsumi D, Ohtani Y, Shimada T, Takagi S (2017) *J Photochem Photobiol A* 353:597–601
76. Sonotani A, Sano K, Wakayama S, Shimada T, Takagi S (2018) *Chem Lett* 47:803–805

77. Novoselov KS, Geim AK, Morozov SV, Jiang D, Zhang Y, Dubonos SV, Grigorieva IV, Dirsov AA (2004) *Science* 306:666
78. Chen F, Tao NJ (2009) *Acc Chem Res* 42:429
79. Bae S, Kim H, Lee Y, Xu X, Park JS, Zheng Y, Balakrishnan J, Lei T, Kim HR, Song YI, Kim YJ, Kim KS, Ozyilmaz B, Ahn JH, Hong BH, Iijima S (2010) *Nat Nanotechnol* 5:574–578

Resonance Energy Transfer in Hybrid Systems of Photoactive Dye Molecules and Layered Inorganics



Juraj Bujdák

Contents

1	Introduction	207
2	Theoretical Basics of Resonance Energy Transfer	208
3	Distribution of Molecules and Intermolecular Distances	211
4	Layered Inorganic Compounds as Hosts for Efficient Energy Transfer	215
4.1	Layered Inorganic Compounds: Structure and Properties	215
4.2	Layered Nanoparticles as the Hosts of Dye Molecules and FRET	216
5	Applications	238
5.1	Control of Photodegradation of Pesticides by FRET	238
5.2	FRET for Sensing	238
5.3	FRET in Bioimaging	241
5.4	FRET in Catalysis	242
6	Future Perspectives	242
	References	243

Abstract The phenomenon of Förster resonance energy transfer (FRET) commonly leads to significant changes in the photophysical properties of systems. FRET is very important for the functioning of photosynthesis, thus inspiring scientists to design new functional materials for the efficient use of light energy. This chapter summarizes existing knowledge about FRET in hybrid systems containing inorganic layered nanoparticles and organic luminescent dyes. The physical principles of the interaction between dye molecules leading to FRET and the effect on the spectral properties of the systems are briefly presented. The main part of the chapter covers the fundamental properties of layered nanoparticles, their interactions with organic dyes, and numerous examples of hybrid materials exhibiting FRET. The focus is on

J. Bujdák (✉)

Department of Physical and Theoretical Chemistry, Faculty of Natural Sciences, Comenius University in Bratislava, Bratislava, Slovakia

Institute of Inorganic Chemistry, Slovak Academy of Sciences, Bratislava, Slovakia

e-mail: juraj.bujdak@uniba.sk; bujdak3@uniba.sk

various hybrids including various types of assemblies, films, composites, and more complex systems, which can be synthesized from several luminescent species, such as ionic dyes, neutral dyes, luminescent polymeric substances, and complexes. Special attention is devoted to the effects of the dye surface concentration and distribution of the molecules, anisotropy, the types of inorganic host, and external stimuli on the controlled energy transfer. Some examples of applications and the relevance of FRET for future research are summarized.

Keywords Energy transfer · Fluorescence · FRET · Layered materials · Layered silicates · Luminescence · Organic dyes

Abbreviations

3D	Three-dimensional
CRET	Chemiluminescence resonance energy transfer
DET	Dexter energy transfer
DNA	Deoxyribonucleic acid
DOC	3,3'-Diethyloxacarbocyanine
EA	Energy acceptor
ED	Energy donor
ET	Energy transfer
FAM	Fluorescein amidite
FLIM	Fluorescence lifetime imaging microscopy
FRET	Förster resonance energy transfer
GO	Graphene oxide
IgE	Antibody immunoglobulin E
Lap	Laponite
LB	Langmuir-Blodgett
LbL	Layer-by-layer
LDH	Layered double hydroxide
LUMO	Lowest unoccupied molecular orbitals
Ox4	Oxazine 4
PDF	Probability density function
PVK	Poly(vinylcarbazole)
R3B	Rhodamine 3B
R6G	Rhodamine 6G
RB	Rhodamine B
rGO	Reduced graphene oxide
Sap	Saponite
UV	Ultraviolet
vis	Visible
VOC	Volatile organic compounds

1 Introduction

Devices of the future that are able to efficiently transfer and manipulate light energy at the molecular level are inspired by nature, namely, by the processes taking place in photosynthetic systems. In green plants, part of the visible (vis) light (blue and red spectral regions) is absorbed by chlorophyll pigments. The chromophore units in the pigments include hundreds of specifically arranged porphyrin molecules that play the role of molecular antennas organized in order to efficiently absorb light. Their spatial orientation allows a highly efficient transfer of the excitation energy to nearby chromophores that reach the reaction center, where the energy can be further utilized for biochemical processes. The chromophoric units are arranged in a protein skeleton to prevent the formation of molecular aggregates that would significantly inhibit the photoactivity and thus reduce energy transfer efficiency. Knowledge about these natural systems can also be applied in strategies and designs of artificial hybrid materials capable of conducting the controlled energy transfer process. Such materials based on zeolites and organic dyes have been extensively investigated [1–3].

In addition to the controlled utilization of light energy, Förster resonance energy transfer (FRET) itself is significant in countless areas of modern industries and in a variety of applications and fields of scientific research. One promising type of system for controlled FRET is hybrid materials. The hosts provide the opportunity to control the separation distance between the interacting molecules and suppress the molecular aggregation. In the hybrid materials, the luminophores could be sufficiently stabilized and protected, especially from atmospheric oxygen and moisture. It is possible to prepare a wide variety of materials with different optical properties merely by combining different ratios of layered hosts, dyes, and other constituents of the materials. Such an approach has potential for the development of new types of devices such as hybrid light-emitting devices, diodes, sensors, white light-emitting systems, etc. The combination of proper dyes and the control of energy transfer processes can help to control the color of emitted light [3]. In some cases, the color variants can be changed by external stimuli. Other phenomena partially related to FRET are photostabilization, photosensitization, photocatalysis, and the photocatalytic decomposition of various pollutants and agrochemicals, etc.

The materials of the future are those whose properties and functionality can be changed by external stimuli. Examples of applications of such systems are chemical sensors or probes. The FRET phenomenon can be used for the analysis of various substances or for the measurements of some physical quantities. From the perspective of nanomaterial research, FRET can serve as a ruler for measuring distances at the molecular level. To describe the dynamics of nanoparticle systems, FRET anisotropy methods have been widely used in molecular biology and macromolecular chemistry. Many optical probes and sensors have important applications in optical microscopy. Fluorescence imaging by optical microscopy is one of the most effective techniques for the noninvasive monitoring of cells and biomolecules in real time and in their natural environments. It is fairly accurate in terms of spatial resolution, specific to target sites, and is a suitable tool for obtaining basic

knowledge of the localization and role of biomolecules in living systems [4]. The simplest types of fluorescence probes are organic dyes that specifically interact with the target site; this interaction is detected as a change in fluorescence properties. The evolution of fluorescence probes continues to advance due to progress in the synthesis of new types of luminophores [4]. The development of FRET probes significantly expands the possibilities of using optical microscopy.

The objective of this chapter is to analyze the most important results and trends in the research of hybrid materials of organic dyes and two-dimensional inorganic hosts, focusing on the phenomenon of FRET and in part on other related photophysical processes and phenomena. The chapter partly follows the author's previous reviews and chapters on the analysis of the general properties of such systems [5–7]. It analyzes several aspects related to FRET in these systems. The first sections briefly describe the theoretical basis of FRET, basic knowledge on the properties of layered nanomaterials, and the nature of their interaction with organic dyes. Based on the essential criteria for efficient energy transfer, the chapter focuses on the problem of the distribution of photoactive molecules in such systems and its crucial effect on FRET. The later sections deal with the analysis of the properties of materials of various types including very complex systems, and some examples and possibilities for their application are discussed.

2 Theoretical Basics of Resonance Energy Transfer

FRET is a phenomenon representing the transfer of the energy from excited dye molecules in a non-radiative way. The first step that is required for the energy transfer to occur is the excitation of a dye molecule, playing the role of an energy donor (ED). The excitation is realized by absorbing a photon, but in principle also other sources of energy could be applied (electrical energy, chemical reaction, etc.). The excited molecule is unstable and rapidly relaxes back to its ground state via several mechanisms, either by emitting a photon or by transferring its energy to nearby molecules. The simplest system to be described is represented by a one-photon event: FRET from the excited ED molecule (ED^*) to an energy acceptor (EA). The energy transfer between the ED^* and EA leads to the formation of an $ED EA^*$ pair:



where the symbol $*$ denotes a molecule in an excited state. The interaction energy β is expressed by the Coulombic U and the exchange E_{ex} interactions:

$$\beta = U - E_{ex} \quad (2)$$

At shorter distances, Dexter energy transfer (DET) can occur, representing a quenching mechanism based on the transfer of an excited electron. In contrast to

FRET, DET requires a wavefunction overlap between the molecules and occurs at very short intermolecular distances, < 1 nm. With FRET, the orbital overlap between the interacting molecules is negligible. The exchange interaction can be neglected and the equation of the interaction energy can be simplified:

$$\beta = U \quad (3)$$

The initial and final states can be expressed as follows:

$$\Psi_i = \Psi_{ED^*} \Psi_{EA} \quad (4)$$

$$\Psi_f = \Psi_{ED} \Psi_{EA^*} \quad (5)$$

The Förster-type interaction is due to relatively weak dipole-dipole coupling, which means that the Coulombic interaction is considerably lower than the bandwidth of the vibronic spectral component. FRET is a common phenomenon occurring in complex systems containing pairs of dye molecules with specific spectral properties. The efficiency of FRET (Φ_{ET}) depends on the competitiveness of this phenomenon relative to other relaxation processes. It can be quantitatively described by the rate constants of fluorescence radiative relaxation (k_f), energy transfer (k_{ET}), and other processes ($\sum k_i$):

$$\Phi_{ET} = \frac{k_{ET}}{k_f + k_{ET} + \sum k_i} = 1 - \frac{\tau_{DA}}{\tau_D} \quad (6)$$

τ_{DA} and τ_D represent the fluorescence lifetimes of the ED which are measured in the presence and absence of the EA, respectively. The ratio of the intensities of emitted light from steady-state spectra can also be used for the estimation of FRET efficiency, but additional factors such as response or instrumental efficiency of the spectrophotometer to detect photons at specific wavelengths, fluorescence quantum yields of the components, etc., must be taken into account. The more straightforward way is, therefore, using the data of time-resolved fluorescence. FRET is only allowed for specific pairs of interacting molecules. High yields are expected if the emission spectrum of ED sufficiently overlaps with the absorption spectrum of EA [8]. This property is quantitatively described by the parameter called the spectral overlap integral (J):

$$J = \int_0^{\infty} I_{\lambda}^D(\lambda) \epsilon_A(\lambda) \lambda^4 d\lambda \quad (7)$$

where $I_{\lambda}^D(\lambda)$ represents the normalized spectral radiant intensity of the ED emission, $\epsilon_A(\lambda)$ is the decadic molar absorption coefficient of EA, and λ is the wavelength. For FRET to occur, suitable spatial arrangements of dye molecules are needed. Non-radiative energy transfer can occur between molecules separated by considerably larger distances than the size of the molecules or their chromophoric units.

FRET efficiency is generally limited to intermolecular distances in the range of 5–10 nm and depends on the spectral overlap integral J (Eq. (7)). The efficiency of FRET in relation to the distance between the ED and EA is defined as:

$$\Phi_{\text{ET}} = \frac{1}{1 + (r/R_0)^6} \quad (8)$$

where R_0 is a constant called the Förster radius, which reflects the distance between interacting ED and EA molecules at which the FRET efficiency is 50%. Due to the dependence of Φ_{ET} on the sixth power of separation distance r , negligible deviations of the distance r from R_0 lead to significant changes in Φ_{ET} . Reducing r with respect to R_0 results in a significant enhancement of Φ_{ET} . However, an increase of the distance r to double or triple the value of R_0 reduces FRET efficiency to 1.5% or 0.14%, respectively. Thus, the changes in FRET efficiency can only be observed over a relatively narrow range of distances close to the value of R_0 . The Förster radius R_0 is specific to an ED/EA pair. The relation between the Förster radius and the spectral overlap integral is expressed by the equation:

$$R_0 = \text{constant} \left(\frac{\kappa^2 \Phi_{\text{D}} J}{n^4} \right) \quad (9)$$

where κ is the orientation factor, Φ_{D} is the fluorescence quantum yield of the energy donor, and n is the refractive index of the medium. There is a direct relationship between the rate constant for FRET and Förster radius:

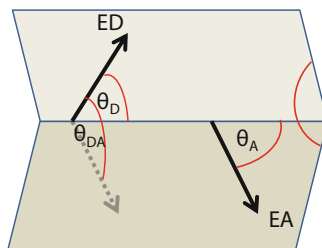
$$k_{\text{ET}} = k_{\text{D}} \left(\frac{R_0}{r} \right)^6 \quad (10)$$

where k_{D} is the rate constant for all the processes deactivating the emissive excited state of the ED in the absence of EA. The equation is often expressed using the reciprocal for the lifetime of the energy donor ($k_{\text{D}} = 1/\tau_{\text{D}}$), which can be easily obtained by time-resolved fluorescence spectroscopy. The efficiency of FRET depends on the orientation of the interacting molecules. κ^2 represents the orientation factor, showing the relative orientation of the transition moments of interacting molecules with the values in the interval [0,4]. For isotropic systems, the contribution of all possible orientations has to be considered, resulting in an orientation factor equal to 2/3. The relationship between κ^2 and the orientation of the transition moments of ED and EA molecules is expressed by Eq. (11), and the meaning of some symbols is explained in Fig. 1 [9]:

$$\kappa^2 = (\cos \theta_{\text{DA}} - 3 \cos \theta_{\text{D}} \cos \theta_{\text{A}})^2 \quad (11)$$

Although the orientation factor can have a wide range of values, it usually does not influence energy transfer efficiency to such an extent as the intermolecular

Fig. 1 Parameters characterizing the orientation factor of the molecules



distance in solution. This is because the orientation of molecules is rarely perfectly anisotropic, and excited fluorophores may undergo a fast reorientation over a timescale much shorter than the lifetime of the excited state of a molecule. Hence, modulating the distance between the interacting ED and EA molecules and the spectral overlap integral are considered the two main ways to change the energy transfer efficiency [4].

In its physical nature, FRET also includes a phenomenon called energy migration. This takes place between the molecules of the same type and can compete with FRET between different fluorophore molecules. To be effective, the energy migration must be rapid enough to compete not only with FRET but also other concurrent processes, such as spontaneous emissions and quenching. The factors influencing an energy migration are very similar to those for FRET: a high spectral overlap integral and sufficiently small intermolecular distances. Logically, the dyes that have a small Stokes shift would be most appropriate for the energy migration. A specific example of energy migration is also the energy transfer between molecules inside an individual supramolecule of a J-type assembly.

3 Distribution of Molecules and Intermolecular Distances

The distance between ED and EA molecules plays an essential role in the FRET process (Eq. (8)). When a single pair of ED and EA molecules are involved in FRET, the distance between the molecules can be relatively well estimated. For example, if the molecules are fixed to a biopolymer chain, the intermolecular distance represents the distance between the sites on the polymer chains where the molecules are attached. In this case, it is relatively simple to estimate FRET efficiency. However, if FRET occurs in a system in which a large number of interacting molecules coexist together, then all the interactions of the participating molecules must be taken into account. Even homogeneous systems, such as a mixed two-dye solution, are relatively complex. On the other hand, conventional dilute solutions of organic dyes give only very small FRET quantum yields. The reason for this is the relatively large intermolecular distances. The yields only become significant at relatively high concentrations. Under these conditions, it is also possible to observe a radiant energy transfer, when emitted light is re-absorbed. The re-absorption can be efficiently

Table 1 Relationship between average intermolecular distance and molar concentration of dye molecules in homogeneous systems

$c, \text{ mol L}^{-1}$	$\sigma_N, \text{ nm}^{-3}$	$1/\sigma_N, \text{ nm}^3$	$\bar{d}, \text{ nm}$
10^{-3}	6.02×10^{-4}	1.66×10^3	11.8
10^{-4}	6.02×10^{-5}	1.66×10^4	25.5
10^{-5}	6.02×10^{-6}	1.66×10^5	55.0
10^{-6}	6.02×10^{-7}	1.66×10^6	118.4
10^{-7}	6.02×10^{-8}	1.66×10^7	255.1
10^{-8}	6.02×10^{-9}	1.66×10^8	549.7

c is molar concentration in mol L^{-1} . σ_N denotes the number density of molecules in nm^{-3} , and $1/\sigma_N$ is the reciprocal number density, which denotes the volume per molecule in the solution. \bar{d} is the average distance between homogeneously distributed molecules in space (assuming an ordered cubic packing)

suppressed by a suitable setup of the measurement and using solutions with absorbance < 0.1 . For a better understanding of the effect of intermolecular distances on FRET, Table 1 shows the change in the average distance between molecules, depending on the concentration of molecules in homogeneous solutions. These data provide only an approximate insight, as the calculation also considers homogeneity at the molecular level and considers the molecules to be dimensionless points. Relatively large distances were calculated for each concentration. Only the solution with the highest concentration ($10^{-3} \text{ mol L}^{-1}$) achieved distances of 11.8 nm, which came close to values that are theoretically suitable for FRET to occur.

The distance between the molecules in solutions is not constant over space and time, but is subject to a statistical distribution in space and a rapid diffusion over time. In particular, the occurrence of distances that are much smaller than the average value can significantly affect the quantum yields of FRET. For the precise description of a system, it is necessary to determine the occurrence of different intermolecular distances and their statistical impact on FRET. This is what the Poisson distribution can predict from a known average concentration. The Poisson statistics assume a random and independent occurrence of all theoretically possible arrangements, and any intermolecular interactions are neglected. Calculating probabilities for narrow intervals of intermolecular distances can lead to the approximation of probability density functions (PDFs). They define the probability of the occurrence for the distance r between the interacting molecules depending on the concentration expressed by the number density (σ_N) (number of molecules per unit volume) [10]. r is a predictor variable defined as the distance between molecules in 3D space ($0 < r < \infty$):

$$f(r, \sigma_N) = 4\pi\sigma_N r^2 e^{-\frac{4}{3}\sigma_N \pi r^3} \quad (12)$$

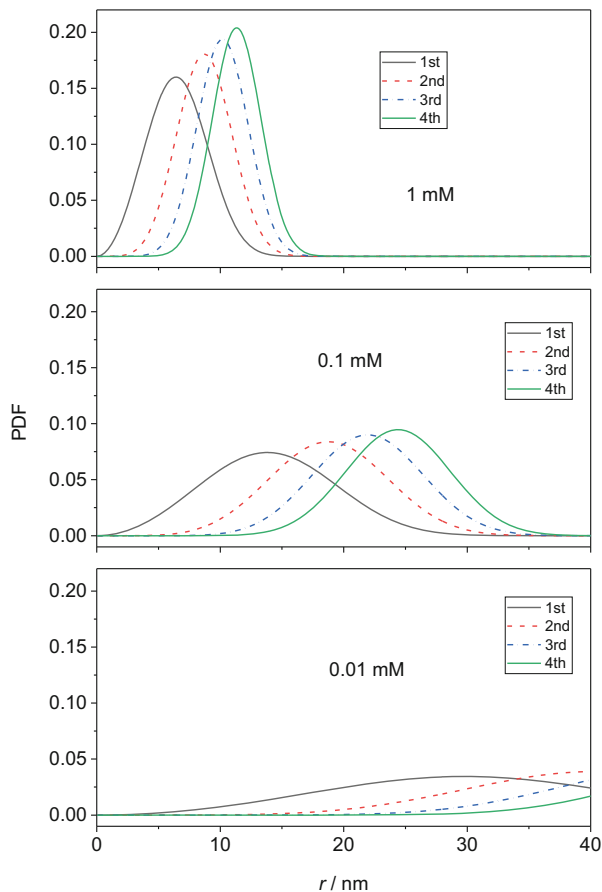
In our previous study, only FRET to the nearest EA molecule was considered in the model utilized for the two-dimensional process [11]. FRET to the second-, third-, and forth-nearest EA molecule can also be considered, although the efficiency would always be much lower than for the nearest molecule. The formula for calculating

probability density functions of the occurrence of the n th nearest molecule is shown below [10]:

$$f(r, \sigma_N) = 3 \left(\frac{4}{3} \pi \sigma_N \right)^n r^{3n-1} e^{-\frac{4}{3} \sigma_N \pi r^3} \quad (13)$$

Figure 2 shows a PDF of the occurrence of EA molecules near EDs over short distances (<40 nm) for EA concentrations of 1.0, 0.1, and 0.01 mmol L⁻¹. At the highest concentration, a fraction of the intermolecular distances is also within the range 0–10 nm, which are intermolecular distances which might be efficient for FRET. Much broader functions are observed if the concentration was reduced tenfold (0.1 mmol L⁻¹), and only the nearest neighboring molecule can be found within the efficient range of distances. The second-, third-, and fourth-nearest molecule would mainly occur at distances over 10 nm from the ED molecule. The concentration 10⁻² mmol L⁻¹ represents more or less the upper concentration limit,

Fig. 2 Probability density functions (PDFs) of intermolecular distances between ED and EA molecules in homogeneous solutions. The functions are calculated using Eq. (13)



at which no significant molecular aggregation and quenching occurs. As shown in Fig. 2, the occurrence of the neighboring molecules in the range of high FRET efficiency is highly unlikely at this concentration. Combining Eqs. (8) and (13), one can calculate the values of the FRET efficiency similarly to the way it has been described for two-dimensional FRET [11]. The expected value of the FRET efficiency $\overline{\Phi_{\text{ET}}}$ can be calculated by integrating the inner product of the probability density function $f(r, \sigma_N)$ and the function for the FRET efficiency $\Phi_{\text{ET}}(r)$:

$$\overline{\Phi_{\text{ET}}} = \int_{r=0}^{\infty} \Phi_{\text{ET}}(r) f(r, \sigma_N) dr \quad (14)$$

FRET efficiency, $\Phi_{\text{ET}}(r)$, between the ED and EA molecules, is defined as a function of the distance between the molecules r . It depends on the parameter R_0 , which is specific for an ED/EA pair (Eq. (8)). The expected value of the FRET efficiency $\overline{\Phi_{\text{ET}}}$ can be estimated for solutions of any concentration of dye molecules. The real energy transfer efficiency would be partially enhanced relative to this idealized model by the diffusion of ED and EA molecules. During the migration, the distances between neighboring molecules may significantly change over time. These changes occur over the timescale of the relaxation of excited molecules. Dye molecules can travel relatively long distances from the time of excitation to the time of the return of the molecule to its electronic ground state. Such a phenomenon is more likely to occur at higher diffusion rates and for the molecules which form stable excited states with long lifetimes.

It is not easy to achieve a system with a high degree of organization of fluorophore molecules, with assemblies of controlled intermolecular distances and molecular orientations, and exhibiting an efficient FRET. Difficulties also occur due to the limits of the size of the assemblies to be applicable for devices. The large ordered systems have been produced quite easily using a supramolecular organization and self-assembly in two or three dimensions. In these cases, the functionality often suffers from a luminescence quenching due to the formation of inactive molecular aggregates. One strategy for preparing artificial photosynthetic devices or multifunctional systems was the development of molecular *Dyads* and *Triads*. Such systems incorporated several functional molecules into a single one, combining at least two photoactive components performing different photophysical processes. An example is the combination of molecules of chromophores and luminophores, which represent light antennas, energy and/or electron transfer components, and photosensitizers. The molecules can be bound via a covalent linkage. As for the functionality of such systems, not only the properties of the individual components but also their specific combination and their relative orientation in space can play a crucial role in their performance and efficiency. The cost of such complex entities is very high, and their use is mostly limited to fundamental research with little chance of finding broad commercial applications. On the other hand, using nanoparticle hosts can also be applied to connect and concentrate fluorophore molecules, thus promoting their photophysical interaction. Hence, such hybrid materials can perform

in a similar way as are achieved with *Dyads* and *Triads*. Of note are the types of hybrid materials that are based on an inorganic host which is photochemically inactive but can incorporate photoactive organic molecules into its skeleton. For example, zeolite L has proven to be a suitable host material that allows for the controlled intercalation of dye molecules into internal channels suitable for this purpose. Basic knowledge is summarized, e.g., in the work of Calzaferri [1]. In several hybrid materials of this type, efficient FRET over relatively large distances has been confirmed, in which energy migration between dye molecules of the same type was effectively involved. Efficient FRET along a zeolite crystal is only possible if the dye molecules are suitably ordered, arranged, and oriented in the channels [1–3]. Besides the host materials with a 3D structure, inorganic hosts composed of two-dimensional particles also need to be considered as templates for photoactive hybrid systems exhibiting efficient FRET (see reviews [5, 7, 12–14]). A detailed analysis of such systems is provided in the sections below.

4 Layered Inorganic Compounds as Hosts for Efficient Energy Transfer

4.1 Layered Inorganic Compounds: Structure and Properties

There are several reviews and book chapters devoted to the chemistry of layered nanoparticles [15–18]. Several types of inorganic compounds are composed of layered particles with thicknesses at the sub-nanometer or nanometer level. There are many types of layered inorganic compounds, and their chemistry is relatively variable. They include graphene, graphene oxide (GO), oxides, hydroxides, LDH, layered chalcogenides, carbonates, metal phosphates, vanadates, niobates, titanates, layered perovskites, and layered silicates. The structure, properties, and their hybrid materials have been reviewed [17, 19, 20]. Nanosheets composed of atoms of one type are structurally the simplest platelet-like particles (graphene). Their atoms are often partially functionalized GO. Some types of nanosheets are composed of polyhedrons. Nanosheets of layered double hydroxides (LDHs) built from octahedrons are a typical example. More complex nanolayered particles can be composed of covalently linked sheets of different polyhedrons [17]. Complex layers are the case of layered silicates of 2:1 type, represented by smectites (naturally occurring clay minerals) or synthetic expandable layered silicates. The structure of an individual layer is based on a sheet of octahedrons ($[\text{MO}_4(\text{OH})_2]^{z-}$) covalently bound and sandwiched between the two sheets of tetrahedrons ($[\text{SiO}_4]^{4-}$). One of the most important properties of these materials is the layer charge, which plays a key role in the stability of the colloidal systems. The layer charge affects many important properties and plays a dominant role in the interaction with ionic organic substances. Layered particles can bear either a positive or negative charge. For example, particles of layered silicates of the 2:1 type bear a permanent negative charge caused

by the presence of non-equivalent isomorphic substitutions in the structure. Graphene or chalcogenides are typical examples of materials based on particles with no original surface charge. They need to be modified or functionalized to get them to disperse in polar solvents. The charge of some materials can be induced by redox reactions or by protolytic reactions.

4.2 Layered Nanoparticles as the Hosts of Dye Molecules and FRET

Hybrid materials consisting of organic dyes and layered hosts are, at first sight, a relatively well-defined group of systems and materials. In fact, these materials can be very diverse in terms of the combination of an almost infinite number of types of substances. The variability could be even higher when considering structurally different variants of the materials based on the same components. The presence of other substances, which are often included to stabilize the systems and to preserve the photoactivity of the dyes, opens up further possibilities for the preparation of very diverse ternary, multicomponent, and very complex hybrid materials. These hybrid systems include various types ranging from colloids, through solid materials, thin films to nanocomposites with polymers. The photoactive component, which is represented by organic dyes, can be in the form of neutral molecules or ions of conventional dyes, but also luminophore-labeled surfactant molecules, luminescent polymeric substances, biopolymers, and conventional polymers labeled with luminophores. Inorganic components can be represented by photochemically inactive particles or by the properties of semiconductors, conductors, and luminescent materials. Depending on the nature of an organic dye, different types of adsorption and interactions between the components occur. In addition to most frequent electrostatic interactions, covalent and coordination bonds can be applied to attach fluorophore groups onto the particles. In some cases, van der Waals forces and hydrogen bonding significantly contribute to the binding of organic dyes in specific materials.

4.2.1 Complexes with Ionic Dyes

The most frequent type of hybrid system is based on charged nanoparticles that are counterbalanced by organic ions with an opposite charge. The organic dyes may include ionic chromophores or molecules modified with ionic groups. An example of the latter type is derivatives of neutral dyes modified with alkylamine groups, which hydrolyze to form positively charged species [21]. To date, many papers on complexes of layered silicates with cationic dyes have been published and reviewed [5, 7, 13, 14, 22–24]. An opposite example in terms of the charge of the individual components is LDH systems with positively charged layers and anionic dyes [25, 26]. The main advantages of using ionic dyes are their relatively good solubility

in polar solvents, easy combination with polar and charged nanoparticles, and the successful synthesis of hybrid systems. The ionic character of the components allows the preparation of a broad range of types of materials. Here, it is important to mention layer-by-layer (LbL) assemblies as a type of supramolecular systems, whose preparation is primarily based on the electrostatic interaction between components. Quite a lot of papers have been published related to systems based on ionic dyes and layered inorganics in which FRET was observed. Due to the ease of preparation of these hybrid systems, the distribution of ED and EA molecules was controlled by the concentrations of the individual components used in the preparation of these materials. Some examples of the numerous papers on FRET using layered inorganic templates are summarized in Table 2.

The organization of ED and EA ions is controlled by the adsorption promoted by ion exchange at the surface of the particles of inorganic hosts. The distribution of the dye ions is controlled by their local concentration, which is analyzed in detail in Sect. 4.2.3. In some cases, the combination of a pair of dyes of opposite charge has been successfully applied and their interaction proved by FRET [46, 47]. For example, an efficient FRET proved that both of the dyes RB and anionic dye fluorescein were co-adsorbed onto negatively charged particles of zirconium phosphate [46]. The binding of the fluorescein molecules forming anions could be due to the presence of

Table 2 Energy transfer occurring in hybrids based on layered compounds and electrostatically bound ionic dyes

Reference	Layered compound	ED/EA + other information
[11]	Sap	R6G/Ox4, distribution modeling
[25]	LDH	Anionic indigo molecules
[27]	Sap	LB films, surfactants with fluorophores
[28]	Sap	R3B/Ox4, colloids
[29]	LDH	Anionic porphyrin and pyrene derivatives
[30]	Montmorillonite	Effect of layer charge
[31]	Sap	R6G/RB, colloids/films
[32]	Lap	Surfactants with luminophoric groups, LB films
[33]	Lap	Surfactants with luminophoric groups, LB films
[34]	Sap	Cationic porphyrins
[35]	Sap	Three dyes, two-step FRET
[36]	Sap	Cationic porphyrins
[37]	Lap	Acriflavine/RB, colloids, ion sensing
[38]	Sap	Porphyrin dyes
[39]	Lap	Acriflavine/RB, colloids, LbL films
[40]	Sap	R6G/Ox4, LbL assemblies
[41]	Lap	Acriflavine/RB, colloids, ion sensing
[42]	Sap	Ir(III) complexes, LbL films
[43]	Sap	Porphyrins, orientation factor
[44]	Sap	Various dyes, cascade FRET, films
[45]	Sap	R6G/Ox4, solid films

the electric double layer around colloidal particles, which concentrate both ions of positive and negative charge. The association of ions of opposite charges or the formation of *particle-inorganic cation-anionic dye* bridges cannot also be neglected. This phenomenon has not been studied in depth, although FRET would be an ideal method. The effect of pH indicates that the charge of dye molecules plays an important role in their adsorption and the stability of the system, which was confirmed by FRET [47]. It was proven directly by FRET that the adsorption of zwitterionic RB is much weaker than that of cationic R6G [31]. This interpretation was based on the repulsive electrostatic forces between the negatively charged group of the RB and the negatively charged surface of the particles [31]. Interestingly, this only occurred at high dye concentrations with respect to the adsorption capacity of the particles. At low surface concentrations, both the RB and the cationic R6G were adsorbed quantitatively and did not compete with each other. The modification of the surface of nanoparticles is a strategy for creating adsorption sites for both types of ions. For example, a phyllosilicate with amino-alkyl groups on the surface proved to be an optimal type of material to form complexes with dye molecules with anionic groups [48].

4.2.2 Quenching by Molecular Aggregates

Planar heteroaromatic systems have a large tendency for molecular aggregation and strong metachromatic properties. The result of their molecular aggregation is not only a loss of dye photoactivity but also strong photo-quenching properties. The formation of molecular aggregates is a relatively complex phenomenon that takes place in hybrid colloidal systems. The high charge density leads to a high density of the adsorbed counterions of dye, which are favorable conditions for the formation of H-aggregates with a sandwich-type structure. To date, various types of strategies have been developed to avoid the formation of molecular aggregates in hybrid systems with layered nanoparticles. For ionic dyes, the choice of a layered host of a relatively low surface charge density often helps to reduce the dye molecular aggregation. The main literature on this topic was reviewed recently [5], and only the most important facts are mentioned here. The use of surfactants as the third component is a very effective and commonly used strategy to reduce the concentration of dye molecules, thereby preventing the formation of molecular aggregates. An effective method is also to select dyes whose molecular structure is non-planar and contains bulky groups. Competitive FRET between photoactive species and the aggregates in the systems with layered silicates has been reported [49]. Similar processes are illustrated in the scheme explaining competitive fluorescence quenching and FRET occurring in systems of rhodamine and oxazine dyes (Fig. 3). The molecular aggregation rarely leads to improved photophysical properties or an increased photoactivity. Rare cases involve the formation of J-aggregates and the phenomenon of aggregation-induced emission, which occur in special cases of dyes with very specific structures [5].

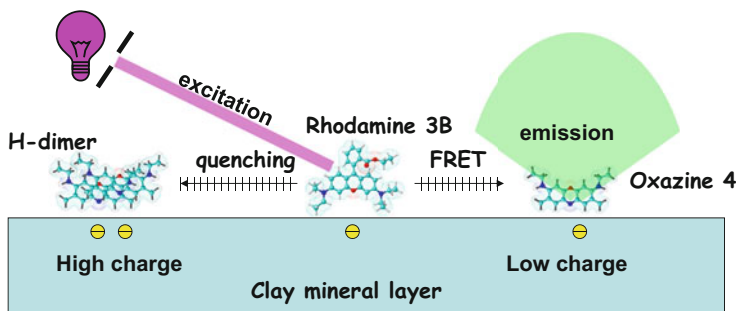


Fig. 3 Scheme showing two parallel FRET processes and fluorescence quenching which occurs in a hybrid system of layered silicate and two laser dyes [50]. Part of the excitation energy from ED molecules (represented by R3B) is quenched by the molecular aggregates of the same dye and part is transferred to EA molecules (represented by Ox4). The high density of the layer charge promotes the formation of dye aggregates and fluorescence quenching. Reprinted from *Journal of Colloid and Interface Science*, 306/2, Czímerová, A., Iyi, N., Bujdák, J., Energy transfer between rhodamine 3B and oxazine 4 in synthetic-saponite dispersions and films, 316–322, Copyright (2007), with permission from Elsevier

4.2.3 Distribution of Molecules and FRET in Hybrid Systems

As mentioned in Sect. 3, homogeneous solutions do not provide sufficiently small intermolecular distances for efficient FRET. Non-radiative energy transfer only occurs in highly concentrated solutions and with very low yields. In addition, high concentrations produce other phenomena such as high light absorption and low transparency, reabsorption of an emitted light (radiative energy transfer), and molecular aggregation. One possible way to prepare systems with relatively high FRET efficiencies is by using colloidal dispersions that contain particles that effectively adsorb dye molecules onto their surface. Depending on the degree of adsorption and the concentrations of the components, it is possible to control the surface concentration and the intermolecular distances of the adsorbed dye molecules (Fig. 4). Essentially, this strategy is not limited to the type or shape of the particles, and efficient adsorption of dye molecules can occur on the surfaces of spherical, two-dimensional, or one-dimensional nanoparticles. As mentioned in Sect. 1, nanoporous materials have been used for this adsorption to concentrate dye molecules in the cavities for controlled energy transfer. Layered nanomaterials are also very good substrates for such a purpose. Some of them can fully expand in water or other liquids to form colloidal systems based on completely dispersed individual nanoparticles. The stability of such systems and, optionally, the size of particles significantly affect the optical properties of such colloids. It is advantageous if the particle size is smaller than the wavelength of vis light, so that the colloidal dispersion would be transparent and the light scattering minimized.

FRET could be used as a method to estimate the distribution of adsorbed dye molecules on an inorganic surface [51]. The possibility of regulating intermolecular

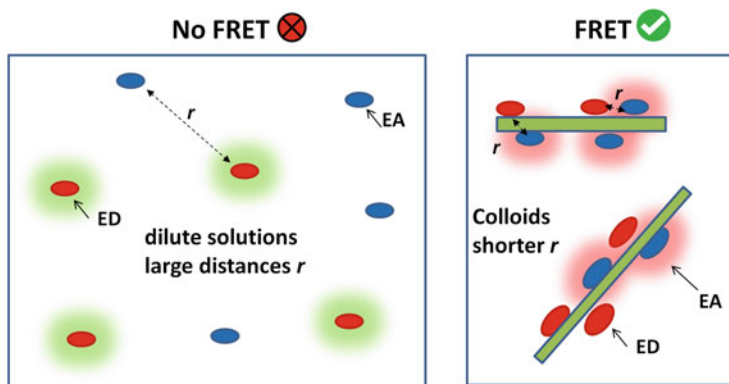


Fig. 4 Scheme showing the concentration of dye molecules by adsorption on layered particles leading to shorter intermolecular distances that promote FRET

distances and FRET is clearly documented by an experiment based on the hybrid colloidal systems of layered silicate and two dyes, R6G and Ox4 [11]. The dyes formed a suitable couple for FRET with an R_0 of approximately 5.5 nm. The FRET efficiency can be controlled simply by adjusting the amounts of dye molecules and adsorbent to an appropriate ratio. Due to the quantitative adsorption of the dye cations onto the surface of layered silicate, the dyes/Sap ratio essentially determined the concentration of the dye molecules on the silicate particles. As it turned out, changes in just the Sap concentration in the colloid resulted in significant color changes of the emitted light with the same dye concentrations (Fig. 5). When the concentration of Sap was relatively high, there was a large excess of Sap, resulting in a relatively low surface concentration of the adsorbed dye molecules. Such systems were characterized by large intermolecular distances and low FRET efficiencies. The selective excitation of R6G resulted in the emission of green light from this dye. However, by lowering the concentration of Sap, and at the same time keeping the bulk concentrations of both the dyes the same, a higher density of the adsorbed dye molecules can be achieved. In this case, smaller intermolecular distances between the dye molecules led to an increase in FRET efficiency. The green light emission from R6G molecules decreased in favor of red light emission from Ox4 (Fig. 5).

As with a three-dimensional FRET (see Sect. 3), a two-dimensional FRET can also be modeled by the statistical distribution of the intermolecular distances. Typically, the real values of FRET efficiency are significantly higher than one would expect based on the calculated average intermolecular distances (Fig. 6). Heterogeneous distribution leading to the occurrence of smaller intermolecular distances significantly affects the actual FRET yields. Similarly to the three-dimensional systems, FRET efficiency can also be modeled for the dye adsorption onto the particles in colloids. The models are based on Poisson statistics applied for the probability of intermolecular distances $f(r, \Gamma)$ for two-dimensional systems (Eq. 15) which can be derived from Eq. 13:

$$f(r, \Gamma) = 2\pi\Gamma r e^{-\Gamma\pi r^2} \quad (15)$$

where r represents the intermolecular distance and Γ is the surface concentration of the molecules [m^{-2}]. If we neglect the particle edges as minor sites for the adsorption of the molecules, the basal surface of two-dimensional layered particles essentially has two opposite planes of the surfaces on which the adsorption of the molecules occurs. Ordinary R_0 reaches far higher values than the distances between opposite surfaces. When calculating the energy transfer efficiency, it is possible to neglect the distances of opposite surfaces (~ 1 nm) of an individual layered particle and evaluate the energy transfer as if it was realized on the one plane created by merging the two planes of opposing surfaces. In such a case, the dye concentration is essentially doubled compared to the real concentration on one of the surface planes of a particle.

A further increase in the dye concentration in such hybrid systems may also occur with the flocculation of the particles. The simplest example is the association of two particles. An agglomerate can be formed by joining two individual particles with already adsorbed dye molecules. In the agglomerate, two sides of the particles share

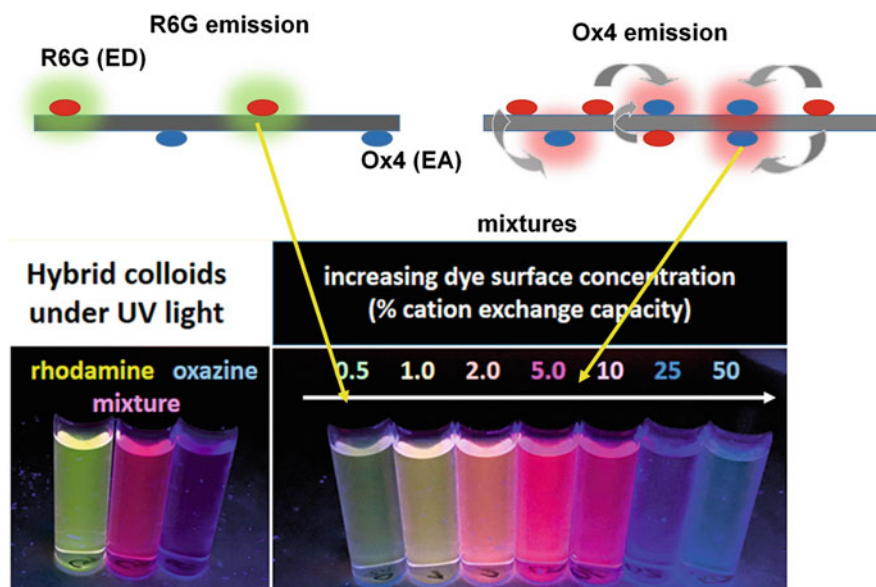


Fig. 5 Photographs showing the effect of the surface concentration of dyes (R6G and Ox4) adsorbed onto saponite particles in colloidal dispersion [11]. Dye bulk concentrations were the same for all the specimens. Only the concentration of saponite particles was changed, which controlled the surface concentration and the intermolecular distances of the adsorbed dye molecules. The distances influenced the efficiency of energy transfer, changing the color of the emitted light. The photographs were taken under UV light in the dark. Reprinted and partially modified with permission from (Belušáková, S., Martínez-Martínez, V., Arbeloa, I.L., Bujdák, J., 2017. Resonance Energy Transfer between Dye Molecules in Colloids of a Layered Silicate. The Effect of Dye Surface Concentration. *J. Phys. Chem. C* 121, 8300–8309) Copyright (2017) American Chemical Society

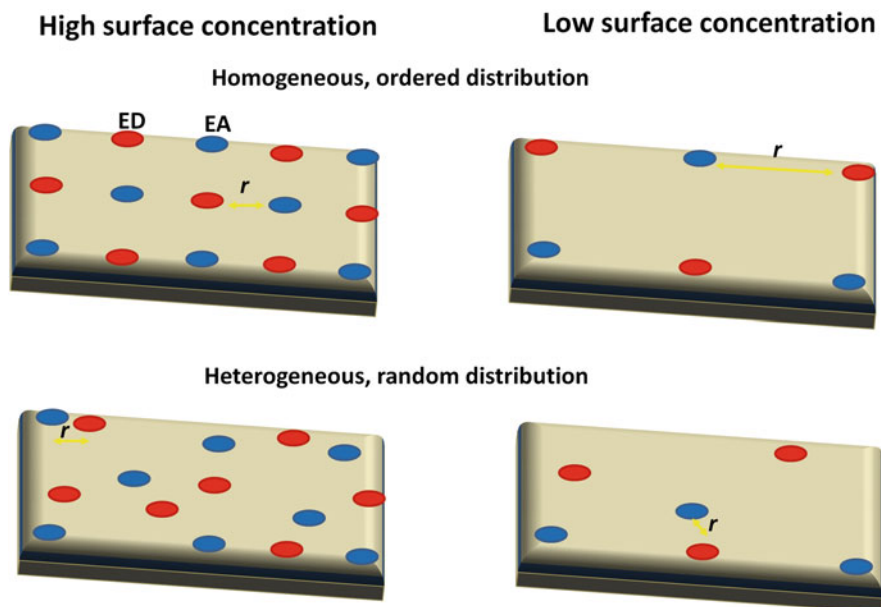


Fig. 6 Scheme showing an underestimation of the occurrence of short intermolecular distances in the model of a homogeneous ordered distribution. A heterogeneous or random distribution of the molecules on the surface of particles (lower) leads to the occurrence of both shorter and longer than average distances between molecules (upper). The shorter distances between ED and EA significantly contribute to the enhancement of FRET efficiency. Left – high surface concentration, right – low surface concentration

a common interlayer space formed by a face-to-face association. In the interlayer thus formed, the dye concentration increases to twice the value that it was prior to the coupling of the particles. From this point of view, the destabilization of colloids followed by the interparticle association is a significant factor that can also contribute to an increased FRET efficiency, but also to other, undesirable effects such as molecular aggregation and enhanced light scattering. Colloidal systems have been frequently used as the precursors of hybrid solid materials or thin solid films. By associating multiple particles into larger agglomerates, the character of the FRET is also changed from two- to three-dimensional. Substantially higher yields are achieved for three-dimensional FRET, although the dye/substrate ratio remains the same [11, 31, 45].

The model of the distribution of dye molecules shown above considers a completely random distribution of both ED and EA molecules on both the adjacent planes of the surface of particles, without any preference to either side. However, more complex views on this topic have been reported, and segregation of the molecules has also been considered [34, 52, 53]. The ways in which the molecules can be distributed on the surface of particles is shown in the scheme (Fig. 7). The first hypothesis on the possible segregation occurring in hybrid colloidal systems was

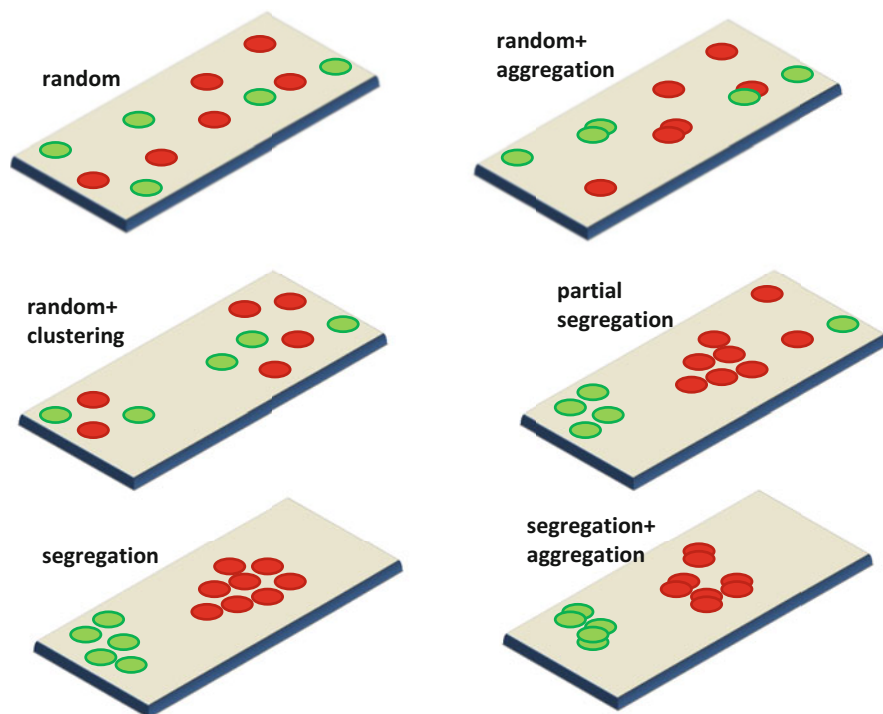


Fig. 7 Different models of the distribution of dye molecules on a particle surface

assumed based on a low efficiency of electron transfer between adsorbed $[\text{Ru}(\text{bpy})_3]^{2+}$ and methylviologen [54]. However, later on, similar materials exhibited no segregation [55], which was later confirmed for various types of materials [11, 36, 56]. The segregation of adsorbed dye molecules may be due to a specific adsorption mechanism. The adsorption is usually controlled by diffusion of the dye molecules from the solution to the surface of the particles [5]. In this case, the adsorption can be completed more rapidly than the effective mixing of the solution and the colloid [57]. As a consequence, the segregation and non-homogeneous distribution of the dye molecules may occur. However, recent studies on the kinetics of the molecular aggregation of dyes indicate an almost instantaneous adsorption is followed by further processes, including the rearrangement and redistribution of the molecules [57, 58]. In addition, a piece of direct evidence has also been obtained that dye molecules are exchanged between particles [11]. This evidence emerged from the results of an experiment for preparing Sap colloids with two laser dyes, R6G and Ox4. In the first step, two Sap colloid systems were prepared, each containing one of a pair of the dyes. The experiment tested whether such *forced segregation* would also remain after the mixing of the two colloids. After mixing the systems, the dye molecules were gradually exchanged between the particles. This was effectively monitored by the increasing efficiency of the energy transfer between the dye

molecules over time. Within a few seconds, mixed systems with a random distribution of both types of dyes emerged [11]. On the other hand, the segregation of dye molecules has been experimentally proven for some specific systems. Such segregation could be promoted when the dye molecules are structurally very different species. Examples are an ED and EA pair based on a polymer and a compound of much smaller molecular size [59, 60]. In this case, the segregation has been proven and led to an increase in molecular aggregation. Segregation can also relate to the strong adsorption of dye molecules, which prevents their migration and redistribution. For example, some porphyrins can migrate onto the surface of individual clay mineral particles, but cannot move from one particle to another [36]. The segregation of the molecules can be greatly influenced by an appropriate interaction between the dye molecules and the particle surface. If the adsorption of the dye molecules is dominated by electrostatic forces, the distribution of charged groups in the dye molecules should match sites with an opposite charge on the particles. Appropriate parameters would lead to the optimal adsorption and distribution of the molecules (random distribution). A model that describes the rules for achieving these optimal conditions has been elaborated in detail [34, 36, 38, 56, 61–63]. However, in some cases, nanoparticles may exhibit a heterogeneous charge distribution, which may lead to the distribution of qualitatively different properties of a portion of the particles with respect to dye adsorption. If ED and EA are dyes with significantly different properties, some molecules can be selectively adsorbed onto part of the particles and another dye on another part, which is, in fact, the segregation of the molecules. One example is a system based on porphyrin and viologen molecules on the surface of a synthetic Sap [53]. Although porphyrin was effectively quenched at high concentrations of viologen molecules, some of the porphyrin fluorescence remained to indicate the presence of the segregated phases of the molecules. To reduce molecular segregation, the proper selection of components and preliminary tests by FRET seem to be the best strategies. However, an encapsulation of dye molecules in cavitands can also play a significant role and may improve the properties of the system in this respect [52].

The distances between the molecules can be controlled not only by the number of dye molecules with respect to the surface of particles but also by incorporating another component to dilute the concentration of the adsorbed dye molecules. In some cases, organic surfactants, which are inactive in terms of photophysics, were used as a part of the mixture with dye molecules. This helped to reduce the concentration of the dye molecules and prevented their aggregation. An example is multilayer hybrid films containing amphiphilic cationic complexes of Ir^{III} adsorbed onto synthetic Sap [42]. The distance between the two Ir^{III} complexes, representing the emitters of blue and red light, was controlled by the presence of stearylammmonium cations. Another strategy was adopted for LbL films [29]. The efficiency of FRET was strongly influenced by the change in the distance between the interacting dye molecules, which was altered by the insertion of one or multiple photo-inactive layers of poly(styrene sulfonic acid) between the layers containing the photoactive dyes [29]. A similar strategy was applied for the LbL assemblies based on laser dyes and Sap particles [64].

4.2.4 Complexes with Neutral Dye Molecules

Systems based on uncharged organic dye molecules are very rare. One simple reason is the relatively low solubility of this type of compounds, especially in polar solvents that are compatible with nanoparticle systems. Another major reason for the application of this type of compounds being problematic is the relatively weak adsorption of neutral molecules to the polar surfaces of nanoparticles compared to the stronger electrostatic binding of ionic dyes. And last but not least, the formation of molecular aggregates and the so-called phenomenon of metachromasia, which frequently leads to the disappearance of a dye's photoactivity, occurs more easily in systems with uncharged molecules. Although ionic dyes also exhibit molecular aggregation, the degree of the aggregation can be at least partially reduced by electrostatic repulsion between ions of the same charge and by the hydration of the ions. With ionic dyes, the dye aggregation can be suppressed more easily than with neutral molecules. Nevertheless, the successful application of neutral dye molecules has also been realized. The solubilization of otherwise insoluble dyes was achieved in the presence of layered templates, such as Sap, which led to the enhancement of their photoactivity [65]. There are a few papers reporting FRET for systems with neutral dye molecules and layered inorganic templates. For example, FRET was studied with systems based on pyrene and acriflavine, the former dye component was in a neutral form. FRET efficiency doubled in the presence of Lap compared to the mixed solution, and a similar effect was observed for the systems with DNA [66]. Cavitands have been used to overcome the problems with molecular aggregation and the low solubility of neutral dyes in water and to achieve an enhancement of photoactivity (Fig. 8). The cavitands were also applied to improve the properties of hybrid systems to optimize FRET efficiency [49, 52, 67, 68]. A cationic organic cavitand was used to incorporate neutral organic dyes (neutral pyrene and 2-acetyl-anthracene) to improve their solubility and incorporate them into hydrophilic hybrid systems with

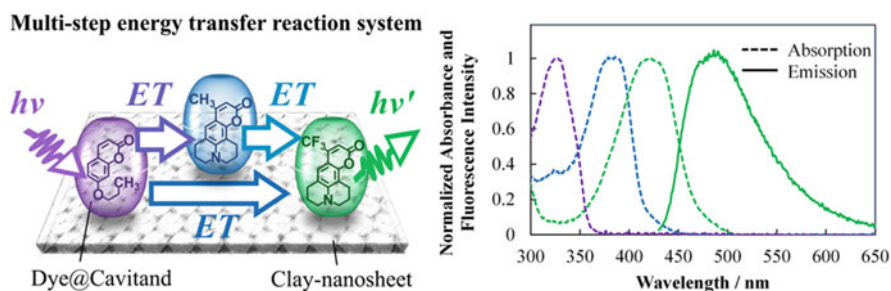


Fig. 8 Scheme showing energy transfer between neutral molecules of organic dyes embedded in cavitands adsorbed onto clay mineral particles [68]. The dye molecules achieved better solubility and enhanced photoactivity and effectively absorbed visible light in the range of 300–450 nm and emitted light at 450–600 nm. Reprinted (adapted) with permission from (Tsukamoto, T., Ramasamy, E., Shimada, T., Takagi, S., Ramamurthy, V., 2016. Supramolecular Surface Photochemistry: Cascade Energy Transfer between Encapsulated Dyes Aligned on a Clay Nanosheet Surface. *Langmuir* 32, 2920–2927). Copyright (2016) American Chemical Society

a layered silicate [52]. Both aromatic compounds are not very soluble in water and were solubilized by encapsulating their molecules in the cavities. At the same time, the incorporation of the dyes in the cavitand protected them against molecular aggregation and prevented fluorescence quenching. Highly efficient FRET was achieved, even with relatively high loadings of the encapsulated dye molecules [52]. In similar work, the pair of tetracationic Zn-porphyrin and neutral aromatic molecule of 2-acetyl-anthracene encapsulated inside the cavity of a cationic organic cavitand was used [67]. Under the condition of an intermolecular distance of only 2.4 nm, an almost 100% efficiency of FRET was observed. In some cases, the modification using ionic surfactants makes the materials suitable for the adsorption of neutral molecules. Hostasol red is a hydrophobic and strongly luminescent dye in aprotic solvents, but its luminescence is significantly quenched in polar solvents. Its quenching was also observed when the dye was adsorbed onto a zeolite L surface [69]. An increase in luminescence quantum yield could be achieved if the potassium cations in the zeolite were exchanged for imidazolium cations. The dye molecules embedded within the channels protected by perylene dye co-adsorbed onto the external surface, resulting in highly luminescent materials in which FRET from the perylene dye to Hostasol red occurred. Effective FRET was also applied at an ED/EA ratio of 100:1 [69]. Another example is hydrogels, which were based on Lap, cationic cyclodextrins, pseudorotaxenes, and organic dyes exhibiting high quantum yields and efficient FRET [70]. Adjusting the various ratios of the interacting dyes led to different colors of emitted light, including white light composed of a proper spectrum of polychromatic light. The tunable luminescent properties of the hydrogel will open up new possibilities for the preparation of new luminescent materials.

4.2.5 Covalently Bound Dye Molecules

Relatively stable hybrid materials can be prepared in particular by covalently attaching chromophoric groups to the surface of nanoparticles. This method requires the use of reactive dyes or precursors that can react with specific groups on the surface of the particles. An example can be the coupling of reactive silanes with chromophore groups by reacting with the OH groups on the surface of silicate nanoparticles [51, 71]. Occasionally, such reactive precursors may be used as part of reaction mixtures for the synthesis of hybrid nanoparticles [72, 73]. Surface heterogeneity at the nanometer scale is a very important factor in the modification of nanoparticles with dyes. An example is the selective modification of silicate particle edges [51, 71]. Some such systems exhibited very efficient FRET [51, 72, 73]. The pair of coumarin and cyanine dye derivatives were used in an energy transfer study [72]. The coumarin moieties were incorporated into the phyllosilicate structure during the synthesis of the silicate. A reactive silane derivative with a coumarin group was used. The second dye was intercalated into the coumarin/silicate complex (Fig. 9). In this work, the phenomenon of energy transfer was investigated in detail, and it was possible to distinguish the transfer by both radiation and non-radiation mechanisms [72]. The photophysical interaction could be

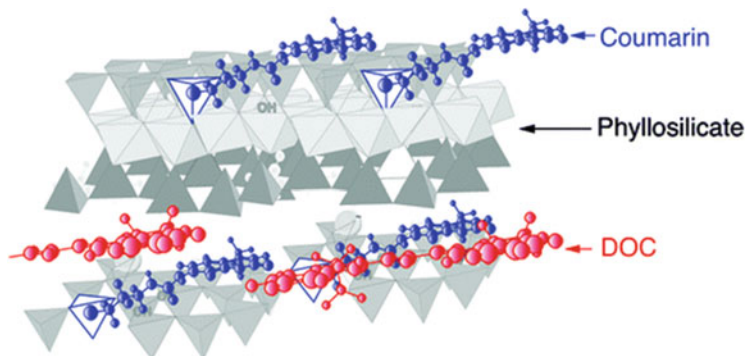


Fig. 9 Scheme showing the structure of the synthesized hybrid material of phyllosilicate with covalently bound coumarin moieties (blue) and intercalated cyanine dye (DOC, red) molecules [72]. Reprinted with permission from (Kuroda, T., Fujii, K., Sakoda, K., 2010. Ultrafast Energy Transfer in a Multichromophoric Layered Silicate. *J. Phys. Chem. C* 114, 983–989). Copyright (2010) American Chemical Society

controlled by the ratio of the embedded luminophores [73]. Similar systems were investigated using R6G as the EA [73]. The fluorescence spectra significantly changed mainly at higher loadings of R6G, indicating the formation of molecular aggregates. In another study, the reactivity of hydroxyl groups at the edges of smectite layers was used to prepare a system exhibiting FRET [51]. The hydroxyl groups were selectively modified with a reactive pyrene derivative playing the role of ED. The adsorption of the cationic porphyrin was realized via an ion exchange reaction in another step. FRET was used to characterize the distribution of cations of the porphyrin. The energy transfer was very effective to the molecules located near the particle edges bearing moieties of the pyrene derivative. It appeared that a significant proportion of porphyrin cations were adsorbed near the center of the particles and did not participate in the energy transfer [51].

4.2.6 FRET in Hybrids with Polymers

Types of Polymers and Formation of Polymer Nanocomposites

Some hybrids based on layered nanoparticles and organic dyes also included macromolecular substances as one of the components. In general, various types of polymeric substances can be used in these materials. For example, molecules of polyelectrolytes are electrostatically attracted to the surfaces of particles with an opposite charge. Another type of polymers is polar but neutral macromolecules that are soluble in water and polar solvents. In contrast to neutral small molecules, a relatively strong adsorption of such polymers on the surfaces of hydrophilic nanoparticles occurs. A specific category of macromolecular substances is technical,

hydrophobic polymers and their nanocomposites. The compatibility of industrial polymers with nanoparticles of various types has been a major topic of materials science in recent decades. Macromolecules as one of the components in hybrid materials or nanocomposites can be either inactive or active in terms of photochemistry. Common technical polymers or biopolymers are typical examples of photoinactive substances. In this case, the photoactivity is achieved by the addition of photoactive components or by modifying either layered particles or the polymer with photoactive moieties. The presence of chromophore or luminophore groups in the chains of polymers usually plays a minor role in their chemical and physical properties. The presence of luminophore labels mostly does not affect the binding of a polymer to nanoparticles, because only low contents of such groups are needed for an optical or photophysical activity of the material [71]. One of the challenges of using polymer nanocomposites as optical materials is their transparency in the relevant range of the electromagnetic spectrum [74]. The protecting role of the polymer and nanoparticles in such materials is very important, especially with dyes that are sensitive to oxidation or humidity [74, 75].

Polymer nanocomposites can be prepared by traditional routes; the most common method of synthesis is the mixing of a polymer with nanoparticles by the adsorption of macromolecules from their solutions or melt extrusion. In a few cases, polymerization from monomers was also performed. An example is the polymerization of styrene, which together with R6G and a polymerization initiator was pre-intercalated in an organically modified fluoro-mica [76]. The final composite materials exhibited improved thermal and chemical stability and energy migration [76]. In another study, the degree of polymerization influenced the properties of the dye component in the material. In situ polymerization leading to the formation of poly(norbornene) affected the molecular aggregation of oxazine 1 and FRET between oxazine 1 monomers and J-aggregates [59]. In another study, the presence of an inert and photochemically inactive polymer suppressed the molecular aggregation of the dye and significantly improved the photoactivity of the composite [60].

Polyelectrolytes in LbL Assemblies

Polyelectrolytes can significantly alter their surface charge, depending on the density of the charged groups in the polymer chains and the charge distribution on the surface of the modified particles. Polyelectrolytes have been applied in numerous works, many dealing with the synthesis of photoactive LbL films [40, 77]. For example, the anionic block copolymer poly(tert-butyl acrylate-co-ethyl acrylate-co-methacrylic acid) was deposited alternatively with LDH nanosheets to form an LbL film [78]. The polymer phase formed multicomponent micelles carrying the complex of Zn^{II} (8-hydroxyquinolate)₂ and a merocyanine dye. Different types of FRET were observed in this film: zero-dimensional FRET inside the micelles and two-dimensional between the micelles [78]. In another study, FRET was used as a very effective method for monitoring changes in photoactive substances during the deposition of LbL assemblies [40]. The films were based on a layered silicate, a

cationic polymer, and laser dyes. The extent to which molecular aggregates were formed or changed with the deposition of new layers was determined. The desorption of part of the dyes from the outer surface during the deposition of new layers was clearly identified, but the stability of the layers inside the film was confirmed [40].

Composites of Luminescent Polymers

Various materials derived from polymeric substances with photoactive groups have been reported. For example, materials with the properties of light-emitting diodes were produced as nanocomposites of conjugated polymers and organoclays [75]. Two-dimensional composite materials have been shown to be the most effective at polychromatic light emission, with high efficiency and good environmental stability. Energy migration played a significant role in the photophysical properties of such materials [75]. In a few cases, merely the presence of inorganic particles may induce a higher photoactivity of luminescent polymer substances. An example is the mixture of a luminescent poly(fluorene) with kaolinite [79]. No intercalation of the polymer chains took place, but the positive effect of the clay mineral on the photoactivity of the polymer was apparent. There are about a dozen examples of FRET occurring in hybrid materials based on nanoparticles which also include luminescent polymeric substances, if we omit energy migration between the same type of luminophores and fluorescence quenching, which are more frequent. For example, two-step FRET has been achieved in blue light-emitting materials based on zeolite and several photoactive substances [80]. Before preparing the composite, zeolite was modified with oxonine dye, which was incorporated inside the cavities of the host. The external surface of the zeolite was grafted with thiophene-based fluorophores and modified with a fluorene-based copolymer. The photoactive luminophores interacted via FRET starting from the polymeric phase, via the dye molecules anchored on the external surface and ending inside the zeolite cavities [80]. Slightly different arrangements were adopted for the hybrids based on layered nanoparticles. The intercalation of both the polymeric and non-polymeric luminescent substances is the most frequent procedure for the preparation of such materials. One example is FRET from a luminescent organosilicon compound – polyhedral oligomeric silsesquioxane – to RB intercalated in Sap [81]. The structure of polymer molecules can be significantly changed upon their intercalation between layered particles. This may secondarily affect the conjugation of the polymer [82]. For example, the conjugated polymer poly(9,9-dioctylfluorene), which emits in the blue light region, was intercalated between the layers of the layered metal dichalcogenides MoS_2 and SnS_2 . The polymer formed two distinct phases that differed in their extent of polymer conjugation: The phase of the planar-extended conjugation, which was identified as a fraction of the polymer present in the interlayer spaces, exhibited a red-shifted absorption with respect to the common form of the polymer. An efficient energy transfer occurred from the bulk phase to the planar one, resulting in a shift in the wavelength of emitted light [82].

Examples in Sensor Applications

Systems with luminescent polymers are often designed to serve as sensors for various analytical purposes. For example, a hybrid material based on LbL assemblies composed from perylene, poly(*N*-vinylcarbazole), and LDH nanoparticles exhibited a reversible switching of the emission of two colors: violet and blue [83]. The switching was achieved by modulating FRET from poly(*N*-vinylcarbazole) to perylene by changing the concentration of vapors of organic volatile solvents. The phenomenon was explained by the migration of solvent molecules inside the films leading to swelling and increased distances between the ED and EA. This led to the inhibition of the FRET, which was reversible upon the repeated removal or increase in the vapor pressure of the solvents [83]. For this purpose, proper polymers must be chosen to sensitively respond to the presence of solvent vapors. Films of similar properties were designed on the same type of polymer and the complex tris [2-(4,6-difluorophenyl)pyridinato- C^2,N]Ir^{III} [84]. Cyan luminescence from the Ir^{III} complex due to triplet Ir^{III}-to-ligand and ligand-to-Ir^{III} charge transfer and also under conditions of the selective excitation of the polymer proved the occurrence of FRET. The process was described as two-dimensional and achieved high efficiency. The presence of the vapors of various volatile organic solvents could interrupt the energy transfer process [85]. Some of the developed polymeric materials can be also applied in cancer therapy (Fig. 10). Microcapsules based on MoS₂ and a pH-responsive polymer (a copolymer of 2-(diethylamino)-ethyl methacrylate and butyl methacrylate) with fluorescent rhodamine end groups are a typical example of a sensor which can easily penetrate inside the cells. The MoS₂ inside the capsules played the role of an efficient FRET quencher. The changes in pH in the environment of the microcapsules induced the conformation changes in the polymer chains, which sensitively affected the efficiency of FRET [86].

4.2.7 Molecular Orientation and Anisotropy

The spatial orientation of EA and ED molecules is a parameter that significantly affects FRET efficiency. It is a challenge to synthesize systems with a high degree of organization of fluorophores with controlled intermolecular distances and orientation and a high photoactivity. The difficulties occur due to the limits of the size of assemblies that can be applicable for devices. Large ordered systems might be produced quite easily using a supramolecular organization and self-assembly in two or three dimensions. However, the functionality of such systems often suffers from luminescence quenching due to the formation of molecular aggregates.

The orientation of dye molecules on the surface of nanoparticles is quite important for FRET efficiency. Determining it for colloidal hybrid systems is quite problematic, but the orientation of dye molecules in oriented films can be determined relatively easily using linearly polarized spectroscopy, e.g., [35, 87–89]. The optical anisotropy of the oriented hybrid films is due to the two-dimensional nature of the particles and their alignment on the surface and at the same time a preferential

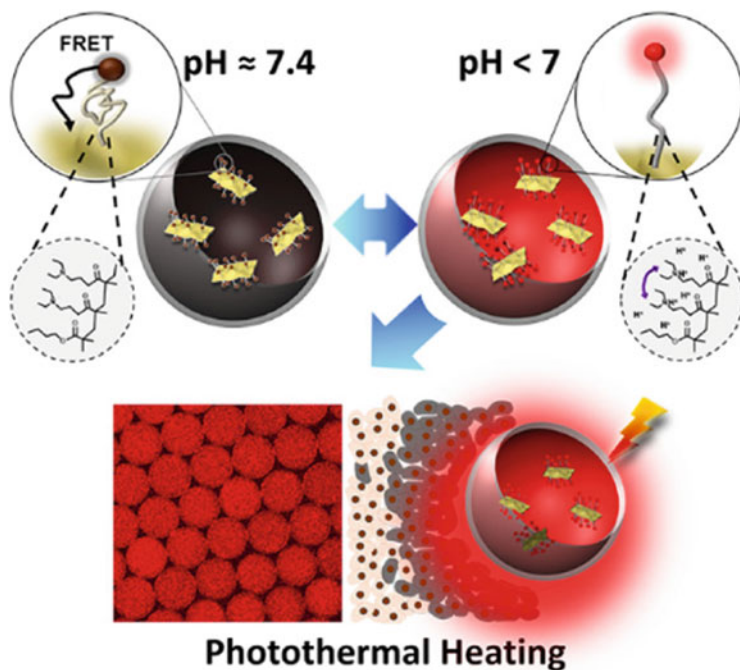


Fig. 10 Scheme of microcapsules as suitable materials for in situ pH sensing and their photothermal properties [86]. The microcapsules contain MoS₂ particles with a semi-permeable polymeric coating. The MoS₂ were functionalized with pH-responsive polymers with fluorescent end groups. Changing pH results in a change in the conformation of the polymers, which results in a change in the distances between the end groups, easily measured by FRET. Reprinted with permission from (Park, C.H., Lee, S., Pornnoppadol, G., Nam, Y.S., Kim, S.H., Kim, B.J., 2018. Microcapsules Containing pH-Responsive, Fluorescent Polymer-Integrated MoS₂: An Effective Platform for in Situ pH Sensing and Photothermal Heating. *ACS Appl. Mater. Interfaces* 10, 9023–9031). Copyright (2018) American Chemical Society

orientation of dye molecules [90–92]. With layered particles, it is easy to achieve at least a partial anisotropy by ordering the layers in anisotropic three-dimensional structures. For example, such ordering takes place when the films are prepared from colloidal precursors by the preferential alignment of the layered particles with respect to the surface of a substrate. The layered particles in such films are arranged in a face-to-face alignment, lying parallel with respect to the substrate. A higher degree of anisotropy can be achieved by spin coating. For the dye molecules adsorbed on the surface of layered particles, a preferential orientation is expected due to specific dye-surface or dye-dye interactions.

Molecular orientation is significantly affected by molecular aggregation. For example, H-aggregates of some dyes were characterized by a nearly perpendicular orientation with respect to the plane of the layers, while non-aggregated molecules or those forming J-aggregates were almost parallel with respect to the substrate surface

[90–92]. In specific cases, the changes in the orientation led to the formation of photoactive molecular aggregates, resulting in a phenomenon called aggregation-induced emission [93]. Systems based on organic dyes and layered nanoparticles are mostly composed of a mixture of various types of molecular assemblies coexisting together with non-aggregated dye molecules [5]. Although a parallel alignment between interacting transition dipole moments is the most suitable for FRET to occur, this phenomenon proceeds at a lower extent with variable configurations [23]. A typical example is the energy transfer from monomers and H-dimers to J-aggregates; the result of such an interaction can be monitored by the red-shifted fluorescence [23]. The energy transfer produces a partial depolarization of the polarized light used for the excitation, but a complete depolarization is rarely achieved [35, 44].

It has been concluded that the orientation is individually related to dye structure and in particular to the interactions that occur between molecules and particles [92]. The topography of a particle surface can also influence the molecular orientation that results from the structure of the particle surface. Different orientations can occur in colloidal systems and in solids, even if the components of the materials are the same. It is not simple to generalize the relatively different behaviors of different types of organic dyes depending on the properties of both of the components. In rare cases, a perpendicular orientation is preferred. If the dye has more ionic groups, these cause electrostatic interactions with the particle surface supporting a parallel orientation [43, 94]. Significant effects of various solvents have also been observed which, due to the interactions between the individual components, could significantly influence or possibly alter the orientation of dye molecules by changing the vapor pressure of the solvent [43, 56]. The phenomenon was investigated for porphyrin dyes whose molecules were adsorbed onto the basal surfaces of phyllosilicate particles. When changing the composition of the vapors surrounding this hybrid material, the angle of the orientation of the adsorbed dye molecules changed in some cases. It has been assumed that the change in orientation resulted in significant changes in the efficiency of FRET between different porphyrin molecules. In this way, the energy transfer can be changed by an external stimulus, which is caused by the change of molecular orientation. This technique could be useful in constructing photofunctional switches or sensors [43].

4.2.8 Cascade Energy Transfer

Cascade FRET or multi-step FRET can be defined as a non-radiative process of the transfer of excitation energy that occurs between more than one pair of ED and EA on the scale of intermolecular distances < 10 nm. By its nature, multi-step FRET is more efficient than the one-step process, which is limited to only a pair of the first and end member of the cascade. It is claimed that a multi-step process can be realized beyond the distance conventionally achieved for single-step processes [95]. If there are several molecules of different dyes with different photophysical properties in the vicinity of an excited ED molecule, then a selective transfer of energy takes place not

only on the basis of the smallest intermolecular distance but also on the basis of spectral overlap criterion. Assuming that the distances in a macrosystem are statistically the same for all the dye components involved, then the spectral properties are the most important criterion.

There are several examples of systems with layered nanoparticles as hosts of at least three different types of dyes exhibiting multi-step FRET. Blue-emitting neutral poly(vinylcarbazole), tris-(8-hydroxy-quinoline) aluminum, tris [2-(4,6-difluorophenyl) pyridinato-C 2,N] iridium (III), and 4-(dicyano-methylene)-2-methyl-6-(4-dimethylamino-styryl)-4H-pyran were chosen as fluorophores with blue, green, and orange emission, respectively [84]. The fluorophores were assembled in the films of LDH applying an LbL assembly method and efficiently interacted as ED and EA in FRET. Two-dimensional FRET was achieved with enhanced orange fluorescence from the final member of the cascade. The efficiency of FRET was significantly affected by the presence of different organic solvents [84]. The phenomenon of controlled multi-step energy transfer can lead to novel materials with efficient light absorption over a broad spectral range. One such material is Sap nanolayers with three adsorbed cationic dyes, one fluorine derivative, and two porphyrins. The material exhibited efficient absorption over a broad range of wavelengths [96]. FRET in more than one step was also observed for the dyes pyrene, acriflavine, and RB [95]. Pyrene and RB played the role of ED and EA, respectively, and acriflavine molecules mediated and increased the efficiency of the transfer. The presence of Lap significantly increased the FRET efficiency [95]. The two-step FRET process was observed for films of Sap and three laser dyes [35]. A FRET process was confirmed by the results of steady-state and time-resolved fluorescence spectroscopies. The depolarization of light determined by fluorescence anisotropy helped to identify the most efficient steps of FRET [35]. Complex systems based on the films of Sap with embedded six dyes were also constructed, and multi-step FRET proceeding at a very low concentration of the dyes was characterized [44].

4.2.9 Energy Transfer in Solids and Assembled Films

In addition to the variability of the individual components that make up the hybrid systems, there is a relatively broad spectrum of material types. Besides conventional colloidal systems and solid powders or films that can be prepared from colloidal precursors, there are some special types of solid hybrid materials [7, 12, 24, 97]. The most frequent examples of solid materials are transparent thin films that can be prepared by various procedures (Fig. 11). Very thin films can be made by depositing LbL assemblies using the charge of individual components in the deposition process to prepare alternating assemblies of the layers. Several films of this type exhibited efficient FRET [29, 39, 40, 64, 78, 83, 98, 99]. The films of LB type which represent monomolecular assemblies can be prepared by combining nanoparticles and surfactant molecules. Luminescent LB films can be prepared by applying either the surfactants with luminescent groups or incorporating common dye molecules into

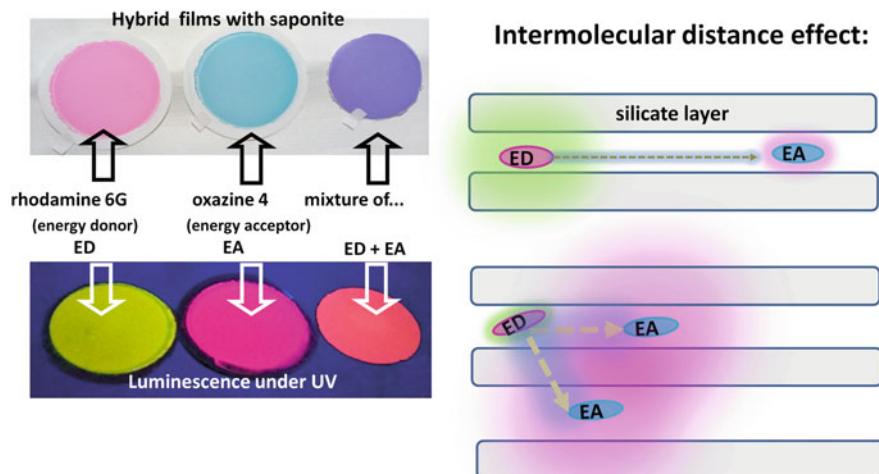


Fig. 11 Hybrid films of saponite with intercalated laser dyes, rhodamine 6G and oxazine 4, prepared by a vacuum filtration method (left) and scheme showing three-dimensional FRET and its dependence on the distances between intercalated ED and EA molecules (right) [45]. Reprinted from *Applied Clay Science*, Vol 155, Belušáková, S., Sola-Llano, R., Arbeloa, I.L., Martínéz-Martínéz, V., Bujdák, J., Resonance energy transfer between dye molecules in hybrid films of a layered silicate, including the effect of dye concentration thereon, 57–64, Copyright (2018), with permission from Elsevier

the LB films. Some of them exhibited FRET [27, 32, 33, 42, 100]. An example is LB films comprised of N, N'-dioctadecyl-thiacyanine and octadecyl-RB in the presence of Lap. The dye molecules formed J-aggregates which were active in FRET [33]. The properties of LB films were improved compared to the hybrid dispersions or films of the same systems, in which the hydrophobic dyes had a stronger tendency to aggregate, forming H- and J-type assemblies with lower photoactivities [33]. FRET was effectively used to track changes occurring during the deposition of the LbL films based on the layers of silicate particles with adsorbed cationic laser dyes and polyelectrolyte [40] as already described in Sect. 4.2.6.

4.2.10 Structural Changes in Dye Molecules and FRET

Changing the FRET efficiency can be achieved by an induced change of the integral overlap. It can be done by changing the conditions, notably pH, photochromically, or by interacting with an analyte. One possibility is to change the integral overlap by shifting the wavelength of the absorbed light. Alternatively, the change in the integral overlap may be modulated by changing the molar absorption coefficient without any significant displacements of the absorption bands. The use of

photochromic dyes in FRET can be applied for special systems that enable switching between two forms, thus modulating FRET by the two optical forms of either ED or EA molecules. Another example is the ring-open and ring-closed form of rhodamine dyes controlled by environmental conditions such as the polarity of the solvent. The open-ring forms have high molar absorption coefficients in the vis range, whereas those with the closed ring do not exhibit significant absorption in this region. In addition, these two forms are significantly different in terms of fluorescence and photoactivity. There are several examples of systems including layered silicates exhibiting the phenomena of modulating FRET by changing the structure of interacting dye molecules. For example, using light-sensitive merocyanine as part of the FRET system, UV light can be used to switch off the energy transfer in the system [78]. The process was fully reversible, and the switching on could be performed using vis light irradiation. The switching on/off was not a fast process, taking seconds to minutes [78].

In many cases, the pH of the system can significantly affect the properties of dye molecules participating in FRET. Acidic forms significantly change their properties with respect to the energies of absorbed and emitted light, but also in terms of fluorescence efficiency and the value of molar absorption coefficients. One such example is xanthene dyes [101]. Another example of FRET modulated by pH is the sensitive response of fluorescein to the pH of the medium [47]. The spectral changes of fluorescein sensitively influenced the overlap between its emission spectrum and the absorption spectrum of R6G, as the EA. The electrostatic interaction between the anionic and the cationic dye also led to an efficient FRET in mixed solutions, most likely due to the formation of ionic pairs. However, the presence of Lap contributed to the increase in FRET efficiency. These systems could be used as a pH sensor over a relatively broad range [47].

In addition to pH, other conditions can also affect FRET. For example, solvatochromic properties can be used to influence not only the spectral properties of the dyes but also the efficiency of FRET [56]. Fluorophores can change their properties due to their interaction with layered hosts, which can also be applied in FRET. For example, poly(styrene) chains carrying fluorescent terfluorene side groups significantly changed their spectral properties when intercalated between silicate layers [102]. The hybrid material exhibited deep-blue electroluminescence mainly thanks to FRET taking place between terfluorene and fluorophore groups occurring in different conformations (Fig. 12). The excitons of terfluorene groups in the bulk phase transferred energy to the intercalated polymer chains. The emission occurred mainly from the planar fluorenyl moieties intercalated between the silicate layers, which exhibited enhanced quantum efficiency [102].

4.2.11 Influence of Electrical Properties of Hosts on FRET

The optical properties of the system and the efficiency of FRET can be influenced by the electronic properties of the layered particles. This is essential whether the layered particles has insulating, semiconductive, or electrically conductive properties, or if

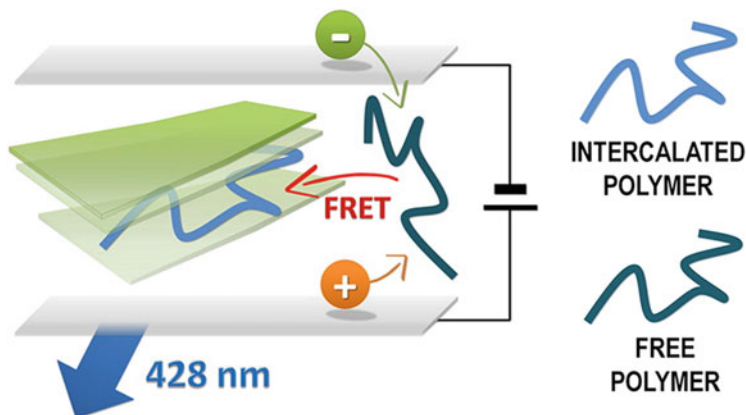


Fig. 12 Scheme showing FRET mechanism occurring in the polymer/layered silicate nanocomposite [102]. Poly(styrene) carrying terfluorene luminescent groups is partially intercalated. The bulk phase transfers energy to the intercalated polymer. Reprinted with permission from (Giovannella, U., Leone, G., Galeotti, F., Mroz, W., Meinardi, F., Botta, C., 2014. FRET-Assisted Deep-Blue Electroluminescence in Intercalated Polymer Hybrids. *Chem. Mater.* 26, 4572–4578.). Copyright (2014) American Chemical Society

they are photoactive. In some cases, their insulating properties play an essential role in the functionality of the material [102]. Charge-induced exciton quenching was effectively prevented with an intercalated fluorescent polymer. The intercalated molecules could not be electrically addressed because of the insulating properties of the silicate layers, and the emitters were electrically isolated from the free polymer phase. The intercalated phase exhibited enhanced fluorescence compared to the bulk phase [102]. The presence of layered particles with luminescent or semiconductive properties allows a direct photophysical interaction of the particles with dye molecules. For example, the energy transfer between J-aggregates of a dye and a monolayer of semiconductive MoS_2 helped to enhance the efficiency of a photodetector [103]. Due to the strong spectral overlap between the J-aggregates and MoS_2 , efficient FRET and Dexter energy transfer took place. This material is a potential prototype of dye-sensitized photodetectors [103].

Another way to increase the efficiency of FRET is to use surface plasmon resonance [104]. This phenomenon is charge oscillations at metal surfaces stimulated by electromagnetic radiation. The electromagnetic waves propagate at the interface between the metal and non-conducting environment, and these oscillations are highly sensitive to the presence of molecules at or near the conducting surface. The local electric field resulting from a surface plasmon located near a metal nanoparticle can lead to an increase in exciton transfer efficiency, even when there are larger separations between the interacting molecules [104]. The emission from rhodamine dye J-aggregates was enhanced by surface plasmons on silica nanoparticles deposited onto the Ag surface [105]. This effect was accompanied

by a complete quenching of the emission of monomers. It was found that a quenching mechanism related to the amplification of the energy transfer from dye monomers to dimers and larger aggregates. Without this enhancement, the J-aggregates were weakly emitting species with a luminescence that was difficult to detect and measure [105]. A few materials combining quantum dots and layered nanoparticles have also been constructed. A few examples include LbL assemblies based on quantum dots attached to the LDH particles [106, 107].

4.2.12 Chemiluminescence Resonance Energy Transfer

Chemiluminescence resonance energy transfer (CRET) has not been investigated as frequently as the basic types of FRET [108]. Unlike FRET, CRET is initiated without an external source of excitation. It is initiated by specific reactions, such as the oxidation of chemiluminescent substrates. Chemiluminescence has many advantages, as to some extent, it minimizes nonspecific signals and light backgrounds and avoids the bleaching of dyes caused by external light excitation [109]. Highly effective CRET can be achieved when the molecules of interacting substances are fixed to the surface of layered nanoparticles [109]. An example is fluorescein dianions fixed onto the LDH surface. Under optimal conditions using peroxyxynitronium dianions as the ED, high CRET efficiency was achieved due to the improvement in the molecular orientation in the LDH matrix and the flatness of the molecules. This led to a remarkable increase in the fluorescence lifetime and quantum yield. This complex material was used for the construction of a device that was able to detect very low concentrations of the analyte, exhibiting operational stability, high reproducibility, and long service life. A flow column was constructed and successfully applied to determine nitrite ions in salami samples [109]. In another study, chemiluminescence was observed after the electrophilic attack of OH radicals on RB molecules adsorbed onto the montmorillonite surface [110]. Increased emissions were attributed to the H-aggregates of RB molecules, leading to an increased electron density on the aromatic rings. High electron density facilitated using the electrophilic reaction with OH radicals as a selective probe to determine these species. Inorganic layered particles can be used to prevent chemiluminescence quenching [111]. For example, the inhibition of chemiluminescence by halide ions in micelles was demonstrated by the fact that micelles formed from cetyltrimethylammonium hydroxide exhibited much higher emissions than those formed with the bromide salt. An elegant solution was to use organoclays based on alkylammonium-exchanged montmorillonite (without halide anions), leading to a large improvement in its chemiluminescence in a peroxyxynitrous acid (ONOOH) system [111].

5 Applications

5.1 Control of Photodegradation of Pesticides by FRET

One of the first types of applications that utilized the FRET phenomenon in a combination of hybrid materials, especially clay minerals, was agriculture. This was connected with controlling the photochemical degradation of pesticides. With FRET, it was possible to either stabilize or accelerate the decomposition of the pesticides. The stabilization was based on the quenching of the pesticides using a substance that interacted via the FRET mechanism. Or, on the contrary, the photosensitizer could be a source of energy to photochemically promote the decomposition of agrochemicals or to accelerate their decomposition. One example was the photochemical degradation of a thiazine-type insecticide adsorbed onto montmorillonite, nontronite, and hectorite [112]. The photodegradation was slower due to significant photostabilization compared to the pesticide in its free form. This was probably due to a charge transfer from the excited state of the pesticide to the Fe^{3+} ions. Further stabilization was achieved when the cationic dye, 3,6-diamino-10-methyl-acridinium, was co-adsorbed with the insecticide. The deactivation of the photodecomposition was carried out by FRET between the two organic molecules adsorbed onto the surface of the mineral [112]. Various mechanisms have been described for the photostabilization of agrochemicals, such as pesticides, using clay minerals modified with organic dyes. The phenomenon of energy transfer often played a dominant role. This was also the case in the stabilization of the photolabile insecticide bioresmethrin in a system of montmorillonite with the cationic dye methyl green [113]. The pesticide was stabilized due to the energy transfer from excited pesticide molecules to the methyl green. Energy transfer processes can also occur from the pesticide to the inorganic host, and the presence of transition metal ions in the structure can be effective energy or electron acceptors. Such a mechanism was observed during the photostabilization of the insecticide tetrahydro-2-(nitromethylene)-2H-1,3-thiazine [113]. Alternatively, photostabilization was achieved by the addition of a cationic dye – acriflavine – when a stereochemical factor played an important role in preventing or slowing down certain photochemical reactions. An example is the photostabilization of the herbicide trifluralin. Energy transfer has also been proven in photostabilizing microbial insecticides such as a toxin isolated from *Bacillus thuringiensis* [113].

5.2 FRET for Sensing

The most frequent applications of FRET are related to sensors. The spectral overlap integral can be altered by the effect of the molecular environment in various ways, in particular by changing the molar absorption coefficient of the ED. As analyzed in Sect. 4.2.10, the absorption spectra of rhodamine dyes are significantly changed by

the reversible reactions of ring formation and ring opening, which are very sensitive to the molecular environment [4]. There are several papers describing the functionality of new types of sensors using organic dyes and layered nanoparticles. There are dozens of examples using such hybrid systems in connection with FRET for sensing various analytes, such as inorganic ions [37, 41]. One typical example is sensing the vapors of various organic liquids [56, 83–85]. For example, the color of emitted light sensitively changed when the dyes/LDH hybrid films were exposed to the vapor of different volatile organic solvents [84]. In the presence of nitrobenzene, the luminescence was totally quenched. This was explained by an electron transfer process to the electron-deficient LUMO orbital of the nitrobenzene molecules. The presence of some organic solvent molecules can affect the swelling of the hybrid film, thus changing its fluorescence properties (Fig. 13). For example, a large degree of swelling with toluene prevented FRET from occurring [84].

ED chromophores based on an electron push-pull system exhibit photophysical properties that are greatly dependent on the solvent polarity. This variability can be explained by the presence of electron-donating and electron-accepting groups in the molecule. The change in the polarity is reflected in different spectral properties of such molecules, also affecting FRET [84]. Another example of solvent sensors is hybrid films based on poly(vinylcarbazole) (PVK) and a complex $[\text{Ir}(\text{F}_2\text{ppy})_3]$ assembled with LDH nanosheets. Cyan luminescence from the Ir^{III} complex (due to triplet Ir^{III} -to-ligand and ligand-to- Ir^{III} charge transfer) was also observed under the conditions of the selective excitation of poly(vinylcarbazole), indicating the occurrence of FRET. The vapors of volatile organic compounds can interrupt this

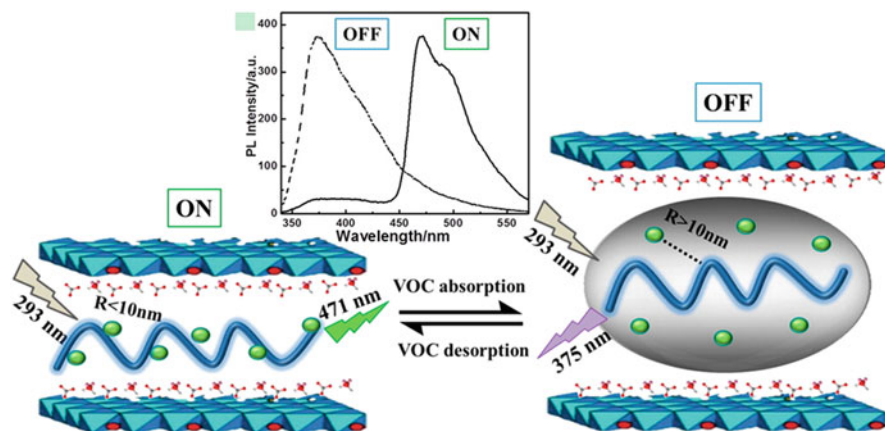


Fig. 13 Effect of swelling of the hybrid material by vapors of volatile solvents affecting FRET between a luminescent polymer and an Ir(III) complex [85]. Reprinted with permission from (Qin, Y., Lu, J., Li, S., Li, Z., Zheng, S., 2014. Phosphorescent sensor based on iridium complex/poly(vinylcarbazole) orderly assembled with layered double hydroxide nanosheets: Two-dimensional Förster resonance energy transfer and reversible luminescence response for VOCs. *J. Phys. Chem. C* 118, 20538–20544). Copyright (2014) American Chemical Society

process and thus be easily detected [85]. The phosphorescence sensor exhibited a fast, but highly reversible, response toward the solvents. The forbidden triplet-singlet exciton excitation energy transfer is the explanation of this interesting phenomenon. The ED(singlet) \rightarrow EA(triplet) energy transfer process was more efficient for sensing applications than the singlet-singlet process [84, 85]. In some cases, the nanoparticles themselves can participate in a FRET process. For example, layered MoS₂ exhibits the properties of an efficient fluorescence quencher, which was used in the selective detection of kanamycin residue in milk [114]. Some hybrid systems can respond to ambient conditions such as temperature [115, 116] or pH [47, 86].

Modern applications also include the sensing of biological compounds. FRET has been successfully applied for new clinical diagnostic methods and protein analytical techniques. Graphene oxide (GO) nanosheets easily dispersible in water were used for sensing immunoglobulin [117]. The GO played the role of a quencher in the selective FRET aptasensor. The luminescence from the fluorescein-labeled aptamer adsorbed onto the surface of GO was quenched by the host via a FRET mechanism. In the presence of the antibody immunoglobulin E (IgE), the bonding of IgE and the aptamer was stronger, which prevented the adsorption of the aptamer to GO. The result of the presence of IgE was the persistence of strong luminescence also in the coexistence of GO in the system [117]. Another example is a specific FRET aptasensor for the detection of the enzyme thrombin (Fig. 14) [118]. It used a dye-labeled aptamer adsorbed onto the surface of graphene, playing the role of the

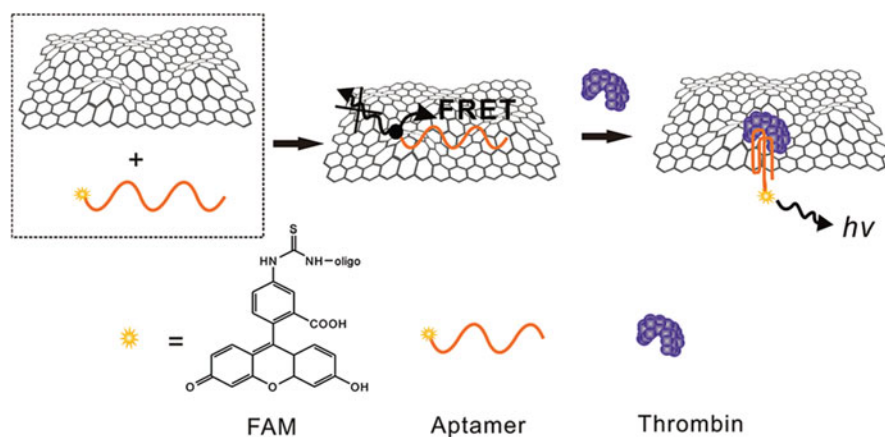


Fig. 14 A specific FRET aptasensor for the detection of thrombin, based on a dye-labeled aptamer assembled on graphene [118]. Quenching occurs due to the non-covalent association between graphene and the aptamer. The addition of thrombin leads to fluorescence regeneration due to the formation of aptamer-thrombin complexes that do not adsorb onto the graphene. Reprinted with permission from (Chang, H.X., Tang, L.H., Wang, Y., Jiang, J.H., Li, J.H., 2010. Graphene Fluorescence Resonance Energy Transfer Aptasensor for the Thrombin Detection. *Anal. Chem.* 82, 2341–2346). Copyright (2010) American Chemical Society

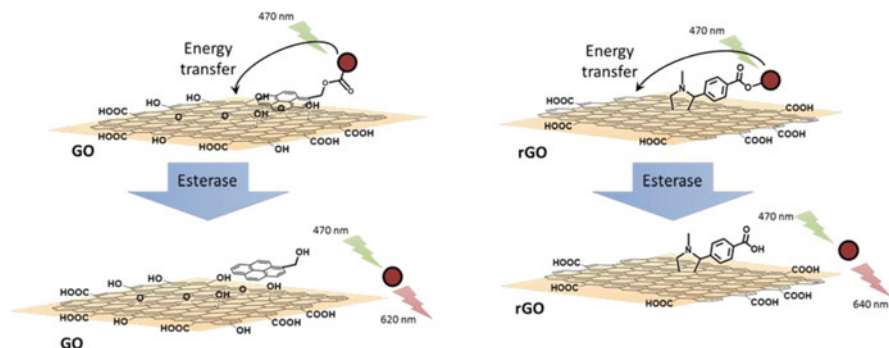


Fig. 15 Sensor for esterase activity based on Ru^{II} complexes attached to graphene oxide particles [119]. The interaction between the conjugates was studied by esterase hydrolysis. Hydrolysis caused the separation between donor and acceptor units, thus affecting FRET efficiency. Reprinted with permission from (Chi-Ming Leung, F., Wing-Wah Yam, V., 2018. Covalent and Non-covalent Conjugation of Few-Layered Graphene Oxide and Ruthenium(II) Complex Hybrids and Their Energy Transfer Modulation via Enzymatic Hydrolysis. *ACS Appl. Mater. Interfaces* 10, 15582–15590). Copyright (2018) American Chemical Society

quencher. Due to the non-covalent bond between the aptamer and graphene, the fluorescence of the luminophores linked to the aptamer was effectively quenched. The addition of thrombin led to the generation of fluorescence due to the formation of thrombin-aptamer complexes, which had a weak affinity for the surface of graphene [118]. The energy transfer phenomenon between pyrene and $[\text{Ru}(\text{bipy})_3]^{2+}$, which are connected in the complex molecule, was applied to track the hydrolysis of the bonds connecting these photoactive components (Fig. 15) [119]. The pyrene- Ru^{II} complexes were non-covalently attached onto the sheets of GO particles through their high affinity via π -interactions. The energy transfer could reflect changing separation distances between the ED and EA units during the hydrolysis reaction. These systems are promising for the detection of enzymes [119].

FRET from luminescent MoS_2 particles to polyaniline was achieved, which led to quenching of the luminescence of the nanoparticles [120]. The quenching was increased by increasing the concentration of polyaniline. In the presence of bovine serum albumin, the intense fluorescence of MoS_2 was recovered. Only nM concentrations of the biopolymer were needed to switch on the luminescence. The phenomenon was presented as potentially useful for sensing the biopolymer [120].

5.3 FRET in Bioimaging

A large number of fluorescent probes for bioimaging have been synthesized and applied as highly effective tools for monitoring biological tissues, microorganisms, and biomolecules. Thanks to high-resolution optical microscopy methods, living

systems can be monitored in real time, at high resolution and in their natural environment. Some limitations such as low fluorescence intensity and concentration limits, excitation wavelength limits, etc., can be overcome by using FRET [4]. Fluorescence probes in combination with layered nanoparticles are rarely used. Even other options that have not yet been exploited are for hybrid probe types using FRET. Fluorescence lifetime imaging (FLIM) is based on the fact that the lifetime of excited states of a fluorophore depends on its environment, but not its concentration. FLIM provides very useful information in combination with FRET, which is not accessible by steady-state FRET techniques. It can distinguish fractions of interacting and non-interacting probe molecules to obtain information on the ratio of the interacting molecules and on intermolecular distances [121]. FLIM would be an optimal method for detecting FRET occurring in hybrid systems probes.

5.4 FRET in Catalysis

Some hybrid materials exhibiting FRET can be applied as selective catalysts. The molecules of metalloporphyrin and subporphyrin in the roles of the photocatalyst and photo-antenna, respectively, were adsorbed onto particles of phyllosilicates [122, 123]. Highly efficient FRET from the subporphyrin to the metalloporphyrin was achieved, reaching 98%. Moreover, the photocatalyst exhibited a high efficiency to catalyze the photochemical conversion of cyclohexene. The cyclohexane reaction was initiated by the formation of a cation radical by electron transfer from the porphyrin and produced oxygenated and halogenated products of this alkene [123].

6 Future Perspectives

Recently, new types of layered inorganic compounds have been developed. The most interesting materials are those with conductive and luminescent properties, semiconductors and also superconductors. New inert and photochemically inactive layered substances are also important. New methods have been developed that can be applied to expand the layered solid crystals to obtain layered nanoparticles. Not only inorganic hosts but also new organic dyes, as the active components of these materials, are constantly being developed [124]. With the help of experts in organic synthesis, thousands of new luminescent dyes have been prepared in the last few decades, and some of them have found commercial use. The main and traditional applications include sensors or tunable lasers, but there is now a demand for fluorescent dyes that absorb and emit light in the NIR region. NIR radiation has better penetration through biological tissues, which makes such dyes promising for biomedical and biophotonic applications or as photosensitizers in photodynamic therapy. Light harvesting and transfer of the light energy via radiative or resonance mechanisms can overcome some problems occurring in the systems based on a

single type of dye. Many organic dyes exhibit a small Stokes shift, which is a drawback for some applications. Using energy transfer systems, a large pseudo-Stokes shift can be achieved, and the photoactivation can be performed at a spectral range significantly different from that of the expected emission [124]. Templates based on layered nanoparticles can be very useful for the construction of such systems. There are still many opportunities to develop novel layered nanoparticle hybrid materials. One example is utilizing or including the transfer of plasmon energy. Plasmonic metal nanoparticles have larger absorption cross sections than organic chromophores. The efficiency of energy transfer decreases more slowly with increasing distance between the nanoparticle and EA molecules than in FRET. Another advantage is the possibility of using an excitation wavelength longer than that of the absorption peak of the EA. The Stokes shift that is known to occur with molecular luminophores does not occur in plasmonics. The radiative deactivation from plasmonics via light scattering occurs earlier than non-radiative relaxation, and the wavelength profile of the emitted light is almost identical to that of the absorption cross section. Plasmon energy transfer does not consider meeting the conditions required by FRET, but is strongly dependent on the electronic properties of plasmons. This phenomenon can be used in photoelectrochemical cells, photocatalysis, and photovoltaics [125]. Other possibilities include other photophysical and photochemical phenomena such as chemiluminescence, bioluminescence, and triboluminescence. The energy transfer can find new applications in photosensitization, in photocatalysis, and in searching for new photosensors and in the construction of smart and multifunctional materials.

Acknowledgments This work was supported by the Slovak Research and Development Agency under contract No. APVV-15-0347, APVV-15-0741, and APVV-18-0075. Support from the VEGA grant agency (1/0227/20) is also gratefully acknowledged.

References

1. Calzaferri G (2010) Artificial photosynthesis. *Top Catal* 53(3-4):130–140. <https://doi.org/10.1007/s11244-009-9424-9>
2. Calzaferri G (2008) Energy transfer in nanochannels. *Nuovo Cimento Soc Ital Fis B* 123 (10–11):1337–1367. <https://doi.org/10.1393/ncb/i2008-10721-5>
3. Gartzia-Rivero L, Bañuelos J, López-Arbeloa I (2017) Photoactive nanomaterials inspired by nature: LTL zeolite doped with laser dyes as artificial light harvesting systems. *Materials* 10 (5):495. <https://doi.org/10.3390/ma10050495>
4. Yuan L, Lin W, Zheng K, Zhu S (2013) FRET-based small-molecule fluorescent probes: rational design and bioimaging applications. *Acc Chem Res* 46(7):1462–1473. <https://doi.org/10.1021/ar300273v>
5. Bujdák J (2018) The effects of layered nanoparticles and their properties on the molecular aggregation of organic dyes. *J Photochem Photobiol C* 35:108–133. <https://doi.org/10.1016/j.jphotochemrev.2018.03.001>
6. Bujdák J (2017) Hybrids with photoactive dyes. In: Nakato T, Kawamata J, Takagi S (eds) *Inorganic nanosheets and nanosheet-based materials: fundamentals and applications of two-dimensional systems*. Springer, Tokyo

7. Bujdák J (2015) Hybrid systems based on organic dyes and clay minerals: fundamentals and potential applications. *Clay Miner* 50(5):549–571. <https://doi.org/10.1180/claymin.2015.050.5.01>
8. Forster T (1946) Energiewanderung und Fluoreszenz. *Naturwissenschaften* 33(6):166–175. <https://doi.org/10.1007/BF00585226>
9. Dale RE, Eisinger J, Blumberg WE (1979) The orientational freedom of molecular probes. The orientation factor in intramolecular energy transfer. *Biophys J* 26(2):161–193. [https://doi.org/10.1016/S0006-3495\(79\)85243-1](https://doi.org/10.1016/S0006-3495(79)85243-1)
10. Zwillinger D (2003) 7.1.8 geometric probability. In: Zwillinger D (ed) *CRC standard mathematical tables and formulae*, 31st edn. CRC Press, London, p equation 7.1.46
11. Belušáková S, Martínez-Martínez V, Arbeloa IL, Bujdák J (2017) Resonance energy transfer between dye molecules in colloids of a layered silicate. The effect of dye surface concentration. *J Phys Chem C* 121(15):8300–8309. <https://doi.org/10.1021/acs.jpcc.7b00947>
12. Schoonheydt RA (2002) Smectite-type clay minerals as nanomaterials. *Clays Clay Miner* 50(4):411–420
13. Bujdák J (2006) Effect of the layer charge of clay minerals on optical properties of organic dyes. A review. *Appl Clay Sci* 34(1-4):58–73. <https://doi.org/10.1016/j.clay.2006.02.011>
14. Liu P, Zhang LX (2007) Adsorption of dyes from aqueous solutions or suspensions with clay nano-adsorbents. *Sep Purif Technol* 58:32–39. <https://doi.org/10.1016/j.seppur.2007.07.007>
15. Chen Y (2015) *Nanotubes and nanosheets: functionalization and applications of boron nitride and other nanomaterials*. CRC Press, New York
16. Auerbach SM, Carrado KA, Dutta PK (2004) *Handbook of layered materials*. CRC Press, New York
17. Nakato T, Kawamata J, Takagi S (2017) *Inorganic nanosheets and nanosheet-based materials: fundamentals and applications of two-dimensional systems*. Springer, Tokyo
18. Miyamoto N, Ohseda Y, Nakato T (2017) Colloidal nanosheets. In: Nakato T, Kawamata J, Takagi S (eds) *Inorganic nanosheets and nanosheet-based materials: fundamentals and applications of two-dimensional systems*. Springer, Tokyo
19. Nakato T (2017) Synthetic nanosheets from ion-exchangeable layered solids. In: Nakato T, Kawamata J, Takagi S (eds) *Inorganic nanosheets and nanosheet-based materials: fundamentals and applications of two-dimensional systems*. Springer, Tokyo
20. Schoonheydt RA, Umemura Y (2017) Clay minerals as natural nanosheets. In: Nakato T, Kawamata J, Takagi S (eds) *Inorganic nanosheets and nanosheet-based materials: fundamentals and applications of two-dimensional systems*. Springer, Tokyo
21. Wang T, Hu XB, Zheng SD, Liu XX, Wang CY, Tong Z (2012) Adsorption of fluorophores and N-isopropylacrylamide on Laponite. *Appl Clay Sci* 58:102–107. <https://doi.org/10.1016/j.clay.2012.01.021>
22. Li HY, Li QA (2003) Organic dye-layered silicate optical functional nanocomposites. *Prog Chem* 15(2):135–140
23. Arbeloa FL, Martínez VM, Arbeloa T, Arbeloa IL (2007) Photoresponse and anisotropy of rhodamine dye intercalated in ordered clay layered films. *J Photochem Photobiol C* 8:85–108. <https://doi.org/10.1016/j.jphotochemrev.2007.03.003>
24. Zhou CH, Shen ZF, Liu LH, Liu SM (2011) Preparation and functionality of clay-containing films. *J Mater Chem* 21(39):15132–15153
25. Costa AL, Gomes AC, Pereira RC, Pillinger M, Gonçalves IS, Pineiro M, Seixas De Melo JS (2018) Interactions and supramolecular organization of sulfonated indigo and thioindigo dyes in layered hydroxide hosts. *Langmuir* 34(1):453–464. <https://doi.org/10.1021/acs.langmuir.7b03735>
26. Mandal S, Natarajan S, Raja S, Vijayalakshmi N, Muralidharan C, Mandal AB (2013) Adsorption of acid dyes on hydrotalcite-like anionic clays. In: Mishra T, Das N (eds) *Layered clay materials for functional applications*. Key engineering materials, vol 571, pp 57–69. <https://doi.org/10.4028/www.scientific.net/KEM.571.57>

27. Ras RHA, van Duffel B, Van der Auweraer M, De Schryver FC, Schoonheydt RA (2003) Molecular and particulate organisation in dye-clay films prepared by the Langmuir-Blodgett method. In: 2001 – A clay odyssey. Elsevier, Amsterdam, pp 473–480
28. Czímerová A, Bujdák J, Iyi N (2007) Fluorescence resonance energy transfer between laser dyes in saponite dispersions. *J Photochem Photobiol A* 187(2-3):160–166. <https://doi.org/10.1016/j.jphotochem.2006.10.011>
29. Yui T, Kameyama T, Sasaki T, Torimoto T, Takagi K (2007) Pyrene-to-porphyrin excited singlet energy transfer in LBL-deposited LDH nanosheets. *J Porphyrins Phthalocyanines* 11(5-6):428–433
30. Czímerová A, Iyi N, Bujdák J (2008) Fluorescence resonance energy transfer between two cationic laser dyes in presence of the series of reduced-charge montmorillonites: effect of the layer charge. *J Colloid Interface Sci* 320(1):140–151. <https://doi.org/10.1016/j.jcis.2007.10.055>
31. Bujdák J, Chorvát D, Iyi N (2010) Resonance energy transfer between rhodamine molecules adsorbed on layered silicate particles. *J Phys Chem C* 114(2):1246–1252. <https://doi.org/10.1021/jp9098107>
32. Hussain SA, Chakraborty S, Bhattacharjee D, Schoonheydt RA (2010) Fluorescence resonance energy transfer between organic dyes adsorbed onto nano-clay and Langmuir-Blodgett (LB) films. *Spectrochim Acta A Mol Biomol Spectrosc* 75(2):664–670. <https://doi.org/10.1016/j.saa.2009.11.037>
33. Hussain SA, Schoonheydt RA (2010) Langmuir-Blodgett monolayers of cationic dyes in the presence and absence of clay mineral layers: N,N'-dioctadecyl thiocyanine, octadecyl rhodamine B and laponite. *Langmuir* 26(14):11870–11877. <https://doi.org/10.1021/la101078f>
34. Ishida Y, Shimada T, Masui D, Tachibana H, Inoue H, Takagi S (2011) Efficient excited energy transfer reaction in clay/porphyrin complex toward an artificial light-harvesting system. *J Am Chem Soc* 133(36):14280–14286. <https://doi.org/10.1021/ja204425u>
35. Bujdák J, Czímerová A, Arbeloa FL (2011) Two-step resonance energy transfer between dyes in layered silicate films. *J Colloid Interface Sci* 364(2):497–504. <https://doi.org/10.1016/j.jcis.2011.08.042>
36. Ishida Y, Masui D, Tachibana H, Inoue H, Shimada T, Takagi S (2012) Controlling the microadsorption structure of porphyrin dye assembly on clay surfaces using the “size-matching rule” for constructing an efficient energy transfer system. *ACS Appl Mater Interfaces* 4(2):811–816. <https://doi.org/10.1021/am201465a>
37. Dey D, Bhattacharjee D, Chakraborty S, Hussain SA (2013) Development of hard water sensor using fluorescence resonance energy transfer. *Sensors Actuators B Chem* 184:268–273. <https://doi.org/10.1016/j.snb.2013.04.077>
38. Shimada T, Hamatani S, Onodera S, Ishida Y, Inoue H, Takagi S (2013) Investigation of adsorption behavior and energy transfer of cationic porphyrins on clay surface at low loading levels by picosecond time-resolved fluorescence measurement. *Res Chem Intermed* 39(1):269–278. <https://doi.org/10.1007/s11164-012-0647-1>
39. Dey D, Bhattacharjee D, Chakraborty S, Hussain SA (2013) Effect of nanoclay laponite and pH on the energy transfer between fluorescent dyes. *J Photochem Photobiol A* 252:174–182
40. Bujdák J (2014) Layer-by-layer assemblies composed of polycationic electrolyte, organic dyes, and layered silicates. *J Phys Chem C* 118(13):7152–7162. <https://doi.org/10.1021/jp411155x>
41. Dey D, Saha J, Roy AD, Bhattacharjee D, Hussain SA (2014) Development of an ion-sensor using fluorescence resonance energy transfer. *Sensors Actuators B Chem* 195:382–388. <https://doi.org/10.1016/j.snb.2014.01.065>
42. Sato H, Ochi M, Kato M, Tamura K, Yamagishi A (2014) Energy transfer in hybrid Langmuir-Blodgett films of iridium complexes and synthetic saponite: dependence of transfer efficiency on the interlayer distance. *New J Chem* 38(12):5715–5720. <https://doi.org/10.1039/c4nj00818a>

43. Eguchi M, Watanabe Y, Ohtani Y, Shimada T, Takagi S (2014) Switching of energy transfer reaction by the control of orientation factor between porphyrin derivatives on the clay surface. *Tetrahedron Lett* 55(16):2662–2666. <https://doi.org/10.1016/j.tetlet.2014.03.027>
44. Belušáková S, Lang K, Bujdák J (2015) Hybrid systems based on layered silicate and organic dyes for cascade energy transfer. *J Phys Chem C* 119:21784–21794. <https://doi.org/10.1021/acs.jpcc.5b04982>
45. Belušáková S, Sola-Llano R, Arbeloa IL, Martínez-Martínez V, Bujdák J (2018) Resonance energy transfer between dye molecules in hybrid films of a layered silicate, including the effect of dye concentration thereon. *Appl Clay Sci* 155:57–64. <https://doi.org/10.1016/j.clay.2018.01.001>
46. Liu Q, Yan HJ, Su YM, Shi SK, Ye JP (2014) Energy transfer studies of dye chromophores in modified zirconium phosphate framework. *J Lumin* 152:238–240. <https://doi.org/10.1016/j.jlumin.2014.01.077>
47. Saha J, Datta Roy A, Dey D, Chakraborty S, Bhattacharjee D, Paul PK, Hussain SA (2015) Investigation of fluorescence resonance energy transfer between fluorescein and rhodamine 6G. *Spectrochim Acta A Mol Biomol Spectrosc* 149:143. <https://doi.org/10.1016/j.saa.2015.04.027>
48. Rao KV, Datta KKR, Eswaramoorthy M, George SJ (2012) Light-harvesting hybrid assemblies. *Chem Eur J* 18(8):2184–2194. <https://doi.org/10.1002/chem.201103601>
49. Fujii K, Iyi N, Sasai R, Hayashi S (2008) Preparation of a novel luminous heterogeneous system: rhodamine/coumarin/phyllsilicate hybrid and blue shift in fluorescence emission. *Chem Mater* 20(9):2994–3002. <https://doi.org/10.1021/cm0716452>
50. Czímerová A, Iyi N, Bujdák J (2007) Energy transfer between rhodamine 3B and oxazine 4 in synthetic-saponite dispersions and films. *J Colloid Interface Sci* 306(2):316–322. <https://doi.org/10.1016/j.jcis.2006.10.040>
51. Nakayama A, Mizuno J, Ohtani Y, Shimada T, Takagi S (2018) Elucidation of the adsorption distribution of cationic porphyrin on the inorganic surface by energy transfer as a molecular ruler. *J Phys Chem C* 122(8):4365–4371. <https://doi.org/10.1021/acs.jpcc.7b12104>
52. Ishida Y, Kulasekharan R, Shimada T, Takagi S, Ramamurthy V (2013) Efficient singlet-singlet energy transfer in a novel host-guest assembly composed of an organic cavitand, aromatic molecules, and a clay nanosheet. *Langmuir* 29(6):1748–1753. <https://doi.org/10.1021/la305148j>
53. Konno S, Fujimura T, Otani Y, Shimada T, Inoue H, Takagi S (2014) Microstructures of the porphyrin/viologen mono layer on the clay surface: segregation or integration? *J Phys Chem C* 118(35):20504–20510. <https://doi.org/10.1021/jp5076274>
54. Ghosh PK, Bard AJ (1984) Photochemistry of tris(2,2'-bipyridyl)ruthenium(II) in colloidal clay suspensions. *J Phys Chem* 88(23):5519–5526. <https://doi.org/10.1021/j150667a012>
55. Kakegawa N, Ogawa M (2004) Effective luminescence quenching of tris(2,2-bipyridine) ruthenium(II) by methylviologen on clay by the aid of poly(vinylpyrrolidone). *Langmuir* 20(17):7004–7009. <https://doi.org/10.1021/la036213u>
56. Takagi S, Shimada T, Ishida Y, Fujimura T, Masui D, Tachibana H, Eguchi M, Inoue H (2013) Size-matching effect on inorganic nanosheets: control of distance, alignment, and orientation of molecular adsorption as a bottom-up methodology for nanomaterials. *Langmuir* 29(7):2108–2119. <https://doi.org/10.1021/la3034808>
57. Baranyaiová T, Bujdák J (2016) Reaction kinetics of molecular aggregation of rhodamine 123 in colloids with synthetic saponite nanoparticles. *Appl Clay Sci* 134:103–109. <https://doi.org/10.1016/j.clay.2016.01.036>
58. Baranyaiová T, Bujdák J (2018) Effects of dye surface concentration on the molecular aggregation of xanthene dye in colloidal dispersions of montmorillonite. *Clay Clay Miner* 66(2):114–126. <https://doi.org/10.1346/ccmn.2018.064089>
59. Leone G, Giovannella U, Porzio W, Botta C, Ricci G (2011) In situ synthesis of fluorescent poly(norbornene)/oxazine-1 dye loaded fluoromica hybrids: supramolecular control over dye arrangement. *J Mater Chem* 21(34):12901–12909. <https://doi.org/10.1039/c1jm11281c>

60. Giovanella U, Leone G, Ricci G, Virgili T, Lopez IS, Rajendran SK, Botta C (2012) Oxazine-1 J-aggregates in polymer nanohybrids. *Phys Chem Chem Phys* 14(39):13646–13650. <https://doi.org/10.1039/c2cp42361h>
61. Sonotani A, Shimada T, Takagi S (2017) “Size-matching effect” in a cationic porphyrin-titania nanosheet complex. *Chem Lett* 46(4):499–501. <https://doi.org/10.1246/cl.161146>
62. Takagi S, Aratake Y, Konno S, Masui D, Shimada T, Tachibana H, Inoue H (2011) Effects of porphyrin structure on the complex formation behavior with clay. *Microporous Mesoporous Mater* 141(1-3):38–42. <https://doi.org/10.1016/j.micromeso.2009.11.011>
63. Egawa T, Watanabe H, Fujimura T, Ishida Y, Yamato M, Masui D, Shimada T, Tachibana H, Yoshida H, Inoue H, Takagi S (2011) Novel methodology to control the adsorption structure of cationic porphyrins on the clay surface using the “size-matching rule”. *Langmuir* 27(17):10722–10729. <https://doi.org/10.1021/la202231k>
64. Czimerová A, Čeklovský A (2017) Resonance energy transfer between rhodamine dyes in saponite thin films: a step towards novel photofunctional nanohybrids. *Clay Miner* 52(2):263–273. <https://doi.org/10.1180/claymin.2017.052.2.06>
65. Felbeck T, Mundinger S, Lezhnina MM, Staniford M, Resch-Genger U, Kynast UH (2015) Multifold fluorescence enhancement in nanoscopic fluorophore-clay hybrids in transparent aqueous media. *Chem Eur J* 21(20):7582–7587. <https://doi.org/10.1002/chem.201406416>
66. Roy AD, Saha J, Dey D, Bhattacharjee D, Hussain SA (2016) Influence of clay and DNA on fluorescence resonance energy transfer between two laser dyes pyrene and acriflavine. *Adv Sci Lett* 22(1):149–153. <https://doi.org/10.1166/asl.2016.6810>
67. Ishida Y, Kulasekharan R, Shimada T, Ramamurthy V, Takagi S (2014) Supramolecular-surface photochemistry: supramolecular assembly organized on a clay surface facilitates energy transfer between an encapsulated donor and a free acceptor. *J Phys Chem C* 118(19):10198–10203. <https://doi.org/10.1021/jp502816j>
68. Tsukamoto T, Ramasamy E, Shimada T, Takagi S, Ramamurthy V (2016) Supramolecular surface photochemistry: cascade energy transfer between encapsulated dyes aligned on a clay nanosheet surface. *Langmuir* 32(12):2920–2927. <https://doi.org/10.1021/acs.langmuir.5b03962>
69. Devaux A, Calzaferri G, Belsler P, Cao P, Brühwiler D, Kunzmann A (2014) Efficient and robust host-guest antenna composite for light harvesting. *Chem Mater* 26(23):6878–6885. <https://doi.org/10.1021/cm503761q>
70. Zhang Y, Chen Y, Li J, Liang L, Liu Y (2018) Construction and luminescent behavior of supramolecular hydrogel with white-light emission. *Acta Chim Sin* 76(8):622–626. <https://doi.org/10.6023/A18040171>
71. Sas S, Danko M, Bizovská V, Lang K, Bujdák J (2017) Highly luminescent hybrid materials based on smectites with polyethylene glycol modified with rhodamine fluorophore. *Appl Clay Sci* 138:25–33. <https://doi.org/10.1016/j.clay.2016.12.034>
72. Kuroda T, Fujii K, Sakoda K (2010) Ultrafast energy transfer in a multichromophoric layered silicate. *J Phys Chem C* 114(2):983–989. <https://doi.org/10.1021/jp910341f>
73. Fujii K, Kuroda T, Sakoda K, Iyi N (2011) Fluorescence resonance energy transfer and arrangements of fluorophores in integrated coumarin/cyanine systems within solid-state two-dimensional nanopore. *J Photochem Photobiol A* 225(1):125–134. <https://doi.org/10.1016/j.jphotochem.2011.10.009>
74. Kunz DA, Schmid J, Feicht P, Erath J, Fery A, Breu J (2013) Clay-based nanocomposite coating for flexible optoelectronics applying commercial polymers. *ACS Nano* 7(5):4275–4280. <https://doi.org/10.1021/nn400713e>
75. Lee TW, Park OO, Yoon J, Kim JJ (2001) Polymer-layered silicate nanocomposite light-emitting devices. *Adv Mater* 13(3):211–213. [https://doi.org/10.1002/1521-4095\(200102\)13:3<211::AID-ADMA211>3.0.CO;2-H](https://doi.org/10.1002/1521-4095(200102)13:3<211::AID-ADMA211>3.0.CO;2-H)
76. Leone G, Giovanella U, Bertini F, Porzio W, Meinardi F, Botta C, Ricci G (2013) Poly(styrene)-graft-rhodamine 6G-fluoromica hybrids: synthesis, characterization and

- photophysical properties. *J Mater Chem C* 1(7):1450–1460. <https://doi.org/10.1039/c2tc00533f>
77. Chakraborty U, Singha T, Chianelli RR, Hansda C, Paul PK (2017) Organic-inorganic hybrid layer-by-layer electrostatic self-assembled film of cationic dye Methylene Blue and a clay mineral: spectroscopic and Atomic Force microscopic investigations. *J Lumin* 187:322–332. <https://doi.org/10.1016/j.jlumin.2017.03.039>
78. Li Z, Liang R, Xu S, Liu W, Yan D, Wei M, Evans DG, Duan X (2016) Multi-dimensional, light-controlled switch of fluorescence resonance energy transfer based on orderly assembly of 0D dye@micro-micelles and 2D ultrathin-layered nanosheets. *Nano Res* 9(12):3828–3838. <https://doi.org/10.1007/s12274-016-1252-1>
79. Tozoni JR, Guimarães FEG, Atvars TDZ, Nowacki B, Marlleta A, Akcelrud L, Bonagamba TJ (2011) De-aggregation of a polyfluorene derivative in clay nanocomposites: a photophysical study. *Eur Polym J* 47(12):2259–2265. <https://doi.org/10.1016/j.eurpolymj.2011.09.023>
80. Vohra V, Calzaferri G, Destri S, Pasini M, Porzio W, Botta C (2010) Toward white light emission through efficient two-step energy transfer in hybrid nanofibers. *ACS Nano* 4(3):1409–1416. <https://doi.org/10.1021/nn9017922>
81. Olivero F, Carniato F, Bisio C, Marchese L (2014) Promotion of forster resonance energy transfer in a saponite clay containing luminescent polyhedral oligomeric silsesquioxane and rhodamine dye. *Chem Asian J* 9(1):158–165. <https://doi.org/10.1002/asia.201300936>
82. Aharon E, Albo A, Kalina M, Frey GL (2006) Stable blue emission from a polyfluorene/layered-compound guest/host nanocomposite. *Adv Funct Mater* 16(7):980–986. <https://doi.org/10.1002/adfm.200500458>
83. Li Z, Lu J, Li S, Qin S, Qin Y (2012) Orderly ultrathin films based on perylene/poly(N-vinyl carbazole) assembled with layered double hydroxide nanosheets: 2d fluorescence resonance energy transfer and reversible fluorescence response for volatile organic compounds. *Adv Mater* 24(45):6053–6057. <https://doi.org/10.1002/adma.201203040>
84. Qin Y, Shi J, Gong X, Tian Z, Zhang P, Lu J (2016) A luminescent inorganic/organic composite ultrathin film based on a 2D cascade FRET process and its potential VOC selective sensing properties. *Adv Funct Mater* 26(37):6752–6759. <https://doi.org/10.1002/adfm.201601087>
85. Qin Y, Lu J, Li S, Li Z, Zheng S (2014) Phosphorescent sensor based on iridium complex/poly(vinylcarbazole) orderly assembled with layered double hydroxide nanosheets: two-dimensional foster resonance energy transfer and reversible luminescence response for VOCs. *J Phys Chem C* 118(35):20538–20544. <https://doi.org/10.1021/jp505448d>
86. Park CH, Lee S, Pornnoppadol G, Nam YS, Kim SH, Kim BJ (2018) Microcapsules containing pH-responsive, fluorescent polymer-integrated MoS₂: an effective platform for in situ pH sensing and photothermal heating. *ACS Appl Mater Interfaces* 10(10):9023–9031. <https://doi.org/10.1021/acsami.7b19468>
87. Arbeloa FL, Martinez V, Arbeloa T, Arbeloa IL (2010) Fluorescence anisotropy to study the preferential orientation of fluorophores in ordered bi-dimensional systems: rhodamine 6G/laponite layered films. In: Geddes CD (ed) *Reviews in fluorescence 2008*. Reviews in fluorescence, vol 5. Kluwer Academic, New York, pp 1–35. https://doi.org/10.1007/978-1-4419-1260-2_1
88. López Arbeloa F, Martínez Martínez V (2006) Orientation of adsorbed dyes in the interlayer space of clays. 2 fluorescence polarization of rhodamine 6G in laponite films. *Chem Mater* 18(6):1407–1416
89. Martínez VM, Arbeloa FL, Prieto JB, Arbeloa IL (2005) Orientation of adsorbed dyes in the interlayer space of clays. 1. Anisotropy of Rhodamine 6G in Laponite films by Vis-absorption with polarized light. *Chem Mater* 17(16):4134–4141. <https://doi.org/10.1021/cm050728k>
90. Iyi N, Sasai R, Fujita T, Deguchi T, Sota T, López Arbeloa F, Kitamura K (2002) Orientation and aggregation of cationic laser dyes in a fluoromica: polarized spectrometry studies. *Appl Clay Sci* 22(3):125–136

91. Iyi N, Sasai R, Fujita T, Deguchi T, Sota T, Arbeloa FL, Kitamura K (2002) Orientation and aggregation of cationic laser dyes in a fluoromica: polarized spectrometry studies. *Appl Clay Sci* 22(3):125–136
92. Bujdák J, Iyi N (2005) Molecular orientation of rhodamine dyes on surfaces of layered silicates. *J Phys Chem B* 109(10):4608–4615
93. Hirose M, Ito F, Shimada T, Takagi S, Sasai R, Okada T (2017) Photoluminescence by intercalation of a fluorescent β -diketone dye into a layered silicate. *Langmuir* 33(47):13515–13521. <https://doi.org/10.1021/acs.langmuir.7b03460>
94. Kafunkova E, Taviot-Gueho C, Bezdicka P, Klementova M, Kovar P, Kubat P, Mosinger J, Pospisil M, Lang K (2010) Porphyrins intercalated in Zn/Al and Mg/Al layered double hydroxides: properties and structural arrangement. *Chem Mater* 22(8):2481–2490. <https://doi.org/10.1021/cm903125v>
95. Saha J, Dey D, Roy AD, Bhattacharjee D, Hussain SA (2016) Multi step FRET among three laser dyes Pyrene, Acriflavine and Rhodamine B. *J Lumin* 172:168–174. <https://doi.org/10.1016/j.jlumin.2015.12.004>
96. Ohtani Y, Kawaguchi S, Shimada T, Takagi S (2017) Energy transfer among three dye components in a nanosheet-dye complex: an approach to evaluating the performance of a light-harvesting system. *J Phys Chem C* 121(4):2052–2058. <https://doi.org/10.1021/acs.jpcc.6b10372>
97. Zhuk A, Sukhishvili SA (2013) Stimuli-responsive layer-by-layer nanocomposites. *Soft Matter* 9(21):5149–5154
98. Kehlbeck JD, Hagerman ME, Cohen BD, Eliseo J, Fox M, Hoek W, Karlin D, Leibner E, Nagle E, Nolan M, Schaefer I, Toney A, Topka M, Uluski R, Wood C (2008) Directed self-assembly in laponite/CdSe/polyaniline nanocomposites. *Langmuir* 24(17):9727–9738
99. Hansda C, Chakraborty U, Hussain SA, Bhattacharjee D, Paul PK (2016) Layer-by-layer films and colloidal dispersions of graphene oxide nanosheets for efficient control of the fluorescence and aggregation properties of the cationic dye acridine orange. *Spectrochim Acta A* 157:79–87. <https://doi.org/10.1016/j.saa.2015.12.006>
100. Chakraborty S, Bhattacharjee D, Hussain SA (2014) Formation and control of excimer of a coumarin derivative in Langmuir-Blodgett films. *J Lumin* 145:824–831. <https://doi.org/10.1016/j.jlumin.2013.09.001>
101. Lewkowicz A, Synak A, Grobelna B, Kułak L, Bojarski P (2014) Spectroscopic properties of Rhodamine B entrapped in hybrid porous nanolayers at high dye concentration. *Chem Phys* 439:121–127. <https://doi.org/10.1016/j.chemphys.2014.05.016>
102. Giovanella U, Leone G, Galeotti F, Mroz W, Meinardi F, Botta C (2014) FRET-assisted deep-blue electroluminescence in intercalated polymer hybrids. *Chem Mater* 26(15):4572–4578. <https://doi.org/10.1021/cm501870e>
103. Cheng CH, Li Z, Hambarde A, Deotare PB (2018) Efficient energy transfer across organic-2D inorganic heterointerfaces. *ACS Appl Mater Interfaces* 10(45):39336–39342. <https://doi.org/10.1021/acsami.8b12291>
104. Akhavan S, Akgul MZ, Hernandez-Martinez PL, Demir HV (2017) Plasmon-enhanced energy transfer in photosensitive nanocrystal device. *ACS Nano* 11(6):5430–5439. <https://doi.org/10.1021/acsnano.6b08392>
105. Rangelowa-Jankowska S, Jankowski D, Bogdanowicz R, Grobelna B, Bojarski P (2012) Surface plasmon-coupled emission of rhodamine 110 aggregates in a silica nanolayer. *J Phys Chem Lett* 3(23):3626–3631. <https://doi.org/10.1021/jz301728y>
106. Li Z, Zhou Y, Yan D, Wei M (2017) Electrochemiluminescence resonance energy transfer (ERET) towards trinitrotoluene sensor based on layer-by-layer assembly of luminol-layered double hydroxides and CdTe quantum dots. *J Mater Chem C* 5(14):3473–3479. <https://doi.org/10.1039/C7TC00100B>
107. Liang R, Xu S, Yan D, Shi W, Tian R, Yan H, Wei M, Evans DG, Duan X (2012) CdTe quantum dots/layered double hydroxide ultrathin films with multicolor light emission via layer-by-layer assembly. *Adv Funct Mater* 22(23):4940–4948. <https://doi.org/10.1002/adfm.201201367>

108. Zhong J, Yuan Z, Lu C (2016) Layered-nanomaterial-amplified chemiluminescence systems and their analytical applications. *Anal Bioanal Chem* 408(30):8731–8746. <https://doi.org/10.1007/s00216-016-9449-4>
109. Wang Z, Teng X, Lu C (2013) Universal chemiluminescence flow-through device based on directed self-assembly of solid-state organic chromophores on layered double hydroxide matrix. *Anal Chem* 85(4):2436–2442. <https://doi.org/10.1021/ac303487b>
110. Cao Y, Sui D, Zhou W, Lu C (2016) Highly selective chemiluminescence detection of hydroxyl radical via increased π -electron densities of rhodamine B on montmorillonite matrix. *Sensors Actuators B Chem* 225:600–606. <https://doi.org/10.1016/j.snb.2015.11.084>
111. Chen S, Zhou W, Cao Y, Xue C, Lu C (2014) Organo-modified montmorillonite enhanced chemiluminescence via inactivation of halide counterions in a micellar solution. *J Phys Chem C* 118(5):2851–2856. <https://doi.org/10.1021/jp411290z>
112. Rozen H, Margulies L (1991) Photostabilization of tetrahydro-2-(nitromethylene)-2H-1,3-thiazine adsorbed on clays. *J Agric Food Chem* 39(7):1320–1325
113. Margulies L, Rozen H, Stern T, Rytwo G, Rubin B, Ruzo LO, Nir S, Cohen E (1993) Photostabilization of pesticides by clays and chromophores. *Arch Insect Biochem Physiol* 22(3-4):467–486
114. Wang Y, Ma T, Ma S, Liu Y, Tian Y, Wang R, Jiang Y, Hou D, Wang J (2017) Fluorometric determination of the antibiotic kanamycin by aptamer-induced FRET quenching and recovery between MoS₂ nanosheets and carbon dots. *Microchim Acta* 184(1):203–210. <https://doi.org/10.1007/s00604-016-2011-4>
115. Yan D, Lu J, Wei M, Han J, Ma J, Li F, Evans DG, Duan X (2009) Ordered poly(p-phenylene)/layered double hydroxide ultrathin films with blue luminescence by layer-by-layer assembly. *Angew Chem Int Ed Engl* 48(17):3073–3076. <https://doi.org/10.1002/anie.200900178>
116. Yan D, Lu J, Ma J, Wei M, Evans DG, Duan X (2011) Reversibly thermochromic, fluorescent ultrathin films with a supramolecular architecture. *Angew Chem Int Ed Engl* 50(3):720–723. <https://doi.org/10.1002/anie.201003015>
117. Hu K, Yang H, Zhou J, Zhao S, Tian J (2012) Aptasensor for amplified IgE sensing based on fluorescence quenching by graphene oxide. *Luminescence* 28(5):662–666. <https://doi.org/10.1002/bio.2412>
118. Chang HX, Tang LH, Wang Y, Jiang JH, Li JH (2010) Graphene fluorescence resonance energy transfer aptasensor for the thrombin detection. *Anal Chem* 82(6):2341–2346. <https://doi.org/10.1021/ac9025384>
119. Chi-Ming Leung F, Wing-Wah Yam V (2018) Covalent and non-covalent conjugation of few-layered graphene oxide and ruthenium(II) complex hybrids and their energy transfer modulation via enzymatic hydrolysis. *ACS Appl Mater Interfaces* 10(18):15582–15590. <https://doi.org/10.1021/acsami.7b18663>
120. Swaminathan H, Balasubramanian K (2018) Forster resonance energy transfer between MoS₂ quantum dots and polyaniline for turn-on bovine serum albumin sensing. *Sensors Actuators B Chem* 264:337–343. <https://doi.org/10.1016/j.snb.2018.02.182>
121. Becker W (2012) Fluorescence lifetime imaging – techniques and applications. *J Microsc* 247(2):119–136. <https://doi.org/10.1111/j.1365-2818.2012.03618.x>
122. Tsukamoto T, Shimada T, Takagi S (2013) Photochemical properties of mono-, tri-, and pentacationic antimony(V) metalloporphyrin derivatives on a clay layer surface. *J Phys Chem A* 117(33):7823–7832. <https://doi.org/10.1021/jp405767s>
123. Tsukamoto T, Shimada T, Takagi S (2018) Artificial photosynthesis model: photochemical reaction system with efficient light-harvesting function on inorganic nanosheets. *ACS Omega* 3(12):18563–18571. <https://doi.org/10.1021/acsomega.8b02594>
124. Gartzia-Rivero L, Bañuelos J, López-Arbeloa I (2015) Excitation energy transfer in artificial antennas: from photoactive materials to molecular assemblies. *Int Rev Phys Chem* 34(4):515–556. <https://doi.org/10.1080/0144235X.2015.1075279>
125. Li J, Cushing SK, Meng F, Senty TR, Bristow AD, Wu N (2015) Plasmon-induced resonance energy transfer for solar energy conversion. *Nat Photonics* 9(9):601–607. <https://doi.org/10.1038/nphoton.2015.142>

Photofunctions of Dye-Clay Hybrids: Recent Developments



Tetsuo Yamaguchi, Jae-Min Oh, and Makoto Ogawa

Contents

1	Introduction	253
2	Characteristics of Dye-Clay Hybrids for Photochemical Studies and Photofunctional Materials	253
3	Surface Modification	256
4	Photophysics of Dye-Clay Hybrid Systems	257
4.1	Changes in the Absorption Properties, Color Change, and Stability	257
4.2	Changes in the Photoluminescence Properties	266
4.3	Alignment of Dyes by Host-Guest Interactions: Study by Linear Polarized Light .	272
5	Photochemical Reactions	275
5.1	Intramolecular Reactions Affected by Host-Guest Interactions	275
5.2	Intermolecular Reactions	284
5.3	Uses of Photochemical Reactions as Trigger for Photoinduced Phenomena	287
6	Conclusions and Future Perspectives	294
	References	295

Abstract Precise design of hybrid nanostructures based on dyes in hybrid materials toward controlled photochemical reactions and novel photoinduced phenomena is overviewed with the emphasis on the recent developments. Various clays and clay minerals with different origins and characteristics have been used as hosts to control the location, orientation, and aggregation as well as the dynamic states (rotation and diffusion) of the dyes. The designed nanostructures affect photochemical properties such as efficiency, selectivity, and the rate of some photochemical reactions. Using the photochemical reactions in nanospaces, unique photoinduced phenomena such

T. Yamaguchi and M. Ogawa (✉)
School of Energy Science and Engineering, Vidyasirimedhi Institute of Science and
Technology, Rayong, Thailand
e-mail: makoto.ogawa@vistec.ac.th

J.-M. Oh
Department of Energy and Materials Engineering, Dongguk University-Seoul, Seoul, South
Korea
e-mail: jaemin.oh@dongguk.edu

as nanostructural/morphological change and adsorption/desorption triggered by irradiation have been found.

Keywords Clays and clay minerals · Host-guest · Photochemistry · Photoinduced phenomena · Photophysics

Abbreviations

[Ru(bpy) ₃] ²⁺	Tris(2,2-bipyridine)ruthenium(II)
AFM	Atomic force microscopy
ATR	Attenuated total reflection
AZ	Azobenzene
C ₁₂ TMA	Dodecyltrimethylammonium ion
C ₁₆ TMA	Hexadecyltrimethylammonium ion
CEC	Cation exchange capacity
CT	Charge transfer
DMSO	Dimethylsulfoxide
HE	A synthetic hectorite (Sumecton SWF)
KF	A natural montmorillonite (Kunipia F)
LB	Langmuir-Blodgett
LbL	Layer-by-layer deposition
LDH	Layered double hydroxide
LP-RD	A synthetic hectorite (Laponite RD)
LP-XLG	A synthetic hectorite (Laponite XLG)
MC	Merocyanine
MV ²⁺	Methyl viologen
PEMA	Poly(ethyl methacrylate)
PIC	<i>Pseudoisocyanine</i>
PMMA	Poly(methyl methacrylate)
PSS	Poly(styrene sulfonate)
PVP	Poly(vinyl pyrrolidone)
R6G	Rhodamine 6G
SA	A synthetic saponite (Sumecton SA)
SP	Spiropyran
STN ⁺	Stilbazolium ion
SWy-1	A Na-montmorillonite from Wyoming, USA
SYn-1	A synthetic mica-montmorillonite
TEOS	Tetraethoxysilane
TMA	Tetramethylammonium ion
TPP	Tetraphenylporphine
TSM	Fluoro-tetrasilicic mica

1 Introduction

Photochemical reactions in heterogeneous systems may differ significantly from analogous reactions in homogeneous liquids/solutions or gas phases [1–6]. Important roles of the media/supports to control such parameters as the reaction rates/yields and product selectivity have been recognized so far, so that various photofunctional hybrids have been designed by organizing molecular species in/on solid surfaces. The location (proximity), orientation, association/aggregation, as well as the freedom (rotation and diffusion) of molecules on the surfaces or in the solids vary depending on the host-guest interactions at the interface to affect the characteristics and functions. The molecular and supramolecular designs (by the selection of host and guest and their composition and the additives) have been done using nanospace materials such as zeolites, mesoporous silicas, MOFs, COFs, and layered materials for organizing molecular and polymeric photofunctional species, and unique/useful photofunctions of the resulting hybrids have been reported [7–11]. Materials with defined (ordered) nanospaces have advantages as supports to accommodate guest species because their structure-property relationships will provide indispensable information on designing materials with controlled properties [12]. Spectroscopic properties, which are very sensitive to the environment, of the immobilized species, have given insights to the nanoscopic structures of the host-guest systems where conventional instrumental analysis does not have access [11–16]. By utilizing photoprocesses, one can obtain such information as distribution [17–20], orientation [21, 22], and mobility [23] of the guest species on/in nanospaces.

In this chapter, among possible host-guest systems, the studies on the organization of photofunctional species on/in clays (more accurately clay minerals and their synthetic analogs) will be summarized with the emphasis on the developments in the last two decades. The attention will mainly be focused on the role of the nanostructures, which directly and indirectly correlate the photofunctions of the guest species and the host-guest systems (Fig. 1).

2 Characteristics of Dye-Clay Hybrids for Photochemical Studies and Photofunctional Materials

Smectites have been used most extensively for a wide range of application including environmental and biomedical ones [24–28]. Smectites are a type of swellable 2:1 type layered clay minerals and consist of negatively charged silicate layer and charge compensating interlayer cations which are exchangeable [29–31]. The negative charge in the layers is generated by isomorphous substitution of framework metal cations with similar size and lower valency, and to compensate this negative charge, metal cations such as sodium and calcium occupy the interlayer space. The terms of bentonite and montmorillonite have often confused, bentonite is a term of a natural resource, and montmorillonite is the name of a clay mineral. The amount as well as

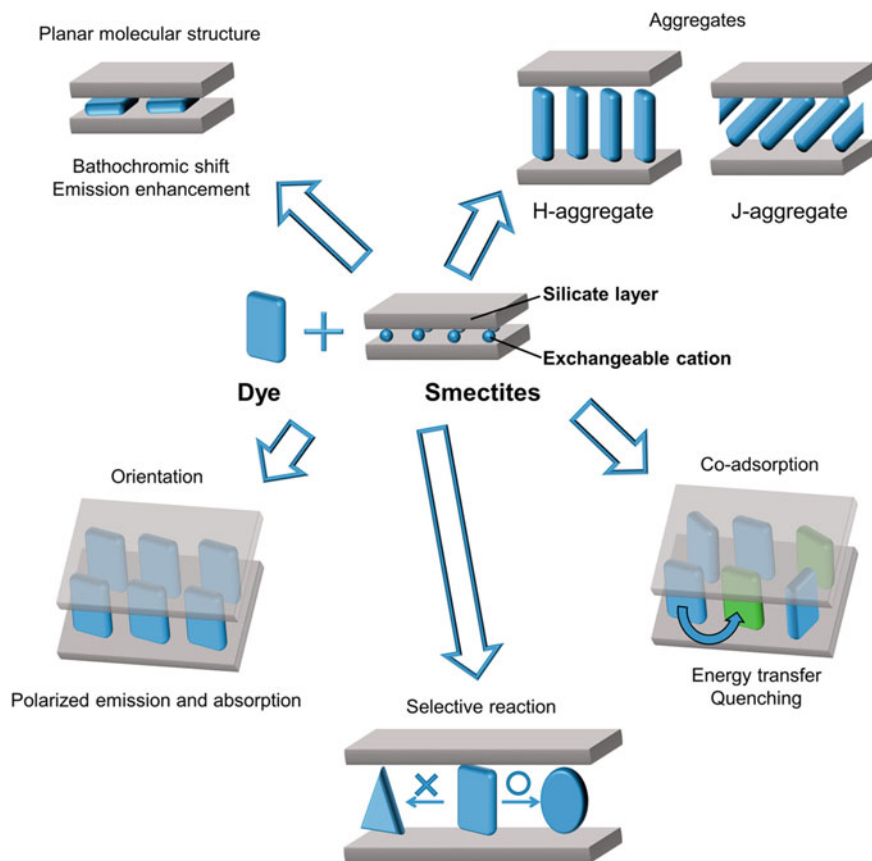


Fig. 1 Possible effects of dye-smectite hybridization

the site of the isomorphous substitution influences the surface and colloidal properties of smectites. Impurities present both within the structure and on the particle surface, and elements and their amounts vary depending on the source of the clay minerals. Synthetic analogs of smectites, i.e., hectorite (Laponite, Rockwood Ind. Co. and Sumecton SWF, Kunimine Ind. Co.) [32], saponite (Sumecton SA, Kunimine Ind. Co.) [33], and swelling mica (sodium-fluor-tetrasilic mica, TSM, Topy Ind. Co. and others) [33], do not contain colored impurities so that they are advantages for the photochemical studies. In addition to the commercially available ones, synthetic analogs of smectite have been prepared in the laboratory and used for the adsorption of dyes [25, 34]. The interlayer cation, which compensates the negative charge of the silicate layer, is exchangeable by the reactions in suspension and in solid state [35–37].

Cation exchange with interlayer exchangeable cations and the adsorption of polar molecules by ion-dipole interactions with interlayer cations and/or hydrogen bonding with the surface oxygen atom of the silicate sheets are known driving forces for

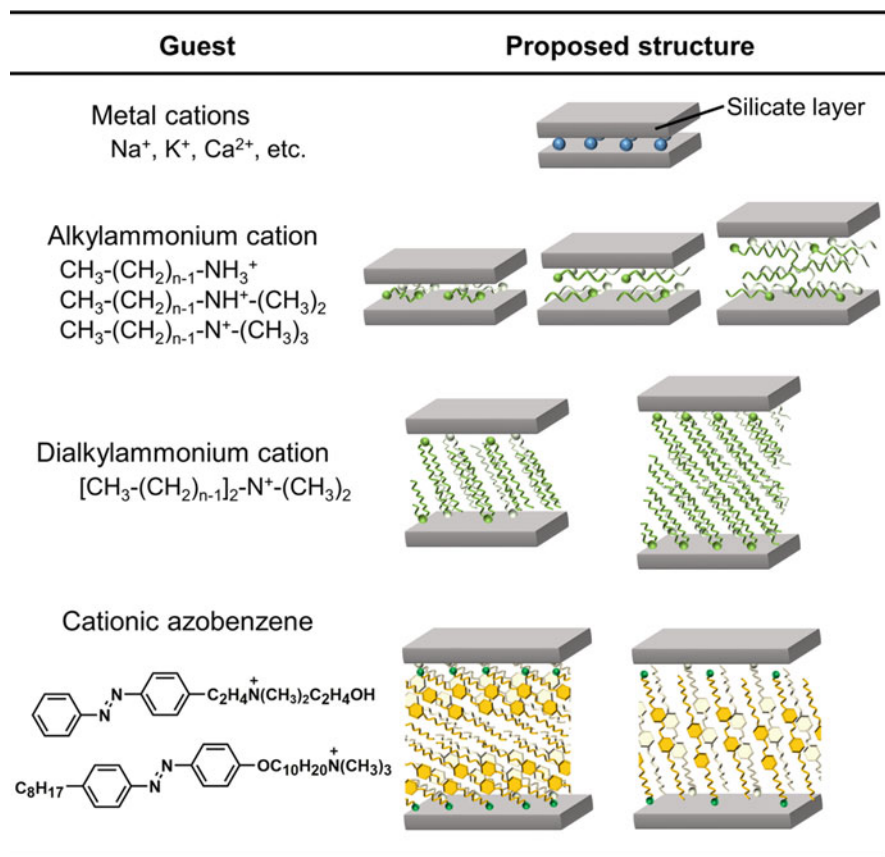


Fig. 2 Examples of organic cationic dyes and schematic drawing for possible arrangements of alkylammonium cations [62, 63]

the intercalation [38–52]. One of the characteristic features of smectites is the possible surface modification. Nanoporous pillared smectites have been obtained using inorganic particles and small organic cations as pillars [53–55]. Organophilic modification has been conducted by the cation exchange with cationic surfactants of various structures (Fig. 2) [26, 33, 56–61]. Due to the variation of the layer charge density and the molecular structures of the surfactants, host-guest systems with controlled microstructures and properties have been obtained.

Layered alkali silicates, namely, magadiite ($\text{Na}_2\text{Si}_{14}\text{O}_{29}\cdot n\text{H}_2\text{O}$) and octosilicate ($\text{Na}_2\text{Si}_8\text{O}_{17}\cdot n\text{H}_2\text{O}$), which are characterized by the higher layer charge density than smectites, have also been used as hosts to construct photofunctional dye-silicate hybrids. The reactions of the layered alkali silicates involve covalent attachments through the reactions with the surface silanol groups [20, 64]. On the other hand, layered double hydroxides (LDHs) are composed of positively charged brucite-type layers of mixed-metal hydroxides and exchangeable anions located at the interlayer

spaces, which compensate for the positive charge of the brucite-type layers [65]. Due to the structural characteristics and compositional variation, the application of LDHs in such areas as adsorption/separation of ions [65–69], catalysis [66–68], polymer additives [66–68], and medical and biochemical uses [66, 68] has been proposed so far. The chemical composition of the LDHs is expressed as $[M(II)_{1-x}M(III)_x(OH)_2][A^{n-}_{x/n}]^{x-}$ where $M(II) = Mg, Co, Ni, \text{ etc.}$; $M(III) = Al, Cr, Fe, \text{ etc.}$; and A is an interlayer anion such as CO_3^{2-} and Cl^- .

In addition to the crystalline structures, the particle size and its distributions of layered solids are key issues in order to achieve optimum performance of layered solids and their intercalates; accordingly, attention has been paid for the powder morphology during the syntheses as well as classification [27, 70, 71]. Powders [36, 72], suspensions [73, 74], and thin films [55, 75–77] have been used for the evaluation of the photoprocesses, as well as for other application [78]. One of the unique and attractive properties of smectites is their spontaneous swelling in water. Platy particles pile up with their *ab* plane parallel to the substrate to form a film when the suspension is evaporated on a flat substrate [55, 75, 79]. The preparation of thin films by the Langmuir-Blodgett technique (LB technique) from exfoliated platelets of clays has also been reported [80, 81]. Inorganic-organic multilayered films have also been prepared via alternate adsorption of a cationic species and an anionic sheet of an exfoliated layered solid (layer-by-layer deposition technique, hereafter abbreviated as LbL technique) [82–86].

3 Surface Modification

In addition to the structural and compositional variation of smectites and other clay minerals (Table 1), the possible surface modification with organic/inorganic cations and polymers makes the variation of the material more versatile (Fig. 2) [87]. Long-chain alkylammonium ions have been studied most extensively in the chemistry of organophilic smectites, and the practical application of the organophilic smectites as adsorbents [25, 88] has been extensively reported. Phospholipids have been utilized for the construction of environmentally benign organoclay [89, 90]. Several non-ionic surfactants have also been used for the surface modification of smectites [75, 91–93]. Intercalation of alkylammonium ions with more complex structures into layered silicates to precisely design hydrophobic nanospace, and, recently, flexibility of the interlayer surfactant aggregates has been discussed based on quasi-elastic neutron scattering data [57].

Microporous and mesoporous solids have been obtained by crosslinking the nanosheets. The pioneering example is the pillaring with polyoxocations (e.g., $[AlO_4Al_{12}(OH)_{24}(H_2O)_{12}]^{7+}$) [94, 95]. Nanoporous solids composed of silicate layers and metal/metal oxide finite particles have been prepared [96–100]. The microporous solids composed of silicate nanosheet and small organoammonium cations (e.g., tetramethylammonium ion, TMA) have been prepared and used for the separation/sensing and other functional materials [101–107]. The adsorptive

Table 1 Abbreviation of specific clays discussed in this chapter

Abbreviation in this chapter	Product name	Type and origin	Producer/authorization company
KF	Kunipia F	Na-montmorillonite from Tsukinuno, Yamagawa, Japan	Kunimine Ind. Co., Reference Clay Sample of Clay Science Society of Japan
SWy-1		Na-montmorillonite from Wyoming, USA	Source Clays Repository of the Clay Minerals Society
SYn-1	Barasym SSM-100	Synthetic mica-montmorillonite	Source Clays Repository of the Clay Minerals Society
SA	Sumecton SA	Synthetic saponite	Kunimine Ind. Co., Reference Clay Sample of Clay Science Society of Japan
HE	Sumecton SWF	Synthetic hectorite	Kunimine Ind. Co.
LP-XLG	Laponite XLG	Synthetic hectorite	Laporte Industry
LP-RD	Laponite RD	Synthetic hectorite	Laporte Industry
TSM		Fluor-tetrasilicic mica	Topy Industry Co.

properties of smectites modified with aliphatic and aromatic ammonium ions have also been investigated [101, 108, 109]. Pore size and porosity are controlled by selecting pillaring agents.

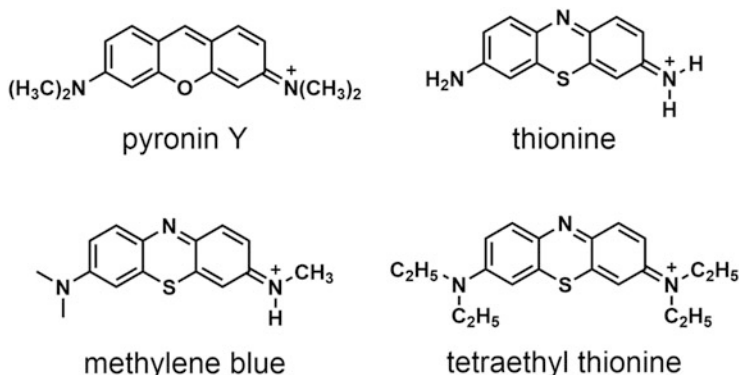
Synthetic clays by hydrothermal method have been developed as summarized in Table 1 and become necessary products for clay research thanks to the high purities and regular chemical equations. The careful syntheses of the clay minerals have been done to control the size of the silicate layers and layer charge densities. The research about the ion exchange led to the development of organically modified clays, which enabled to intercalate non-polar organic compounds into the interlayer spaces [110, 111]. The LB and LbL techniques have been used to fabricate thin films, while the effective swelling and subsequent evaporation of organically modified clays [76] led the thick films with improved quality.

4 Photophysics of Dye-Clay Hybrid Systems

4.1 Changes in the Absorption Properties, Color Change, and Stability

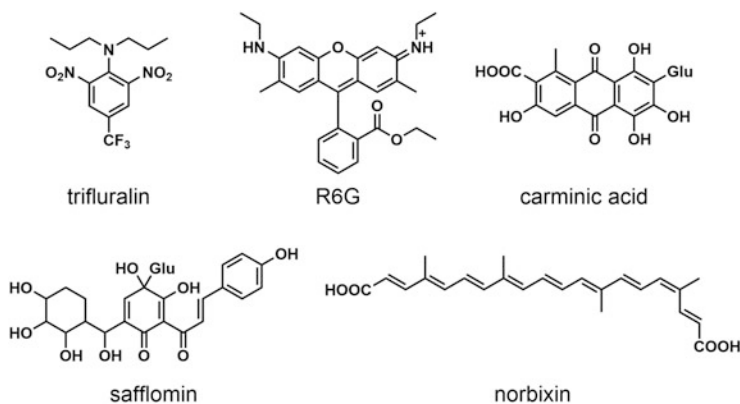
4.1.1 Effects of Host-Guest Interactions

The interactions between lone pair of the oxygen atom of silicate layer of clays and π -electron of dyes were proposed to affect for relatively planar structured dyes such as crystal violet [38, 39, 45–47], rhodamine B [48], pyronin Y [49], thiazines [50–



Scheme 1 Molecular structures of pyronin Y and thiazines

52], and methylene blue [40–44, 112, 113]. The adsorption of pyronin Y (Scheme 1) has been examined in aqueous suspensions of smectites (Wyoming bentonite from Wards Natural Establishment Inc., a natural bentonite from Ünye, Turkey and LP-XLG) [49, 114]. Depending on the concentration and the dye-clay ratios, the absorption shifted, which has been explained as a result of the interactions between pyronin Y and silicate layer as well as the dye aggregation, although this latter effect will be exhaustively explained in Sect. 4.1.2. Thiazine dyes such as thionine [51], methylene blue [41, 42, 51], and tetraethyl thionine [51] (Scheme 1) showed hypsochromic shifts in clay suspensions [41, 51]. Thionine had absorption at 595 and 560 nm in an aqueous solution, which were attributed to a π - π^* transition of monomer and the absorption of H-dimer (see further details on aggregation types in Sect. 4.2.1), respectively [51]. By the addition of a Na-montmorillonite, a new absorption appeared at 528 nm, which was proposed to be caused by the interactions between the π -electron of thionine and the oxygen of the silicate layers, and another new absorption at 690 nm appeared, which was ascribed to J-aggregate (consult Sect. 4.1.2). Methylene blue [40, 115] and tetraethyl thionine [51] also showed hypsochromic shifts of monomer and a new absorption appeared by the addition of a montmorillonite. In LP-XLG, the absorption of thionine and tetraethyl thionine did not shift compared to the solution [51]. It was thought that the thionines had weaker π -interactions with the silicate layer than those with the bentonites. In the presence of a vermiculite (obtained from Zonolite), the absorption of the dimer increased and that of the monomer decreased, while the absorption shift was not observed [51]. The authors thought that the limited interlayer expansion for the vermiculite restricted the molecular conformation of thiazines to interact with the vermiculate. Thus, the hypsochromic shifts of the absorption of the dimers of pyronin and thiazines in the clay suspensions were observed by the interactions between lone pair of oxygen atom of silicate layer and π -electron of dyes. It suggested that the pyronin formed dimer in an aqueous solution, while it was de-aggregated and adsorbed in the interlayer space of the clays. The polarized IR spectra of the film of pyronin Y in LP-XLG and the Wyoming montmorillonite [49] suggested that the



Scheme 2 Molecular structures of dyes, which were reported to be stabilized by the host-guest interactions with clays

interactions between the oxygen of the layered silicates and the π -electron of the dyes made the molecular orientation of the dyes parallel to the silicate layer.

Stability of dyes is one of the prerequisites for the practical application, and the dye-clay interactions have been expected to play a role in it [116–126]. The improvements of the stability of the dyes upon irradiation and heating have been seen in (1) cationic dyes with smectites, (2) anionic dyes with layered double hydroxides (LDHs), and (3) nonionic dyes with organically modified smectites and LDHs. The improvements of the stabilities of the dyes by the hybridization with the layered materials were explained as results of reducing the intensity of the incident light by the absorption and scattering with the host [127–129], electronic stabilization of the dye [130–132], and suppressed gas diffusion mainly oxygen in the hydrophobic environment [111, 133–139].

An example of the improved chemical stability of the anthocyanin by the interactions with SA was shown by the color change upon exposure to acidic and basic atmospheres repeatedly [102]. Such natural dyes as β -carotene, anthocyanin, carmine, annatto, and carthamus yellow were adsorbed on a hydrotalcite [111, 139] and organically modified montmorillonite [110, 111]. Carminic acid, safflomin, and norbixin (Scheme 2) are the main components of carmine, carthamus yellow, and annatto, respectively [132]. When interacted with the hydrotalcite, the absorption spectra of carmine showed bathochromic shift as shown in Fig. 3a. The absorption shift was explained by the electrostatic interactions between carmine and the hydrotalcite and the planar molecular conformation induced by the adsorption on the hydrotalcite. As a result, the photostability was improved. Carthamus yellow showed the same trend as carmine. On the other hand, the stability of annatto was not affected in the presence of the hydrotalcite, suggesting the adsorption of annatto at the external surface of the hydrotalcite. The planar conformation was induced by the intercalation and was thought to contribute to the photostability of the dyes through the decrease of the lifetime of the excited state by the effective internal conversion. It

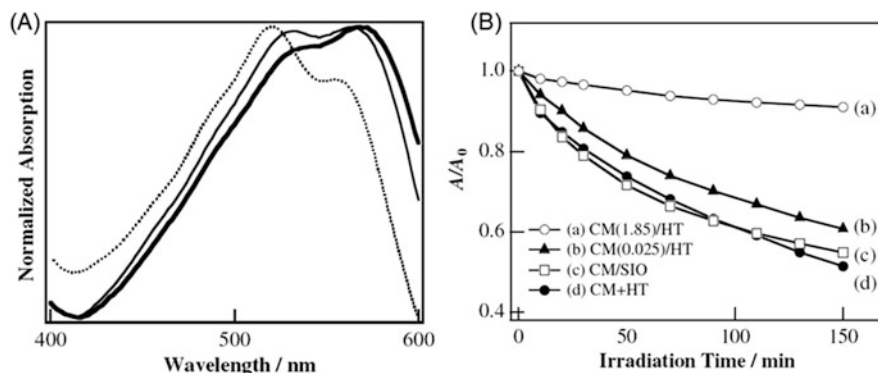


Fig. 3 (a) Diffuse reflectance UV-vis spectra of carmine intercalated in the hydrotalcite at the amount of 0.025 g/g (*dotted line*), 0.46 g/g (*thin line*), and 1.85 g/g (*thick line*). (b) Change of the absorbance during the irradiation for carmine intercalated in the hydrotalcite with the amount of (a) 1.85 g/g and (b) 0.025 g/g, (c) carmine mixed with SiO₂, and (d) carmine mixed with the hydrotalcite (Reproduced from the reference [132] with permission)

is known that a rate constant of internal conversion is limited by Franck-Condon factor which is the overlap integral of vibrational parts of wave functions in the states before and after the transition [140]. Carmine and carthamus yellow were reported to have planar molecular conformations in hydrotalcite, expecting similar molecular conformation in excited state to that of the ground state. The conformation similarity increased the Franck-Condon factor and increased an effective internal conversion from the excited states. The opposite phenomenon (the dyes adsorbed on the external surface of smectites exhibited a decreased internal conversion rate) was also reported as discussed in Sect. 4.2.1. The change of the molecular conformation of the adsorbed dyes in the excited states was allowed on the external surface, while the molecular vibration was suppressed if compared with those in solutions.

Photodecomposition of trifluralin (Scheme 2) was reported as a cyclization between an alkylamino group and one of two nitro groups to form an imidazole ring [141]. The adsorption of trifluralin onto SWy-1 suppressed the molecular motion to form the imidazole ring improving the photostability [142].

Rhodamine 6G (R6G in Scheme 2) was intercalated into smectites, KF, SA, and synthetic hectorites (HE and LP-RD) [143]. The stability of R6G against irradiation was remarkably improved on KF in both of a suspension and a film. As shown in Fig. 4, the emission intensity of R6G depended on the clays, and there is a linear correlation between the photoluminescence intensity and the dye stability, suggesting the quenching of the excited state of R6G was the key parameter to determine the stability. The stability of R6G was substantially modified upon the adsorption onto KF, where the energy transfer from R6G to KF led shorter lifetime of the excited state of R6G.

Improvement of the stability of R6G upon visible light irradiation was also reported for a polymer-smectite intercalation compound [143, 144]. R6G was intercalated in SA with poly(vinyl pyrrolidone) (PVP) to obtain a film, which the

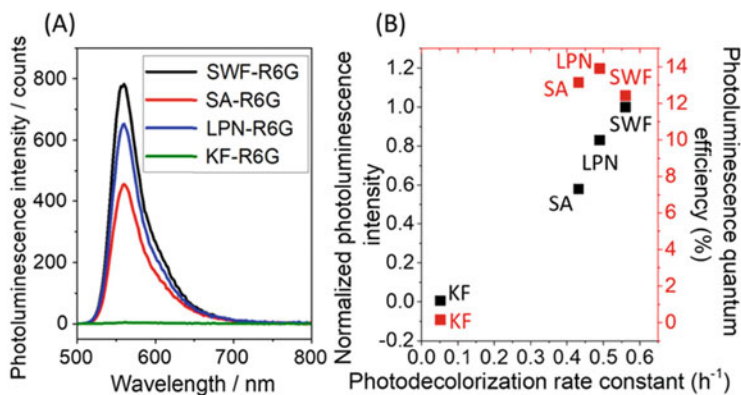


Fig. 4 (a) Photoluminescence spectra and (b) the relationship between the photodecolorization rate constant and the photoluminescence intensity (*black squares*) and the photoluminescence quantum efficiency (*red squares*) of R6G in HE, SA, LPN, and KF suspensions (Reproduced from the reference [143] with permission)

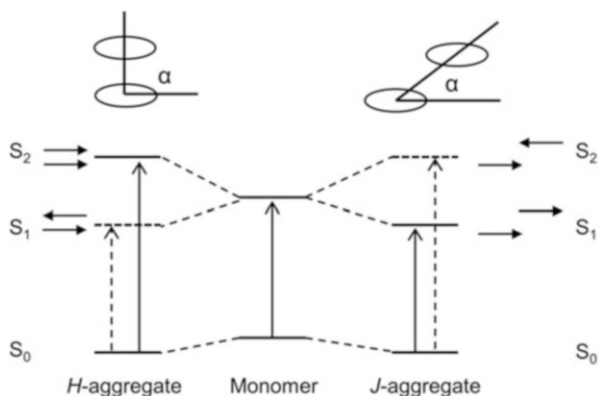
decoloration suppressed upon visible light irradiation over the R6G in SA or in PVP [144]. It was thought that the suppressed oxygen diffusion in the layered structure of SA-PVP contributed to the observed stability.

Another important process is charge transfer (CT) interactions from dyes to layered materials which induce bathochromic shift of absorption spectra [145, 146]. Hybridization of biphenyl with a synthetic hectorite (laponite)-induced absorption at 320 nm attributed to the CT transition, where the biphenyl acted as an electron donor and electron-deficient sites or Lewis acid sites of laponite were electron acceptors [147]. The CT interactions induced a triplet state of biphenyl by recombination from the CT state, and subsequent phosphorescence at 480 nm was observed at 130°C which was stronger than the fluorescence.

Anthraquinone-2-sulfonic acid was hybridized with MgAl-LDH ($\text{Mg}_{0.65}\text{Al}_{0.35}(\text{OH})_2(\text{CO}_3)_{0.01}$), and the hybrid showed photoinduced reduction of the anthraquinone in formamide as shown by the color change from colorless to red [148]. The red color returned to the initial colorless in the dark. The mono-anionic and di-anionic anthraquinones with different lifetime were observed (13.9 and 16.9 min). The solvent was thought to act as the electron donor, and a surface of the MgAl-LDH provides a high pH environment to stabilize the anionic anthraquinone.

Another example is the diverse coloration of retinal Schiff base by the interactions with different smectites. Retinal in rhodopsin as a photoreceptive unit exists as a protonated Schiff base in a *cis*-isomeric state [149], and the rhodopsin provides three different environments for the retinal Schiff base to give blue ($\lambda_{\text{max}} = 425$ nm), green ($\lambda_{\text{max}} = 530$ nm), and red ($\lambda_{\text{max}} = 560$ nm) colors with broad absorption [150]. The similar absorption changes of the retinal Schiff base were observed by mixing the retinal Schiff base with three montmorillonites, Bengel Bright 11 obtained from Wyoming, USA (Hojun Ind. Co., Japan) (479 nm), a

Fig. 5 Schematic representation of the relationship between the dye arrangement and energy level change by molecular aggregation

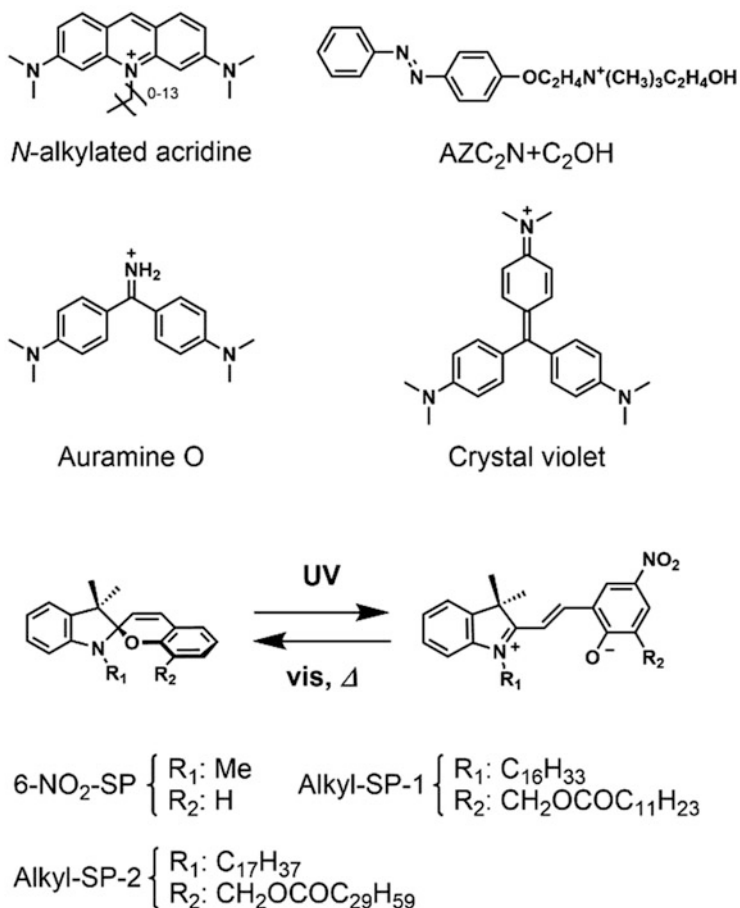


montmorillonite obtained from Mikawa, Japan (503 nm), and Bengel A obtained from China (Hojun Ind. Co., Japan) (532 nm) [151]. This is a rare example for the retinal Schiff base to show the color variation after the isolation from the protein.

4.1.2 Effect of the Dye Aggregation

Aggregation of such dyes [152–156] as acridine orange [157–159], methylene blue [23, 40, 160], azobenzenes [62, 161–169], merocyanines [170, 171], rhodamines [172–178], nile blue A [179], and porphyrins [180–182] has been reported to be induced by the interactions with layered materials [183, 184]. According to Kasha's molecular exciton theory [185], J- and H-aggregates are distinguished by an angle between the line connecting centers of the dyes and the long axis of the dye molecule (α in Fig. 5). When the angle α is larger than 54.7° as shown on the left side in Fig. 5, the transition from S₀ to S₂ is allowed, it is called H-aggregate, and it's characterized by a hypsochromic shift in the absorption band. When the angle α is smaller than 54.7° as shown on the right side in Fig. 5, the head-to-head aggregate is stabilized, and the transition from S₀ to S₁ is allowed. The aggregate shows a bathochromic shift (redshift) upon aggregation and is J-aggregate. Some dyes were intercalated into layered materials as monomolecular or bimolecular layers. The tilt angle between the silicate layer and dyes transition moment may cause shifts in the absorption spectra.

The effects of the length of the alkyl chain of the guest molecules were shown to affect the stability of aggregates in layered materials [159, 171]. Equilibrium constants K_b (M^{-1}) of the adsorption of *N*-alkylated acridine oranges [158], whose alkyl chains were methyl to tetradecyl (Scheme 3), onto KF were estimated [159]. The rate constant of disaggregation k_m ($M^{-1} s^{-1}$) was estimated by the change in the absorption change of the monomer. As shown in Fig. 6, the second-order rate constants k_m increased by increasing the length of the alkyl group for short alkyl chains (number of C atoms up to 4), and the opposite behavior was observed for large alkyl chains (C atoms > 4). The variation of k_m was thought to be due to a



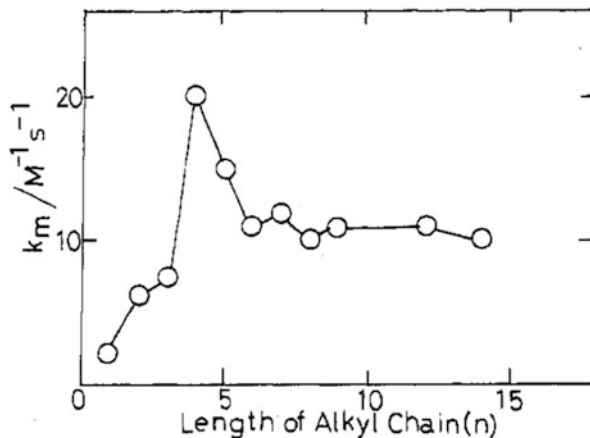
Scheme 3 Molecular structures of dyes which formed aggregates in layered materials

compromise between the steric repulsion and the hydrophobic attraction between the alkyl chains, respectively.

By freeze-drying the suspensions, auramine O (Scheme 3) was hybridized with three montmorillonites SYn-1, SAz-1, and SWy-1 obtained from Source Clays Repository of the Clay Minerals Society [63]. The basal spacings of SYn-1 and SAz-1 did not change by the hybridization, while the absorption due to H-aggregate was observed. The authors proposed that auramine O was adsorbed on the external surface of SYn-1 and SAz-1 as H-aggregates. The absorption and the emission of J- and the H-aggregates of auramine O were observed for SWy-1 depending on the dye loading.

Structure of the intercalation compounds of an amphiphilic cationic azobenzene ($\text{AZC}_2\text{N}^+\text{C}_2\text{OH}$, in Scheme 3) KF was proposed from the basal spacing (1.86 nm, corresponding to the gallery height of 0.9 nm) and the bathochromic shift of the

Fig. 6 Dependence of the second-order rate constant, k_m , on the alkyl chain length of 1–14 (Reproduced from the reference [159] with permission)

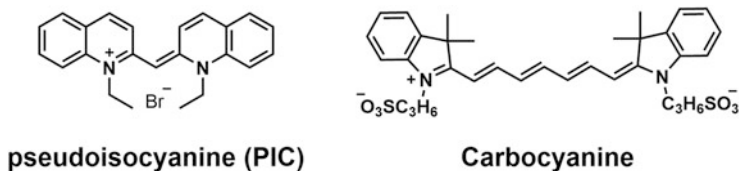


visible absorption spectra, which was thought to be due to the head-to-tail orientation [62]. Considering the molecular size of $AZC_2N^+C_2OH$ and the observed bathochromic shifts of the visible absorption spectrum, it was proposed that $AZC_2N^+C_2OH$ formed J-aggregate as monolayer or bilayer as shown in Fig. 2. The absorption spectrum of $AZC_2N^+C_2OH$ intercalated in magadiite showed a hypsochromic shift, indicating the formation of H-aggregate, which has a gallery height of 1.57 nm [165, 186]. It was considered that the larger layer charge density of magadiite led the $AZC_2N^+C_2OH$ with the higher tilt angle to the silicate layer than that in KF to lead the H-aggregate (head-to-tail dimer).

The absorption spectra of methylene blue (Scheme 1) in the aqueous dispersions of smectites, whose layer charge densities were reduced by Hofmann-Klemen effect, was investigated [23, 115]. The phenomenon called Hofmann-Klemen effect is attributed to the migration of interlayer lithium ions to the vacancies in the octahedral sheet of smectites by heating. The absorption of J-aggregate decreased, and the dimer increased by reducing the layer charge density of the montmorillonite (obtained from Apache Country, Arizona) [115]. The same trend was seen in montmorillonites obtained from San Diego Country, California, and Horní Dunajovice, Czech Republic; a beidellite obtained from Stebno, Czech Republic; and a smectite obtained from Grand Country, Washington.

Dialkylated spiropyrans (Alkyl-SP-1 and Alkyl-SP-2 in Scheme 3) were intercalated into a film of a didodecyldimethylammonium exchanged montmorillonite, and the aggregation of photochemically formed merocyanines was investigated [171]. A photomerocyanine formed from 6- NO_2 -SP has a characteristic absorption at 552 nm, while those of Alkyl-SP-1 and Alkyl-SP-2 absorbed at 493 and 617 nm, which were attributed to H- and J-aggregates, respectively.

Aggregation of dyes in the interlayer space has been reported. The emission of dyes is weaker for H-aggregate due to that the transition dipoles weaken each other [187, 188], while the emission of J-aggregate is intense, and the Stokes shift is smaller than those of the monomer [189–191]. Aggregates of pseudoisocyanine (PIC



Scheme 4 Molecular structures of cyanines adsorbed on clays

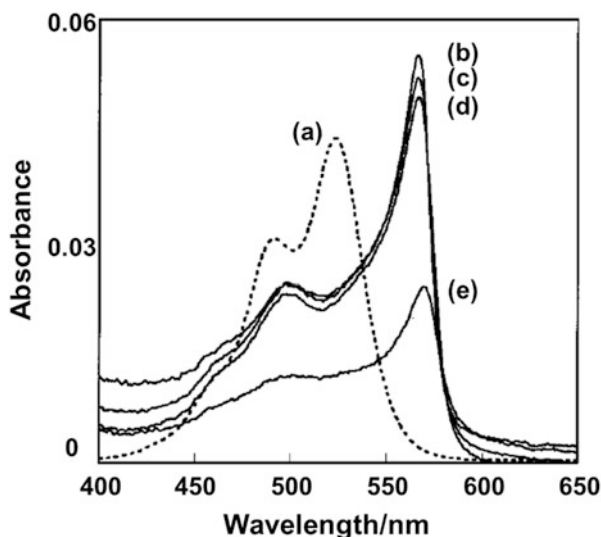


Fig. 7 Absorption spectra of the (a) 5×10^{-6} M PIC aqueous solution and aqueous mixtures containing (b) 20, (c) 10, (d) 5, and (e) 1 mg of KF and 100 mL of 5×10^{-6} M PIC aqueous solution (Reproduced from the reference [193] with permission)

in Scheme 4) have been studied from 1935 [192] and those in layered materials have been reported from 1996 [193]. PIC has absorption at 490 and 520 nm in an aqueous solution, and the absorption of J-aggregate at 577 nm is seen only at high concentration [194]. An aqueous suspension of KF (10 mg/L) with PIC (5×10^{-6} M) showed absorption at 570 nm, which was attributed to the J-aggregate as shown in Fig. 7. The absorption of J-aggregates increased with increasing the concentration of KF. The aggregation of PIC was investigated using montmorillonites (SWy-1, SAz-1, and SYn-1 supplied from Source Clays Repository of the Clay Minerals Society and KF), SA, synthetic hectorites (SWN supplied from Coop Chemical and LP-RD), TSM [195–200], and magadiite [201] to find H-aggregate in SWy-1, SWN, LP-RD, and SA [197, 199, 202, 203]. For TSM, KF, SAz-1, and SYn-1, the absorption of J-aggregate was observed, and the absorption of the H-aggregate increased with the increase of the loading amount of PIC. There was no clear correlation between the cation exchange capacity (CEC) and the types of aggregates. It was proposed that the particle size of the clays can be a factor to determine the aggregation. The broadening of the absorption spectra of PIC due to the aggregation

was observed for magadiite and dodecyltrimethylammonium (C_{12} TMA)-exchanged magadiite [201]. Because, in magadiite, the absorption shift was smaller and the Stokes shift was larger than those of J-aggregate observed in other clays, PIC formed aggregates in magadiite, while they were not the H- and the J-aggregates.

The H- and the J-aggregates of PIC were switched by swelling of host SA [204]. A SA film with 46.4 meq/100 g (70%CEC) of PIC had absorption of the monomer and a shoulder of the H-aggregate. By adding DMSO, the absorption of the J-aggregate increased, and the monomer and the H-aggregate decreased. The absorption spectrum returned to the initial shape by removing DMSO by washing with ethanol and subsequently drying.

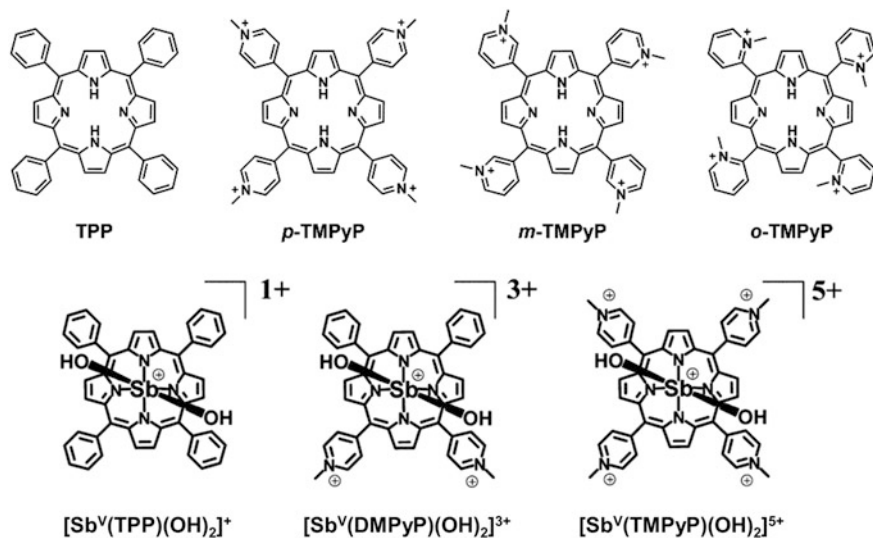
Aggregation of rhodamine 6G (R6G, Scheme 2) in the films of Wyoming montmorillonites [176, 205] and laponites [172, 174–176] was investigated. R6G had absorption at 527 nm in an aqueous solution, [172] and, by adding the montmorillonite, absorption at 534 nm due to J-aggregate and two shoulders at around 500 and 470 nm appeared [205]. The absorption at 500 nm increased, and the shift of the monomer absorption from 527 to 538 nm was observed in a laponite film, which corresponded to the formation of the H- and the J-aggregates [172]. H- and J-aggregates were observed in the absorption and emission spectra of the film of a hexadecyltrimethylammonium (C_{16} TMA) exchanged KF [206]. Effective quenching of the emission from the H-aggregate [207] was observed for auramine O in SYn-1 powder [63], PIC in LP-RD powder [196], and merocyanine 540 in a bentonite (obtained from Ordu/Ünye in Turkey) and the bentonite exchanged with C_{16} TMA [208].

4.2 Changes in the Photoluminescence Properties

4.2.1 Effects of the Host-Guest Interactions

Adsorption on the external surface and in the interlayer space of layered materials suppresses molecular motion of dyes and induces a planar conformation [183, 209–217]. Three different effects of electrostatic interactions and the suppression of the molecular motion on the emission spectra have been proposed: (1) the bathochromic shift of emission by electrostatic interactions, (2) smaller Stokes shift than that in solutions owing to the similar molecular conformation of the excited and ground states inducing hypsochromic shift and increase intensity of the hypsochromic emission, or (3) decrease of the internal conversion rate due to the fixation of the molecular conformation in the excited state on the external surface. These effects were reported for porphyrins [17, 218–222], auramine O [223], and triphenylbenzene derivatives [224].

Porphyrins have two π - π^* transitions known as Soret band at around 400–500 nm and Q-band at around 500–700 nm. The Soret band and the Q-band of tetraphenylporphine (TPP, Scheme 5) and Fe(III)-TPP shifted by the adsorption on a purified Wyoming bentonite from 416 to 445 nm and 620 to 664 nm, respectively [218]. The shift of the absorption was explained by the coplanar structure of the



Scheme 5 Molecular structures of porphyrin derivatives and Sb-porphyrin complexes adsorbed on clays (Reproduced from the reference [225] with permission)

porphyrin moieties and the phenyl substituents on the silicate layer. The relationship between the shift of the Soret band and the molecular structure of porphyrins has been studied to find that the matching of the intercharge distance of the porphyrins and the distance of the adjacent negative charge of the silicate layer was important [17, 219–221]. The shifts of the Soret bands of *p*-TMPyP, *m*-TMPyP, and *o*-TMPyP (Scheme 5) on SA were 30, 12, and 6 nm compared to their aqueous solutions [221]. The shifts were larger when the intercharge distance of the porphyrins (*p*-TMPyP, 1.05; *m*-TMPyP, 0.99; and *o*-TMPyP, 0.88 nm) was closer to the distance of the adjacent negative surface charge (1.19 nm). The planar structure of the three porphyrin derivatives on SA was proposed to be a reason for the shift of the fluorescence to longer wavelength region as shown in Fig. 8 [225, 226]. Fluorescence quantum yields and rate constants of the internal conversion of $[Sb^V(TPP)(OH)_2]^+$ and $[Sb^V(DMPyP)(OH)_2]^{3+}$ (Scheme 4) increased by the adsorption because the excited states of the two derivatives had more similar structures to the ground states than those in solutions. Among the three tested porphyrins, $[Sb^V(TMPyP)(OH)_2]^{5+}$ adsorbed on SA had the fluorescence quantum yield same as that in an aqueous solution, while the internal conversion rate was lower than those of the others, suggesting the suppression of the molecular motion to keep the molecular structure in the excited state by the stronger electrostatic interactions with SA if compared with $[Sb^V(TPP)(OH)_2]^+$ and $[Sb^V(DMPyP)(OH)_2]^{3+}$.

The fluorescence of methyl viologen (MV^{2+}) shown in Scheme 6 in hectorite and montmorillonite was observed as a result of the photoinduced charge transfer from the silicate layers to MV^{2+} [227]. Change of the emission spectra of MV^{2+} by the adsorption on layered materials has been studied [227]. MV^{2+} and viologen derivatives have been intercalated into montmorillonites [227–231], saponite [232, 233],

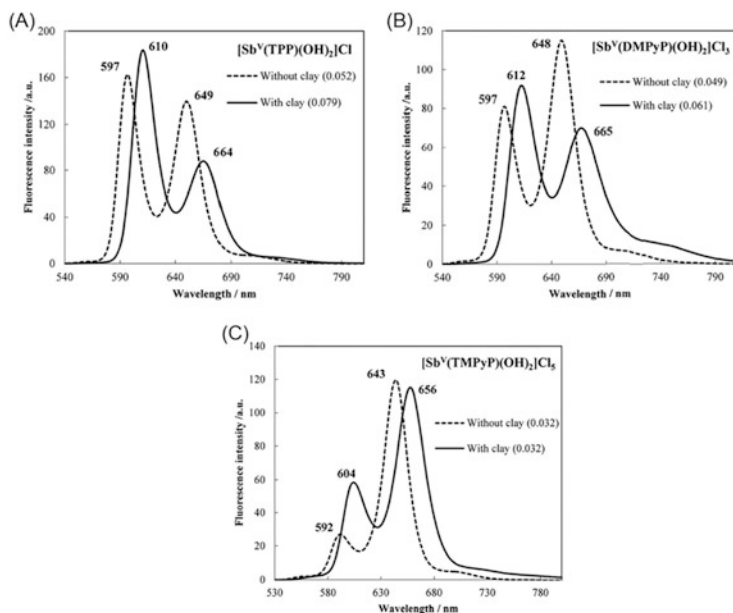
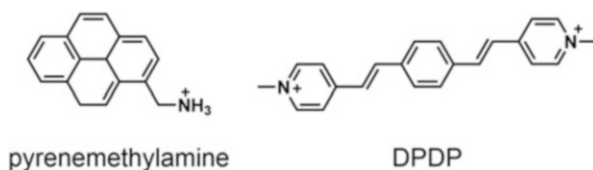


Fig. 8 Fluorescence spectra of *p*-TMPyP (A), *m*-TMPyP (B), and *o*-TMPyP (C) with clay (*solid line*) and without clay (*dashed line*) (Reproduced from the reference [226] with permission)



Scheme 6 Molecular structures of dyes which form excimer in the interlayer space

hectorite [227, 231], nontronite [227, 231], vermiculite [229], titanates [234], niobates [235–238], and layered zirconium phosphate [239, 240]. The absorption spectra of MV^{2+} showed bathochromic a shift by the intercalation into smectites (KF, SA, and LP-XLG) [233], the layered zirconium phosphate/phosphonates [239, 240], and niobate [235–238]. The intercalated hybrid showed reversible color change to blue by the photoinduced charge transfer from the host. Non-emissive MV^{2+} showed fluorescence in an aqueous suspension of a hectorite (San Bernardino) and a montmorillonite (Clay Spur, Wyoming), and this phenomenon was explained by the planar structure of MV^{2+} on the silicate layer [231]. This phenomenon can be explained as “adsorption-induced emission.” The emission intensity of MV^{2+} increased by the decrease of the loading amount (by the increase of the concentration of the clays). The self-quenching of fluorescence of MV^{2+} on

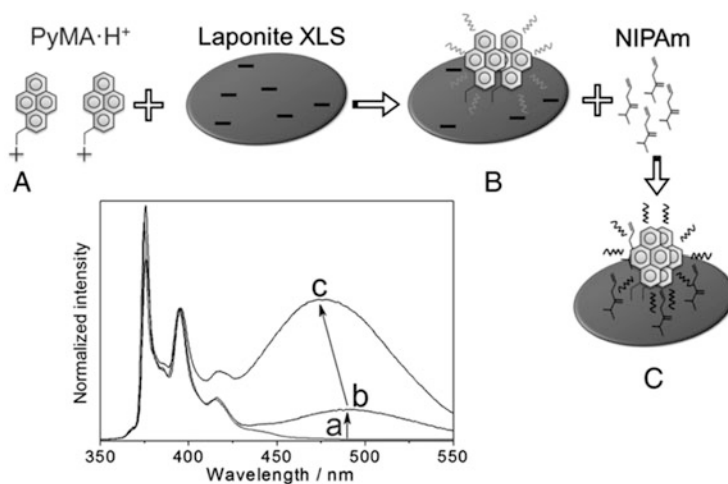


Fig. 9 Schematic illustration of the adsorption of pyrenemethylamine and *N*-isopropylacrylamide on LP-XLS and the corresponding normalized emission spectra. (a) Pyrenemethylamine in the aqueous solution; (b) pyrenemethylamine adsorption on LP-XLS; (c) co-adsorption of *N*-isopropylacrylamide on LP-XLS. The spectra a, b, and c correspond to the conditions A, B, and C (Reproduced from the reference [253] with permission)

the clays was proposed as a reason of the weaker emission at the high loading amount.

Absorption at 410 and 450 nm appeared in powder of pyrene hybridized with LP-RD by UV irradiation. Electron spin resonance experiment with and without O₂ (triplet quencher) indicated that the absorption was from a triplet state of radical cation of pyrene [241]. The radical cation of pyrene was thought to be generated by the photoinduced charge transfer from pyrene to LP-RD. The color of the hybrid was different depending on the pre-activation temperature of LP-RD. The intensity of the ESR signal was higher when the pre-activation temperature was lower, suggesting the interactions of the surface water/OH groups with the adsorbed pyrene.

4.2.2 Excimer Formation

Pyrene has been used as a probe to investigate the surface chemistry [242–247] and refractive index [248] of clays as well as the surface modification with alkylammonium surfactants [249–252]. Excimer emission of pyrenemethylamine (Scheme 6) was enhanced by adding LP-XLS to an aqueous solution of pyrenemethylamine, suggesting change in the intermolecular distance between the adjacent pyrenemethylamine molecules [253]. As shown in Fig. 9, co-adsorption of *N*-isopropylacrylamide further enhanced the excimer emission, suggesting that *N*-isopropylacrylamide reduced the intermolecular distance of pyrenemethylamines to induce effective intermolecular interactions.

Packing of DPDP [254] (Scheme 6) changed by the swelling of SA with DMSO [255]. DPDP was intercalated into SA film with various loading amounts from 0.033 to 49.7 meq/100 g (from 0.05 to 75%CEC). At the loading from 0.033 to 26.5 meq/100 g, the emission of the monomer at 482 nm decreased, while new emission at 588 nm of excimer appeared by the increase of the concentration. The gallery height of the hybrid increased from 0.48 to 0.93 nm by the swelling of SA with DMSO and the excimer emission enhanced, suggesting that the swollen SA provides the interlayer expansion large enough for the π - π stacking of DPDP.

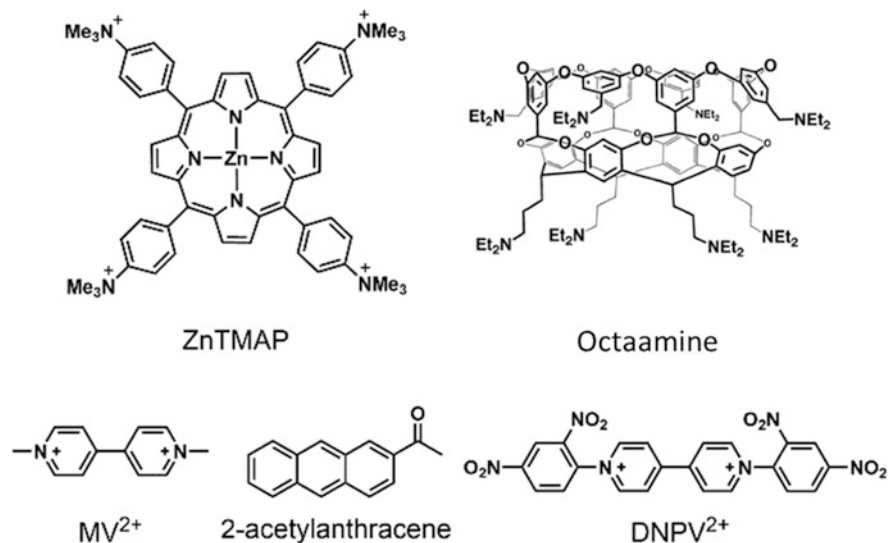
4.2.3 Energy and Electron Transfer Between Molecules Adsorbed on Clays

The construction of photocatalyst by energy transfer in the interlayer space is a topic of interest [256–262]. Adsorption on layered materials is a way to concentrate dyes and to control the proximity, which resulted in efficient energy [19, 263–269] and electron transfer [18, 31, 270, 271]. Expected effects of hybridization of dyes and layered materials are (1) efficient quenching of the excited state of the dyes for photostabilization, (2) separation of the photosensitizer from photocatalyst to avoid the photocatalytic decomposition of sensitizer, and (3) directional energy and electron transfer by locational and orientational design.

A possible way to improve the photostability is quenching the photoexcited state by energy transfer as discussed in Sect. 4.1. The stability of herbicides [272–274], bioresmethrin [275], and norflurazon [276] was improved by energy or electron transfers to methyl green co-adsorbed on montmorillonite and to thioflavin T on SWy-1. The separation of the photosensitizer from the photocatalyst (anatase particle) by smectite nanosheet induced durability of the photosensitizer. The photocatalytic oxidation of benzene to phenol was done in an aqueous suspension of anatase with the tris(2,2-bipyridine)ruthenium(II) (designated as $[\text{Ru}(\text{bpy})_3]^{2+}$)-synthetic saponite, resulting in a high yield of benzene decomposition and selectivity of phenol. The hybrid was processed as a film to be used as the photocatalyst layer to obtain a photocatalytic flow reactor [277, 278].

The fluorescence of $[\text{Ru}(\text{bpy})_3]^{2+}$ was quenched by SO_2 gas [107] suggesting a possible gas sensor application. The fluorescence of $[\text{Ru}(\text{bpy})_3]^{2+}$ was quenched by the MV^{2+} co-adsorbed on smectites, and the quenching efficiency was higher when smectites with larger particle sizes (e.g., TSM) was used if compared with those on clays with smaller particle sizes (e.g., SA and LP-XLG) [279]. Such quenchers as cyanine, MV^{2+} , and anthraquinone derivatives were co-adsorbed with cyanine dyes on laponite RDS (Southern Clay Products, Inc.) to quench the fluorescence of the J-aggregate of the cyanine [280].

MV^{2+} (Scheme 7) in the interlayer space of smectites acted as an electron acceptor [232, 233, 281–284]. It was reported the photoinduced electron transfer from TPP (Scheme 5) to MV^{2+} under visible light irradiation to form the TPP radical cation and MV^+ radical cation [281]. The color of MV^{2+} intercalated in a hectorite-like layered silicate changed by the adsorption of *N,N*-dimethylaniline and

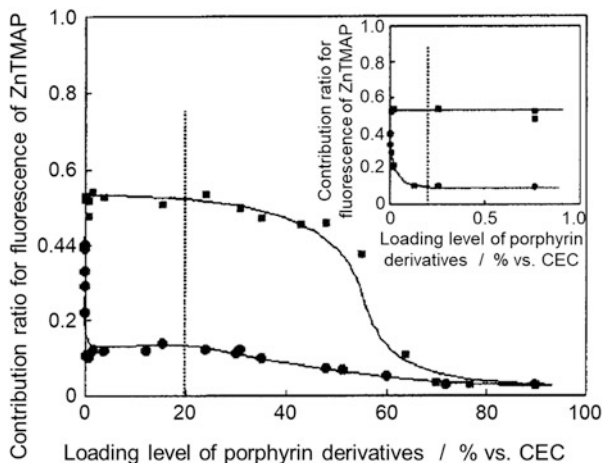


Scheme 7 Molecular structures of dyes exhibited energy and electron transfer on layered materials

2,4-dichlorophenol [285], and the color depended on the layer charge density and the concentration of the adsorbents. The hectorite-like layered silicate was synthesized from LiF, Mg(OH), and SiO₂ sol with various ratios to vary the layer charge density [286]. The color of the hybrids of the hectorite and MV²⁺ changed from yellow to purple green and purple by the adsorption of *N,N*-dimethylaniline depending on the layer charge density and the increase of the concentration of *N,N*-dimethylaniline. Color changed from yellow to orange was seen by the adsorption of 2,4-dichlorophenol. The color of the hybrids with *N,N*-dimethylaniline was explained to the formation of methyl violet, and that with 2,4-dichlorophenol was attributed to the charge-transfer complexes.

Effects of the molecular location and orientation on the energy transfer between adjacent molecules have been investigated in porphyrin-smectites systems [19, 211, 260, 264, 266, 284]. Energy transfer from Zn complexed aniline-substituted porphyrin (ZnTMPAP, Scheme 7) to pyridine-substituted porphyrin (*p*-TMPyP, Scheme 5) was investigated in SA suspension by monitoring the contribution of the fluorescence from ZnTMPAP excited at 428 nm, which matched the absorption of Soret band of ZnTMPAP [287]. When the two porphyrins adsorbed on SA individually and subsequently mixed, the contribution of the fluorescence intensity of ZnTMPAP was the same in the concentration region of the porphyrins to 6.6 meq/100 g (10%CEC, for each), while the contribution decreased in the higher concentration region (Fig. 10). When the two porphyrins were co-adsorbed on SA, the contribution of the fluorescence intensity of ZnTMPAP was decreased from 0.6 to 0.1 with increase of the concentration of the two porphyrins to 0.066 meq/100 g (0.1%/CEC for each), and then, the contribution of ZnTMPAP gradually decreased and become negligibly small at 29.8 meq/100 g (45%CEC for each) as shown in Fig. 10. These results

Fig. 10 Contribution of ZnTMAP for fluorescence at various porphyrin loading levels for independent adsorption (*squares*) and co-adsorption (*circles*) (Reproduced from the reference [287] with permission)



suggested that the energy transfer between SA layers was major in the suspension prepared with SAs that adsorbed porphyrins individually, while the intralayer energy transfer was major in the suspension prepared with SA with porphyrins by the co-adsorption.

The sequential energy and electron transfers from 2-acetylanthracene to Zn-*p*-TMPyP to DNPV²⁺ (Scheme 6) on SA were reported [288]. 2-Acetylanthracene was encapsulated in octaamine to be adsorbed on SA with 1:1 ratio of Zn-*p*-TMPyP. In a suspension of SA with 2-acetylanthracene in octaamine and Zn-*p*-TMPyP, the decrease of fluorescence of 2-acetylanthracene and the increase of that of Zn-*p*-TMPyP compared to suspensions were seen, suggesting the energy transfer from 2-acetylanthracene in octaamine to Zn-*p*-TMPyP. The shorter lifetime of Zn-*p*-TMPyP in a suspension of SA with DNPV²⁺ than that in a suspension without DNPV²⁺ suggested the electron transfer from Zn-*p*-TMPyP to DNPV²⁺.

4.3 Alignment of Dyes by Host-Guest Interactions: Study by Linear Polarized Light

Film of propylammonium-exchanged titanate (Na₂Ti₃O₇) was prepared by casting an aqueous suspension and used as a host of cationic dyes. Pseudoisocyanine (PIC in Scheme 7) intercalated in the titanate film showed absorption anisotropy [289] as shown in Fig. 11. The absorbance in the visible region with 5° of the angle between the film plane and the incident light was decreased by the rotation of the incident polarized light from 0° to 90°, while the small absorption change was observed with 90° of the angle between the substrate plane and the incident light. It suggests that a transition moment of PIC, which corresponds to the long molecular axis, was parallel to the substrate.

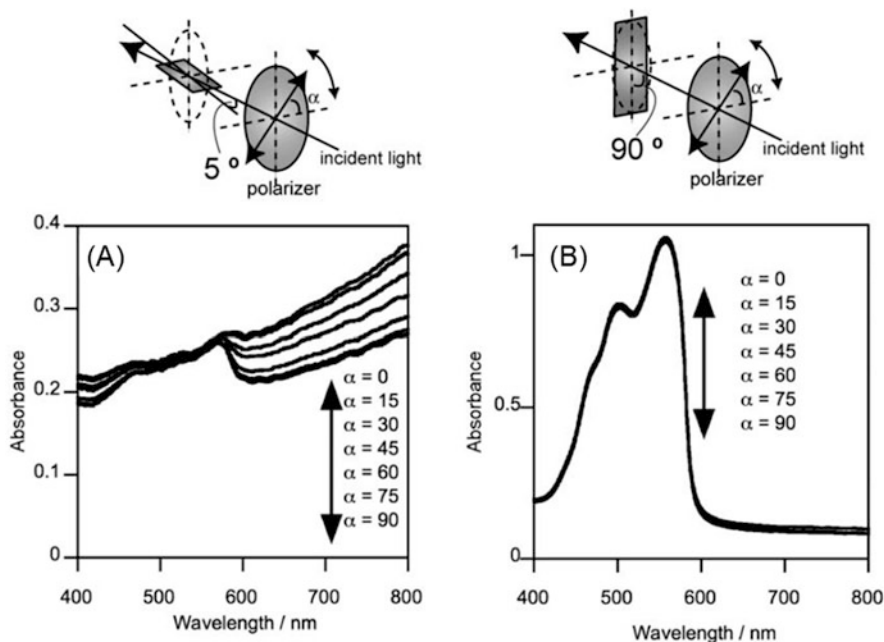


Fig. 11 Polarized visible spectra of a film of PIC-Ti₃O₇. The angle between the substrate plane and the incident light was set to (a) 5° and (b) 90° by rotating the film; α represents the angle between the polarization direction of the incident light and the rotation axis of the film (Reproduced from the reference [289] with permission)

The angles between molecular axes of the following porphyrin derivatives, *p*-TMPyP, *trans*-DMPyP, and *cis*-DMPyP (Scheme 4), and the silicate layer of SA were estimated by polarized visible light attenuated total reflection (polarized vis-ATR) spectra [290]. Figure 12 shows that the absorbance of *p*-TMPyP of s-polarized light was larger than that of the p-polarized light. A similar difference in the polarized absorption spectra was observed in *trans*-DMPyP and *cis*-DMPyP. The angles between the molecular axes of the three porphyrins and the surface of the silicate layer were estimated to be less than 5°.

Fluorescent dyes adsorbed in layered materials showed linearly polarized emission, suggesting the alignment of the dye dipole in the interlayer space [291–293]. A laponite film was prepared by spin-coating an aqueous suspension and was used to accommodate rhodamine 6G (R6G, in Scheme 2) by cation exchange by immersing the film in an R6G solution [206, 294, 295]. Fluorescence intensity excited by horizontally polarized light depended on the direction of the polarizer. The angle between the long axis of R6G and the silicate layer was estimated to be 28° from the difference of the fluorescence intensities observed with horizontal or vertical axes of the film.

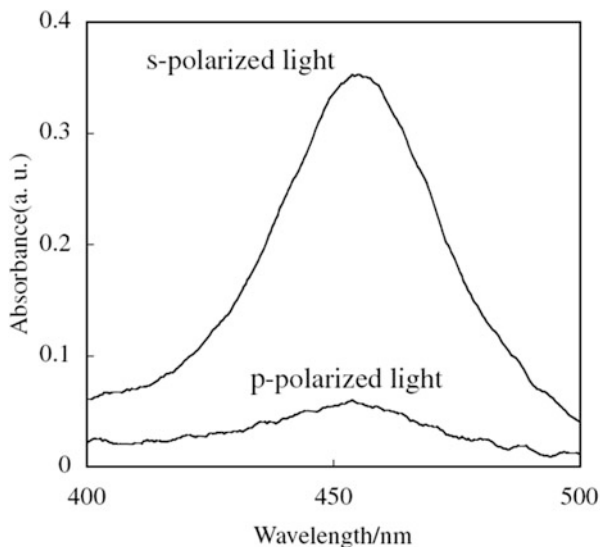


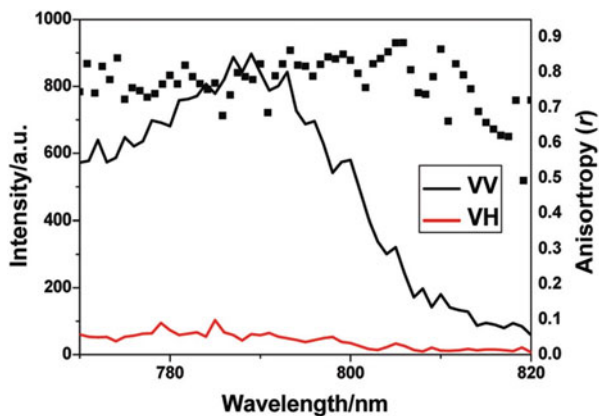
Fig. 12 Polarized vis-ATR spectra of *p*-TMPyP with s- and p-polarized light (Reproduced from the reference [290] with permission)

Polarized fluorescence of rhodamine B [296], fluorescein [297], pyrene [298], cyanine [299], niflumic acid [300], bis(*N*-methylacridinium) [301], tris (8-hydroxyquinolate-5-sulfonate)aluminum(III) [302], polyphenylene [303], and polythiophene [304] in LDH films prepared by LbL technique was reported. The anisotropic value r as defined by Eq. (1) was derived to discuss the dye orientation from emission anisotropy.

$$r = \frac{I_{VV} - I_{VH}}{I_{VV} + 2I_{VH}} \quad (1)$$

In (1), I_{VV} and I_{VH} are emission intensities with vertical and horizontal directions excited by vertical light [305]. The fluorescence spectra of a carbocyanine (Scheme 4) intercalated in a MgAl-LDH [303] showed anisotropy (Fig. 13) with the r value as high as 0.8, where the value was higher than that in a solution (0.2) and nearly twice of the theoretical highest value in the case without macroscopic alignment (0.4) [299]. The r value of the carbocyanine was larger than pyrene (0.26) [298], fluorescein (0.3) [297], and fluorenone derivatives (0.25) [306], which have planar molecular structures. The orientation of the intercalated dye in MgAl-LDH was thought to induce the anisotropy.

Fig. 13 Polarized fluorescence with the intensities of I_{VV} and I_{VH} and the r value for the hybrid of the carbocyanine in MgAl-LDH (Reproduced from the reference [303] with permission)



5 Photochemical Reactions

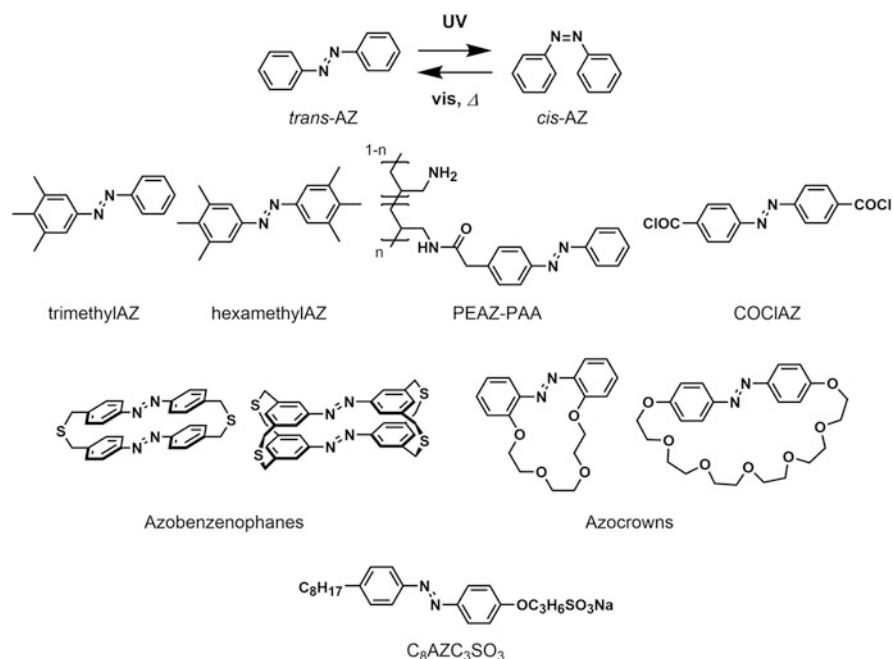
5.1 Intramolecular Reactions Affected by Host-Guest Interactions

Molecular reactions of organic compounds interacted in clays are different from those in solutions. The molecular reactions of the organic molecules were affected by the polarity of interlayer space and/or by the suppression of molecular vibration in the interlayer space [8, 10, 307].

5.1.1 Azobenzene

Azobenzene (AZ) shows photoisomerization from *trans*- to *cis*-isomer by UV irradiation, and the *cis*-isomer returns to the initial *trans*-isomer by heat or visible light irradiation as shown in Scheme 8. The half-lives of the thermal isomerization of the *cis*-isomer to the *trans*-isomer of AZ in a benzene solution at room temperature and 60°C were 119 [308] and 1.5 h [309], respectively, in the dark following first-order kinetics. The polarity and the viscosity of the solvent affect the photoisomerization of AZ [310, 311], and the photoisomerization was suppressed in packed states [312]. Accordingly, the host-guest interactions are expected to affect the photoisomerization.

Here, a fraction of the *cis*-isomer of AZ is used as a measure of photoisomerization. The fractions of the *cis*-isomer of AZ at the photostationary state in cyclohexane [313] and in toluene [314] solutions were 80 and 90%, respectively. Although the fraction of the *cis*-isomer is different depending on the substituents of the azobenzene and the wavelength of the incident light [315], the fraction of the *cis*-isomer in polymethyl methacrylate (PMMA) was as high as that in the toluene solution [316]. The fraction of the *cis*-isomer became smaller in poly(styrenesulfonate) (PSS) [317], azobenzene polymer [318], SiO₂ [316], and zeolite



Scheme 8 Molecular structures of azobenzenes introduced in this chapter

[313] as summarized in Table 2. The fraction (83%) of the *cis*-isomer of trimethylAZ was larger than that (60%) of hexamethylAZ in the methylcyclohexane-isohehexane 2:1 solution [319] and that (64%) of $\text{C}_1\text{AZC}_2\text{OH}$ (in Table 2) in a SiO_2 film prepared by a sol-gel reaction with tetraethoxysilane (TEOS), but it was smaller than that (93%) in the ethanol solution [316] (Table 2). It was explained that the steric repulsion between the azobenzene derivatives and the media is an important factor to change the molecular fraction of the *cis*-isomer. The azobenzene derivatives, which were introduced as building blocks of co-polymers (PEAZ and COCIAZ in Scheme 8), showed a smaller fraction (65–70% for PEAZ and 50% in a swelled film for COCIAZ) of the *cis*-isomer than that in the AZ solution of cyclohexane. The steric repulsion between the azobenzene part and the other part of the polymer suppressed the isomerization. LB films with amphiphilic azobenzene derivatives (as summarized in Table 2) have been studied [320–332]. The fraction of the *cis*-isomer was as high as 90% in the LB films of $\text{C}_8\text{AZC}_3\text{SO}_3$ (Scheme 8) with poly (diallyldimethylammonium chloride) [332].

AZ was adsorbed on a sodium montmorillonite by solid-solid reactions [334] and from vapor [335]. Adsorption of AZ on a kaolinite from aqueous solution was also reported [217]. Photochemical studies of AZ in layered materials were initiated by Ogawa et al., and the first one was that on the AZ intercalated in an organically modified montmorillonite [334]. Then, amphiphilic cationic azobenzenes were intercalated into a montmorillonite [161], followed by the intercalation of various

Table 2 Fraction of *cis*-isomer of azobenzene derivatives

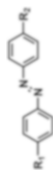
Derivative	State	<i>cis</i> -isomer fraction	Excitation wavelength (nm)	Reference
AZ	Cyclohexane	80%	254	Kojima et al. [313]
	Toluene	91%	365	Fischer et al. [314]
	Zeolite NaY (pore size: 0.74 nm)	80%	313	Kojima et al. [313]
	Sodium mordenite (pore size: 0.7 × 0.65 nm)	50%	313	Kojima et al. [313]
TrimethylAZ	Methylcyclohexane-isohehexane 2:1	83%	313	Gegiou et al. [319]
HexamethylAZ	Methylcyclohexane-isohehexane 2:1	60%	313	Gegiou et al. [319]
C ₁ AZC ₂ OH	Ethanol	93%	365	Ueda et al. [316]
	PMMA ($M_n = 1.0 \times 10^5$, $T_g = 105^\circ\text{C}$)	93%	365	Ueda et al. [316]
	SiO ₂ (sol-gel film)	64%	365	Ueda et al. [316]
PEAZ-PAA	Multilayer film with polystyrenesulfonate (PSS)	Dry film: 31% Swollen film: 50%	320–380	Suzuki et al. [317]
COCIAZ	Introduced as a part of polymers in <i>N,N</i> -dimethylacetamide	65–70%	370–400	Beattie et al. [318]
AZC ₂ N ⁺ C ₂ OH	MCM-41 with 3.2 nm pore size	70%	350	Ogawa et al. [333]
C ₈ AZC ₂₀ Py ⁺	LB film with dimyristoylphosphatidic acid (DMPA)	Ca. 90%	365	Maak et al. [332]

ionic azobenzenes (summarized in Table 3) into layered clay minerals [62, 163–165, 167, 186, 336–340], layered double hydroxide (LDH) [341], potassium hexaniobate (K₄Nb₆O₁₇) [342], and a titanoniobate [343] by ion exchange reactions.

The photochromism of AZ was observed in organically modified KF [334] and TSM [162, 349]. The fraction of the *cis*-isomer of AZ in didodecyldimethylammonium (2C₁₈2C₁N⁺)-TSM was about 80% at the

Table 3 Molecular structures of cationic azobenzenes intercalated in smectites

Derivatives	R ₁	R ₂	References
C ₁ AZC ₂ OH	OCH ₃	OC ₂ H ₄ OH	Okada et al. [344]
AminoAZ	H	NH ₂	Ogawa et al. [345]
AZN ⁺	H	N ⁺ (CH ₃) ₃	Ogawa et al. [345]
AZC1N ⁺	H	CH ₂ N ⁺ (CH ₃) ₃	Bujdák et al. [337]
AZC ₂ N ⁺ C ₂ OH	H	C ₂ H ₄ N ⁺ (CH ₃) ₂ C ₂ H ₄ OH	Ogawa et al. [167, 186, 344, 346]
C ₂ AZC ₂ N ⁺	C ₂ H ₅	OC ₂ H ₄ N ⁺ (CH ₃) ₃	Okada et al. [344]
C ₈ AZC ₁₀ N ⁺	C ₈ H ₁₇	OC ₁₀ H ₂₀ N ⁺ (CH ₃) ₃	Ogawa et al. [161, 165]
C ₈ AZC ₁₀ N ⁺ C ₂ OH	OC ₈ H ₁₇	OC ₁₀ H ₂₀ N ⁺ (CH ₃) ₂ C ₂ H ₄ OH	Takagi et al. [347]
C ₁₂ AZC ₅ N ⁺	OC ₁₂ H ₂₅	OC ₅ H ₁₀ N ⁺ (CH ₃) ₃	Ogawa et al. [62, 161, 163–165]
N ⁺ AZN ⁺	N ⁺ (CH ₃) ₃	N ⁺ (CH ₃) ₃	Umemoto et al. [348]
N ⁺ C ₁ AZC ₁ N ⁺	CH ₂ N ⁺ (CH ₃) ₃	CH ₂ N ⁺ (CH ₃) ₃	Bujdák et al. [337]



photostationary state under a 500 W super high-pressure Hg lamp [162], while that in octadecyltrimethylammonium cation ($C_{18}3C_1N^+$)-TSM was about 35% under a 100 W high-pressure Hg lamp [349]. The difference of the fraction of the *cis*-isomer is thought to be due to the molecular packing of the surfactants in the interlayer space. The thermal *cis*- to *trans*-isomerization of AZ in $C_{18}3C_1N^+$ -TSM took 2 days [349] which was faster than the half-life of *cis*-AZ in a benzene solution (5 days) [308]. The thermal isomerization of *cis*-AZ in the solution followed a first-order kinetics while in such polymers as poly(methyl methacrylate) (PMMA) [350] and poly(ethyl methacrylate) (PEMA) [351] and a silica gel synthesized by sol-gel method did not follow the first-order kinetics [350], indicating that the azobenzene molecules were in several environments in these solid-state materials.

The photochromism of cationic azobenzenes in montmorillonites [62, 161, 344], saponites [163, 337, 352], a fluorohectrite [337], taeniolite [163], and magadiite [164, 165, 186, 346] was reported [167]. Organically modified fluoro-tetrasilicic mica [345], montmorillonite [353], and beidellite [353] were also used. As summarized in Table 2, the fraction of the *cis*-isomer of $AZC_2N^+C_2OH$ in mesoporous silica (MCM-41) with the pore size of 3.2 nm was 70% [333], and those of AZ in a zeolite NaY (pore size: 0.74 nm) and a sodium mordenite (pore size: 0.7×0.65 nm) were 80 and 50%, respectively [313]. The fraction of *cis*-isomer of the cationic azobenzene ($AZC_2N^+C_2OH$, Table 3) in magadiite at room temperature was 80%, similar to AZ in a cyclohexane solution [165]. It was thought that the structural change of azobenzenes was accommodated by the change of the basal spacing to achieve the relatively high yield of *cis*-isomer. The thermal isomerization of *cis*-isomer of $AZC_2N^+C_2OH$ in magadiite followed the first-order kinetics, indicating that $AZC_2N^+C_2OH$ was homogeneously distributed in magadiite. The fraction of *cis*-isomer at the photostationary state decreased in KF [161] and magadiite [165] at low temperatures. The fraction of *cis*-isomer of the cationic azobenzenes ($C_8AZC_{10}N^+$ and $C_{12}AZC_5N^+$, in Table 3) in KF at room temperature was about 50%, while *cis*-isomer was practically not detected at the temperature lower than 200 K, suggesting that the molecular motion was suppressed in the interlayer space of KF.

There are several examples of the suppression of the *trans*- to *cis*-isomerization. In a fluorohectorite (obtained from Corning Inc.) in both suspensions and films, photoisomerization of $N^+C_1AZC_1N^+$ (Table 3) was suppressed, while AZC_1N^+ isomerized as shown by the change in the absorption spectrum (Fig. 14) [337]. It was explained that attractive electrostatic forces between the silicate layers and the dicationic $N^+C_1AZC_1N^+$ hindered the isomerization. Photoisomerization of N^+AZN^+ (Table 3) was suppressed by the adsorption on SA [348]. Both *trans*- and *cis*-isomers of N^+AZN^+ were exchanged on SA. The *cis*-isomer showed photoisomerization to the *trans*-isomer on SA by 420 nm light irradiation with a higher quantum yield than that in an aqueous solution (without clay), while *trans*-isomer on SA did not show photoisomerization. The suppression of the *trans*- to *cis*-isomerization was thought to be due to the matching of the interchange distance of the *trans*-isomer and that of the adjacent negative surface charge of the silicate layer. The *trans*-isomer interacted with the silicate layer with both of two cationic moieties

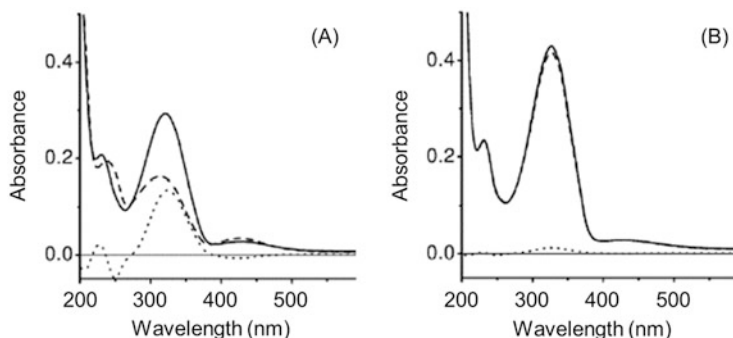


Fig. 14 UV-vis absorption spectra of (a) AZC_1N^+ and (b) $N^+C_1AZC_1N^+$ in a fluorohectorite dispersion. The spectra were recorded before (*solid line*) and after the UV irradiation (*dashed line*). Difference spectra were derived by subtracting the spectrum before the irradiation from that of the irradiated solution (*dotted line*) (Reproduced from the reference [337] with permission)

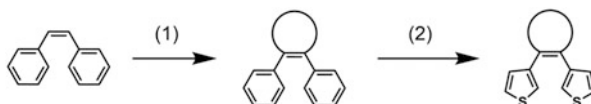
and the molecular motion was suppressed. In the case of the *cis*-isomer, one of the two cationic moieties interacted with the surface charge, leading that the *cis*-form isomerized to the *trans*-isomer.

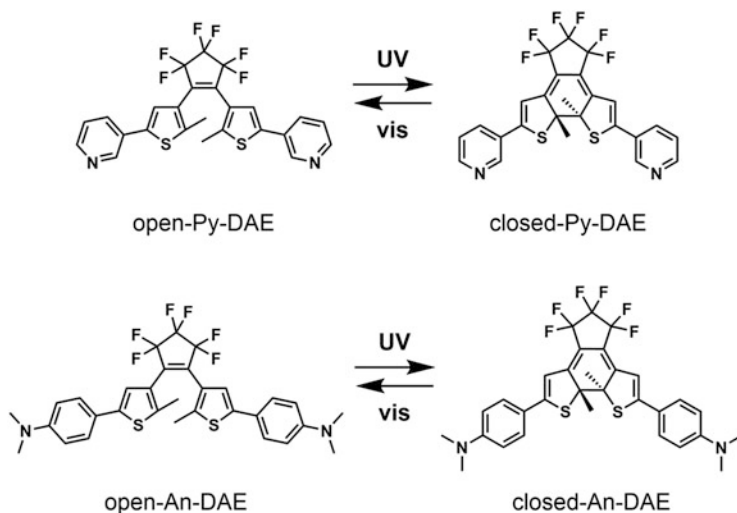
Nonionic azobenzenes intercalated in organically modified clays and cationic azobenzenes exchanged on clays showed photochromism with the relatively high fraction of the *cis*-isomer at the photostationary state. When a dicationic azobenzene was adsorbed on SA, the isomerization of the *trans*-isomer was suppressed. By the design of the interlayer space of clays, the control of the photochromism of azobenzene such as the fraction of the *cis*-isomer, thermal fading speed to achieve quick response, and bistability is expected.

5.1.2 Diarylethene

Photochromism of diarylethenes is attributed to reversible photocyclization between two aryl rings [354]. Open-ring isomer of diarylethenes shows photocyclization under UV irradiation and closed-ring isomer with a planar π -system forms. Both of the open-ring and the closed-ring isomers do not show the thermal isomerization to give P-type (thermally irreversible, but photochemically reversible) photochromism. The reversibility and the durability of the diarylethenes have been investigated by Irie through molecular design [354]. The points are (1) substitution with a ring structure to suppress the *cis-trans* isomerization of stilbene and (2) substitution with thiophene rings to stabilize the closed-ring isomer as shown in Scheme 9. The open-ring isomer of the diarylethenes has two molecular conformations,

Scheme 9 Molecular design of diarylethenes

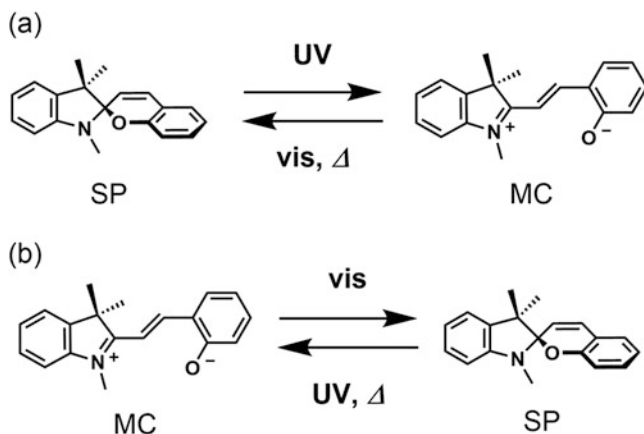




Scheme 10 Molecular structures of diarylethenes hybridized with clays

photoinactive parallel and photoactive antiparallel conformations, and the ratio of these conformations are almost equal in solution [354]. In addition to the photoinduced oxidation of thiophen rings [355], a photoinactive isomer, which formed by the condensation of two thiophen rings, was reported as a deactivation process of diarylethenes [356–359]. In order to improve the reversibility and the yield of photocyclization, control of the molecular conformation of the diarylethene has been examined by the molecular and supramolecular designs using such intramolecular interactions as hydrogen bonds [360, 361], intramolecular steric repulsion [362, 363], as well as the host-guest interactions in nanospaces [364, 365]. Almost unity quantum yield (98%) of a ring-closing reaction of a diarylethene derivative was achieved in a hexane solution by restricting the molecular motion with intramolecular hydrogen bonds, being smaller in polar solvents (in methanol solution: 54%) [360, 361].

Restricted molecular motion by host-guest interactions is expected to affect the ring-closing reaction. A pyridine- and aniline-substituted diarylethenes (Py-DAE and An-DAE, Scheme 10) were intercalated into KF and magadiite by cation exchange [366, 367] and covalent functionalization [368, 369], respectively. An interchange distance in the parallel conformation of Py-DAE (0.9 nm), which was shorter than that of the antiparallel conformation (1.3 nm), matched with the distance between adjacent negative charge of KF (0.9 nm) so that the parallel conformation was preferred on KF. As a result, a change of absorption owing to the photocyclization of Py-DAE in KF suspension was smaller than that in a solution (without clay) [367]. The reversibility of Py-DAE photochromism was improved by co-intercalation of dodecylpyridinium ion [366]. The formation of the parallel conformation was suppressed by the co-intercalation of dodecylpyridinium.



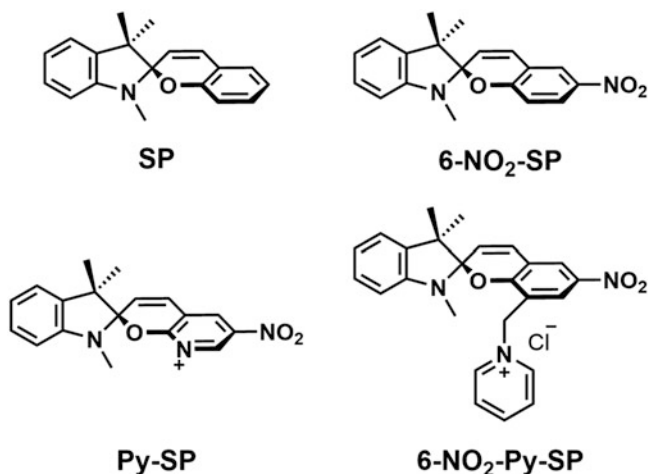
Scheme 11 The photochromism of spiropyran in (a) non-polar and (b) polar environment

An-DAE covalently bound on magadiite gave improved reversibility of the photocyclization compared with that in an ethanol solution [368, 369]. The molecular rotation from the antiparallel to the parallel conformation of An-DAE was suppressed by the covalent attachment to the silicate layer. Reversibility of photochromisms was also improved by restricting the molecular motion by the confinements. It was also claimed that the suppression of the parallel conformation improved the reversibility. The suppression of the generation of the photoinactive isomer was also concerned for the reversibility.

5.1.3 Spiropyran

Photochromism of spiropyran is dependent on the polarity of the molecular environment. In a non-polar environment, spiropyran (SP) is more stable than photomerocyanine (photoMC) (Scheme 11) as zwitter ionic structure [370]. 6-NO₂-MC is photochemically formed from 6-nitrospiropyran (6-NO₂-SP, in Scheme 12) in toluene showing blue color with a half-life of 5.6 s at room temperature, while 6-NO₂-MC in ethanol was red and the half-life is 17 min [371]. The phenoxy moiety of merocyanine is protonated in acidic condition, and the protonated merocyanine shows yellow; thus, photochromism of spiropyran in the acidic condition is related to three isomers of spiropyran, merocyanine, and protonated merocyanine forms [370, 372, 373].

SP, the protonated MC, and 6-NO₂-SP were intercalated into KF by mixing in a mixed solvent of methanol and water and subsequent filtration [170]. The hybrids of KF were yellow, suggesting that SP and 6-NO₂-SP converted to the protonated MC, which was stabilized by the interactions with hydroxyl groups at the edge of the silicate layer. 6-NO₂-MC generated from 6-NO₂-SP is red in a toluene suspension of



Scheme 12 Chemical structures of spiropyrans hybridized in clays

HE by the UV irradiation [374], indicating that 6-NO₂-MC adsorbed on HE by the host-guest interactions.

Dihydropyrenes [375], Stenhouse salts [376, 377], and binaphthyl-bridged imidazole dimers [378, 379] showed negative photochromism (opposite behavior to normal photochromism in non-polar environment; photodecoloration by visible light and thermal coloration) (Scheme 11b). High conversion of the photoisomerization of the negative photochromic compounds with respect to normal photochromism is possible because of the absence of the visible light absorption by the photochemically formed colorless isomer. In polar environments such as in mesoporous silicas [380–383], zeolites [383–385], and LDHs [386, 387], MC form is thermally more stable than SP form. These characteristics were utilized to control negative photochromism [380, 381, 388]. Both of Py-SP and 6-NO₂-Py-SP showed negative photochromism on KF [389, 390]. It was thought that the cationic parts of pyridine and aniline moieties electrostatically interacted with negative charges on the silicate layers and the merocyanine forms were stabilized.

Nonionic spiropyran, SP and 6-NO₂-SP, and a cationic spiropyran, 6-NO₂-Py-SP, showed normal photochromism in a cetyltrimethylammonium (CTA⁺) exchanged KF [170, 391, 392]. The CTAB provided the hydrophobic environment for the spiropyran derivatives to show normal photochromism [171]. The hydrophobicity of the clays is controlled by intercalating a wide variety of surfactants.

5.2 Intermolecular Reactions

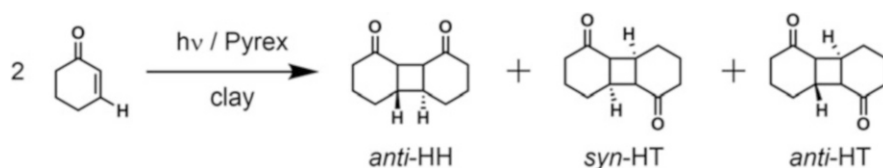
The intermolecular reactions in/on nanospaces have been used for (1) stereoselective reaction and (2) trigger of photoinduced phenomena [393]. Intermolecular distance and orientation of guests in layered materials have been utilized to control the stereoselective reactions [394, 395].

5.2.1 Diels-Alder Reaction in Clay Interlayer

Diels-Alder reaction is known as a [4 + 2] cycloaddition between a π -conjugated diene and an alkene to form a six-membered ring. A major reaction product is predicted by Woodward-Hoffman rules, while some by-products are included in the products [394, 395]. Because the kinetically stable product is the major product of Diels-Alder reaction (endo rules), high temperatures are not recommended to accelerate Diels-Alder reaction with keeping the reaction selectivity. The addition of the catalyst, which does not affect the reaction selectivity, is proposed to increase the rate constant for Diels-Alder reaction. Acceleration of the dimerization of 1,3-cyclohexadiene [396] and the cycloaddition between 2,3-dimethyl-1,3-butadiene and acrolein [397] in the presence of a montmorillonite (K10) with Fe(III) was reported. A reaction yield of the dimerization of 1,3-cyclohexadiene increased to 49% even at 0°C for 10 h by adding K10 with Fe(III) with keeping the product selectivity the same compared to a reaction yield (30%) at 200°C for 20 h without K10 [398]. The yield (80% at 20°C for 3 h in water) of the cycloaddition increased to 95% at 20°C for 0.3 h by adding the K10 with Fe(III). The reaction condition was optimized to -24°C for 4 h in dichloromethane to achieve the yield of 96% with keeping the product isomer ratio. Though the role of the clay for the improved selectivity of Diels-Alder reaction was not explained clearly [396, 397], molecular packing of guests in clays are thought to contribute [176, 193].

5.2.2 [2 + 2] Photocycloaddition

According to Woodward-Hoffman rules, a [2 + 2] cycloaddition does not progress by heat and is photochemically allowed. Some of the stereoisomers are obtained by the [2 + 2] cycloaddition due to a biradical process [399]. Packing (orientation) at the



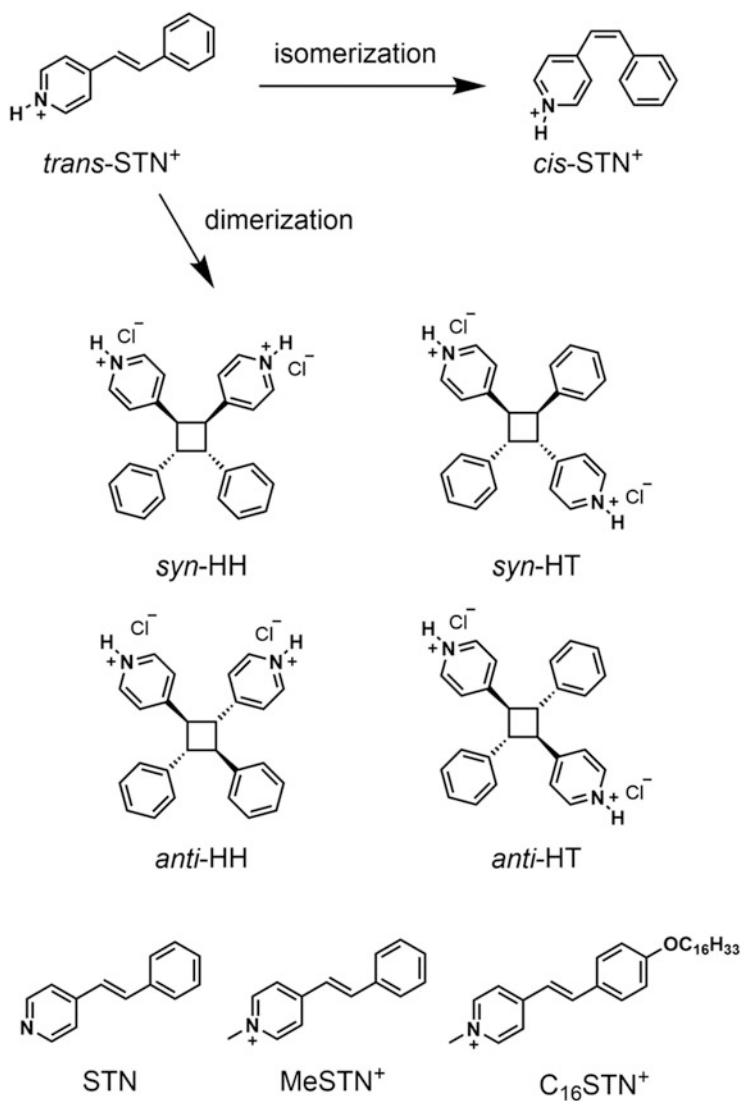
Scheme 13 Photocycloaddition of 2-cyclohexene-1-one

initial state and the molecular conformation of the intermediates affect the stereoselective [2 + 2] cycloaddition. Three products are possible by the cycloaddition of 2-cyclohexene-1-one in a solution as shown in Scheme 13. The reaction yield of photocycloaddition of 2-cyclohexene-1-one in the benzene solution under UV irradiation for 10 h (without clay) was 25%, and the ratio of the products of *anti*-HH, *syn*-HT, and *anti*-HT was 8:0.1:29 (Scheme 13) [400, 401]. By adding SA, the reaction yield remarkably increased to 72%, and the ratio of the products of *anti*-HH, *syn*-HT, and *anti*-HT was 82:0.1:5 [400, 401]. It was proposed that 2-cyclohexene-1-one aggregated in a parallel fashion, which led the effective photocycloaddition to *anti*-HT. The photoluminescence of the excimer of 2-cyclohexene-1-one was observed for the clay suspension.

Stilbene shows *cis-trans* isomerization and dimerization. Four possible photodimers of the stilbene are obtained as shown in Scheme 14. The photochemistry of stilbazolium ion (STN⁺, Scheme 14) has been investigated to find stereoselective photodimerization [214, 402–410]. A higher reaction yield of photodimerization of STN⁺ (the total yield, 98%, and the *cis*-isomer, 14%; *syn*-HT, 70%, and *syn*-HH, 5%, respectively) under UV irradiation for 30 min in an aqueous suspension of a saponite than that in a solution (the total yield, 69%, and the *cis*-isomer, 67%, *syn*-HT, 2%, and *anti*-HH, 2%, respectively) was reported [402]. Cyano- and methyl-substituted STN⁺ were used to show that the hetero dimer was a major product thanks to the formation of the exciplex between the electron-donating methyl-substituted and the electron-accepting cyano-substituted stilbenes in the interlayer space of SA [404]. Recently, three stilbazolium derivatives, STN, MeSTN⁺, and C₁₆STN⁺ (in Scheme 14), were intercalated into a *N*-(2-(2,2,3,3,4,4,4-heptafluorobutanamido)ethyl)-*N,N*-dimethylhexadecan-1-ammonium bromide exchanged SA by mixing in HCl aqueous solution to examine the selectivity of the photochemical reactions [409]. Three factors, (1) electronic interactions between the negatively charges SA surface and the stilbazolium derivatives, (2) hydrophobic interactions among the long alkyl chains of the surfactants, and (3) both hydrophobic and lipophobic interactions of the perfluoropropyl moieties of the surfactant, affected the selectivity.

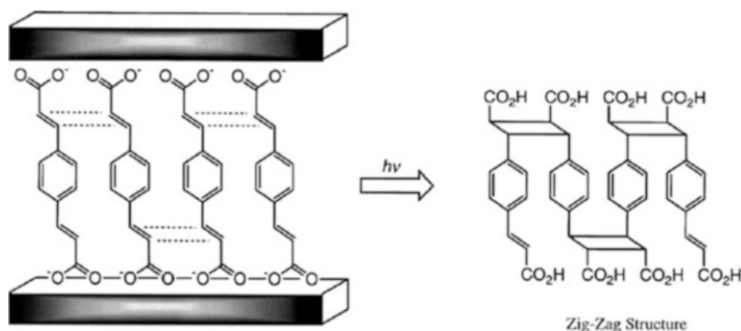
A [2 + 2] cycloaddition in the interlayer space of a hydrotalcite [411] led oligomer of phenylenediacrylate with a head-to-head structure [412]. *p*-Phenylenediacrylate was exchanged on a hydrotalcite (Alcamac Cl supplied by Kyowa Chemicals Ltd.) and was irradiated a 300 W medium pressure Hg lamp for 6 h in the aqueous suspension under stirring. The ratio of monomer, dimer, trimer, and oligomer was 0:22:31:47 after the irradiation for 6 h. In contrast, the ratio of the monomer and the dimer in an aqueous solution of *p*-phenylenediacrylate (without the hydrotalcite) was 74:26, and the trimer and the oligomer were not obtained. The polymerization degree was up to 10. The oligomer was assigned to the *syn*-head-to-head structure as shown in Scheme 15. The oligomer of *p*-phenylenediacrylate was not obtained by the irradiation to the powder.

The stereoselective cycloaddition was achieved by the molecular packing in the interlayer space of clays. Aspect ratio [413] and layer charge density [414–417] affected the yield and the selectivity. The selective cycloadditions were also reported



Scheme 14 Molecular structures of stilbene derivatives and photoreaction of *trans*-stilbene

in such nanospace materials [418] as zeolites [419, 420], mesoporous silicas [421], and a surfactant intercalated graphite oxide [422].



Scheme 15 Oligomerization of *p*-phenylenediacrylate in the interlayer space of the hydrotalcite (Reproduced from the reference [412] with permission)

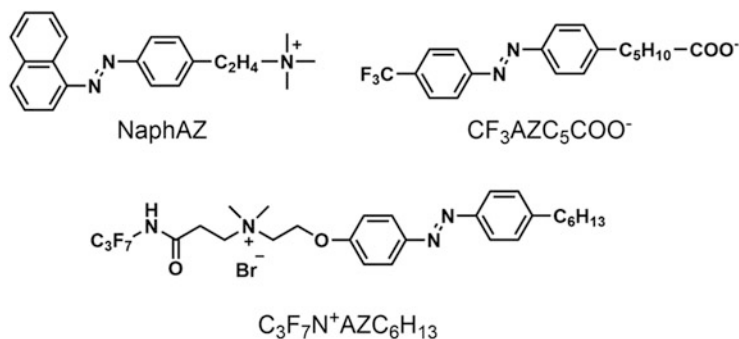
5.3 Uses of Photochemical Reactions as Trigger for Photoinduced Phenomena

5.3.1 Photoinduced Change in the Basal Spacing

The change in the basal spacing by photoirradiation is the first example of photoinduced structural change in intercalation compounds [334]. Azobenzene (AZ) shows reversible photoisomerization between a rod-like-shaped *trans*-isomer and a bending structured *cis*-isomer (Scheme 8), and a molecular size of a long axis was switched between 1.21 nm for the *trans*-isomer and 0.74 nm for the *cis*-isomer. AZ was intercalated into *n*-dodecylammonium exchanged KF by mechanical mixing without a solvent [334]. The basal spacing of the organically modified KF increased from 1.8 to 3.0 nm by the intercalation of AZ. The basal spacing of the hybrid increased from 3.0 to 3.1 nm by UV irradiation, which is the first example of photoinduced change in the basal spacing.

It was reported that the basal spacing of magadiite intercalated with $\text{AZC}_2\text{N}^+\text{C}_2\text{OH}$ (Table 3) changed from 2.69 to 2.75 nm under UV irradiation and returned to 2.69 nm by visible irradiation [165, 186], while those of KF intercalated $\text{C}_8\text{AZC}_{10}\text{N}^+$ and $\text{C}_{12}\text{AZC}_5\text{N}^+$ (Table 3) did not change by the isomerization of the cationic azobenzenes in the interlayer space [161]. Basal spacings of the montmorillonite with a cation exchange capacity of 143 meq/100 g intercalated aminoAZ and 4,4'-diaminoazobenzene were simulated [423]. The simulated basal spacings with the *trans*-isomers of aminoAZ and 4,4'-diaminoazobenzene were 2.0 and 2.1 nm, and those with the *cis*-isomers were 1.8 nm. The simulation did not match the experimental observations, suggesting that the photoswitching of the basal spacing was not explained simply by the isomerization of azobenzene.

To state the point, more recently, it was reported that the basal spacing of $\text{AZC}_2\text{N}^+\text{C}_2\text{OH}$ -magadiite under humidity of 5% was negligibly small [346], while the change between 2.69 and 2.75 nm was observed when the reaction was conducted under ambient condition [165, 186]. It suggests that the basal spacing



Scheme 16 Molecular structure of a naphthalene-substituted azobenzene and a trifluoromethyl-substituted anionic azobenzene

change was induced by the adsorption of vapors. The basal spacing of a naphthalene-substituted cationic azobenzene (NaphAZ in Scheme 16)-magadiite was observed during UV irradiation [346]. The basal spacing decreased by UV irradiation from 2.89 to 2.79 nm and did not return to the initial value, indicating that the molecular packing after the UV irradiation changed from the initial state.

The change of the basal spacing of clays was also induced by photoisomerization of a pyridine-substituted spiropyran (Py-SP in Scheme 12) [389]. Py-SP was intercalated into KF by two methods, (1) ion exchange with the interlayer sodium cation and (2) guest replacement using the ion exchange of the interlayer sodium cation with cetyltrimethylammonium bromide (CTAB) and subsequent exchange with Py-SP. The basal spacing of the hybrid prepared by the ion exchange was switched between 1.55 and 1.40 nm by 365 nm UV and 600 nm visible light irradiation, respectively. The basal spacing (1.55 nm) for the spiropyran form with a twisted molecular structure was larger than that for the merocyanine form with a planar molecular structure (1.40 nm). In contrast, the basal spacing (1.38 nm) of the hybrid prepared by the guest replacement did not change. The co-existing CTAB in KF expanded the inter-layer distance to accommodate Py-SP and Py-SP isomerized without changing the basal spacing.

The irradiation induced another change of a microscopic region. An azobenzene derivative with fluoroalkyl chain ($\text{C}_3\text{F}_7\text{N}^+\text{AZC}_6\text{H}_{13}$ in Scheme 16) was intercalated in potassium hexaniobate ($\text{K}_2\text{Nb}_6\text{O}_{17}$) [342, 424] to obtain a spiral tube structure [424]. The interlayer distance of the tube was changed by irradiation of 368 nm UV and 463 nm visible light irradiation with a simultaneous structure change of the tube [342]. The size changes of the tube from 244 to 93 nm and to 170 nm by UV and visible irradiation, respectively, were observed (Fig. 15). As shown in Fig. 16, a bottom edge of a hybrid film of $\text{C}_3\text{F}_7\text{N}^+\text{AZC}_6\text{H}_{13}$ and the niobate was slid out by UV irradiation (point A) up to 1.5 μm , and the edge returned to the initial position by the subsequent visible light irradiation (point C) [352, 425]. These reports suggest that the basal spacing change by photoisomerization of $\text{C}_3\text{F}_7\text{N}^+\text{AZC}_6\text{H}_{13}$ with a nanometer scale induced the structure change with a micrometer scale.

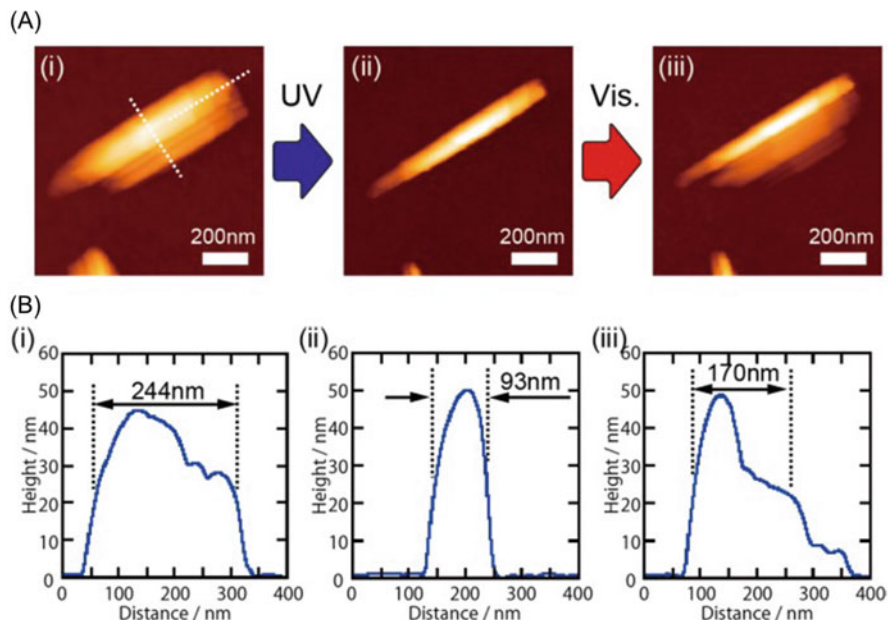


Fig. 15 Atomic force microscopic (AFM) images of morphological change of a hybrid of $C_3F_7N^+AZC_6H_{13}$ and the hexaniobate: (A) AFM top-view and (B) cross sections at the white dash lines of parallel of the short axis of the tube (Reproduced from the reference [342] with permission)

5.3.2 Photoswitching of Wettability

Photoswitching of surface properties of layered material films [426] by functionalization with photochromic compounds is expected owing to polarity change with photoisomerizations. Photoswitching of wettability of a layered double hydroxide film (ZnAl- NO_3 -LDH film) was reported by functionalization with a trifluoromethyl-substituted anionic azobenzene ($CF_3AZC_5COO^-$ in Scheme 16) [427]. The film was synthesized by putting a porous anodic alumina/aluminum (PAO/Al) substrate into the solution containing zinc nitrate and ammonium nitrate [428] and the subsequent intercalation of $CF_3AZC_5COO^-$. The morphology of the film of the LDH crystal seemed to have a curved hexagonal sheet structure (Fig. 17a). A water contact angle of the film was $151 \pm 1^\circ$, while the contact angle decreased to $73 \pm 1^\circ$ by 365 nm UV irradiation (Fig. 17b, c). The contact angle was returned to the initial value by subsequent visible light (420 nm) irradiation. The *cis*-isomer of azobenzene has larger polarity owing to the bending structure, indicating that the surface of the film with the *cis*-isomer had higher polarity than that with the *trans*-isomer. An advantage of this system is thought to be an easy preparation method of ion exchange method [35, 36, 283], which is expected to make a film with a large area compared to other films that showed photoswitching of wettability [429, 430].

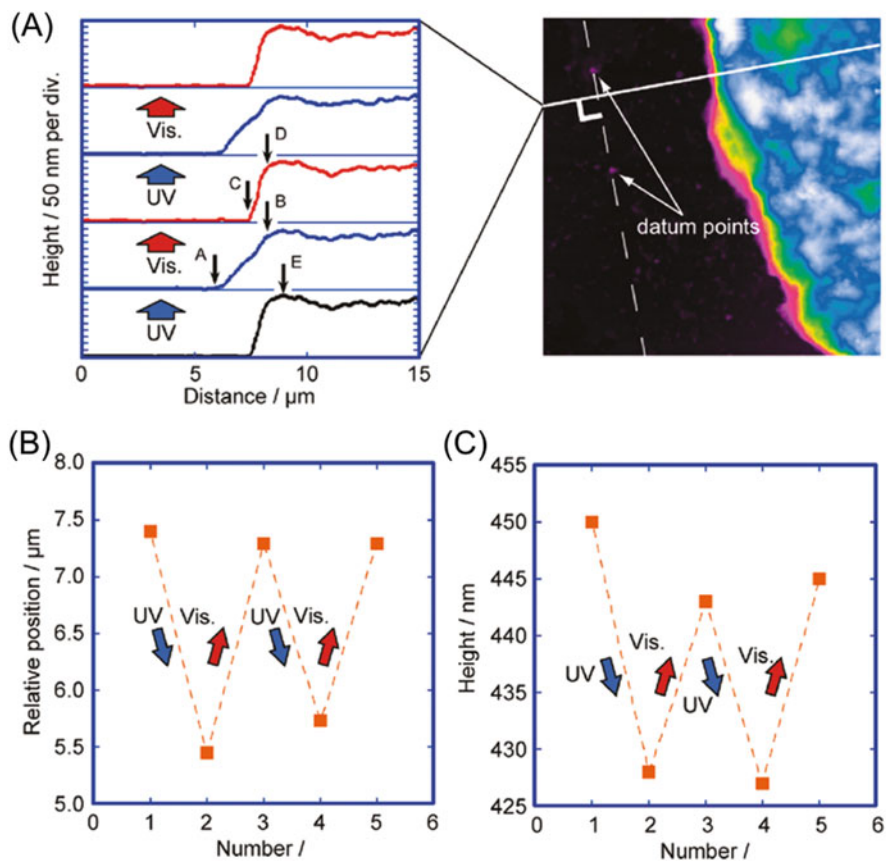


Fig. 16 3D morphology changes in the hybrid film. (a) Height profile of the hybrid film. (b) Relative distance from the reference point to the film edge vs the number of irradiation cycles. (c) Film thickness at a point E located a constant distance from the reference point vs the number of irradiation cycles (Reproduced from the reference [425] with permission)

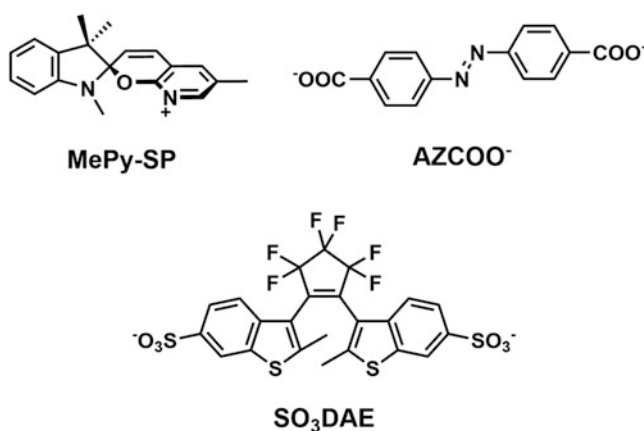


Fig. 17 SEM images of the top and cross section views of the hybrid of $\text{CF}_3\text{AZC}_5\text{COO}^-$ intercalated ZnAl-LDH (a) and shapes of a water droplet on the hybrid film surface (b) before the UV irradiation and (c) after the UV irradiation (Reproduced from the reference [427] with permission)

5.3.3 Photoswitching of Magnetism

Photoswitching of magnetism of layered double hydroxides (LDHs) was reported by intercalation of photochromic compounds of spiropyrans [431–435], azobenzenes [436, 437], and diarylethenes [438–440]. Two main contributions of intralayer superexchange interactions between metal cations and interlayer dipole interactions between the LDH layers were claimed to control the magnetism of the LDHs [441]. Because the photochromic compounds change shapes, sizes, and polarities by irradiation, the photochromic compounds affected the magnetism of the LDHs-dye hybrids.

Magnetism of layered $(\text{C}_3\text{H}_7)_4\text{N}[\text{Fe}^{\text{II}}\text{Fe}^{\text{III}}(\text{C}_2\text{O}_2\text{S}_2)_3]$ was explained by charge transfer at 120 and 6.5 K between Fe^{II} and Fe^{III} [432, 442, 443]. The phase transition at 120 K was attributed to the charge transfer between Fe^{II} (spin angular momentum $S = 1/2$) and Fe^{III} ($S = 2$) (the authors named high-temperature phase) to form the state with Fe^{III} ($S = 5/2$) and Fe^{II} ($S = 0$) (low-temperature phase). The layered $(\text{C}_3\text{H}_7)_4\text{N}[\text{Fe}^{\text{II}}\text{Fe}^{\text{III}}(\text{C}_2\text{O}_2\text{S}_2)_3]$ showed ferromagnetism below 6.5 K due to the charge transfer between the Fe^{III} ($S = 5/2$) and the Fe^{II} ($S = 0$). A hybrid of $[\text{Fe}^{\text{II}}\text{Fe}^{\text{III}}(\text{C}_2\text{O}_2\text{S}_2)_3]$ with MePy-SP (Scheme 17) [431, 433, 434] showed the charge transfer phase transition from the high-temperature phase to the low-temperature phase at 75 K and the ferromagnetic phase transition at 5 K [434]. Upon UV irradiation (365 nm), the intercalated MePy-SP isomerized to a merocyanine form (MePy-MC), and the isomerization induced the charge transfer between Fe^{II} and Fe^{III} . As a result, the charge transfer phase transition from the high-temperature phase to the low-temperature phase was not observed, and the ferromagnetic phase transition was observed at 22 K. Taking into account that an alkylammonium surfactant with a long alkyl chain stabilized the high-temperature phase and



Scheme 17 Anionic photochromic compound intercalated into LDHs for photoswitching of magnetism

increased the ferromagnetic phase transition temperature T_C , [431] the longer molecular length of MePy-MC than that of MePy-SP increased T_C .

The magnetism of LDHs depended on the dipole interactions between the LDH layers which are smaller with longer interlayer distance [441]. A CoAl-LDH ($\text{Co}_{0.69}\text{Al}_{0.31}(\text{OH})_2(\text{CO}_3)_{0.155}(\text{H}_2\text{O})_{0.3}$) had spontaneous magnetization below the critical temperature T_M at 4.7 K [444]. T_M of a CoAl-LDH ($\text{Co}_{0.65}\text{Al}_{0.35}(\text{OH})_2$) was switched by the *cis-trans* photoisomerization of the intercalated dicarboxylazobenzene (designated as AZCOO^-) [436]. T_M of the CoAl-LDH hybrid (4.5 K) increased to 5.2 K by 355 nm UV irradiation accompanied by the basal spacing change from 20.29 to 20.18 nm, suggesting that the change in the nanostructure was the reason of the increase of T_M . The basal spacing did not revert to the initial value by visible light irradiation in acetonitrile, while it reverted by exposure of water under the visible light irradiation. As discussed in Sect. 5.3.1, vapor played an important role in the change in the basal spacing [346]. It is thought that the adsorption of the water molecules triggered the backward reaction to the initial molecular packing.

Magnetism of alkylcarboxylate intercalated layered Co and Cu hydroxides ($\text{Co}_7(\text{OH})_{11.6}$ and $\text{Cu}_2(\text{OH})_2$) depended on the length and π -conjugate system of the alkylcarboxylate surfactants due to the interlayer ferromagnetic interaction [445]. The photocyclization of diarylethene, which accompanies the switching of the π -conjugate system, affected the magnetic interactions of two nitronyl nitroxide moieties substituted to the phenylthiophene moieties of the diarylethene [446, 447]. T_C of a hybrid of a layered $\text{Co}_4(\text{OH})_7$ (designated as Co-LDH) intercalated an open-ring isomer of SO_3DAE in Scheme 17 was 9 K, while that after UV irradiation increased to 20 K [439]. Although the mechanism was not reported in detail [438, 440], the photoswitch of the π -conjugate system of the intercalated SO_3DAE seemed to affect the magnetism of Co-LDH [446, 447].

The photoswitching of the π -conjugate system by the photocyclization and the photoswitching of the basal spacing caused by photochromism affected to the magnetism of the LDHs. As discussed in Sects. 5.2.2 and 5.3.1, the design of the hybrids and the photoinduced adsorption of vapor are expected to make these phenomena effective, suggesting that the elucidation and improvement of the photoinduced phenomena of the hybrids induce the effective magnetism switching.

5.3.4 Photoinduced Adsorption

As discussed in Sect. 5.3.1, adsorption of vapor during the photochromic changes induced the change in the basal spacing [346]. Adsorption of phenol onto organically modified clay from an aqueous solution was also reported [101, 282, 448, 449]. Motivated by the phenomena, photoinduced adsorption of phenol was examined [166, 167, 344]. $\text{AZC}_2\text{N}^+\text{C}_2\text{OH}$ and $\text{C}_2\text{AZC}_2\text{N}^+$ (Table 3) intercalated KF were mixed with neat phenol. As shown in Fig. 18, gallery heights increased from 0.81 to 1.5 nm and 0.96 to 2.6 nm by mixing with phenol, respectively [344]. The gallery heights of the hybrids $\text{AZC}_2\text{N}^+\text{C}_2\text{OH-KF}$ with phenol increased further from 1.5 to

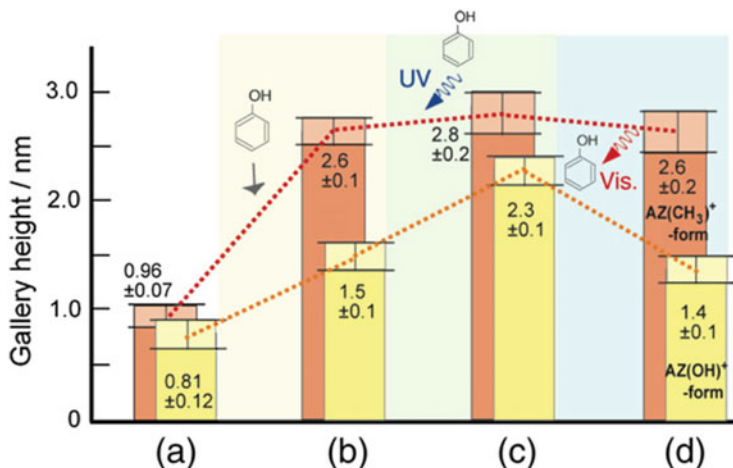


Fig. 18 The changes in the basal spacings of KF intercalated $AZC_2N^+C_2OH$ and $C_2AZC_2N^+$; (a) before the intercalation of phenol, (b) after phenol intercalation, (c) after UV irradiation, and (d) after subsequent visible light irradiation (Reproduced from the reference [344] with permission)

Table 4 Photoinduced expansion of basal spacings of azobenzene exchanged clays

Adsorbent	CEC/ meq/ 100 g	Adsorbed amount of $AZC_2N^+C_2OH$ / meq/100 g	Before intercalation of phenol	$d_{(001)}/nm$ before UV irradiation	After UV irradiation	After visible light irradiation
KF	108	105	1.76	2.56	3.16	2.56
		91	1.63	2.56, 1.54	3.40, 2.56, 1.54	2.56, 1.54
		66	1.54	1.54	1.54	1.54
TSM	84	52	1.89	2.45	3.45, 2.45	2.45
SA	71	76	1.53	1.57	1.57	1.57

2.3 nm by UV irradiation. The large change of the gallery heights (0.8 nm) indicated that the phenol was intercalated into the hybrid by the UV irradiation. On the other hand, the gallery height of $C_2AZC_2N^+-KF$ increased from 2.6 to 2.8 nm by the UV irradiation in the presence of phenol. Because the polarity of $C_2AZC_2N^+$ was thought to be smaller than that of $AZC_2N^+C_2OH$ from a comparison of dipole moments of *cis*-AZ (0.41 Debye) and 4-ethylazobenzene (0.34 Debye), the adsorbed amount of phenol in $C_2AZC_2N^+-KF$ intercalated with phenol was thought to be smaller than that of $AZC_2N^+C_2OH-KF$. The basal spacing changes of $AZC_2N^+C_2OH-KF$ with the adsorbed amount of 105, 91, and 66 meq/100 g were determined as summarized in Table 4 [167]. Observation of several basal spacing with 91 meq/100 g suggested the inhomogeneous adsorption of phenol. The changes in the basal spacings of $AZC_2N^+C_2OH$ -smectites with varied CEC were also

examined to find $C_2AZC_2N^+$ -clay (with CEC of 108 and 84 meq/100 g) increased by the UV irradiation, while that with 71 meq/100 g did not change. Changes of the basal spacings of KF, TSM, and SA intercalated $AZC_2N^+C_2OH$ in the presence of phenol by the UV irradiation are summarized in Table 4 [167]. The fraction of the *cis*-isomer of $AZC_2N^+C_2OH$ in TSM was estimated to be ca. 50%, and it was larger than that in KF (ca. 30%).

To enhance the structural change by the photoinduced adsorption, the following parameters were proposed: (1) fraction of *cis*-isomer at the photostationary state [167, 344], (2) amount [344], and (3) orientation [167] of azobenzene derivative (corresponding to the surface coverage).

The photoinduced adsorption of photochromic compounds was also reported recently [374, 382, 450, 451]. As discussed in Sect. 5.1.3, photochromism of spiroopyran was affected by the presence of nanospace materials including mesoporous silicas and smectites. Color of 6-NO₂-MC (Scheme 12) photochemically formed from 6-NO₂-SP was blue in toluene under UV irradiation, while the color of it was red in the presence of HE [374]. Red-colored sediment was collected by storing the suspension in the dark so that the adsorbed amount of MC onto HE was followed, showing that the 6-NO₂-SP was adsorbed on HE with the first-order kinetics [374]. The adsorbed amount of 6-NO₂-MC was 2.8 mg/100 g. The photoinduced adsorption is thought as molecular migration between hydrophobic and hydrophilic phases by using the bistability of the photochromic compound.

Mesoporous silicas were used as adsorbent of photo 6-NO₂-MC, which is named as “photoinduced adsorption” [382, 450, 452]. Photoinduced migration of SA/MC between the mesoporous silicas and the organophilic clay [381, 382] was reported to lead the reversibility of the negative photochromisms. The organically modified clay was thought to host less polar 6-NO₂-SP, which formed by the negative photochromisms of 6-NO₂-MC accommodated in the mesoporous silica. The thermal coloration of 6-NO₂-SP to 6-NO₂-MC accelerated by using the mesoporous silicas with larger pore size [382] and that whose external surface was functionalized with phenyl groups [451], suggesting that the diffusion inside the pore is important and the intraparticle diffusion was more efficient than the interparticle diffusion.

6 Conclusions and Future Perspectives

Recent developments on the preparation and the photofunctions of dye-clay hybrids are reviewed. Photofunctions have been systematically controlled and discussed based on the variation of hosts, guests, and their compositions. These developments led to further understanding of the structure and composition-property relationships, which may provide advance knowledge to optimize materials' performances. Not only the nanostructure design by using host-guest interfaces has been revised, but the search for raw materials and their synthesis of new host materials have been also done. Successful morphosyntheses of known materials to obtain well-defined particles and single crystals with narrow particle size distribution expanded the

possibilities of the materials and made detailed characterization possible. Taking the advantages of the morphosyntheses, interfacial design and the developments of fabrication techniques, some dye-clay systems have been prepared as thin films. The application covers traditional pigments application to agriculture (on soil contamination), optical devices including light-emitting ones, sensors, photocatalysts, etc. Though the practical application is not seen, various unique photoinduced phenomena have been also ascribed.

Acknowledgments This work was supported by the Research Chair Grant 2017 (grant number FDA-CO-2560-5655) from the National Science and Technology Development Agency (NSTDA), Thailand.

References

1. Matsuura T, Anpo M (eds) (1989) *Photochemistry on solid surfaces*. Elsevier Science, Amsterdam
2. Anpo M (ed) (1996) *Surface photochemistry*. Wiley, Chichester
3. Klafter J, Drake J (eds) (1989) *Molecular dynamics in restricted geometries*. Wiley Interscience, New York
4. Ramamurthy V (ed) (1991) *Photochemistry in organized and constrained media*. VCH Publishers, New York
5. Ramamurthy V, Schanze KS (eds) (2000) *Solid state and surface photochemistry*. Marcel Dekker, New York
6. Fendler JH (ed) (1994) *Membrane-mimetic approach to advanced materials*. Springer-Verlag, Berlin
7. Yamaguchi T, Ogawa M (2019) Photochromic reactions in nanospace; host-guest interactions and opportunity. In: Douhal A, Anpo M (eds) *Chemistry of silica and zeolite-based materials Synthesis, characterization and applications*. Elsevier, Amsterdam, pp 163–177
8. Sohmiya M, Saito K, Ogawa M (2015) Host-guest chemistry of Mesoporous Silicas: precise Design of Location, density and orientation of molecular guests in Mesopores. *Sci Technol Adv Mater* 16:54201. <https://doi.org/10.1088/1468-6996/16/5/054201>
9. Ogawa M, Kuroda K (1995) Photofunctions of intercalation compounds. *Chem Rev* 95:399–438
10. Ogawa M, Saito K, Sohmiya M (2015) Possible roles of the spatial distribution of organic guest species in mesoporous silicas to control the properties of the hybrids. *Eur J Inorg Chem*:1126–1136. <https://doi.org/10.1002/ejic.201402651>
11. Ogawa M (2002) Photoprocesses in mesoporous silicas prepared by a supramolecular templating approach. *J Photochem Photobiol C: Photochem Rev* 3:129–146. [https://doi.org/10.1016/S1389-5567\(02\)00023-0](https://doi.org/10.1016/S1389-5567(02)00023-0)
12. Alberti G, Bein T (eds) (1996) *Solid-state supramolecular chemistry: two- and three-dimensional inorganic networks*. Pergamon, Oxford
13. Thomas JK (1987) Characterization of surfaces by excited states. *J Phys Chem* 91:267–276. <https://doi.org/10.1021/j100286a008>
14. Thomas JK (1993) Physical aspects of photochemistry and radiation chemistry of molecules adsorbed on silica, gamma-alumina, zeolites, and clays. *Chem Rev* 93:301–320. <https://doi.org/10.1021/cr00017a014>
15. Turro NJ, Grätzel M, Braun AM (1980) Photophysical and photochemical processes in micellar systems. *Angew Chem Int Ed* 19:675–696. <https://doi.org/10.1002/anie.198006751>

16. Thomas JK (1988) Photophysical and photochemical processes on clay surfaces. *Acc Chem Res* 21:275–280. <https://doi.org/10.1021/ar00151a004>
17. Fujimura T, Shimada T, Hamatani S, Onodera S, Sasai R, Inoue H, Takagi S (2013) High density intercalation of porphyrin into transparent clay membrane without aggregation. *Langmuir* 29:5060–5065. <https://doi.org/10.1021/la4003737>
18. Konno S, Fujimura T, Otani Y, Shimada T, Inoue H, Takagi S (2014) Microstructures of the porphyrin/viologen monolayer on the clay surface: segregation or integration? *J Phys Chem C* 118:20504–20510. <https://doi.org/10.1021/jp5076274>
19. Nakayama A, Mizuno J, Ohtani Y, Shimada T, Takagi S (2018) Elucidation of the adsorption distribution of cationic porphyrin on the inorganic surface by energy transfer as a molecular ruler. *J Phys Chem C* 122:4365–4371. <https://doi.org/10.1021/acs.jpcc.7b12104>
20. Sohmiya M, Nakamura T, Sugahara Y, Ogawa M (2018) Distribution control-oriented intercalation of a cationic metal complex into layered silicates modified with organosulfonic-acid moieties. *Langmuir* 34:4762–4773. <https://doi.org/10.1021/acs.langmuir.8b00547>
21. Eguchi M, Takagi S, Inoue H (2006) The orientation control of dicationic porphyrins on clay surfaces by solvent polarity. *Chem Lett* 35:14–15. <https://doi.org/10.1246/cl.2006.14>
22. Sasai R, Shichi T, Gekko K, Takagi K (2000) Continuously changing the conformational dependence of saponite hybrid materials on the intercalation degree: electric linear dichroism of stilbazolium derivatives intercalated in saponite clay. *Bull Chem Soc Jpn* 73:1925–1931. <https://doi.org/10.1246/bcsj.73.1925>
23. Neumann MG, Gessner F, Schmitt CC, Sartori R (2002) Influence of the layer charge and clay particle size on the interactions between the cationic dye methylene blue and clays in an aqueous suspension. *J Colloid Interface Sci* 255:254–259. <https://doi.org/10.1006/jcis.2002.8654>
24. Okada T, Ide Y, Ogawa M (2012) Organic-inorganic hybrids based on ultrathin oxide layers: designed nanostructures for molecular recognition. *Chem Asian J* 7:1980–1992. <https://doi.org/10.1002/asia.201101015>
25. Okada T, Seki Y, Ogawa M (2014) Designed nanostructures of clay for controlled adsorption of organic compounds. *J Nanosci Nanotechnol* 14:2121–2134. <https://doi.org/10.1166/jnn.2014.8597>
26. Ruiz-Hitzky E, Aranda P, Akkari M, Khaorapapong N, Ogawa M (2019) Photoactive nanoarchitectures based on clays incorporating TiO₂ and ZnO nanoparticles. *Beilstein J Nanotechnol* 10:1140–1156. <https://doi.org/10.3762/bjnano.10.114>
27. Deepracha S, Vibulyaseak K, Ogawa M (2019) Complexation of TiO₂ with clays and clay minerals for hierarchically designed functional hybrids. In: *Advanced supramolecular nanoarchitectonics*. Elsevier, Amsterdam, pp 125–150
28. Intasard SG, Ogawa M (2018) Layered silicates as a possible drug carrier. In: Tamanoi F (ed) *Mesoporous silica-based Nanomaterials and biomedical applications, part B*. Elsevier, Amsterdam, pp 117–136
29. Ogawa M (1998) Organized molecular assemblies on the surfaces of inorganic solids-photofunctional inorganic-organic supramolecular systems. *Annu Rep Prog Chem Sect C Phys Chem* 94:209. <https://doi.org/10.1039/pc094209>
30. Lagaly G, Ogawa M, Dékány I (2006) Chapter 7.3 clay mineral organic interactions. *Dev Clay Sci* 1:309–377
31. Shichi T, Takagi K (2000) Clay minerals as photochemical reaction fields. *J Photochem Photobiol C: Photochem Rev* 1:113–130. [https://doi.org/10.1016/S1389-5567\(00\)00008-3](https://doi.org/10.1016/S1389-5567(00)00008-3)
32. Granquist WT, Pollack SS (1960) *A study of the synthesis of hectorite*. Pergamon Press, Oxford
33. Ogawa M, Wada T, Kuroda K (1995) Intercalation of pyrene into alkylammonium-exchanged swelling layered silicates: the effects of the arrangements of the interlayer alkylammonium ions on the states of adsorbates. *Langmuir* 11:4598–4600. <https://doi.org/10.1021/la00011a068>

34. Klopogge JT, Komarneni S, Amonette JE (1999) Synthesis of smectite clay minerals: a critical review. *Clay Clay Miner* 47:529–554. <https://doi.org/10.1346/CCMN.1999.0470501>
35. Ogawa M, Handa T, Kuroda K, Kato C (1990) Formation of organoammonium-montmorillonites by solid-solid reaction. *Chem Lett* 19:71–74
36. Intasard SG, Imwiset K, Bureekaew S, Ogawa M (2018) Mechanochemical methods for the preparation of intercalation compounds, from intercalation to the formation of layered double hydroxides. *Dalton Trans* 47:2896–2916. <https://doi.org/10.1039/C7DT03736H>
37. Nakamura T, Ogawa M (2013) Adsorption of cationic dyes within spherical particles of poly (*N*-isopropylacrylamide) hydrogel containing Smectite. *Appl Clay Sci* 83–84:469–473. <https://doi.org/10.1016/j.clay.2013.05.005>
38. Yariv S, Ghosh DK, Hepler LG (1991) Metachromasy in clay-mineral systems: adsorption of cationic dyes crystal violet and ethyl violet by kaolinite from aqueous and organic solutions. *J Chem Soc Faraday Trans* 87:1201–1207. <https://doi.org/10.1039/FT9918701201>
39. Yariv S, Nasser A, Bar-on P (1990) Metachromasy in clay minerals. Spectroscopic study of the adsorption of crystal violet by laponite. *J Chem Soc Faraday Trans* 86(1593). <https://doi.org/10.1039/ft9908601593>
40. Bergmann K, O’Konski CT (1963) A spectroscopic study of methylene blue monomer, dimer, and complexes with Montmorillonite. *J Phys Chem* 67:2169–2177. <https://doi.org/10.1021/j100804a048>
41. Yariv S, Lurie D (1971) Metachromasy in clay minerals. Part I. Sorption of methylene-blue by montmorillonite. *Isr J Chem* 9:537–552. <https://doi.org/10.1002/ijch.197100070>
42. Samuels M, Mor O, Rytwo G (2013) Metachromasy as an indicator of photostabilization of methylene blue adsorbed to clays and minerals. *J Photochem Photobiol B Biol* 121:23–26. <https://doi.org/10.1016/j.jphotobiol.2013.02.004>
43. Hang PT (1970) Methylene blue absorption by clay minerals. Determination of surface areas and cation exchange capacities (clay-organic studies XVIII). *Clays Clay Miner* 18:203–212. <https://doi.org/10.1346/CCMN.1970.0180404>
44. Brindley GW, Thompson TD (1970) Methylene blue absorption by montmorillonites. Determinations of surface areas and exchange capacities with different initial cation saturations (clay-organic studies XIX). *Isr J Chem* 8:409–415. <https://doi.org/10.1002/ijch.197000047>
45. Hepler LG, Yariv S, Dobrogowska C (1987) Calorimetric investigation of adsorption of an aqueous metachromic dye (crystal-violet) on montmorillonite. *Thermochim Acta* 121:373–379. [https://doi.org/10.1016/0040-6031\(87\)80187-9](https://doi.org/10.1016/0040-6031(87)80187-9)
46. Schramm LL, Yariv S, Ghosh DK, Hepler LG (1997) Electrokinetic study of the adsorption of ethyl violet and crystal violet by montmorillonite clay particles. *Can J Chem* 75:1868–1877. <https://doi.org/10.1139/v97-620>
47. Lapedes I, Yariv S, Golodnitsky D (2002) Simultaneous DTA-TG study of montmorillonite mechanochemically treated with crystal-violet. *J Therm Anal Calorim* 67:99–112. <https://doi.org/10.1023/A:1013737914178>
48. Grauer Z, Malter AB, Yariv S, Avnir D (1987) Sorption of rhodamine B by montmorillonite and laponite. *Colloids Surf* 25:41–65. [https://doi.org/10.1016/0166-6622\(87\)80268-8](https://doi.org/10.1016/0166-6622(87)80268-8)
49. Grauer Z, Grauer GL, Avnir D, Yariv S (1987) Metachromasy in clay minerals. Sorption of pyronin Y by montmorillonite and laponite. *J Chem Soc Faraday Trans* 1 83:1685. <https://doi.org/10.1039/f19878301685>
50. Bose IS, Sunwar CB, Chakravarti SK (1987) Metachromasy of thiazine dyes when sorbed onto clay minerals (Montmorillonite). *Indian J Chem* 26:944–946
51. Sunwar CB, Bose H (1990) Effect of clay minerals on the visible spectra of thiazine dyes. *J Colloid Interface Sci* 136:54–60. [https://doi.org/10.1016/0021-9797\(90\)90077-2](https://doi.org/10.1016/0021-9797(90)90077-2)
52. Breen C, Rock B (1994) The competitive adsorption of methylene blue on to montmorillonite from binary solution with thioflavin T, proflavine and acridine yellow, steady-state and dynamic studies. *Clay Miner* 29:179–189. <https://doi.org/10.1180/claymin.1994.029.2.04>
53. Figueras F (1988) Pillared clays as catalysts. *Catal Rev* 30:457–499. <https://doi.org/10.1080/01614948808080811>

54. Gil A, Korili SA, Trujillano R, Vicente MA (eds) (2010) Pillared clays and related catalysts. Springer, New York
55. Ogawa M, Takahashi M, Kato C, Kuroda K (1994) Oriented microporous film of tetramethylammonium pillared saponite. *J Mater Chem* 4:519–523. <https://doi.org/10.1039/jm9940400519>
56. Ogawa M, Kuroda K (1997) Preparation of inorganic-organic nanocomposites through intercalation of organoammonium ions into layered silicates. *Bull Chem Soc Jpn* 70:2593–2618
57. Imwiset KJ, Hayakawa T, Fukushima Y, Yamada T, Ogawa M (2019) Novel flexible supramolecular assembly of dioleilydimethylammonium ion in a two-dimensional nanospace studied by neutron scattering. *Langmuir* 35:13977–13982. <https://doi.org/10.1021/acs.langmuir.9b02504>
58. Ogawa M (1997) Preparation of layered silica–dialkyldimethylammonium bromide nanocomposites. *Langmuir* 13:1853–1855. <https://doi.org/10.1021/la9608775>
59. Lagaly G (1986) Interaction of alkylamines with different types of layered compounds. *Solid State Ionics* 22:43–51. [https://doi.org/10.1016/0167-2738\(86\)90057-3](https://doi.org/10.1016/0167-2738(86)90057-3)
60. Kanoh T, Shichi T, Takagi K (1999) Mono- and bilayer equilibria of stearate self-assembly formed in hydrotalcite interlayers by changing the intercalation temperature. *Chem Lett* 28:117–118. <https://doi.org/10.1246/cl.1999.117>
61. Burgentzlé D, Duchet J, Gérard JF, Jupin A, Fillon B (2004) Solvent-based nanocomposite coatings: I. Dispersion of organophilic montmorillonite in organic solvents. *J Colloid Interface Sci* 278:26–39. <https://doi.org/10.1016/j.jcis.2004.05.015>
62. Ogawa M (1996) Preparation of a cationic azobenzene derivative-montmorillonite intercalation compound and the photochemical behavior. *Chem Mater* 8:15–17. <https://doi.org/10.1021/cm950602v>
63. Valandro SR, Poli AL, Neumann MG, Schmitt CC (2015) Photophysics of auramine O adsorbed on solid clays. *J Lumin* 161:209–213. <https://doi.org/10.1016/j.jlumin.2015.01.023>
64. Takahashi N, Kuroda K (2011) Materials design of layered silicates through covalent modification of interlayer surfaces. *J Mater Chem* 21:14336–14353. <https://doi.org/10.1039/c1jm10460h>
65. Wijitwongwan RP, Intasard SG, Ogawa M (2019) Preparation of layered double hydroxides toward precisely designed hierarchical organization. *ChemEngineering* 3:68. <https://doi.org/10.3390/chemengineering3030068>
66. Taviot-Guého C, Prévot V, Forano C, Renaudin G, Mousty C, Leroux F (2018) Tailoring hybrid layered double hydroxides for the development of innovative applications. *Adv Funct Mater* 28:1–33. <https://doi.org/10.1002/adfm.201703868>
67. Intasard S, Bureekaew S, Ogawa M (2019) Efficient production of MgAl layered double hydroxide nanoparticle. *J Ceram Soc Jpn*:11–17. <https://doi.org/10.2109/jcersj2.18140>
68. Park DH, Hwang SJ, Oh JM, Yang JH, Choy JH (2013) Polymer-inorganic supramolecular nano-hybrids for red, white, green, and blue applications. *Prog Polym Sci* 38:1442–1486. <https://doi.org/10.1016/j.progpolymsci.2013.05.007>
69. Li W, Yan D, Gao R, Lu J, Wei M, Duan X (2013) Recent advances in stimuli-responsive photofunctional materials based on accommodation of chromophore into layered double hydroxide nanogallery. *J Nanomater* 2013. <https://doi.org/10.1155/2013/586462>
70. Akkari M, Aranda P, Ben Rhaïem H, Ben Haj Amara A, Ruiz-Hitzky E (2016) ZnO/clay Nanoarchitectures: synthesis, characterization and evaluation as photocatalysts. *Appl Clay Sci* 131:131–139. <https://doi.org/10.1016/j.clay.2015.12.013>
71. Aranda P, Kun R, Martín-Luengo MA, Letaïef S, Dékány I, Ruiz-Hitzky E (2008) Titania-sepiolite nanocomposites prepared by a surfactant templating colloidal route. *Chem Mater* 20:84–91. <https://doi.org/10.1021/cm702251f>
72. Hayakawa T, Minase M, Fujita K, Ogawa M (2016) Green synthesis of Organophilic clays; solid-state reaction of acidic clay with organoamine. *Ind Eng Chem Res* 55:6325–6330. <https://doi.org/10.1021/acs.iecr.5b03344>

73. Ide Y, Matsuoka M, Ogawa M (2012) Controlled photocatalytic oxidation of benzene in aqueous clay suspension. *ChemCatChem* 4:628–630. <https://doi.org/10.1002/cctc.201200043>
74. Hayakawa T, Oya M, Minase M, Fujita K, Teepakakorn AP, Ogawa M (2019) Preparation of sodium-type bentonite with useful swelling property by a mechanochemical reaction from a weathered bentonite. *Appl Clay Sci* 175:124–129. <https://doi.org/10.1016/j.clay.2019.04.009>
75. Ogawa M, Kanaoka N, Kuroda K (1998) Preparation of smectite/dodecyltrimethylamine *N*-oxide intercalation compounds. *Langmuir* 14:6969–6973. <https://doi.org/10.1021/la980173q>
76. Minase M, Hayakawa T, Oya M, Fujita K, Ogawa M (2019) Improved rheological properties of organophilic-clay suspensions by a simple pretreatment with a wet type jet mill. *Bull Chem Soc Jpn* 92:1329–1334. <https://doi.org/10.1246/bcsj.20190051>
77. Tetsuka H, Ebina T, Tsunoda T, Nanjo H, Mizukami F (2007) Flexible organic electroluminescent devices based on transparent clay films. *Nanotechnology* 18:355701. <https://doi.org/10.1088/0957-4484/18/35/355701>
78. Deepracha S, Bureekaew S, Ogawa M (2019) Synergy effects of the complexation of a titania and a smectite on the film formation and its photocatalyst' performance. *Appl Clay Sci* 169:129–134. <https://doi.org/10.1016/j.clay.2018.12.005>
79. Isayama M, Sakata K, Kunitake T (1993) Preparation of a self-supporting, multilayered film of montmorillonite. *Chem Lett* 22:1283–1286. <https://doi.org/10.1246/cl.1993.1283>
80. Hotta Y, Taniguchi M, Inukai K, Yamagishi A (1997) Clay-modified electrodes prepared by the Langmuir-Blodgett method. *Clay Miner* 32:79–88. <https://doi.org/10.1180/claymin.1997.032.1.09>
81. Suzuki Y, Tenma Y, Nishioka Y, Kawamata J (2012) Efficient nonlinear optical properties of dyes confined in interlayer nanospaces of clay minerals. *Chem Asian J* 7:1170–1179. <https://doi.org/10.1002/asia.201200049>
82. Kleinfeld ER, Ferguson GS (1994) Stepwise formation of multilayered nanostructural films from macromolecular precursors. *Science* 265:370–373. <https://doi.org/10.1126/science.265.5170.370>
83. Kleinfeld ER, Ferguson GS (1996) Healing of defects in the stepwise formation of polymer/silicate multilayer films. *Chem Mater* 8:1575–1578. <https://doi.org/10.1021/cm960073a>
84. Lvov Y, Ariga K, Ichinose I, Kunitake T (1996) Formation of ultrathin multilayer and hydrated gel from montmorillonite and linear polycations. *Langmuir* 12:3038–3044. <https://doi.org/10.1021/la951002d>
85. Lotsch BV, Ozin GA (2008) Clay Bragg stack optical sensors. *Adv Mater* 20:4079–4084. <https://doi.org/10.1002/adma.200800914>
86. Ariga K, Ji Q, McShane MJ, Lvov YM, Vinu A, Hill JP (2012) Inorganic nanoarchitectonics for biological applications. *Chem Mater* 24:728–737. <https://doi.org/10.1021/cm202281m>
87. Nakamura T, Ogawa M (2012) Attachment of the sulfonic acid group in the interlayer space of a layered alkali silicate, octosilicate. *Langmuir* 28:7505–7511. <https://doi.org/10.1021/la300390s>
88. Leodopoulos C, Doulia D, Gimouhopoulos K (2014) Adsorption of cationic dyes onto Bentonite. *Sep Purif Rev* 44:74–107. <https://doi.org/10.1080/15422119.2013.823622>
89. Kukkadapu RK, Boyd SA (1995) Tetramethylphosphonium- and tetramethylammonium-smectites as adsorbents of aromatic and chlorinated hydrocarbons: effect of water on adsorption efficiency. *Clay Clay Miner* 43:318–323. <https://doi.org/10.1346/CCMN.1995.0430306>
90. Lawrence MAM, Kukkadapu RK, Boyd SA (1998) Adsorption of phenol and chlorinated phenols from aqueous solution by tetramethylammonium- and tetramethylphosphonium-exchanged montmorillonite. *Appl Clay Sci* 13:13–20. [https://doi.org/10.1016/S0169-1317\(98\)00009-X](https://doi.org/10.1016/S0169-1317(98)00009-X)
91. Deng Y, Dixon JB, White GN (2006) Bonding mechanisms and conformation of poly(ethylene oxide)-based surfactants in interlayer of smectite. *Colloid Polym Sci* 284:347–356. <https://doi.org/10.1007/s00396-005-1388-0>
92. Guégan R (2010) Intercalation of a nonionic surfactant (C₁₀E₃) bilayer into a Na-montmorillonite clay. *Langmuir* 26:19175–19180. <https://doi.org/10.1021/la1039267>

93. Guégan R, Veron E, Le Forestier L, Ogawa M, Cadars S (2017) Structure and dynamics of nonionic surfactant aggregates in layered materials. *Langmuir* 33:9759–9771. <https://doi.org/10.1021/acs.langmuir.7b01831>
94. Van Olphen H (1977) *An introduction to clay colloid chemistry*. Wiley-Interscience, New York
95. Auerbach SM, Carrado KA, Dutta PK (2004) Clay-organic interactions: organoclay complexes and polymer-clay nanocomposites. In: Auerbach SM, Carrado KA, Dutta PK (eds) *Handbook of layered materials*. Marcel Dekker, New York, pp 91–154
96. Galarneau A, Barodawalla A, Pinnavaia TJ (1995) Porous clay heterostructures formed by gallery-templated synthesis. *Nature* 374:529–531. <https://doi.org/10.1038/374529a0>
97. Michot LJ, Barrès O, Hegg EL, Pinnavaia TJ (1993) Cointercalation of Al₁₃ polycations and nonionic surfactants in montmorillonite clay. *Langmuir* 9:1794–1800. <https://doi.org/10.1021/la00031a030>
98. Nakatsuji M, Ishii R, Wang ZM, Ooi K (2004) Preparation of porous clay minerals with organic-inorganic hybrid pillars using solvent-extraction route. *J Colloid Interface Sci* 272:158–166. <https://doi.org/10.1016/j.jcis.2003.11.039>
99. Malla PB, Ravindranathan P, Komarneni S, Roy R (1991) Intercalation of copper metal clusters in montmorillonite. *Nature* 353:412–414
100. Yamauchi Y, Itagaki T, Yokoshima T, Kuroda K (2012) Preparation of Ni nanoparticles between montmorillonite layers utilizing dimethylaminoborane as reducing agent. *Dalton Trans* 41:1210–1215. <https://doi.org/10.1039/c1dt11395j>
101. Seki Y, Ogawa M (2010) The removal of 2-phenylphenol from aqueous solution by adsorption onto organoclays. *Bull Chem Soc Jpn* 83:712–715. <https://doi.org/10.1246/bcsj.20090191>
102. Ogawa M, Takee R, Okabe Y, Seki Y (2017) Bio-Geo Hybrid Pigment; Clay-Anthocyanin Complex Which Changes Color Depending on the Atmosphere. *Dye Pigment* 139:561–565. <https://doi.org/10.1016/j.dyepig.2016.12.054>
103. Sanchez C, Julián B, Belleville P, Popall M (2005) Applications of hybrid organic-inorganic nanocomposites. *J Mater Chem* 15:3559–3592. <https://doi.org/10.1039/b509097k>
104. Parola S, Julián-López B, Carlos LD, Sanchez C (2016) Optical properties of hybrid organic-inorganic materials and their applications. *Adv Funct Mater* 26:6506–6544. <https://doi.org/10.1002/adfm.201602730>
105. Bujdák J (2017) Hybrids with functional dyes. In: Nakato T, Kawamata J, Takagi S (eds) *Inorganic nanosheets and nanosheet-based materials*. Springer, Tokyo, pp 419–465
106. Ngulube T, Gumbo JR, Masindi V, Maity A (2017) An update on synthetic dyes adsorption onto clay based minerals: a state-of-art review. *J Environ Manag* 191:35–57. <https://doi.org/10.1016/j.jenvman.2016.12.031>
107. Okada T, Konno T, Ogawa M (2008) Luminescence quenching of tris(2,2'-bipyridine)ruthenium(II) in the interlayer space of saponite by sulfur dioxide. *Clay Sci* 14:43–47. https://doi.org/10.11362/jcssjclayscience.14.1_43
108. Jaynes WF, Boyd SA (1991) Hydrophobicity of siloxane surfaces in smectites as revealed by aromatic hydrocarbon adsorption from water. *Clay Clay Miner* 39:428–436. <https://doi.org/10.1346/CCMN.1991.0390412>
109. Jaynes WF (1999) Sorption of benzene, toluene, Ethylbenzene, and xylene (BTEX) compounds by hectorite clays exchanged with aromatic organic cations. *Clay Clay Miner* 47:358–365. <https://doi.org/10.1346/CCMN.1999.0470312>
110. Kakegawa N, Ogawa M (2002) The intercalation of β -carotene into the organophilic interlayer space of dialkyldimethylammonium-montmorillonites. *Appl Clay Sci* 22:137–144. [https://doi.org/10.1016/S0169-1317\(02\)00145-X](https://doi.org/10.1016/S0169-1317(02)00145-X)
111. Kohno Y, Asai S, Shibata M, Fukuhara C, Maeda Y, Tomita Y, Kobayashi K (2014) Improved photostability of hydrophobic natural dye incorporated in organo-modified hydrotalcite. *J Phys Chem Solids* 75:945–950. <https://doi.org/10.1016/j.jpcs.2014.04.010>
112. Liu P, Zhang L (2007) Adsorption of dyes from aqueous solutions or suspensions with clay nano-adsorbents. *Sep Purif Technol* 58:32–39. <https://doi.org/10.1016/j.seppur.2007.07.007>

113. Elmoubarki R, Mahjoubi FZ, Tounsadi H, Moustadraf J, Abdennouri M, Zouhri A, El Albani A, Barka N (2015) Adsorption of textile dyes on raw and decanted moroccan clays: kinetics, equilibrium and thermodynamics. *Water Resour Ind* 9:16–29. <https://doi.org/10.1016/j.wri.2014.11.001>
114. Meral K, Yılmaz N, Kaya M, Tabak A, Onganer Y (2011) The molecular aggregation of pyronin Y in natural bentonite clay suspension. *J Lumin* 131:2121–2127. <https://doi.org/10.1016/j.jlumin.2011.05.023>
115. Bujdák J (2001) Methylene blue interactions with reduced-charge smectites. *Clay Clay Miner* 49:244–254. <https://doi.org/10.1346/CCMN.2001.0490307>
116. Teepakakorn AP, Yamaguchi T, Ogawa M (2019) The improved stability of molecular guests by the confinement into nanopspaces. *Chem Lett* 48:398–409. <https://doi.org/10.1246/cl.181026>
117. Van Olphen H (1966) Maya blue: a clay-organic pigment? *Science* 154:645–646. <https://doi.org/10.1126/science.154.3749.645>
118. Teixeira-Neto AA, Izumi CMS, Temperini MLA, Ferreira AMDC, Constantino VRL (2012) Hybrid materials based on smectite clays and nutraceutical anthocyanins from the Açai fruit. *Eur J Inorg Chem*:5411–5420. <https://doi.org/10.1002/ejic.201200702>
119. Chiari G, Giustetto R, Ricchiardi G (2003) Crystal structure refinements of palygorskite and Maya Blue from molecular modelling and powder synchrotron diffraction. *Eur J Mineral* 15:21–33. <https://doi.org/10.1127/0935-1221/2003/0015-0021>
120. Tilocca A, Fois E (2009) The color and stability of Maya Blue: TDDFT calculations. *J Phys Chem C* 113:8683–8687. <https://doi.org/10.1021/jp810945a>
121. Fuentes ME, Peña B, Contreras C, Montero AL, Chianelli R, Alvarado M, Olivas R, Rodríguez LM, Camacho H, Montero-Cabrera LA (2008) Quantum mechanical model for Maya Blue. *Int J Quantum Chem* 108:1664–1673. <https://doi.org/10.1002/qua.21646>
122. Leitão IMV, Seixas De Melo JS (2013) Maya Blue, an ancient guest-host pigment: synthesis and models. *J Chem Educ* 90:1493–1497. <https://doi.org/10.1021/ed300425c>
123. Sánchez-Ochoa F, Cocoltzi GH, Canto G (2017) Trapping and diffusion of organic dyes inside of palygorskite clay: the ancient Maya blue pigment. *Microporous Mesoporous Mater* 249:111–117. <https://doi.org/10.1016/j.micromeso.2017.04.060>
124. Bernardino ND, Constantino VRL, De Faria DLA (2018) Probing the indigo molecule in Maya Blue simulants with resonance Raman spectroscopy. *J Phys Chem C* 122:11505–11515. <https://doi.org/10.1021/acs.jpcc.8b01406>
125. Ribeiro HL, de Oliveira AV, Brito ESd, Ribeiro PRV, Souza Filho MM, Azeredo HMC (2018) Stabilizing effect of montmorillonite on Acerola juice anthocyanins. *Food Chem* 245:966–973. <https://doi.org/10.1016/j.foodchem.2017.11.076>
126. Marangoni R, Bouhent M, Taviot-Guého C, Wypych F, Leroux F (2009) Zn₂Al layered double hydroxides intercalated and adsorbed with anionic blue dyes: a physico-chemical characterization. *J Colloid Interface Sci* 333:120–127. <https://doi.org/10.1016/j.jcis.2009.02.001>
127. Raha S, Ivanov I, Quazi NH, Bhattacharya SN (2009) Photo-stability of rhodamine-B/montmorillonite nanopigments in polypropylene matrix. *Appl Clay Sci* 42:661–666. <https://doi.org/10.1016/j.clay.2008.06.008>
128. Smitha VS, Manjumol KA, Ghosh S, Brahmakumar M, Pavithran C, Perumal P, Warriar KG (2011) Rhodamine 6G intercalated montmorillonite nanopigments-polyethylene composites: facile synthesis and ultravioletstability study. *J Am Ceram Soc* 94:1731–1736. <https://doi.org/10.1111/j.1551-2916.2010.04326.x>
129. Yang L, Qian L, Feng Y, Tang P, Li D (2014) Acid blue 129 and salicylate cointercalated layered double hydroxides: assembly, characterization, and photostability. *Ind Eng Chem Res* 53:17961–17967. <https://doi.org/10.1021/ie502893f>
130. Guo S, Evans DG, Li D (2006) Preparation of C.I. Pigment 52:1 anion-pillared layered double hydroxide and the thermo- and photostability of the resulting intercalated material. *J Phys Chem Solids* 67:1002–1006. <https://doi.org/10.1016/j.jpcs.2006.01.017>

131. Liu P, Liu P, Zhao K, Li L (2015) Photostability enhancement of azoic dyes adsorbed and intercalated into Mg-Al-layered double hydroxide. *Opt Laser Technol* 74:23–28. <https://doi.org/10.1016/j.optlastec.2015.05.008>
132. Kohno Y, Totsuka K, Ikoma S, Yoda K, Shibata M, Matsushima R, Tomita Y, Maeda Y, Kobayashi K (2009) Photostability enhancement of anionic natural dye by intercalation into hydrotalcite. *J Colloid Interface Sci* 337:117–121. <https://doi.org/10.1016/j.jcis.2009.04.065>
133. Ogawa M, Sohmiya M, Watase Y (2011) Stabilization of photosensitizing dyes by complexation with clay. *Chem Commun* 47:8602–8604. <https://doi.org/10.1039/c1cc12392k>
134. Kohno Y, Hoshino R, Matsushima R, Tomita Y, Kobayashi K (2015) Stabilization of flavylum dyes by incorporation in the clay interlayer. *J Jpn Soc Colour Mater* 80:6–12. <https://doi.org/10.4011/shikizai1937.80.6>
135. Ambrogi V, Nocchetti M, Latterini L (2014) Promethazine-montmorillonite inclusion complex to enhance drug photostability. *Langmuir* 30:14612–14620. <https://doi.org/10.1021/la5033898>
136. Chakraborty C, Dana K, Malik S (2012) Lamination of cationic perylene in montmorillonite nano-gallery: induced J-aggregated nanostructure with enhanced PHOTOPHYSICAL AND THERMOGRAVIMETRIC aspect. *J Phys Chem C* 116:21116–21123. <https://doi.org/10.1021/jp307293r>
137. Fahn R, Fenderl K (1983) Reaction products of organic dye molecules with acid-treated montmorillonite. *Clay Miner* 18:447–458. <https://doi.org/10.1180/claymin.1983.018.4.10>
138. Chakraborty C, Dana K, Malik S (2011) Intercalation of perylene diimide dye into LDH clays: enhancement of photostability. *J Phys Chem C* 115:1996–2004. <https://doi.org/10.1021/jp110486r>
139. Kohno Y, Kinoshita R, Ikoma S, Yoda K, Shibata M, Matsushima R, Tomita Y, Maeda Y, Kobayashi K (2009) Stabilization of natural anthocyanin by intercalation into montmorillonite. *Appl Clay Sci* 42:519–523. <https://doi.org/10.1016/j.clay.2008.06.012>
140. Turro NJ, Ramamurthy V, Scaiano JC (2010) Modern molecular photochemistry of organic molecules. University Science Books, California
141. Soderquist CJ, Crosby DG, Moilanen KW, Seiber JN, Woodrow JE (1975) Occurrence of trifluralin and its photoproducts in air. *J Agric Food Chem* 23:304–309. <https://doi.org/10.1021/jf60198a003>
142. Margulies L, Margulies L, Stern T, Ruzo LO, Rubin B (1992) Photostabilization of trifluralin adsorbed on a clay matrix. *J Agric Food Chem* 40:152–155. <https://doi.org/10.1021/jf00013a030>
143. Teepakakorn AP, Bureekaew S, Ogawa M (2018) Adsorption induced dye stability of cationic dyes on clay nanosheet. *Langmuir* 34:14069–14075. <https://doi.org/10.1021/acs.langmuir.8b02978>
144. Sohmiya M, Omata S, Ogawa M (2012) Two dimensional size controlled confinement of poly (vinyl pyrrolidone) in the interlayer space of swelling clay mineral. *Polym Chem* 3:1069. <https://doi.org/10.1039/c2py00465h>
145. Sackett DD, Fox MA (1990) Adsorption of alkyl-substituted phenols onto montmorillonite: investigation of adsorbed intermediates via visible absorption spectroscopy and product analysis. *Langmuir* 6:1237–1245. <https://doi.org/10.1021/la00097a008>
146. Grigoryan L, Yakushi K, Liu CJ, Takano S, Wakata M, Yamauchi H (1993) Evolution of optical absorption and superconductivity in bi-2212 and 2223 oxides intercalated by metal-phthalocyanines. A systematical study as a function of intercalation level. *Phys C Superconduct Appl* 218:153–163. [https://doi.org/10.1016/0921-4534\(93\)90278-X](https://doi.org/10.1016/0921-4534(93)90278-X)
147. Mao Y, Zhang G, Thomas JK (1993) Surface complexes as precursors of photoinduced radical cations of biphenyl and subsequent hydroxylation on laponite. *Langmuir* 9:1299–1305. <https://doi.org/10.1021/la00029a024>
148. Lee JH, Chang J, Cha JH, Jung DY, Kim SS, Kim JM (2010) Anthraquinone sulfonate modified, layered double hydroxide nanosheets for dye-sensitized solar cells. *Chem A Eur J* 16:8296–8299. <https://doi.org/10.1002/chem.201000703>

149. Kato HE, Zhang F, Yizhar O, Ramakrishnan C, Nishizawa T, Hirata K, Ito J, Aita Y, Tsukazaki T, Hayashi S, Hegemann P, Maturana AD, Ishitani R, Deisseroth K, Nureki O (2012) Crystal structure of the channelrhodopsin light-gated cation channel. *Nature* 482:369–374. <https://doi.org/10.1038/nature10870>
150. Kandori H, Ichioka T, Sasaki M (2002) Photoisomerization of the rhodopsin chromophore in clay interlayers at 77 K. *Chem Phys Lett* 354:251–255. [https://doi.org/10.1016/S0009-2614\(02\)00096-9](https://doi.org/10.1016/S0009-2614(02)00096-9)
151. Furutani Y, Ido K, Sasaki M, Ogawa M, Kandori H (2007) Clay mimics color tuning in visual pigments. *Angew Chem Int Ed* 46:8010–8012. <https://doi.org/10.1002/anie.200702368>
152. Margulies L, Rozen H (1986) Adsorption of methyl green on montmorillonite. *J Mol Struct* 141:219–226. [https://doi.org/10.1016/0022-2860\(86\)80326-X](https://doi.org/10.1016/0022-2860(86)80326-X)
153. Kovar L, DellaGuardia R, Thomas JK (1984) Reaction of radical cations of tetramethylbenzidine with colloidal clays. *J Phys Chem* 88:3595–3599. <https://doi.org/10.1021/j150660a043>
154. Bujdák J, Iyi N (2006) Spectral and structural characteristics of oxazine 4/ hexadecyltrimethylammonium montmorillonite films. *Chem Mater* 18:2618–2624. <https://doi.org/10.1021/cm052715c>
155. Bujdák J, Rátulovská J, Donauerová A, Bujdáková H (2016) Hybrid materials based on luminescent alkaloid berberine and saponite. *J Nanosci Nanotechnol* 16:7801–7804. <https://doi.org/10.1166/jnn.2016.12550>
156. Hirose M, Ito F, Shimada T, Takagi S, Sasai R, Okada T (2017) Photoluminescence by intercalation of a fluorescent β -diketone dye into a layered silicate. *Langmuir* 33:13515–13521. <https://doi.org/10.1021/acs.langmuir.7b03460>
157. Cohen R, Yariv S (1984) Metachromasy in clay minerals. sorption of acridine orange by montmorillonite. *J Chem Soc Faraday Trans 1* 80:1705. <https://doi.org/10.1039/f19848001705>
158. Taniguchi M, Yamagishi A, Iwamoto T (1990) Effects of alkyl chain length on the adsorption of an *N*-alkylated acridine orange cation by colloiddally dispersed zirconium phosphate. *J Phys Chem* 94:2534–2537. <https://doi.org/10.1021/j100369a057>
159. Yamagishi A, Soma M (1981) Aliphatic tail effects on adsorption of acridine orange cation on a colloidal surface of montmorillonite. *J Phys Chem* 3398:3090–3092
160. Valenty SJ (1979) Monolayer films of surfactant derivatives of methylene blue. *J Colloid Interface Sci* 68:486–491. [https://doi.org/10.1016/0021-9797\(79\)90306-0](https://doi.org/10.1016/0021-9797(79)90306-0)
161. Ogawa M, Ishikawa A (1998) Controlled microstructures of amphiphilic cationic azobenzene-montmorillonite intercalation compounds. *J Mater Chem* 8:463–467. <https://doi.org/10.1039/a706507h>
162. Ogawa M, Hama M, Kuroda K (1999) Photochromism of azobenzene in the hydrophobic interlayer spaces of dialkyldimethylammonium-fluor-tetrasilicic mica films. *Clay Miner* 34:213–220. <https://doi.org/10.1180/000985599546127>
163. Ogawa M, Goto R, Kanegawa N (2000) Intercalation of an amphiphilic azobenzene derivative into the interlayer space of clays. *Clay Sci* 11:231–241. <https://doi.org/10.1017/CBO9781107415324.004>
164. Ogawa M, Yamamoto M, Kuroda K (2001) Intercalation of an amphiphilic azobenzene derivative into the interlayer space of a layered silicate, magadiite. *Clay Miner* 36:263–266. <https://doi.org/10.1180/000985501750177988>
165. Ogawa M (2002) Photoisomerization of azobenzene in the interlayer space of magadiite. *J Mater Chem* 12:3304–3307. <https://doi.org/10.1039/B204031J>
166. Okada T, Watanabe Y, Ogawa M (2004) Photocontrol of the adsorption behavior of phenol for an azobenzene-montmorillonite intercalation compound. *Chem Commun* 1:320–321
167. Okada T, Watanabe Y, Ogawa M (2005) Photoregulation of the intercalation behavior of phenol for azobenzene-clay intercalation compounds. *J Mater Chem* 15:987. <https://doi.org/10.1039/b412707b>

168. Rouliá M, Vassiliadis AA (2005) Interactions between C.I. basic blue 41 and aluminosilicate sorbents. *J Colloid Interface Sci* 291:37–44. <https://doi.org/10.1016/j.jcis.2005.04.085>
169. Giustetto R, Wahyudi O (2011) Sorption of red dyes on palygorskite: synthesis and stability of red/purple Mayan nanocomposites. *Microporous Mesoporous Mater* 142:221–235. <https://doi.org/10.1016/j.micromeso.2010.12.004>
170. Takagi K, Kurematsu T, Sawaki Y (1991) Intercalation and photochromism of spiropyran on clay interlayers. *J Chem Soc Perkin Trans 2*:1517. <https://doi.org/10.1039/p29910001517>
171. Tomioka H, Itoh T (1991) Photochromism of spiropyran in organized molecular assemblies. Formation of J- and H-aggregates of photomerocyanines in bilayers-clay matrices. *J Chem Soc Chem Commun*:532–533. <https://doi.org/10.1039/C39910000532>
172. Martínez VM, Arbeloa FL, Prieto JB, Arbeloa IL (2005) Characterization of rhodamine 6G aggregates intercalated in solid thin films of laponite clay. 2 fluorescence spectroscopy. *J Phys Chem B* 109:7443–7450. <https://doi.org/10.1021/jp050440i>
173. Martínez Martínez V, López Arbeloa F, Bañuelos Prieto J, Arbeloa López T, López Arbeloa I (2004) Characterization of rhodamine 6G aggregates intercalated in solid thin films of laponite clay. 1. absorption spectroscopy. *J Phys Chem B* 108:20030–20037. <https://doi.org/10.1021/jp047552e>
174. Tapia Estévez MJ, López Arbeloa F, López Arbeloa T, López Arbeloa I, Schoonheydt RA (1994) Spectroscopic study of the adsorption of rhodamine 6G on laponite B for low loadings. *Clay Miner* 29:105–113. <https://doi.org/10.1180/claymin.1994.029.1.12>
175. Estévez MJT, Arbeloa FL, Arbeloa TL, Arbeloa IL (1994) On the monomeric and dimeric states of rhodamine 6G adsorbed on laponite B surfaces. *J Colloid Interface Sci* 162:412–417. <https://doi.org/10.1006/jcis.1994.1055>
176. Grauer Z, Avnir D, Yariv S (1984) Adsorption characteristics of rhodamine 6G on montmorillonite and laponite, elucidated from electronic absorption and emission spectra. *Can J Chem* 62:1889–1894. <https://doi.org/10.1139/v84-324>
177. Baranyaiová T, Bujdák J (2018) Effects of dye surface concentration on the molecular aggregation of xanthene dye in colloidal dispersions of montmorillonite. *Clay Clay Miner* 66:114–126. <https://doi.org/10.1346/CCMN.2018.064089>
178. Fujii K, Iyi N, Sasai R, Hayashi S (2008) Preparation of a novel luminous heterogeneous system: rhodamine/coumarin/phyllsilicate hybrid and blue shift in fluorescence emission. *Chem Mater* 20:2994–3002. <https://doi.org/10.1021/cm0716452>
179. Huang M, He S, Liu W, Yao Y, Miao S (2015) Spectral inspections on molecular configurations of Nile blue a adsorbed on the elementary clay sheets. *J Phys Chem B* 119:13302–13308. <https://doi.org/10.1021/acs.jpcc.5b05188>
180. Banik S, Bhattacharjee J, Hussain SA, Bhattacharjee D (2015) Clay induced aggregation of a tetra-cationic metalloporphyrin in layer by layer self assembled film. *J Phys Chem Solids* 87:128–135. <https://doi.org/10.1016/j.jpccs.2015.08.008>
181. Park IY, Kuroda K, Kato C (1989) Preparation of a layered double hydroxide–porphyrin intercalation compound. *Chem Lett* 18:2057–2058. <https://doi.org/10.1246/cl.1989.2057>
182. Kameyama H, Suzuki H, Amano A (1988) Intercalation of co(II) meso-tetrakis(1-methyl-4-pyridyl)porphyrin into montmorillonite. *Chem Lett* 17:1117–1120. <https://doi.org/10.1246/cl.1988.1117>
183. Bujdák J (2006) Effect of the layer charge of clay minerals on optical properties of organic dyes. A review. *Appl Clay Sci* 34:58–73. <https://doi.org/10.1016/j.clay.2006.02.011>
184. Bujdák J (2018) The effects of layered nanoparticles and their properties on the molecular aggregation of organic dyes. *J Photochem Photobiol C: Photochem Rev* 35:108–133. <https://doi.org/10.1016/j.jphotochemrev.2018.03.001>
185. Kasha M, Rawls HR, El-Bayoumi MA (1965) The exciton model in molecular spectroscopy. *Pure Appl Chem* 11:371–392. <https://doi.org/10.1351/pac196511030371>
186. Ogawa M, Ishii T, Miyamoto N, Kuroda K (2001) Photocontrol of the basal spacing of azobenzene-magadiite intercalation compound. *Adv Mater* 13:1107–1109. [https://doi.org/10.1002/1521-4095\(200107\)13:14<1107::AID-ADMA1107>3.0.CO;2-O](https://doi.org/10.1002/1521-4095(200107)13:14<1107::AID-ADMA1107>3.0.CO;2-O)

187. Kuykendall VG, Thomas JK (1991) Photophysical investigation of the degree of dispersion of aqueous colloidal clay. *Langmuir* 7:610–610. <https://doi.org/10.1021/la00051a036>
188. Quites FJ, Germino JC, Atvars TDZ (2014) Improvement in the emission properties of a luminescent anionic dye intercalated between the lamellae of zinc hydroxide-layered. *Colloids Surf A Physicochem Eng Asp* 459:194–201. <https://doi.org/10.1016/j.colsurfa.2014.07.009>
189. Hestand NJ, Spano FC (2018) Expanded theory of H- and J-molecular aggregates: the effects of vibronic coupling and intermolecular charge transfer. *Chem Rev* 118:7069–7163. <https://doi.org/10.1021/acs.chemrev.7b00581>
190. Schoonheydt RA, Cenens J, De Schrijver FC (1986) Spectroscopy of proflavine adsorbed on clays. *J Chem Soc Faraday Trans 1* 82:281. <https://doi.org/10.1039/f19868200281>
191. Hill EH, Zhang Y, Whitten DG (2015) Aggregation of cationic *p*-phenylene ethynyls on laponite clay in aqueous dispersions and solid films. *J Colloid Interface Sci* 449:347–356. <https://doi.org/10.1016/j.jcis.2014.12.006>
192. Jelley EE (1936) Spectral absorption and fluorescence of dyes in the molecular state. *Nature* 138:1009–1010. <https://doi.org/10.1038/1381009a0>
193. Ogawa M, Kawai R, Kuroda K (1996) Adsorption and aggregation of a cationic cyanine dye on smectites. *J Phys Chem* 100:16218–16221. <https://doi.org/10.1021/jp960261o>
194. Bricks JL, Slominskii YL, Panas ID, Demchenko AP (2018) Fluorescent J-aggregates of cyanine dyes: basic research and applications review. *Methods Appl Fluoresc* 6. <https://doi.org/10.1088/2050-6120/aa8d0d>
195. Miyamoto N, Kawai R, Kuroda K, Ogawa M (2000) Adsorption and aggregation of a cationic cyanine dye on layered clay minerals. *Appl Clay Sci* 16:161–170. [https://doi.org/10.1016/S0169-1317\(99\)00051-4](https://doi.org/10.1016/S0169-1317(99)00051-4)
196. Valandro SR, Poli AL, Correia TFA, Lombardo PC, Schmitt CC (2017) Photophysical behavior of isocyanine/clay hybrids in the solid state. *Langmuir* 33:891–899. <https://doi.org/10.1021/acs.langmuir.6b03898>
197. Boháč P, Czimerová A, Bujdák J (2016) Enhanced luminescence of 3,3'-Diethyl-2,2'-thiacyanine cations adsorbed on saponite particles. *Appl Clay Sci* 127–128:64–69. <https://doi.org/10.1016/j.clay.2016.04.008>
198. Sato N, Fujimura T, Shimada T, Tani T, Takagi S (2015) J-aggregate formation behavior of a cationic cyanine dye on inorganic layered material. *Tetrahedron Lett* 56:2902–2905. <https://doi.org/10.1016/j.tetlet.2015.04.084>
199. Debnath P, Chakraborty S, Deb S, Nath J, Dey B, Bhattacharjee D, Soda H, Tominaga M, Suzuki Y, Kawamata J, Hussain SA (2017) Effect of nano clay laponite on stability of SHG active J-aggregate of a thiacyanine dye onto LB films. *Appl Clay Sci* 147:105–116. <https://doi.org/10.1016/j.clay.2017.07.013>
200. Mekhroum MEM, Essassi EM, Qaiss A, Bouhfid R (2016) Fluorescent bio-nanocomposites based on chitosan reinforced hemicyanine dye-modified montmorillonite. *RSC Adv* 6:111472–111481. <https://doi.org/10.1039/c6ra23320a>
201. Miyamoto N, Kawai R, Kuroda K, Ogawa M (2001) Intercalation of a cationic cyanine dye into the layer silicate magadiite. *Appl Clay Sci* 19:39–46. [https://doi.org/10.1016/S0169-1317\(01\)00054-0](https://doi.org/10.1016/S0169-1317(01)00054-0)
202. Chakraborty S, Debnath P, Dey D, Bhattacharjee D, Hussain SA (2014) Formation of fluorescent H-aggregates of a cyanine dye in ultrathin film and its effect on energy transfer. *J Photochem Photobiol A Chem* 293:57–64. <https://doi.org/10.1016/j.jphotochem.2014.07.018>
203. Chakraborty S, Bhattacharjee D, Soda H, Tominaga M, Suzuki Y, Kawamata J, Hussain SA (2015) Temperature and concentration dependence of J-aggregate of a cyanine dye in a Laponite film fabricated by Langmuir-Blodgett technique. *Appl Clay Sci* 104:245–251. <https://doi.org/10.1016/j.clay.2014.11.039>
204. Matejdes M, Himeno D, Suzuki Y, Kawamata J (2017) Controlled formation of pseudoisocyanine J-aggregates in the interlayer space of synthetic saponite. *Appl Clay Sci* 140:119–123. <https://doi.org/10.1016/j.clay.2017.02.007>

205. Estévez MJT, Arbeloa FL, Arbeloa TL, Arbeloa IL (1993) Absorption and fluorescence properties of rhodamine 6G adsorbed on aqueous suspensions of Wyoming montmorillonite. *Langmuir* 9:3629–3634. <https://doi.org/10.1021/la00036a045>
206. Sasai R, Itoh H, Iyi N, Fujita T, Arbeloa FL, Martínez VM, Takagi K (2004) Luminescence properties of rhodamine 6G intercalated in surfactant/clay hybrid thin solid films. *Langmuir* 20:4715–4719. <https://doi.org/10.1021/la049584z>
207. Wu L, Lv G, Liu M, Li Z, Liao L, Pan C (2015) Adjusting the layer charges of host phyllosilicates to prevent luminescence quenching of fluorescence dyes. *J Phys Chem C* 119:22625–22631. <https://doi.org/10.1021/acs.jpcc.5b07243>
208. Kaya M, Meral K, Onganer Y (2015) Molecular aggregates of merocyanine 540 in aqueous suspensions containing natural and CTAB-modified bentonite. *J Mol Struct* 1083:101–105. <https://doi.org/10.1016/j.molstruc.2014.11.046>
209. Giannelis EP (1990) Highly organized molecular assemblies of porphyrin guest molecules in mica-type silicates: influence of guest–host interactions on molecular organization. *Chem Mater* 2:627–629. <https://doi.org/10.1021/cm00012a002>
210. Carrado KA, Winans RE (1990) Interactions of water-soluble porphyrins and metalloporphyrins with smectite clay surfaces. *Chem Mater* 2:328–335. <https://doi.org/10.1021/cm00009a027>
211. Bergaya F, Van Damme H (1982) Stability of metalloporphyrins adsorbed on clays: a comparative study. *Geochim Cosmochim Acta* 46:349–360. [https://doi.org/10.1016/0016-7037\(82\)90226-5](https://doi.org/10.1016/0016-7037(82)90226-5)
212. Carrado KA, Thiyagarajan P, Winans RE, Botto RE (1991) Hydrothermal crystallization of porphyrin-containing layer silicates. *Inorg Chem* 30:794–799. <https://doi.org/10.1021/ic00004a034>
213. Grando SR, Santos FDS, Gallas MR, Costa TMH, Benvenuti EV, Rodembusch FS (2012) Photophysics of aminobenzazole dyes in silica-based hybrid materials. *J Sol-Gel Sci Technol* 63:235–241. <https://doi.org/10.1007/s10971-012-2720-z>
214. Kudo N, Tsukamoto T, Tokieda D, Shimada T, Takagi S (2018) Fluorescence enhancement behavior of hemicyanine derivatives on the clay nanosheets: aggregation induced emission (AIE) vs. surface-fixation induced emission (S-FIE). *Chem Lett* 47:636–639. <https://doi.org/10.1246/cl.180043>
215. Tokieda D, Tsukamoto T, Ishida Y, Ichihara H, Shimada T, Takagi S (2017) Unique fluorescence behavior of dyes on the clay minerals surface: surface fixation induced emission (S-FIE). *J Photochem Photobiol A Chem* 339:67–79. <https://doi.org/10.1016/j.jphotochem.2017.01.013>
216. Kawamata J, Suzuki Y, Tominaga M (2018) From adsorbed dyes to optical materials. In: *Developments in clay science*. Elsevier, Amsterdam, pp 361–375
217. Zhang X, Hong H, Li Z, Guan J, Schulz L (2009) Removal of azobenzene from water by kaolinite. *J Hazard Mater* 170:1064–1069. <https://doi.org/10.1016/j.jhazmat.2009.05.073>
218. van Damme H, Crespin M, Obrecht F, Cruz MI, Fripiat JJ (1978) Acid-base and complexation behavior of porphyrins on the intracrystal surface of swelling clays: meso-tetraphenylporphyrin and meso-tetra(4-pyridyl)porphyrin on montmorillonites. *J Colloid Interface Sci* 66:43–54. [https://doi.org/10.1016/0021-9797\(78\)90182-0](https://doi.org/10.1016/0021-9797(78)90182-0)
219. Takagi S, Shimada T, Yui T, Inoue H (2001) High density adsorption of porphyrins onto clay layer without aggregation: characterization of smectite-cationic porphyrin complex. *Chem Lett* 30:128–129. <https://doi.org/10.1246/cl.2001.128>
220. Takagi S, Shimada T, Eguchi M, Yui T, Yoshida H, Tryk DA, Inoue H (2002) High-density adsorption of cationic porphyrins on clay layer surfaces without aggregation: the size-matching effect. *Langmuir* 18:2265–2272. <https://doi.org/10.1021/la011524v>
221. Ishida Y, Masui D, Shimada T, Tachibana H, Inoue H, Takagi S (2012) The mechanism of the porphyrin spectral shift on inorganic nanosheets: the molecular flattening induced by the strong host–guest interaction due to the “size-matching rule”. *J Phys Chem C* 116:7879–7885. <https://doi.org/10.1021/jp300842f>

222. Ogawa M, Handa T, Kuroda K, Kato C, Tani T (1992) Photochemical hole burning of 1,4-dihydroxyanthraquinone intercalated in a pillered layered clay mineral. *J Phys Chem* 96:8116–8119
223. Ferreira AUC, Poli AL, Gessner F, Neumann MG, Schmitt Cavalheiro CC (2013) Interaction of auramine O with montmorillonite clays. *J Lumin* 136:63–67. <https://doi.org/10.1016/j.jlumin.2012.11.022>
224. Tsukamoto T, Shimada T, Takagi S (2013) Unique photochemical properties of *p*-substituted cationic triphenylbenzene derivatives on a clay layer surface. *J Phys Chem C* 117:2774–2779. <https://doi.org/10.1021/jp3092144>
225. Tsukamoto T, Shimada T, Takagi S (2013) Photochemical properties of mono-, tri-, and pentacationic antimony(V) metalloporphyrin derivatives on a clay layer surface. *J Phys Chem A* 117:7823–7832. <https://doi.org/10.1021/jp405767s>
226. Tsukamoto T, Shimada T, Takagi S (2015) Structure resembling effect of clay surface on photochemical properties of meso-phenyl or pyridyl-substituted monocationic antimony (V) porphyrin derivatives. *RSC Adv* 5:8479–8485. <https://doi.org/10.1039/C4RA15650A>
227. Villemure G, Detellier C, Szabo AG (1986) Fluorescence of clay-intercalated methylviologen. *J Am Chem Soc* 108:4658–4659. <https://doi.org/10.1021/ja00275a071>
228. Miyata H, Sugahara Y, Kuroda K, Kato C (1987) Synthesis of montmorillonite-viologen intercalation compounds and their photochromic behaviour. *J Chem Soc Faraday Trans 1* 83:1851–1858. <https://doi.org/10.1039/F19878301851>
229. Raupach M, Emerson WW, Slade PG (1979) The arrangement of paraquat bound by vermiculite and montmorillonite. *J Colloid Interface Sci* 69:398–408. [https://doi.org/10.1016/0021-9797\(79\)90129-2](https://doi.org/10.1016/0021-9797(79)90129-2)
230. Hayes MHB, Pick ME, Toms BA (1978) The influence of organocation structure on the adsorption of mono- and of bipyridinium cations by expanding lattice clay minerals. *J Colloid Interface Sci* 65:254–265. [https://doi.org/10.1016/0021-9797\(78\)90156-X](https://doi.org/10.1016/0021-9797(78)90156-X)
231. Villemure G, Detellier C, Szabo AG (1991) Fluorescence of methylviologen intercalated into montmorillonite and hectorite aqueous suspensions. *Langmuir* 7:1215–1221. <https://doi.org/10.1021/la00054a032>
232. Okada T, Ogawa M (2003) 1,1'-dimethyl-4,4'-bipyridinium-smectites as a novel adsorbent of phenols from water through charge-transfer interactions. *Chem Commun*:1378–1379. <https://doi.org/10.1039/b302144k>
233. Kakegawa N, Kondo T, Ogawa M (2003) Variation of electron-donating ability of smectites as probed by photoreduction of methyl viologen. *Langmuir* 19:3578–3582. <https://doi.org/10.1021/la020763v>
234. Miyata H, Sugahara Y, Kuroda K, Kato C (1988) Synthesis of a viologen-tetratitanate intercalation compound and its photochemical behaviour. *J Chem Soc Faraday Trans* 84:2677–2682. <https://doi.org/10.1039/F19888402677>
235. Nakato T, Kuroda K, Kato C (1989) Photoreduction of methylviologen in the interlayer of $K_4Nb_6O_{17}$. *J Chem Soc Chem Commun* 1144. <https://doi.org/10.1039/c39890001144>
236. Nakato T, Kuroda K, Kato C (1992) Syntheses of intercalation compounds of layered niobates with methylviologen and their photochemical behavior. *Chem Mater* 4:128–132. <https://doi.org/10.1021/cm00019a027>
237. Nakato T, Ito K, Kuroda K, Kato C (1993) Photochemical behavior of perovskite-related layered niobates $HA_2Nb_3O_{10}$ ($a = Ca, Sr$) intercalated with methylviologen. *Microporous Mater* 1:283–286. [https://doi.org/10.1016/0927-6513\(93\)80071-2](https://doi.org/10.1016/0927-6513(93)80071-2)
238. Nakato T, Miyata H, Kuroda K, Kato C (1988) Synthesis of methylviologen-HTiNbO₅ intercalation compound and its photochemical behavior. *React Solids* 6:231–238. [https://doi.org/10.1016/0168-7336\(88\)80063-9](https://doi.org/10.1016/0168-7336(88)80063-9)
239. Vermeulen LA, Snover JL, Sapochak LS, Thompson ME (1993) Efficient photoinduced charge separation in layered zirconium viologen phosphonate compounds. *J Am Chem Soc* 115:11767–11774. <https://doi.org/10.1021/ja00078a015>

240. Vermeulen LA, Thompson ME (1992) Stable photoinduced charge separation in layered viologen compounds. *Nature* 358:656–658. <https://doi.org/10.1038/358656a0>
241. Liu X, Iu KK, Thomas JK (1992) Studies of surface properties of clay Laponite using pyrene as a photophysical probe molecule. 2. Photoinduced electron transfer. *Langmuir* 8:539–545. <https://doi.org/10.1021/la00038a038>
242. Viaene K, Caigui J, Schoonheydt RA, De Schryver FC (1987) Study of the adsorption on clay particles by means of a fluorescent probe. *Langmuir* 3:107–111. <https://doi.org/10.1021/la00073a019>
243. Viaene K, Schoonheydt RA, Crutzen M, Kuniyima B, De Schryver FC (1988) Study of the adsorption on clay particles by means of fluorescent probes. *Langmuir* 4:749–752. <https://doi.org/10.1021/la00081a044>
244. Labbé P, Reverdy G (1988) Adsorption characteristics of polycyclic aromatic compounds on clay: pyrene as a photophysical probe on Laponite. *Langmuir* 4:419–425. <https://doi.org/10.1021/la00080a028>
245. Kuniyima B, Viaene K, Khalil MMH, Schoonheydt RA, Crutzen M, De Schryver FC (1990) Study of the adsorption and polymerization of functionalized organic ammonium derivatives on a clay surface. *Langmuir* 6:482–486. <https://doi.org/10.1021/la00092a031>
246. Liu X, Thomas JK (1991) Study of surface properties of clay Laponite using pyrene as a photophysical probe molecule. *Langmuir* 7:2808–2816. <https://doi.org/10.1021/la00059a065>
247. Ikeda M, Yoshii T, Matsui T, Tanida T, Komatsu H, Hamachi I (2011) Montmorillonite–supramolecular hydrogel hybrid for fluorocolorimetric sensing of polyamines. *J Am Chem Soc* 133:1670–1673. <https://doi.org/10.1021/ja109692z>
248. Kavanagh RJ, Iu KK, Thomas JK (1992) Spectroscopic determination of refractive index and dielectric constant at interfaces, using photophysical probe molecules. *Langmuir* 8:3008–3013. <https://doi.org/10.1021/la00048a026>
249. Nakamura T, Thomas JK (1986) The interaction of alkylammonium salts with synthetic clays. A fluorescence and laser excitation study. *J Phys Chem* 90:641–644. <https://doi.org/10.1021/j100276a032>
250. Nakamura T, Thomas JK (1987) Formation of surfactant double layers on Laponite clay colloids. *Langmuir* 3:234–239. <https://doi.org/10.1021/la00074a016>
251. DellaGuardia RA, Thomas JK (1983) Photoprocesses on colloidal clay systems. 2. Quenching studies and the effect of surfactants on the luminescent properties of pyrene and pyrene derivatives adsorbed on clay colloids. *J Phys Chem* 87:3550–3557
252. DellaGuardia RA, Thomas JK (1984) Photoprocesses on colloidal clay systems. 3. Interaction of dodecanol and its micelles with colloidal montmorillonite. *J Phys Chem* 88:964–970. <https://doi.org/10.1021/j150649a024>
253. Wang T, Hu X, Zheng S, Liu X, Wang C, Tong Z (2012) Adsorption of fluorophores and *N*-isopropylacrylamide on Laponite. *Appl Clay Sci* 58:102–107. <https://doi.org/10.1016/j.clay.2012.01.021>
254. Kawamata J, Suzuki Y, Tenma Y (2010) Fabrication of clay mineral-dye composites as nonlinear optical materials. *Philos Mag* 90:2519–2527. <https://doi.org/10.1080/14786430903581304>
255. Tominaga M, Oniki Y, Mochida S, Kasatani K, Tani S, Suzuki Y, Kawamata J (2016) Clay-organic hybrid films exhibiting reversible fluorescent color switching induced by swelling and drying of a clay mineral. *J Phys Chem C* 120:23813–23822. <https://doi.org/10.1021/acs.jpcc.6b07537>
256. Barloy L, Battioni P, Mansuy D (1990) Manganese porphyrins supported on montmorillonite as hydrocarbon mono-oxygenation catalysts: particular efficacy for linear alkane hydroxylation. *J Chem Soc Chem Commun*:1365–1367. <https://doi.org/10.1039/C39900001365>
257. Gaillon L, Bedioui F, Devynck J, Battioni P (1993) Electrochemical characterization of manganese Porphyrins fixed onto silica and layered Dihydroxide matrices. *J Electroanal Chem* 347:435–442. [https://doi.org/10.1016/0022-0728\(93\)80108-T](https://doi.org/10.1016/0022-0728(93)80108-T)

258. Liu J, Zhang G (2014) Recent advances in synthesis and applications of clay-based photocatalysts: a review. *Phys Chem Chem Phys* 16:8178–8192. <https://doi.org/10.1039/c3cp54146k>
259. Kameyama H, Narumi F, Hattori T, Kameyama H (2006) Oxidation of cyclohexene with molecular oxygen catalyzed by cobalt porphyrin complexes immobilized on montmorillonite. *J Mol Catal A Chem* 258:172–177. <https://doi.org/10.1016/j.molcata.2006.05.022>
260. Tsukamoto T, Shimada T, Takagi S (2018) Artificial photosynthesis model: photochemical reaction system with efficient light-harvesting function on inorganic nanosheets. *ACS Omega* 3:18563–18571. <https://doi.org/10.1021/acsomega.8b02594>
261. Remello SN, Kuttassery F, Mathew S, Thomas A, Yamamoto D, Nabetani Y, Sano K, Tachibana H, Inoue H (2018) Two-electron oxidation of water to form hydrogen peroxide catalysed by silicon-porphyrins. *Sustain Energy Fuels* 2:1966–1973. <https://doi.org/10.1039/c8se00102b>
262. Tatsumi D, Tsukamoto T, Honna R, Hoshino S, Shimada T, Takagi S (2017) Highly selective photochemical epoxidation of cyclohexene sensitized by Ru(II) porphyrin/clay hybrid catalyst. *Chem Lett* 46:1311–1314. <https://doi.org/10.1246/cl.170521>
263. Jain A, Achari A, Eswaramoorthy M, George SJ (2016) Light induced: in situ post-modification of clay-chromophore hybrids for multiple white light emissions. *J Mater Chem C* 4:2748–2751. <https://doi.org/10.1039/c5tc03319e>
264. Ishida Y, Shimada T, Masui D, Tachibana H, Inoue H, Takagi S (2011) Efficient excited energy transfer reaction in clay/porphyrin complex toward an artificial light-harvesting system. *J Am Chem Soc* 133:14280–14286. <https://doi.org/10.1021/ja204425u>
265. Takagi S, Eguchi M, Shimada T, Hamatani S, Inoue H (2007) Energy transfer reaction of cationic porphyrin complexes on the clay surface: effect of sample preparation method. *Res Chem Intermed* 33:177–189. <https://doi.org/10.1163/156856707779160889>
266. Takagi S, Shimada T, Ishida Y, Fujimura T, Masui D, Tachibana H, Eguchi M, Inoue H (2013) Size-matching effect on inorganic nanosheets: control of distance, alignment, and orientation of molecular adsorption as a bottom-up methodology for nanomaterials. *Langmuir* 29:2108–2119. <https://doi.org/10.1021/la3034808>
267. Rao KV, Datta KKR, Eswaramoorthy M, George SJ (2013) Highly pure solid-state white-light emission from solution-processed soft-hybrids. *Adv Mater* 25:1713–1718. <https://doi.org/10.1002/adma.201204407>
268. Sato K, Matsubara K, Hagiwara S, Saito K, Yagi M, Takagi S, Yui T (2015) Remarkable stimulation of emission quenching on a clay surface. *Langmuir* 31:27–31. <https://doi.org/10.1021/la504597t>
269. Takagi S, Eguchi M, Tryk DA, Inoue H (2006) Porphyrin photochemistry in inorganic/organic hybrid materials: clays, layered semiconductors, nanotubes, and mesoporous materials. *J Photochem Photobiol C: Photochem Rev* 7:104–126. <https://doi.org/10.1016/j.jphotochemrev.2006.04.002>
270. Nakato T, Iwata Y, Kuroda K, Kaneko M, Kato C (1993) Intercalation of a free-base porphyrin into layered tetrahedral acid. *J Chem Soc Dalton Trans*:1405–1409. <https://doi.org/10.1039/DT9930001405>
271. Sasai R, Kato Y, Soontornchaiyakul W, Usami H, Masumori A, Norimatsu W, Fujimura T, Takagi S (2017) Photoinduced electron transfer in layer-by-layer thin solid films containing cobalt oxide nanosheets, porphyrin, and methyl viologen. *Phys Chem Chem Phys* 19:5611–5616. <https://doi.org/10.1039/c6cp07250j>
272. Gu Z, Gao M, Lu L, Liu Y, Yang S (2015) Montmorillonite functionalized with zwitterionic surfactant as a highly efficient adsorbent for herbicides. *Ind Eng Chem Res* 54:4947–4955. <https://doi.org/10.1021/acs.iecr.5b00438>
273. Si Y, Zhou J, Chen H, Zhou D (2004) Photostabilization of the herbicide bensulfuron-methyl by using organoclays. *Chemosphere* 54:943–950. <https://doi.org/10.1016/j.chemosphere.2003.09.033>

274. El-Nahhal Y, Nir S, Margulies L, Rubin B (1999) Reduction of photodegradation and volatilization of herbicides in Organo-clay formulations. *Appl Clay Sci* 14:105–119. [https://doi.org/10.1016/S0169-1317\(98\)00053-2](https://doi.org/10.1016/S0169-1317(98)00053-2)
275. Margulies L, Rozen H, Cohen E (1985) Energy transfer at the surface of clays and protection of pesticides from photodegradation. *Nature* 315:658–659. <https://doi.org/10.1038/315658a0>
276. Undabeytia T, Nir S, Tel-Or E, Rubin B (2000) Photostabilization of the herbicide norflurazon by using organoclays. *J Agric Food Chem* 48:4774–4779. <https://doi.org/10.1021/jf9912405>
277. Goto T, Ogawa M (2015) Visible-light-responsive photocatalytic flow reactor composed of Titania film photosensitized by metal complex-clay hybrid. *ACS Appl Mater Interfaces* 7:12631–12634. <https://doi.org/10.1021/acsami.5b03128>
278. Goto T, Ogawa M (2016) Efficient photocatalytic oxidation of benzene to phenol by metal complex-clay/TiO₂ hybrid photocatalyst. *RSC Adv* 6:23794–23797. <https://doi.org/10.1039/c5ra25430b>
279. Kakegawa N, Ogawa M (2004) Effective luminescence quenching of Tris (2,2-bipyridine) ruthenium (II) by methylviologen on clay by the aid of poly (vinylpyrrolidone). *Langmuir* 20:7004–7009
280. Lu L, Jones RM, McBranch D, Whitten D (2002) Surface-enhanced superquenching of cyanine dyes as J-aggregates on Laponite clay nanoparticles. *Langmuir* 18:7706–7713. <https://doi.org/10.1021/la0259306>
281. Kanegawa N, Ogawa M (2003) The synthesis of dihexadecylviologen- intercalation compounds and the photochemical reactions. *Clay Sci* 12:153–157
282. Okada T, Ogawa M (2002) Adsorption of phenols onto 1,1'-dimethyl-4,4'-bipyridinium-smectites. *Chem Lett* 31:812–813
283. Yui T, Tsuchino T, Itoh T, Ogawa M, Fukushima Y, Takagi K (2005) Photoinduced one-electron reduction of MV²⁺ in titania nanosheets using porphyrin in mesoporous silica thin films. *Langmuir* 21:2644–2646. <https://doi.org/10.1021/la047385+>
284. Yui T, Kobayashi Y, Yamada Y, Yano K, Fukushima Y, Torimoto T, Takagi K (2011) Photoinduced electron transfer between the anionic porphyrins and viologens in titania nanosheets and monodisperse mesoporous silica hybrid films. *ACS Appl Mater Interfaces* 3:931–935. <https://doi.org/10.1021/am101281n>
285. Okada T, Matsutomo T, Ogawa M (2010) Nanospace engineering of methylviologen modified hectorite-like layered silicates with varied layer charge density for the adsorbents design. *J Phys Chem C* 114:539–545. <https://doi.org/10.1021/jp9089886>
286. Ogawa M, Matsutomo T, Okada T (2008) Preparation of hectorite-like swelling silicate with controlled layer charge density. *J Ceram Soc Jpn* 116:1309–1313. <https://doi.org/10.2109/jcersj2.116.1309>
287. Takagi S, Tryk DA, Inoue H (2002) Photochemical energy transfer of cationic porphyrin complexes on clay surface. *J Phys Chem B* 106:5455–5460. <https://doi.org/10.1021/jp0200977>
288. Fujimura T, Ramasamy E, Ishida Y, Shimada T, Takagi S, Ramamurthy V (2016) Sequential energy and electron transfer in a three-component system aligned on a clay nanosheet. *Phys Chem Chem Phys* 18:5404–5411. <https://doi.org/10.1039/c5cp06984j>
289. Miyamoto N, Kuroda K, Ogawa M (2004) Exfoliation and film preparation of a layered titanate, Na₂Ti₃O₇, and intercalation of pseudoisocyanine dye. *J Mater Chem* 14:165. <https://doi.org/10.1039/b308800f>
290. Eguchi M, Tachibana H, Takagi S, Tryk DA, Inoue H (2007) Dichroic measurements on dicationic and tetracationic porphyrins on clay surfaces with visible-light-attenuated total reflectance. *Bull Chem Soc Jpn* 80:1350–1356. <https://doi.org/10.1246/bcsj.80.1350>
291. Takenawa R, Komori Y, Hayashi S, Kawamata J, Kuroda K (2001) Intercalation of nitroanilines into kaolinite and second harmonic generation. *Chem Mater* 13:3741–3746. <https://doi.org/10.1021/cm010095j>

292. Yan D, Lu J, Wei M, Evans DG, Duan X (2011) Recent advances in photofunctional guest/layered double hydroxide host composite systems and their applications: experimental and theoretical perspectives. *J Mater Chem* 21:13128–13139. <https://doi.org/10.1039/c1jm11594d>
293. Yan D, Lu J, Wei M, Qin S, Chen L, Zhang S, Evans DG, Duan X (2011) Heterogeneous transparent ultrathin films with tunable-color luminescence based on the assembly of photoactive organic molecules and layered double hydroxides. *Adv Funct Mater* 21:2497–2505. <https://doi.org/10.1002/adfm.201002446>
294. López Arbeloa F, Martínez Martínez V (2006) Orientation of adsorbed dyes in the interlayer space of clays. 2 fluorescence polarization of rhodamine 6G in Laponite films. *Chem Mater* 18:1407–1416. <https://doi.org/10.1021/cm051518a>
295. López Arbeloa F, Martínez Martínez V, Arbeloa T, López Arbeloa I (2007) Photoresponse and anisotropy of rhodamine dye intercalated in ordered clay layered films. *J Photochem Photobiol C: Photochem Rev* 8:85–108. <https://doi.org/10.1016/j.jphotochemrev.2007.03.003>
296. Yan D, Lu J, Wei M, Evans DG, Duan X (2009) Sulforhodamine B intercalated layered double hydroxide thin film with polarized photoluminescence. *J Phys Chem B* 113:1381–1388. <https://doi.org/10.1021/jp8084217>
297. Wang Z, Teng X, Lu C (2013) Universal chemiluminescence flow-through device based on directed self-assembly of solid-state organic chromophores on layered double hydroxide matrix. *Anal Chem* 85:2436–2442. <https://doi.org/10.1021/ac303487b>
298. Shi W, Lin Y, Kong X, Zhang S, Jia Y, Wei M, Evans DG, Duan X (2011) Fabrication of pyrenetetrakisulfonate/layered double hydroxide ultrathin films and their application in fluorescence chemosensors. *J Mater Chem* 21:6088–6094. <https://doi.org/10.1039/c1jm00073j>
299. Yan D, Lu J, Ma J, Wei M, Li S, Evans DG, Duan X (2011) Near-infrared absorption and polarized luminescent ultrathin films based on sulfonated cyanines and layered double hydroxide. *J Phys Chem C* 115:7939–7946. <https://doi.org/10.1021/jp2002029>
300. Zhao Y, Lin H, Chen M, Yan D (2014) Niflumic anion intercalated layered double hydroxides with Mechano-induced and solvent-responsive luminescence. *Ind Eng Chem Res* 53:3140–3147. <https://doi.org/10.1021/ie404054v>
301. Yan D, Lu J, Chen L, Qin S, Ma J, Wei M, Evans DG, Duan X (2010) A strategy to the ordered assembly of functional small cations with layered double hydroxides for luminescent ultra-thin films. *Chem Commun* 46:5912–5914. <https://doi.org/10.1039/c0cc00522c>
302. Li S, Lu J, Ma H, Xu J, Yan D, Wei M, Evans DG, Duan X (2011) Ordered blue luminescent ultrathin films by the effective coassembly of tris(8-hydroxyquinolate-5-sulfonate)aluminum and polyanions with layered double hydroxides. *Langmuir* 27:11501–11507. <https://doi.org/10.1021/la202139f>
303. Yan D, Lu J, Ma J, Wei M, Wang X, Evans DG, Duan X (2010) Anionic poly(*p*-phenylenevinylene)/layered double hydroxide ordered ultrathin films with multiple quantum well structure: a combined experimental and theoretical study. *Langmuir* 26:7007–7014. <https://doi.org/10.1021/la904228b>
304. Yan D, Lu J, Ma J, Wei M, Evans DG, Duan X (2011) Fabrication of an anionic polythiophene/layered double hydroxide ultrathin film showing red luminescence and reversible pH photoresponse. *AICHE J* 57:1926–1935. <https://doi.org/10.1002/aic.12400>
305. Valeur B, Berberan-Santos MN (2012) Molecular fluorescence. Wiley-VCH Verlag GmbH & Co. KGaA, Weinheim
306. Yan D, Zhao Y, Wei M, Liang R, Lu J, Evans DG, Duan X (2013) Regular assembly of 9-fluorenone-2,7-dicarboxylate within layered double hydroxide and its solid-state photoluminescence: a combined experiment and computational study. *RSC Adv* 3:4303. <https://doi.org/10.1039/c3ra23064c>
307. Jain A, Achari A, Mothi N, Eswaramoorthy M, George SJ (2015) Shining light on clay-Chromophore hybrids: layered templates for accelerated ring closure photo-oxidation. *Chem Sci* 6:6334–6340. <https://doi.org/10.1039/c5sc02215k>

308. Hartley GS (1938) 113. The *cis*-form of azobenzene and the velocity of the thermal *cis*→*trans*-conversion of azobenzene and some derivatives. *J Chem Soc*:633–642. <https://doi.org/10.1039/JR9380000633>
309. Ciccone S, Halpern J (1959) Catalysis of the *cis* - *trans* isomerization of azobenzene by acids and cupric salts. *Can J Chem* 37:1903–1910. <https://doi.org/10.1139/v59-278>
310. Siampiringue N, Guyot G, Monti S, Bortolus P (1987) The *cis* → *trans* photoisomerization of azobenzene: an experimental re-examination. *J Photochem* 37:185–188. [https://doi.org/10.1016/0047-2670\(87\)85039-6](https://doi.org/10.1016/0047-2670(87)85039-6)
311. Bortolus P, Monti S (1979) *Cis-trans* photoisomerization of azobenzene. solvent and triplet donors effects. *J Phys Chem* 83:648–652. <https://doi.org/10.1021/j100469a002>
312. Saremi F, Tieke B (1998) Photoinduced switching in self-assembled multilayers of an azobenzene bolaamphiphile and polyelectrolytes. *Adv Mater* 10:389–391. [https://doi.org/10.1002/\(SICI\)1521-4095\(199803\)10:5<389::AID-ADMA388>3.0.CO;2-9](https://doi.org/10.1002/(SICI)1521-4095(199803)10:5<389::AID-ADMA388>3.0.CO;2-9)
313. Kojima M, Takagi T, Goshima T (2000) Photoisomerization of Azobenzene in zeolite cavities. *Mol Cryst Liq Cryst Sci Technol Sect A* 344:179–184. <https://doi.org/10.1080/10587250008023833>
314. Fischer E, Frankel M, Wolovsky R (1955) Wavelength dependence of photoisomerization equilibria in azocompounds. *J Chem Phys* 23:1367–1367. <https://doi.org/10.1063/1.1742302>
315. Bandara HMD, Burdette SC (2012) Photoisomerization in different classes of azobenzene. *Chem Soc Rev* 41:1809–1825. <https://doi.org/10.1039/c1cs15179g>
316. Ueda M, Kim HB, Ikeda T, Ichimura K (1992) Photoisomerization of an azobenzene in sol-gel glass films. *Chem Mater* 4:1229–1233. <https://doi.org/10.1021/cm00024a022>
317. Suzuki I, Ishizaki T, Hoshi T, Anzai J (2002) Fully reversible isomerization of azobenzene chromophores in polyelectrolyte layered assemblies. *Macromolecules* 35:577–580. <https://doi.org/10.1021/ma010388y>
318. Beattie MS, Jackson C, Jaycox GD (1998) Azobenzene modified poly(aryl ether ketone amide)s. 2. Photo- and thermo-responsive behaviour in dilute solution. *Polymer* 39:2597–2605. [https://doi.org/10.1016/S0032-3861\(97\)00559-4](https://doi.org/10.1016/S0032-3861(97)00559-4)
319. Gegiou D, Muszkat KA, Fischer E (1968) Temperature dependence of Photoisomerization. V the effect of substituents on the photoisomerization of stilbenes and azobenzenes. *J Am Chem Soc* 90:3907–3918. <https://doi.org/10.1021/ja01017a002>
320. Yabe A, Kawabata Y, Niino H, Tanaka M, Ouchi A, Takahashi H, Tamura S, Tagaki W, Nakahara H, Fukuda K (1988) *cis-trans* isomerization of the azobenzenes included as guests in Langmuir–Blodgett films of amphiphilic β-cyclodextrin. *Chem Lett* 17:1–4. <https://doi.org/10.1246/cl.1988.1>
321. Nishiyama K, Fujihira M (1988) *cis-trans* reversible photoisomerization of an amphiphilic azobenzene derivative in its pure LB film prepared as polyion complexes with polyallylamine. *Chem Lett* 17:1257–1260. <https://doi.org/10.1246/cl.1988.1257>
322. Matsumoto M, Tachibana H, Sato F, Terretaz S (1997) Photoinduced self-organization in Langmuir–Blodgett films. *J Phys Chem B* 101:702–704. <https://doi.org/10.1021/jp9629093>
323. Matsumoto M, Miyazaki D, Tanaka M, Azumi R, Manda E, Kondo Y, Yoshino N, Tachibana H (1998) Reversible light-induced morphological change in Langmuir–Blodgett films. *J Am Chem Soc* 120:1479–1484. <https://doi.org/10.1021/ja970577p>
324. Tachibana H, Goto A, Nakamura T, Matsumoto M, Manda E, Niino H, Yabe A, Kawabata Y (1989) Photoresponsive conductivity in Langmuir–Blodgett films. *Thin Solid Films* 179:207–213. [https://doi.org/10.1016/0040-6090\(89\)90184-3](https://doi.org/10.1016/0040-6090(89)90184-3)
325. Tachibana H, Nakamura T, Matsumoto M, Komizu H, Manda E, Niino H, Yabe A, Kawabata Y (1989) Photochemical switching in conductive Langmuir–Blodgett films. *J Am Chem Soc* 111:3080–3081. <https://doi.org/10.1021/ja00190a061>
326. Nishiyama K, Kurihara MA, Fujihira M (1989) Photochromism of an amphiphilic azobenzene derivative in its Langmuir–Blodgett films prepared as polyion complexes with ionic polymers. *Thin Solid Films* 179:477–483. [https://doi.org/10.1016/0040-6090\(89\)90224-1](https://doi.org/10.1016/0040-6090(89)90224-1)

327. Seki T, Tamaki T, Ichimura K, Aoki K (1989) Photochemical alignment regulation of a nematic liquid crystal by Langmuir-Blodgett layers of azobenzene polymers as "command surfaces". *Macromolecules* 22:3505–3506
328. Tachibana H, Azumi R, Nakamura T, Matsumoto M, Kawabata Y (1992) New types of photochemical switching phenomena in Langmuir-Blodgett films. *Chem Lett*:173–176. <https://doi.org/10.1246/cl.1992.173>
329. Tachibana H, Manda E, Azumi R, Nakamura T, Matsumoto M, Kawabata Y (1992) Multiple photochemical switching device based on Langmuir-Blodgett films. *Appl Phys Lett* 61:2420–2421. <https://doi.org/10.1063/1.108184>
330. Tachibana H, Manda E, Matsumoto M (1995) Conductivity switching of Langmuir-Blodgett films using photoisomerization of phenylazonaphthalene. *Mol Cryst Liq Cryst Sci Technol Sect A Mol Cryst Liq Cryst* 267:341–346. <https://doi.org/10.1080/10587259508034014>
331. Tachibana H, Azumi R, Tanaka M, Matsumoto M, Sako SI, Sakai H, Abe M, Kondo Y, Yoshino N (1996) Structures and photoisomerization of the polyion complex Langmuir-Blodgett films of an amphiphile bearing two azobenzene units. *Thin Solid Films* 284–285:73–75. [https://doi.org/10.1016/S0040-6090\(95\)08274-3](https://doi.org/10.1016/S0040-6090(95)08274-3)
332. Maack J, Ahuja RC, Möbius D, Tachibana H, Matsumoto M (1994) Molecular cis-trans switching in amphiphilic monolayers containing azobenzene moieties. *Thin Solid Films* 242:122–126. [https://doi.org/10.1016/0040-6090\(94\)90514-2](https://doi.org/10.1016/0040-6090(94)90514-2)
333. Shimura N, Ogawa M (2004) Preparation of aluminum-containing self-standing mesoporous silica films. *Bull Chem Soc Jpn* 77:1599–1606. <https://doi.org/10.1246/bcsj.77.1599>
334. Ogawa M, Fujii K, Kuroda K, Kato C (1991) Preparation of montmorillonite-*p*-aminoazobenzene intercalation compounds and their photochemical behavior. *Mater Res Soc Symp Proc* 233:89–94
335. Adams JM, Reid PI (1977) Azobenzene intercalates of montmorillonite. *Clay Clay Miner* 25:228–230
336. Ogawa M, Okutomo S, Kuroda K (1998) Control of interlayer microstructures of a layered silicate by surface modification with organochlorosilanes. *J Am Chem Soc* 120:7361–7362. <https://doi.org/10.1021/ja981055s>
337. Bujdák J, Iyi N, Fujita T (2003) Isomerization of cationic azobenzene derivatives in dispersions and films of layered silicates. *J Colloid Interface Sci* 262:282–289. [https://doi.org/10.1016/S0021-9797\(03\)00235-2](https://doi.org/10.1016/S0021-9797(03)00235-2)
338. Koteja A, Matusik J (2016) Preparation and characterization of azobenzene-smectite photoactive mineral nanomaterials. *Geol Geophys Environ* 41:99. <https://doi.org/10.7494/geol.2015.41.1.99>
339. Kosuge K, Yamazaki A, Tsunashima A, Otsuka R (1992) Hydrothermal synthesis of magadiite and kenyaite. *J Ceram Soc Jpn* 100:326–331. <https://doi.org/10.2109/jcersj.100.326>
340. Okutomo S, Kuroda K, Ogawa M (1999) Preparation and characterization of silylated-magadiites. *Appl Clay Sci* 15:253–264. [https://doi.org/10.1016/S0169-1317\(99\)00010-1](https://doi.org/10.1016/S0169-1317(99)00010-1)
341. Iyi N, Kurashima K, Fujita T (2002) Orientation of an organic anion and second-staging structure in layered double-hydroxide intercalates. *Chem Mater* 14:583–589. <https://doi.org/10.1021/cm0105211>
342. Nabetani Y, Takamura H, Uchikoshi A, Hassan SZ, Shimada T, Takagi S, Tachibana H, Masui D, Tong Z, Inoue H (2016) Photo-induced morphological winding and unwinding motion of nanoscrolls composed of niobate nanosheets with a polyfluoroalkyl azobenzene derivative. *Nanoscale* 8:12289–12293. <https://doi.org/10.1039/C6NR02177H>
343. Tong Z, Sasamoto S, Shimada T, Takagi S, Tachibana H, Zhang X, Tryk DA, Inoue H (2008) Preparation and photochemical behavior of polyfluorinated cationic azobenzene-titanoniobate intercalation compounds. *J Mater Chem* 18:4641. <https://doi.org/10.1039/b805879b>
344. Okada T, Sakai H, Ogawa M (2008) The effect of the molecular structure of a cationic azo dye on the photoinduced intercalation of phenol in a montmorillonite. *Appl Clay Sci* 40:187–192. <https://doi.org/10.1016/j.clay.2007.09.001>

345. Ogawa M, Kimura H, Kuroda K, Kato C (1996) Intercalation and the photochromism of azo dye in the hydrophobic interlayer spaces of organoammonium-fluor-tetrasilicic micas. *Clay Sci* 65:57–65. <https://doi.org/10.11362/jcssjclayscience1960.10.57>
346. Okada T, Nozaki N, Seo J, Kwon JE, Park SY, Hashizume H, Sasaki T, Ogawa M (2017) Photoinduced structural changes of cationic azo dyes confined in a two dimensional nanospace by two different mechanisms. *RSC Adv* 7:8077–8081. <https://doi.org/10.1039/C6RA27749G>
347. Ohtani O, Itoh T, Monna Y, Sasai R, Shichi T, Yui T, Takagi K (2005) Design of photofunctional laminated organized thin films: photochromism of ammoniumazobenzene arenecarboxylates cast on silica glass. *Bull Chem Soc Jpn* 78:698–702. <https://doi.org/10.1246/bcsj.78.698>
348. Umemoto T, Ohtani Y, Tsukamoto T, Shimada T, Takagi S (2014) Pinning effect for photoisomerization of a dicationic azobenzene derivative by anionic sites of the clay surface. *Chem Commun* 50:314–316. <https://doi.org/10.1039/c3cc47353h>
349. Fujita T, Iyi N, Klapyta Z (1998) Preparation of azobenzene-mica complex and its photoresponse to ultraviolet irradiation. *Mater Res Bull* 33:1693–1701
350. Ueda M, Kim HB, Ichimura K (1994) Photochemical and thermal isomerization of azobenzene derivatives in sol-gel bulk materials. *Chem Mater* 6:1771–1775. <https://doi.org/10.1021/cm00046a033>
351. Eisenbach CD (1978) Effect of polymer matrix on the *cis-trans* isomerization of azobenzene residues in bulk polymers. *Macromol Chem Phys* 179:2489–2506. <https://doi.org/10.1002/macp.1978.021791014>
352. Nabetani Y, Takamura H, Hayasaka Y, Sasamoto S, Tanamura Y, Shimada T, Masui D, Takagi S, Tachibana H, Tong Z, Inoue H (2013) An artificial muscle model unit based on inorganic nanosheet sliding by photochemical reaction. *Nanoscale* 5:3182–3193. <https://doi.org/10.1039/c3nr34308a>
353. Koteja A, Szczerba M, Matusik J (2017) Smectites intercalated with azobenzene and aminoazobenzene: structure changes at nanoscale induced by UV light. *J Phys Chem Solids* 111:294–303. <https://doi.org/10.1016/j.jpcs.2017.08.015>
354. Irie M, Fukaminato T, Matsuda K, Kobatake S (2014) Photochromism of diarylethene molecules and crystals: memories, switches, and actuators. *Chem Rev* 114:12174–12277
355. Taniguchi H, Shinpo A, Okazaki T, Matsui F, Irie M (1992) Photodegradation mechanism of photochromic diarylethene derivatives. *Nippon Kagaku Kaishi* 112:1138–1140. <https://doi.org/10.1246/nikkashi.1992.1138>
356. Irie M, Lifka T, Uchida K, Kobatake S, Shindo Y (1999) Fatigue resistant properties of photochromic dithienylethenes: by-product formation. *Chem Commun*:747–748
357. Higashiguchi K, Matsuda K, Kobatake S, Yamada T, Kawai T, Irie M (2000) Fatigue mechanism of photochromic 1,2-bis(2,5-dimethyl-3-thienyl)perfluorocyclopentene. *Bull Chem Soc Jpn* 73:2389–2394. <https://doi.org/10.1246/bcsj.73.2389>
358. Yokoyama S, Hirose T, Matsuda K (2015) Photoinduced four-state three-step ordering transformation of photochromic terthiophene at a liquid/solid interface based on two principles: photochromism and polymorphism. *Langmuir* 31:6404–6414. <https://doi.org/10.1021/acs.langmuir.5b01404>
359. Frath D, Sakano T, Imaizumi Y, Yokoyama S, Hirose T, Matsuda K (2015) Diarylethene self-assembled monolayers: cocrystallization and mixing-induced cooperativity highlighted by scanning tunneling microscopy at the liquid/solid interface. *Chem A Eur J* 21:11350–11358. <https://doi.org/10.1002/chem.201500804>
360. Fukumoto S, Nakashima T, Kawai T (2011) Photon-quantitative reaction of a dithiazolylarylene in solution. *Angew Chem Int Ed* 50:1565–1568. <https://doi.org/10.1002/anie.201006844>
361. Iijima S, Nakashima T, Kawai T (2016) Stereoselective photoreaction in P-stereogenic dithiazolylbenzo[*b*]phosphole chalcogenides. *New J Chem* 40:10048–10055. <https://doi.org/10.1039/c6nj02446g>

362. Yokoyama Y, Shiozawa T, Tani Y, Ubukata T (2009) A unified strategy for exceptionally high diastereoselectivity in the photochemical ring closure of chiral diarylethenes. *Angew Chem Int Ed* 48:4521–4523. <https://doi.org/10.1002/anie.200901156>
363. Yokoyama Y, Hasegawa T, Ubukata T (2011) Highly diastereoselective photochromic ring closure of bisbenzothienylethenes possessing dual fluorinated stereocontrollers. *Dyes Pigments* 89:223–229. <https://doi.org/10.1016/j.dyepig.2010.03.008>
364. Okada H, Nakajima N, Tanaka T, Iwamoto M (2005) Improvement in photocyclization efficiency of diaryl ethenes by adjusting the pore size of mesoporous silica. *Angew Chem Int Ed* 44:7233–7236. <https://doi.org/10.1002/anie.200501992>
365. Fukagawa M, Kawamura I, Ubukata T, Yokoyama Y (2013) Enantioselective photochromism of diarylethenes in human serum albumin. *Chem A Eur J* 19:9434–9437. <https://doi.org/10.1002/chem.201301459>
366. Sasai R, Ogiso H, Shindachi I, Shichi T, Takagi K (2000) Photochromism in oriented thin films prepared by the hybridization of diarylethenes in clay interlayers. *Tetrahedron* 56:6979–6984. [https://doi.org/10.1016/S0040-4020\(00\)00519-6](https://doi.org/10.1016/S0040-4020(00)00519-6)
367. Sasai R, Itoh H, Shindachi I, Shichi T, Takagi K (2001) Photochromism of clay - diarylethene hybrid materials in optically transparent gelatin films. *Chem Mater* 13:2012–2016. <https://doi.org/10.1021/cm000822v>
368. Shindachi I, Hanaki H, Sasai R, Shichi T, Yui T, Takagi K (2004) The effect of layered sodium-magadiite on the photochromic reversibility of diarylethene immobilized on its surfaces. *Chem Lett* 33:1116–1117. <https://doi.org/10.1246/cl.2004.1116>
369. Shindachi I, Hanaki H, Sasai R, Shichi T, Yui T, Takagi K (2007) Preparation and photochromism of diarylethene covalently bonded onto layered sodium-magadiite surfaces. *Res Chem Intermed* 33:143–153. <https://doi.org/10.1163/156856707779160870>
370. Klajn R (2014) Spiropyran-based dynamic materials. *Chem Soc Rev* 43:148–184. <https://doi.org/10.1039/C3CS60181A>
371. Wojtyk JTC, Wasey A, Kazmaier PM, Hoz S, Bunzel E (2000) Thermal reversion mechanism of *N*-functionalized merocyanines to spiropyrans: a solvatochromic, solvatokinetic, and semi-empirical study. *J Phys Chem A* 104:9046–9055. <https://doi.org/10.1021/jp001533x>
372. Shimizu I, Kokado H, Inoue E (1969) Photoreversible photographic systems. V. Reverse photochromism of (photospiran/acid) system in acetone. *Bull Chem Soc Jpn* 42:1726–1729. <https://doi.org/10.1246/bcsj.42.1726>
373. Raymo FM, Giordani S (2001) Signal processing at the molecular level. *J Am Chem Soc* 123:4651–4652. <https://doi.org/10.1021/ja005699n>
374. Yamaguchi T, Ogawa M (2018) Photochromism of a spiropyran in the presence of a synthetic hectorite. *Chem Lett* 47:189–191. <https://doi.org/10.1246/cl.170982>
375. Mitchell RH, Ward TR, Chen Y, Wang Y, Weerawarna SA, Dibble PW, Marsella MJ, Almutairi A, Wang Z (2003) Synthesis and photochromic properties of molecules containing [e] -annelated dihydropyrenes. two and three way π -switches based on the valence isomerization. *J Am Chem Soc* 125:2974–2988
376. Honda K, Komizu H, Kawasaki M (1982) Reverse photochromism of stenhouse salts. *J Chem Soc Chem Commun*:253. <https://doi.org/10.1039/c39820000253>
377. Lerch MM, Szymański W, Feringa BL (2018) The (photo)chemistry of stenhouse photoswitches: guiding principles and system design. *Chem Soc Rev* 47:1910–1937. <https://doi.org/10.1039/c7cs00772h>
378. Hatano S, Horino T, Tokita A, Oshima T, Abe J (2013) Unusual negative photochromism via a short-lived imidazolyl radical of 1,1'-binaphthyl-bridged imidazole dimer. *J Am Chem Soc* 135:3164–3172. <https://doi.org/10.1021/ja311344u>
379. Yamaguchi T, Kobayashi Y, Abe J (2015) Fast negative photochromism of 1,1'-binaphthyl-bridged phenoxyl–imidazolyl radical complex. *J Am Chem Soc* 138:906–913. <https://doi.org/10.1021/jacs.5b10924>

380. Yamaguchi T, Ogawa M (2018) Hydrophilic internal pore and hydrophobic particle surface of organically modified mesoporous silica particle to host photochromic molecules. *Chem Lett* 48:170–172
381. Yamaguchi T, Maity A, Polshettiwar V, Ogawa M (2018) Negative photochromism based on molecular diffusion between hydrophilic and hydrophobic particles in the solid-state. *Inorg Chem* 57:3671–3674
382. Yamaguchi T, Leelapaththaraphan NN, Shin H, Ogawa M (2019) Acceleration of photochromism and negative photochromism by the interactions with mesoporous silicas. *Photochem Photobiol Sci* 18:1742–1749. <https://doi.org/10.1039/C9PP00081J>
383. Schomburg C, Wark M, Rohlfling Y, Schulz-Ekloff G, Wöhrle D (2001) Photochromism of spiropyran in molecular sieve voids: effects of host–guest interaction on isomer status, switching stability and reversibility. *J Mater Chem* 11:2014–2021. <https://doi.org/10.1039/b101516h>
384. Casades I, Constantine S, Cardin D, García H, Gilbert A, Márquez F (2000) Ship-in-a-bottle synthesis and photochromism of spiropyran encapsulated within zeolite Y supercages. *Tetrahedron* 56:6951–6956. [https://doi.org/10.1016/S0040-4020\(00\)00515-9](https://doi.org/10.1016/S0040-4020(00)00515-9)
385. Kahle I, Spange S (2010) Internal and external acidity of faujasites as measured by a solvatochromic spiropyran. *J Phys Chem C* 114:15448–15453. <https://doi.org/10.1021/jp1048106>
386. Tagaya H, Kuwahara T, Sato S, Kadokawa J, Karasu M, Chiba K (1993) Photoisomerization of indolinespirobenzopyran in layered double hydroxides. *J Mater Chem* 3:317. <https://doi.org/10.1039/jm9930300317>
387. Tagaya H, Sato S, Kuwahara T, Kadokawa J, Masa K, Chibaa K (1994) Photoisomerization of Indolinespirobenzopyran in anionic clay matrices of layered double hydroxides. *J Mater Chem* 4:1907. <https://doi.org/10.1039/jm9940401907>
388. Aiken S, Edgar RJL, Gabbutt CD, Heron BM, Hobson PA (2018) Negatively photochromic organic compounds: exploring the dark side. *Dyes Pigments* 149:92–121. <https://doi.org/10.1016/j.dyepig.2017.09.057>
389. Kinashi K, Kita H, Misaki M, Koshiba Y, Ishida K, Ueda Y, Ishihara M (2009) Fabrication and optical properties of photochromic compound/clay hybrid films. *Thin Solid Films* 518:651–655. <https://doi.org/10.1016/j.tsf.2009.07.042>
390. Saso N, Yamamoto T, Umemura Y, Einaga Y (2008) Normal photochromism of spiropyran in montmorillonite interlayer. *Colloids Surf A Physicochem Eng Asp* 317:309–315. <https://doi.org/10.1016/j.colsurfa.2007.10.036>
391. Seki T, Ichimura K (1990) Thermal isomerization behaviors of a spiropyran in bilayers immobilized with a linear polymer and a smectitic clay. *Macromolecules*:31–35
392. Takagi K, Kurematsu T, Sawaki Y (1995) Photochromic behaviour of surfactant spiro[2*H*-1-benzopyran-2,2′-[2,3]-dihydroindole]s (spiropyran) adsorbed into clay interlayers. *J Chem Soc Perkin Trans 2*:1667–1671. <https://doi.org/10.1039/P29950001667>
393. Mal NK, Fujiwara M, Tanaka Y (2003) Photocontrolled reversible release of guest molecules from coumarin-modified mesoporous silica. *Nature* 421:350–353. <https://doi.org/10.1038/nature01337.1>
394. Bach T (1998) Stereoselective intermolecular [2+2]-photocycloaddition reactions and their application in synthesis. *Synthesis*:683–703
395. González-López M, Shaw JT (2009) Cyclic anhydrides in formal cycloadditions and multicomponent reactions. *Chem Rev* 109:164–189. <https://doi.org/10.1021/cr8002714>
396. Laszlo P, Lucchetti J (1984) Catalysis of the diels-alder reaction in the presence of clays. *Tetrahedron Lett* 25:1567–1570. [https://doi.org/10.1016/S0040-4039\(01\)90012-7](https://doi.org/10.1016/S0040-4039(01)90012-7)
397. Laszlo P, Lucchetti J (1984) Acceleration of the diels-alder reaction by clays suspended in organic solvents. *Tetrahedron Lett* 25:2147–2150. [https://doi.org/10.1016/S0040-4039\(01\)81184-9](https://doi.org/10.1016/S0040-4039(01)81184-9)
398. Valentine D, Turro NJ, Hammond GS (1964) Thermal and photosensitized dimerizations of cyclohexadiene. *J Am Chem Soc* 86:5202–5208. <https://doi.org/10.1021/ja01077a033>

399. Schuster DI, Lem G, Kaprinidis NA (1993) New insights into an old mechanism: [2 + 2] photocycloaddition of enones to alkenes. *Chem Rev* 93:3–22. <https://doi.org/10.1021/cr00017a001>
400. Usami H, Takagi K, Sawaki Y (1992) Regioselective photocyclodimerization of cyclohexenones intercalated on clay layers. *Chem Lett* 21:1405–1408. <https://doi.org/10.1246/cl.1992.1405>
401. Madhavan D, Pitchumani K (2002) Photodimerisation of enones in a clay microenvironment. *Photochem Photobiol Sci* 1:991–995. <https://doi.org/10.1039/b208030c>
402. Takagi K, Usami H, Fukaya H, Sawaki Y (1989) Spatially controlled photocycloaddition of a clay-intercalated stilbazolium cation. *J Chem Soc Chem Commun*:1174. <https://doi.org/10.1039/c39890001174>
403. Usami H, Takagi K, Sawaki Y (1990) Controlled photocycloaddition of stilbazolium ions intercalated in saponite clay layers. *J Chem Soc Perkin Trans 2*:1723. <https://doi.org/10.1039/p29900001723>
404. Usami H, Takagi K, Sawaki Y (1992) Clay-inclusion photocyclodimerization: intercalation and migration of stilbazolium ions. *J Chem Soc Faraday Trans 88*:77–81. <https://doi.org/10.1039/FT9928800077>
405. Nakahira T, Hama M, Fukuchi O, Okamura T, Iwabuchi S, Shimazu S, Uematsu T, Kikuchi H (1995) Control of photochemistry of stilbazolium ion by adsorption to poly(potassium vinylsulfate) and to hectorite clay. *Macromol Rapid Commun* 16:717–723. <https://doi.org/10.1002/marc.1995.030161003>
406. Shichi T, Takagi K, Sawaki Y (1996) Organized photocycloaddition of 4-benzoylbenzoate with unsaturated carboxylates in hydrotalcite clay interlayers. *Chem Lett* 25:781–782. <https://doi.org/10.1246/cl.1996.781>
407. Takagi K, Nakamura T, Katsu H, Itoh M, Sawaki Y, Imae T (1996) Photochemical cyclodimerization of cinnamic acids included in surfactant amine oxides. *Mol Cryst Liq Cryst Sci Technol Sect A Mol Cryst Liq Cryst* 276–277:135–138. <https://doi.org/10.1080/10587259608046014>
408. Elsherbiny AS, Salem MA, Ismail AA (2012) Influence of the alkyl chain length of cyanine dyes on their adsorption by Na⁺-montmorillonite from aqueous solutions. *Chem Eng J* 200–202:283–290. <https://doi.org/10.1016/j.cej.2012.06.050>
409. Yui T, Takagi K, Inoue H (2018) Microscopic environment and molecular orientation of guest molecules within polyfluorinated surfactant and clay hybrids: photochemical studies of stilbazolium derivatives. *J Photochem Photobiol A Chem* 363:61–67. <https://doi.org/10.1016/j.jphotochem.2018.05.022>
410. Zhong J, Cui X, Guan W, Lu C (2018) Direct observation of adsorption kinetics on clays by cation- π interaction-triggered aggregation luminescence. *J Mater Chem C* 6:13218–13224. <https://doi.org/10.1039/c8tc04837a>
411. Sasai R, Shin'ya N, Shichi T, Takagi K, Gekko K (2002) Molecular alignment and photodimerization of 4'-Chloro-4-stilbenecarboxylic acid in hydrotalcite clays: bilayer formation in the interlayers. *Langmuir* 15:413–418. <https://doi.org/10.1021/a980699a>
412. Shichi T, Yamashita S, Takagi K (1998) Photopolymerization of 4-vinylbenzoate and *m*- and *p*-phenylenediacrylates in hydrotalcite interlayers. *Supramol Sci* 5:303–308. [https://doi.org/10.1016/S0968-5677\(98\)00023-6](https://doi.org/10.1016/S0968-5677(98)00023-6)
413. Kalo H, Möller MW, Kunz DA, Breu J (2012) How to maximize the aspect ratio of clay nanoplatelets. *Nanoscale* 4:5633–5639. <https://doi.org/10.1039/c2nr31322g>
414. Hofmann U, Klemen R (1950) Verlust der Austauschfähigkeit von Lithiumionen an Bentonit durch Erhitzung. *Zeitschrift für Anorg Chemie* 262:95–99. <https://doi.org/10.1002/zaac.19502620114>
415. Zemanová M, Link G, Takayama S, Nüesch R, Janek M (2006) Modification of layer charge in smectites by microwaves. *Appl Clay Sci* 32:271–282. <https://doi.org/10.1016/j.clay.2006.01.002>

416. Skoubris EN, Chryssikos GD, Christidis GE, Gionis V (2013) Structural characterization of reduced-charge montmorillonites. Evidence based on FTIR spectroscopy, thermal behavior, and layer-charge systematics. *Clays Clay Miner* 61:83–97. <https://doi.org/10.1346/CCMN.2013.0610207>
417. Takahashi K, Ishii R, Suzuki A, Nakamura T, Yoshida M, Ebina T (2017) Preparation of Lignin–Montmorillonite nanocomposite films and its characterization for electronic devices. *Clay Sci* 21:1–6. https://doi.org/10.11362/jcssjclayscience.21.1_1
418. Ramamurthy V, Sivaguru J (2016) Supramolecular photochemistry as a potential synthetic tool: photocycloaddition. *Chem Rev* 116:9914–9993. <https://doi.org/10.1021/acs.chemrev.6b00040>
419. Ramamurthy V, Corbin DR, Kumar CV, Turro NJ (1990) Modification of photochemical reactivity by zeolites: cation controlled photodimerisation of acenaphthylene within faujasites. *Tetrahedron Lett* 31:47–50. [https://doi.org/10.1016/S0040-4039\(00\)94330-2](https://doi.org/10.1016/S0040-4039(00)94330-2)
420. Lalitha A, Pitchumani K, Srinivasan C (2000) Photodimerization of *trans*-2-styrylpyridine in zeolite cages. *J Photochem Photobiol A Chem* 134:193–197. [https://doi.org/10.1016/S1010-6030\(00\)00271-9](https://doi.org/10.1016/S1010-6030(00)00271-9)
421. Kim SW, Son SU, Lee SI, Hyeon T, Chung YK (2000) Cobalt on mesoporous silica: the first heterogeneous pauson-khand catalyst. *J Am Chem Soc* 122:1550–1551. <https://doi.org/10.1021/ja9939237>
422. Matsuo Y, Fukunaga T, Fukutsuka T, Sugie Y (2002) Photochemical dimerization of acenaphthylene in hydrophobized graphite oxide. *Mol Cryst Liq Cryst Sci Technol Sect A Mol Cryst Liq Cryst* 386:45–50. <https://doi.org/10.1080/10587250290113178>
423. Heinz H, Vaia RA, Koerner H, Farmer BL (2008) Photoisomerization of azobenzene grafted to layered silicates: simulation and experimental challenges. *Chem Mater* 20:6444–6456. <https://doi.org/10.1021/cm801287d>
424. Tong Z, Takagi S, Shimada T, Tachibana H, Inoue H (2006) Photoresponsive multilayer spiral nanotubes: intercalation of polyfluorinated cationic azobenzene surfactant into potassium niobate. *J Am Chem Soc* 128:684–685. <https://doi.org/10.1021/ja0564564>
425. Nabetani Y, Takamura H, Hayasaka Y, Shimada T, Takagi S, Tachibana H, Masui D, Tong Z, Inoue H (2011) A Photoactivated artificial muscle model unit: reversible, photoinduced sliding of nanosheets. *J Am Chem Soc* 133:17130–17133. <https://doi.org/10.1021/ja207278t>
426. Guo W, Yu C, Li S, Yang J, Liu Z, Zhao C, Huang H, Zhang M, Han X, Niu Y, Qiu J (2017) High-stacking-density, superior-roughness LDH bridged with vertically aligned graphene for high-performance asymmetric supercapacitors. *Small* 13:1–9. <https://doi.org/10.1002/smll.201701288>
427. Chen T, Xu S, Zhang F, Evans DG, Duan X (2009) Formation of photo- and thermo-stable layered double hydroxide films with photo-responsive wettability by intercalation of functionalized azobenzenes. *Chem Eng Sci* 64:4350–4357. <https://doi.org/10.1016/j.ces.2009.07.005>
428. Zhang F, Zhao L, Chen H, Xu S, Evans DG, Duan X (2008) Corrosion resistance of superhydrophobic layered double hydroxide films on aluminum. *Angew Chem Int Ed* 47:2466–2469. <https://doi.org/10.1002/anie.200704694>
429. Uchida K, Izumi N, Sukata S, Kojima Y, Nakamura S, Irie M (2006) Photoinduced reversible formation of microfibrils on a photochromic diarylethene microcrystalline surface. *Angew Chem Int Ed* 45:6470–6473. <https://doi.org/10.1002/anie.200602126>
430. Wang S, Song Y, Jiang L (2007) Photoresponsive surfaces with controllable wettability. *J Photochem Photobiol C: Photochem Rev* 8:18–29. <https://doi.org/10.1016/j.jphotochemrev.2007.03.001>
431. Kashima I, Okubo M, Qno Y, Itoi M, Kida N, Hikita M, Enomoto M, Kojima N (2005) Ferromagnetism and its photo-induced effect in 2D Iron mixed-valence complex coupled with photochromic spiropyran. *Synth Met* 155:703–706. <https://doi.org/10.1016/j.synthmet.2005.09.033>

432. Enomoto M, Kojima N (2005) Charge transfer phase transition and ferromagnetism in a novel iron mixed-valence complex $(n\text{-C}_3\text{H}_7)_4\text{N}[\text{Fe}^{\text{II}}\text{Fe}^{\text{III}}(\text{tto})_3]$ ($\text{tto}=\text{C}_2\text{O}_2\text{S}_2$). *Synth Met* 152:457–460. <https://doi.org/10.1016/j.synthmet.2005.07.177>
433. Kida N, Hikita M, Kashima I, Enomoto M, Itoi M, Kojima N (2009) Mössbauer spectroscopic study of photo-sensitive organic-inorganic hybrid system, $(\text{SP})[\text{Fe}^{\text{II}}\text{Fe}^{\text{III}}(\text{dto})_3]$ ($\text{dto}=\text{C}_2\text{O}_2\text{S}_2$, SP = spiropyran). *Polyhedron* 28:1694–1697. <https://doi.org/10.1016/j.poly.2008.10.060>
434. Kida N, Hikita M, Kashima I, Okubo M, Itoi M, Enomoto M, Kato K, Takata M, Kojima N (2009) Control of charge transfer phase transition and ferromagnetism by photoisomerization of spiropyran for an organic-inorganic hybrid system, $(\text{SP})[\text{Fe}^{\text{II}}\text{Fe}^{\text{III}}(\text{dto})_3]$ (SP = spiropyran, $\text{dto}=\text{C}_2\text{O}_2\text{S}_2$). *J Am Chem Soc* 131:212–220. <https://doi.org/10.1021/ja806879a>
435. Tanaka N, Okazawa A, Sugahara A, Kojima N (2015) Development of a photoresponsive organic-inorganic hybrid magnet: layered cobalt hydroxides intercalated with spiropyran anions. *Bull Chem Soc Jpn* 88:1150–1155. <https://doi.org/10.1246/bcsj.20150129>
436. Abellán G, Coronado E, Martí-Gastaldo C, Ribera A, Jordá JL, García H (2014) Photo-switching in a hybrid material made of magnetic layered double hydroxides intercalated with azobenzene molecules. *Adv Mater* 26:4156–4162. <https://doi.org/10.1002/adma.201400713>
437. Abellán G, Jordá JL, Atienzar P, Varela M, Jaafar M, Gómez-Herrero J, Zamora F, Ribera A, García H, Coronado E (2015) Stimuli-responsive hybrid materials: breathing in magnetic layered double hydroxides induced by a thermoresponsive molecule. *Chem Sci* 6:1949–1958. <https://doi.org/10.1039/C4SC03460K>
438. Okubo M, Enomoto M, Kojima N (2005) Study on photomagnetism of 2-D magnetic compounds coupled with photochromic diarylethene cations. *Synth Met* 152:461–464. <https://doi.org/10.1016/j.synthmet.2005.07.181>
439. Shimizu H, Okubo M, Nakamoto A, Enomoto M, Kojima N (2006) Enhancement of the curie temperature by isomerization of diarylethene (DAE) for an organic-inorganic hybrid system: $\text{Co}_4(\text{OH})_7(\text{DAE})_{0.5}\cdot 3\text{H}_2\text{O}$. *Inorg Chem* 45:10240–10247. <https://doi.org/10.1021/ic061498u>
440. Kojima N, Okubo M, Shimizu H, Enomoto M (2007) Control of magnetism by isomerization of intercalated molecules in organic-inorganic hybrid systems. *Coord Chem Rev* 251:2665–2673. <https://doi.org/10.1016/j.ccr.2007.08.025>
441. Abellán G, Coronado E, Martí-Gastaldo C, Waerenborgh J, Ribera A (2013) Interplay between chemical composition and cation ordering in the magnetism of Ni/Fe layered double hydroxides. *Inorg Chem* 52:10147–10157. <https://doi.org/10.1021/ic401576q>
442. Kojima N, Aoki W, Itoi M, Ono Y, Seto M, Kobayashi Y, Maeda Y (2001) Charge transfer phase transition and ferromagnetism in a mixed-valence iron complex, $(n\text{-C}_3\text{H}_7)_4\text{N}[\text{Fe}^{\text{II}}\text{Fe}^{\text{III}}(\text{dto})_3]$ ($\text{dto}=\text{C}_2\text{O}_2\text{S}_2$). *Solid State Commun* 120:165–170. [https://doi.org/10.1016/S0038-1098\(01\)00366-0](https://doi.org/10.1016/S0038-1098(01)00366-0)
443. Ono Y, Okubo M, Kojima N (2003) Crystal structure and ferromagnetism of $(n\text{-C}_3\text{H}_7)_4\text{N}[\text{Co}^{\text{II}}\text{Fe}^{\text{III}}(\text{dto})_3]$ ($\text{dto}=\text{C}_2\text{O}_2\text{S}_2$). *Solid State Commun* 126:291–296. [https://doi.org/10.1016/S0038-1098\(02\)00825-6](https://doi.org/10.1016/S0038-1098(02)00825-6)
444. Carrasco JA, Abellán G, Coronado E (2018) Influence of morphology in the magnetic properties of layered double hydroxides. *J Mater Chem C* 6:1187–1198. <https://doi.org/10.1039/c7tc05569b>
445. Hornick C, Rabu P, Drillon M (2000) Hybrid organic-inorganic multilayer materials: influence of π electrons as magnetic media in a series of bridged-layer compounds $\text{M}_2(\text{OH})_{4-x}\text{A}_{x/2}$ ($\text{M}=\text{Cu}(\text{II})$ or $\text{Co}(\text{II})$, $a=\text{dicarboxylate anion}$). *Polyhedron* 19:259–266. [https://doi.org/10.1016/S0277-5387\(99\)00355-1](https://doi.org/10.1016/S0277-5387(99)00355-1)
446. Matsuda K, Irie M (2000) Photoswitching of intramolecular magnetic interaction: a diarylethene photochromic spin coupler. *Chem Lett* 29:16–17. <https://doi.org/10.1246/cl.2000.16>

447. Bousquet D, Peltier C, Masselin C, Jacquemin D, Adamo C, Ciofini I (2012) A DFT study of magnetic interactions in photoswitchable systems. *Chem Phys Lett* 542:13–18. <https://doi.org/10.1016/j.cplett.2012.05.040>
448. Okada T, Morita T, Ogawa M (2005) Tris(2,2'-bipyridine)ruthenium(II)-clays as adsorbents for phenol and chlorinated phenols from aqueous solution. *Appl Clay Sci* 29:45–53. <https://doi.org/10.1016/j.clay.2004.09.004>
449. Seki Y, Ide Y, Okada T, Ogawa M (2015) Concentration of 2-phenylphenol by organoclays from aqueous sucrose solution. *Appl Clay Sci* 109–110:64–67. <https://doi.org/10.1016/j.clay.2014.12.021>
450. Yamaguchi T, Maity A, Polshettiwar V, Ogawa M (2017) Photochromism of a spiropyran in the presence of a dendritic fibrous nanosilica; simultaneous photochemical reaction and adsorption. *J Phys Chem A* 121:8080–8085. <https://doi.org/10.1021/acs.jpca.7b08466>
451. Yamaguchi T, Ogawa M (2018) Hydrophilic internal pore and hydrophobic particle surface of organically modified mesoporous silica particle to host photochromic molecules. *Chem Lett* 48:170–172. <https://doi.org/10.1246/cl.180908>
452. Okabe Y, Ogawa M (2015) Photoinduced adsorption of spiropyran into mesoporous silicas as photomerocyanine. *RSC Adv* 5:101789–101793. <https://doi.org/10.1039/C5RA18252B>

Photophysicochemical Processes Directed Within Nano-Containers



Mahesh Pattabiraman and Arunkumar Natarajan

Contents

1	Introduction	324
2	Host-Guest Chemistry and Nano-Containers	325
3	Fluorescence	327
4	Phosphorescence	331
5	Twisted-Intramolecular Charge Transfer	338
6	Excimers and Exciplexes	343
7	Energy Transfer Cascade	349
8	Singlet Oxygen	351
9	Photocycloaddition Reactions Within Cavitands	355
10	Photo-Fries Rearrangement	361
11	Conclusion and Future Perspectives	363
	References	364

Abstract Directing excited-state behavior of photoactive molecules without covalent modification has been more frequently achieved through inclusion within cavitands than by any other supramolecular approach. Such efforts have led to interesting photophysicochemical phenomena and their applications. This includes employing strategies such as use of chromo-/luminophore-cavitand interactions to perturb the electronic states to affect quantum efficiencies of radiative processes or structural pre-orientation of reactants to achieve chemoselectivity. The influence of nano-containers such as macrocyclic cavitands, nanocages, and capsules on the photoactive molecules has been observed in solution phase as well as the solid state, which has been studied through spectroscopy, product selectivity analysis, and computational chemistry. This chapter will highlight prominent works in the past

M. Pattabiraman (✉)
Department of Chemistry, University of Nebraska Kearney, Kearney, NE, USA
e-mail: pattabiramm2@unk.edu

A. Natarajan
GE Aviation, West Chester, OH, USA
e-mail: natararu@ge.com

two decades that studied the nano-container-photoactive guest systems whose significance extends well beyond the domain of supramolecular photochemistry. The crucial nature of such works in gaining new insight into electronic, bonding, and dynamics nature of chemical interactions or their role in realizing new applications is discussed herein. The contents are organized on the basis of named photochemical reactions or photophysical activity affected through nano-container mediation contrasted with that of the free chromophore or luminophore. Three cavitands (families) cyclodextrins, cucurbiturils, and octa acids are primarily focused due to their literature predominance leading to a comprehensive understanding of their effects, with relatively less frequent instances of calixarenes and crown-ethers. Differences in physicochemical influences affected by the various cavitand families as well as that within the oligomers of a given family will be discussed wherever possible, and diversity in such effects is analyzed on the basis of “supramolecular cause-and-effect” relationship.

Keywords Cavitands · Cucurbiturils · Cyclodextrins · Excited state · Fluorescence · Molecular orbitals · Octa acid · Phosphorescence · Photochemistry · Photophysics · Singlet · Supramolecular chemistry · Triplet

Abbreviations

α -CD	α -cyclodextrin
β -CD	β -cyclodextrin
γ -CD	γ -cyclodextrin
λ_{fl}	Fluorescence wavelength
τ_F	Fluorescence lifetime
Φ	Quantum yield
Φ_F	Fluorescence quantum yield
ACN	Acenaphthylene
ADT	Adamantathione
ANT	Anthracene
aPS	Activatable photosensitizers
BP	Biphenyl bipyridinium guest
CA	Cinnamic acid
CB	Cucurbituril
CB7	Cucurbit[7]uril
CB8	Cucurbit[8]uril
CD	Cyclodextrin
CE	Crystal engineering
CHT	Camphorhione
Coum-n	Coumarins
D-A	Donor-acceptor
DBA	Dibenzal acetone
DMABN	N,N-Dimethylaminobenzonitrile

DNC	Dinaphthyl crown ether
E*	Excimer
FNT	Fenchthione
HH	Head-to-head
HOMO	Highest occupied molecular orbital
HT	Head-to-tail
IC	Internal conversion
ISC	Intersystem crossing
ITC	Intramolecular charge transfer
L	Linker
LE	Local excited state
LUMO	Lowest unoccupied molecular orbital
M*	Excited-state monomer
MM	Molecular mechanics
MO	Molecular orbital
NBS	N-benzyl succinimide
NpE	Naphthyl benzoates
NPM	N-phenylmaleimide
OA	Octa acid
OAm	Octa amine
P*	Excited-state product
PAH	Polyaromatic hydrocarbon
PCA	Photocycloaddition
Pd-NC	Palladium nanocage
PDT	Photodynamic therapy
Py	Pyrene
R*	Excited-state reactant
RH	Rebek's host
RTP	Room temperature phosphorescence
SOG	Singlet oxygen generator
SQ	Squaraines
STB	4,4'-dimethyl stilbene
ST-n	Stilbazole guests
TB-B	Biotinylated toluidine blue
TF	Thioflavin
TICT	Twisted intramolecular charge transfer
TP ⁺	2,4,6-triphenylpyrylium
TPOR	Tetranaphthyl-substituted porphyrin
VSEPR	Valence shell electron pair repulsion

1 Introduction

Photochemistry is the study of physical and chemical processes following absorption of photons; it aims to understand the electronic and structural characteristics of the molecule in excited state and deduce mechanism of chemical change. Since its formal recognition as a separate field of study that had begun in the earlier half of the eighteenth century, photochemistry has provided fundamental insights regarding the chemical nature of matter: structure and electronic properties of electronically excited species [1, 2]. This has also resulted in technological advancements ranging from photonic devices and high-density storage media to nanocircuits, synthetic transformations, and drug delivery systems [3, 4]. As a complementary science to ground-state reactions driven by thermal energy, photochemistry also possesses several complementary advantages over ground-state reactions: light being a concentrated form of energy, chromophoric transparency, functional group specificity, faster mechanistic timescales, low operating temperature, access to highly strained structures, etc. However, the awesome potential of photochemistry was not fully realized until the emergence of the subdiscipline of supramolecular photochemistry. The ability of weak intermolecular interaction to control molecular structure in the excited state has provided a new dimension of exploration and exploitation of this field. Manipulation of electronic and structural properties of photoactive molecules in ground and excited state has allowed photochemists to study previously unobserved phenomena, which were predicted but were not realized.

Unlike thermal organic reactions where functional group chemistry is generally consistent and predictable based on qualitative valence shell electron repulsion (VSEPR) considerations, photochemical reactions are difficult to predict due to high sensitivity to electronic structure and need for knowledge of molecular orbitals (MOs), which cannot be deduced without rigorous mathematical treatment of molecular systems. Supramolecular photochemistry has served as a useful means for predicting the feasibility of reactions and phenomena on several occasions. Thus, the influence of supramolecular chemistry on photochemical reactions has led to a great expansion of the significance of the latter field as a science for understanding the chemical nature of the natural world.

Supramolecular interactions have been utilized for controlling ground- [5] and excited-state property of chemical entities [6–8]. Several supramolecular approaches exist for dictating molecular behavior: inter and intramolecular weak interactions in solid state [9–13], mechanical interlocking [14, 15], and host-guest chemistry [12, 16, 17]. Among these approaches, host-guest approach to controlling structure and directing chemical dynamics has been responsible for the most progress made in supramolecular photochemistry [6, 18]. A molecular host is a chemical framework that encapsulates a relatively smaller entity, wholly or partly [16, 19, 20]. As an associative phenomenon, host-guest complexation is driven by either attractive weak interactions between host and guest or repulsive solvophobic interactions between host or guest and the surrounding medium. Molecular host systems such as cavitands [21–24], micelles [25, 26], and microporous materials such as zeolites [27, 28] and

metal organic frameworks [29] have enabled exploration of otherwise unexplored aspects of excited-state processes. The range of photoreactions explored within cavitands is wide, and their utility in understanding fundamental aspects of photochemistry is profound. Comparison of photophysical events of free and encapsulated molecules has provided innate understanding about the electronic properties of excited states; such efforts have also benefited the supramolecular community as the interpretation of observed deviation from photochemistry of nascent chromophores providing insight into the nature of supramolecular interactions that drive that change. On the applied side, host-guest interactions have provided the niche required for realizing photochemical technologies [30–32]. This chapter will present a conceptual overview of the fundamental science underlying the latest advancement in the field of supramolecular chemistry.

2 Host-Guest Chemistry and Nano-Containers

Encapsulation of photoactive guest molecules within macrocyclic hosts has been a very efficient and simple approach to directing molecular behavior (Fig. 1). The advantage of host-guest approach over others derives from the convenience due to reversibility and qualitative predictability of complex structure. If a specific photoactive guest structure is desired at ground or excited state to achieve a directed photochemical outcome, host-guest approach contains the necessary interactions in the supramolecular toolkit. Formation of host-guest inclusion complex is driven by two types of interactions: attractive host-guest and/or solvophobic interactions. Combination of host-guest, guest-guest, host-solvent, and guest-solvent interactions has been skillfully employed by chemists to precisely control excited-state behavior. Unlike solid- and crystalline state supramolecular interactions, which are difficult to predict due to the numerous interactions, inclusion complexes have fewer interactions, which confer greater predictability and control.

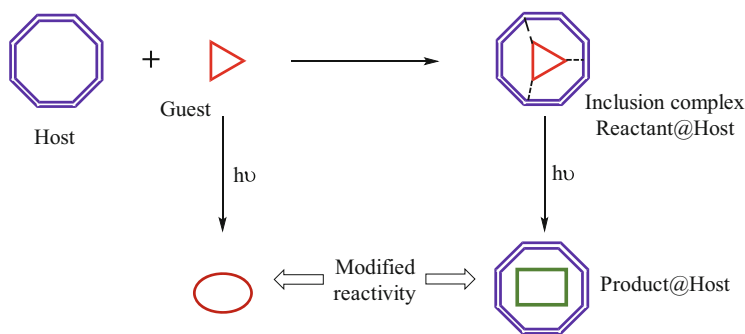


Fig. 1 Representation of host-guest inclusion complex formation and differential reactivity of free and bound guest

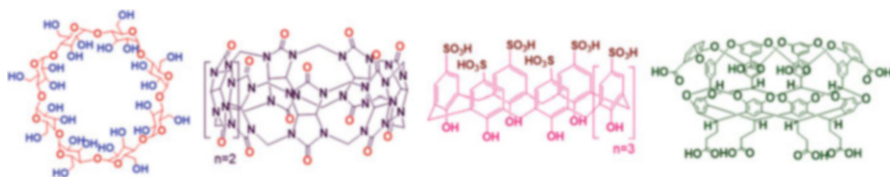


Fig. 2 Chemical structures of common molecular cavitands used to control excited-state chemistry of organic molecules

Several hosts are available for supramolecular chemists currently, though a few macrocycles have been employed more frequently than others. Cyclodextrins (CDs) and cucurbiturils (CBs) are arguably the most commonly utilized organic hosts due to their supramolecular versatility, easy synthetic accessibility, and aqueous amenability. Calixarenes (CAs) are the next most commonly utilized host, though to a much lower extent than the former. Each family of aforementioned macrocycles possesses oligomers that are of comparable dimensions to each other, due to which they affect similar photochemical outcome in many instances. At the same time, differences in their chemical functionalities, therefore different modes of interactions, have led to markedly different photochemistry as well. Octa acid (OA) is a relatively newly synthesized host with unique host characteristics, which has given rise to previously unobserved inclusion dynamics and therefore supramolecular photochemistry. The chemical structures of common hosts are provided in Fig. 2, and their dimensions and comparative 3-D structures rendered through molecular modeling are provided in Fig. 3.

Cucurbiturils (CBs) have gained prominence in supramolecular chemistry due to their easy synthetic accessibility and strong binding affinity toward cationic guests; they bind to neutral and anionic guests, though at much lower strengths. CB8, which is composed of eight glycoluril units, is well-known for its ability to form ternary (2:1 or 1:1:1) guest-host complexes (represented as guest₂@host). Inclusion of neutral guests in CB8 is primarily driven by hydrophobic effect as the cavity is less polar than water and the interior is hydrophobic. Binding to cationic guests, in addition to hydrophobic effect, is driven by cation-dipole interaction between the oxygen atoms of the carbonyl portals and the guest's positive charge. As improving efficiency of photocycloaddition (PCA) would require proximal placement of two alkene molecules to increase the chance of molecular encounter within the window of excited-state reactivity, CB8 has been an excellent choice of host for effecting this reaction.

Cyclodextrins (CDs) are the earliest and most studied family of macrocyclic cavitands. CDs are composed of α -D-glucopyranose monomer units. The hexa-, hepta-, and octameric members of the family are known as α -, β -, and γ -CDs; the host-guest and supramolecular chemistry of these have been extensively studied. Similar to CB8, γ -CD possesses a cavity conducive for promoting PCA. Inclusion of guests in the significantly nonpolar cavity of CDs is driven by hydrophobic effects. Composed of hydroxy benzenesulfonic acid units calixarenes are yet another family of cavitands. Like CB8 and γ -CD, the octa- and hexameric members of the

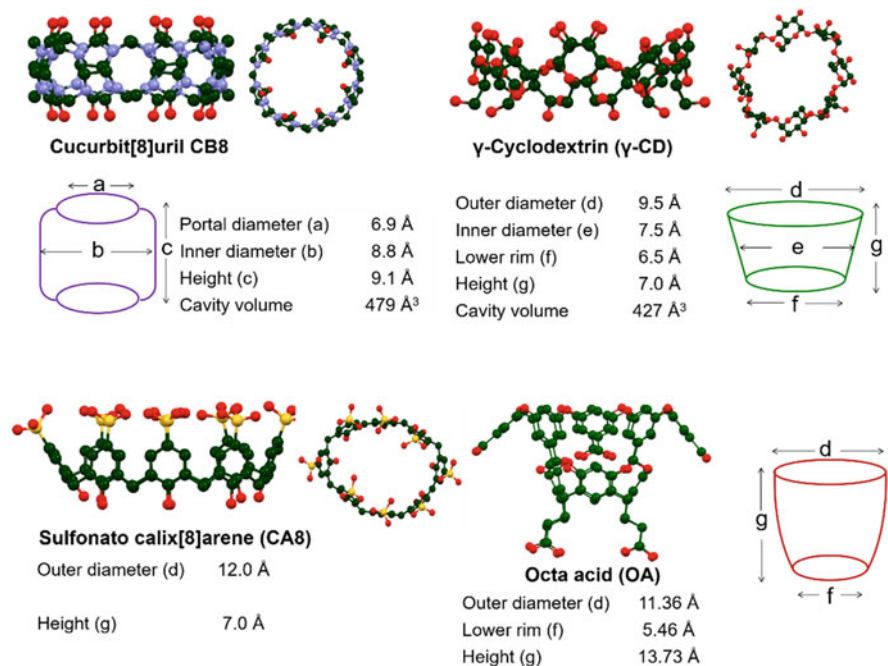


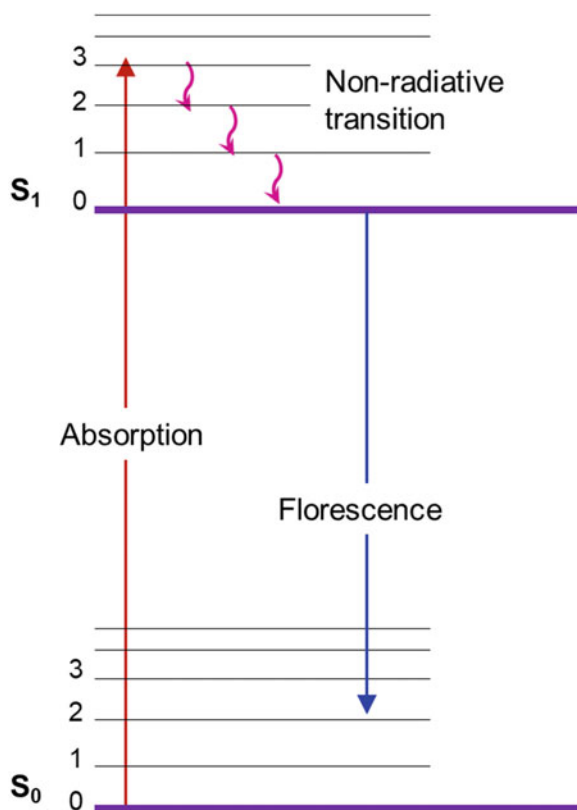
Fig. 3 Representation of cavitands frequently used in supramolecular photochemistry and their dimensions. Color coding: red (oxygen), blue (nitrogen), green (carbon), and yellow (sulfur). Hydrogens are omitted for clarity

calixarene family, calix[8]arene and calix[6]arene (CA8 and CA6), possess cavity volume suitable for PCA reactions. A comparative chart outlining cavity dimensions and shapes of the cavitands is provided in Fig. 3.

3 Fluorescence

Fluorescence is the emission of light by a molecule in its excited singlet state (Fig. 4) [33]. In organic photochemistry majority of the molecules are of singlet multiplicity in their ground state (S_0), which upon absorption of light is converted to the singlet excited state (S_1 , purple arrow). Following thermal relaxation (red arrow) to the lower vibrational state in electronic excited state, radiative transition from $S_1 \rightarrow S_0$ results in emission of light (green arrow), which is referred to as fluorescence. Some of the general characteristics of fluorescence are (a) the emitted light has a longer wavelength, and therefore lower energy, than the absorbed radiation, which is referred to Stokes shift, (b) fluorescence is often a mirror image of absorption spectrum of the molecule, (c) fluorophore lifetimes in excited state typically range

Fig. 4 Jablonski diagram to represent fluorescence



between pico- to hundreds of nanoseconds, and (d) the quantum yield of fluorescence (Φ_f) is independent of wavelength of excitation. Fluorescence has many practical applications, including bio- and material imaging, medicine, sensing, labeling, and optical devices.

Efficiency of fluorescence is increased by reducing the efficiency of other competing pathways such as intersystem crossing (ISC, $S_1 \rightarrow T_1$), energy transfer (ET), non-radiative relaxation, or other competing processes such as photochemical change. Supramolecular strategies for enhancing fluorescence should, therefore, involve the use of weak interactions to thwart the competing pathways. Cavitands have been employed to enhance fluorescence by increasing rigidity of fluorophores to prevent $S_1 \rightarrow S_0$ IC (which requires conformational freedom), thwarting autoquenching by reducing aggregation, and promoting energy transfer of previously excited chromophore.

One such representative approach to observing fluorescence through energy transfer between aromatic hydrocarbons and squaraines (SQ) was demonstrated by Mako et al. [34]. Energy transfer between excited anthracene and ground-state squaraine to exhibit its near-infrared emission, after UV excitation, was achieved through supramolecular association. This energy transfer occurs inside the

γ -cyclodextrin cavity, with up to 35% emission observed from energy transfer compared with exciting SQ directly. Due to the complete lack of spectral overlap between anthracene and squaraines, such energy transfer from ANT to SQ is unprecedented. In particular, γ -CD was used to promote energy transfer from five common polycyclic aromatic hydrocarbons (PAHs) to near-infrared-emitting squaraine dyes, as illustrated in Fig. 5. They demonstrated efficient energy transfer from anthracene (ANT) to a near-infrared-emitting squaraine (SQ) fluorophore acceptor within γ -CD. For instance, Fig. 5 shows the wavelength-dependent emission of the ANT.SQ@ γ -CD ternary complex wherein direct photoexcitation of ANT at 360 nm and SQ at 620 nm resulted in predominant emission of the respective fluorophores. Energy transfer between ANT and SQ was ascertained through increasing SQ emission upon photoexcitation at 360 nm; this was further validated when increasing concentration of γ -CD increases SQ emission while that of ANT decreases.

Similar ET fluorescence emission from SQ was observed for four other PAHs including pyrene (Py), wherein presence of γ -CD under photoexcitation conditions showed increase in SQ emission with concomitant decrease in excimer emission of Py. This energy transfer setup, which occurs via the formation of ternary complexes, is analogous to a sensor array wherein the presence of PAHs could be detected through emission from near IR emitter [35].

Manipulating fluorescence through cavitand-controlled fluorophore rigidity was demonstrated by Rebek's group using their synthetic molecular host [36]. Rebek's host (RH, Fig. 6) is a synthetic "deep cavitand" with one opening, therefore only one portal, through which guest molecules could enter its cavity. It consists of the C-undecylcalix[4]resorcinarene basin with four 1,4-pyrazyl-amido pillars. The urea (amido) units in the host, capable of hydrogen bonding, enable the host to self-assemble into a dimeric capsule (RH•RH) in nonpolar solvents. The interior of the capsule provides well-protected and isolated molecular spaces for guests, which has been utilized efficiently for controlling molecular behavior [37]. RH is also capable of forming an elongated self-assembled capsule through hydrogen-bonding glycoluril linkers Ls (Fig. 6).

Trans-stilbenes are known to give weak to moderate fluorescence in solution due to their high quantum efficiency for photochemical change (*trans* \rightarrow *cis*) and lack of structural rigidity, whereas it is known to exhibit strong emission within constrained environment such as antibody interior, yielding an intense blue fluorescence [38–40]. Though the reason for enhanced emission within constrained media is attributed to the reduced quantum efficiency of photoisomerization, little is known about the photophysical nature of its excited state. Rebek's group utilized the constraining effect of their molecular hosts to study the factors controlling behavior of stilbenes in a sterically constrained environment. For example, 4,4'-dimethyl stilbene STB exhibits moderate fluorescence in solution (Fig. 7, black solid line); encapsulation of the same in self-assembled RH•RH capsule resulted in a near quantitative fluorescence quenching (red solid line). This loss in fluorescence, despite encapsulation within the capsule, was remarkable especially in the context of what was observed within antibody environments. The loss of emission was attributed to the

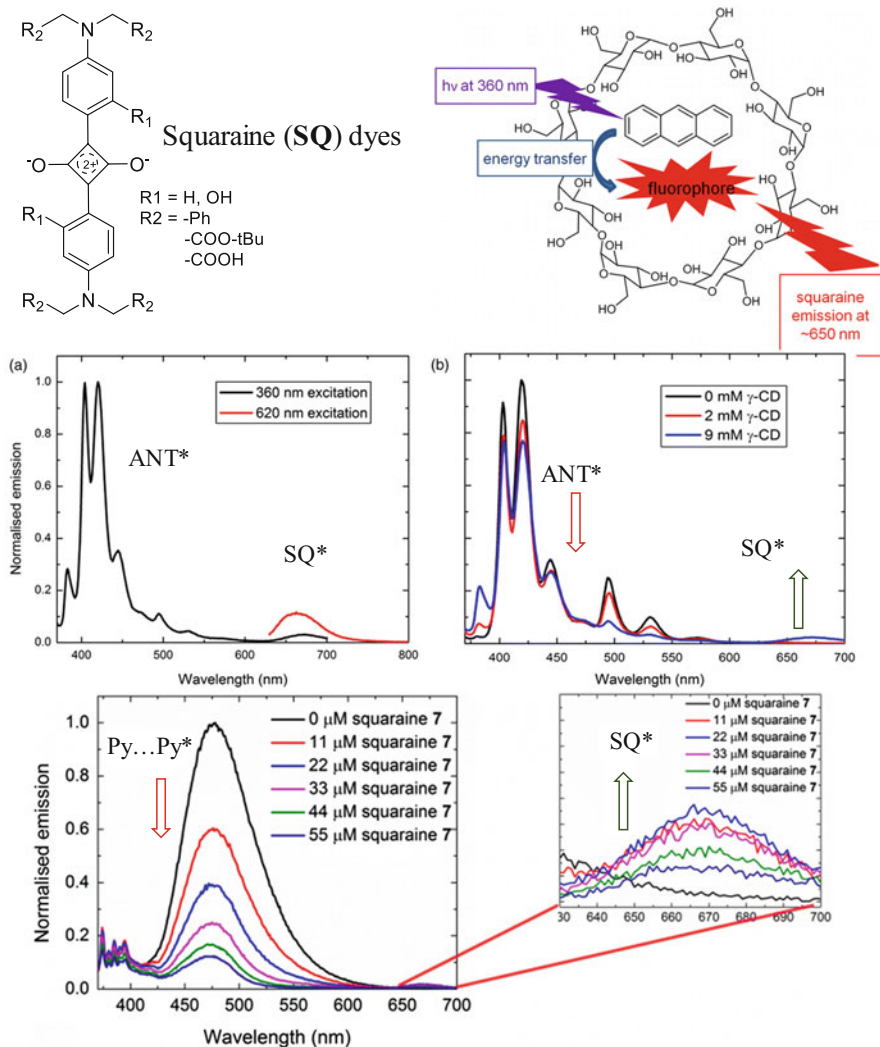


Fig. 5 Formation of ternary complex of anthracene (ANT), squaraines (SQ), and γ -CD. Photoexcitation of ANT transfers energy to SQ co-guest which fluoresces in near IR. Spectra, (top left) comparison of fluorescence spectra from excitation at 360 nm to excitation at 620 nm (9 mM γ -CD, 45 μM ANT, and 11 μM SQ) and (top right) fluorescence spectra at different concentrations of γ -CD (45 μM ANT and 53 μM SQ). (Bottom) Excimer emission spectrum of pyrene (Py) decreases as SQ fluorescence increases (inset) in ternary complexes with 40 μM Py, SQ, and 9 mM γ -CD. Spectra are used with permission from Taylor and Francis [34]

nonplanar geometry between phenyl rings (45°) enforced by the host, which is a consequence of the dihedral angle between the two monomeric units of the capsules (Fig. 7). When the complex was elongated by incorporating glycoluril spacers to form the $\text{RH}\cdot\text{L}_4\cdot\text{RH}$, STB was able to adapt a fully coplanar arrangement, and

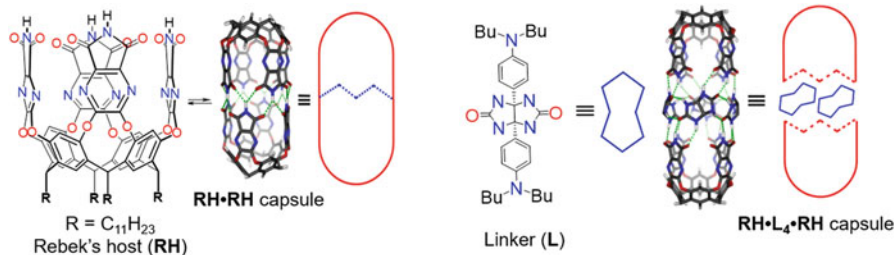


Fig. 6 Structure of cavitaand: Rebek's hosts (RH) and its dimeric (capsule) structure on left. RH binds with linker L to form an extended capsule on right. Structures from open access journal used with permission from author [41]

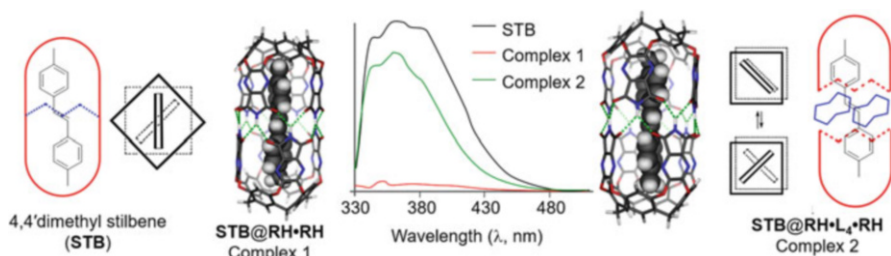


Fig. 7 Controlling fluorescence of *trans*-stilbene by manipulating its geometry within dimeric capsule with and without linker (left and right). Fluorescence spectra of STB under complexed and uncomplexed conditions (middle). Structures from open access journal used with permission from author of published work [41]

fluorescence returned (Fig. 7, green solid line). Thus, controlled systematic variation of fluorophore geometry manipulated through nano-container enabled the study of photophysics of stilbene. Many fluorescent sensors have been reported in the literature; however, they usually respond to chemical changes rather than purely geometrical ones. Here, self-assembly of an external host system was utilized for turning on and off stilbene fluorescence through geometrical control of the stilbene's surroundings [41].

4 Phosphorescence

Phosphorescence (Fig. 8) occurs when photoexcited molecules' intersystem crosses to the lower-energy triplet state ($S_1 \rightsquigarrow T_1$), ISC, and radiatively deactivates to the ground state ($T_1 \rightarrow S_0$) by phosphorescence [33, 42]. Phosphorescence is spin-forbidden but occurs in those systems in which the spin-orbit coupling is favored, for instance, by the presence of heavy halogen atoms (heavy atom effect). Phosphorescence occurs at a shorter rate constant (longer lifetime) compared to fluorescence with emission lifetimes generally ranging from microseconds to milliseconds.

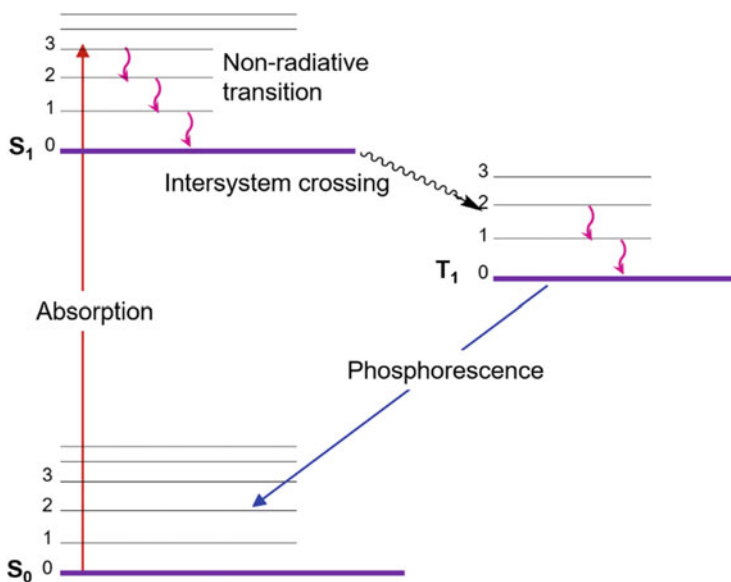


Fig. 8 Jablonski diagram to represent phosphorescence

However, some compounds have triplet lifetimes up to minutes or even hours, allowing these substances to effectively store light energy in the form of very slowly degrading excited electron states. Due to the long lifetimes required for the spin-forbidden $T_1 \rightarrow S_0$ transition, other faster processes such as fluorescence, photochemical reactions, energy transfer, etc. often preempt phosphorescence, and consequently the phosphorescence quantum yields are generally very low. In fact, drastic conditions (i.e., in frozen solutions) are generally required to detect phosphorescence emissions in organic systems. Therefore, phosphorescence measurements are generally performed at low temperatures in which the phosphore could be “trapped” in the lower-energy triplet state; solutions are also purged to remove molecular oxygen which efficiently quenches the triplet state through energy transfer.

Cavitands have been utilized in the past to facilitate room temperature phosphorescence (RTP) of organic molecules with recent reports taking advantage of unique supramolecular strategies to achieve the same even in the presence of molecular oxygen. Once a photoactivable molecule forms a host-guest inclusion with a cavitand, the physicochemical properties of the guest, especially the water solubility, is modified significantly. The host molecules affect molecular behavior as it provides a rigid environment for the guest molecules to limit the vibrational freedom of the guest molecules, suppressing the non-radiative relaxation of the triplet states, and effectively protect the phosphorescence from the triplet oxygen which will quench the luminance of guest molecules, thereby generating strong room temperature phosphorescence.

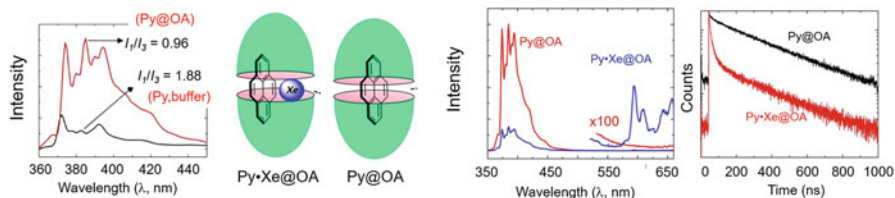


Fig. 9 (Left) Monomer emission of pyrene with different I_1/I_3 band intensities indicating cavitand hydrophobicity. (Middle) Complex structures of pyrene (Py), xenon (Xe), and octa acid (OA). (Right) Phosphorescence observed from Py due to co-complexation with Xe in OA. Spectra and structures used with permission from the American Chemical Society [43]

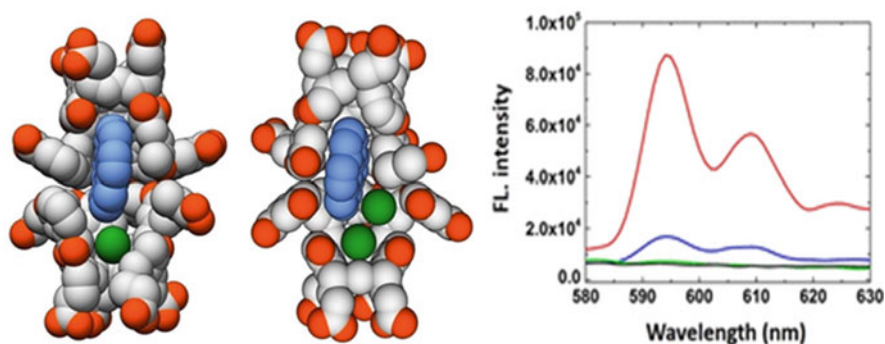


Fig. 10 (Left) Representation of inclusion complex of Xe atom and Py encapsulated within OA at different ratios. (Right) Phosphorescence spectra of Py@OA: aerated (black), after N₂-purged (blue), after Xe purged (red), and after O₂ purged (green). Spectra and structures used with permission from the American Chemical Society [43]

Ramamurthy's group demonstrated the application of deep cavitand OA capsules in achieving RTP of pyrene (Py) by co-encapsulating the luminophore with heavy atom effect [43]. Phosphorescence from pyrene especially at room temperature is uncommon. This emission was recorded utilizing a combination of supramolecular inclusion complex and the heavy atom effect. Poor intersystem crossing from S_1 to T_1 , small radiative rate constant from T_1 , and large rate constant for oxygen quenching hinder the phosphorescence of aromatic hydrocarbons like pyrene (Py). However, such limitations were overcome by encapsulating Py within OA (Fig. 9) and increasing its interaction with xenon (Xe). As demonstrated in previous examples, OA forms a capsule with pyrene, and the ratio of intensities of I_1 vs. I_3 emission bands of Py suggests a benzene-like hydrophobicity [44, 45]. In the presence of xenon gas, the three entities (OA, Py, and Xe) form a 2:1:1 complex. The close interaction between the Py and the heavy atom effect facilitated in the three-component supramolecular assembly resulted in phosphorescence from pyrene (Figs. 9 and 10 red line) observed as a structured emission between 580 and 630 nm. Encapsulation of pyrene within OA suppressed oxygen quenching by serving as a physical barrier for triplet energy transfer. Xenon enabled the

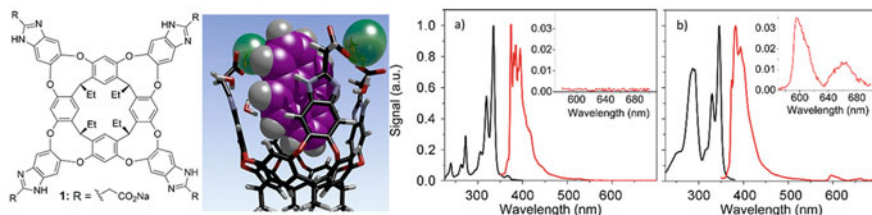


Fig. 11 (Left) Chemical structure of deep cavitaand. (Middle) Its complex structure rendered in 3-D (middle). (Right) Excitation (black) and emission (red) spectra for Py@SDS micelles vs. Py@deep cavitaand in aerated aqueous medium with 6 mM Py and 10 mM Ti^+ . (Inset) Phosphorescence is observed between 550 and 700 nm. Spectra and structures used with permission from the American Chemical Society [47]

intersystem crossings ($S_1 \rightsquigarrow T_1$ as well as $T_1 \rightarrow S_0$) through heavy atom effect [46] as evidenced by the fast fluorescence decay of excited pyrene in Py•Xe@OA₂ compared to the same in absence of Xe (Py@OA₂). Computational modeling and NMR studies supported the postulate that Py and at least one Xe atom were present within the OA capsule (Fig. 10), which resulted in high degree of RTP. Py lacked any significant RTP under all other conditions wherein Xe was not present: as a free luminophore, complexed to OA in aerated and N_2 -purged solutions (Fig. 10, black, blue, and green).

Another example of water-soluble deep cavitaand host in eliciting RTP from Py was reported by Easley et al. [47]. Similar to OA, the deep cavitaand reported by Easley is a water-soluble host (Fig. 11), which was used to encapsulate the aromatic molecule pyrene in its interior while also simultaneously binding Ti^+ ions at its carboxylate periphery. Steady-state and time-resolved spectroscopic experiments, along with quantum yield measurements, quantify the enhancements of intersystem crossing and room temperature phosphorescence due to cavitaand encapsulation. The combination of selective binding and strong Ti^+ recognition by the cavitaand enhanced the intersystem crossing and decreases the phosphorescence radiative lifetime from ~ 30 to 0.23 s. The cavitaand also decreases the rate of O_2 quenching by a factor of 100. All these factors had demonstrably enhanced the RTP efficiency of Py by several orders of magnitude, allowing it to be detected in water without O_2 removal.

Enhancement of phosphorescence of 2,4,6-triphenylpyrylium cation (TP^+) was demonstrated by encapsulating it within the rigid host CB8. TP^+ forms host-guest complexes with cucurbiturils (CBs) in acidic aqueous solutions [48]. ^1H NMR spectroscopic data indicated that complexation takes place by encapsulation of the phenyl ring para to oxonium CB (green, Fig. 12).

The tendency to complex with smaller hosts CB6 and CB7 was minimal as indicated in NMR chemical shifts, and no complexation to cyclodextrin hosts (β -, γ -) was observed; the former is attributed to size, while the latter is attributed to lack of electronic complementarity between the ionic guest and nonpolar cavity. Free TP^+ fluoresces at ~ 460 nm in solution. With CB6 and CB7, minor shifts in the

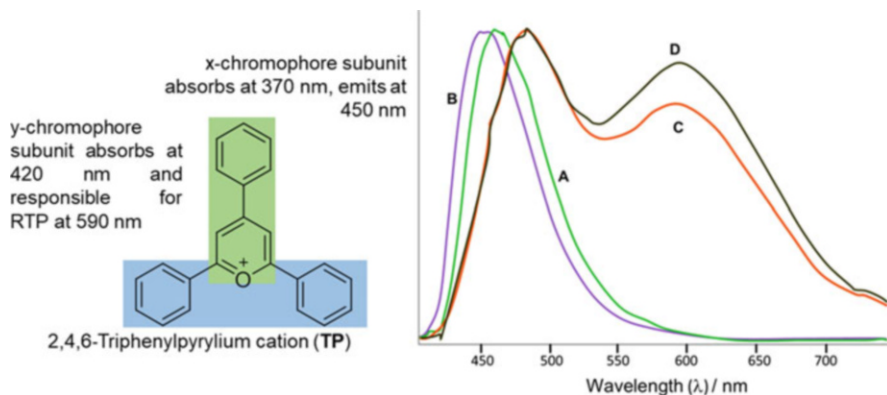


Fig. 12 TP⁺ cation structure (left) showing pure fluorescence (A, B) and dual emission with fluorescence and phosphorescence (C, D). Emission spectrum of aqueous solutions of TP⁺ BF₄⁻ (10⁻⁵ M, pH 1) in the absence (A) or in the presence of a ~10⁻³ M of CB7 (B) and different amounts of CB[8] (C and D) at λ_{ex} = 420 nm. A, B, and C. For spectrum D λ_{ex} = 370 nm. Spectra reproduced from published work [48]

fluorescence wavelength maximum (λ_{fl}) or quantum yield (Φ_{fl}) were observed as well. In sharp contrast, for complexes with CB8, the emission resulted in the simultaneous observation of bathochromic fluorescence (λ_{fl} = 480 nm, Φ_{fl} = 0.05) and room temperature phosphorescence (Fig. 12, λ_{ph} = 590 nm, Φ_{ph} = 0.15).

Achieving RTP of Py discussed above is relatively straightforward, compared to TP⁺, as Py being a rigid molecule is more emissive (reduced Φ for non-radiative) and heavy atom effect favors phosphorescence; such advantages do not exist for TP⁺ as it is far less rigid and no heavy atom effect was involved. Moreover, there is a dramatic difference in emission spectra between TP⁺@CB8 and smaller CB hosts. In order to understand this, MM2 molecular mechanics calculations were employed, which suggests that this effect arises from locking the conformational mobility of the 2- and 6-phenyl rings as a result of CB8 encapsulation.

Plot of host-guest inclusion complex stabilization energy (computed, MM2) of CB7 and CB8 as a function of the distance from the center of the organic capsule to the center of the 4-phenyl ring (relative distance) was deduced (Fig. 13). It could be noticed that the energy minimum does not coincide for CB7 and CB8. For the defined relative distance (Host_{center-to-phenyl}_{center}), the energy minimum for CB8 was recorded at 0 Å while that for CB7 was at 1 Å. This indicated that the phenyl ring of the pyrylium ion was not able to penetrate as deeply into the capsule for CB7, and the difference is attributed to the width of the capsule and the repulsive interactions between the oxygen atoms of the CB carbonyl portals and the ortho hydrogen atoms of the phenyl groups at the 2- and 6-positions of the TP⁺ ion. This, along with theoretical conformational analysis for 2- and 6-phenyl rings, indicated that CB8 imposes conformational locking onto TP⁺ cation leading to phosphorescence from the localized excitation of 2,6-diphenylpyrylium structure (y-unit, Fig. 12). Lack of

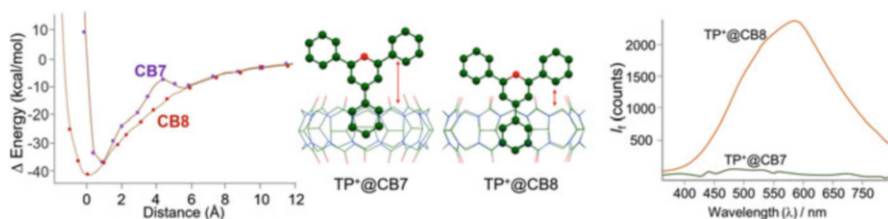


Fig. 13 (Left) Energy vs. cavity TP⁺ wherein horizontal axis represents relative distance from center of cavity to center of included phenyl ring. (Middle) complex structure of TP⁺ with CB7 and CB8. (Right) emission spectrum of OLED device constructed using the TP⁺ complexes with CB7 (green) and CB8 (orange) as the active layers at an operating potential of 10 V. Structure and graphs reproduced from published work [48]

such conformational locking in TP⁺@CB7 resulted in radiationless relaxation of the triplet state ($T_1 \sim \rightarrow S_0$) and, hence, no emission.

The remarkably high room temperature phosphorescence quantum yield of the TP⁺@CB8 complex resulted in a noticeable characteristic yellow color to the medium. An electroluminescent light-emitting device was developed based on this system with TP⁺@CB8 layer coated indium tin oxide (anode)/aluminum (cathode). OLED cells thus designed showed visual emission of bright yellow light, correlating with solution-phase emission, under operating potential of 10 V (Fig. 13). An equivalent cell developed with TP⁺@CB7 layer did not show any luminescence.

Thiocarbonyl compounds possess unusual photophysical properties as they fluoresce from the second excited state (S_2) owing to the typical large energy between their S_1 ($n-\pi^*$) and S_2 ($\pi-\pi^*$) states. Thioketones present one of the rare instances of $S_0 \rightarrow T_1$ absorption, near-unity quantum yield for $S_1 \rightarrow T_1$ transition owing to strong internal spin-orbit coupling [49–51]. However, they are not phosphorescent due to diffusion-controlled self-quenching at concentrations higher than 10^{-6} M [52, 53]; they phosphoresce from T_1 at extremely low concentrations or other conditions where self-quenching interactions are minimized [54]. In addition to self-quenching, thioketone phosphorescence is further inhibited by triplet oxygen quenching and oxidation by singlet oxygen [55].

Ramamurthy et al. demonstrated the use of a nano-container to observe phosphorescence from thioketones at room temperature in aqueous solution at high concentrations [56]. The capsule of OA has been shown to afford a protective barrier for photophysicochemical processes. In this case of thioketone photochemistry, OA eliminated the diffusion-limited self-quenching and oxygen quenching, which presents a reliable general strategy that has allowed observation of record phosphorescence from a series of thioketones (fenchthione – FNT, camphorthione – CHT, and adamantathione – ADT) in aqueous solution at room temperature (Fig. 14). The remarkable ability of OA capsules to facilitate phosphorescence of three thioketones at high concentrations is shown in Figs. 14 and 15. Three thioketones were explored, which do not exhibit phosphorescence in liquid media at concentrations around 10^{-4} M. However, in the presence of 1.2 eq of OA host, all the ketones exhibited intense phosphorescence, which increased proportionally to the concentration of OA

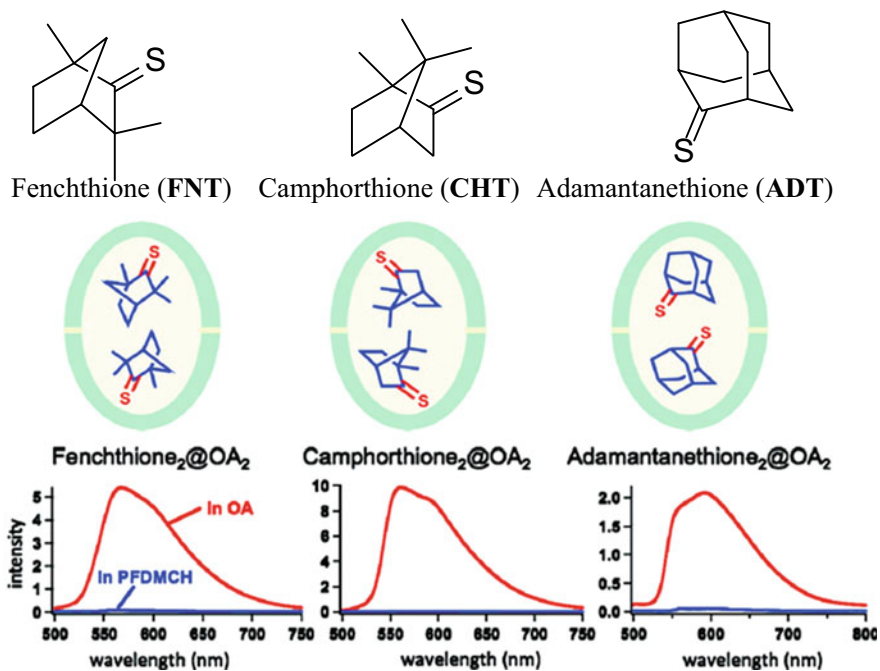


Fig. 14 (Top) Structure of thioketones and representation of their inclusion complexes. (Bottom) Recorded phosphorescence spectra of free (blue) in perfluoro-1,3-dimethylcyclohexane and OA₂-bound thioketones (red) in aqueous solution. Concentrations of thioketones ~0.1 mM. Spectra and structures used with permission from the American Chemical Society [56]

in titration experiments (Fig. 14). The host-guest complex stoichiometry was determined to be 2:2 quaternary complex, wherein two guests were complexed within the capsular assembly made of two OA units. In these supramolecular complexes, despite two thiocarbonyl compounds being present in proximity, no self-quenching was observed within the confined space due to highly restricted rotational mobility.

Other macrocyclic hosts were also explored in this study: CB7 and CB8. These hosts do not form capsules like OA, due to which the thioketones formed 1:1 complex. As seen in Fig. 15, these hosts also provided the required ambience for the thioketones to exhibit strong phosphorescence. Photophysical measurements were performed by the authors which showed that the triplet lifetimes of complexed thioketones increased manifold within compared to that in water indicating protection from self-quenching. Although phosphorescence could also be observed when these thioketones are included within CBs, the closed container made up of octa acid is found to be the best medium to observe phosphorescence from thioketones whose excited-state chemistry is essentially controlled by self-quenching [57]. Camphorhthione (CHT), in spite of having a reasonably high spin-forbidden radiative rate constant, is well-known not to emit phosphorescence at room temperature in solution [55, 58]. The triplet state is efficiently quenched by oxygen and by

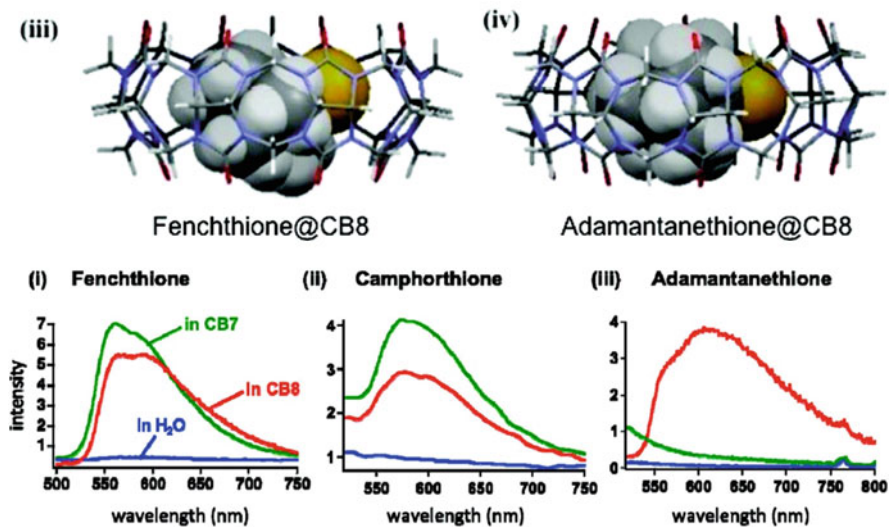


Fig. 15 (Top) Structure of thioketones and representation of their inclusion complexes. (Bottom) Recorded phosphorescence spectra of free (blue), CB7 (green)- and CB8 (red)-bound thioketones (red) in aqueous solution. Concentrations of thioketones ~ 0.01 mM. Spectra and structures used with permission from the American Chemical Society [56]

neighboring ground-state thione through self-quenching (Fig. 15). The above results relating to the excited-state photophysics of the thiones proved to be an efficient and simple approach to enhancing the RTP of otherwise inefficient luminophores.

5 Twisted-Intramolecular Charge Transfer

The majority of fluorescence ($S_1 \rightarrow S_0$) of organic molecules results from the excited singlet state. However, molecules that can undergo chemical change in the excited state due to nuclear and electronic reorganization, from reactant (R^*) to product (P^*), can undergo radiative transitions from both the species leading to dual fluorescence; in many cases such dual fluorescence could be observed simultaneously. The phenomenon of twisted intramolecular charge transfer (TICT emission) is one such example (Fig. 16) [59, 60]. TICT is an electron transfer process that occurs upon photoexcitation in molecules that usually consist of electron donor and acceptor units (D-A) linked by a single bond. Conjugated systems with D-A linkage are planar and maintain their geometry in the so-called local excited S_1 (R^*). R^* could also undergo a dihedral conformational twist to the staggered orthogonal conformation following $D \rightarrow A$ electron transfer, which is called the TICT state (P^*). TICT state should then undergo red-shifted fluorescence relative to “locally excited” LE or relax non-radiatively. TICT emission is often sensitive to environmental properties

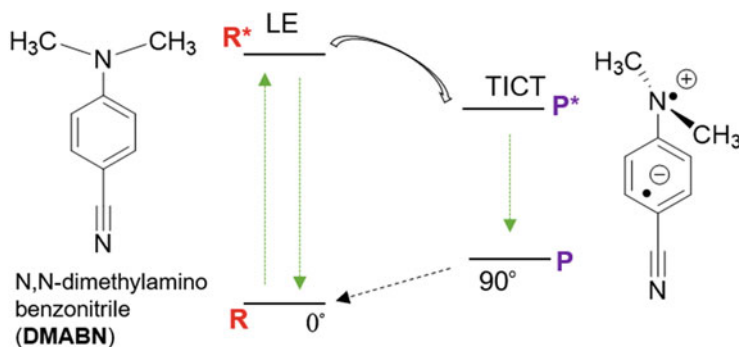


Fig. 16 Depiction of photoexcitation of DMABN and its normal emission from locally excited (LE) state and twisted intramolecular charge-transfer (TICT) state

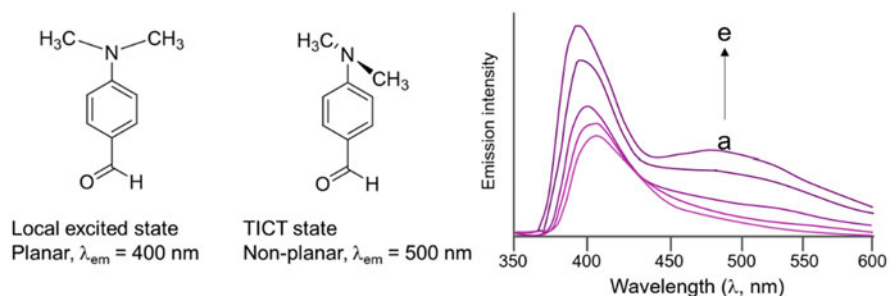


Fig. 17 Normal and TICT emission of DMABA (0.01 mM) within β -CD with increasing concentration of cavitant (a. 0.0 mM \rightarrow e. 8 mM). Spectra reproduced from published work [61]

that could influence excited-state conformational change, such as viscosity and molecular (electronic, steric) rotational barriers, which makes TICT-based fluorophores ideal sensors. Dimethylaminobenzonitrile (DMABN) is one of the simplest representative examples for TICT emission wherein the donor dimethylamino group is coplanar with the benzonitrile chromophore in ground state (Fig. 16). Upon excitation, emission from the locally excited coplanar structure was observed at ~ 350 nm, whereas emission from a twisted excited (coupled with electron transfer) state was observed at ~ 450 nm.

Earlier influence of cavitant on TICT emission was explored for dimethylaminobenzaldehyde (DMABA). With regard to host-guest chemistry involving TICT chromophores, cyclodextrins have been the only cavitants used in the past due to lack of other alternatives at that time. Encapsulation of DMABA reported by Kundu et al. [61] within the three CD oligomers leads to different outcomes, which were interpreted in terms of the structure of the complex and polarity of the CD cavity (Fig. 17). However, due to the expansion of supramolecular and host-guest chemistry, the last decade has seen utilization of several new hosts in manipulating TICT behavior, which has led to newer insights about these D-A

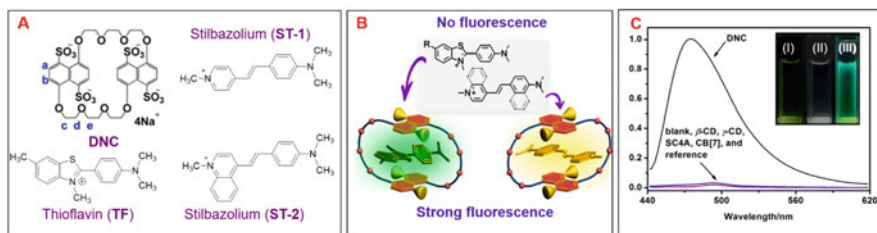


Fig. 18 (a) Structure of host and guests. (b) Representation of complex structure between fluorophore and host. (c) Accessing TICT emission of D-A conjugated molecules exclusively using dansyl crown ether (DNC, black) hosts through π - π interaction, which is not observed in CBs and CDs due to lack of the π -electronic interaction (blue, purple, red). Spectra and structures used with permission from the American Chemical Society [62]

systems and some exciting new examples of potential applications. Especially, comparison of differential effects of cavity polarity and dimension on the relative LE vs. TICT emission and their cumulative intensities affords wealth of information that has not been previously available.

Zhang et al. [62] explored conformational locking in excited state achieved by electron-deficient TICT chromophores that operate based on a push-pull design in tandem with electron-rich host such as bis(4,8-disulfonato-1,5-naphtho)-32-crown-8 (DNC, Fig. 18). Spectroscopic and microcalorimetric titrations revealed that the binding affinity in these artificial host-guest pairs could reach up to a nearly 10^7 M^{-1} , which indicates strong binding. Such high degree of binding strength is attributed to π -stacked charge-transfer interaction and electrostatic interactions predominantly, with minor but significant contributions from hydrophobic and hydrogen-bonding interactions as well. Binding of these guests with both CB and CD hosts was much weaker.

Zhang et al. showed that the intrinsically hydrophobic cavity of DNC possesses abundant electronic “anchoring points,” which could be used to stabilizing the TICT state of push-pull fluorophores. With the aid of positive supramolecular cooperativity based on electron-rich host donor and electron-deficient guest, the inclusion complexation with DNC was used to dynamically modulate the photophysical behaviors of the three push-pull molecules listed in Fig. 18 (thioflavin TF, stilbazoles ST-1 and ST-2). Thioflavin (TF) is a well-known fluorophore, which contains the electron-rich dimethylamino phenyl (D) unit directly linked to the benzothiazole acceptor unit, whereas stilbazoles ST-1 and ST-2 structure contain the D and A connected through a conjugating alkene functionality. Despite the difference in structure and dimension, DNC facilitates TICT emission by stabilizing the twisted geometry upon photoexcitation. The inferences deduced from DNC-TF system could have potential value in biomedical application as TF is used as a fluorescent biomarker for detection of amyloid fibrils; the use of DNC as a model receptor could lead to better understanding and application of its photophysics. This finding also promotes the use of DNC as a model host for mimicking and

investigating the complexation behaviors of other receptor-ligand binding systems and stimulates the mechanistic study in molecular detail.

Dong et al. reported the use of cavitand to control stilbazole ST1, a TICT fluorophore, in supramolecular microcrystals [63] with temperature-controlled tunability. Stilbazoles lack emissivity which is a crystalline state due to aggregation-induced quenching. This disadvantage was overcome by inclusion chemistry, which afforded dual advantage of aggregate prevention and conformational control. The authors report broadband tunable microlasers built by incorporating a highly polarized organic intramolecular charge-transfer (ICT) compound with β -CD, which resulted in a 1:1 inclusion complex. As the LE and TICT emission occur at different wavelengths, controlling the planar vs. nonplanar conformations of the fluorophore in excited states would afford ability to control visible color emitted by designed material (Fig. 19). It was deduced for stilbazolium fluorophores (ST-1) that at lower temperatures (-60°C), the lack of energy to overcome rotational barrier prevents geometric transition from planar to nonplanar conformation resulting in exclusive emission from the lower-wavelength LE state at 550 nm. Whereas at higher temperatures (120°C), the TICT state is accessed more easily leading to mixed (LE + TICT) emission at a higher wavelength (670 nm). The spatial confinement of the ICT dye, imposed using β -CD, facilitated generation of an optimized energy level system that favors controlled population distribution between the LE and TICT states. As a result, the authors realized a wide tuning of lasing wavelengths in the organic supramolecular microcrystals based on temperature-controlled population transfer from the LE to TICT state. The results provided a useful demonstration of rational design of miniaturized lasers with tunable optical performances.

Schoder et al. reported a series of easily accessible bipyridinium fluorophores, whose emission is quenched by a TICT mechanism [64]. The donor-acceptor arrangement for TICT emission based on the bispyridyl-biphenyl duo has not been explored before (Fig. 20). Based on experimental and theoretical studies, absorption bands were attributed to HOMO-LUMO transitions, with the HOMO being centered on the biphenyl and the LUMO on the bipyridinium parts. Photoexcitation of BP in homogeneous media does not result in emission from LE state due to quenching mechanism from the TICT structure (through a metastable state, MSS), which is easily accessible at room temperature given its low rotational barrier (c.a. 15 kJ/mol). Therefore, it was reasoned that encapsulation of the fluorophores in macrocyclic cavitands capable of enforcing co-planarity by destabilizing TICT geometry should enhance the LE emission.

BP-Et was investigated for its luminescence in three different hosts (CB7, CB8, and β -CD) which offer a unique insight into the effect of bonding and steric supramolecular variations on the excited-state dynamics. Encapsulation of BP in a CB7 host gave a 1:1 complex exhibiting a moderate emission increase (Fig. 21, blue spectrum) due to destabilization of the TICT state inside the relatively less polar cucurbituril cavity. On the other hand, CB8 formed both 1:2 and 2:2 complexes with a much stronger fluorescence enhancement which is observed in 2:2 complexes. This was attributed to the additional conformational restriction of rotations around the aryl/aryl bonds (Fig. 21, purple spectrum) due to reduced cavity volume from

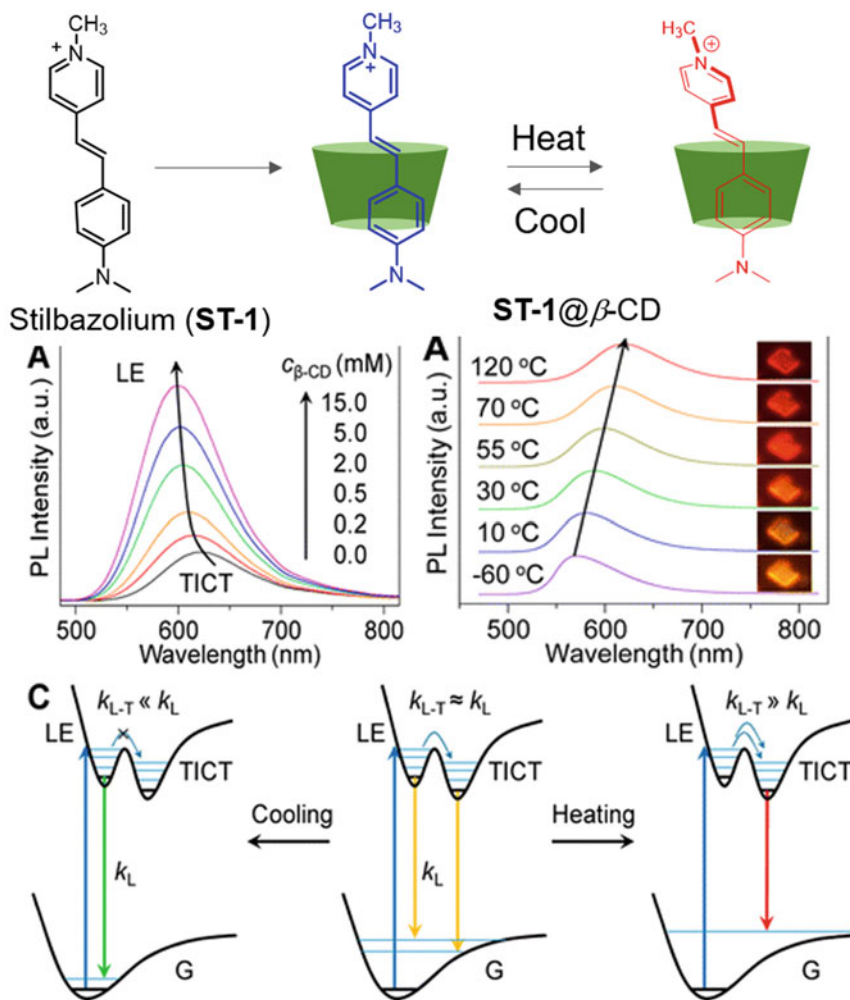


Fig. 19 (Top) Representation of complexation processes. (Middle) Temperature control of LE vs. TICT emission of TICT fluorophore: (left) effect of increasing β -CD proportion on emission and (right) effect of temperature on inclusion complex. (Bottom) Depiction of effect of temperature on conformational change in excited energy surface. Spectra and images used with permission from the American Chemical Society [63]

multiple guest occupancy. In comparison, β -CD did not yield any noticeable emission enhancement owing to poor conformational control on the guest. This is due to well-known weaker binding strength of β -CD host as well as confinement of its binding interaction to just the biphenyl moiety (Fig. 21, red spectrum). The lack of emission of free BP and BP@ β -CD, and its increased emission in CB7 and CB8, respectively, through control of the TICT mechanism, demonstrates versatility of the host-guest photochemistry.

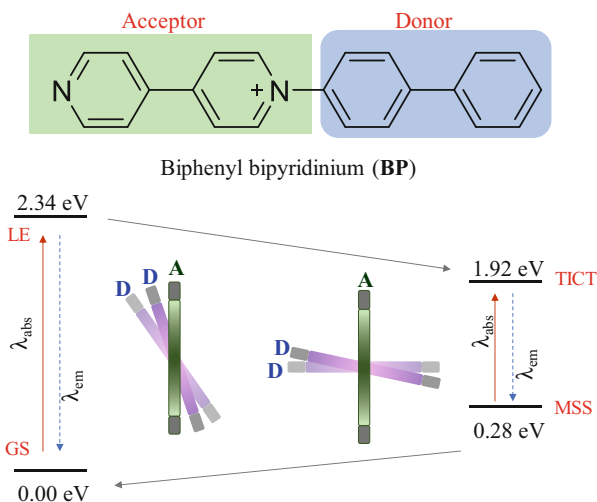


Fig. 20 (Top) Structure of the BP fluorophore. (Bottom) Conformational change between near-planar LE and near-orthogonal TICT states and their relative energies. Details reproduced from published work [64]

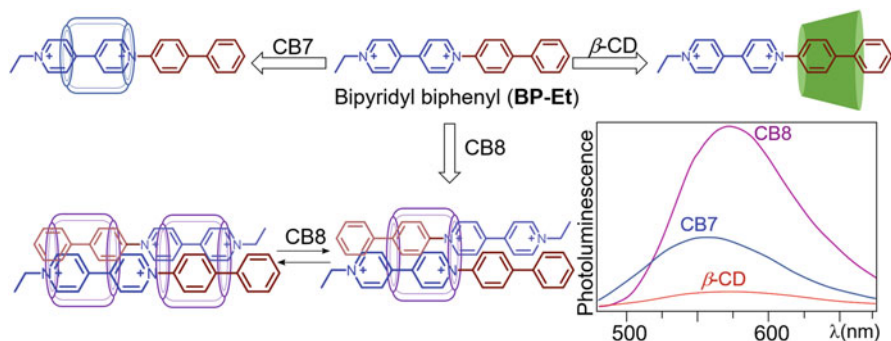


Fig. 21 Complexation equilibria of biphényl/bipyridinium TICT fluorophores and difference in their emissions controlled supramolecularly. The emission spectra are that for BP complexed to CB8 (purple), CB7 (blue), and β -CD (red), respectively. Structures and spectra reproduced from published work [64]

6 Excimers and Exciplexes

Excimers (and exciplexes) are emissive metastable species [65–67] (MSS) that are electronically aggregated dimeric entities in the excited state whose chromophores remain dissociated otherwise. Electronic interaction between an excited chromophore M^* and a ground-state chromophore M leads to an aggregated species ($M^* \dots M$), which is referred to as the excimer (E^* , Fig. 22). Homochemical

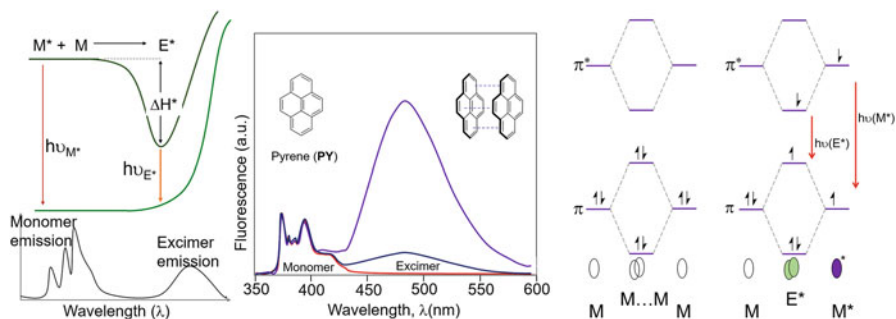


Fig. 22 (Left) Energy diagram depicting excimer formation and emission. (Middle) Monomer emission of pyrene (Py) is a structured spectrum and occurs between 350 nm and 425 nm, while that for excimer emission is broad and occurs between 450 and 600 nm. (Right) Molecular orbital picture depicting electronic interactions leading to excimer formation. Spectra reproduced from published work [65]

excited-state aggregation is referred to as an excimer, while heterochemical equivalents are referred to as exciplexes. The excited-state aggregated dimer (excimer) E^* is particularly different from a ground-state charge-transfer complex (CT), due to electronic complementarity, which will exhibit a new bathochromic absorption; absorption spectrum of excimer chromophores is unchanged.

Excimers and exciplexes are fluorescent, with broad structureless emissions that appear at lower-energy region (higher wavelength) compared to that of the excited monomer. Excimer formation is a physical reaction analogous to a bimolecular chemical reaction. The reaction can be initiated by a short (10^{-9} s) light flash, and the subsequent variations in the concentrations of the reacting species can be monitored by observation of the intensities of fluorescence of the excited monomer and excimer (Fig. 22). Excimer formation is understood in terms of electronic interaction between the half-filled HOMO of the excited species M^* and LUMO of the ground-state species M as depicted in Fig. 22, whereas ground-state interaction between two monomers ($M \dots M$) will result in no net stabilization of dimer.

Excimer formation is best represented by the photophysics of pyrene. The fluorescence spectrum consists of two components: a structured violet emission band which is characteristic of the excited monomer (M^*) and a structureless blue emission band which is characteristic of the excimer ($M \dots M^*$) formed by the association of an excited molecule M^* and an unexcited molecule (M) to form excimer. As the molar concentration of the monomer is increased, the fluorescence quantum yield of M^* decreases due to concentration-based quenching, and the fluorescence quantum yield $M \dots M^*$ increases. The shape of the absorption spectrum, which is characteristic of the monomer, is independent of concentration, showing that the excimer is not present in the ground state but that it dissociates on emission (Fig. 22, right). This behavior of pyrene is typical of many other aromatic hydrocarbons, including benzene, naphthalene, anthracene, perylene, and their derivatives. In some compounds, the excimer fluorescence is difficult to detect in solution at room temperature because of the low solubility or the low excimer

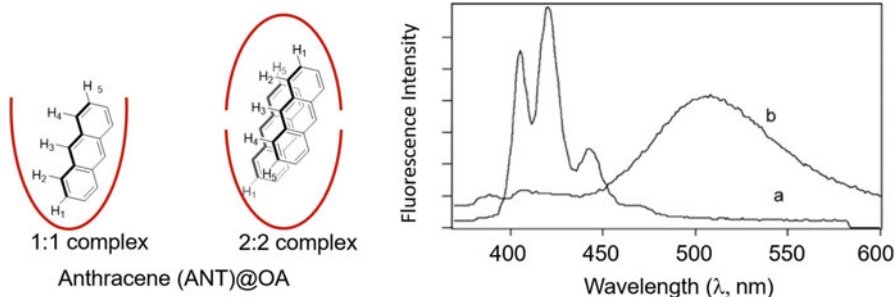


Fig. 23 Left depiction of inclusion based on cavitand and capsule complexes (caviplex/capsuleplex) formation. Emission spectra of ANT (10 mM) showing monomer emission in absence (a) and excimer emission in presence 1 eq. OA host. Spectra used with permission from the American Chemical Society [68]

fluorescence yield, but it can often be observed at low temperatures or in the pure liquid or crystalline states. In other compounds, such as anthracene, tetracene, and pentacene, the dimer interaction is so strong that a stable chemical dimer (photodimer) is formed either from or in competition with the excimer.

Octa acid (OA, Figs. 2 and 3) is a synthetic cavitand with a deep binding pocket, which is rendered soluble in basic aqueous media ($\text{pH} > 8.5$, solubility up to 10^{-2} M) through its four carboxylic acid-terminated side arms. At concentrations above 10^{-3} M, it aggregates into a dimeric capsule. Both the monomeric cavitand and dimeric capsule bind to guests to form 1:1, 2:1, or 2:2 host/guest complexes, referred to caviplex or capsuleplex, respectively.

One of the most remarkable deviations from normal excited-state behavior of fluorophore in the context of excimer emission involving cavitands was demonstrated using octa acid by Kaanumalle et al. (Fig. 23) [68]. Anthracene (ANT), well-known to dimerize with a limiting quantum yield of 1.0, does not show any excimer emission in solution. Its excimer emission has only been recorded by photofragmenting the synthetic dimer either in the crystalline state or in an organic glass at 77 K. Typical emission of anthracene spectrum reveals strong monomer emission ($\lambda_{\text{max}} \sim 420$ nm) and only a weak excimer emission ($\lambda_{\text{max}} \sim 530$ nm; $\tau < 2$ ns). Consequently, studies of the anthracene excimer have focused on low-temperature (< 77 K) photodissociation of ANT dimer in either rigid glass or the crystalline state. These studies have identified two kinds of excimer: the first, termed “stable dimer,” is speculated to involve two ANT monomers at an angle of 55° with respect to the short axis, rather than being π -stacked. The stable dimer has a short lifetime, estimated to be less than 10 ns. The second one, known as the “sandwich excimer,” is a symmetrical π -stacked excimer with a longer lifetime (> 200 ns) especially at lower temperatures. Within the OA capsule, two molecules of the sparingly water-soluble anthracene could be included in a slipped geometry. This complex, upon irradiation, showed intense excimer emission but did not dimerize. The long lifetime of this emission ($\tau = 263$ ns) is consistent with the sandwich excimer ($\tau > 200$ ns) formed upon photofragmentation of the anthracene dimer in the crystalline state. The

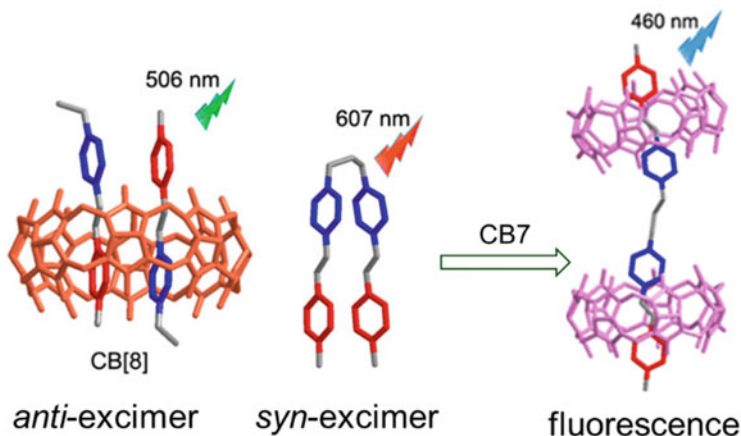


Fig. 24 Depiction of excimer emission of stilbazoles resulting from *anti*-arrangement of ST-3 (left) facilitated by CB8. ST-4 exhibits *syn*-excimer emission in its free (middle) form, while complexation to CB7 inhibits aromatic ring overlap resulting in fluorescence (right). Images used with permission from the American Chemical Society [68]

absence of dimerization could be attributed to the slipped arrangement and to the tight space that prevented the anthracene molecules from realigning to form bonds across 9,9' and 10,10' positions.

This work by Kaanumalle et al. stands out from other cavitand-mediated emissions for two reasons: excimer emission within cavitands predominantly involves pyrene as the chromophore and that the excited-state dynamics of anthracene was directed away from a highly facile photodimerization pathway. This provided a wealth of structural information pertinent to the slipped-sandwich arrangement of the guests stacked within the OA capsule cavity.

Another example of a fluorophore that is usually not known to exhibit excimer emission was affected through host-guest inclusion as demonstrated by Li et al. [69] (Fig. 24). Styrylpyridines are known for their photoisomerization reaction, which often competes (and precludes) photodimerization. They are not well-known for their fluorescence and even less so for excimer emission. Inclusion of cationic styrylpyridines ST-3 and ST-4 (Fig. 25) forms of these compounds within CB8 forms ternary complexes, which presents the required proximity to engage in excited-state aggregation to undergo radiative internal conversion for excimer emission.

As cationic guests, the ternary complexes between two isolated monomeric styrylpyridinium molecules ST3 and CB8 resulted in a head-to-tail (*anti*) arrangement, wherein the pyridinium moieties faced away from each other due to electrostatic repulsion. For ST4, tethering at the phenyl rings resulted in the head-to-head (*syn*) pro-excimer arrangement, which was further favored through encapsulation with CB8. Both arrangements facilitated through complexation resulted in distinct excimer emissions, a phenomenon that has not been previously studied (Fig. 25).

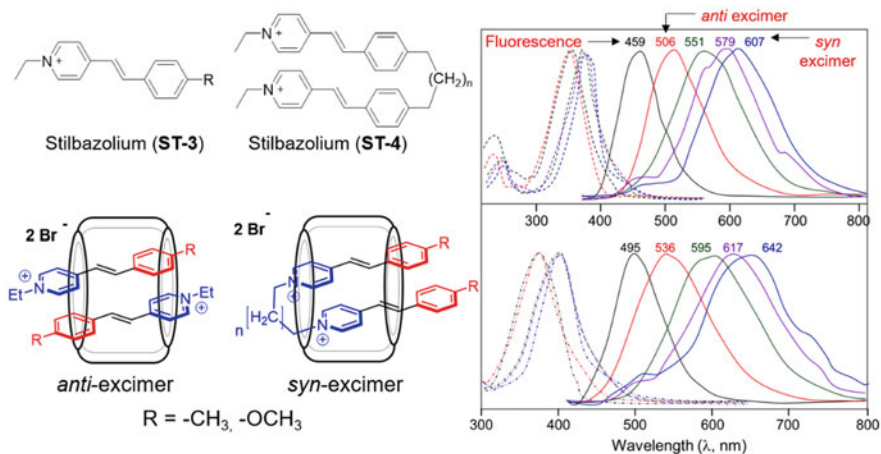


Fig. 25 Excimer emission of stilbazoles through encapsulation. (Top left) structure of stilbazolium fluorophores. (Bottom left) Depiction of head-to-tail complex structure of $ST_3_2@CB8$ and head-to-head $ST_4@CB8$ complex. (Right top $R = -CH_3$, bottom $R = O-CH_3$) Normalized absorption (dotted lines) and emission (solid lines) spectra. Black free ST-3; red, green, purple, and blue are CB8 complexes of ST-3, ST-4 ($n = 5, 4, 3$), respectively. Structure and spectra reproduced from published work [68]

The difference in stacking arrangement of luminophore within the cavitant yielded emission spectra that were markedly different as well: the excimer emission of free and CB8-complexed ST-3 s was observed in the hypsochromic region, while that of complexed ST-4 s was observed in the bathochromic side. Upon complexing to CB7, ST4 showed no excimer band as all its emission completely switched toward fluorescence (~ 450 nm) due to cavity-enforced separation of the two fluorophore units.

The fluorescence quantum yield and lifetime (Φ_F , τ_F) of free and CB8-bound STs were measured. It was observed that both the quantum yield of emission and the lifetime of the excited species were generally higher for the bound guests (STs@CB8) compared to the free guest. It was deduced that increase in quantum yield is a consequence of cavity-enforced electronic aggregation between the luminophores, whereas increase in lifetime could be due to decreased quantum efficiencies of other non-radiative pathways. More interestingly, the HT-excimer of ternary complex of $ST-3@CB8$ and the syn-excimer of $ST-4_{(n=5)}@CB8$ were quite similar except for difference in their λ_{max} . The authors were able to achieve supramolecular manipulation of luminescence to design a reversible color-tunable luminescent assembly, including near white-light emission into the visible region ranging (between 465 and 607 nm).

The photophysics of thioflavin (TF) and instance of aromatic crown ether-stabilized twisted state and enhancement of TICT emission were discussed in Sect. 5. Now, the effect of a wider cavitant (CB8) on complex structure and its influence on photophysical activity leading to excimer emission are discussed. Host-guest

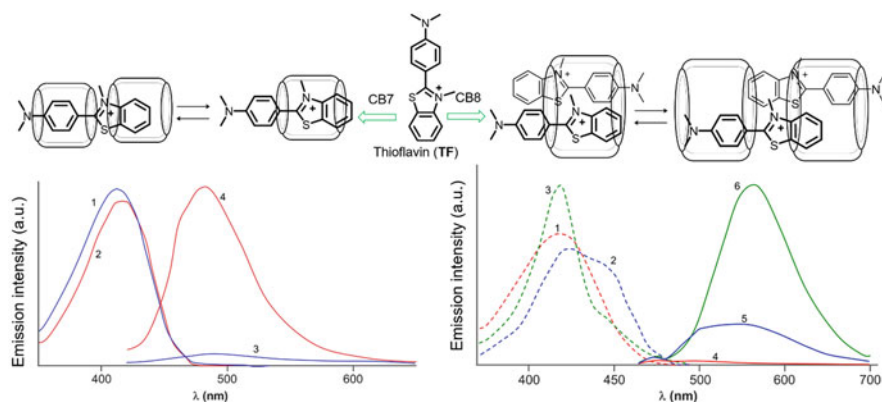


Fig. 26 (Top) Excimer emission of thioflavin (TF) through ternary complex formation with CB8. (Left) Absorption (1, 2) and emission (3,4) of 3 μM TF in the presence of 0 and 1 eq. CB7. (Right) Absorption (1–3) and emission (4–6) of 2 μM TF in the presence of 0, 1, and 10 of eq. CB8. All spectra were recorded in aqueous media. Spectra and structure reproduced from published work [72]

approach to studying emissive properties of TF is of particular importance considering its role in biomedical imaging. TF is a cationic benzothiazole dye that has been extensively applied in the early detection of amyloid fibril formation in tissues to diagnose chronic disorders such as Alzheimer's and Parkinson's diseases. Binding of TF with protein fibrils is shown to be quite specific, and detection is mainly based on the characteristic fluorescence of TF ($\Phi_f = 0.0003$) at 490 nm, which increases dramatically ($\sim 1,000$ -fold) upon binding to cavities in the amyloid fibrils. In recent years, the use of TF as an extrinsic fluorescent dye has increased significantly, due to its versatility, sensitivity, and suitability for high-throughput screening in detecting amyloid fibrils in tissues. Though the application of TF for the analysis of different aggregating systems is rapidly rising [70], the exact mechanism for TF binding into the cavities of the amyloid fibrils causing dramatic changes in its fluorescence properties remains to be fully understood [71].

Excimer emission of TF was observed when fluorometric titration was performed with CB8, which differed significantly from that observed for titration with CB7 as reported by Mohanty et al. [72]. Titration of solution of TF with increasing CB8 concentration resulted in shift in absorption band from 412 nm toward 445 nm with a well-defined isosbestic point at 428 nm, and on further addition of CB8, the absorption peak retracts to 415 nm with another isosbestic point at 426 nm; the final spectrum remains markedly different from the spectrum of TF alone, as shown in Fig. 26.

Excimer emission effected by CB8 was studied in the presence of metal ions, as cations are known to competitively bind to cucurbituril portal. Addition of a strongly competitive cation-like Ca^{2+} resulted in a loss of fluorescence as well as excimer emission from the molecule suggesting an efficient displacement of the guest from the cavity. Based on the combination of photochemistry, computational chemistry,

and NMR titration, the authors demonstrated the control over the supramolecular excimer assembly between a benzothiazole dye (thioflavin TF) and a macrocyclic host (CB8). The strong ion-dipole interactions provided by the carbonyl portals of the CB8 adequately support the stabilization of two π -stacked TF, both in 1:2 (CB8-TF) and 2:2 stoichiometric ratio. The noncovalently stabilized assembly brings out an intense novel excimer emission band at 570 nm, tunable in the presence of Ca^{2+} . Such tunable host-guest molecular assemblies find immense implications in activating non-diffusional- and stoichiometry-controlled photoinduced processes and excimer-based fluorescence on/off switches and provide design criteria for tailor-made molecular assemblies based on supramolecular interactions [73, 74].

7 Energy Transfer Cascade

Energy transfer can occur between a photoexcited chromophore (donor) and a fluorophore (acceptor) when their LUMO energies are close to each other, especially when acceptor LUMO is lower than that of donor's. Energy transfer in a two-component system is well-known, but there are only a few reports of multistep energy transfer in three-component systems. Controlled energy transfer between a three chromo-fluorophore sequence was demonstrated with the use of cavitands. The cationic analog of octa acid host, the octa ammonium host (Fig. 27, OAm^{8+}), which consists of eight ammonium-terminated side arms, was synthesized by Ramamurthy's group. The host was utilized to demonstrate the concept of three-component energy cascade system [75] by adsorbing dye-encapsulated OAm^{8+} capsules onto clay surfaces. The octa amine host was specifically advantageous in this scenario as the ionic interaction between negative electrostatic charge on clay

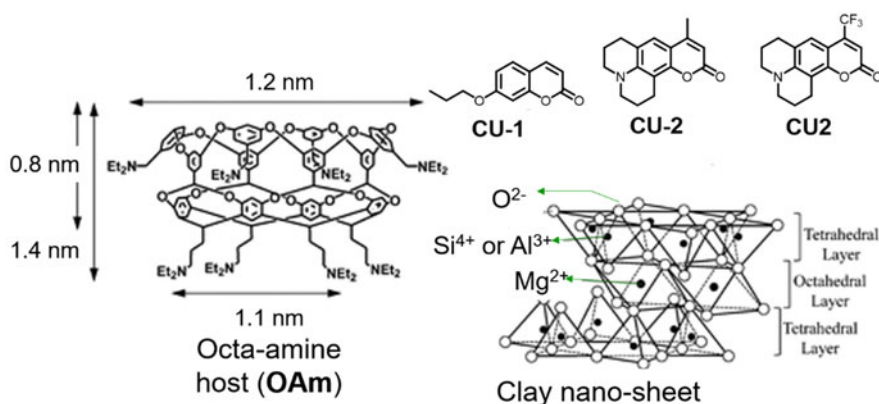


Fig. 27 (Left) structure of octa amine host (OAm). (Right, top) Structures of coumarin chromo-/fluorophores used in the energy transfer cascade system. (Right, bottom) Representation of clay nano-sheets. Images used with permission from the American Chemical Society [75]

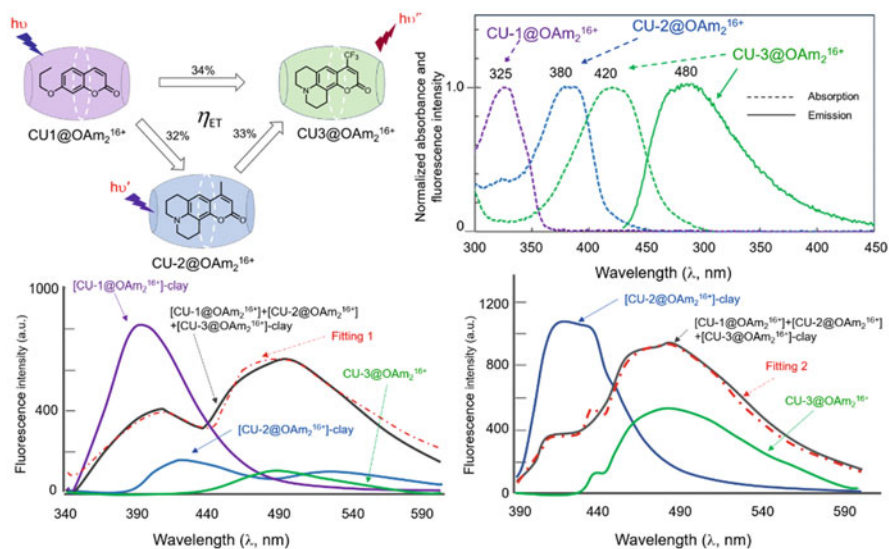


Fig. 28 (Top left) Depiction of energy cascade sequence. (Top right) Absorption spectra of CU-1, CU-2, and CU-3, respectively, and emission spectrum of CU-3. (Middle) Depiction of the energy cascade. (Right) Emission spectra. (Bottom left: purple, blue, and green) Emission spectra of individual encapsulated CUs within OAm₂ adsorbed to clay. Black spectra are emissions of mixture of CUs@OAm₂ adsorbed to clay (left 320 nm, right 380 nm). Red spectra are best fitting generated based on mathematical models to determine individual ET efficiencies. Raman scattering at 360 is not represented for sake of clarity. Top right spectrum used with permission from the American Chemical Society and other images reproduced from published work [75]

surface and cationic arms of OAm⁸⁺ resulted in a strongly adsorbed energy cascade system.

Three coumarin derivatives (7-propoxy coumarin, coumarin-480, and coumarin-540a: CU-1, CU-2, and CU-3, respectively) having different absorption and emission spectra were encapsulated within a water-soluble organic capsule formed by the two positively charged ammonium-functionalized cavitand octaamines; none of the dyes were adsorbed on the clay surface directly. The coumarins 1–3 absorb in ultraviolet, violet, and blue regions and emit in violet, blue, and green regions, respectively (Fig. 28, top right). Energy transfer between the three coumarins encapsulated within OAm₂ (OAm⁸⁺ dimeric capsule) complexes assembled on the surface of a saponite clay nanosheet was investigated by the authors in steady-state and time-resolved emission techniques. The choice of coumarins based on their ground and excited-state energy levels was such that singlet-singlet energy transfer proceeded CU-1 → CU-2 → CU-3 alongside CU-1 → CU-3 and CU-2 → CU-3. Expected performance of the cascade was realized as evidenced by the emission profiles of mixture of OAm₂-encapsulated coumarins, which were aligned on a clay surface (Fig. 28) upon photoexcitation of CU-1.

The ET efficiencies (η_{ET}) of two-component systems were studied first with one absorbing donor and one emissive acceptor for CU-1* → CU-2, CU-2* → CU-3,

CU-1* \rightarrow CU-3 (Fig. 28 bottom left: purple, blue, green). Emission spectra of mixture of the three coumarins encapsulated within OAm₂ on clay showed predominant emission from the energy acceptor CU-3 irrespective of which donor was excited (CU-1 at 320 nm and CU-2 at 380 nm, Fig. 28 bottom right). Mathematically generated best-fit emission spectra based on individual ET efficiencies and statistical analysis of surface distribution of the donor-acceptor arrangement were almost identical to the empirical data (dotted red line vs. black line). The best-fit spectrum was also useful in determining the individual ET efficiencies, which was comparable to that of the two-component systems upon normalization. Comparison of energy transfer efficiencies of the two-component and three-component systems clearly demonstrated that excitation of CU-1 leads to emission from CU-3 (Fig. 28) through an energy cascade pathway. Successful merging of supramolecular chemistry and surface chemistry by demonstrating novel multistep energy transfer in a three-component dye-encapsulated system on a clay surface opens newer opportunities for exploring such systems in an artificial light-harvesting phenomenon.

8 Singlet Oxygen

Singlet oxygen is the common name of an electronically excited state of molecular oxygen which is less stable than molecular oxygen in the electronic ground state, which is a triplet species (Fig. 29).

Molecular oxygen in its ground state contains two unpaired electrons due to two degenerate orbitals in its HOMO (${}^3\Sigma_g^-$, Fig. 29, right). Two excited singlet (electron-coupled) states exist for oxygen – ${}^1\Sigma_g^+$ and ${}^1\Delta_g$ – that are higher in energy by 150 and 95 kJ/mol, respectively [76]. Under typical experimental conditions, the ${}^1\Sigma_g^+$ (upper excited) state rapidly relaxes to the lower-energy ${}^1\Delta_g$ state; therefore, majority of the photophysicochemical phenomena of singlet oxygen are observed

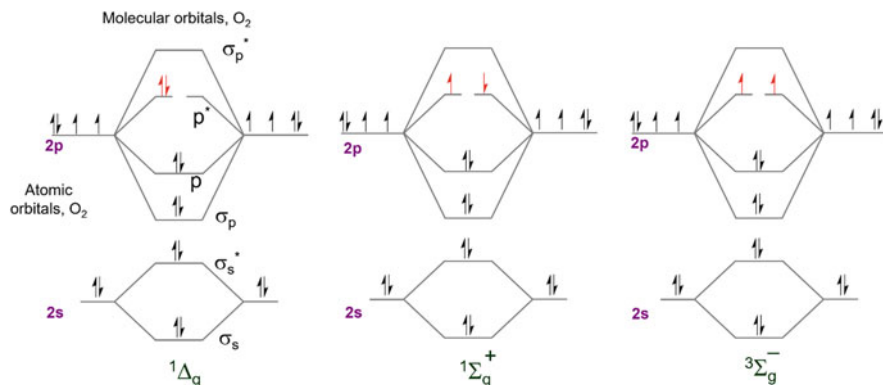


Fig. 29 Molecular orbital energy diagram for the two excited singlet states of oxygen (left, and middle) and triplet ground state

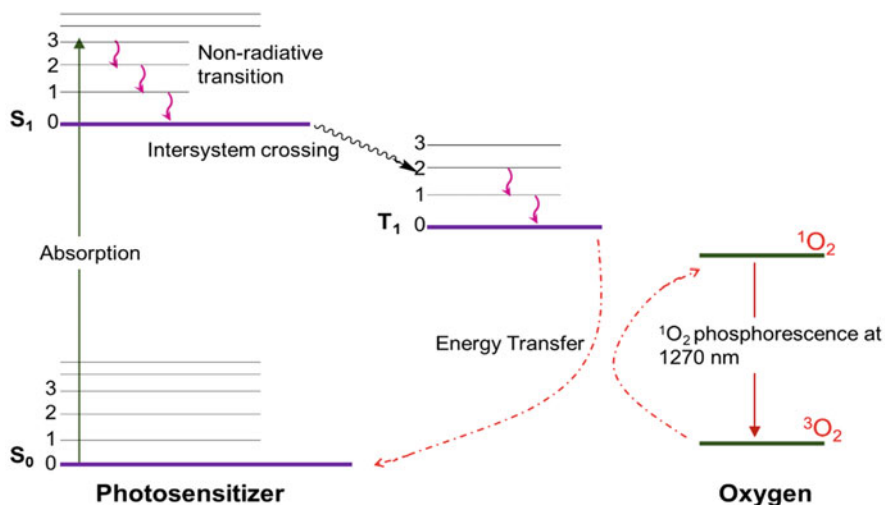


Fig. 30 Jablonski diagram representing singlet oxygen generation through triplet energy transfer from photosensitizer

from the $^1\Delta_g$ state. Singlet oxygen is typically generated via energy transfer from the excited state of a photosensitizer (dyes) to the oxygen molecule (Fig. 30). Photoexcitation of a dye molecule, which possesses high ISC rates, engages in efficient spin-coupled triplet energy transfer ($T_{1,dye} \rightarrow S_{0,dye}$) to triplet oxygen ($T_{1,O_2} \rightarrow S_{1,O_2}$). Singlet oxygen thus generated is a much more reactive form of oxygen, engaging in redox chemistry or weakly phosphoresces in the infrared region.

Singlet oxygen science has tremendous implications in biomedicine, materials science, drug delivery, and organic synthesis. For example, photodynamic therapy (PDT) is a treatment modality wherein its in situ generation is an efficient and relatively benign approach to tumor cytotoxicity. As a highly reactive species, controlling singlet oxygen generation has great value in protecting material surfaces.

Cavitand-regulated activatable photosensitizer with dual role as singlet oxygen generator (SOG) and fluorescent imager was reported by Wang et al. (Fig. 31) [77]. Activatable photosensitizers (aPSs) are photodynamic therapy (PDT) agents that possess the ability to simultaneously image cancer location and its selective ablation. Traditional synthetic approaches to designing aPSs are inefficient and tedious due to the need for combining various modules (photo-, physio-, and biochemical) covalently. An efficient approach to construction of ternodal system could be achieved through host-guest inclusion based on supramolecular interactions. The system reported by Wang is based on the host-guest interaction between the biotinylated toluidine blue (TB-B) and CB8 to form ternary TB-B₂@CB8 complex. This is a three-component system with biotin unit acting as a cell-receptor-anchoring unit, toluidine blue as a singlet oxygen generator and fluorophore, and CB8 as a function regulator as depicted in Fig. 31 (left).

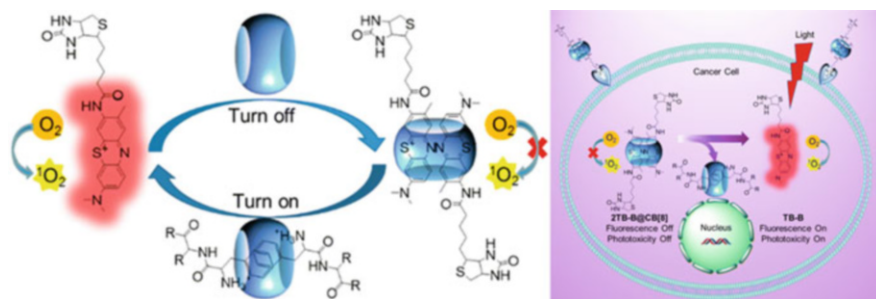


Fig. 31 (Left) Cavitand-based activatable photosensitizer (aPS) assembly for singlet oxygen generation and simultaneous imaging. (Right) Utility of aPS for simultaneous cellular PDT and imaging. Images used with permission from the American Chemical Society [77]

TB-B is a phenothiazine dye with dual activity as an efficient SOG and fluorophore. As a free, uncomplexed dye, TB-B generated singlet oxygen, which was monitored through the endoperoxidation of anthracene 9,10-dipropionic acid [78]. As a luminophore, free TB-B also possesses strong fluorescence at ~ 650 nm. In the presence of added CB8, the dye self-assembles into a ternary complex (TB-B₂@CB8) with head-to-tail guest arrangement owing to steric interaction between the bulky biotin side arms. With CB8 acting as a physical barrier, the SOG ability of TB-B is suspended; as two dyes are included within the cavity, TB-B also loses its ability to fluoresce due to self-quenching. Releasing complexed TB-B through competitive guests known to have very high affinity for CB8, such as N-terminated aromatic peptides, restored its photophysical activity. The utility of such a system for simultaneous tumor ablation and imaging is presented in Fig. 31 (right): biotin arm anchors the photoinactive ternary complex (TB-B₂@CB8) onto cell-surface receptor, which is then transported into the cell where intracellular N-terminated aromatic peptides would release TB-B restoring its photodynamic activity and fluorescence.

The role of CB in a self-assembled polymeric network capable of generating singlet oxygen was demonstrated by Liu et al. [79] Hyperbranched supramolecular polymers were obtained by mixing a tetranaphthyl-substituted porphyrin (TPOR, Fig. 32) derivative and CB8 in aqueous solution, which was driven by host-guest interactions. The formation of a supramolecular polymeric structure can cause disruption of the porphyrin aggregation, thus leading to enhancement of their singlet oxygen generation (SOG) efficiency. Unlike the previous example (Fig. 32) where complexation-induced suspension in SOG efficiency was observed, TPOR polymeric network is photoinactive when uncomplexed and generates singlet oxygen upon inclusion and polymer formation. This is because porphyrins are poor SOGs, in general, as they remain aggregated due to their large, rigid, planar structures, which leads to aggregation-induced photodeactivation. Affinity of CB8 for cationic guests disaggregates the TPOR units, while its ability to include two guests simultaneously results in formation of an extended . . . TPOR..CB..TPOR..CB..TPOR. . . network.

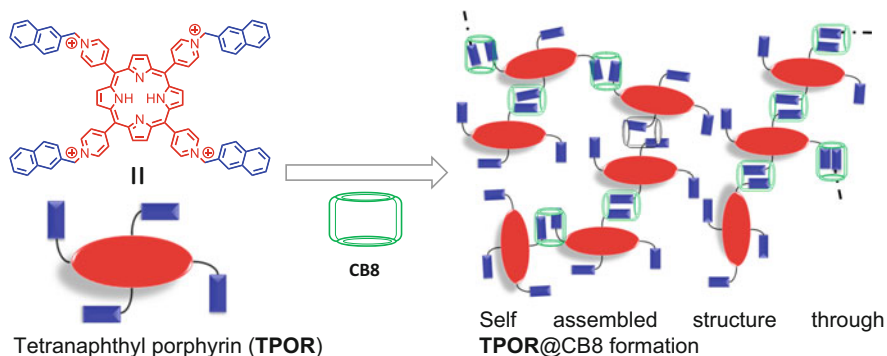


Fig. 32 Cucurbituril-mediated enhancement of singlet oxygen generation efficiency of naphthyl TPOR: Structure of TPOR and complexation of CB to form TPOR-CB8 network. Image reproduced from published work [79]

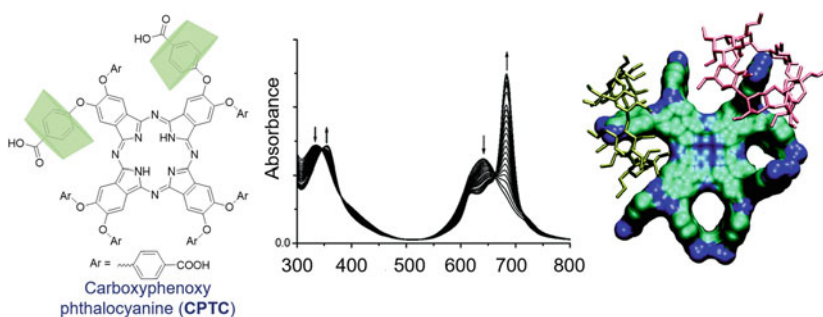


Fig. 33 (Left) Chemical structure of CPTC and its complexation with host to form CPTC@ β -CD₂ complex. (Middle) Complexation-induced changes in UV-Vis absorption spectrum. (Right) Energy minimized structure of complex. Image used with permission from the American Chemical Society [80]

Another example of enhanced SOG of an otherwise photoactive dye rendered inactive due to aggregation-induced photodeactivation was reported by Leng et al. (Fig. 33) [80]. Carboxyphenoxy phthalocyanines were synthesized and tested for their nascent SOG efficiency, which was quite low due to strong tendency for π -stacked aggregation. Disaggregation through complexation using β -CD to form a 1:2 (CPTC@ β -CD) complex showed significant changes in absorption and emission characteristics as well as its SOG efficiency.

The use of CBs in manipulating SOG efficiency of TPOR and its antibacterial efficacy in solid state was reported by Liu et al. [81]. The previous examples demonstrate the value of cavitands in SOG in homogeneous media; the same in solid state is even more difficult as there is greater tendency for aggregation among dyes. Employing neutral hosts such as cyclodextrins does not guarantee disaggregation in solid state as protruded units of the guests could engage in aggregation leading to photochemical deactivation. This tendency for aggregation despite

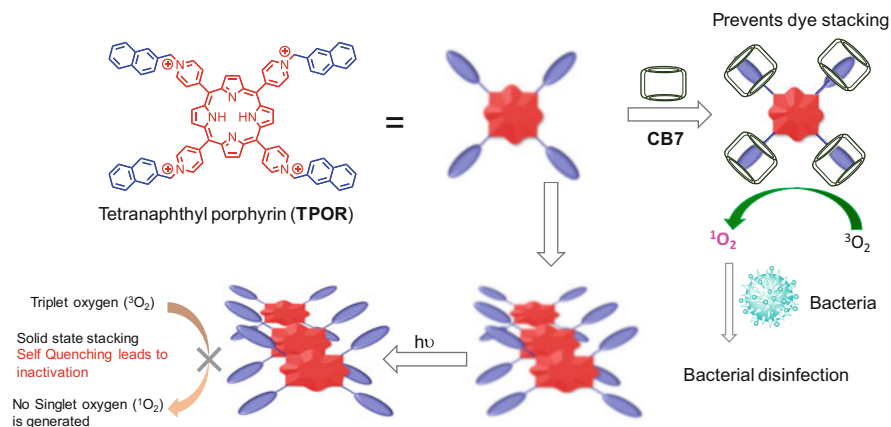


Fig. 34 Depiction of cucurbituril-TPOR complex capable of generating singlet oxygen for bacterial disinfection. Reproduced based on published work [81]

complexation could be avoided if ionic dyes were employed. Liu et al. reported lowering of aggregation-induced deactivation upon complexation to CB as shown in Fig. 34. The dye, owing to its cationic charge, was also well-adsorbed onto gram-negative bacteria (*E. Coli*). This led to strong bacterial disinfection efficacy even in solid state.

9 Photocycloaddition Reactions Within CavitanDs

Photocycloadditions (PCA) are symmetry-allowed pericyclic excited-state reactions that follow to the Woodward-Hoffmann orbital selection rules resulting in cyclic products [82–84]. They are one of the most studied photochemical reactions performed within macrocyclic cavitanDs with contrastable outcomes between free and supramolecularly controlled reactions [31, 85, 86]. As a bimolecular reaction, they suffer from significant entropic unfavorability and stand to benefit the most from cavitanD mediation; self-assembly of two alkene reactants and a cavitanD into a termolecular inclusion complex (1:2 host:guest) provide the necessary condition for an efficient bimolecular PCA. Though there has been a consistent activity of cavitanD-mediated PCA in supramolecular photochemistry literature, there has been notable evolution in its complexity, efficiency, and yield since the turn of this century facilitated by advancement in computational chemistry and hardware and spectroscopic and colorimetric instrumentation.

PCA is often precluded by the unimolecular photoisomerization in acyclic and larger cycloalkenes. Moreover, even upon dimerization, as many as eleven stereo-/regio-isomeric dimers can result in homodimerization (homo-PCA) reaction between identical alkenes (Fig. 35). As the bimolecular reaction is doubly disadvantaged entropically, and due to the low probability of fruitful molecular collision

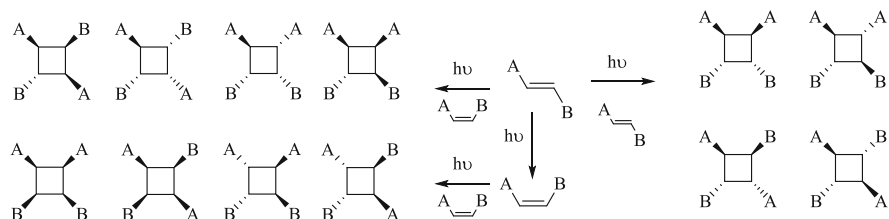


Fig. 35 Alkene photochemistry leading to isomerization and the various possible isomeric dimers

occurring within the excited-state lifetime (typically in the range of nano- to micro-seconds), PCAs generally suffer from low quantum yields. PCAs from excited triplet state are less likely to occur with regio- and/or stereoselectively.

The supramolecular approach employed to promote PCA of alkenes falls under two categories: crystal engineering (CE), and cavitand mediation. The CE approach achieves controlled PCA based on reduced rotational and translational freedom experienced by molecules in organized solid state [87, 88]. This approach, pioneered by G. M. J. Schmidt, is referred to as topochemical solid-state transformation [89]. However, the inability to predict molecular packing of organic molecules in crystals renders this method less general and very reactant-specific. The other method, more general and reliable, for directing the reactivity of alkenes is the cavitand-mediation approach. This involves confining two reacting alkenes in the cavity of a large cavitand (Fig. 36) and pre-orienting them based on supramolecular interactions toward a specific dimeric product upon excitation. Cavitand-mediated photodimerization of alkenes has been known since the early 1980s. Early studies were carried with cyclodextrins as templates.

The 2+2 PCA within cavitands has been demonstrated for several families of alkenes, and each of them presents unique perspective into this reaction. Such efforts focus on two main aspects of this reaction that are of fundamental science significance: quantum efficiency of dimerization and chemoselectivity. Quantum efficiency of photodimerization, over isomerization, indicates stability/dynamism of ground-state termolecular complex, and stereoselectivity is an indication of multiplicity of excited-state and ground-state complex structure; however, it should also be recognized that multiplicity and efficiency are interrelated. Several instances of PCA of alkenes affected within cavitands have served as a proof of feasibility of cycloadditions that either are not possible without supramolecular mediation or are difficult to predict theoretically. This section will present a series of simple and predictable PCAs affected within cavitands and its usefulness in understanding molecular structure and bonding, which is deducible from weak interactions between encapsulated guests.

Cinnamic acids (CAs) have been at the forefront of the study of PCA since Schmidt studied their reactivity to deduce topochemical information (relative structure and orientation) of reactants, wherein the quantum efficiency of dimerization was directly proportional to the proximity of the alkene bonds. Cucurbituril-mediated PCA of CAs was reported by our group (Fig. 36) [90, 91]. Both quantum

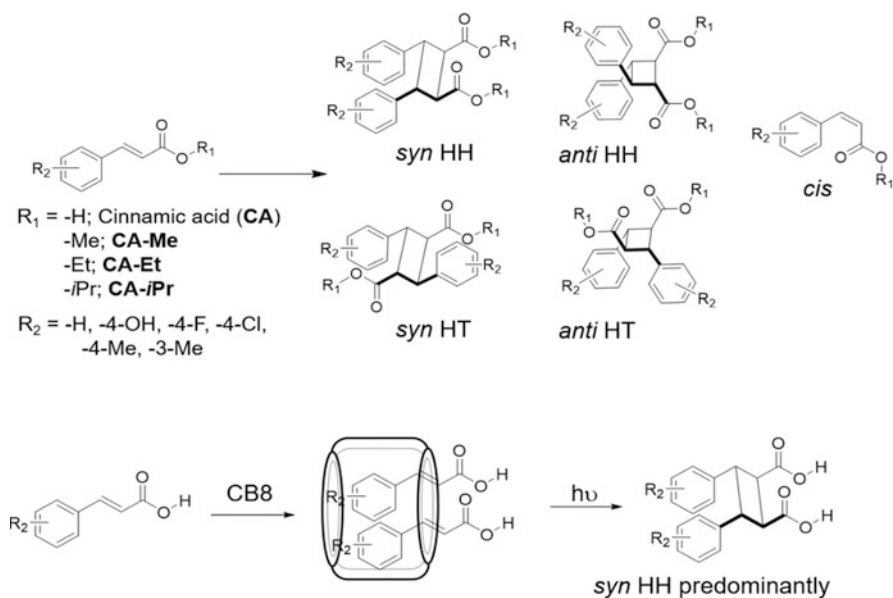


Fig. 36 Product distribution in photochemistry of cinnamic acids (CAs). Four isomeric dimers are possible *syn*-HH (*syn*-head-to-head); *anti* HH (*anti* head-to-head); *syn* HT (head-to-tail); and *anti*-HT (*anti* head-to-tail)

yield of dimerization and stereoselectivity in favor of the *syn*-head-to-head (*syn*-HH, Fig. 36) were observed for CAs irrespective of the substituent on the aromatic ring. Inferences regarding the complex stability were derived from this work as high dimerization efficiency corresponded to the proximity of the alkene bond. However, at that time, no inferences regarding the complex structure (i.e., electronic/steric origins of HT vs. HH arrangement, Fig. 36) based on stereoselectivity were derived. Later studies, especially in the last decade, including our group [92], have delved into the stereoselectivity aspect of these reactions and deduced their supramolecular implications.

For instance, photoactivation of alkyl cinnamates (Fig. 37, $R_1 = -Me, -Et, -iPr$) within cavitands yielded *anti*-HT dimers [92]. The dominance of the HT dimer, with respect to the *syn*-HH dimer, was directly proportional to the size of the alkyl group; methyl cinnamate afforded approximately equal amounts of HH and HT dimers; and isopropyl cinnamates yielded exclusively *anti*-HT dimers, while CAs yielded exclusively *syn*-HH dimers in all cases. This progressive inversion in dimer stereoselectivity from free carboxylic acid to isopropyl ester indicated the impact of supramolecular interaction (alkyl...alkyl sterics) on the relative alignment of alkenes within the cavitand. However, a more important, previously unstated, inference was also derived from this work. The fact that CAs exclusively afforded *syn*-HH dimer suggests that HH arrangement is favored within the cavity, which could be attributed to two directing interactions, π - π (aromatic rings) and hydrogen-bonding interaction (carboxylic acids). However, whether either or both interactions

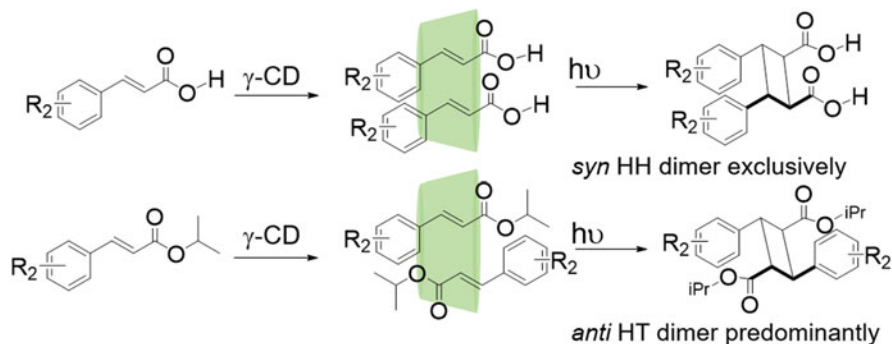


Fig. 37 Controlling regio- and stereoselectivity of CA dimerization using cavitannds

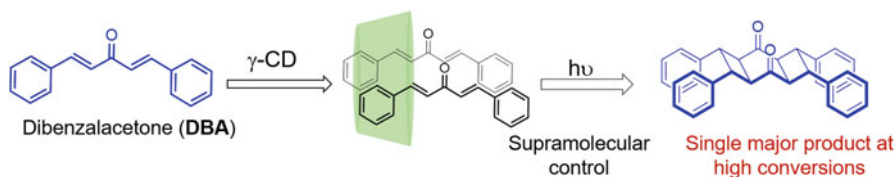


Fig. 38 Longitudinal photodimerization of cross-conjugated dienes affected within cavitant

are directing the reactants' relative orientation was resolved by photochemistry of alkyl cinnamates. Replacing the acidic hydrogens with methyl groups eliminated contribution of hydrogen-bonding interaction in complex structure. Therefore, if steric interactions between methyl groups were not counteracted, *anti*-HT should be the only product; however, equal amounts of HH and HT dimers were observed, which indicated that the steric conflict between two methyl groups is qualitatively balanced by the π - π interaction. Thus, the role of both π - π interaction and hydrogen bonding was inferred.

The directing influence of π - π interaction, more than that of hydrogen bonding, could be deduced from the fact that PCA of CAs within cucurbituril in homogeneous aqueous media also yielded the *syn*-HH dimer. The self-directing influence between two CAs remained essentially unchanged despite change in macrocyclic host as well as the medium. While both hosts are similar in dimensions, CDs encapsulate guests through hydrophobic effects while CBs through dipole-dipole interaction. Moreover, the presence of water in homogeneous aqueous medium would compete with hydrogen bonding between the free acids; similar competition for CA-CA hydrogen-bonding interaction could be expected from the alcoholic groups in (cyclodextrins) CDs as well as remanence of residual water used for complexation. Thus, this presents a strong evidence for aromatic ring being the strong driving force behind the HH alignment of CAs while in proximity.

The ability of cavitannds to affect previously unexplored 2+2 PCA of alkenes, such as cross-conjugated, extended alkenes [93], has been demonstrated. Dibenzalacetones (DBA, Fig. 38) are cross-conjugated 1,4-pentadiene systems

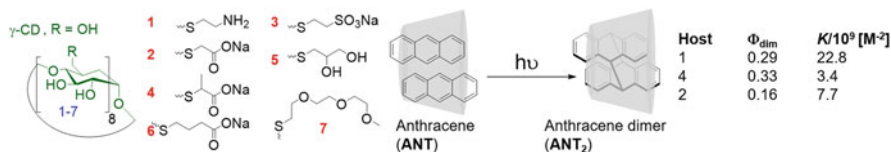


Fig. 39 Photocycloaddition [4+4] of anthracene within cyclodextrin thioether hosts. Reproduced from published work [94]

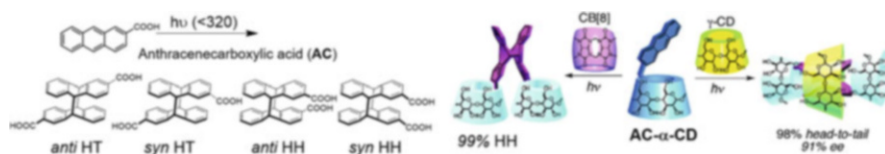


Fig. 40 PCA of anthracene carboxylates within CD and CB and corresponding differences in regioselectivity. Used with permission from the American Chemical Society [95]

with two cyclizable π -bonds. Despite the presence of two reactive centers in the molecule and propensity of such system to yield multitude of unintended products, the ternary complex of the guest with γ -CD resulted in perfectly stacked arrangement leading to formation of the *syn*-HH dimer.

The [4+4] PCA of polyaromatic hydrocarbons is also highly dependent on intermolecular distance between the reactants. However, due to lack of a competing photoisomerization pathway, and dimerization being the only reaction, aromatics such as anthracenes (ANT) undergo only 4+4 PCA upon irradiation in homogeneous solution. Wang et al. showed that the quantum yield of anthracene dimerization is significantly increased when encapsulated within water-soluble cyclodextrin complexes rendered soluble through polar functionalization (Fig. 39) [94].

Though PCA of water-soluble anthracene derivatives has been performed before, the same for ANT complexes in homogeneous solutions has not been possible as the inclusion compounds of ANT in native β -CD or γ -CD are completely insoluble in water. Several conjugate base-functionalized CDs were synthesized, which encapsulated two ANTs within the cavity leading to water-soluble complexes. Efficiency of 4+4 PCA varied significantly between the various water-soluble hosts (Fig. 39). The quantum yield of dimerization (Φ_{dim}) did not correlate with the binding constant K ; therefore, it was inferred that Φ_{dim} is a function complex structure and ANT...ANT orientation as opposed to strength of binding interaction.

Photocyclodimerization of α -cyclodextrin-appended anthracene (AC- α -CD, Fig. 40) was studied in the presence of γ -CD and CB8 hosts to manipulate the stereo-differentiating photoreaction occurring inside the cavity by the bulky attachment located outside [95]. The γ -CD-mediated photodimerization afforded the HT photodimers in 98% combined yield, in particular, the *syn* HT photodimer in 68% yield. This is much greater than 44% yield obtained with unmodified anthracene carboxylate within γ -CD. The use of CB8 on the other hand led to a striking inversion of the head-to-tail/head-to-head selectivity, affording exclusively the

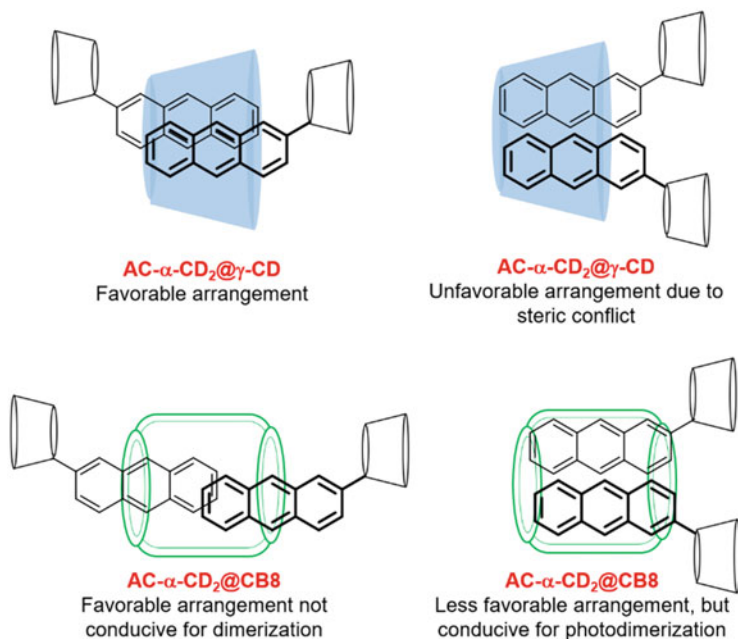


Fig. 41 Difference in regioselectivity demonstrates effect of cavitand's depth on complex structure and product selectivity. Reproduced from published work [95]

head-to-head (HH) photodimers in 99% combined yield. The difference in regioselectivity of the product is deduced to be due to difference in cavitand depth between the two hosts. Though the width of the two cavitands is comparable, CBs (9.1 Å) are significantly taller than CDs (7.0 Å). Thus CDs allow 4+4 PCA of the internal aromatic nucleus of ANT while in H-T arrangement, which is favored due to avoidance of steric interaction between the tethered CDs (Fig. 41), whereas the deeper cavity of CBs does not allow the required proximity of inner nuclei of tethered ANT for PCA. Thus, the only arrangement conducive for dimerization, despite its steric unfavorability, is the HH orientation.

Despite its importance, most of the reports of PCA, both free and supramolecularly controlled, are focused on the reaction between identical alkenes (homodimerization), while PCA between non-identical alkenes (cross-dimerization) has not been explored well. The first example of a highly efficient instance of cross-dimerization between dual photoactive alkene pairs was reported by Fujita's groups affected within their then newly synthesized palladium nanocage (Fig. 42) [96]. The palladium nanocage Pd-NC synthesized by his group is a hemicarcer and constructed based on the coordination of tripyridyltriazine and ethylene diamine (EDA) ligands with Pd²⁺, wherein the aromatic ligands formed the four alternating faces of the octahedron with the metal ion in the apexes and the EDA capping the external coordination site. The resulting structure contained hydrophobic interior, which encapsulated organic guests predominantly through hydrophobic interactions.

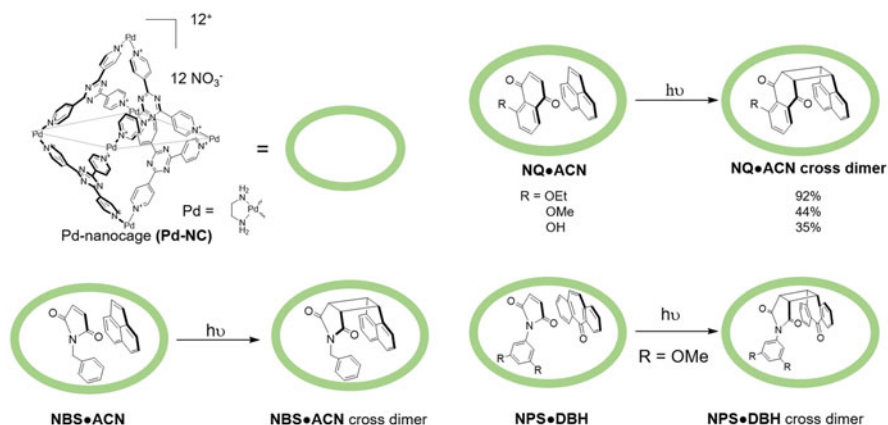


Fig. 42 Cross-photodimerization between alkenes affected by palladium nanocage (Pd-NC). Naphthoquinone (NQ), acenaphthylene (ACN), *N*-benzyl succinimide (NBS), *N*-phenylsuccinimide (NPS), dibenzocycloheptanone (DBH)

The tight spaces within the palladium nanocage were demonstrated to be conducive for selective inclusion of a series of hetero-alkene pairs: acenaphthylene (ACN) and *N*-benzyl succinimide (NBS), acenaphthylene and naphthoquinones (NQ), dibenzosuberone (DBH), and disubstituted-*N*-phenylmaleimides (NPM). This approach was based on the strategy of size-complementarity selective inclusion of alkenes to form the ternary 1:1:1 complex, which yielded the *syn* heterodimers exclusively in majority of the reactions. Some of the selectivity reported in nanocage is perhaps the highest for the reaction reported in a homogeneous medium for cross-dimerization reactions to date. While the chemoselectivity for crossdimers over homodimers is explained based on cavitand/guest size-complementarity, the stereochemical selectivity for *syn* is also explained in terms of the spatial limitations as the *anti*-dimer (and hence the precursor arrangement) is too large to fit within the cage. Despite its remarkable efficiency, there were fewer reports involving the nanocage for PCA (homo and cross) that followed the aforementioned work. This is perhaps due to the spectral interference from aromatic ligands in the nanocage, which acted as an internal absorption filter. Other instances of cross-photodimerization mediated by cavitands such as CDs [97] and OAs could be found in literature.

10 Photo-Fries Rearrangement

Photo-Fries rearrangement reaction [98] involves the homolytic cleavage of a carbon-heteroatom bond (C–O, C–S, and C–N, of esters, thioesters, and amides). The radical mechanism of the photo-Fries rearrangement is well-established, and it is currently understood to occur mainly through the excited singlet state [99, 100]. Photo-Fries rearrangement of aromatic esters has been used to assess

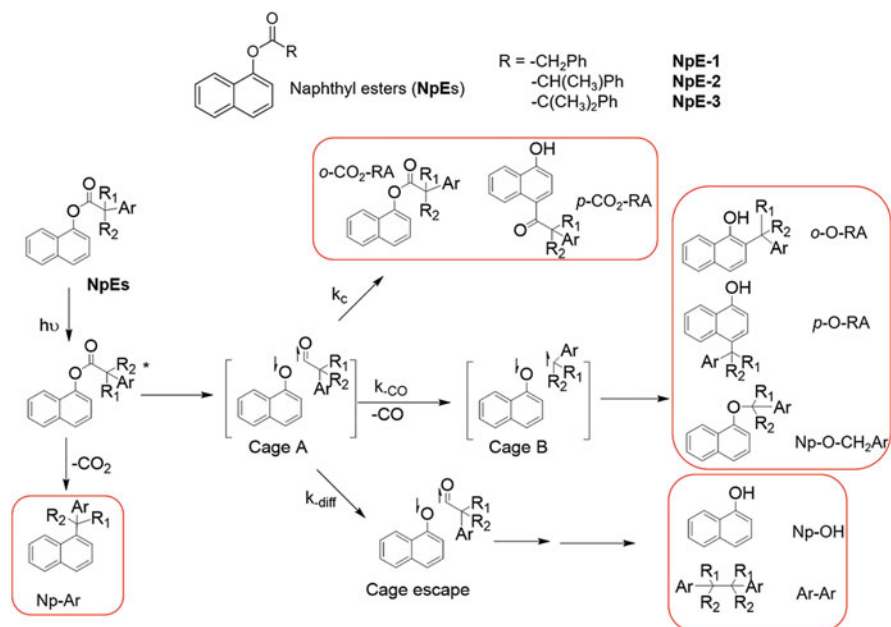


Fig. 43 Photochemistry of naphthyl benzoates leading to different products

molecular cavities of host systems such as cavitands [101, 102], micelles [103–105], and other organized media [106].

Photochemistry of naphthyl benzoates (NpE-1) occurs from their excited singlet state to yield singlet geminate radical pair: naphthoxy and phenyl acetyl radicals (Fig. 43). The fate of the radical pair thus generated is sensitive to the molecular cage surrounding it: when a confining molecular environment is present, in-cage recombination preempts any other facile process such as decarbonylation and decarboxylation, leading to ortho- and para-rearranged products *o*-CO₂-RA and *p*-CO₂-RA. Decarbonylation of phenylacetyl radical within the cage results in the radical pair B which leads to naphthoxy and benzyl radical pair; reactions of these radical pairs B either within or outside the cage result in decarbonylated product Np-O-CH₂Ar or its rearranged products *o*-O-RA and *p*-O-RA. Naphthol (Np-OH) and the coupled alkane products (Ar-Ar) result exclusively from proton abstraction and radical coupling from the cage-escaped radical pair. Thus, different products from the reaction represent different degrees of molecular confinement experienced by the radical pair, which is interpreted as how “leakproof” a given cavitand is. The rearranged products *o*- and *p*-CO₂-RA would result from cage effect that remains effective within the singlet timescale (nanoseconds) capable of affecting recombination before decarboxylation or decarbonylation could occur. Formation of decarbonylated products (Np-O-CH₂Ar, *o*-O-RA and *p*-O-RA) is indicative of moderate degree of cage effect, whereas the presence of Np-OH and Ar-Ar in product mixture indicates lack of any radical caging, which is typically the case in non-supramolecular solution-phase reactivity.

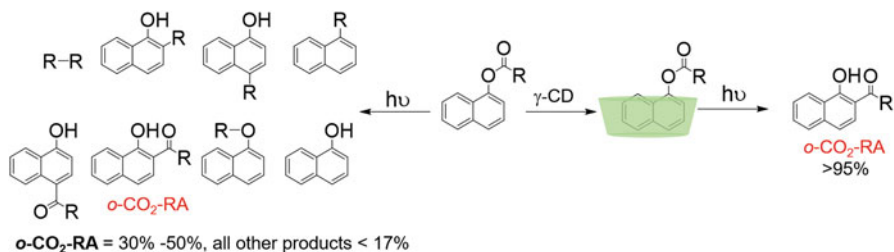


Fig. 44 Photochemistry of naphthyl benzoates: product distribution in hexane and selectivity observed within γ -CD

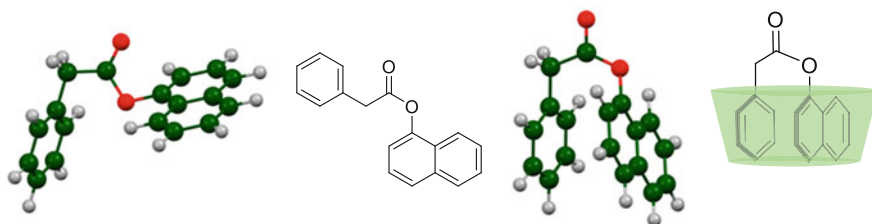


Fig. 45 Computed structure of naphthyl phenyl acylates of free and folded conformations simulating a bound guest. Structure and details reproduced from published work [107]

Photochemistry of NpEs (Fig. 44) investigated by Ramamurthy's group [107] in hexane yielded a broad mixture of products resulting from both in-cage and cage-escape pathways. The presence of *o*- and *p*-CO₂-RA between 30% and 50% in product mixture indicated influence of solvent cage effect on the radical pair. On the other hand, photochemistry of the NpEs complexed to γ -CD yielded the *o*-CO₂-RA in near quantitative proportions (>95%, Fig. 44). This remarkable switch in selectivity could be unambiguously attributed to the high degree of cage effect conferred by the cavitand. However, more structural information was elucidated by the authors using computational chemistry. Analysis of energy minimized structure of reactant in its free and bound (@ γ -CD) form compared to that of the product structure, which suggested that the reactants adapt into a folded conformation (Fig. 45) within the host, which is responsible for the high proportion of *o*-CO₂-RA as opposed to the para isomer.

11 Conclusion and Future Perspectives

Examples discussed in this chapter have represented supramolecular inclusion phenomena as an effective strategy and in many occasions as reliable toolkit, for controlling their physical and chemical behavior to direct excited-state processes. Such utilization of cavitands for fluorochrome manipulation has expanded

significantly since the turn of this millennia. New incidences of cavity-influenced photophysical phenomena such as singlet oxygen generation and anthracene phosphorescence have been demonstrated, while previously demonstrated phenomena such as TICT and photocycloaddition have been studied in greater detail. CDs dominated this area of research till the turn of this century, while CBs and OAs allowed supramolecular photochemists to explore new frontiers since the early 2000s. Though the modern cavitands (CBs and OAs) were markedly different from CDs with far superior binding strengths and unprecedented structure control on guest, they are still in the same single/small molecule dimension, relatively simple binding site characteristics, and cavity function. Future cavitands of larger dimension and complexity could be envisioned, which would allow photochemists to alter and study molecular behavior in unprecedented manner.

As represented in this chapter, the inter-subdisciplinary area of supramolecular photochemistry has predominantly explored familiar excited-state phenomena in newer chemical contexts. Future expansion in this area is expected to occur alongside synthesis/discovery of newer cavitands. As novel cavitands with wider supramolecular capabilities emerge, the opportunities to study previously unexplored excited-state dynamics would also arise. In addition to unraveling fundamental scientific knowledge of the excited-state characteristics, modern host-guest photochemistry has also realized very interesting applications using a rational approach, such as optical devices, synthetic utility, and disinfectants. Another notable activity in this area is the evolution of this strategy from molecular realm to macroscopic and material domains. It is anticipated that future researchers in this area would result in commercializable technology with real-time use.

Acknowledgments AN thanks GE Additive to support and approve the publication content. MP would like to thank his professional and life partner, Dr. Surabhi Chandra, for her support and patience during the preparation of this chapter. He also expresses his gratitude to Dr. Richard Mocarski (Assistant Vice Chancellor for Research) for his passionate support for research and providing new opportunities for researchers at UNK.

References

1. Bach T (2015) More chemistry with light! More light in chemistry! *Angew Chem Int Ed* 54:11294–11295
2. Roth HD (2001) Twentieth century developments in photochemistry. Brief historical sketches. *Pure Appl Chem* 73:395–403
3. Chan BP (2010) Biomedical applications of photochemistry. *Tissue Eng Part B Rev* 16:509–522
4. Pape M (1975) Industrial applications of photochemistry. *Pure Appl Chem* 41:535–558
5. Steed JW, Atwood JL (eds) (2009) *Supramolecular chemistry*. 2nd edn. Wiley, Chichester
6. Balzani V (1990) Supramolecular photochemistry. *Pure Appl Chem* 62:1099–1102
7. Turro NJ (1996) Supramolecular photochemistry. A paradigm for the 1990s? *J Photochem Photobiol A Chem* 100:53–56
8. Ramamurthy V, Schanze KS (2003) Photochemistry of organic molecules in isotropic and anisotropic media. In: *Molecular and supramolecular photochemistry*, vol 9. Marcel Dekker, New York

9. Atwood JL, Gokel GW, Barbour LJ, MacGillivray LR (eds) (2017) *Comprehensive supramolecular chemistry II. Volume 7: Supramolecular engineering: designing the solid state*. Elsevier, Amsterdam
10. Dalgarno SJ (ed) (2017) *Comprehensive supramolecular chemistry II. Volume 6: Supramolecular engineering: discrete molecular assemblies*. Elsevier, Amsterdam
11. Gokel GW, Barbour LJ (eds) (2017) *Comprehensive supramolecular chemistry II. volume 1: general principles of supramolecular chemistry and molecular recognition*. Elsevier, Amsterdam
12. Credi A (2012) *Supramolecular photochemistry controlling photochemical processes*. Edited by V. Ramamurthy and Yoshihisa Inoue. *Angew Chem Int Ed* 51:6311–6312
13. Tanaka K, Toda F (2002) *Organic photoreaction in the solid state*. In: Toda F (ed) *Organic solid-state reactions*. Springer, Dordrecht
14. Mena-Hernando S, Perez EM (2019) Mechanically interlocked materials. Rotaxanes and catenanes beyond the small molecule. *Chem Soc Rev* 48:5016–5032
15. Xu Y, von Delius M (2019) The supramolecular chemistry of strained carbon nano hoops. *Angew Chem Int Ed* 59(2):559–573
16. Cram DJ, Cram JM (eds) (1997) *Container molecules and their guests*. Royal Society of Chemistry, London
17. Bortolus P, Grabner G, Koehler G, Monti S (1993) Photochemistry of cyclodextrin host-guest complexes. *Coord Chem Rev* 125:261–268
18. Balzani V, Credi A (1996) *Supramolecular photochemistry: recent advances*. NATO ASI Ser C 485:163–177
19. Voegtle F, Weber E (eds) (1985) *Host guest complex chemistry: synthesis, structures, applications*. Springer, Berlin
20. Laeri F, Schueth F, Simon U, Wark M (eds) (2003) *Host-guest-systems based on nanoporous crystals*. Wiley, Amsterdam
21. Bortolus P, Monti S (1996) Photochemistry in cyclodextrin cavities. *Adv Photochem* 21:1–133
22. Ueno A, Ikeda H (2001) *Supramolecular photochemistry of cyclodextrin-related materials*. *Mol Supramol Photochem* 8:461–503
23. Ayitou A, Pemberton BC, Kumarasamy E, Vallavoju N, Sivaguru J (2011) Fun with photons: selective light induced reactions in solution and in water soluble nanocontainers. *Chimia* 65:202–209
24. Chemikova EY, Fedorov YV, Fedorova OA (2012) Cucurbituril as a new “host” of organic molecules in inclusion complexes. *Russ Chem Bull* 61:1363–1390
25. Mori T, Inoue Y (2012) Photochemistry in alternative media. In: Griesbeck, Oelgemoller, Ghetti (eds) *CRC handbook of organic photochemistry and photobiology*, 3rd edn. CRC Press, Boca Raton, FL, pp 249–275
26. Coyle EE, Oelgemoller M (2008) *Micro-photochemistry: photochemistry in microstructured reactors. The new photochemistry of the future?* *Photochem Photobiol Sci* 7:1313–1322
27. Ramamurthy V, Sivaguru J (2011) Controlling photoreactions through noncovalent interactions within zeolite nanocages, pp 389–442
28. Ramamurthy V (1990) *Photochemistry in zeolite cavities*. In: Atwood JL (ed) *Inclusion phenomena and molecular recognition*. Springer, Boston, MA
29. Jing X, He C, Zhao L, Duan C (2019) Photochemical properties of host-guest supramolecular systems with structurally confined metal-organic capsules. *Acc Chem Res* 52:100–109
30. Qu D-H, Wang Q-C, Zhang Q-W, Ma X, Tian H (2015) Photoresponsive host-guest functional systems. *Chem Rev* 115:7543–7588
31. Ramamurthy V, Sivaguru J (2016) *Supramolecular photochemistry as a potential synthetic tool: photocycloaddition*. *Chem Rev* 116:9914–9993
32. Chretien MN (2007) *Supramolecular photochemistry in zeolites: from catalysts to sunscreens*. *Pure Appl Chem* 79:1–20
33. Lakowicz JR (1983) *Principles of fluorescence spectroscopy*. Plenum, New York

34. Mako T, Marks P, Cook N, Levine M (2012) Fluorescent detection of polycyclic aromatic hydrocarbons in ternary cyclodextrin complexes. *Supramol Chem* 24:743–747
35. Serio N, Miller K, Levine M (2013) Efficient detection of polycyclic aromatic hydrocarbons and polychlorinated biphenyls via three-component energy transfer. *Chem Commun* 49:4821–4823
36. Heinz T, Rudkevich DM, Rebek Jr J (1998) Pairwise selection of guests in a cylindrical molecular capsule of nanometer dimensions. *Nature* 394:764–766
37. Heinz T, Rudkevich DM, Rebek Jr J (1999) Molecular recognition within a self-assembled cylindrical host. *Angew Chem Int Ed* 38:1136–1139
38. Debler EW, Kaufmann GF, Meijler MM, Heine A, Mee JM, Pljevaljcic G, Di Bilio AJ, Schultz PG, Millar DP, Janda KD, Wilson IA, Gray HB, Lerner RA (2008) Deeply inverted electron-hole recombination in a luminescent antibody-stilbene complex. *Science* 319:1232–1235
39. Armitage BA, Berget PB (2008) An enlightening structure-function relationship. *Science* 319:1195–1196
40. Matsushita M, Meijler MM, Wirsching P, Lerner RA, Janda KD (2005) A blue fluorescent antibody-cofactor sensor for mercury. *Org Lett* 7:4943–4946
41. Ams MR, Ajami D, Craig SL, Yang JS, Rebek J (2009) Control of stilbene conformation and fluorescence in self-assembled capsules. *Beilstein J Org Chem* 5:79
42. Itoh T (2012) Fluorescence and phosphorescence from higher excited states of organic molecules. *Chem Rev* 112:4541–4568
43. Mohan Raj A, Sharma G, Prabhakar R, Ramamurthy V (2019) Room-temperature phosphorescence from encapsulated pyrene induced by xenon. *J Phys Chem A* 123:9123–9131
44. Kalyanasundaram K, Thomas JK (1977) Environmental effects on vibronic band intensities in pyrene monomer fluorescence and their application in studies of micellar systems. *J Am Chem Soc* 99:2039–2044
45. Dong DC, Winnik MA (1984) The Py scale of solvent polarities. *Can J Chem* 62:2560–2565
46. Koziar JC, Cowan DO (1978) Photochemical heavy-atom effects. *Acc Chem Res* 11:334–341
47. Easley CJ, Mettry M, Moses EM, Hooley RJ, Bardeen CJ (2018) Boosting the heavy atom effect by cavitand encapsulation: room temperature phosphorescence of pyrene in the presence of oxygen. *J Phys Chem A* 122:6578–6584
48. Montes-Navajas P, Teruel L, Corma A, Garcia H (2008) Specific binding effects for cucurbit [8]uril in 2,4,6-triphenylpyrylium-cucurbit[8]uril host-guest complexes: observation of room-temperature phosphorescence and their application in electroluminescence. *Chem Eur J* 14:1762–1768
49. Steer RP, Ramamurthy V (1988) Photophysics and intramolecular photochemistry of thiones in solution. *Acc Chem Res* 21:380–386
50. Rao VP (1992) The photoreactivity of thiocarbonyl compounds. *Sulfur Rep* 12:359–403
51. Maciejewski A, Steer RP (1993) The photophysics, physical photochemistry, and related spectroscopy of thiocarbonyls. *Chem Rev* 93:67–98
52. Rajee R, Ramamurthy V (1979) Energy wastage in organic photochemistry: self-quenching in thiones. *J Photochem* 11:135–138
53. Maciejewski A (1988) The role of T1 self-quenching in photochemical decay of aromatic thiones. *J Photochem Photobiol A Chem* 43:303–312
54. Ramesh V, Ramamurthy V (1982) Inhibition of self-quenching in thioketones by micellar compartmentalization. *J Photochem* 20:47–52
55. Ramesh V, Ramnath N, Ramamurthy V (1982) Efficiency of singlet oxygen production by thiocarbonyls. *J Photochem* 18:293–299
56. Jayaraj N, Maddipatla MV, Prabhakar R, Jockusch S, Turro NJ, Ramamurthy V (2010) Closed nanocontainer enables thioketones to phosphoresce at room temperature in aqueous solution. *J Phys Chem B* 114:14320–14328

57. Jagadesan P, Samanta SR, Choudhury R, Ramamurthy V (2017) Container chemistry: manipulating excited state behavior of organic guests within cavitands that form capsules in water. *J Phys Org Chem* 30:e3728
58. De Mayo P (1976) Photochemical synthesis. 62. Thione photochemistry, and the chemistry of the S2 state. *Acc Chem Res* 9:52–59
59. Grabowski ZR, Dobkowski J (1983) Twisted intramolecular charge transfer (TICT) excited states: energy and molecular structure. *Pure Appl Chem* 55:245–252
60. Grabowski ZR, Rotkiewicz K, Rettig W (2003) Structural changes accompanying intramolecular electron transfer: focus on twisted intramolecular charge-transfer states and structures. *Chem Rev* 103:3899–4031
61. Kundu S, Chattopadhyay N (1995) Dual luminescence of dimethylaminobenzaldehyde in aqueous β -cyclodextrin: non-polar and TICT emissions. *J Photochem Photobiol A Chem* 88:105–108
62. Zhang YM, Zhang XJ, Xu X, Fu XN, Hou HB, Liu Y (2016) Rigid organization of fluorescence-active ligands by artificial macrocyclic receptor to achieve the thioflavin t-amyloid fibril level association. *J Phys Chem B* 120:3932–3940
63. Dong H, Wei Y, Zhang W, Wei C, Zhang C, Yao J, Zhao YS (2016) Broadband tunable microlasers based on controlled intramolecular charge-transfer process in organic supramolecular microcrystals. *J Am Chem Soc* 138:1118–1121
64. Schoder S, Schroder HV, Cera L, Puttreddy R, Guttler A, Resch-Genger U, Rissanen K, Schalley CA (2019) Strong emission enhancement in pH-responsive 2:2 cucurbit[8]uril complexes. *Chemistry* 25:3257–3261
65. Foerster T (1969) Excimers. *Angew Chem Int Ed Engl* 8:333–343
66. Birks JB (1970) Photophysics of aromatic molecules. Wiley monographs in chemical physics. Wiley, London, p 301
67. Birks JB (1975) Organic molecular photophysics, vol 2. Wiley, New York, p 159
68. Kaanumalle LS, Gibb CL, Gibb BC, Ramamurthy V (2005) A hydrophobic nanocapsule controls the photophysics of aromatic molecules by suppressing their favored solution pathways. *J Am Chem Soc* 127:3674–3675
69. Li SH, Xu X, Zhou Y, Zhao Q, Liu Y (2017) Reversibly tunable white-light emissions of styrylpyridiniums with cucurbiturils in aqueous solution. *Org Lett* 19:6650–6653
70. Hawe A, Sutter M, Jiskoot W (2008) Extrinsic fluorescent dyes as tools for protein characterization. *Pharm Res* 25:1487–1499
71. Amdursky N, Erez Y, Huppert D (2012) Molecular rotors: what lies behind the high sensitivity of the thioflavin-T fluorescent marker. *Acc Chem Res* 45:1548–1557
72. Mohanty J, Choudhury SD, Upadhyaya HP, Bhasikuttan AC, Pal H (2009) Control of the supramolecular excimer formation of thioflavin T within a cucurbit[8]uril host: a fluorescence on/off mechanism. *Chem Eur J* 15:5215–5219
73. Ansari S, Alahyan M, Marston SB, El-Mezgueldi M (2008) Role of caldesmon in the Ca²⁺ regulation of smooth muscle thin filaments: evidence for a cooperative switching mechanism. *J Biol Chem* 283:47–56
74. Bhasikuttan AC, Dutta Choudhury S, Pal H, Mohanty J (2011) Supramolecular assemblies of thioflavin T with cucurbiturils: prospects of cooperative and competitive metal ion binding. *Isr J Chem* 51:634–645
75. Tsukamoto T, Ramasamy E, Shimada T, Takagi S, Ramamurthy V (2016) Supramolecular surface photochemistry: cascade energy transfer between encapsulated dyes aligned on a clay nanosheet surface. *Langmuir* 32:2920–2927
76. Nonell S, Flors C (eds) (2016) Singlet oxygen: applications in biosciences and nanosciences, volume 1. *Comprehensive series in photochemical and photobiological sciences*, vol 13. RSC, Cambridge
77. Wang XQ, Lei Q, Zhu JY, Wang WJ, Cheng Q, Gao F, Sun YX, Zhang XZ (2016) Cucurbit[8]uril regulated activatable supramolecular photosensitizer for targeted cancer imaging and photodynamic therapy. *ACS Appl Mater Interfaces* 8:22892–22899

78. Lindig BA, Rodgers MAJ, Schaap AP (1980) Determination of the lifetime of singlet oxygen in water-d₂ using 9,10-anthracenedipropionic acid, a water-soluble probe. *J Am Chem Soc* 102:5590–5593
79. Liu Y, Huang Z, Liu K, Kelgtermans H, Dehaen W, Wang Z, Zhang X (2014) Porphyrin-containing hyperbranched supramolecular polymers: enhancing 1O₂-generation efficiency by supramolecular polymerization. *Polym Chem* 5:53–56
80. Leng X, Choi C-F, Luo H-B, Cheng Y-K, Ng DKP (2007) Host-guest interactions of 4-carboxyphenoxy phthalocyanines and β -cyclodextrins in aqueous media. *Org Lett* 9:2497–2500
81. Liu K, Liu Y, Yao Y, Yuan H, Wang S, Wang Z, Zhang X (2013) Supramolecular photosensitizers with enhanced antibacterial efficiency. *Angew Chem Int Ed Engl* 52:8285–8289
82. McLeod D, Thøgersen MK, Jessen NI, Joergensen KA, Jamieson CS, Xue X-S, Houk KN, Liu F, Hoffmann R (2019) Expanding the frontiers of higher-order cycloadditions. *Acc Chem Res* 52:3488–3501
83. Woodward RB, Hoffmann R (1965) Stereochemistry of electrocyclic reactions. *J Am Chem Soc* 87:395–397
84. Woodward RB, Hoffmann R (1969) Conservation of orbital symmetry. *Angew Chem Int Ed Engl* 8:781–853
85. Pattabiraman M, Sivaguru J, Ramamurthy V (2018) Cucurbiturils as reaction containers for photocycloaddition of olefins. *Isr J Chem* 58:264–275
86. Ramamurthy V, Parthasarathy A (2011) Chemistry in restricted spaces: select photodimerizations in cages, cavities, and capsules. *Isr J Chem* 51:817–829
87. Hutchins KM, MacGillivray LR (2016) Crystal engineering [2 + 2] photodimerizations via templates and hydrogen bonds: case of styrylthiophenes. *Photochemistry* 43:321–329
88. Natarajan A, Bhogala BR (2011) Bimolecular photoreactions in the crystalline state. In: Ramamurthy V, Yoshihisa I (eds) *Supramolecular photochemistry: controlling photochemical processes*. John Wiley & Sons, Inc, Hoboken, NJ, pp 175–228
89. Green BS, Lahav M, Schmidt GMJ (1975) Reactions in chiral crystals. Principles governing asymmetric synthesis via topochemically controlled solid-state photodimerization. *Mol Cryst Liq Cryst* 29:187–200
90. Pattabiraman M, Kaanumalle LS, Natarajan A, Ramamurthy V (2006) Regioselective photodimerization of cinnamic acids in water: templation with cucurbiturils. *Langmuir* 22:7605–7609
91. Pattabiraman M, Natarajan A, Kaanumalle LS, Ramamurthy V (2005) Templating photodimerization of trans-cinnamic acids with cucurbit[8]uril and gamma-cyclodextrin. *Org Lett* 7:529–532
92. Nguyen N, Clements AR, Pattabiraman M (2016) Using non-covalent interactions to direct regioselective 2+2 photocycloaddition within a macrocyclic cavitand. *New J Chem* 40:2433–2443
93. Kashyap A, Bokosike TK, Bhuvanesh N, Pattabiraman M (2018) Stereo- and regioselective photocycloaddition of extended alkenes using γ -cyclodextrin. *Org Biomol Chem* 16:6870–6875
94. Wang HM, Wenz G (2013) Topochemical control of the photodimerization of aromatic compounds by gamma-cyclodextrin thioethers in aqueous solution. *Beilstein J Org Chem* 9:1858–1866
95. Yang C, Mori T, Origane Y, Ko YH, Selvapalam N, Kim K, Inoue Y (2008) Highly stereoselective photocyclodimerization of alpha-cyclodextrin-appended anthracene mediated by gamma-cyclodextrin and cucurbit[8]uril: a dramatic steric effect operating outside the binding site. *J Am Chem Soc* 130:8574–8575
96. Yoshizawa M, Takeyama Y, Okano T, Fujita M (2003) Cavity-directed synthesis within a self-assembled coordination cage: highly selective [2 + 2] cross-photodimerization of olefins. *J Am Chem Soc* 125:3243–3247

97. Clements AR, Pattabiraman M (2015) γ -Cyclodextrin mediated photo-heterodimerization between cinnamic acids and coumarins. *J Photochem Photobiol A Chem* 297:1–7
98. Anderson JC, Reese CB (1960) Photo-induced fries rearrangement. *Proc Chem Soc Lond* 6:217
99. Meyer JW, Hammond GS (1972) Mechanism of photochemical reactions in solution. LXX. Photolysis of aryl esters. *J Amer Chem Soc* 94:2219–2228
100. Gritsan NP, Tsentalovich YP, Yurkovskaya AV, Sagdeev RZ (1996) Laser flash photolysis and CIDNP studies of 1-naphthyl acetate photo-fries rearrangement. *J Phys Chem* 100:4448–4458
101. Banu HS, Pitchumani K, Srinivasan C (1999) Effect of cyclodextrin complexation on photo-Fries rearrangement of naphthyl esters. *Tetrahedron* 55:9601–9610
102. Veglia AV, de Rossi RH (1993) β -Cyclodextrin effects on the photo-Fries rearrangement of aromatic alkyl esters. *J Org Chem* 58:4941–4944
103. Iguchi D, Erra-Balsells R, Bonesi SM (2016) Photo-fries rearrangement of aryl acetamides: regioselectivity induced by the aqueous micellar green environment. *Photochem Photobiol Sci* 15:105–116
104. Kaanumalle LS, Nithyanandhan J, Pattabiraman M, Jayaraman N, Ramamurthy V (2004) Water-soluble dendrimers as photochemical reaction media: chemical behavior of singlet and triplet radical pairs inside dendritic reaction cavities. *J Am Chem Soc* 126:8999–9006
105. Siano G, Crespi S, Mella M, Bonesi SM (2019) Selectivity in the photo-fries rearrangement of some aryl benzoates in green and sustainable media. Preparative and mechanistic studies. *J Org Chem* 84:4338–4352
106. Gu W, Weiss RG (2001) Extracting fundamental photochemical and photophysical information from photorearrangements of aryl phenylacrylates and aryl benzyl ethers in media comprised of polyolefinic films. *J Photochem Photobiol C* 2:117–137
107. Koodanjeri S, Pradhan AR, Kaanumalle LS, Ramamurthy V (2003) Cyclodextrin-mediated regioselective photo-Fries reaction of 1-naphthyl phenyl acrylates. *Tetrahedron Lett* 44:3207–3210

Functional Nanohybrids Based on Dyes and Upconversion Nanoparticles



Juan Ferrera-González, María González-Béjar, and Julia Pérez-Prieto

Contents

1	Introduction	373
1.1	UCNP Properties	373
2	Pre-requirements When Designing Photoactive Nanohybrids by Combining UCNPs and Chromophores	378
3	Sensing with UCNH	379
3.1	Inner Filter	380
3.2	Lanthanide-Based Resonant Energy Transfer	380
3.3	pH Sensing	381
3.4	Biomolecules and Ions Sensing	385
4	Photodynamic Therapy	387
5	Theragnosis	388
6	Conclusion Remarks	392
	References	392

Abstract Upconversion nanoparticles (UCNPs) and dyes are combined to make nanohybrid systems, which take advantage of the synergic relationship between lanthanide (Ln)-based UCNPs and dyes. Ln-UCNPs are inorganic nanophosphors which absorb NIR light and emit narrow emission bands in the UV-NIR region with long luminescence lifetimes. These unique properties, when coordinated properly with dyes of the appropriate photophysical features, produce nanosystems with new photophysical properties. In this context, the UCNP-dye nanohybrids are very promising for potential sensing (ions and biomolecules) and theragnosis (imaging and therapy, e.g. photodynamic therapy).

Keywords Dyes · Imaging · Photodynamic therapy · Sensors · Upconversion nanoparticles

J. Ferrera-González, M. González-Béjar (✉), and J. Pérez-Prieto (✉)
Departamento de Química Orgánica, Instituto de Ciencia Molecular (ICMol), Universidad de Valencia, Valencia, Spain
e-mail: maria.gonzalez@uv.es; julia.perez@uv.es

Abbreviation

AuNP	Gold nanoparticle
BCH	A benzopyrylium-coumarin-based hydrogen peroxide-sensitive probe
BODIPY	Boron-dipyrrromethene
BSA	Bovine serum albumin
CB	Cucurbit[7]uril
Ce6	Chlorin e6
CT	Computed tomography
DNA	Deoxyribonucleic acid
ET	Energy transfer
FITC	Fluorescein isothiocyanate
GSH	Glutathione
IBDP	Diiodo-substituted BODIPY
Ln	Lanthanide
LOD	Limit of detection
LRET	Lanthanide-based resonant energy transfer
MC540	Merocyanine 540
MRI	Magnetic resonance imaging
NI	1,8-Naphthalimide
NIR	Near-infrared
NP	Nanoparticle
PDT	Photodynamic therapy
PEG	Polyethylene glycol
PP	N-aminobacterio-purpurinimide porphyrin
PPy	Polypyrrole
PS	Photosensitizer
QD	Quantum dot
ROS	Reactive oxygen species
TCG	Thiol-coumarin-based glutathione-sensitive probe
UC _{Er}	β -NaYF ₄ :Yb,Er
UC _{Ho}	β -NaYF ₄ :Yb,Ho
UCNH	Upconversion nanohybrid
UCNP	Upconversion nanoparticle
UC _{Tm}	β -NaYF ₄ :Yb,Tm
UC _{YbErTm}	β -NaYF ₄ :Yb,Er,Tm.
UV	Ultraviolet
Vis	Visible
Zn-PC	Zinc phthalocyanine

1 Introduction

UCNPs are being decorated with chromophores with interesting photophysical properties, such as high extinction coefficients, high fluorescence or triplet quantum yields or capability to generate singlet oxygen. According to the chromophore or dye features, the prepared nanohybrids would be applied to different purposes, namely, sensing, imaging, photodynamic therapy (PDT) and so on [1, 2].

This chapter focuses on the requirements needed to succeed when designing a photoactive functional nanohybrid based on the combination of Ln-UCNPs and dyes.

For a detailed description of the preparation methods of this kind of nanohybrids, the reader is directed to recent published reviews and the references cited therein [3, 4]. Briefly, several synthetic protocols have been outlined to load a high concentration of chromophores on the UCNP surface or its periphery by means of, e.g. interdigitation of amphiphilic molecules, direct anchoring to the NP surface, ionic or covalent linkage to the NP ligand or ligand oxidation [3–5].

Along this chapter, a few representative examples have been selected to illustrate the advances in the application of the luminescence of UCNPs to transfer energy to conventional dyes and the applications emerging from these photophysical events.

Accordingly, we have set out this chapter in sections dealing, first, with a description of the UCNPs and, next, with each type of applications. Thus, two main types of applications are introduced in the last two sections: sensing and photodynamic therapy. Finally, a brief section about theragnosis is also presented.

1.1 UCNP Properties

UCNPs are usually made of a nanometre-sized inorganic photochemically inert matrix, such as NaYF_4 , doped with at least two photoactive trivalent lanthanide cations. One of them serves as sensitizer, absorbs NIR light and transfers it to the other one, the activator, which emits at certain characteristic wavelengths [6, 7].

The unique intrinsic properties of UCNPs such as NIR excitation and multiple long-lifetime emission in the UV-NIR region have attracted the attention as nanomaterials for being implemented in (bio)imaging, sensing, optoelectronics and theragnosis with incredible potential in bioassays.

1.1.1 NIR Excitation

Commonly used organic bioprobes and nanoparticles – such as quantum dots (QDs) or carbon dots – are excited in the UV-Vis region. Consequently, there is an important limitation for in vivo or in vitro applications due to the limited penetration depth of UV-Vis light. UV-Vis radiation cannot penetrate effectively in the

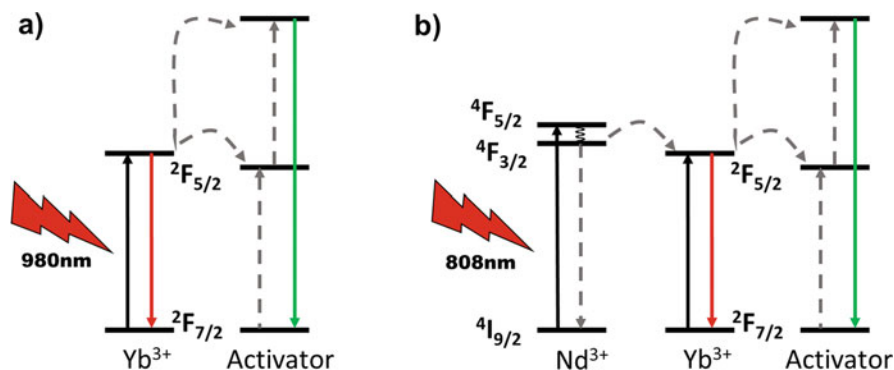


Fig. 1 Proposed mechanism for excitation of UCNPs (a) NaYF₄:Yb,Er at 980 nm and (b) NaYF₄:Yb,Er@Nd at 808 nm

biological tissue because of two reasons: the tissue scattering and the absorption of the biomolecules naturally present in the organisms [8–12]. These factors can be minimized by shifting the excitation to longer wavelengths where the highest transparency of biological samples occurs.

In this context, UCNPs can be excited at near-infrared (NIR) wavelengths thanks to the presence of Yb³⁺, which is the most used sensitizer to absorb the excitation energy due to its relatively large absorption cross section at ~980 nm [13, 14]. Nd³⁺ is also used due to its absorption at 808 nm (where water absorption is minimal). This is of high relevance for aqueous samples (especially in biological samples) to avoid their heating.

Thus, UCNPs are excited in the first biological window (NIR-I). They can be excited at 980 (or 915 nm) and 808 nm, when doped with Nd³⁺ and Yb³⁺ and at 980 nm (or 915 nm) when doped with Yb³⁺ (Fig. 1) [6, 7, 13, 15–17]. Due to the water absorption at 980 nm, 915 and 808 nm are being explored as preferable wavelengths. It has been reported that 915 nm light-triggered photodynamic therapies dramatically diminished overheating [18]. Even so, similar therapeutic effects were achieved in comparison with those triggered by 980 nm light. Also, the absorption of Yb³⁺ is higher at 980 than at 915 nm, so a higher number of photons is absorbed.

Equally important, the efficiency of the Yb,Nd-codoped UCNP is usually lower than the Yb-doped UCNP because the first one involves one more energy transfer (ET) step, specifically that from Nd³⁺ to Yb³⁺ (Fig. 1b) [16]. In any case, NIR irradiation allows for deeper penetration in biological tissues than shorter excitation wavelengths [19]. UCNPs also exhibit excellent chemical and thermal stability and present relatively low (cyto)toxicity [6, 20].

As a consequence of the sensitizer excitation, consecutive resonance ET to higher energy levels of the activators – such as Er³⁺, Tm³⁺ or Ho³⁺ – occurs, giving rise to different long-lived sharp emissions in the UV, Vis and/or NIR, i.e. the upconversion emission spectrum usually consists of multiple narrow emission bands in the UV-

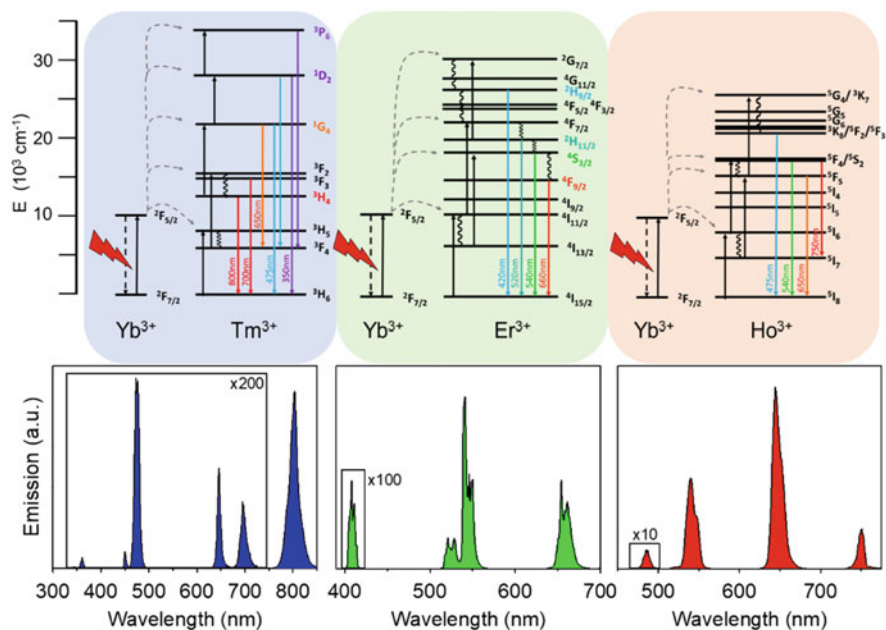


Fig. 2 Proposed mechanism for 980 nm excitation of (left) NaYF₄:Yb,Tm (UC_{Tm}); (centre) NaYF₄:Yb,Er (UC_{Er}) and (right) NaYF₄:Yb,Ho (UC_{Ho}) and their corresponding emission spectra

Vis-NIR attributed to the different transitions on the activator. Figure 2 shows three representative examples; one of them is the process occurring in NaYF₄:Yb,Tm (UC_{Tm}) upon excitation at 980 nm and the resulting emission spectrum (Fig. 2, left) [6, 7]. The spectrum has the characteristic Tm³⁺ narrow emission bands below 500 nm, which correspond to ¹I₆ → ³F₄ (345 nm), ¹D₂ → ³H₆ (368 nm), ¹D₂ → ³F₄ (450 nm) and ¹G₄ → ³H₆ (475 nm) transitions together with the bands at 650 nm and 800 nm, which correspond to ¹G₄ → ³F₄ and ³H₄ → ³H₆ transitions, respectively. The second one is (Fig. 2, centre) the process occurring upon excitation of NaYF₄:Yb,Er (UC_{Er}) at 980 nm and the resulting emission spectrum [6, 7]. The spectrum has the characteristic Er³⁺ narrow emission bands due to the transfer of photons from Yb³⁺ ions to the Er³⁺ excited states, which correspond to ²H_{9/2} → ⁴I_{15/2} (420 nm), ⁴S_{3/2} → ⁴I_{15/2} (ca. 550 nm), ²H_{11/2}, ⁴S_{3/2} → ⁴I_{15/2} (ca. 520 nm) and ⁴F_{9/2} → ⁴I_{15/2} (670 nm).

Similarly, for the third one (Fig. 2, right), following 980 nm excitation, the emission of NaYF₄:Yb,Ho UCNPs (UC_{Ho}) involves the transfer of two photons from Yb³⁺ to Ho³⁺. The emissions centred at 486 nm and 541 nm correspond to the emission from the ⁵F₃ → ⁵I₈ and ⁵S₂ → ⁵I₈ transitions, respectively. The red emissions observed at 647 and 751 nm are attributed to the ⁵F₅ → ⁵I₈ and ⁵F₄ and ⁵S₂ → ⁵I₇ transitions, respectively [21].

Figure 3 shows the emission intervals in the electromagnetic spectrum of these three activators (Er³⁺, Tm³⁺ and Ho³⁺) when combined with Yb³⁺ as sensitizer in an

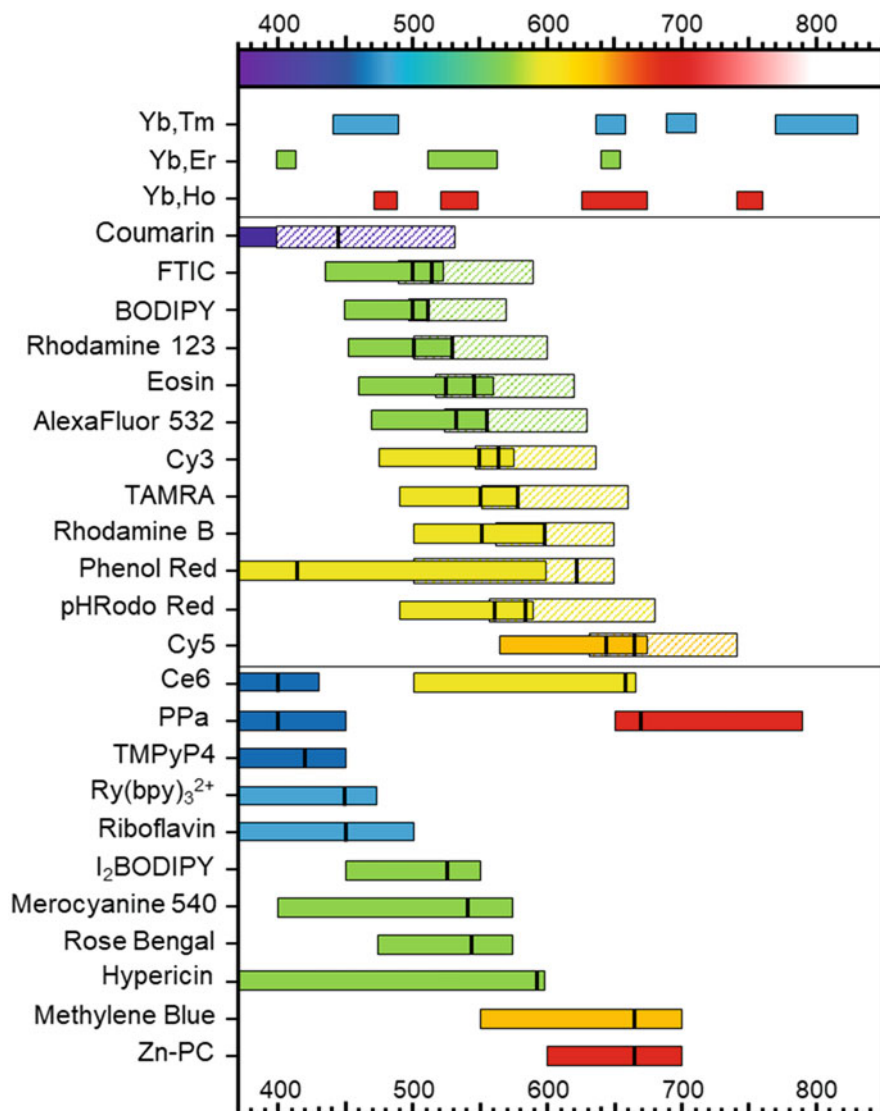
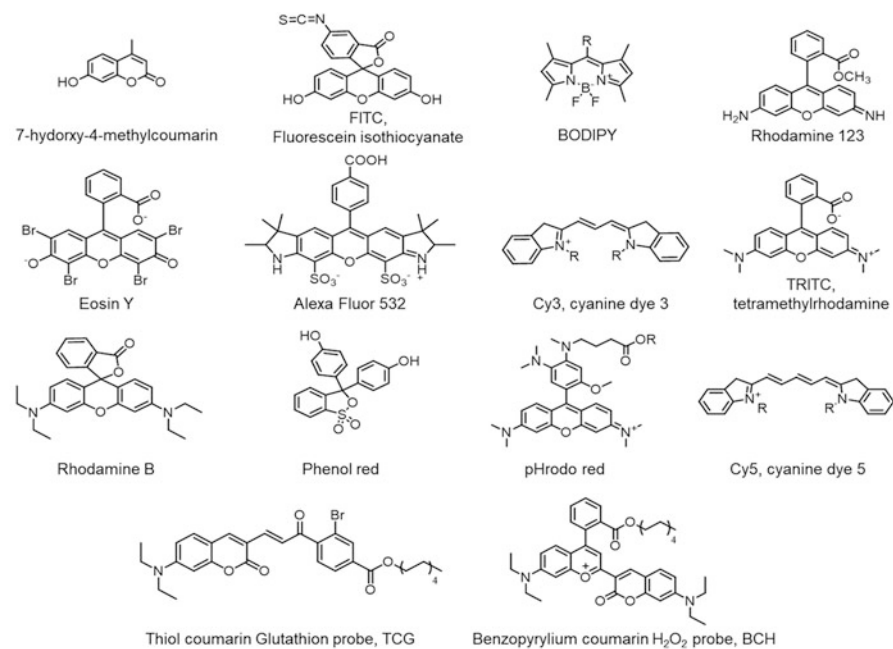


Fig. 3 Upconversion emission intervals in the electromagnetic spectrum of NaLnF_4 : Yb, X (X = Er, Tm or Ho). The absorption (coloured) and emission (dashed) intervals of several chromophores used for sensing or PDT are also presented. Black vertical lines in the squares represent the maximum absorption or emission

inert matrix of NaYF_4 . The absorption and emission intervals of several chromophores are also presented (from shorter to longer wavelengths) to illustrate their possible overlap with the emission of the UCNP according to their doping composition (Fig. 3). Moreover, Chart 1 displays the structures of these chromophores included in Fig. 3.



Photosensitizers

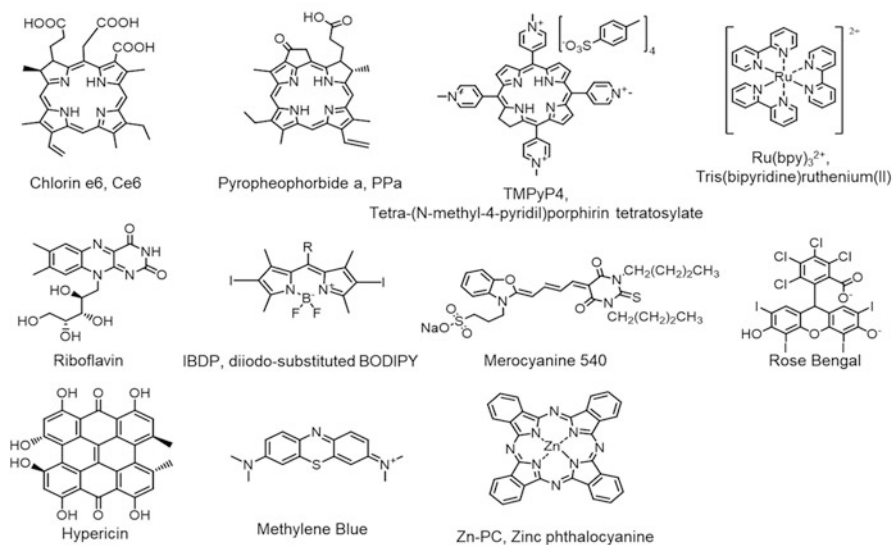


Chart 1 Structures of some of the chromophores presented in Fig. 3, which are commonly combined with UCNPs either for sensing or for photodynamic therapy

1.1.2 Tunable Long-Lifetime Emission

All this considered, the different sharp emission peaks, together with their respective long lifetimes, make UCNPs doped with different ions of interest for multicolour imaging and time-resolved photoluminescence imaging [22, 23]. In fact, UCNP emissions possess long lifetime, usually in the order of several hundreds of μs , as compared to the ns scale of common organic fluorophores. As a result, the autofluorescence of the biomolecules can be completely removed just by selecting the appropriate detection window in a time-gated imaging strategy [22, 24].

The sharp long-lived emission of the lanthanides embedded in the UCNP is attributed to the shielded partially allowed intra f-f electronic transitions of lanthanide dopants. The upconversion emission is the result of the combined effect of the crystal field, the staggered nature of lanthanides electronic configuration and the characteristic long-lived lifetime of their excited state. In the ET upconversion mechanism, the Yb^{3+} plays an important role because of its high absorption cross section, its long-lived excited state and its energy gap, which is similar to the energy gap between higher excited states of the activators. The feeding of superior excited states produces multiple sharp power-dependent emissions from the activator(s) [6, 7, 16, 25, 26].

Even more, by controlling several parameters, such as the doping ratio, the inorganic matrix, the presence of other dopants, the size, the temperature or the presence of shells (active or inactive), it is possible to tune the UCNP emission features [6, 13, 15, 27]. Moreover, although the upconversion emission is the special feature of the UCNPs, they also display the typical downconversion emission of the doping lanthanides, which usually happens in the second biological window (NIR-II) [10, 28, 29]. Often UV-Vis emission region has been applied in theragnostics and sensing [26, 30, 31], while the downconversion emission has been especially useful in bioimaging [28, 29].

2 Pre-requirements When Designing Photoactive Nanohybrids by Combining UCNPs and Chromophores

The absorbing species (dye or nanoparticle) selected to make upconversion nanohybrids (UCNHs) must absorb at the activator's emissions present in the UCNP, if the purpose is to enable NIR-induced lanthanide ET processes. A huge variety of dyes can then be used: cationic dyes (e.g. methylene blue) [32–35], BODIPYs [36–38] and phthalocyanines [32, 39–41]. See Chart 1 for more examples.

Then, according to the photophysical properties of the absorbing species present in the nanohybrid, one would select the application of the UCNH. Several possibilities can be outlined for the absorbing species:

- (i) It filters the UCNP emission, but has no emission and does not induce reactive oxygen species generation.
- (ii) It absorbs the UCNP emission leading to an emission in a wavelength range different to that of the UCNP, and this emission is used as a part of the ratiometric response of the sensor instead of those of the UCNP emission.
- (iii) It absorbs the UCNP emission leading to its characteristic emission; however, it is ignored for the sensor response.
- (iv) It absorbs the UCNP emission generating reactive oxygen species (e.g. singlet oxygen).

These four possibilities regarding the photophysical pathways after NIR excitation will determine the capabilities of the UCNH to be used in different applications. Next sections present several examples in order to illustrate each option either for sensing (i–iii) or for PDT applications (iv).

3 Sensing with UCNH

The unique features of UCNP have been exploited and combined with other photoactive species (molecules and nanoparticles) to obtain new sensors. Adequate combinations may produce significant and selective differences in the luminescence response of the UCNH when an analyte is present in the medium. The common configuration of UCNH sensors benefits from the photophysical properties of the UCNP and the sensing properties of known chromophores. NIR excitation of the UCNP produces emissions in the UV-Vis spectral region. These emissions eventually lead to the excitation of the chromophore, which is a well-known molecular probe sensitive to pH, temperature or analyte concentration (e.g. ions, proteins, or DNA) [26, 31].

At the microscale cellular level, the sensors based on UCNP offer superior sensing properties than organic probes or other NPs. Fluorescence sensors supply higher sensitivity and selectivity than absorption sensors, but their usual limitation is that direct fluorescence measurements are sensible to interferences, such as photobleaching or photoblinking, dye leaching or the instability of the lamps or detectors. Ratiometric or time-resolved measurements suppress many of these factors and, consequently, are preferable [42]. UCNP can be used in both ways since they have multiple narrow emissions (enabling ratiometric measurements) and long lifetime for time-resolved imaging [22, 26, 31].

According to the interaction between the UCNP and the photoactive species mentioned above, we can classify UCNHs into two groups: inner-filter (i) or resonant ET (ii–iii) nanohybrids. In any case, both mechanisms require an efficient spectral overlap between the emission of the donor (the lanthanide acting as activator) and the absorption of the acceptor (chromophore).

3.1 Inner Filter

The inner-filter mechanism (i) follows a trivial mechanism, where the donor (the UCNP) emits light at a wavelength where the acceptor (the chromophore) absorbs. In this case, the detection system will detect a quenching of the fluorescence intensity of the donor but without affecting the donor emission lifetime [35, 43].

Wolfbeis et al. [44] developed a NH_3 film sensor by mixing $\text{NaYF}_4:\text{Yb,Er}$ and phenol red, a pH probe, (Fig. 3, Chart 1), inside a polystyrene matrix which is impermeable to protons but permeable to NH_3 molecules (Fig. 4a). The absorption spectrum of phenol red changes with the pH, and as a consequence, the relative intensity of the Er emissions changes. They designed a reversible stable ratiometric sensor by using the Er emissions at 540 and 650 nm, whose intensity ratio exhibited a linear response from 0.4 to 10 mM NH_3 [44].

3.2 Lanthanide-Based Resonant Energy Transfer

Lanthanide-based resonance energy transfer (LRET) in UCNHs involves a dipole coupling which causes a non-radiative virtual photon transfer from the donor to the acceptor [27, 46].

Deactivation of the excited state of the donor by using an acceptor (quencher) will follow a dynamic quenching scheme, where the emission lifetime of the donor is reduced due to the presence of the acceptor at short distances of the UCNP surface [43, 47–53].

These short distances can be effectively obtained only in a UCNH in which the fluorophore is close to the UCNP surface. Huang et al. [45] developed a DNA sequence case (ii) and (iii) (in Sect. 2) sensor (Fig. 4b) which consists of $\text{NaYF}_4:\text{Yb,Er}$

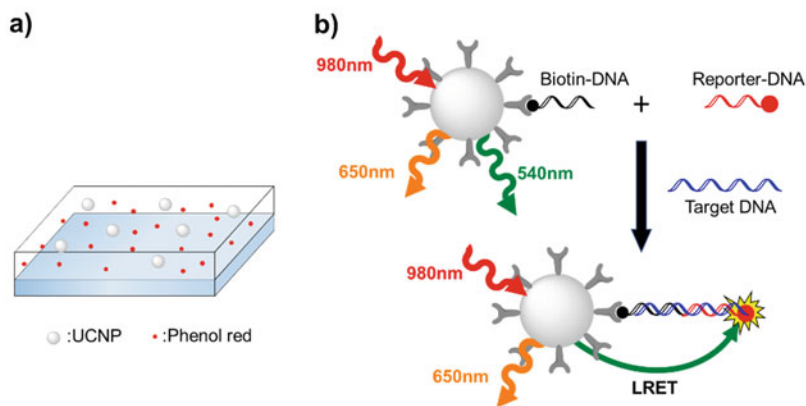


Fig. 4 Schematic representation of (a) the NH_3 inner-filter sensor film developed by Wolfbeis et al. [44] and (b) the sensing mechanism of the DNA LRET-based sensor built by Huang et al. [45]

functionalized with streptavidin. When the UCNH is dispersed in a solution with the target DNA, the capture DNA linked to biotin and the reporter DNA linked to a dye (a tetramethylrhodamine), the specific interaction between the DNA strands produces a quenching in the 520–540 nm Er emission band, even at low concentrations. The ratiometric sensor showed linear response from 10 to 50 nM target DNA when comparing the 540 nm emission band with either the dye emission at 580 nm or the Er emission at 650 nm.

Our group also developed a ratiometric case (iii) LRET-based sensor. It consisted of a β -NaYF₄:Yb,Tm UCNP functionalized with fluorescein, a pH probe (Fig. 3, Chart 1, Table 1 entry 21), which allowed for pH sensing. The fluorescein pH-dependent absorption affects the 475 nm Tm emission band, while the Tm band at 800 nm remained unaffected. The ratiometric sensor was built referencing the 800 nm emission to that at 475 nm and proved to be linear in the pH range 3–5 (Fig. 5) [54].

Taking into account that many UCNHs have been developed as potential intracellular pH sensors, we have devoted special consideration to the pH sensing topic in the following section. Last but not least, other biomolecules and ions sensors will be briefly discussed afterwards.

3.3 pH Sensing

pH plays a crucial role in cellular behaviour, being involved in several cellular processes such as the metabolism and cell cycle [49, 63, 66]. Depending on the cell compartment, differences in the pH may be observed. Moreover, an abnormal acidic pH may symbolize dysfunctions of cells and diseases [66]. Therefore, a lot of efforts have been made in order to develop efficient pH optical sensors. In this way, many UCNP-based nanoplatfroms have been developed since 2009. Table 1 displays some pH sensors organized according to their mechanism (i–iii). Some publications have been selected and discussed below.

Wang et al. developed a case (i) inner-filter pH sensor by loading pH dyes, such as bromothymol blue and rhodamine B (Fig. 3, Chart 1, Table 1 entry 10), into bovine serum albumin (BSA), which was attached to the surface of a core-shell NaYF₄:Yb,Er@silica UCNP. By varying the pH of the media, the absorption of the dye and the intensity of the Er emission band at 540 nm vary. The ratio between Er emission bands at 540 and 650 nm showed a good linearity in the 6–8 and 5–6.5 pH ranges for bromothymol blue and rhodamine B, respectively.

Giri et al. [51] recently reported a case (ii) dopamine sensor which could be also used for pH sensing. The system consists of a core-shell β -NaYF₄:Yb,Tm@NaYbF₄ UCNPs capped with a mesoporous silica shell to facilitate the physical loading of dopamine molecules (Table 1 entry 20). At neutral and basic pHs, dopamine undergoes autoxidation to the quinone form, which has an absorption band at 450 nm, and quenches the Tm emission band at the same wavelength (Fig. 6). The sensor shows good linearity in the 5–8 pH range.

Table 1 pH sensors based on upconversion nanohybrids (UCNHs)

n.	Cooperative species	UCNP	UCNH size (nm)	pH linear response	Detection	Year	Ref.
<i>Case (i) Inner-filter mechanism</i>							
1.	Bromothymol blue	NaYF ₄ :Yb,Er	50 × 950	6–10	I ₆₅₈ (Er)	2009	[55]
2.	Phenol red	NaYF ₄ :Yb,Er	60–90	6–8	I ₅₄₁ (Er)/I ₆₅₅ (Er)	2010	[44]
3.	Polyglutamic porphyrin dendrimers	β-NaYF ₄ :Yb, Er	23	6–9	I _{520–540} (Er)/I ₆₆₀ (Er)	2012	[56]
4.	ETH 5418	β-NaYF ₄ :Yb,Er	200 × 1,000	6–11	I ₆₅₆ (Er)/I ₅₄₂ (Er)	2012	[57]
5.	Bromocresol green	Y ₂ O ₃ :S:Yb,Er	200–300	5–10	I ₆₇₁ (Er)/I ₆₆₁ (Er)	2014	[58]
6.	Neutral red	Gd ₂ O ₃ :S:Yb,Er	1,500	6–8	I _{520–540} (Er)/I ₆₅₀ (Er)	2014	[59]
7.	Bromothymol blue	NaGdF ₄ :Yb,Er	200 × 1,200	6–8	I _{650–700} (Er)	2014	[60]
8.	Bromocresol green + bromothymol blue	α-NaYF ₄ :Yb,Mn,Eu @α-NaYF ₄ @PEG	24	3–8	I _{592 + 609} (Eu)/I ₇₀₀ (Eu)	2014	[61]
9.	Aza-BODIPY dimethylamino	NaCaY _{0.2} Yb _{0.7} Tm _{0.02} Ho _{0.08} (MoO ₄) ₃	Bulk	7–10	I ₇₉₇ (Tm)/I ₆₄₅ (Ho)	2016	[36]
10.	Bromothymol blue Rhodamine B	β-NaYF ₄ :Yb,Er@SiO ₂ @BSA	240	6–8 5–6.5	I ₅₄₀ (Er)/I ₆₅₅ (Er) I ₅₅₀ (Er)/I ₆₅₅ (Er)	2017	[62]
11.	Bromophenol-BODIPY derivatives	β-NaYF ₄ :Yb,Tm@PEI	27	5–7 7–9	A _{500–600} (dye)/A _{630–675} (Tm)	2019	[38]
<i>Case (ii) LRET and dye resonant emission play a role in the sensor response</i>							
12.	pHrodo red™	β-NaYF ₄ :Yb,Er@SiO ₂	28 × 36	3–6.7	I ₅₉₀ (dye)/I ₅₅₀ (Er)	2014	[63]
13.	pHrodo red™	β-NaYF ₄ :Yb,Er@PEI	23 × 27	3–7	I ₅₉₀ (dye)/I ₅₅₀ (Er)	2016	[49]
14.	Fluorescein isothiocyanate	β-NaYF ₄ :Yb,Tm@SiO ₂	23	4–10	I ₅₁₉ (dye)/I ₄₆₅ (Tm)	2016	[48]
15.	Fluorescein	β-NaGdF ₄ :Yb,Tm @β-NaGdF ₄ :Nd,Yb@β-NaYF ₄	22	5–8	I ₅₁₅ (dye)/I ₆₄₅ (Tm)	2017	[50]
16.	Hemicyanine derivative	β-NaGdF ₄ @β-NaYF ₄ :Yb,Tm @β-NaYF ₄ @PAA	30	6.8–9	I ₆₅₀ (Tm)/I ₅₁₃ (dye)	2017	[64]
17.	GM-Ag ₂ S nanodots	α-NaGdF ₄ :Yb,Tm@SiO ₂	70	4–9	I ₇₉₅ (GM-Ag ₂ S)/I ₅₄₀ (Er)	2019	[52]

Case (iii) LRET but sensor response is based on the UCNP emission

18.	Xylenol orange	β -NaYF ₄ :Yb,Tm@SiO ₂	50	4–8	I ₄₅₀ (Tm)/I ₆₄₆ (Tm)	2015	[65]
19.	Fluorescein isothiocyanate	β -NaYF ₄ :Yb,Tm@PEI	22	3–7	I ₄₇₅ (Tm)/I ₆₄₅ (Tm)	2016	[66]
20.	Dopamine	β -NaYF ₄ :Yb,Tm@NaYbF ₄ @SiO ₂	50	5–8	I ₄₅₀ (Tm)	2019	[51]
21.	Fluorescein	β -NaYF ₄ :Yb,Tm @CB@Y	24 × 29	3.2–4.8	I ₈₂₅ (Tm)/I ₄₇₅ (Tm)	2020	[54]
<i>Cases (ii) and (iii)</i>							
22.	Calcium red Alizarin red S	β -NaYF ₄ :Yb,Er@ β -NaYF ₄ @PEI/PMA	25–30	4.6–5.2 4.4–6.4	I ₅₄₀ (Er)/I ₆₅₀ (Er)	2019	[53]

PEG polyethylene glycol, PEI polyethylenimine, BSA bovine serum albumin, PAA poly(acrylic acid), GM glutathione and mercaptopropionic acid, PMA poly(isobutylene-*alt*-maleic anhydride), CB cucurbit[7]uril

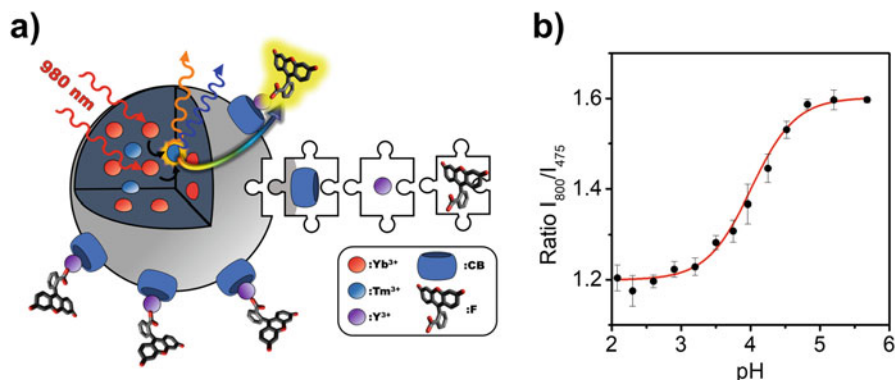


Fig. 5 (a) Schematic representation of the upconversion nanohybrids UC@CB@Y@F consisting of UCNP, cucurbit[7]uril (CB), Y^{3+} and fluorescein and the NIR-triggered emission of the organic probe after excitation of UCNP followed by energy transfer to the probe F and (b) ratiometric response of the emission intensity (area under the curve) of 800 (I_{800}) and 475 nm (I_{475}) emissions of the UC_{Tm}@CB@Y@F, showing a linear response in the 3–5 pH range. Adapted with permission of John Wiley & Sons Ltd. from N. Estebanez, J. Ferrera-González, I. A. Cortez-, M. González-Béjar, J. Pérez-Prieto, *Adv. Opt. Mater.* 2020 [54]

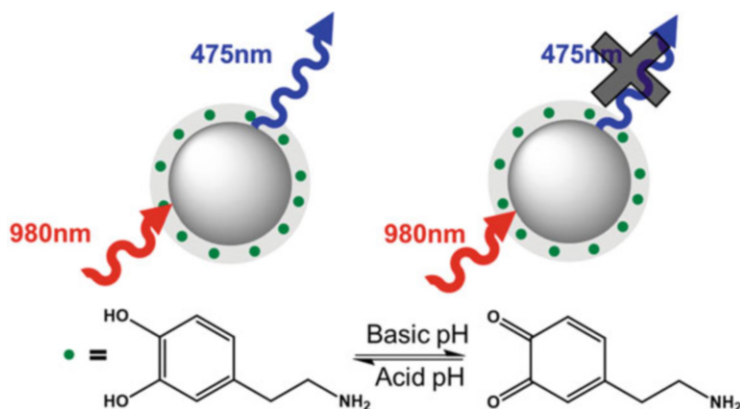


Fig. 6 Schematic representation of the sensing mechanism of the pH sensor proposed by Giri et al. [51]

Also, Kong et al. [66] developed a ratiometric case (iii) LRET-based sensor, which consisted of β -NaYF₄:Yb,Er UCNP functionalized with fluorescein isothiocyanate (FITC), a pH probe (Fig. 3, Chart 1, Table 1 entry 19), which allowed for the intracellular pH sensing. The fluorescein pH-dependent absorption affects the 475 nm Tm emission band, while the Tm band at 650 nm remained identical. Therefore, the response was calculated from the dependence of the I_{475}/I_{650} ratio on the pH. The sensor proved to be sensitive, linear in the pH range 3.0–7.0 and reversible.

Different nanoparticles, such as Ag₂S nanodots and graphene oxide, have also been used to build UCNH-based pH sensors. As an example, Xian et al. [52] built a case (iii) LRET-based nanosensor based on the interaction of NaYF₄:Yb,Er dense silica-coated UCNPs and a NIR Ag₂S nanodot pH probe (Table 1 entry 17). The higher the pH (up to 10), the higher the emission of the probe (due to higher RET efficiency between the UCNP and the nanodot). The ratio between the nanodot emission at 800 nm and the emission band of Er at 540 nm showed a linear response from pH 4 to 10 and good reversibility. In addition, it allowed for pH imaging in living cells and in Zebrafish model.

Other dye-UCNP-based pH sensors can be found in Table 1. Please, check references cited therein for further information.

3.4 Biomolecules and Ions Sensing

Recently Zhang et al. [67] reported a UCNH case (iii) RET-based sensor for the synchronous detection of glutathione (GSH) and H₂O₂ in vivo (Fig. 7a). The UCNH consisted of a NaYF₄:Yb,Er,Tm UCNP co-functionalized with two probes: a thiol-coumarin-based GSH-sensitive probe (TCG) and a benzopyrylium-coumarin-based H₂O₂-responsive probe (BCH), respectively (Chart 1).

The probes were selected to quench different emissions of the UCNP, 540 (Er) and 650 nm (Tm), respectively, and each signal was referenced to another unaffected upconversion emission at 800 nm (Tm) (Fig. 7b). The resulting sensing proved to be selective and reached limits of detection (LOD) in the order of 10⁻³ M for GSH and 10⁻⁶ M for H₂O₂.

Similarly, Li et al. [68] built a case (i) and (ii) hypochlorite (ClO⁻) nanosensor which was based on the interaction between an Er core-shell nanoparticle, specifically β-NaYF₄:Yb,Nd,Er@β-NaYF₄:Nd, and a cyanine 3 (Cy3; Fig. 3, Chart 1) ClO⁻ probe. The absorption of the ClO⁻-sensitive Cy3 affects the intensity of the 540 nm Er emission band, while that of the 650 nm Er emission remains identical. As a result, the ratiometric response was obtained between those bands. This sensor showed good linearity, a LOD of 27 ppb, high selectivity and a rapid response. Moreover, it was successfully tested in vitro and in vivo.

Other nanoparticles have also been used as acceptors to develop sensors. Even if it is out of the scope of the present chapter, a representative example is commented below. Zourob et al. [69] designed a case (iii) complex DNA sensor based on the quenching of the UCNP emissions by a gold nanoparticle (AuNP). The nanoplatfrom consists of polystyrene-co-acrylic acid core capped with dense silica and functionalized with α-NaYF₄:Yb,Tm UCNPs. The platform is attached to a AuNP nanoparticle through a single-strand DNA probe. When the specific single-strand DNA sequence hybridizes the DNA probe, it induces a lengthening in the AuNP-UCNP distance, and, consequently, the UCNP emissions are recovered.

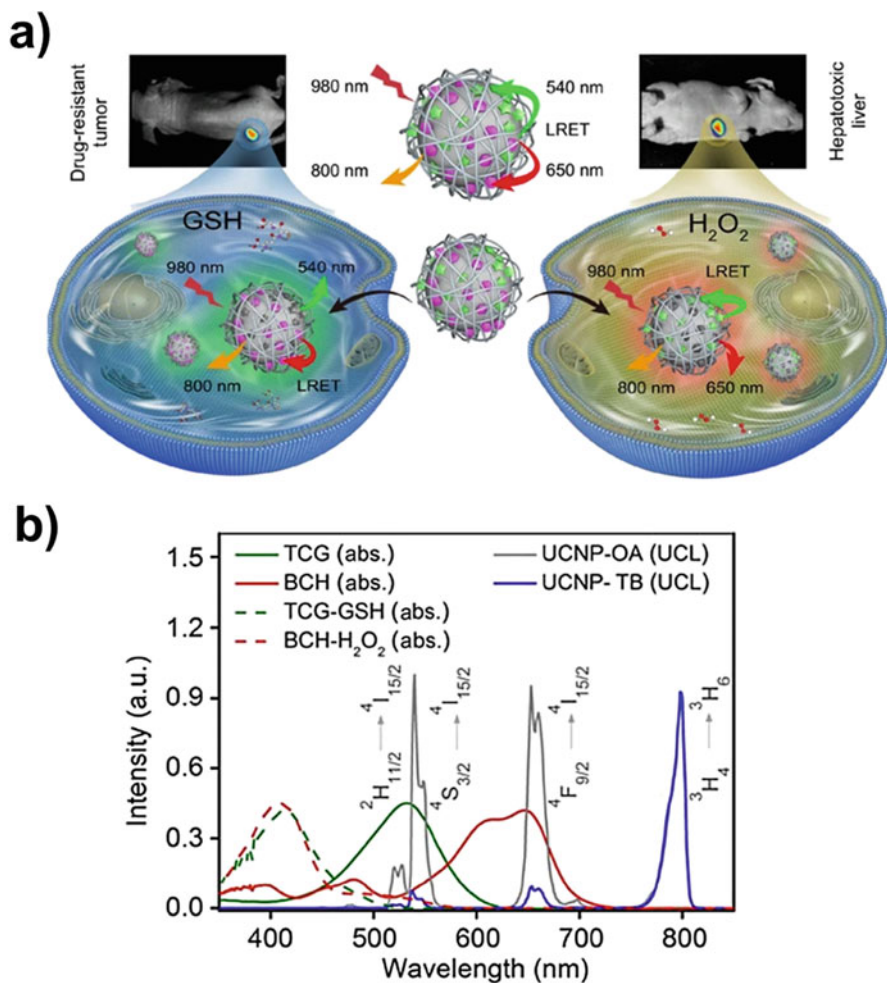


Fig. 7 (a) Proposed mechanism of the synchronous in vivo sensor of GSH and H_2O_2 and (b) the absorption spectra of the GSH and H_2O_2 probes (TCG and BCH, respectively) in the absence (green and orange lines) and presence of GSH and H_2O_2 (green and orange dashed lines), together with the emission spectrum of the UCNPs (grey line) and the nanohybrid (blue line). Adapted with permission from [67]. Copyright 2019 Springer Nature

Several platforms have been developed for sensing other ions [47, 70–74], proteins [75–78], DNA [79–84], molecules [51, 85–87], hypoxia [88] and temperature [89]. More information can be found in the next review articles and references cited therein [4, 6, 26, 30, 31, 90].

4 Photodynamic Therapy

Photodynamic therapy (PDT) uses light of the appropriate wavelength to activate a chromophore, commonly known as photosensitizer (PS). The generation of the PS singlet excited state is followed by intersystem crossing to the triplet excited state. Thus, ground state molecular oxygen (triplet oxygen, $^3\text{O}_2$) can quench the PS triplet state by ET to generate singlet oxygen $^1\Delta_g$, as well as by electron transfer to produce reactive radicals; these reactive oxygen species (ROS) are capable of damaging biomolecules and killing cells in the irradiated area [91, 92]. The extent of each process will be determined by the photophysical features of the PS. For example, ideally, for singlet oxygen generation, the PS would have very low fluorescence quantum yield, high intersystem crossing quantum yield (Φ_{ISC}), long triplet lifetime and high singlet oxygen sensitization (Φ_{Δ}).

Some of the limitations faced by common PSs are photobleaching, limited cell-penetrating capacity due to their easy aggregation and poor solubility in aqueous solutions [93]. An approach that is being explored to circumvent these limitations is the combination of photosensitizers and nanomaterials [94]. Hence, the search for efficient PDT-photosensitizer/nanomaterial nanohybrids has been pursued in the last decade. Silica nanoparticles [91], magnetic nanoparticles [94], quantum dots [95], and metallic nanoparticles [96, 97] (among others) are examples of nanomaterials used for this purpose.

Along this line, UCNPs are also being explored as functional carriers of PDT-PSs in order to take advantage of their ability to absorb light in the NIR and use the generated upconversion emission at the PSs absorption wavelength [39, 91]. For a successful design, the PS selected to make an UCNH must absorb at the preferred activator's emission, to allow for NIR-induced LRET processes leading to pathway (iv); that is, the PS absorbs the UCNP emission(s) leading to reactive oxygen species [97].

The reader is referred to other revisions and book chapters for detailed methods of synthetic protocols to make water-dispersible UCNPs [3, 5]. Briefly, coating UCNPs with polymers or mesoporous silica to embed or attach PSs, grafting PSs onto the UCNP surface and ligand exchange are the general methods for this purpose. Here we focus on the right combination of UCNP composition and PSs according to their photophysical features.

So far, for PDT applications, some PSs have been combined with UCNPs and are presented in Chart 1: pyropheophorbide a [98], cationic porphyrin TMPyP4 [99], riboflavin [100], I-BODIPY [2], rose bengal [101], methylene blue [33], zinc phthalocyanine (ZnPc) [40, 102–105], fullerene derivatives (hyaluronated fullerene; HAC₆₀ [106] and fullerene monomalonate; C₆₀-MA [107]), Ru(bpy)₃²⁺ [108], hypericin [109], chlorin e6 (Ce6) [110, 111] and merocyanine 540 [112].

Zhang et al. [113] studied the distance-dependent RET between an UCNP, $\beta\text{-NaYF}_4\text{:20\%Yb, 2\%Er}$ and an organic singlet oxygen generator, namely, rose bengal. Er-doped UCNP was chosen because its maximum upconversion emission band overlaps properly with the absorption band of the rose bengal. The donor-

acceptor distances were controlled by building an inactive silica shell around the UCNP core. The thickness of the silica shell bears an influence on the upconversion luminescence (in particular, increasing brightness by reducing superficial defects and quenching by solvent molecules) as well as in ET efficiency. Interestingly, shorter distances between the UCNP surface and rose bengal did not translate into higher ET efficiency which was achieved when the separation was about 6 nm.

We have also prepared an UCNH consisting of a NaYF₄:Yb,Er UCNP, capped with polyethylene glycol (PEG), and a diiodo-substituted BODIPY (IBDP) as the photosensitizer, i.e., UCNP-IBDP@PEG UCNHs [2]. The IBDP absorption spectrum overlaps the green luminescence of NaYF₄:Yb,Er. This UCNH showed a decrease in its green to red emission compared to that of the precursor (NaYF₄:Er³⁺, Yb³⁺ UCNP) upon NIR excitation. Time-resolved experiments demonstrated that the quenching of the green upconverted emission was due to resonance ET from the UCNP to the IBDP [37]. Moreover, singlet oxygen was detected by using a chemical probe, and then, the UCNH was tested to check its feasibility for cell killing. In vitro assays with SH-SY5Y human neuroblastoma-derived cells proved that the UCNH induced about 50% cancer cell death after NIR light irradiation (Fig. 8).

Remarkably, the combination of PSs with UCNPs has been optimized to make the most out of it by simultaneously activating two photosensitizers for enhanced PDT. For example, Zn-PC and merocyanine 540 has been encapsulated in NaYF₄:Yb,Er nanoparticles coated with mesoporous silica. The UCNP efficiently upconverted the energy of NIR light to Vis light (green and red emissions) and transferred it to the encapsulated photosensitizers since their absorption matched perfectly well the upconversion emission. The results of this study showed that this nanohybrid was capable of enhancing the therapeutic efficacy of PDT when activated at a single 980 nm wavelength [114].

Later on, IR-808-sensitized UCNHs carrying dual PSs as PDT agent have been designed [115]. The UCNH consisted of a core-shell NaGdF₄:Yb,Er@NaGdF₄:Nd, Yb nanoparticle, Ce6 covalently conjugated to mesoporous silica shell and MC540 loaded inside the silica channels via electrostatic interactions. This UCNH enabled the generation of cytotoxic ROS under 808 nm light thanks to the absorption of the upconverted green and red light by each PS (MC540 and Ce6, respectively) [115].

5 Theragnosis

Theragnosis has emerged as a new concept in next-generation medicine to include combinations of simultaneous imaging (e.g. for diagnosis) and targeted therapy. Cutting-edge nanotheranostic agents are designed to contain those combinations in single integrated nanohybrids aiming to offer individualized treatments based on in vivo molecular images to allow for a comprehensive diagnosis [116–118]. Several NPs have been used as platforms for theragnosis based on nanoparticles [119, 120], such as magnetic NPs [121], gold nanoparticles [122], silica NPs [123, 124], carbon nanotubes [125, 126], quantum dots [127] and UCNPs [6, 128] among others.

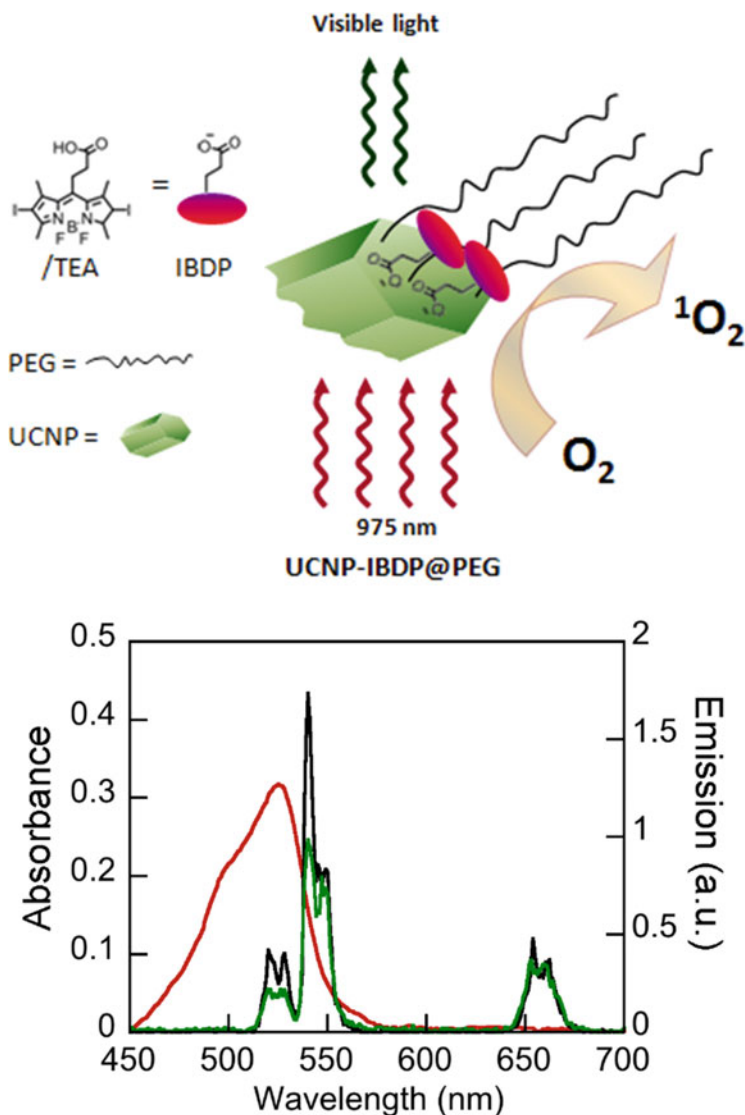


Fig. 8 (Top) Oversimplified scheme illustrating how UCNP@PEG transfers its energy (wavy green arrows) to IBDP (pink ovals: see structure on the left) coordinated to the UCNP surface after being excited with NIR leading to oxygen leads to singlet oxygen generation. (Middle) IBDP (1.7 μM) UV-visible absorption spectrum (red line) and luminescence emission spectra of solutions of UCNP@PEG (1 mg mL^{-1} , black line) and UCNP-IBDP@PEG (1 mg mL^{-1} , green line) in PBS. (Bottom) Semithin and ultrathin sections of SH-SY5Y cells after irradiation with NIR. Control (UCNP@PEG: **a** and **b**) and UCNP-IBDP@PEG incubated cells (**c** and **d**) are compared in a NIR light-irradiated zone and in a non-irradiated area of the same Petri dish. The nanohybrid-treated cells of the irradiated area (**d**) show exceptionally large vacuoles (black arrows) and signs of cellular damage. Reproduced from Ref. [37] with permission from The Royal Society of Chemistry

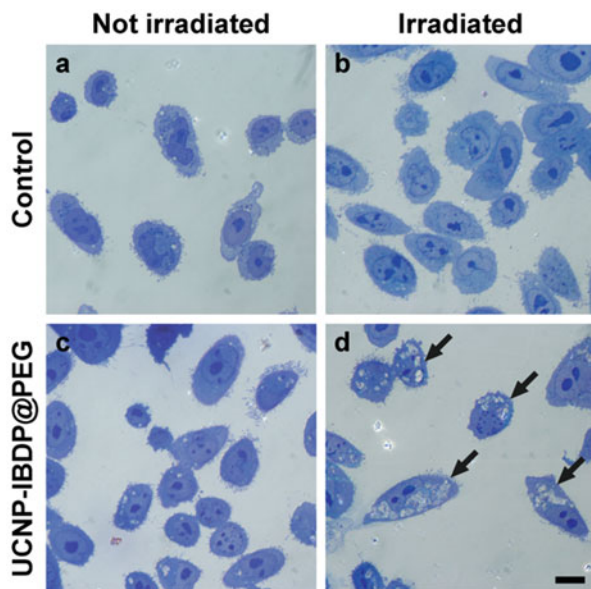


Fig. 8 (continued)

In the field of UCNPs, research has gone one step forward and opened up new alternatives for successful and non-invasive antitumoural theragnosis, thus proving how it is possible to perform Vis imaging tracking without triggering therapy by having another dye present on the nanohybrid surface with no absorption overlapping with the UCNP emission, thus allowing direct absorption (either Stokes or anti-Stokes via two-photon absorption) for innocuous tracking (Fig. 9) [1].

Thus, the UCNH consisted of a tridoped UCNP ($\text{NaYF}_4:\text{Yb,Er,Tm}$ ($\text{UC}_{\text{YbErTm}}$)) emitting in the UV, Vis and NIR; a broadband-absorbing natural porphyrin (PP) in the UV-to-NIR range but from 580 to 675 nm; and a 1,8-naphthalimide (NI) with two absorption bands (UV, Vis) and dual emission. The production of cytotoxic reactive oxygen species took place upon NIR excitation due to the co-localization of UCNP that allowed for effective RET from the UCNP to dyes. In fact, *in vitro* assays demonstrated that $\text{UC}_{\text{YbErTm}}@\text{PP/NI}$ UCNH was non-cytotoxic and extremely effective for NIR-induced cancer cell death upon NIR irradiation while offering fluorescence tracking features without therapy when specifically exciting NI.

Multifunctional $\text{NaYF}_4:\text{Yb,Er}@$ polypyrrole (PPy) core-shell nanoplates can also be simultaneously used for cancer diagnosis and photothermal therapy. In this nanohybrid, the core serves as an efficient nanoprobe for upconversion luminescence (UCL)/X-ray computed tomography (CT) dual-modal imaging, whereas the shell of PPy also shows strong NIR absorption, which makes it effective in photothermal ablation of cancer cells and infrared thermal imaging *in vivo* [129]. Therefore, in this particular example, the UCL is used for imaging but not for PPy activation.

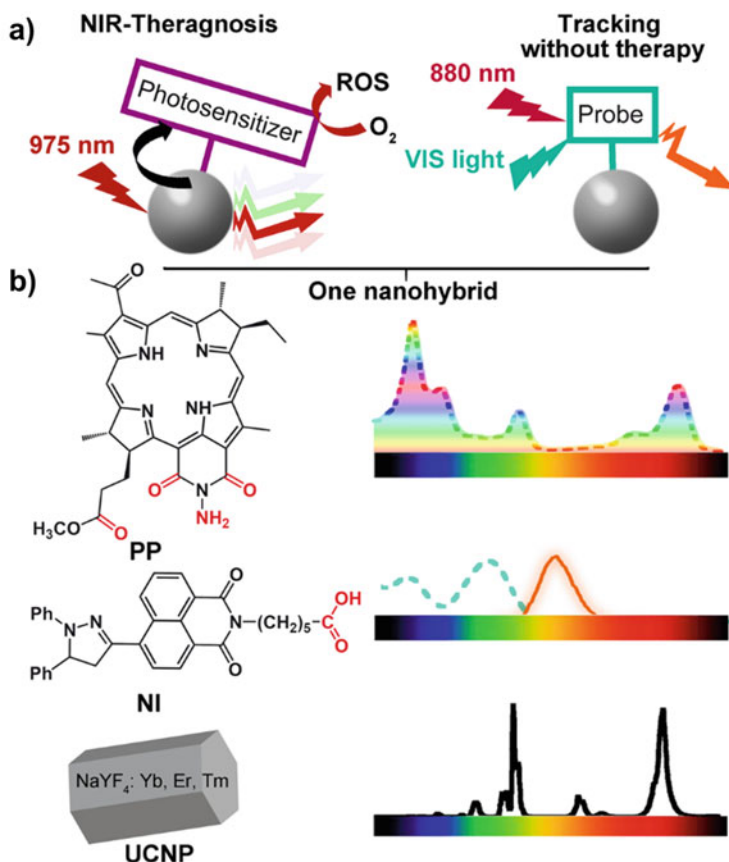


Fig. 9 (a) Schematic representation of the components required for a NIR-responsive NH with NIR theragnosis and fluorescence tracking without therapy capacity. (b) Structure of the components used for building the NH consisting of N-aminobacterio-purpurinimide (PP), 1,8-naphthalimide (NI) and UCNP (NaYF₄:Yb, Er, Tm); absorption (dashed lines) and emission (thick lines) spectra of the components (PP, NI and UCNP). Reprinted with permission from L. Frances-Soriano, M. A. Zakharko, M. González-Béjar, P. A. Panchenko, V. Herranz-Perez, D. A. Pritmov, M. A. Grin, A. F. Mironov, J. M. Garcia-Verdugo, O. A. Fedorova, J. Pérez-Prieto, *Chem. Mater.* 2018, 30, 3,677. Copyright 2018 American Chemical Society [1]

In addition, the IR-808-sensitized core-shell NaGdF₄:Yb,Er@(NaGdF₄:Nd,Yb) nanoparticles carrying Ce6 and MC540 as PSs, which were mentioned in the previous section, also showed the upconversion luminescence, MRI (magnetic resonance imaging) and CT imaging properties under a single 808 nm light excitation, revealing its potential for imaging-guided PDT [115].

6 Conclusion Remarks

The photophysical features of UCNPs and dyes must be carefully selected when making functional UCNHs for further applications. Several examples illustrating successful syntheses of UCNHs containing an UCNP (e.g. UC_{Er}, UC_{Tm} or UC_{Er,Tm}) and the appropriate dye useful in sensing, PDT and/or theragnosis have been reviewed in this chapter.

Briefly, the selected dye must absorb at some of the emissions of the activator present in the UCNP. The photophysical and sensing properties of the dye will determine the application of the UCNH. Several mechanisms can be outlined for the photophysical processes following the UCNP emission: inner-filter effect or LRET. Whenever the absorption or emission wavelength range of the dye changes, at least one of the UCNP sharp emissions will vary. This could be used to register the ratiometric response of a sensor (either referring to another UCNP emission or to the dye fluorescence if that were the case).

Moreover, if the dye is able to generate reactive oxygen species, the UCNHs can be used in PDT.

Last but not least, dyes not interfering with these photophysical events (i.e. not absorbing or filtering the UCNP emission) can also be included in the UCNH design to make independent tracking without applying therapy possible, thus allowing for efficient theragnosis.

Acknowledgments The authors thank Ministerio de Economía, Industria y Competitividad (CTQ2017-82711-P partially cofinanced with FEDER and AEI); Ministerio de Economía y Competitividad (RTC-2016-5114-5, partially cofinanced with FEDER; MDM-2015-0538; RYC-2013-14063 (M.G.B), FPU (J.G.F.)); Generalitat Valenciana (IDIFEDER/2018/064 and PROMETEO/2018/138, partially cofinanced with FEDER); and Fundación Ramón Areces (M.G. B.).

References

1. Frances-Soriano L, Zakharko MA, González-Béjar M, Panchenko PA, Herranz-Perez V, Pritimov DA, Grin MA, Mironov AF, Garcia-Verdugo JM, Fedorova OA, Pérez-Prieto J (2018) *Chem Mater* 30:3677
2. González-Béjar M, Liras M, Francés-Soriano L, Voliani V, Herranz-Pérez V, Duran-Moreno M, Garcia-Verdugo JM, Alarcon EI, Scaiano JC, Pérez-Prieto J (2014) *J Mater Chem B* 2:4554
3. Francés-Soriano L, González-Béjar M, Pérez-Prieto J (2016) In: Altavilla C (ed) *Upconverting nanomaterials: perspectives, synthesis, and applications*. CRC Press, Boca Raton, pp 101–138
4. Andresen E, Resch-Genger U, Schäferling M (2019) *Langmuir* 35:5093
5. Sedlmeier A, Gorris HH (2015) *Chem Soc Rev* 44:1526
6. Chen G, Qiu H, Prasad PN, Chen X (2014) *Chem Rev* 114:5161
7. Li X, Zhang F, Zhao D (2015) *Chem Soc Rev* 44:1346
8. Smith AM, Mancini MC, Nie S (2009) *Nat Nanotechnol* 4:710
9. Hong G, Antaris AL, Dai H (2017) *Nat Biomed Eng* 1:0010

10. He S, Song J, Qu J, Cheng Z (2018) *Chem Soc Rev* 47:4258
11. Hemmer E, Benayas A, L egar e F, Vetrone F (2016) *Nanoscale Horiz* 1:168
12. Wang F, Banerjee D, Liu Y, Chen X, Liu X (2010) *Analyst* 135:1839
13. Chen G,  gren H, Ohulchanskyy TY, Prasad PN, Agren H, Ohulchanskyy TY, Prasad PN (2015) *Chem Soc Rev* 44:1680
14. Chen G, Yang C, Prasad PN (2013) *Acc Chem Res* 46:1474
15. Resch-Genger U, Gorris HH (2017) *Anal Bioanal Chem* 409:5855
16. Xie X, Li Z, Zhang Y, Guo S, Pendharkar AI, Lu M, Huang L, Huang W, Han G (2017) *Small* 13:1
17. Estebanez N, Ferrera-Gonz alez J, Franc es-Soriano L, Arenal R, Gonz alez-B ejar M, P erez-Prieto J (2018) *Nanoscale* 10:12297
18. Huang Y, Xiao Q, Hu H, Zhang K, Feng Y, Li F, Wang J, Ding X, Jiang J, Li Y, Shi L, Lin H (2016) *Small* 12:4200
19. Zhou Z, Song J, Nie L, Chen X (2016) *Chem Soc Rev* 45:6597
20. Gnach A, Lipinski T, Bednarkiewicz A, Rybka J, Capobianco JA (2015) *Chem Soc Rev* 44:1561
21. Naccache R, Vetrone F, Mahalingam V, Cuccia LA, Capobianco JA (2009) *Chem Mater* 21:717
22. Zhang KY, Yu Q, Wei H, Liu S, Zhao Q, Huang W (2018) *Chem Rev* 118:1770
23. Deng R, Liu X (2014) *Nat Photonics* 8:10
24. Tu D, Liu L, Ju Q, Liu Y, Zhu H, Li R, Chen X (2011) *Angew Chem Int Ed* 50:6306
25. B unzli J-CG, Eliseeva SV (2011) H nninen P, H rm  H (eds) *Lanthanide luminescence: photophysical, analytical and biological aspects*. Springer, Berlin, pp 1–46
26. Gu B, Zhang Q (2018) *Adv Sci* 5:1700609
27. Wang X, Valiev RR, Ohulchanskyy TY,  gren H, Yang C, Chen G (2017) *Chem Soc Rev* 46:4150
28. Naczynski DJ, Tan MC, Zevon M, Wall B, Kohl J, Kulesa A, Chen S, Roth CM, Riman RE, Moghe PV (2013) *Nat Commun* 4:1–10
29. Dang X, Gu L, Qi J, Correa S, Zhang G, Belcher AM, Hammond PT (2016) *Proc Natl Acad Sci U S A* 113:5179
30. Shi J, Tian F, Lyu J, Yang M (2015) *J Mater Chem B* 3:6989
31. Wang C, Li X, Zhang F (2016) *Analyst* 141:3601
32. Tian G, Ren W, Yan L, Jian S, Gu Z, Zhou L, Jin S, Yin W, Li S, Zhao Y (2013) *Small* 9:1929
33. Chen F, Zhang S, Bu W, Chen Y, Xiao Q, Liu J, Xing H, Zhou L, Peng W, Shi J (2012) *Chem Eur J* 18:7082
34. Tada DB, Vono LLR, Duarte EL, Itri R, Kiyohara PK, Baptista MS, Rossi LM (2007) *Langmuir* 23:8194
35. Chen S, Yu YL, Wang JH (2018) *Anal Chim Acta* 999:13
36. Strobl M, Mayr T, Klimant I, Borisov SM (2017) *Sens Actuators B Chem* 245:972
37. Franc es-Soriano L, Liras M, Kowalczyk A, Bednarkiewicz A, Gonz alez-B ejar M, P erez-Prieto J (2016) *Nanoscale* 8:204
38. Radunz S, Andresen E, W rth C, Koerdt A, Tschiche HR, Resch-Genger U (2019) *Anal Chem* 91:7756
39. Hamblin MR (2018) *Dalton Trans* 47:8571
40. Qian HS, Guo HC, Ho PC-L, Mahendran R, Zhang Y (2009) *Small* 5:2285
41. Gvozdev DA, Lukashev EP, Gorokhov VV, Pashchenko VZ (2019) *Biochemist* 84:911
42. Wencel D, Abel T, McDonagh C (2014) *Anal Chem* 86:15
43. Lakowicz JR (2006) *Principles of fluorescence spectroscopy*. Springer, New York, pp 278–330
44. Mader HS, Wolfbeis OS (2010) *Anal Chem* 82(12):5002
45. Chen Z, Chen H, Hu H, Yu M, Li F, Zhang Q, Zhou Z, Yi T, Huang C (2008) *J Am Chem Soc* 130:3023

46. Lakowicz JR (2006) Principles of fluorescence spectroscopy. Springer, New York, pp 443–476
47. Xu S, Xu S, Zhu Y, Xu W, Zhou P, Zhou C, Dong B, Song H (2014) *Nanoscale* 6:12573
48. Wu Y-X, Zhang X-B, Zhang D-L, Zhang C-C, Li J-B, Wu Y, Song Z-L, Yu R-Q, Tan W (2016) *Anal Chem* 88:1639
49. Näreoja T, Deguchi T, Christ S, Peltomaa R, Prabhakar N, Fazeli E, Perälä N, Rosenholm JM, Arppe R, Soukka T, Schäferling M (2017) *Anal Chem* 89:1501
50. Du S, Hernández-Gil J, Dong H, Zheng X, Lyu G, Bañobre-López M, Gallo J, Sun L, Yan C, Long NJ (2017) *Dalton Trans* 46:13957
51. Kumar B, Murali A, Giri S (2019) *Chem Select* 4:5407
52. Ding C, Cheng S, Zhang C, Xiong Y, Ye M, Xian Y (2019) *Anal Chem* 91:7181
53. Tsai ES, Himmelstoß SF, Wiesholler LM, Hirsch T, Hall EAH (2019) *Analyst* 144:5547
54. Estebanez N, Ferrera-González J, Cortez-Cevallos IA, González-Béjar M, Pérez-Prieto J (2020) *Adv Opt Mater* 8:1902030
55. Sun L-N, Peng H, Stich MIJ, Achatz D, Wolfbeis OS (2009) *Chem Commun* 33:5000
56. Esipova TV, Ye X, Collins JE, Sakadžić S, Mandeville ET, Murray CB, Vinogradov SA, Sakadžić S, Mandeville ET, Murray CB, Vinogradov SA (2012) *Proc Natl Acad Sci* 109:20826
57. Xie L, Qin Y, Chen H-Y (2012) *Anal Chem* 84:1969
58. Wang F, Raval Y, Chen H, Tzeng TRJ, Desjardins JD, Anker JN (2014) *Adv Healthc Mater* 3:197
59. Meier RJ, Simbürger JMB, Soukka T, Schäferling M (2014) *Anal Chem* 86:5535
60. Wang S, Feng J, Song S, Zhang H (2014) *RSC Adv* 4:55897
61. Wang Z, Feng J, Song S, Sun Z, Yao S, Ge X, Pang M, Zhang H (2014) *J Mater Chem C* 2:9004
62. Liu X, Zhang S-QQ, Wei X, Yang T, Chen M-LL, Wang J-HH (2018) *Biosens Bioelectron* 109:150
63. Arppe R, Näreoja T, Nylund S, Mattsson L, Koho S, Rosenholm JM, Soukka T, Schäferling M (2014) *Nanoscale* 6:6837
64. Li H, Dong H, Yu M, Liu C, Li Z, Wei L, Sun LD, Zhang H (2017) *Anal Chem* 89:8863
65. Ma T, Ma Y, Liu S, Zhang L, Yang T, Yang H-RR, Lv W, Yu Q, Xu W, Zhao Q, Huang W (2015) *J Mater Chem C* 3:6616
66. Li C, Zuo J, Zhang L, Chang Y, Zhang Y, Tu L, Liu X, Xue B, Li Q, Zhao H, Zhang H, Kong X (2016) *Sci Rep* 6:38617
67. Zheng J, Wu Y, Xing D, Zhang T (2019) *Nano Res* 12:931
68. Zou X, Liu Y, Zhu X, Chen M, Yao L, Feng W, Li F (2015) *Nanoscale* 7:4105
69. Jesu Raj JG, Quintanilla M, Mahmoud KA, Ng A, Vetrone F, Zourob M (2015) *ACS Appl Mater Interfaces* 7:18257
70. Li H, Wang L (2013) *Analyst* 138:1589
71. Zou X, Zhou X, Cao C, Lu W, Yuan W, Liu Q, Feng W, Li F (2019) *Nanoscale* 11:2959
72. Liu Y, Jiang A, Jia Q, Zhai X, Liu L, Ma L, Zhou J (2018) *Chem Sci* 9:5242
73. Liu X, Ding N, Wang J, Chen H, Chen X, Wang Z, Peng X (2019) *RSC Adv* 9:30917
74. Peng J, Xu W, Teoh CL, Han S, Kim B, Samanta A, Er JC, Wang L, Yuan L, Liu X, Chang YT (2015) *J Am Chem Soc* 137:2336
75. Wu M, Wang X, Wang K, Guo Z (2017) *Talanta* 174:797
76. Wang Y, Shen P, Li C, Wang Y, Liu Z (2012) *Anal Chem* 84:1466
77. Liu L, Zhang H, Wang Z, Song D (2019) *Biosens Bioelectron* 141:111403
78. Li Y, Jia D, Ren W, Shi F, Liu C (2019) *Adv Funct Mater* 1903191:1
79. Ren H, Long Z, Shen X, Zhang Y, Sun J, Ouyang J, Na N (2018) *ACS Appl Mater Interfaces* 10:25621
80. Wu B, Cao Z, Zhang Q, Wang G (2018) *Sens Actuators B Chem* 255:2853
81. Zhang P, Rogelj S, Nguyen K, Wheeler D (2006) *J Am Chem Soc* 128:12410
82. Ye WW, Tsang MK, Liu X, Yang M, Hao J (2014) *Small* 10:2390

83. Zhang C, Yuan Y, Zhang S, Wang Y, Liu Z (2011) *Angew Chem Int Ed* 50:6851
84. Alonso-Cristobal P, Vilela P, El-Sagheer A, Lopez-Cabarcos E, Brown T, Muskens OL, Rubio-Retama J, Kanaras AG (2015) *ACS Appl Mater Interfaces* 7:12422
85. Zhang H, Fang C, Wu S, Duan N, Wang Z (2015) *Anal Biochem* 489:44
86. Hu J, Zhan S, Wu X, Hu S, Wu S, Liu Y (2018) *RSC Adv* 8:21505
87. Deng R, Xie X, Vendrell M, Chang YT, Liu X (2011) *J Am Chem Soc* 133:20168
88. Li H, Lei W, Wu J, Li S, Zhou G, Liu D, Yang X, Wang S, Li Z, Zhang J (2018) *J Mater Chem B* 6:2747
89. Brites CDS, Balabhadra S, Carlos LD (2019) *Adv Opt Mater* 7:1
90. Tsang MK, Bai G, Hao J (2015) *Chem Soc Rev* 44:1585
91. Wang C, Cheng L, Liu Z (2013) *Theranostics* 3:317
92. Dougherty TJ (1993) *Photochem Photobiol* 58:895
93. Ideta R, Tasaka F, Jang W-D, Nishiyama N, Zhang G-D, Harada A, Yanagi Y, Tamaki Y, Aida T, Kataoka K (2005) *Nano Lett* 5:2426
94. Roy I, Ohulchanskyy TY, Pudavar HE, Bergoy EJ, Oseroff AR, Morgan J, Dougherty TJ, Prasad PN (2003) *J Am Chem Soc* 125:7860
95. Samia ACS, Chen X, Burda C (2003) *J Am Chem Soc* 125:15736
96. Voliani V, Signore G, Vittorio O, Faraci P, Luin S, Peréz-Prieto J, Beltram F (2013) *J Mater Chem B* 1:4225
97. García Calavia P, Bruce G, Pérez-García L, Russell DA (2018) *Photochem Photobiol Sci* 17:1534
98. Zhou A, Wei Y, Wu B, Chen Q, Xing D (2012) *Mol Pharm* 9:1580
99. Yuan Q, Wu Y, Wang J, Lu D, Zhao Z, Liu T, Zhang X, Tan W (2013) *Angew Chem Int Ed* 52:13965
100. Khaydukov EV, Mironova KE, Semchishen VA, Generalova AN, Nechaev AV, Khochenkov DA, Stepanova EV, Lebedev OI, Zvyagin AV, Deyev SM, Panchenko VY (2016) *Sci Rep* 6:35103
101. Liu K, Liu X, Zeng Q, Zhang Y, Tu L, Liu T, Kong X, Wang Y, Cao F, Lambrechts SAG, Aalders MCG, Zhang H (2012) *ACS Nano* 6:4054
102. Cui S, Chen H, Zhu H, Tian J, Chi X, Qian Z, Achilefu S, Gu Y (2012) *J Mater Chem* 22:4861
103. Cui S, Yin D, Chen Y, Di Y, Chen H, Ma Y, Achilefu S, Gu Y (2013) *ACS Nano* 7:676
104. Xiao Q, Ji Y, Xiao Z, Zhang Y, Lin H, Wang Q (2013) *Chem Commun* 49:1527
105. Guo H, Qian H, Idris NM, Zhang Y (2010) *Nanomed Nanotechnol Biol Med* 6:486
106. Wang X, Yang CX, Chen JT, Yan XP (2014) *Anal Chem* 86:3263
107. Liu X, Zheng M, Kong X, Zhang Y, Zeng Q, Sun Z, Buma WJ, Zhang H (2013) *Chem Commun* 49:3224
108. Guo Y, Kumar M, Zhang P (2007) *Chem Mater* 19:6071
109. Yang X, Xiao Q, Niu C, Jin N, Ouyang J, Xiao X, He D (2013) *J Mater Chem B* 1:2757
110. Wang C, Tao H, Cheng L, Liu Z (2011) *Biomaterials* 32:6145
111. Il Park Y, Kim HM, Kim JH, Moon KC, Yoo B, Lee KT, Lee N, Choi Y, Park W, Ling D, Na K, Moon WK, Choi SH, Park HS, Yoon S-Y, Suh YD, Lee SH, Hyeon T (2012) *Adv Mater* 24:5755
112. Zhang P, Steelant W, Kumar M, Scholfield M (2007) *J Am Chem Soc* 129:4526
113. Wang Y, Liu K, Liu X, Dohnalová K, Gregorkiewicz T, Kong X, Aalders MCG, Buma WJ, Zhang H (2011) *J Phys Chem Lett* 2:2083
114. Idris NM, Gnanasammandhan MK, Zhang J, Ho PC, Mahendran R, Zhang Y (2012) *Nat Med* 18:1580
115. Xu J, Yang P, Sun M, Bi H, Liu B, Yang D, Gai S, He F, Lin J (2017) *ACS Nano* 11:4133
116. Gražú V, Moros M, Sánchez-Espinel C (2012) In: de la Fuente JM, Grazu V (eds) *Nanobiotechnology*, vol 4. Elsevier, Amsterdam, pp 337–440. <https://www.sciencedirect.com/bookseries/frontiers-of-nanoscience/vol/4/suppl/C>
117. Muthu MS, Leong DT, Mei L, Feng S-S (2014) *Theranostics* 4:660

118. Rai P, Mallidi S, Zheng X, Rahmanzadeh R, Mir Y, Elrington S, Khurshid A, Hasan T (2010) *Adv Drug Deliv Rev* 62:1094
119. Choi KY, Liu G, Lee S, Chen X (2012) *Nanoscale* 4:330
120. Liu G, Swierczewska M, Lee S, Chen X (2010) *Nano Today* 5:524
121. Gao Y, Lim J, Teoh S-H, Xu C (2015) *Chem Soc Rev* 44:6306
122. Gao Y, Li Y (2016) Gold nanostructures for cancer imaging and therapy. In: Dai Z (ed) *Advances in nanotheranostics I: design and fabrication of theranostic nanoparticles*. Springer, Berlin, pp 53–101
123. Santra S, Dutta D, Moudgil BM (2005) *Food Bioprod Process* 83:136
124. Vivero-Escoto JL, Huxford-Phillips RC, Lin W (2012) *Chem Soc Rev* 41:2673
125. Fraczek-Szczypta A (2014) *Mater Sci Eng C* 34:35
126. Tran PA, Zhang L, Webster TJ (2009) *Adv Drug Deliv Rev* 61:1097
127. Ho Y-P, Leong KW (2010) *Nanoscale* 2:60
128. Tao K, Sun K (2020) In: Choi S (ed) *Micro and nano technologies*. Elsevier, Amsterdam, pp 177–204. <https://www.sciencedirect.com/book/9780128178409/photonanotechnology-for-therapeutics-and-imaging>
129. Huang X, Li B, Peng C, Song G, Peng Y, Xiao Z, Liu X, Yang J, Yu L, Hu J (2016) *Nanoscale* 8:1040

Index

A

Aggregation-induced emission (AIE), 196, 218
Ag-zeolite multicomponent system, 86, 90
Anthracene (ANT), 329, 330, 345, 359
Artificial photonic antenna
 blue fluorescence, POPOP, 52
 DMPOPOP, 53
 energy transfer experiments, 57
 FRET, 59
 geometrical constraints, 51
 LSC, 56
 luminescence dynamics, 53, 54
 photonic dye₂, dye₁-ZL antenna, 54–55
 Py⁺ and Ox⁺ dyes, 50–51
 stopcock-driven self-assembling, ZL
 crystals, 56
 three-dye antenna composite, 51, 52
 time-space and spectrally resolved
 characterization, 53
 trapping energy from and injecting energy
 into dye-ZL nano antenna, 57
Artificial photosynthesis system, 201
Azobenzene (AZB/AZ)
 adsorption, 276
 bulk materials, 117
 cationic AZ intercalated in smectites, 278
 cis-isomer, 275, 277
 crystal structures, 120, 121
 derivatives, 276
 DSC measurements, 119
 E and *Z* isomers, 123
 electron density, 120
 elemental and thermogravimetric analyses,
 117
 ethanol, 119

 fingerprint region, 122
 fluorine atoms, 122
 gas-phase loading process, 117
 guest-to-host transmission, 119
 host structure, 117, 118
 IR spectroscopy, 120
 light-induced encapsulation and release,
 119, 120
 light irradiation, 118
 molecular properties, 118
 molecular structures, 276
 N₂ adsorption isotherms, 118, 119
 nitrogen adsorption isotherms, 126
 nonionic, 280
 phenyl rings, 123
 photoactive molecule, 119
 photochromic behavior, 125
 photochromic dye, 117
 photochromic hybrid materials, 122
 photochromic properties, 119
 photochromism, 277–279
 photoisomerization, 275
 photoswitching, 119, 122
 polymers/organic solvents, 122
 PSS, 118
 suppression, *trans*-to *cis*-isomerization,
 279–280
 thin films, 117
 UV/*vis* spectra, 125, 126
 XRPD, 117, 118, 120

B

Bacteria-{Py⁺-ZL} assembly, 60
Basal spacing

- Basal spacing (*cont.*)
 AZC₂N⁺C₂OH-magadiite, 287–288
 azobenzene derivative with fluoroalkyl
 chain, 288, 289
 montmorillonite with cation exchange
 capacity, 287
 NaphAZ, 288
 photoinduced change, 287
 photoisomerization, Py-SP, 288
 1,4-Benzene dicarboxylate (BDC), 171
 Biomolecules, 378, 385–386
 2,2'-Bipyridine, 159, 175, 176
 Bovine serum albumin (BSA), 381
 Breast cancer, 62
 Brønsted acidity, 34, 37, 39
- C**
 Calixarenes (CAs), 326
 Camphorhione (CHT), 336, 337
 Carbon dots, 373
 Carboxylate groups, 160
 Cascade energy transfer
 definition, 232
 types of dyes, 233
 Catalysis
 heterogeneous, 113
 ZL, 3, 15, 63
 Cation exchange, 6, 13, 53, 82, 83, 85, 254
 Cation exchange capacity (CEC), 188, 191
 Cavitands, 327
 Cellular processes, 381
 Cetyltrimethylammonium bromide (CTAB),
 283, 288
 Characterization techniques, Ag-exchanged
 zeolites
 ESR spectroscopy and TGA, 92, 94
 fluorescence spectroscopy, 91
 FT-IR spectroscopy, 88–89
 luminescent silver clusters, 88
 microscopy, 91
 TEM, 91–92
 theoretical modeling, 90
 UV-Vis spectroscopy, 87–88
 X-ray-based techniques, 89–90
 Charge-transfer (CT) band, 116
 Chemical reducing agents, 81
 Chemiluminescence resonance energy transfer
 (CRET), 237
 Chromism behavior, 201
 Chromism effects, 200, 201
 Chromophores, 186, 373, 378–379
 Cinnamic acids (CAs)
 alkyl cinnamates, 357
 dimerization, 358
 and PCA, 356
 photochemistry, 357
 Clays and clay minerals
 bentonite and montmorillonite, 253
 dye-clay systems (*see* Dye-clay hybrid
 systems)
 intermolecular reactions
 Diels-Alder reaction, 284
 [2 + 2] photocycloaddition, 284–287
 and photoinduced phenomena
 (*see* Photoinduced phenomena)
 intramolecular reactions
 AZ (*see* Azobenzene (AZB/AZ))
 DAE, 280–282
 SP, 282–283
 smectites, 253, 254
 surface modification, 256–257
 synthetic clay, 257
 Cluster
 Ag clusters (*see* Silver clusters)
 bimetallic clusters in ZL, 12
 Pt cluster in ZL, 48, 49
 PtCo clusters, 49
See also Metal clusters
 Colloidal systems, 222
 Confined spaces, 83, 121–123, 337
 Confocal fluorescence microscopy images, 17,
 19, 20, 28
 Copolymerization, 22
 Covalently bound dye molecules
 luminophores, 227
 photophysical interaction, 226
 reactive precursors, 226
 Crystalline sponge method, 113
 Crystallization inclusion technique, 115, 161
 Cucurbiturils (CBs), 326, 334, 354, 358, 364
 Cyclodextrins (CDs), 326, 340, 359, 360, 364
 Cyclohexane, 117
- D**
 Deoxyribonucleic acid (DNA), 78–79
 Dexter energy transfer (DET), 208, 209
 Diagnostics, 2, 3, 63, 240
 4',6-Diamidino-2-phenylindole (DAPI), 61
 Diarylethene (DAE), 134–136, 280–282
 Diels-Alder reaction, 284
 Diffusion processes, 115
 Dimethylaminobenzonitrile (DMABN), 339
 Dimethylformamide (DMF), 200
 Dithienylethenes, 136

- DNA-templated luminescent Ag nanoclusters, 78, 79
- Drug delivery, 2, 3, 59, 61, 156, 352
- Dye-clay complexes, 200
- Dye-clay hybrid systems
- aggregation, dyes, 262–266
 - alignment of dyes, linear polarized light, 272–275
 - energy and electron transfer, 270–272
 - excimer formation, 269–270
 - host-guest interactions
 - anthocyanin with SA, 259
 - anthraquinone-2-sulfonic acid, 261
 - carmine and carthamus yellow, 260
 - linearly polarized emission, 273
 - molecular structures, 259
 - photoluminescence properties, 266–269
 - planar structured dyes, 257–258
 - pyronin Y and thiazines, 258
 - retinal Schiff base, 261
 - rhodamine 6G (R6G), 260–261
 - stability of dyes, 259
- Dyes
- aggregation, 262–266
 - dye-ZL composites, 30, 32, 34
 - HR, 42
 - length comparison, 10
 - molecular structures, 259
 - molecules, 223
 - organic, 39
 - Py⁺ and Ox⁺, 13, 50–51
 - TSPCU, 20
- Dye-smectite hybridization, 253, 254
- Dye-ZL nano antenna, 57
- E**
- Electrical conductivity, 107
- Electromagnetic radiation, 108
- Electronic transition, 111
- Electronic transition dipole moment (ETDM), 28, 43–45
- Emission enhancement, 196–198
- Emission of dyes, 186–187
- Energy gap, 111
- Energy transfer (ET), 374
- cascade, 349–351
- Excimers and exciplexes
- ANT, 345
 - cationic guests, 346
 - electronic interaction, 343
 - fluorophore, 346
 - formation, 344
 - octa acid, 345
 - pyrene, 344
 - stilbazoles, 347
- Exciton coupling, 43–48
- Exciton splitting, 45, 46
- Extended X-ray absorption fine structure (EXAFS), 86, 87, 90
- F**
- Fluorenone-ZL composites, 9, 11, 12, 29, 32
- Fluorescein isothiocyanate (FITC), 384
- Fluorescence, 187
- efficiency, 328
 - ET, 329
 - Jablonski diagram, 327–328
 - moderate, 329
 - monomeric units, 330
 - squaraines (SQ), 328
 - trans*-stilbene, 331
- Förster resonance energy transfer (FRET)
- anisotropy methods, 207
 - bioimaging, 241–242
 - catalysis, 242
 - dye molecules, 234–235
 - ED and EA molecules, 210
 - energy migration, 211
 - estimation, 209
 - hosts, electrical properties, 235–237
 - ligands in ship-in-the-bottle synthesis, 9
 - molecules
 - distribution, 219
 - dye concentration, 221
 - dye molecules, 224
 - forced segregation, 223
 - non-radiative energy transfer, 219
 - porphyrins, 224
 - quantitative adsorption, 220
 - two-dimensional systems, 220
- non-radiative energy transfer, 210
- optical probes and sensors, 207
- orientation factor, 211
- pesticides, 238
- polymers, 227–229
- sensing
- applications, 240
 - aptasensor, 240
 - ED chromophores, 239
 - esterase activity, 241
 - hybrid material, 239
 - rhodamine dyes, 238
- in solids and assembled films, 223–234
- stopcock molecules, 16

Förster resonance energy transfer (FRET)
 (*cont.*)
 theoretical basis, 208
 zeolite crystal, 214
 Franck-Condon parameters, 175

G

Gas phase loading processes, 115
 Glutathione (GSH), 385
 Gold clusters, 77
 Gold nanoparticle (AuNP), 385
 Guest molecule, 114
 Guest-ZL composites
 confocal luminescence spectroscopy, 28
 dye-ZL composites, 29–30
 fluorenone-ZL composite, 29, 32–33
 host ZL, 28
 hybrid tb-DXP-ZL composite, 30
 MeAcr⁺-ZL composite, 31–32
 methylviologen cation MV²⁺, 28–29
 non-framework K⁺ configuration, 28
 Ox⁺-ZL composites, 31
 perylene dyes, 30
 powder neutron diffraction, 28
 vibrational spectroscopy, 28

H

Heterogeneous systems, 201
 High-angle annular dark-field scanning
 transmission electron microscopy
 (HAADF-STEM), 92, 93
 Hostasol red (HR), 42, 43, 52, 56, 226
 Host-guest composites
 Brønsted acidity, 39
 diffuse reflectance techniques, 33
 electronic properties, 33
 exciton coupling, organic guests, 43–48
 IMZ⁺ influence on HR-ZL composites, 42,
 43
 luminescence enhancement, 42
 luminescence properties, 33
 NZL composites, 41, 42
 organic guest-ZL composites, 34–37
 oscillator strength, 37–39
 polarized absorption and fluorescence
 properties, 36
 Host-guest inclusion, 325
 Humidity sensors, 95–96
 Hybrid materials, 113, 117, 122, 125, 140,
 147, 148

Hydrophobic interaction, 200
 Hypochlorite, 3, 11, 385

I

Incorporation, composition and resulting effects
 (ICEs), 115, 116
 Inner filter, 380
 Intramolecular electronic transitions, 111
 Ions sensing, 385–386
 Isomerization, 110
 Isorecticular approach, 146
 Isorecticular MOFs (IR-MOFs), 113

L

Langmuir-Blodgett (LB) films, 217, 233–234
 Lanthanide-based resonance energy transfer
 (LRET), 380–381
 Layered inorganic compounds
 graphene/chalcogenides, 216
 hybrid materials, 216
 nanoparticles (*see* Layered nanoparticles)
 nanosheets, 215
 types, 215
 Layered materials
 color tuning, 198–199
 complex of dyes
 CEC, 191
 clay-dye complexes, 191, 192
 electrostatic and hydrophobic
 interactions, 190
 hydrophobic interactions, 190
 methylene blue, 190, 191
 photochemical reaction systems, 190
 photo-functional materials, 190
 porphyrin, 191
 SSA-p-TMPyP complex, 191, 192
 photochemical property, 189–190
 Layered nanoparticles
 cationic R6G, 218
 ED and EA ions, 217
 energy transfer, 217
 hybrid materials, 216
 ionic dyes, 216–217
 molecules and FRET, 219
 organic dyes, 216
 quenching, 218–219
 Layered silicates, 187–189
 LB technique, 256, 257
 Lead (Pb) clusters, 97–99
 Ligand-to-metal charge transfer (LMCT), 88

- Light-induced structural changes, 110
- Limits of detection (LOD), 385
- Linde type A zeolite (LTA)
 - Ag-LTA systems, 87
 - Pb clusters, 97–99
 - silver-exchanged zeolites, 83
- Linde type L zeolite (LTL), 92
- Linker molecules, 113
- Liquid phase epitaxial growth (LPE), 127
- Lower-energy triplet state, 331, 332
- Luminescence
 - dynamics, 53, 54
 - host-guest composites (*see* Host-guest composites)
 - microscopy images, 9
 - quenching, 27
 - Ru²⁺ complex, 24
 - ZL single crystals, 19
- Luminescent polymers, 229
- Luminescent silver clusters in zeolites
 - activation, 83
 - optoelectronic properties, 86–87
 - parameters, 85
 - photophysical properties, 83–85
 - silver-exchanged zeolites, 82–83
 - space-confinement, 83
 - structure-to-properties relationship, 85–86
 - synthesis strategy, 82, 85, 86
- Luminescent silver-zeolite composites
 - advanced matrix codes, 97
 - humidity sensors, 95–96
 - OLED, 96
 - optically encoded microcarriers, 96
 - optoelectronic devices, 96
 - phosphors, lighting applications, 94–95
 - ZEOLED, 97
- Luminescent solar concentrators (LSC), 56
- Luminescent stopcocks, 16

- M**
- Magnetic properties, 107
- Magnetic resonance imaging (MRI), 391
- Magnetism
 - alkylcarboxylate intercalated layered Co and Cu hydroxides, 292
 - anionic photochromic compound, 291
 - LDHs, 291–292
 - photoswitching, 291–292
- Melting processes, 115
- Memory devices, 107
- Merocyanine (MC), 111, 136

- Metal building block (MBB), 156–158, 160, 168, 174
- Metal clusters
 - catalytic activity, 77
 - DNA-templated luminescent Ag nanoclusters, 78–80
 - gold clusters, 77
 - molecule-like energy gaps, 77
 - photoluminescence, 77
 - selective synthesis, 78
 - small metal clusters, 77
 - stabilization protocols, 78
 - thiolates, 77
 - See also* Silver clusters
- Metal organic frameworks (MOFs)
 - applications, 157
 - bathochromic shift, 168
 - catalytic sites, 157
 - crystal structure, 168
 - decay parameters, 170
 - emission decays, 169
 - emission lifetimes, 169
 - energy level diagram, 170
 - extrinsic introduction, 113–114
 - functional porous materials, 156, 157
 - geometry, 156
 - Huang-Rhys parameters, 168
 - intrinsic introduction, 113–114
 - with lanthanides ions, 82
 - photoactive guests, 158–160
 - photophysical properties, 167
 - RuBpy
 - crystallization inclusion technique, 161
 - direct synthetic methods, 166
 - emission decays, 164, 165
 - Huang-Rhys factors, 163
 - isostructural HKUST-1(Zn) MOF, 161
 - molecules, 166
 - parameters, 164, 165
 - photophysical properties, 161
 - physical properties, 162
 - RuBpy@HKUST-1(Zn), 164
 - RuBpy@HUKUST-1(Zn), 166
 - RuBpy@USF2, 164
 - state decay pathways, 164
 - steady-state emission spectra, 161–163
 - USF2, 161
 - water and alcohols, 166
- RWLC-3
 - biexponential function, 172
 - bnb* network, 171
 - cavity environment, 174

- Metal organic frameworks (MOFs) (*cont.*)
 emission decays, 172, 173
 emission lifetimes, 174
 ethanol, 172
 excited state potential surfaces, 172, 173
 honeycomb network, 171
 steady-state emission, 172
- RWLC-5, 174–176
- RWLC-6
 BTE ligands, 177
 carboxylate groups, 177
 cavities, 177
 electron density, 177
 emission decays, 178, 179
 emission lifetimes, 178
 energy level diagram, 179
 Franck-Condon parameters, 177
 kinetic parameters, 178
 steady-state emission, 177, 178
 solvothermal conditions, 167
 steady-state emission spectra, 168
 transition metal polyimines, 159–160
 versatility, 156
 Zn-carboxylate-based polyhedral, 160–161
 Zn₂OH clusters, 167
- Metal-to-ligand charge transfer states (MLCT), 159
- Micro contact printing (mCP), 21, 26
- Molecular building blocks (MBBs), 156
- Molecular orientation and anisotropy
 aggregation, 231
 dye-surface/dye-dye interactions, 230, 231
 photoactive molecular, 232
- Molecules and intermolecular distances
 average distance, 212
 density functions, 213
 ED and EA molecules, 211
 fluorophore molecules, 214
 Poisson distribution, 212
- Monomeric species, 196
- Mordenite zeolite (MOR), 92
- N**
- Nanochannel materials, 2
- Nanohybrids, 373
- Nanomaterials, 387
- Nanoparticles, 385
- Nanosized ZL (NZL) composites, 41, 42
- Naphthalene substituted cationic azobenzene (NaphAZ), 288
- Neutral dye molecules
 aromatic compounds, 226
 energy transfer, 225
 luminescence quantum, 226
 organic, 225
- NIR excitation
 biological window, 374
 biomolecules, 374
 chromophores, 376, 377
 doping composition, 376
 efficiency, 374
 electromagnetic spectrum, 375, 376
 mechanism, 374, 375
 nanoparticles, 373
 organic bioprobes, 373
 photons, 375
 UV-Vis light, 373
- O**
- Octa acid (OA), 326, 333, 337
- Optoelectronic devices, 96
- Organic dyes
 binding, 216
 conventional dilute solutions, 211
 hybrid materials, 208
 and zeolites, 207
- Organic light emitting diode (OLED), 96, 336
- Organic molecules, 113
- Oscillator strength, 37–39
- P**
- Para-terphenyl (pTP), 11
- Patterns, ZL crystals
 arrangements, 26–28
 bio-hybrid micro-robots, optical assembly, 27
 elongated chains, 26
 formation of files, 26
 hexagonal patterns, 26–27
 MCP, 26
 oriented monolayers, 24
 Ru-ph4-TMS stopcock, 26
 self-assembly, 23, 24
 solubilization and self-assembly, 25
 supramolecular organization, 23
- Peptide-protected silver clusters, 80–81
- Perovskites, 99, 157
- Perylene dyes, 30, 34, 36, 47, 226
- 2-Phenylazopyridine (PAP), 124
- Phosphorescence
 cavitands, 332, 333
 CB carbonyl portals, 335
 CB8 encapsulation, 335

- intersystem, 331
 - Jablonski diagram, 332
 - RTP efficiency, 334
- Phosphors, 94–96, 99
- Photoactive guests, 159–160, 325
- Photoactive metal organic frameworks, 158–159
- Photoactive moiety, 108
- Photoactive molecules, 113
- Photoactive nanohybrids, 378–379
- Photochemical properties, 189–190
 - absorption spectra, 192, 193
 - cationic molecule, 194
 - clay nanosheet, 194
 - fluorescence quantum yield, 193
 - intramolecular motion, 193
 - layered silicates, 193
 - porphyrin molecule, 192, 193
 - radiative deactivation process, 193
 - saponite, 193, 194
 - Sb(V)porphyrin derivatives, 194, 195
- Photochemical reactants, 158–159
- Photochemistry, 324
 - alkene, 356
 - cavitands, 327
 - ground-state reactions, 324
 - in heterogeneous systems, 253
 - modes of interactions, 326
 - NpEs, 362, 363
 - physical and chemical processes, 324
 - state energy diagram of molecule, 186
 - thioketone, 336
- Photochromic behavior, 134
- Photochromic dyes, 147, 148
- Photochromic moiety, 114
- Photochromic molecules, 108
- Photochromic properties, 108, 112
- Photochromic unit, 114
- Photochromism, 108–110
- Photocycloadditions (PCA)
 - alkene photochemistry, 356
 - bimolecular, 355
 - non-identical alkenes, 360
 - palladium nanocage, 361
 - polyaromatic hydrocarbons, 359
 - supramolecular approach, 356
 - unimolecular, 355
- Photocyclodimerization, 359
- Photodynamic therapy (PDT), 387–388
- Photo-Fries rearrangement reaction
 - carbon-heteroatom bond, 361
 - decarbonylated products, 362
 - naphthyl benzoates, 362
 - photochemistry, 363
 - radical mechanism, 361
- Photoinduced phenomena
 - basal spacing, 287–289
 - magnetism, photoswitching, 291–292
 - photoinduced adsorption of phenol, 292–294
 - wettability, photoswitching, 289, 290
- Photoluminescence
 - in copper clusters, 77–78
 - 2-cyclohexene-1-one, photocycloaddition, 285
 - silver-exchanged zeolites, 83
 - UCNP emissions, 378
- Photophysics
 - dye-clay hybrid systems (*see* Dye-clay hybrid systems)
 - luminescent silver-zeolite composites, 83–85
 - RuBpy complex, 159, 180
 - stilbene fluorescence, 331
 - thioflavin (TF), 347
 - thione, 338
- Photosensitizer (PS), 387
- Photostationary state (PSS), 114, 118
- Photoswitch, 114
- pH sensing, 381–385
- Physicochemical environment, 114
- Pigments, 2, 3, 63, 207
- Planar aromatic molecules, 199, 200
- Polyelectrolytes, 228–229
- Polyethylene glycol (PEG), 388
- Polymer-encapsulated silver clusters, 81
- Polymers
 - industrial, 228
 - luminescent, 229
 - nanocomposites, 228
 - polyelectrolytes, 228–229
 - type, 227
- Poly(methyl methacrylic acid) (PMAA), 81
- Polyoxoanions, 166
- Polyoxometalates (POMs), 166
- Poly(tetrafluoroethylene) (PTFE), 5, 10
- Porous coordination polymer (PCP), 117
- Porous interpenetrated zirconium-organic frameworks (PIZOFs), 113
- Porphyrin macrocycles, 158–159
- Probability density functions (PDFs), 213
- Pyridine-substituted spiropyran (Py-SP), 283, 288

Q

Quantum dots (QDs), 373
 Quartz crystal microbalance (QCM), 130
 Quenching, 218–219

R

Rare earth, 10, 33, 37, 42
 Reactive oxygen species (ROS), 387
 Resonance energy transfer, 208
 Rho zeolite (RHO), 88, 92
 Ruthenium(II) polyimines, *see* Metal organic frameworks (MOFs)

S

Saponite surface, 199
 Secondary building unit (SBU), 112
 Self-assembly, ZL crystals, 23–25
 Sensing, 2, 3, 42, 59, 63
 Sensor applications, 158–159, 230
 Sensor materials, 107
 Ship-in-a-bottle strategy
 lanthanide complexes, 13
 ligands, organolanthanide complexes, 9
 Pb clusters, 97
 preparation of composites, 14
 rare earth complexes, 10
 Res-ZL composites, 15
 sequential synthesis, 13
 space-confinement, silver clusters, 83
 zeolite A monolayer, 24
 Silver clusters
 Ag-carboxylate nanoclusters, 80
 characterization (*see* Characterization techniques, Ag-exchanged zeolites)
 DNA-templated, 78–80
 in glassy substrates, 81–82
 mass-selected oligoatomic, 78
 MOFs, 82
 peptide-protected, 80–81
 photoluminescence, 77
 physicochemical properties, 87
 polymer-encapsulated, 81
 stabilization protocols, 78
 Silver-exchanged zeolites, 82–83
 Silver-zeolite composite-based LED (ZEOLED), 97
 Singlet oxygen
 Jablonski diagram, 352
 molecular orbital energy diagram, 351
 photosensitizer, 352
 TB-B, 353

Singlet oxygen generation (SOG), 353, 354
 Smart materials, 107, 146
 Smectites
 absorption spectra, methylene blue, 264
 clay minerals, 253
 dye-smectite hybridization, 254
 layered alkali silicates, 255
 molecular structures, cationic azobenzenes, 278
 MV2⁺ co-adsorbed, 270
 nanoporous pillared, 255
 organic cationic dyes, 255
 surface modification, 255, 256
 synthetic analogs, 254
 Sodalite zeolite (SOD), 98
 Solid solvents, 147
 Solid-state switching, 123, 124
 Solute-solvent interactions, 111
 Solvatochromic properties, 112
 Solvatochromism, 110–112, 136
 Spirooxazines, 110, 112
 bimolecular processes, 142
 dye molecules, 142
 IR spectra, 145
 isomerization, 145
 photochromic and solvatochromic response, 144
 photographic images, 144
 SP-Nitro@MOF composites, 145
 SP-O@MOF-5, 145–146
 UV light irradiation, 142
 XPS measurements, 144
 Spiropyran (SP), 108, 110, 136–138, 282–283
 Stilbenes, 110, 116–117, 134
 Stopcock principle, 15–18
 Sub-nanometer silver clusters, 77, 82, 87
 Supramolecular photochemistry, 324
 Supramolecular system, 199
 Surface-fixation induced emission (S-FIE), 196–198
 Switch@MOF systems, 146
 Synthetic clays, 257
 Synthetic procedures, 147

T

Theragnosis
 cancer diagnosis, 390
 cutting-edge nanotheranostic agents, 388
 infrared thermal imaging, 390
 innocuous tracking, 390, 391
 in vitro assays, 390
 MRI and CT, 391

- nanohybrid surface, 390
 - nanoparticles, 388
 - photothermal therapy, 390
 - simultaneous imaging, 388
 - targeted therapy, 388
 - Thermal deactivation, 187
 - Thermal organic reactions, 324
 - Thermogravimetric analysis (TGA), 87, 94, 117
 - Thin MOF films
 - approach, 113
 - 1,4-butanediol, 130, 132
 - chromophore, 140
 - conductance photoswitching, 142
 - conduction properties, 142
 - controlled thermal desorption, 132, 133
 - dipole moments, 130
 - E*-AZB@HKUST-1, 127
 - electronic coupling, 142
 - fluorescence spectroscopic measurements, 139
 - hole injection, 142
 - homogenous morphology, 141
 - host-guest interactions, 140
 - hybrid, 127
 - in situ layer-by-layer growth, 127
 - IR spectroscopy, 128, 129, 134, 142
 - JUC-120, 138
 - light-induced conversion processes, 138
 - N₂ sorption isotherms, 131
 - photochromic dye, 138
 - photochromic properties, 127
 - photochromism, 139, 140
 - photorelaxation, 139
 - photostability, 130
 - photoswitching, 130
 - reversible gas permeation, 132, 133
 - spiropyrans, 141
 - SP-Nitro@UiO-67, 142
 - SP-to-MC conversion, 140
 - tF*-AZB, 130
 - UV light irradiation, 139
 - UV/vis spectra, 127–129
 - XPS, 128, 129
 - XRPD measurements, 138, 141
 - Thiocarbonyl compounds, 336
 - Thioflavin (TF), 340, 347
 - benzothiazole dye, 349
 - excimer emission, 348
 - titration of solution, 348
 - Thioketone photochemistry, 336, 337
 - Time-of-flight secondary ion mass spectrometry (ToF-SIMS), 128
 - Transition metal polyimines, 159–160
 - Transition probability, 186, 187
 - Transmission electron microscopy (TEM), 91–92
 - Triethoxysilylated coumarin dye (TSPCU), 20
 - 1,3,5-Tris(4-carboxyphenyl)benzene (TCPB), 167
 - 1,3,5-Tris[(*N*-pyridinium)aniline-4-yl]-benzene (TPAB), 196, 197
 - Twisted-intramolecular charge transfer (TICT)
 - behavior, 339
 - biphenyl/bipyridinium, 343
 - chromophores, 340
 - complexation processes, 342
 - destabilization, 341
 - DMABN, 339
 - DNC, 340
 - emission, 339
 - geometry, 338
 - locally excited (LE) state, 339
 - stilbazole ST1, 341
- U**
- Upconversion nanoparticles (UCNPs)
 - applications, 373
 - chromophores, 373, 378–379
 - luminescence, 373
 - PDT, 387–388
 - photoactive nanohybrids, 378–379
 - preparation methods, 373
 - properties (*see* NIR excitation)
 - sensing
 - biomolecules, 385–386
 - fluorescence sensors, 379
 - inner filter, 380
 - LRET, 380–381
 - microscale cellular level, 379
 - pH, 381–385
 - photoactive species, 379
 - photophysical properties, 379
 - radiometric/time-resolved measurements, 379
 - synthetic protocols, 373
 - tunable long-lifetime emission, 378
 - UV-Vis irradiation, 81
- V**
- Van der Waals model, 24, 27, 46
- W**
- Water-resistant dye-ZL composite, 11
 - Wettability, 289, 290
 - White-light-emitting diodes (WLEDs), 99

X

- X-ray absorption fine structure (XAFS), 80, 89
- X-ray diffraction (XRD), 89, 93, 127, 128, 139, 200
- X-ray-excited optical luminescence-EXFAS (XEOL-EXAFS), 86, 90
- X-ray powder diffraction, 120

Z

Zeolite L (ZL)

- anionic framework, 3
- in breast cancer cells, 62
- catalysis, 3, 15, 63
- as a catalyst, 48–49
- cationic guests, 7
- composites, 2
- fluorenone structure, 12
- guest-ZL composite, 6–7, 9
- hypochlorite, 3–4
- internalization, 62
- length and diameter, 4
- molecules in the channels, 44
- morphology and structure, 5
- neutral guests, 8
- properties, 4
- Pt cluster, 48, 49
- as synthetic material, 4
- test tube experiment, 3

Zeolites

- Ag-LTA and Ag-FAU, 86
- LTA, 83, 87, 97–99
- luminescent silver clusters
(*see* Luminescent silver clusters in zeolites)
- silver-exchanged, 82–83
- ZL (*see* Zeolite L (ZL))
- Zeolite Socony Mobil-5 (ZSM-5), 91
- ZL crystal
 - biological and biomedical applications, 59–63
 - chemical properties, base and coat, 16
 - connolly surface representations, 21
 - FMOc-APMS, 19
 - functionalization, whole surface, 22–23
 - luminescent stopcocks, 16
 - patterns (*see* Patterns, ZL crystals)
 - robust ZL monolayers, 58
 - solubilization and self-assembly, 25
 - stopcock principle, 15–18
 - TCPCU insertion, 20
- ZL synthesis
 - confocal fluorescence microscopy images, 17, 19, 20
 - hexagonal ZL crystals, 6
 - size and shape distribution, 6
 - supramolecular organization, 6
 - technical grade ZL, 5
 - variations, 6